High-precision tephrostratigraphy: Tracking the time-varying eruption pulse of Mt. Taranaki, North Island, New Zealand

A thesis presented in partial fulfilment of the requirements for the degree of

Doctor of Philosophy

in

Earth Science

at Massey University, Palmerston North, New Zealand.

Magret Damaschke

2017

Mt. Taranaki and the Ahukawakawa Swamp viewed from the Pouakai Tarns, North Island, New Zealand. (December 2014)

Abstract

In this research it was proposed that a more robust record of volcanic activity for Mt. Taranaki (New Zealand) could be derived from tephras (pyroclastic fall deposits) within cores from several lakes and peatlands across a 120^{o} arc, NE-SE of the volcano, covering a range of prevailing down-wind directions. These data were integrated with previous tephrochronology studies to construct one of the longest and most complete volcanic eruption history records ever developed for an andesitic stratovolcano. Using 44 new radiocarbon dates, electron microprobe analysis of glass shard and titanomagnetite chemical composition, along with whole-rock chemistry, a chrono- and chemostratigraphy was established. The new record identifies at least 272 tephra-producing eruptions over the last 30 cal ka BP. Six chemo-stratigraphic groups were identified: A (0.5 – 3 cal ka BP), B (3 – 4 cal ka BP), C (4 – 9.5 cal ka BP), D (9.5 – 14 cal ka BP), E (14 – 17.5 cal ka BP), and F (23.5 – 30 cal ka BP). These were used to resolve previous stratigraphic uncertainties at upper-flank (proximal) and ring-plain (medial) sites. Several well-known "marker tephras" are now recognized as being ~2000 years older than previously determined (e.g., Waipuku, Tariki, and Mangatoki Tephra units) with the prominent Korito Tephra stratigraphically positioned above the Taupo-derived Stent Tephra. Further, new markers were identified, including the Kokowai Tephra unit (~4.7 cal ka BP), at a beach-cliff exposure, 40-km north-east of the volcano. Once age-models were established for each tephra, units were matched between sites using statistical methods. Initial statistical integration showed that the immediate past high-resolution tephrochronological record suffered from a distinctive "old-carbon" effect on its ages (Lake Rotokare). This had biased the most recent probabilistic forecasting and generated artificially high probability estimates (52-59% eruption chance over the next 50 years). Once the Rotokare record was excluded and chemostratigraphy constraints were applied, a reliable multi-site tephra record could be built only for the last ~14 ka BP. The new data confirms a highly skewed distribution of mainly (98% of cases) short intervals between eruptions (mode of ~9 years and average interval ~65 years). Long intervals (up to 580 years) as seen in earlier records were reduced to 2% of the record, but can now be considered real, rather than missing data.

The new data confirm a cyclic pattern of varying eruption frequency (with a five-fold range in annual frequency) on a period of ~1000-1500 years. The new time-varying frequency estimates suggest a lower probability for a new eruption at Mt. Taranaki over the next 50 years of 33-42%. The newly established chemostratigraphy was further used to investigate time-related compositional changes. Whole-lapilli analyses highlighted that a specific very evolved Ca-rich and Fe-poor composition was only found within the easterly and south-easterly depositional sites. This was explained by eruption of a stratified magma reservoir, which holds greater modal proportions of plagioclase and lower proportions of pyroxene within low-density, gas-rich upper conduit regions. During the most explosive phases of eruptions, when plumes reach the stratospheric jet-stream, the lowest-density pumice is thus dispersed by high-level stable westerly winds. Further, two distinct evolutional trends were seen in the long and new tephrochronological record; from 17.5 to 3 cal ka BP and <3 cal ka BP; with whole-lapilli, glass, and titanomagnetite compositions overall evolving over time. The former compositional trend indicates a crystallising and cooling magma source in the deep crust, with multiple, spatially separated magma source regions forming, each generating magmas (i.e., magma batches) with unique titanomagnetite compositions. This trend is interrupted by a distinct shift towards less-evolved compositions and the initiation of a second parasitic vent (Fanthams Peak at the southern flank of Mt. Taranaki).

Acknowledgements

Firstly, I would like to thank my chief supervisor, Prof. Shane J. Cronin (Auckland University) for giving me the opportunity of this PhD and for believing in me in the first place. He guided me throughout this thesis with constructive discussions and feedbacks as well as helping me receive a Massey Doctoral scholarship and the George Mason Charitable Trust scholarship. I also benefited greatly from his extraordinary skills in writing and presenting research papers.

I also wish to thank my co-supervisors Dr. Katherine A. Holt (Massey University), Assoc. Prof. Georg F. Zellmer (Massey University), and Prof. Mark S. Bebbington (Massey University) for the time, support and sheer enthusiasm that you have provided for this project and me. In particular, Dr. Holt is sincerely thanked for her assistance in the field and helpful introduction to various sediment coring procedures. I particularly thank Prof. Bebbington for his expertise and knowledge in the (to me unknown) field of statistics and Assoc. Prof. Zellmer for his guidance regarding my understanding of geochemical processes.

This thesis would not have been possible without the great support and encouragement of two very important people, who have become dearest friends over the past years:
Dr. Clel Wallace (Massey University) – I find it extremely difficult to express my gratitude and appreciation for all that you have done for me during my PhD years. You have not just provided me with knowledge, fruitful discussions, constructive criticism, spelling and grammar checks, excellent reviews, and lots of motivation related to my research, but also welcomed me into your lovely family. I will always cherish the evenings full of good food, plenty of wine and wonderful companions. Please deliver a special thanks to Nicky, and give Topsy & Misty a big hug.
AND
Rafael Torres-Orozco (Massey University) – I would like to thank you for being my best colleague and incognito-supervisor over the course of my PhD. You taught me a lot, professionally and personally, inspired me with new ideas, provided me with a good

deal of patience and time, and always believed in me. Your enthusiasm for volcanology and Mt. Taranaki has had me enthralled. I thank you so much for the numerous times we tried to unravel this monstrosity of a volcano together, climbed his steep flanks not just for work, and occupied long overtime hours accompanied with productive discussions and a high-level coffee consumption.

Special thanks also goes to Mr. David Feek (Massey University), who contributed greatly to many successful coring campaigns by providing his technical skills and excellent sense of humour; and to Dr. Anja Moebis (Massey University) and Mr. Peter Lewis (Massey University) for their helpful instructions and support during laboratory and analytical works. I would also like to thank Dr. Alan Palmer (Massey University) for his field assistance, and Assoc. Prof. Robert B. Stewart (Massey University) for his fruitful discussions regarding the petrology and geochemistry of Mt. Taranaki eruptives as well as helpful introduction and assistance in X-ray powder diffraction (XRD) analysis. I am also very grateful to Prof. Vince E. Neall (Massey University), who's unlimited enthusiasm for, and knowledge about, Mt. Taranaki over so many years inspired and encouraged me throughout my own PhD years. He is also thanked for providing me with previous field samples, notes and ideas, which contributed greatly to my research. I also wish to thank Assoc. Prof. Alan Hogg and Dr. Fiona Petchey (Waikato University) for radiocarbon dating multiple sediment samples during my research, and for your fast response and accuracy.

I want to acknowledge all of those who have assisted me during my research: Thank you Dr. Kate Arentsen (Massey University) for organising hotel and car bookings during my field trips and being able to help me with any administrative concerns. I also would like to thank Assoc. Prof. Ian Smith (Auckland University) for his help and time during the evaluation and interpretation of the geochemical analyses; in particular of the laser ablation–inductively coupled plasma–mass spectrometry (LA-ICP-MS) titanomagnetite data. Mr. Ian Furkert and Mr. Bob Toes (Massey University) are thanked for their assistance within the laboratories, and their reassuring kindness although I almost set the lab on fire once. I am also very grateful to Ms. Julie Palmer (Massey University) and her family, who gave me great support and the opportunity to follow my passion for horse riding. I am grateful to the whole Volcanic Risk Solution

department (Massey University), including Assoc. Prof. Jonathan Procter, Assoc. Prof. Karoly Nemeth, Dr. Gert Lube and colleagues/friends Ermanno Brosch, Marija Voloschina, Kevin Kreutz, Gaby Gomez, Gabor Kereszturi, Szabolcs Kosik for their support and encouragement. I also wish to thank Prof. David J. Lowe (Waikato University), Dr. Alastair Clement (Massey University), and Dr. Victoria C. Smith (Oxford University) for examining my thesis and their helpful comments and feedback.

Many thanks also go to Taranaki landowners Steve Styger, Gary Comarer, Trevor Jane, John & Jack Newsome, Raymond Foster, Brian Rowlands, Alison Rumball, and the Tamblin family for allowing access to their properties for sampling and their unreserved trust in this project.

And lastly, but most importantly, I owe everything to my friends and family back in Germany. My sincere thanks go to my parents, grandparents and my brother, who always supported me in everything I pursued. Your love, care, and understanding is priceless. I could not have done this without you. To my dearest friends, Yvonne Baumann and Julia Pauli, thank you so much for your moral support and unconditional friendship.

This thesis is dedicated to my grandpa, who unexpectedly past away during my stay here in New Zealand. I love you Opi.

Table of contents

List of tables

List of figures

Chapter 1

Introduction

This chapter aims to point out the general objectives of this research and provides a literature review of the geological background and previous tephrochronological research at Mt. Taranaki. It also introduces the study sites examined in this research.

1.1 Introduction

Tephrochronology has been a key tool for establishing eruptive records from explosive volcanoes since around the 1960's. Physical, mineralogical and geochemical characteristics of tephra deposits often produce a unique 'fingerprint', allowing correlation, as well providing information on eruption onset, magnitude and style. This information is particularly important at re-awakening volcanoes, where volcanic activity occurs with variable eruption frequency and manifests with a broad range of eruption behaviour and consequent hazard. In most subduction-zone volcanoes, long periods of quiescence are generally followed by an abrupt awakening, sometimes of catastrophic scale (e.g., the 1991 eruption of Mt. Pinatubo in the Philippines; e.g., Dartevelle et al., 2002; Gaillard, 2006, or the eruption of Soufrière Hills Volcano, Montserrat during 1995-1999; e.g., Druitt and Kokelaar, 2002; Baxter et al., 2005). Through applying the principle 'the past is the key to the future', studies of long, continuous tephra records can contribute to understanding and data to quantify (probabilistically) the likely future volcanic hazard from a given volcano. This study applies this concept at the andesitic stratovolcano of Mt. Taranaki (also known as Mt. Egmont), western North Island, New Zealand.

The Taranaki region hosts 2.6% of New Zealand's total population (Statistics New Zealand, 2014) and is home to 17% of New Zealand's dairy farms, with the largest

dairy factory in the Southern Hemisphere (Fonterra, 2014). It is also rich in hydrocarbon resources; hence, the majority of the oil and gas industry operates out of the Taranaki region (New Zealand Oil and Gas Industry, 2014). Of the 18 natural gas fields in the region, 13 are located onshore in proximity to Mt. Taranaki. Sheep and beef farming, concentrated in the inland hill country, has an important role in the regional economy. Approximately 880 sheep and beef farms in Taranaki stock approximately 679 000 sheep and 131 000 beef cattle. Pig and poultry farms are also common (Taranaki Regional Council, 2014). Overall, agriculture and associated food processing industries in the Taranaki region contribute almost 20% to regional Gross Domestic Product (GDP) (Statistics New Zealand, 2014). Forestry, fishing, mining, cropping, manufacturing, and tourism are other relevant economic activities in the Taranaki region.

Mt. Taranaki, situated in the heart of the Taranaki region, poses significant hazards to these industries, and the communities and infrastructure that service them. Even a minor eruption would have a devastating impact on the environment and subsequent economy (e.g., water poisoning, loss of crops and livestock, power failure, feeding/moving of stock, etc.). In particular, airborne ash, lahars and floods represent a major threat. The current dormant state of Mt. Taranaki for more than a century (Druce, 1966; Platz et al., 2012) contributes to an even higher vulnerability, since people often forget or discount the potential devastation of reawakening volcanoes (e.g., Pinatubo was dormant for 650 years prior to the climactic 1991 eruption; Dartevelle et al., 2002; Gaillard, 2006). Previous studies of the volcanic eruption history of Mt. Taranaki have shown that the volcano was highly active over the last ~170 ka (Alloway et al., 2005; Zernack et al., 2011a), and it has experienced several cone-building and collapse episodes. Eruptions range between effusive events to highly explosive Plinian-scale eruptions, as evidenced by several distal tephra beds recognised in Auckland lakes, about 270 km from the source (Shane, 2005; Molloy et al., 2009). Sub-Plinian to Plinian eruptions commonly produce high eruption columns able to reach the stratosphere and covering large areas with ash falls. The hazard posed from these highly explosive eruptions is documented from previous explosive eruptions of several highly active volcanoes around the world (e.g., 1913 eruption of Volcán de Colima, Saucedo et al., 2010; 1902 eruption of Mt. Pelee, De Boer et al., 2002; 2010 eruption of Mt. Merapi, Jousset et al., 2010).

Therefore it is very important to understand past eruption behaviours of these unpredictable andesitic stratovolcanoes so as to quantify (probabilistically) future volcanic hazard.

1.2 Objectives

Previous tephrochronological work at Mt. Taranaki has necessarily focused on short, patchy records, due to the limitations of geological preservation and exposure (e.g., Neall, 1972; Franks, 1984; Franks et al., 1991; Alloway et al., 1995). Highly detailed volcanic eruption records, of which only a handful are currently available for Mt. Taranaki (e.g., Turner et al., 2008a, 2009, 2011a, Zernack et al., 2011a; Platz et al., 2012), provide an unprecedented insight into the temporal dynamics of the volcano and its magmatic system. However, according to Wang and Bebbington et al. (2012), who tested the Holocene volcanic eruption record of Turner et al. (2008a) for completeness, estimated that the catalogue of explosive eruptions is only 86% complete. Hence, the principle aim of this study was to improve the completeness of, and extend the length of, the eruption history record of Mt. Taranaki. A well defined eruption history record subsequently aimed at refining hazard assessments and understanding the underlying volcanic and magmatic processes. The objectives to meet these aims are listed below.

The primary objective of the present study was to establish a new, high-precision tephrostratigraphy covering the Late Pleistocene to Holocene, for the Taranaki region. Taking advantage of excellent climatic and preservation conditions, several long-cores from lakes and peatlands located within the dominant dispersal axis of major tephra falls from Mt. Taranaki were collected and examined to build a full, composite record of large- and small-scale eruptions. These data are integrated with the existing tephra records of Turner (2008), leading to a reconstruction of a more comprehensive historical eruption record.

A further objective of this project was to investigate chemical and physical properties of the tephras, and their minerals, to develop parameters that will enable identification of the tephras and correlation between coring sites. These correlations were reinforced by

radiocarbon age determinations of selected samples and associated statistical-matching procedures. Once these parameters have been established, correlation between the lake and peatland tephra records to the proximal and medial tephrostratigraphy were sought, thus adding fundamental confidence in the regional tephrochronology and new degree of resolution to the eruption history of Mt. Taranaki.

The third objective of this project was to apply the new, long-period, high-resolution eruption record to interpreting the magmatic and volcanic processes operating at andesitic stratovolcanoes (e.g., changes in magma evolution, systematic and/or one-off changes in frequency, magnitude, and/or geochemical composition; Bryant et al., 2003; Shane, 2005; Turner et al., 2008a, 2008b, 2011b; Moebis et al., 2011; Plunkett et al., 2015). The eruptive mechanism and magma dynamics generating andesitic tephras are still poorly understood, attributable to a lack in historical records and complex emplacement mechanisms that may vary between volcanoes and over time (e.g., Price et al., 2005; Platz et al., 2007a; Pardo et al., 2014). Detailed geochemical observations of tephra layers were used to better understand magma genesis and evolution of andesitic volcanic systems.

The fourth objective of this study was to develop a new hazard evaluation for andesitic ash-fall in the North Island of New Zealand. Many urban and rural areas are potentially affected by a volcanic eruption of Mt. Taranaki, from Hawke's Bay in the NW (Lowe et al., 1999, 2013) to the Waikato area (Hamilton) in the NE (Lowe, 1988a) to Auckland in the N (Sandiford et al., 2001; Shane, 2005; Molloy et al., 2009) to Palmerston North in the SE (Wallace, 1987). In particular, ash fall events may cause enormous impact on people, agriculture, transportation, water supplies, wastewater and other economic activities (e.g., Johnston et al., 2000; Stewart et al., 2006; Bebbington et al., 2008). Therefore it is of great relevance to quantify both the frequency and magnitude of hazard posed by Mt. Taranaki. More precise time-controlled eruption records provide the key to strengthening probabilistic hazard forecasting. Overall, the study of andesitic tephra is of great interest worldwide, since these eruptions are more frequent than silicic events and thus more likely to be a hazard encountered around the world up to several times a year (Jenkins et al., 2012; Whelley et al., 2015).

1.3 Background geology

1.3.1 Regional setting

The present geological and tectonic setting of New Zealand is controlled by its position astride the convergent Pacific/Indo-Australian Plate boundary, extending from the Tonga-Kermadec Trench to the Puysegur Trench (Fig. 1.1). Over a relatively short distance, the complex plate tectonic environment changes significantly along that boundary through New Zealand. While the South Island of New Zealand is occupied by a strike-slip fault system, including the Marlborough faults and the Alpine Fault (e.g., Van Dissen and Yeats, 1991; Holt and Haines, 1995; Norris and Cooper, 2007; Sutherland et al., 2012), oblique subduction of the Pacific Plate beneath the Indo-Australian Plate occurs at the Hikurangi Trench east of the North Island (e.g., Karig, 1970; DeMets et al., 1994; Henrys et al., 2003; Nicol et al., 2007; Wallace et al., 2012) (Fig. 1.1). The Hikurangi Trench defines the southernmost extension of the Tonga-Kermadec Trench, where converging plate motion decrease from c. 70 mm yr^{-1} to c. 40 mm yr^{-1} from N to S (e.g., Walcott, 1978; DeMets et al., 1990, 1994; Parson & Wright 1996; Beavan et al., 2002). At c. 280 km from the Hikurangi Trench, the Wadati-Benioff Zone dips at a steep angle of approximately 50°-70° NE, to a depth of 100 km and continues to a maximum depth of 300 km beneath the south-eastern part of the Taranaki region (Boddington et al., 2004; Reyners et al., 2006, 2011; Fig. 1.2). Along the Hikurangi Trench the subducted oceanic crust of the Pacific Plate has variable crustal thicknesses (i.e., Hikurangi Plateau), which causes the North Island to rotate clockwise at 0.5-3.8 deg Myr^{-1} relative to the Indo-Australian Plate (e.g., Wallace et al., 2004; Rowan et al., 2005; Nicol et al., 2007). Hence, subduction becomes increasingly more oblique to the south, forming a complex subduction-zone that is known as the Taupo-Hikurangi arc-trench system (e.g., Cole and Lewis, 1981; Cole, 1990; Wallace et al., 2012).

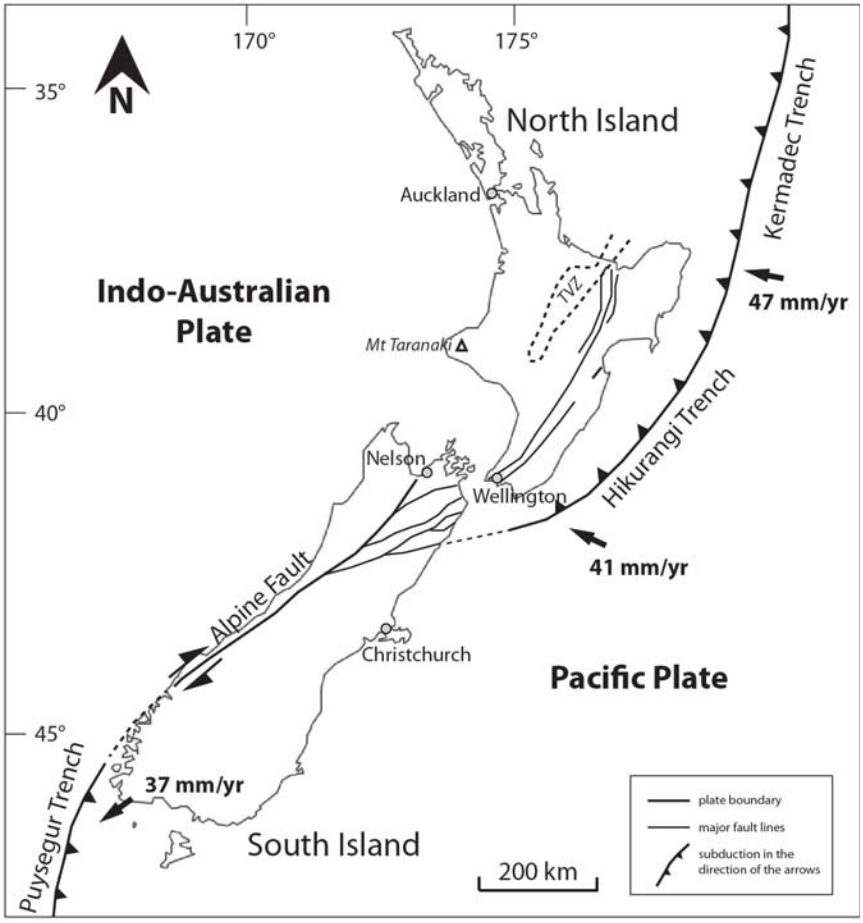

Figure 1. 1 *Plate tectonic setting of New Zealand (modified after Chanier et al., 1999). Arrows indicate plate motion of the Pacific Plate relative to the Indo-Australian Plate with rates adopted from DeMets et al. (1994) and Beavan et al. (2002). The Taupo Volcanic Zone (TVZ) and Mt. Taranaki are also shown.*

The Taupo-Hikurangi arc-trench system is characterised by volcanism in the Taupo Volcanic Zone (TVZ) (Fig. 1.1), which in turn encompasses (1) an active volcanic arc comprising andesite-dacite volcanoes scattering from White Island to the Tongariro Volcanic Centre (TgVC), and (2) an extending back-arc basin in the central part of the North Island (e.g., Cole, 1990; Wilson et al., 1995; Darby et al., 2000; Wilson et al., 2009; Rowland et al., 2010). The central TVZ is divided into four main volcanic centres: Taupo-, Maroa-, Okataina- and Rotorua Volcanic Centres associated with mainly rhyolitic volcanism but with minor amounts of high-Al basalt and dacite (Wilson et al., 1984, 1995 and references therein). A total volume of around 20,000 km^3 of rhyolitic volcanic material, mainly caldera-forming ignimbrites, have been erupted

over 1.6 Myr in the central volcanic region of the TVZ (Houghton et al., 1995; Allan et al., 2008). Volcanic activity in the TVZ was initiated by andesitic, calc-alkaline volcanism (c. 2 Myr ago) that built the most-active stratovolcanoes in the North Island. This andesitic volcanism was joined by rhyolitic volcanism c. 0.4 Myr later (Houghton et al., 1995; Wilson et al., 1995, Graham et al., 1995). The most westerly expression of subduction-related volcanism in the North Island is in the Taranaki region (Hatherton, 1969) (Fig. 1.1).

1.3.2 Taranaki setting

A thumb-shaped peninsula on the western side of the North Island of New Zealand, known as the Taranaki region, hosts a northwest-southeast trending volcanic lineament (Taranaki Volcanic Lineament; e.g., Neall, 1979; Neall et al., 1986; Neall, 2003), and a thick succession of Late Cretaceous to Pleistocene sedimentary rocks that accumulated in the Taranaki graben, which is part of the Taranaki basin (e.g., Pilaar and Wakefield, 1978; Knox, 1982; Palmer and Bulte, 1991; Muir et al., 2000; Gaylord and Neall, 2012; Reilly et al., 2015) (Fig. 1.2).

The Taranaki Volcanic Lineament consists of four andesitic volcanoes: (1) remnants of an older volcanic complex, comprising the Sugar Loaf Islands and Paritutu (1.7 Ma; Neall, 1979) north of the town of New Plymouth (Grant-Taylor, 1964), (2) the Kaitake Volcano (0.57 Ma; Neall, 1979), (3) the Pouakai Volcano (0.25 Ma; Neall, 1979) and (4) Mt. Taranaki (also known as Egmont Volcano; 0.13 Ma; Neall et al., 1986). Volcanic activity migrated along the defined volcanic lineament in a south-east direction, which is nearly orthogonal to the trend of the TVZ. The position of the Sugar Loaf Islands and Paritutu lies slightly to the northeast compared to the principal volcanic line. Another similar volcanic lineament, known as the Alexandra Volcanic Lineament, is found 160 km north of Mt. Taranaki (Fig. 1.2). The emplacement of Alexandra Volcanics is dated between 1.6 and 2.74 Ma (Briggs et al., 1989). Hence, the oldest erupted material of Mt. Taranaki overlaps in age with the youngest eruptives of the Alexandra Volcanics (Price et al., 1992). Volcanic debris form a broad ring plain around the modern cone of Mt. Taranaki and its deeply eroded older volcanic neighbours (Fig. 1.3). The ring plain, of approximately 1000 km^2, is composed of

massive volcanic debris avalanches, lahars and fluvial deposits (Neall et al., 1986; Neall and Alloway, 2004; Alloway et al., 2005). Lava flows are mainly found around the volcanic cones (Stewart et al., 1996; Platz et al., 2007a, 2012). A detailed and most recently described stratigraphic record of debris avalanches is given by Zernack et al. (2011a).

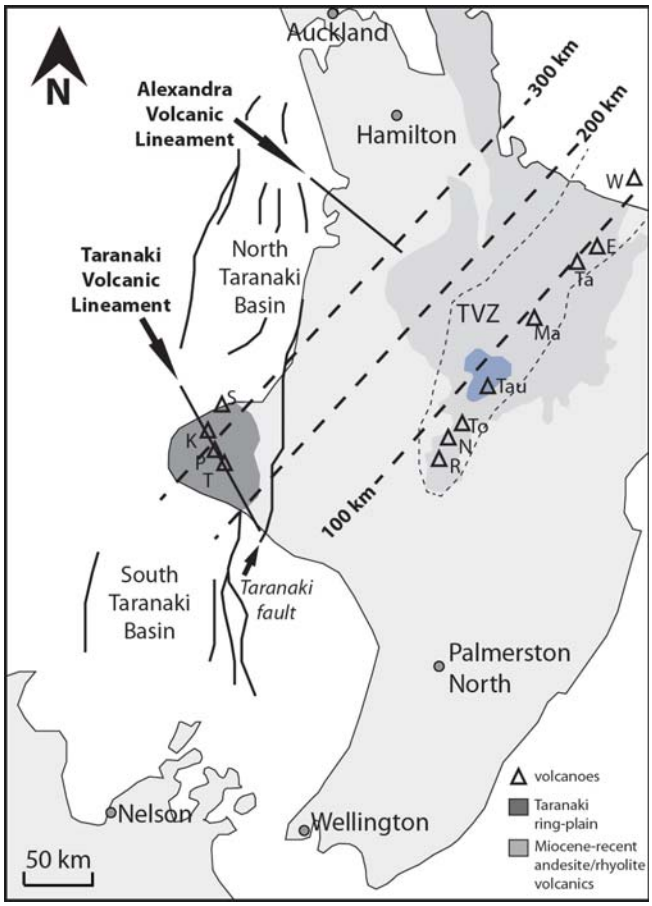

Figure 1. 2 *Tectonic and volcanological setting of the North Island of New Zealand (modified after Price et al., 1999). The Taranaki Volcanic Lineament encompassing Mt. Taranaki (T), Pouakai Volcano (P), Kaitake Volcano (K), and the Sugar Loaf Islands and Paritutu (S). The Taupo Volcanic Zone (TVZ) encompassing Ruapehu Volcano (R), Mt. Ngauruhoe (N), Mt. Tongariro (To), Lake Taupo (Tau), Maroa Volcano (Ma), Mt. Tarawera (Ta), Mt. Edgecumbe (E), and White Island (W). The Alexandra Volcanic Lineament (Briggs et al., 1989) is also shown. Contours show depth to the Wadati–Benioff Zone (Boddington et al., 2004; Reyners et al., 2006, 2011).*

Magma generation along the Taranaki Volcanic Lineament is still a matter of debate. The volcanic succession of Mt. Taranaki represents the most westerly subduction-related volcanism of the Hikurangi arc-trench system (Hatherton, 1969). The depth of the Wadati-Benioff zone beneath the Taranaki region is approximately 300 km according to seismicity analysis (e.g., Adams and Ware, 1977; Boddington et al., 2004; Reyners et al., 2006, 2011). Price et al. (1992) proposed that fluid loss from the slab could be a possible trigger for magma generation along the lineament. They suggested that a north-westerly trending tear or fault in the subducting plate motivated fluid loss from the slab to produce a linear zone of melting in the overlying metasomatised mantle wedge. Temporal propagation of this tear or fault along the subduction slab produced the Taranaki Volcanic Lineament. More recently, Stern et al. (2006) have questioned the presence of an active slab beneath Mt. Taranaki, and rather consider the idea of volcanism being associated with foundering of delaminated, older lithosphere. They invoked the Rayleigh-Taylor instability concept for Taranaki's petrogenesis and suggest that convective removal of once thickened mantle lithosphere to explain high-K volcanism in the western North Island. The "arc" type trace element signature found within Mt. Taranaki's rock suite is hereby caused by recycling of old lithosphere rather than produced by a present-day subduction system. Zernack et al. (2012b) suggested that there could be a relationship between the tectonic block rotation model given by Wallace et al., (2004) and magma evolution.

The Taranaki volcanics overlie the sediments of the Taranaki Basin (Fig. 1.2), which was formed during extension and faulting of the basement associated with the opening of the Tasman Sea in the middle Cretaceous. Subsequent infilling with sediment produced a succession that varies in thickness from 5-10 km and is mainly composed of limestone, coal, silt- and sandstone of Late Cretaceous to Pleistocene age (King and Thrasher, 1996). The 100,000 km^2 Taranaki Basin overlies a basement of calc-alkaline plutonic and metamorphic rocks, which are part of the Median Tectonic Zone (Mortimer et al. 1997). Detailed structural and stratigraphic descriptions of the Taranaki Basin are given by Pilaar and Wakefield (1978), Knox (1982), King and Thrasher (1992, 1996), Muir et al. (2000), and Reilly et al. (2015).

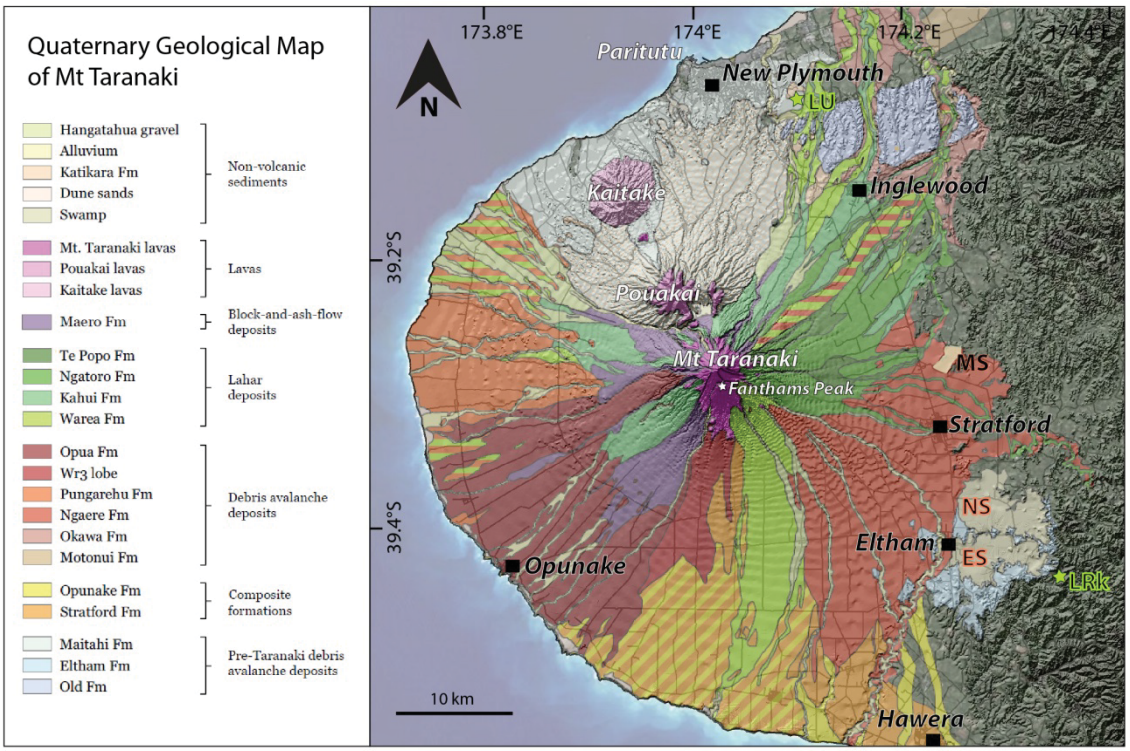

Figure 1. 3 *Volcanic, volcaniclastic and sedimentary deposits shown in the quaternary geological map of Mt. Taranaki (modified after Neall and Alloway, 2004). Sediment coring locations of previous studies (Lees and Neall, 1993; McGlone and Neall, 1994; Turner et al., 2008a, 2009) including the Eltham Swamp (ES), Ngaere Swamp (NS), Midhirst Swamp (MS), Lake Umutekai (LU) and Lake Rotokare (LRk) are also shown.*

1.3.3 The volcanic eruption history of Mt. Taranaki

The youngest volcano of the Taranaki Volcanic Lineament changed name multiple times throughout the history. Maori used to call the volcano *Pukehaupapa*, which was a common term for a snow capped mountain (Wells, 1878). Kahui Maunga people, the first inhabitants of the region, named the volcano *Taranaki*, derived from the Māori words "tara"–mountain and "ngaki"–shining. This name remained until 1770 when British explorer James Cook named the volcano after the Earl of *Egmont*, a man who never set foot in the region. In 1986, the New Zealand Geographic Board (NZGB) sealed both latter names, Mt. Taranaki and Mt. Egmont, as official names used to describe the present geographic feature, whereas the surrounding area is referred to as the Taranaki region or province.

Mt. Taranaki is the second highest mountain (2518 m) in the North Island of New Zealand (Neall et al., 1986). Its symmetrical cone-shaped structure is accompanied by a parasitic cone, known as Fanthams Peak on the southern flank (Fig. 1.3). Its volcanic activity started more than 130 ka ago (Neall et al., 1986; Alloway et al., 2005) and Zernack et al. (2011a) suggested an even older period of volcanic activity based on a ~170 ka old debris avalanche deposit, Mangati Formation, identified among coastal ring-plain successions. The eruption history of the present-day cone (c. 10,000 years old; Neall et al., 1986) is characterised by sub-Plinian eruptions interspersed with effusive events (Alloway et al., 1995). The cone comprises pyroclastic flows, scoria and lava flows, with minor tephra deposits. The presently exposed eruptive deposits represent only a small fraction of the total volume of material erupted from Mt. Taranaki (Neall et al., 1986), since those are prone to rapid erosion and weathering in subaerial environments (Lowe, 1986; Alloway et al., 1995). The last volcanic activity occurred between 1785 AD and 1860 AD (Sisters eruption; Platz et al., 2012).

Fanthams Peak lies approximately 1.5 km to the south of Mt. Taranaki's main cone. The history of Fanthams Peak is complex and as yet poorly understood. Neall et al. (1986) suggested that the cone was present as early as 7000 years ago, with a final cone-building eruption phase at approximately 3300 years ago. Eruptive products from Fanthams Peak are mainly basalt to basaltic-andesite lava flows (Stewart et al., 1996) and mafic fall deposits, which have been considered to be related to the Manganui eruption (Whitehead, 1976).

1.3.4 Petrology and geochemistry of Mt. Taranaki

Igneous rocks at Mt. Taranaki are mainly andesites, and basaltic-andesites with minor basalts (Marshall, 1907; Price et al., 1992). In general, the andesitic rocks are holocrystalline to hypocrystalline and highly porphyritic. They have been classified by Gow (1968) according to their ferromagnesian phenocryst assemblages. The most common andesitic rock type at Mt. Taranaki is augite-hornblende andesite, with augite>hornblende. Other phenocrysts present in most of the rocks are plagioclase, clinopyroxene, titanomagnetite, and small amounts of orthopyroxene and olivine. Most phenocrysts occur as glomerocrysts that range from 25% to 55% by volume (Neall et

al., 1986; Stewart et al., 1996). The high amounts of clinopyroxene and hornblende in Mt. Taranaki rocks are in contrast with andesitic rocks of the TVZ (Ruapehu, Tongariro, and Ngauruhoe), which are dominated by orthopyroxene with rare occurrences of hornblende (Price et al., 1992). Crustal xenoliths are also abundant and are characterised as peridotite, pyroxenite, amphibolite, gabbro, diorite, and meta-sediments; mainly originating from the Median Batholith basement and Cretaceous-Tertiary sediments of the Taranaki Basin (Price et al., 1992; Gruender et al., 2010). Geochemically the rocks of Mt. Taranaki are classified as high-K, low-Si andesites (Gill, 1981). Magmas become progressively more enriched in potassium with time (Stewart et al., 1996; Price et al., 1999, 2005, 2016). Large ion lithiophile elements (LILE) and light rare earth elements (LREE) are significantly enriched in Mt. Taranaki rocks. Further, Mt. Taranaki rocks are depleted in Nb relative to La, and enriched in Pb relative to Ce, indicating a characteristic arc-like trace element signature (Eggins, 1993; Price et al., 1992, 2005). Basalts and basaltic andesites are weakly hypersthene or nepheline normative.

Petrological and geochemical differences between eruptives of Mt. Taranaki and the andesitic rocks of the TVZ highlight possible dissimilarities in magma generation and evolution, crustal structure and heat flow (Neall et al., 1986; Price et al., 1999, 2005, 2016).

1.3.5 Previous tephrostratigraphy at Mt. Taranaki

The first numerical age assigned to a prehistoric tephra deposit from Mt. Taranaki has been defined in 1833 by A.W. Burrell, who documented pumice fragments lodged in the forks of matai (*Prumnopitys taxifolia)* trees near Stratford. Using tree-ring counts Burrell estimated an age of c. AD 1430 for this deposit, formally known as Burrell Lapilli (Oliver, 1931). Dating of charcoals from a Maori oven buried beneath the Burrell Lapilli produced similar ages of 400±60 yr BP and 360±60 yr BP (Oliver, 1931; Fergusson and Rafter, 1957). The most frequently used age of the Burrell eruption is based on dendrochronological analysis of kaikawaka (*Libocedrus bidwillii)* trees and yields an age of AD 1655 (Druce, 1966). The pioneering studies of Oliver (1931) may qualify as the first application of tephrochronology in New Zealand (Lowe, 1990).

First detailed tephrochronological work on Mt. Taranaki was mainly based on soil and peat surveys. Grange and Taylor (1933) recognised two widespread tephra 'showers' (airfalls) by mapping several soil-forming tephra deposits in the Taranaki region. The Stratford Shower (Ash), which is mainly dispersed to the east, and the overlying Egmont Shower (Ash), which is mainly dispersed from the north-east to the south-east. Further studies along the northern coastline of Taranaki by Wellman (1962) documented numerous andesitic ash layers, which were correlated with the Burrell Lapilli (Oliver, 1931), Newall Ash and Stratford Ash (Taylor, 1954). Beneath these ashes another three were grouped into the Stent Ash and another two into the Onaero Pumice (Wellman, 1962). The stratigraphy and chronology of the Stent Ash (silicic, Taupo-derived tephra) is described in detail by Alloway et al. (1994).

The first comprehensive synthesis of the volcanic eruption history of Mt. Taranaki was made by Druce (1966), who mapped and dated pyroclastic deposits on the upper flanks of the volcano during a general soil and vegetation survey. Nine andesitic ash layers, which were erupted during the last phase of volcanic activity at Mt. Taranaki, were grouped into three formations: (1) Tahurangi Formation (AD 1755), (2) Burrell Formation (AD 1655), and (3) Newall Formation (prior AD 1604). Shortly afterwards, Druce's stratigraphy was refined by Tonkin (1970) who studied the influence of these tephras on soil formation in the Dawson Falls region, and Topping (1972) who presented new radiocarbon dates and a detailed description of the widespread Burrell Lapilli, including its deposition and dispersal pattern. Subsequently, Cronin et al. (2003) introduced the term 'Maero Eruptive Period' to represent the latest stage of volcanic activity at Mt. Taranaki.

The investigations of Neall (1972) demonstrated a more extensive andesitic tephrochronological record. He studied the north-western flanks of Mt. Taranaki and documented ten additional ash and lapilli formations deposited during the last 100 ka. Deposits include the formally named Inglewood and Korito Tephra (p2 and p1, respectively of Druce, 1966), the Egmont Shower of Grange and Taylor (1933), which was split into two separate tephra units: (1) Eg 1 – Oakura Tephra (~6970±76 yr BP) and (2) Eg 2 – Okato Tephra and Aa – Ahuahu Lapilli (c. 14,000 yr BP), as well as the underlying Gg – Saunders Ash, which is considered to be a nuées ardentes deposit

(pyroclastic flow - PDC) dated at 16,100±220 yr BP (Neall, 1972). The Koru Lapilli represents a widespread marker bed in older pyroclastic deposits recognised (34,400±1500 yr BP; Neall, 1972). The bottom of the record is characterised by an unconformity, which separates a major ash-group, termed the "New Plymouth Ashes and buried soils", from the overlying deposits. Neall (1972) suggests an age range of 70-100 ka for the lowermost formation, but these were only based on relative stratigraphy, because radiocarbon dating had only been completed on post-12 ka deposits (Alloway et al., 1995).

Whitehead (1976) and Franks (1984) subsequently added new data to previous defined tephra deposits. Whitehead (1976) informally named the Manganui Tephra and Kaupokonui Tephra (p4 of Druce, 1966) as well created detailed isopach maps, which clearly show a multi-lobe distribution pattern (SE, E, and N) for the Manganui Tephra, which imply Fanthams Peak as its source. The documented age of the Manganui Tephra (3200 yr BP) and the age of the Kaupokanui Tephra (1200 yr BP) are estimated ages from their stratigraphic position between dated tephra and/or lahar deposits. Franks (1984) studied the tephra layers on the eastern flanks of Mt. Taranaki. She described and analysed several tephra units below the prominent Manganui Tephra, encompassing the informally named Mahoe, Konini (E1), Kaponga (E2), Waipuku (E3), Tariki (E4), and Mangatoki (E5) tephras, which were correlated to the previously defined Oakura and Okato Tephra Formations of Neall (1972). Although Alloway et al. (1995) outlined the most complete record of the eruptive history of Mt. Taranaki, the pioneering work of Druce (1966), Neall (1972) and Franks (1984) form the basis of all following tephrostratigraphic and tephrochronological investigations.

The study of Alloway et al. (1995) comprises a comprehensive post-28 ka tephra synthesis, which they grouped into sixteen andesitic tephra formations. They recorded 76 eruptive events with volumes of $>10^7$ m^3 and outlined three main tephra successions based on tephra characteristics and stratigraphic position. Those are (1) the upper tephra succession from Manganui to Mahoe Tephra(s) (3 to 11.5 ka period), (2) the upper sequence of the lower tephra succession from Kaihouri to Poto Tephra(s) (12 to 22.7 ka period) and (3) the lower sequence of the lower tephra succession from Tuikonga to Waitepuku Tephra(s) (23.4 to 28 ka period). The distributions of these tephras are

mainly to the NNE and SSE from the present vent, consistent with the dominant prevailing wind directions. Alloway et al. (1995) determined an average eruptive periodicity of one in every c. 330 years, which should be considered as a minimum, since tephras of lower magnitude eruptions are prone to rapid erosion and weathering in ring-plain environments (Lowe, 1986; Alloway et al., 1995). In contrast to previous studies of Turner et al. (2008a, 2009), who suggested a highly cyclic eruption frequency of one per 80 years with a 1500-2000 year periodicity using high-precision lake tephra records.

Alloway et al. (1995) also described two TVZ-sourced silicic tephra layers inter-bedded in the andesitic tephra successions from Mt. Taranaki. Both, the Stent Tephra (first recognised by Wellman, 1962) and the Aokautere Ash (first recognised by Rich, 1959 and named by Cowie, 1964), also known as Kawakawa Tephra (Vucetich and Howorth, 1976), are important stratigraphic marker beds used for age determinations and correlation purposes. The Stent Tephra has an error-weighted mean age of 3970±31 yr BP (Alloway et al., 1994) and the Kawakawa Tephra has a radiocarbon age of 25,360±160 cal yr BP (Vandergoes et al., 2013). Both tephra layers are easy to recognise on the basis of their distinct pale colour and glassy fine ash texture.

During a vegetation study by McGlone and Neall (1994) several andesitic tephra layers were identified in a peat core from the Eltham Swamp, c. 25 km to the SE of Mt. Taranaki's summit (Fig. 1.3). Five tephra layers were correlated with the Burrell Lapilli (295 yr BP), Kaupokonui Tephra (1390±150 yr BP), Manganui Tephra (between 2890±100 to 3320±60 yr BP), Inglewood Tephra (3950±50 yr BP) and Korito Tephra (5000±90 yr BP). A prominent unnamed grey lapilli bed was dated at 10,150±100 yr BP, at the bottom of the peat-core. Dates were determined by radiocarbon dating of peat and wood samples above and/or below tephra layers. Another vegetation study by Lees and Neall (1993), which focused on the impact of volcanic eruption on the vegetation, suggested that the Tahurangi eruption is probably younger than previously estimated by Druce (1966). On the basis of pollen analysis they recognised a >70 year-long soil-forming interval between the Burrell Ash and Burrell Lapilli. Lees and Neall (1993) cored several peat bogs around the volcano including the Midhirst Swamp (Fig. 1.3). A

60 cm long peat core from the Midhirst Swamp contained the Burrell Tephra and the Kaupokonui Tephra.

The medial and distal tephra record of Mt. Taranaki is best preserved in lake and peat environments surrounding the volcano. Andesitic tephra deposits from Mt. Taranaki were identified in lake sediments of the Waikato lakes (Hamilton), c. 200 km to the NNE (Lowe, 1988a), in sediment successions of Lake Umutekai, c. 25 km to the NNE as well as Lake Rotokare, c. 30 km to the SE of the summit (Turner et al. 2008a, 2009; Fig. 1.3) and in sediments of Lake Tutira, c. 250 km to the east in Hawkes Bay (Eden et al., 1993). Further, numerous Mt. Taranaki-sourced tephra deposits occur in lake and maar sediments around Auckland City (i.e., Lake Pupuke, Onepoto Basin, Pukaki Lagoon, Orakei Basin, Hopua Crater), some 270 km N-NW from the source (Sandiford et al., 2001; Shane and Hoverd, 2002; Shane, 2005; Molloy et al., 2009). Distal tephra deposits preserved in lacustrine environments have been shown to be valuable records for high-resolution investigations on large- and small-scale eruption events, due to their continuous sedimentation and good preservation conditions (Lowe, 1986, 1988b). These records are also important for frequency and distribution analysis (Shane, 2005; Turner et al., 2008a, 2009; Bebbington et al., 2011; Green et al., 2013). The records recovered from Auckland sites show many andesitic tephra layers from Mt. Taranaki in the time interval 20-40 ka and minor tephras in the intervals 60-50 ka and 10 ka-present. This variable preservation is possibly explained by different atmospheric circulation conditions in the glacial periods (Horrocks et al., 2005; Molloy et al., 2009). However, near to the volcano, sediments in Lake Umutekai and Lake Rotokare (Turner et al., 2008a, 2009) reveal a high-precision post-10 ka eruption record for Mt. Taranaki. Within a 3.5 m-long core extracted from bottom sediments of Lake Umutekai, 104 individual tephra layers were identified and dated between c. 1550 – 10,000 yr BP, and 42 tephra layers dated between c. 500 – 6250 yr BP were recognised in a 5 m-long core from Lake Rotokare. These temporally-constrained tephra records from the lakes provided statistical data for subsequent volcanic event frequency analysis and probabilistic eruption forecast modelling (Turner et al., 2008a, 2009, 2011b). The data highlighted a pattern of highly cyclic variations in the eruption frequency at Mt. Taranaki, having a 1500-2000 year periodicity.

Further, Turner et al. (2008b) used titanomagnetites as geochemical fingerprints, because andesitic glass shards were geochemically heterogeneous (Shane, 2005) and commonly contain an abundance of microlites, which are difficult to avoid with large-scale electron microprobe beam areas required for glass analysis (Platz et al., 2007b). Turner et al. (2008b) distinguished two eruption styles by examining titanomagnetite textures: (1) slow-ascent eruptions (dome-growth) characterised by exsolved titanomagnetites and (2) fast-ascent eruptions (sub-Plinian) characterised by homogenous titanomagnetites. Further, Turner et al. (2009) predicted a probability of 0.52-0.59 for an eruption occurring in the next 50 years, using the combined eruption record and the mixture-of-Weibulls model (Bebbington and Lai, 1996). Thus, modern tephrochronology has not only focused on the overall chronostratigraphic background of Mt. Taranaki but has also used combined tephra records to understand its long-term eruption behaviour.

Latest work at proximal-medial sites (e.g., Platz et al.,, 2007a, 2012; Turner et al., 2008c, 2011a; Zernack et al., 2011a) focused on detailed re-mapping of ring-plain successions and costal sections so as to build up a more comprehensive record of eruptive behaviour. Interbedded tephra layers were used to build a detailed chronostratigraphic record for the whole volcanic-volcaniclastic succession of Mt. Taranaki. Zernack et al. (2011a) identified at least 14 debris avalanches, which occurred during the last ~170 ka suggesting one major edifice collapse on average every 10-14 ka, with an increase in frequency during the last 40 ka. The estimated age of c. 130 ka (Alloway et al., 2005) for the earliest volcanic activity at Mt. Taranaki has been revised to ~170 ka based on the emplacement age of the newly termed Mangati Formation (Zernack et al., 2011a). Further studies of Zernack et al. (2012) forecasted a potential edifice collapse of 7.9 km^3 in the next 16.2 ka based on volume-frequency models of debris avalanche deposits on Mt. Taranaki. Platz (2007) provides a detailed reconstruction of the latest eruption period, known as the Maero Eruptive Period (<1000 yr BP), which encompasses at least 10 eruptive episodes beginning from the Kaupokonui eruptive event to the latest eruption, newly termed as the Sisters eruption (1785-1820 AD; Platz et al., 2012). Platz et al. (2007a) focused mainly on non-explosive dome-forming eruptions, but identified the causes of rapid changes from effusive to explosive behaviour. Turner et al. (2011a) additionally studied twelve key

stratigraphic locations on the ring-plain of Mt. Taranaki and correlated some of these proximal deposits to the lake record (i.e., Lake Rotokare) on the basis of titanomagnetite chemistry and canonical discriminant function analysis (DFA). This was realised to be the first attempt to connect on-cone deposits with fallout deposits in lake sites. However, correlation of proximal-medial-distal deposits still remains a difficult task at Mt. Taranaki, since no geochemical data is available from on-cone sites, and units in soil sequences are often plagued by poor time-control and incomplete preservation.

Tinkler (2013) studied pollen in a more recent core from the Eltham Swamp. They recovered an 18 m-long core dating back to c. 40,000 cal yr BP This Eltham Swamp core contained 130 tephra layers, which have been correlated to medial deposits of Alloway et al. (1994) on the basis of stratigraphic position, colour, grain-size and sorting, isopach thicknesses and radiocarbon ages. New radiocarbon ages have been determined for several tephra layers. Tinkler (2013) mainly concentrated on palaeo-environmental and -climate reconstructions and created a detailed palaeo-wind record for the Eltham area.

1.3.6 Volcanic hazard at Mt. Taranaki

The Taranaki region is susceptible to a range of volcanic hazards posed by Mt. Taranaki, the most significant of which are volcanic gases, lava flows, pyroclastic flows and lateral blasts, tephra fall, lahars and associated floods, and debris avalanches (Neall and Alloway, 1993, 1995, 1996; Fig. 1.4). During unrest and eruption activity, major earthquakes and ground deformation are also possible threats (Townsend, 1998).

While lava flows are mostly confined to the upper cone (Neall, 1979), lahars and debris avalanches could potentially impact large areas of the ring-plain and many catchments of the Taranaki region (e.g., Neall, 1976; Neall and Alloway, 1993; Zernack et al., 2009; Procter et al., 2009, 2010; Fig. 1.4). Platz et al. (2012) pointed to hazardous, non-eruption-related, mass flows at Mt. Taranaki, which are associated with cooled metastable lava-dome collapses that generate large rock avalanches, extending over 5 km from source. Further, Neall and Alloway (1996) suggested that the potential risk

from future pyroclastic flows at Mt. Taranaki is restricted within a 15 km radius of any active vent, while tephra can be widely distributed by prevailing winds across the most of the North Island; from Manawatu-Wanganui (Wallace, 1987) to Hawke's Bay (Eden et al., 1993) to Waikato (Lowe, 1988a) and all the way up to Auckland, 270 km from the source (Sandiford et al., 2001; Shane, 2005).

The hazard presented by tephra fall is manifold (Neall and Alloway, 1993). Although these may not directly endanger human life, the highly abrasive, corrosive and conductive properties of tephra can dramatically influence public health (e.g., asphyxiation, asthma, bronchitis, and emphysema, Horwell and Baxter, 2006; Hansell et al., 2006), infrastructure and economy (e.g., electricity, transportation, water-supply, communication, Stewart et al., 2006; Bebbington et al., 2008; Wilson et al., 2011), environment (e.g., volcanic ash-leachates, Witham et al., 2005), agriculture and the tourism industry (e.g., Cronin et al., 1998; Johnston et al., 2000).

In general, "probabilistic eruption forecasting consists of estimating the probability of an eruption event and where it sits in a complex multidimensional time-space-magnitude framework" (after Marzocchi and Bebbington, 2012). The most widely applied method in long-term eruption forecasting is stochastic modelling (Bebbington, 2009), where the key information comes from historical and geological evidence of past events. This approach calculates the frequency of past events, assuming that exactly the same frequency holds also for the future (Wickman 1966; Reyment, 1969; Klein, 1982). In a case study of Mt. Taranaki, Turner et al. (2008a, 2009) fitted a mixture of two Weibull distributions to the inter-event times they found between tephras. This was used to calculate a 52-59% chance of an eruption in the next 50 years, depending on the date of the last eruption. A calculation based on a critical-limit size model for the volcano was applied to estimate the probability of edifice failure and the generation of catastrophic debris avalanches at Mt. Taranaki (Zernack et al., 2012). The current annual collapse probability is ~0.00018, with the most likely collapse being small (<2 km^3). Recently Green et al. (2013) demonstrated that the integration of petrological and geochemical data into the estimated hazard function improved the modelling.

All forecasting models strongly rely upon complete eruption-event records and comprehensive age-constrains. These are rarely available from on-cone localities, where small-scale eruptions are poorly preserved due to erosion and weathering processes taking place in soil-forming environments (Lowe, 1986; Alloway et al., 1995) and older deposits have been obliterated by subsequent eruptive activity. The lack of long and detailed geological catalogues will ultimately lead to underestimated frequency calculations and biased forecasts (Wang and Bebbington et al., 2012).

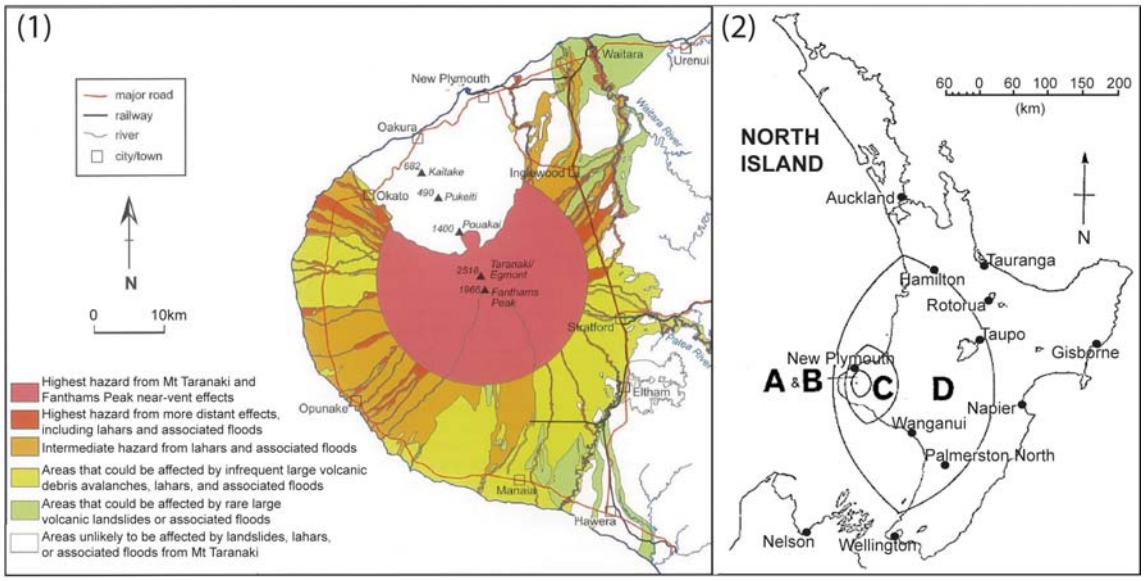

Figure 1. 4 *(1) Volcanic hazard zones for on-ground-type events for the Taranaki region (from Neall and Alloway, 1995). (2) Tephra fall hazard zones (A-D) from future eruptions of Mt. Taranaki (from Neall and Alloway, 1993). Expected thickness for tephra in zone A greater than 25 cm, in zone B between 25-10 cm, in zone C between 10-1 cm, and in zone D between 1-0.1 cm.*

1.4 Background geography

1.4.1 Physiography

The landscape of the Taranaki region (Fig. 1.5) is dominated by the conical-shaped Mt. Taranaki (2518m) and its accompanying parasitic cone, Fanthams Peak. Mt. Taranaki and the remnants of Pouakai Volcano (1399 m) and Kaitake Volcano (682 m) form a NW–SE trending mountain chain, which is surrounded by a voluminous volcanic ring plain occupying most of the Taranaki Peninsula. Another feature of the Taranaki landscape is the deeply dissected hill country to the east, which is entirely composed of late-Tertiary to Quaternary soft sediments (Townsend et al., 2008). A distinct zone of peatlands separates the ring plain from the hill country (i.e., Eltham Swamp, Ngaere Swamp, Tariki Swamp). Several rivers flow in a perfectly radial pattern from the flanks of the volcano to the ring plain (i.e., Waitotara River, Waitara River, Patea River), in contrast to river system occupying the dissected hill country, which show predominantly dendritic pattern with meandering stream channels. Coastal terraces between Hawera and Wanganui, as well as north of Urenui, complete the physiographic picture of the Taranaki region.

1.4.2 Climate

The present day climate of the Taranaki region is mainly influenced by its proximity to the sea, which results in rapidly changing and variable weather patterns. Further, it is also strongly influenced by anticyclones, which approach from the west across the Tasman Sea, and westerly prevailing subtropical winds (Thompson, 1981). Mean annual temperatures range between 11 to 14˚C at low altitudes and below 0˚C around the summit of Mt. Taranaki. Taranaki's coastal regions show mild to warm annual temperatures with few extremes, whereas inland areas have cooler annual temperatures and higher average rainfall, with frosts and fogs being common. Annual rainfall ranges from 900-1600 mm but increases with altitude to about 8000 mm above 2000 m (Fig. 1.5; Coulter 1976; New Zealand Meteorological Service, 1963; NIWA, 2014).

Next to the general mid-latitude westerly prevailing winds over the Taranaki region, low-level winds are generally deflected from the broad-scale flow due to local topographic features, including Mt. Taranaki, with predominantly south-easterlies prevailed at New Plymouth and at Stratford and Hawera the commen winds are from northwest and north, respectively (Chappell, 2014).

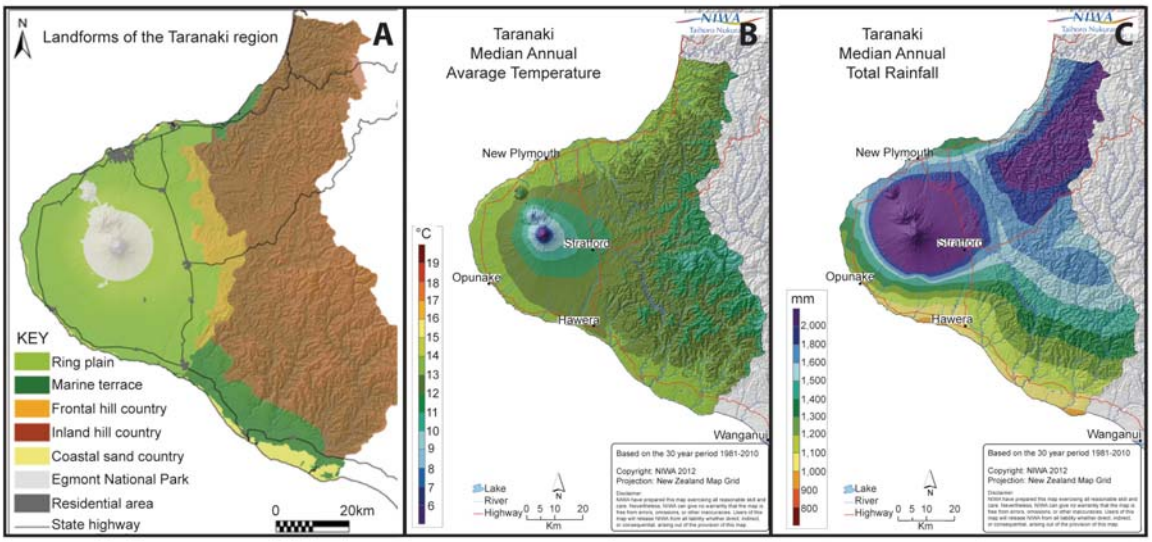

Figure 1. 5 *(A) landforms of the Taranaki region (Taranaki Regional Council, 2014), (B) Taranaki median annual average temperature (NIWA, 2014), (C) Taranaki median annual total rainfall (NIWA, 2014).*

1.4.3 Vegetation and soils

The climate patterns of the Taranaki region are reflected in a distinct zonation of the vegetation (Fig. 1.6; Clarkson, 1986; Newnham and Alloway, 2004). The most predominant vegetation type surrounding Mt. Taranaki, as well as around the Pouakai and Kaitake Ranges between 150-760 m altitude is lowland forest mainly composed of dense, warm-temperate podocarp–angiosperm forest including *Dacrydium cupressinum, Metrosideros robusta* and *Weinmannia racemosa* (McGlone and Neall, 1994). Above 760 m, lowland forest gradually gives way to montane forest, which extends as high as 1050 m. Montane forest is mainly dominated by W*einmannia racemosa* and *Podocarpus hallii*, while above 900 m *Libocedrus bidwillii* is predominant. Above the treeline (1050 m), the subalpine shrubland contains a broad range of species mainly

dominated by *Brachyglottis rotundifolia*. Shrubland grades into shrub–tussockland (i.e., *Hebe odora*) and ultimately, above 1400 m, to alpine tussockland dominated by *Chionochloa rubra* (red tussock). Among the tussocks the ground is covered with herbs and mosses, like *Racomitrium*, which can reach to 1750 m up the mountain (Clarkson, 1986; Bayfield and Benson, 1986; McGlone et al., 1988). The coastal region of Taranaki is dominated by coastal forest up to 1 km inland and semicoastal forest (mainly broadleaved angiosperms) up to 10 km inland. Notwithstanding that these were the original vegetation patterns prior to European settlement, nowadays the land below about 400 m has been cleared for farming and only remnants of the original vegetation remain.

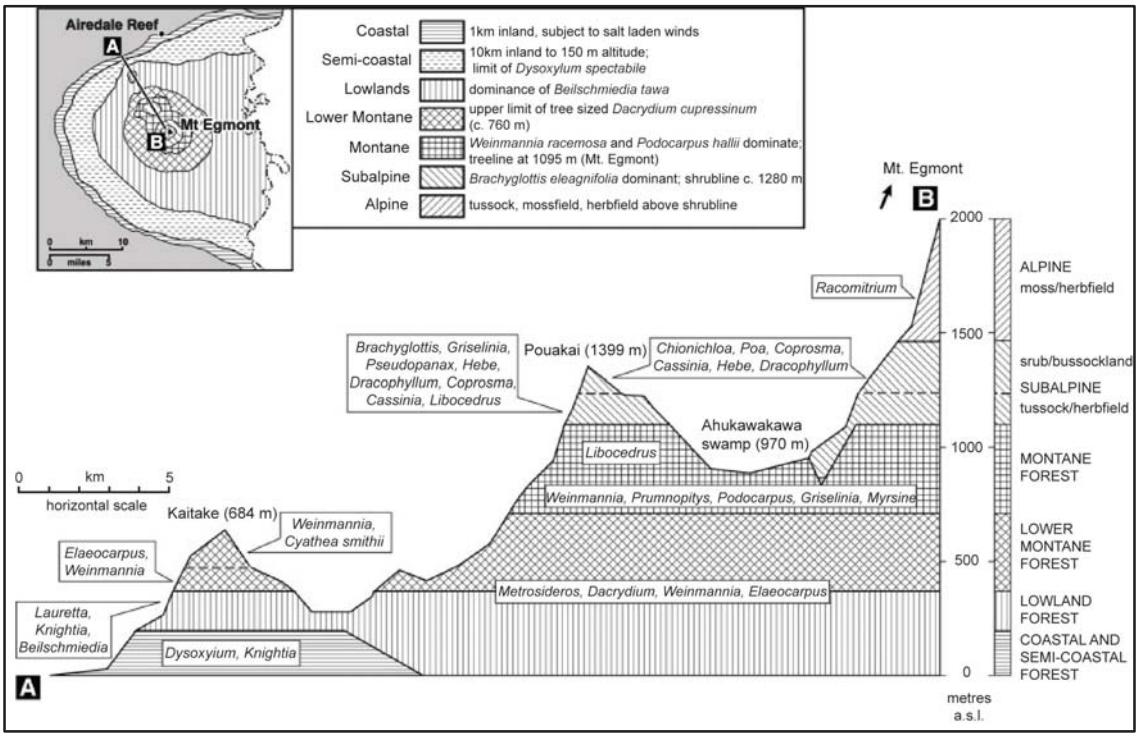

Figure 1. 6 *Vegetation-profile of the Taranaki region (after Newnham and Alloway, 2004).*

The main soil-types in the Taranaki region derive from the volcaniclastic deposits of Mt. Taranaki. The distinct yellow-brown loams are classified as andisols (Herwitt, 1992) and are characterised by high allophane contents and high porosity and permeability, as well as having a strong affinity to organic matter and low bulk density (Stewart et al., 1977, Neall, 1977; Franks et al., 1991). The andesitic volcanic ash soils

of the Taranaki region are highly fertile and therefore highly prised for agricultural uses. Where there are only thin tephric materials over cemented or compacted lahars, the soils are often poorly drained and of lesser value for agriculture.

1.4.4 Palaeoclimate

Palaeoclimate conditions not only play an important role in the formation and evolution of the landscape on which tephra is deposited (peat and lake environments and their response to climate fluctuations over time) but also influence tephra distribution and deposition (e.g., wind directions, fluvial influx, rates of erosion and weathering). Understanding past climate conditions is essential for interpreting lacustrine records and any enclosed tephra beds. Therefore, a brief review of the late Quaternary climate in New Zealand with a focus on the North Island and the Taranaki region is appropriate.

A detailed climate-event stratigraphy for New Zealand spanning the last 30,000 years has been presented by Alloway et al. (2007), Lowe et al. (2013), and Barrell et al. (2013) as part of the NZ-INTIMATE (INTegration of Ice-core, Marine and Terrestrial records) project (Fig. 1.7). Studies of records from the North Island (i.e., Auckland maars, Kaipo and Otamangakau wetlands, Taranaki region, eastern offshore) and South Island (i.e., Okarito wetland, Twin Forks Cave, Galway Tarn, Mount Cook National Park) are mainly based on various climate-proxies including pollen, diatoms, oxygen isotopes in speleothem and marine sediments, total carbon and carbon isotopes in lacustrine sediments, as well as glacial and fluvial deposits, loess and loess-like (aeolian quartz) deposits. Age control derives from radiocarbon dating and stratigraphically well-constrained tephra marker beds (Lowe et al., 2008, 2013). Four major climate periods have been distinguished:

(1) Preceding Interstadial – older than c. 29 cal ka; mild climate conditions.

McGlone et al. (1984) describes cool and extremely wet climate conditions between 40-30 ka, recorded in pollen assemblages in the Inaha Formation, South Taranaki coast. The vegetation was mainly dominated by shrub- and grassland.

(2) Last Glacial Coldest Period (LGCP) – c. 29 to 18 cal ka; mainly cold climate conditions interrupted by two interstadial periods characterised by cool climate conditions (Fig. 1.7).

The LGCP encompasses the Last Glacial Maximum (LGM) *sensu stricto,* defined as the last major glaciation period (c. 21±3 cal ka) with global ice sheets reaching their maximum integrated volume (Mix et al., 2001; Clark and Mix, 2002) and global sea level lowstand of 135 m below present levels (Yokoyama et al., 2000). The onset of the LGM *sensu stricto* has been later redefined by Newnham et al. (2007) to c. 29 cal ka for the New Zealand palaeoclimate record, based on glacial evidence from the South Island and pollen evidence from the North Island, hence, the term 'extended Last Glacial Maximum' – eLGM has been introduced.

The climate in the Taranaki region during the LGCP was mainly cold and dry, which is shown by widespread fluvial and aeolian depositions, which therefore reflect increased erosion across the North Island (Neall, 1975; Pillans et al., 1993). Alloway et al., (1992a) describes an increased quartz influx during two significant periods (at 27 and 21 cal ka) recorded in andesitic soil deposits (andisols) in the Taranaki region. The source of quartz-rich dust is assumed to be the continental shelf of the southern North Island, which was exposed by the low global sea level during the LGCP. The latest study of Tinkler (2013) used aerosolic quartz dust from peat-material from the Eltham Swamp, Taranaki, to reconstruct palaeowind intensities and directions. Major dust peaks at c. 31.4, 21.3 and 18.9 cal ka can be readily correlated with the Vostok ice core (Jouzel at al. 1993), the marine core P69 (Stewart and Neall, 1984) and Onaero/Waitui sample sites in Taranaki (Alloway et al., 1992a).

The end of the LGCP, known as the Termination I (19-18 cal ka), is characterised by an abrupt climate amelioration towards warmer and wetter conditions accompanied by the replacement of pre-existing shrub-grassland taxa with tall podocarp forest communities (e.g., Newnham et al., 2003; Vandergoes et al., 2005; Hajdas et al., 2006). Further, increased fluvial activity due to much higher precipitation rates during Termination I led to increased incision into fluvial terraces in the North Island (Berryman et al., 2000; Litchfield and Berryman, 2006). The transition from last-glacial to post-glacial climate

conditions is marked by the prominent rhyolitic Rerewhakaaitu Tephra (17,900±200 cal yr BP) from the Okataina Volcanic Centre (Newnham et al., 2003; Lowe et al., 2008).

(3) Last Glacial-Interglacial Transition (LGIT) – c. 18 to 12 cal ka; transitional climate conditions characterised by progressive warming conditions with a short cooling period, which is known as the late-glacial cool episode or Late-glacial Reversal (LGR) around 13.8 – 12.5 cal ka (Lowe et al., 2013) (Fig. 1.7).

The general warming trend and rapid expansion of forest during the LGIT reached its maximum between 15.5 – 14 cal ka (e.g., Taranaki region: Durham Road – Alloway et al., 1992b; Eltham Swamp – McGlone and Neall, 1994). The cooling of the LGR is characterised by a decrease in forest vegetation and concomitant expansion of shrub communities. This trend is seen in most pollen records including Taranaki (e.g., Alloway et al., 1992b; McGlone and Neall, 1994; Alloway et al., 2007). Further evidence for a short-time cooling interval in the main deglaciation period is recognised in the total organic carbon (TOC) and isotope curves from marine and lacustrine records from the North Island (e.g., Newnham and Lowe, 2000; Carter et al., 2002; Shane and Hoverd, 2002), as well as glacial sequences from the Southern Alps (Denton and Hendy, 1994). The LGR in New Zealand began slightly later than the start of the Antarctic Cold Reversal and continued through to the end of Younger Dryas time (Alloway et al., 2007).

(4) Holocene Interglacial – c. 11.8 cal ka to present; warm climate conditions with two phases of greatest warmth (early Holocene and mid Holocene).

In general, variations of the Holocene climate are poorly understood, but significant climate fluctuations during this period are recorded (Mayewski et al., 2004; Schaefer et al., 2009; Striewski et al., 2013). Palynological studies (McGlone et al., 1993; Newnham and Lowe, 2000), isotopic sea surface temperature estimates (Weaver et al., 1998), and isotopic analyses on speleothems (Hellstrom et al., 1998; Williams et al., 2004, 2010) indicate a clear, unusually warm, period around 11.5 cal ka, with temperatures between 1.5 and 3.0 ˚C above those recorded at present. After this early Holocene thermal optimum, a drop in temperature occurred between 9 – 7 cal ka

followed by another warm period in mid-Holocene c. 7 – 6.5 cal ka (Williams et al., 2010). The late-Holocene is characterised by even stronger climate fluctuations, which are shown in several studies based on high-precision recording of Holocene glacier activity in New Zealand, particular in the Southern Alps (c. 5 cal ka; Schaefer et al., 2009). Recent studies of Brook et al. (2011) documented a similar trend of glacier expansion in the North Island by investigating glacial moraines on the southern slopes of Mt. Taranaki. Although palynological studies in the Taranaki region are rare, McGlone et al. (1984, 1988) and McGlone and Neall (1994) suggest that climate cooled and became drier, and eventually windier between 3 – 2.5 cal ka and 1.4 – 0.45 cal ka, based on the abundance of *Libocedrus bidwillii* pollen at Mt. Taranaki sites. The arrival of humans at around 650 cal years BP resulted in obscured palynological records since this time (Wilmshurst et al., 1999).

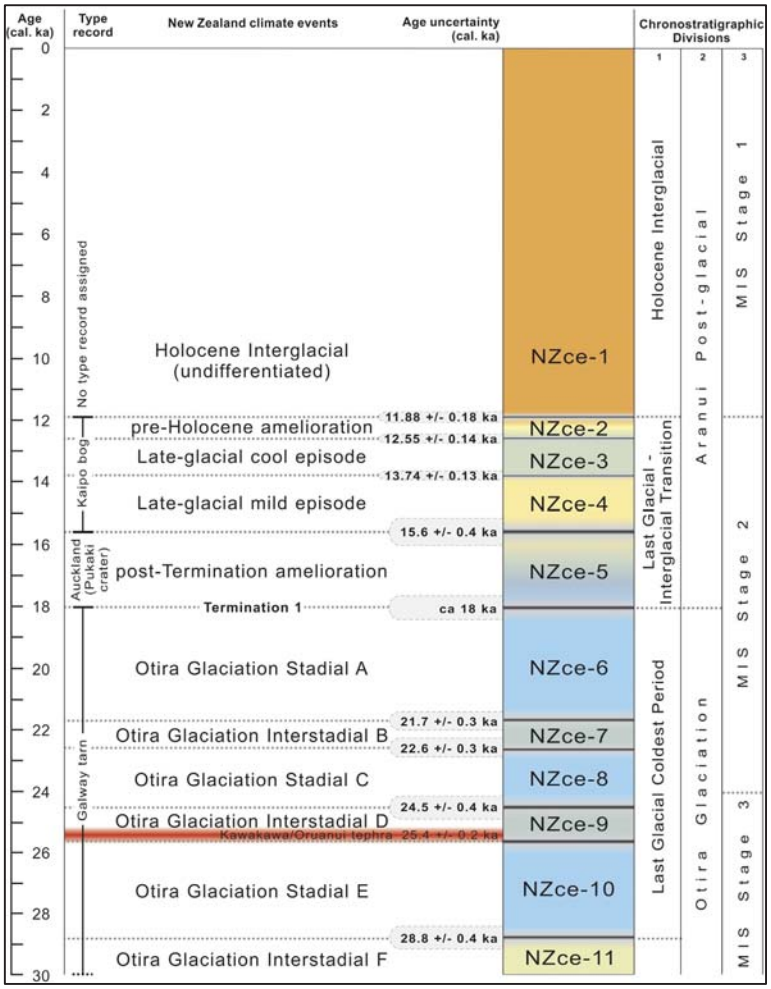

Figure 1. 7 *The NZ-INTIMATE climate event stratigraphy (after Barrell et al., 2013 and Alloway et al., 2007).*

Overall, the environment where tephra is deposited is greatly influenced by climate fluctuations. During moist and warm climate conditions, large forest expanses can be formed and thick peat beds accumulate. Mild/warm and dry conditions result in a change in soil-forming processes and enhanced weathering, which can lead to the development of allophane-rich andisols. Cold and dry climate conditions favour the development of loess-rich, poorly developed soils and the influx of aerosolic quartz dust. Deglaciation periods, or simply wetter climate periods, produce higher fluvial activity and erosion, which can lead to greater sediment influx into lake and peat environments. An increased precipitation rate, or the formation of large volumes of meltwater, can also produce debris avalanches, flash floods and lahars, which can travel great distances from their sources (Zernack et al., 2011a). Collapses from the volcano triggered/or not triggered by climate conditions can deposit large amounts of material across the surrounding ring plain, affectedly changing the pre-existing landscape (e.g., damming streams and rivers, re-routing drainage), and hence, leading to the formation of new environmental settings. The state of the environment is crucial to deposition and preservation of tephra deposits, since andesitic tephra is easily prone to erosion and weathering (Lowe et al., 1988b).

1.5 Study sites

Lakes and peatlands are relatively common on the lower portions of the volcanic ring-plain of Mt. Taranaki, where large debris avalanches and lahar deposits lap up against the deeply dissected hill country to the east (Zernack et al., 2011a) (Fig. 1.8) and have altered or blocked existing drainage patterns, initiating the formation of peats and lakes. One lake and three peatlands located within a 20 to 30 km radius of Mt. Taranaki's summit were selected according to their potential for preserving deep sequences of organic deposits and their positions within the main dispersal axis of mapped tephra falls (Alloway et al., 1995). From north to south, the study sites are Lake Richmond (LRi), Tariki Swamp (TS), Ngaere Swamp (NS), and Eltham Swamp (ES) (Fig. 1.8). To derive the most complete and detailed tephrostratigraphic record I added data from cores at Lake Umutekai (LU) and Lake Rotokare (LR), obtained by Turner (2008), and re-examined in the present study.

Lake Umutekai lies c. 5 km SE of New Plymouth and about 25 km NNE of Mt. Taranaki's summit. It is a 0.02 km^2, shallow (<2 m) closed depression on a gently undulating volcaniclastic surface that is ≥170 ka old (Neall, 1979). The surrounding landscape was densely forested throughout the Holocene (McGlone and Neall, 1994). Lake Umutekai has been cored for a pollen-based vegetation and climate survey (Newnham, 1990) and more recently by Turner et al. (2008a, 2009) who identified 104 tephra layers between c. 1.5 to 10.5 cal ka BP.

Lake Richmond is located c. 5 km NE of Inglewood and about 25 km NE of Mt. Taranaki's summit. The lake is interpreted to be formed by landslide-damming and lies in an N-S oriented valley. It is drained to the north-east by the Mangaonaia Stream and fed by two unnamed streams from the south. The 0.03 km^2 lake has a maximum water depth of 4 m.

Tariki Swamp is located c. 2.5 km SW of Ratapiko and about 22 km ENE of Mt. Taranaki's summit. It is bordered by the Manganui River to the west and the man-made Lake Ratapiko to the east. This small, peat-filled basin is abutted to the north by a massive debris avalanche deposit (Okawa Formation, 105 ka BP; Neall and Alloway,

2004). Alteration of drainage by the emplacement of this deposit is interpreted to have formed the peat bog.

Midhirst Swamp, located along the Salisbury Rd c. 3 km north-east of the village Midhirst, is a small flat peat-filled area of 285m elevation. It has been first studied by Lees and Neall (1993), who collected two cores for pollen analysis from this area. This site is now mainly pasture but a small remnant of lowland forest lies about 1 km to the northeast. Midhirst Swamp is situated on top of a debris avalanche, named Ngaere Formation (c. 23,000 yr BP; Neall and Alloway, 2004; Fig. 1.3).

Eltham Swamp and Ngaere Swamp are large broad peat areas located east of Eltham and separated from each other by a low, east-west trending ridge of Tertiary mudstone. The peatlands lie about 28 km ESE of Mt. Taranaki's summit. At 220m, Ngaere Swamp is 10 m higher than Eltham Swamp. Both are peat-filled basins about 6 km long and 2 km wide. The Eltham Swamp is drained by the Mangimangi Stream to the south and by the Mangawhero Stream to the west. The Ngaere Swamp is drained to the north by the Ngaere Stream, a tributary of the Patea River. These peat bogs formed in response to a series of lahar and debris avalanche deposits emplaced between 23-50 ka BP (Neall and Alloway, 2004; Zernack et al., 2011a). These deposits altered the local topography, provided shallow aquitards, and partially blocked the tributary valleys of the eastern hill country, leading to peat accumulation. The Eltham Swamp has been previously investigated by McGlone and Neall (1994) and Tinkler (2013), who undertook pollen-based palaeovegetation investigations. Pollen analyses of peat-cores from the bog indicate that at ~13 ka BP, towards the end of the Last Glacial Maximum, the region was mainly open grassland. Shortly after (~12.5 ka BP) there was a rapid transition to a forest-dominated landscape. Today, these peatlands are cleared of their original forest, drained and developed into pasture, which has caused the peatland to subside at least 3 m (McGlone and Neall, 1994).

Lake Rotokare lies several kilometres further downwind, approximately 34 km ESE of Mt. Taranaki's summit. This Y-shaped lake was formed by damming of its drainage system following a Holocene landslide (Taranaki Catchment Commission, 1980). It has

an area of 0.25 km^2 and a maximum water depth of 12 m. Turner et al. (2009) identified 42 tephra layers dated between c. 0.5 to 7 cal ka B.P within sediments of this lake.

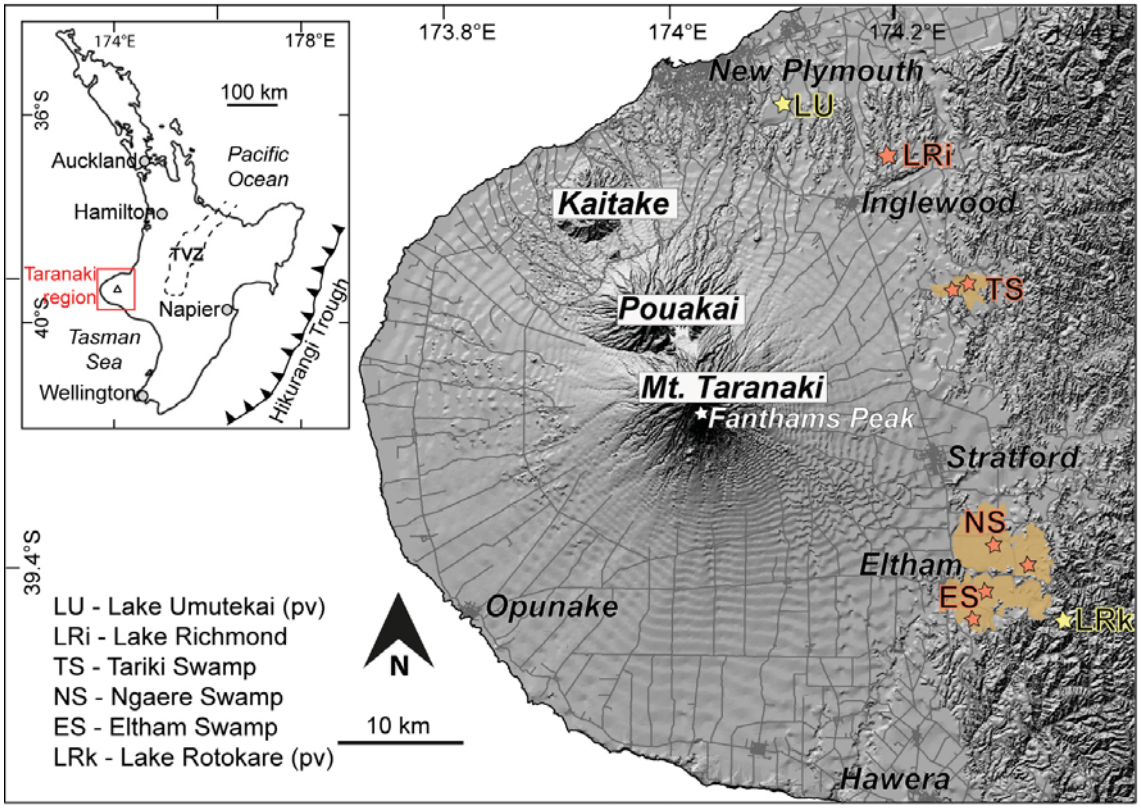

Figure 1. 8 *Location map of the study sites. Peatlands are highlighted by the orange fields; whereas stars represent specific coring location. Lakes are also indicated by stars, whereas green stars indicate previous (pv) coring sites of Turner et al. (2008a, 2009). Note the change in physiographic textures, which is the contrast between the smooth volcanic ring-plain to the west and the dissected mudstone hill country to the east.*

1.6 Thesis outline

This thesis comprises primarily published or submitted manuscripts so there is some degree of repetition between chapters, particularly of the study site description and the methods used.

Chapter 1 provides a broad overview of the background geology and geography of the Taranaki region and outlines previous tephrostratigraphic studies, as well as identifying the aims and objectives of this study. Chapter 2 describes the methods used in this study and potential limitation that may come with them. The development of a robust stratigraphic framework of the eruption record at Mt. Taranaki is contained within Chapter 3 and 4. Chapter 3 considers distal tephra, whereby several lake and peat sediment tephra records are integrated to a composite high-resolution record by using physical and mineral-chemical characteristics, in conjunction with precise age determination of the tephra layers. Chapter 4 applies the techniques of Chapter 3 to on-cone flank and ring-plain proximal deposits and correlates previously defined tephra formations into the composite record to derive an overall revised tephrostratigraphy at Mt. Taranaki. Once this robust eruption record was established, it was used in Chapter 5 to investigate the eruption frequency of Mt. Taranaki, and, in Chapter 6, to model the underlying magmatic system(s) of the volcano. As a result, Chapter 5 focuses on probabilistic estimations, which are realised to be highly sensitive to incomplete and/or biased data sets and provides a revised and more accurate probabilistic eruption and hazard forecast for Mt. Taranaki. Chapter 6 synthesises all the chemical data and provides a detailed interpretation of the magmatic evolution of Mt. Taranaki over the past ~30 cal ka BP. A model is proposed that explains the compositional diversity of analysed tephra layers, e.g., in particular titanomagnetite compositions, in relation to the temporal aspect of magma evolution and eruption history. Chapter 7 closes this thesis with conclusions and recommendations for further work.

The entire data set compiled during this research is presented in the printed and electronic appendices, whereby geochemical analyses are presented as averages (±S.D.) in the printed version and as complete data sets within the electronic version.

1.7 References

Adams, R. D., & Ware, D. E. (1977). Subcrustal earthquakes beneath New Zealand; locations determined with a laterally inhomogeneous velocity model. New Zealand Journal of Geology and Geophysics, 20(1), 59-83.

Allan, A. S., Baker, J. A., Carter, L., & Wysoczanksi, R. J. (2008). Reconstructing the Quaternary evolution of the world's most active silicic volcanic system: insights from an ~1.65 Ma deep ocean tephra record sourced from Taupo Volcanic Zone, New Zealand. Quaternary Science Reviews, 27(25), 2341-2360.

Alloway, B. V., Stewart, R. B., Neall, V. E., & Vucetich, C. G. (1992a). Climate of the last glaciation in New Zealand, based on aerosolic quartz influx in an andesitic terrain. Quaternary Research, 38(2), 170-179.

Alloway, B. V., McGlone, M. S., Neall, V. E., & Vucetich, C. G. (1992b). The role of Egmont-sourced tephra in evaluating the paleoclimatic correspondence between the bio-and soil-stratigraphic records of central Taranaki, New Zealand. Quaternary International, 13, 187-194.

Alloway, B., Lowe, D. J., Chan, R. P. K., Eden, D., & Froggatt, P. (1994). Stratigraphy and chronology of the Stent tephra, a c. 4000 year old distal silicic tephra from Taupo Volcanic Centre, New Zealand. New Zealand Journal of Geology and Geophysics, 37(1), 37-47.

Alloway, B., Neall, V. E., & Vucetich, C. G. (1995). Late Quaternary (post 28,000 year BP) tephrostratigraphy of northeast and central Taranaki, New Zealand. Journal of the Royal Society of New Zealand, 25(4), 385-458.

Alloway, B., McComb, P., Neall, V., Vucetich, C., Gibb, J., Sherburn, S., & Stirling, M. (2005). Stratigraphy, age, and correlation of voluminous debris-avalanche events from an ancestral Egmont Volcano: implications for coastal plain construction and regional hazard assessment. Journal of the Royal Society of New Zealand, 35(1-2), 229-267.

Alloway, B. V., Lowe, D. J., Barrell, D. J., Newnham, R. M., Almond, P. C., Augustinus, P. C., Bertler, N. A., Carter, L., Litchfield, N. J., McGlone, M. S., & Shulmeister, J. (2007). Towards a climate event stratigraphy for New Zealand over the past 30 000 years (NZ-INTIMATE project). Journal of Quaternary Science, 22(1), 9-35.

Barrell, D. J., Almond, P. C., Vandergoes, M. J., Lowe, D. J., Newnham, R. M., & INTIMATE members. (2013). A composite pollen-based stratotype for inter-regional evaluation of climatic events in New Zealand over the past 30,000 years (NZ-INTIMATE project). Quaternary Science Reviews, 74, 4-20.

Baxter, P. J., Boyle, R., Cole, P., Neri, A., Spence, R., & Zuccaro, G. (2005). The impacts of pyroclastic surges on buildings at the eruption of the Soufrière Hills volcano, Montserrat. Bulletin of Volcanology, 67(4), 292-313.

Bayfield, M. A., Benson, M., & Neall, V. E. (1986). Egmont Ecological Region. Department of Lands and Survey.

Beavan, J., Tregoning, P., Bevis, M., Kato, T., & Meertens, C. (2002). Motion and rigidity of the Pacific Plate and implications for plate boundary deformation. Journal of Geophysical Research: Solid Earth, 107(B10).

Bebbington, M. S. (2007). Identifying volcanic regimes using hidden Markov models. Geophysical Journal International, 171(2), 921-942.

Bebbington, M. S. (2009). Volcanic eruptions: stochastic models of occurrence patterns. In Encyclopedia of Complexity and Systems Science (pp. 9831-9861). Springer New York.

Bebbington, M. S. (2010). Trends and clustering in the onsets of volcanic eruptions. Journal of Geophysical Research: Solid Earth, 115(B1).

Bebbington, M. S., & Lai, C. D. (1996). On nonhomogeneous models for volcanic eruptions. Mathematical Geology, 28(5), 585-600.

Bebbington, M., Cronin, S. J., Chapman, I., & Turner, M. B. (2008). Quantifying volcanic ash fall hazard to electricity infrastructure. Journal of Volcanology and Geothermal Research, 177(4), 1055-1062.

Bebbington, M. S., & Cronin, S. J. (2011). Spatio-temporal hazard estimation in the Auckland Volcanic Field, New Zealand, with a new event-order model. Bulletin of Volcanology, 73(1), 55-72.

Boddington, T., Parkin, C. J., & Gubbins, D. (2004). Isolated deep earthquakes beneath the North Island of New Zealand. Geophysical Journal International, 158(3), 972-982.

Briggs, R. M., Itaya, T., Lowe, D. J., & Keane, A. J. (1989). Ages of the Pliocene—Pleistocene Alexandra and Ngatutura Volcanics, western North Island, New Zealand, and some geological implications. New Zealand Journal of Geology and Geophysics, 32(4), 417-427.

Brook, M. S., Neall, V. E., Stewart, R. B., Dykes, R. C., & Birks, D. L. (2011). Recognition and paleoclimatic implications of late-Holocene glaciation on Mt Taranaki, North Island, New Zealand. The Holocene, 21(7), 1151-1158.

Bryant, C. J., Arculus, R. J., & Eggins, S. M. (2003). The geochemical evolution of the Izu-Bonin arc system: A perspective from tephras recovered by deep-sea drilling. Geochemistry, Geophysics, Geosystems, 4(11).

Chanier, F., Ferrière, J., & Angelier, J. (1999). Extensional deformation across an active margin, relations with subsidence, uplift, and rotations: The Hikurangi subduction, New Zealand. Tectonics, 18(5), 862-876.

Chappell, P. R. (2014). The climate and weather of Taranaki. 2nd edition, NIWA Science and Technology Series, 64.

Clark, P. U., & Mix, A. C. (2002). Ice sheets and sea level of the Last Glacial Maximum. Quaternary Science Reviews, 21(1), 1-7.

Clarkson, B. D. (1986). Vegetation of Egmont National Park, New Zealand (No. 5). Balogh Scientific Books.

Cole, J. W. (1990). Structural control and origin of volcanism in the Taupo volcanic zone, New Zealand. Bulletin of Volcanology, 52(6), 445-459.

Cole, J. W., & Lewis, K. B. (1981). Evolution of the Taupo-Hikurangi subduction system. Tectonophysics, 72(1-2), 1-21.

Coulter, J. D. (1976) Weather in Egmont National Park. In: Fullarton, J. H. (ed.) Egmont National Park Handbook. 3rd ed. New Plymouth, Egmont National Park Board. Pp. 51-55.

Cowie, J. D. (1964). Aokautere ash in the Manawatu district, New Zealand. New Zealand Journal of Geology and Geophysics, 7(1), 67-77.

Cronin, S. J., Hedley, M. J., Neall, V. E., & Smith, R. G. (1998). Agronomic impact of tephra fallout from the 1995 and 1996 Ruapehu Volcano eruptions, New Zealand. Environmental Geology, 34(1), 21-30.

Cronin, S. J., Stewart, R. B., Neall, V. E., Platz, T., & Gaylord, D. (2003). The AD1040 to present Maero Eruptive Period of Egmont Volcano, Taranaki, New Zealand. Geol Soc NZ Misc Publ A, 116, 43.

Darby, D. J., Hodgkinson, K. M., & Blick, G. H. (2000). Geodetic measurement of deformation in the Taupo Volcanic Zone, New Zealand: the north Taupo network revisited. New Zealand Journal of Geology and Geophysics, 43(2), 157-170.

Dartevelle, S., Ernst, G. G., Stix, J., & Bernard, A. (2002). Origin of the Mount Pinatubo climactic eruption cloud: Implications for volcanic hazards and atmospheric impacts. Geology, 30(7), 663-666.

De Boer, J. Z., & Sanders, D. T. (2002). Volcanoes in human history: the far-reaching effects of major eruptions. Princeton University Press.

DeMets, C., Gordon, R. G., Argus, D. F., & Stein, S. (1990). Current plate motions. Geophysical Journal International, 101(2), 425-478.

DeMets, C., Gordon, R. G., Argus, D. F., & Stein, S. (1994). Effect of recent revisions to the geomagnetic reversal time scale on estimates of current plate motions. Geophysical Research Letters, 21(20), 2191-2194.

Druce AP (1966) Tree-ring dating of recent volcanic ash and lapilli, Mt Egmont. New Zealand Journal of Botany 4, 3-41.

Druitt, T. H., & Kokelaar, B. P. (Eds.). (2002). The eruption of Soufrière Hills volcano, Montserrat, from 1995 to 1999. Geological Society of London.

Eden, D. N., Froggatt, P. C., Trustrum, N. A., & Page, M. J. (1993). A multiple-source Holocene tephra sequence from Lake Tutira, Hawke's Bay, New Zealand. New Zealand Journal of Geology and Geophysics, 36(2), 233-242.

Eden, D. N., & Froggatt, P. C. (1996). A 6500-year-old history of tephra deposition recorded in the sediments of Lake Tutira, eastern North Island, New Zealand. Quaternary International, 34, 55-64.

Eggins, S. M. (1993). Origin and differentiation of picritic arc magmas, Ambae (Aoba), Vanuatu. Contributions to Mineralogy and Petrology, 114(1), 79-100.

Fergusson, G. J., Rafter, T. A. (1957) N.Z. 14C age measurements - 3. N.Z. Journal of Science and Technology, 38 (7), 732-49.

Fonterra (2014). In: http://www.fonterra.com/nz/en

Franks, A. M. (1984). Soils of Eltham county and the tephrochronology of central Taranaki: a thesis presented in partial fulfilment of the requirements for the degree of Doctor of Philosophy in Soil Science, Massey University, New Zealand.

Franks, A., Neall, V. E., & Pollock, J. (1991). Soils of Eltham County, North Island, New Zealand. DSIR Land Resources Scientific Report No. 14. Lower Hutt, New Zealand. DSIR Land Resources.

Gaillard, J. (2006). Traditional societies in the face of natural hazards: the 1991 Mt. Pinatubo eruption and the Aetas of the Philippines. International Journal of Mass Emergencies and Disasters, 24(1), 5.

Garcia-Aristizabal, A., Selva, J., & Fujita, E. (2013). Integration of stochastic models for long-term eruption forecasting into a Bayesian event tree scheme: a basis method to estimate the probability of volcanic unrest. Bulletin of Volcanology, 75(2), 1-13.

Gaylord, D. R., & Neall, V. E. (2012). Subedifice collapse of an andesitic stratovolcano: The Maitahi Formation, Taranaki Peninsula, New Zealand. Geological Society of America Bulletin, 124(1-2), 181-199.

Gill, J. B. (1981). Geophysical Setting of Volcanism at Convergent Plate Boundaries. In Orogenic Andesites and Plate Tectonics (pp. 44-63). Springer Berlin Heidelberg.

Gow, A. J. (1968). Petrographic and petrochemical studies of Mt Egmont andesites. New Zealand Journal of Geology and Geophysics, 11(1), 166-190.

Graham, I. J., Cole, J. W., Briggs, R. M., Gamble, J. A., & Smith, I. E. M. (1995). Petrology and petrogenesis of volcanic rocks from the Taupo Volcanic Zone: a review. Journal of Volcanology and Geothermal Research, 68(1), 59-87.

Grant-Taylor, T. L. (1964). Volcanic history of western Taranaki. New Zealand Journal of Geology and Geophysics, 7(1), 78-86.

Grant-Taylor, T. L., & Rafter, T. A. (1963). New Zealand natural radiocarbon measurements IV. American Journal of Science.

Grant-Taylor, T. L., & Rafter, T. A. (1971). New Zealand radiocarbon age measurements—6. New Zealand Journal of Geology and Geophysics, 14(2), 364-402.

Grange, L. I., & Taylor, N. H. (1933). Report on soil surveys for 1932-33. NZ Department of Scientific and Industrial Research, Annual Report 1932–33.

Green, R. M., Bebbington, M. S., Cronin, S. J., & Jones, G. (2013). Geochemical precursors for eruption repose length. Geophysical Journal International, 193(2), 855-873.

Gruender, K., Stewart, R. B., & Foley, S. (2010). Xenoliths from the sub-volcanic lithosphere of Mt Taranaki, New Zealand. Journal of Volcanology and Geothermal research, 190(1), 192-202.

Hansell, A. L., Horwell, C. J., & Oppenheimer, C. (2006). The health hazards of volcanoes and geothermal areas. Occupational and Environmental Medicine, 63(2), 149-156.

Hatherton, T. (1969). The geophysical significance of calc-alkaline andesites in New Zealand. New Zealand Journal of Geology and Geophysics, 12(2-3), 436-459.

Hellstrom, J., McCulloch, M., & Stone, J. (1998). A detailed 31,000-year record of climate and vegetation change, from the isotope geochemistry of two New Zealand speleothems. Quaternary Research, 50(2), 167-178.

Henrys, S., Reyners, M., & Bibby, H. (2003). Exploring the plate boundary structure of the North Island, New Zealand. Eos, Transactions American Geophysical Union, 84(31), 289-295.

Hewitt, A. E. (1992). Soil classification in New Zealand-Legacy and lessons. Soil Research, 30(6), 843-854.

Ho, C. H. (1990). Bayesian analysis of volcanic eruptions. Journal of Volcanology and Geothermal Research, 43(1-4), 91-98.

Ho, C. H. (1991). Nonhomogeneous Poisson model for volcanic eruptions. Mathematical Geology, 23(2), 167-173.

Holt, W. E., & Haines, A. J. (1995). The kinematics of northern South Island, New Zealand, determined from geologic strain rates. Journal of Geophysical Research: Solid Earth, 100(B9), 17991-18010.

Horrocks, M., Augustinus, P., Deng, Y., Shane, P., & Andersson, S. (2005). Holocene vegetation, environment, and tephra recorded from Lake Pupuke, Auckland, New Zealand. New Zealand Journal of Geology and Geophysics, 48(1), 85-94.

Horwell, C. J., & Baxter, P. J. (2006). The respiratory health hazards of volcanic ash: a review for volcanic risk mitigation. Bulletin of Volcanology, 69, 1-24.

Houghton, B. F., Wilson, C. J. N., McWilliams, M. O., Lanphere, M. A., Weaver, S. D., Briggs, R. M., & Pringle, M. S. (1995). Chronology and dynamics of a large

silicic magmatic system: central Taupo Volcanic Zone, New Zealand. Geology, 23(1), 13-16.

Jaquet, O., & Carniel, R. (2006). Estimation of volcanic hazards using geostatistical models. Statistics in volcanology. IAVCEI Publications, (1), 89-104.

Jenkins, S., Magill, C., McAneney, J., & Blong, R. (2012). Regional ash fall hazard I: a probabilistic assessment methodology. Bulletin of Volcanology, 74(7), 1699-1712.

Johnston, D. M., Houghton, B. F., Neall, V. E., Ronan, K. R., & Paton, D. (2000). Impacts of the 1945 and 1995–1996 Ruapehu eruptions, New Zealand: an example of increasing societal vulnerability. Geological Society of America Bulletin, 112(5), 720-726.

Jousset, P., Pallister, J., Boichu, M., Buongiorno, M. F., Budisantoso, A., Costa, F., Andreastuti, S., Prata, F., Schneider, D., Clarisse, L., & Humaida, H. (2012). The 2010 explosive eruption of Java's Merapi volcano—a '100-year'event. Journal of Volcanology and Geothermal Research, 241, 121-135.

Jouzel, J., Barkov, N. I., Barnola, J. M., Bender, M., Chappellaz, J., Genthon, C., Kotlyakov, V. M., Lorius, C., Petit, J. R., Raynaud, D., & Raisbeck, G. (1993). Vostok ice cores: extending the climatic records over the penultimate glacial period. Nature, 364(6436), 407-412.

Karig, D. E. (1970). Kermadec arc—New Zealand tectonic confluence. New Zealand Journal of Geology and Geophysics, 13(1), 21-29.

King, P. R., & Thrasher, G. P. (1992). Post-Eocene development of the Taranaki Basin, New Zealand: convergent overprint of a passive margin. Geology and Geophysics of Continental Margins, 53, 93-118.

King, P. R., & Thrasher, G. P. (1996). Cretaceous Cenozoic geology and petroleum systems of the Taranaki Basin, New Zealand (Vol. 2). Institute of Geological & Nuclear Sciences.

Klein, F. W. (1982). Patterns of historical eruptions at Hawaiian volcanoes. Journal of Volcanology and Geothermal Research, 12(1), 1-35.

Knox, G. J. (1982). Taranaki Basin, structural style and tectonic setting. New Zealand Journal of Geology and Geophysics, 25(2), 125-140.

Lees, C. M., & Neall, V. E. (1993). Vegetation response to volcanic eruptions on Egmont Volcano, New Zealand, during the last 1500 years. Journal of the Royal Society of New Zealand, 23(2), 91-127.

Lowe, D. J. (1986). Controls on the rates of weathering and clay mineral genesis in airfall tephras: a review and New Zealand case study. Rates of Chemical Weathering of Rocks and Minerals, 265-330.

Lowe, D. J. (1988a). Stratigraphy, age, composition, and correlation of late Quaternary tephras interbedded with organic sediments in Waikato lakes, North Island, New Zealand. New Zealand Journal of Geology and Geophysics, 31(2), 125-165.

Lowe, D. J. (1988b). Late Quaternary volcanism in New Zealand: towards an integrated record using distal airfall tephras in lakes and bogs. Journal of Quaternary Science, 3(2), 111-120.

Lowe, D. J. (1990). Tephra studies in New Zealand: an historical review. Journal of the Royal Society of New Zealand, 20(1), 119-150.

Lowe, D. J., Newnham, R. M., & Ward, C. M. (1999). Stratigraphy and chronology of a 15 ka sequence of multi-sourced silicic tephras in a montane peat bog, eastern North Island, New Zealand. New Zealand Journal of Geology and Geophysics, 42(4), 565-579.

Lowe, D. J., Shane, P. A., Alloway, B. V., & Newnham, R. M. (2008). Fingerprints and age models for widespread New Zealand tephra marker beds erupted since 30,000 years ago: a framework for NZ-INTIMATE. Quaternary Science Reviews, 27(1), 95-126.

Lowe, D. J., Blaauw, M., Hogg, A. G., & Newnham, R. M. (2013). Ages of 24 widespread tephras erupted since 30,000 years ago in New Zealand, with re-evaluation of the timing and palaeoclimatic implications of the Lateglacial cool episode recorded at Kaipo bog. Quaternary Science Reviews, 74, 170-194.

Marshall, P. (1907). Distribution of the Igneous Rocks of New Zealand. Trans. Aust. Assoc. Adv. Sci, 11, 4.

Marzocchi, W., Sandri, L., & Selva, J. (2008). BET_EF: a probabilistic tool for long- and short-term eruption forecasting. Bulletin of Volcanology, 70(5), 623-632.

Marzocchi, W., & Bebbington, M. S. (2012). Probabilistic eruption forecasting at short and long time scales. Bulletin of Volcanology, 74(8), 1777-1805.

Mayewski, P. A., Rohling, E. E., Stager, J. C., Karlén, W., Maasch, K. A., Meeker, L. D., Meyerson, E. A., Gasse, F., van Kreveld, S., Holmgren, K., & Lee-Thorp, J., (2004). Holocene climate variability. Quaternary Research, 62(3), 243-255.

McGlone, M. S., Neall, V. E., & Pillans, B. J. (1984). Inaha terrace deposits: a late Quaternary terrestrial record in South Taranaki, New Zealand. New Zealand Journal of Geology and Geophysics, 27(1), 35-49.

McGlone, M. S., Neall, V. E., & Clarkson, B. D. (1988). The effect of recent volcanic events and climatic changes on the vegetation of Mt Egmont (Mt Taranaki), New Zealand. New Zealand Journal of Botany, 26(1), 123-144.

McGlone, M. S., Salinger, M. J., & Moar, N. T. (1993). Paleovegetation studies of New Zealand's climate since the last glacial maximum. In: Wright, H. E. Jr., Kutzbach, J. E., Webb, T., et al. (eds.). Global Climates since the Last Glacial Maximum, Universuty of Minnesota Press, pp 569.

McGlone, M. S., & Neall, V. E. (1994). The late Pleistocene and Holocene vegetation history of Taranaki, North Island, New Zealand. New Zealand Journal of Botany, 32(3), 251-269.

Mendoza-Rosas, A. T., & De la Cruz-Reyna, S. (2008). A statistical method linking geological and historical eruption time series for volcanic hazard estimations: applications to active polygenetic volcanoes. Journal of Volcanology and Geothermal Research, 176(2), 277-290.

Mix, A. C., Bard, E., & Schneider, R. (2001). Environmental processes of the ice age: land, oceans, glaciers (EPILOG). Quaternary Science Reviews, 20(4), 627-657.

Moebis, A., Cronin, S. J., Neall, V. E., & Smith, I. E. (2011). Unravelling a complex volcanic history from fine-grained, intricate Holocene ash sequences at the Tongariro Volcanic Centre, New Zealand. Quaternary International, 246(1), 352-363.

Molloy, C., Shane, P., & Augustinus, P. (2009). Eruption recurrence rates in a basaltic volcanic field based on tephra layers in maar sediments: implications for hazards in the Auckland volcanic field. Geological Society of America Bulletin, 121(11-12), 1666-1677.

Mortimer, N., Tulloch, A. J., & Ireland, T. R. (1997). Basement geology of Taranaki and Wanganui Basins, New Zealand. New Zealand Journal of Geology and Geophysics, 40(2), 223-236.

Muir, R. J., Bradshaw, J. D., Weaver, S. D., & Laird, M. G. (2000). The influence of basement structure on the evolution of the Taranaki Basin, New Zealand. Journal of the Geological Society, 157(6), 1179-1185.

Neall, V. E. (1972). Tephrochronology and tephrostratigraphy of western Taranaki (N108–109), New Zealand. New Zealand Journal of Geology and Geophysics, 15(4), 507-557.

Neall, V. E. (1975). Climate-controlled tephra redeposition on Pouakai ring plain, Taranaki, New Zealand. New Zealand Journal of Geology and Geophysics, 18(2), 317-326.

Neall, V. E. (1976). Lahars as major geological hazards. Bulletin of the International Association of Engineering Geology-Bulletin de l'Association Internationale de Géologie de l'Ingénieur, 13(1), 233-240.

Neall, V. E. (1977). Genesis and weathering of Andosols in Taranaki, New Zealand. Soil Science, 123(6), 400-408.

Neall, V. E. (1979). Geological Map of New Zealand 1: 50,000 Sheet P19, P20, & P21: New Plymouth, Egmont and Manaia. New Zealand Geological Survey, Department of Scientific and Industrial Research.

Neall, V. E. (1999). Stony River at the Blue Rata Reserve. Report to the Taranaki Regional Council, Taranaki, p 13.

Neall, V. E. (2003). The volcanic history of Taranaki. Institute of Natural Resources, Massey University.

Neall, V. E., & Jansen, H. S. (1984). Anomalous radiocarbon dates from Mt Egmont. Programme and Abstracts, Geological Society of New Zealand Conference. Geological Society of New Zealand Miscellaneous Publication 31A.

Neall, V. E., Stewart, R. B., & Smith, I. E. M. (1986). History and petrology of the Taranaki volcanoes. Royal Society of New Zealand Bulletin, 23, 251-263.

Neall, V. E., & Alloway, B. V. (1993). Volcanic hazards at Egmont volcano. Volcanic Hazards Working Group of the Scientific Advisory Committee, Ministry of Civil Defence.

Neall, V. E., & Alloway, B. V. (1995). Volcanic hazard map of Taranaki, 1:100,000. Department of Soil Science, Massey University, Occasional report 12.

Neall, V. E., & Alloway, B. E. (1996). Volcanic hazard map of Western Taranaki. Massey Uni Dep Soil Sci Occ Report, 12.

Neall, V. E., & Alloway, B. V. (2004). Quaternary Geological Map of Taranaki, 1: 100 000. Institute of Natural Resources, Massey University.

Newnham, R. M. (1990). Late Quaternary palynological investigations into the history of vegetation and climate in northern New Zealand. Doctoral dissertation, ResearchSpace, Auckland.

Newnham, R. M., & Lowe, D. J. (2000). Fine-resolution pollen record of late-glacial climate reversal from New Zealand. Geology, 28(8), 759-762.

Newnham, R. M., Eden, D. N., Lowe, D. J., & Hendy, C. H. (2003). Rerewhakaaitu Tephra, a land–sea marker for the Last Termination in New Zealand, with implications for global climate change. Quaternary Science Reviews, 22(2), 289-308.

Newnham, R., & Alloway, B. (2004). A terrestrial record of Last Interglacial climate preserved by voluminous debris avalanche inundation in Taranaki, New Zealand. Journal of Quaternary Science, 19(3), 299-314.

Newnham, R. M., Lowe, D. J., Giles, T., & Alloway, B. V. (2007). Vegetation and climate of Auckland, New Zealand, since ca. 32 000 cal yr ago: support for an extended LGM. Journal of Quaternary Science, 22(5), 517-534.

New Zealand Meteorological Service (1963). Summaries of radiosondedata. New Zealand Meteorological Service Miscellaneous Publication 119.

New Zealand's Oil and Gas Industry (2014). In: http://www.energystream.co.nz/

NIWA (2014). In: http://www.niwa.co.nz/climate/national-and-regional-climate-maps/taranaki

Nicol, A., Mazengarb, C., Chanier, F., Rait, G., Uruski, C., & Wallace, L. (2007). Tectonic evolution of the active Hikurangi subduction margin, New Zealand, since the Oligocene. Tectonics, 26(4).

Norris, R. J., & Cooper, A. F. (2007). The Alpine Fault, New Zealand: surface geology and field relationships. A Continental Plate Boundary: Tectonics at South Island, New Zealand, 157-175.

Oliver, W. R. B. (1931). An ancient maori oven on Mount Egmont. The Journal of the Polynesian Society, 40(2 (158), 73-80.

Palmer, J., & Bulte, G. (1991). Taranaki Basin, New Zealand. Active margin basins: AAPG Memoir, 52, 262-282.

Pardo, N., Cronin, S. J., Németh, K., Brenna, M., Schipper, C. I., Breard, E., White, J. D., Procter, J., Stewart, B., Agustín-Flores, J., & Moebis, A. (2014). Perils in distinguishing phreatic from phreatomagmatic ash; insights into the eruption mechanisms of the 6 August 2012 Mt. Tongariro eruption, New Zealand. Journal of Volcanology and Geothermal Research, 286, 397-414.

Parson, L. M., & Wright, I. C. (1996). The Lau-Havre-Taupo back-arc basin: A southward-propagating, multi-stage evolution from rifting to spreading. Tectonophysics, 263(1), 1-22.

Pilaar, W. F. H., & Wakefield, L. L. (1978). Structural and stratigraphic evolution of the Taranaki Basin, offshore North Island, New Zealand. Australian Petroleum Exploration Association Journal, 18, 93-101.

Pillans, B., McGlone, M., Palmer, A., Mildenhall, D., Alloway, B., & Berger, G. (1993). The Last Glacial Maximum in central and southern North Island, New Zealand: a paleoenvironmental reconstruction using the Kawakawa Tephra Formation as a chronostratigraphic marker. Palaeogeography, Palaeoclimatology, Palaeoecology, 101(3), 283-304.

Platz, T. (2007). Understanding aspects of andesitic dome-forming eruptions through the last 1000 yr of volcanism at Mt. Taranaki, New Zealand: a dissertation presented in partial fulfilment of the requirements for the degree of Doctor of Philosophy in Earth Science, Massey University, Palmerston North, New Zealand.

Platz, T., Cronin, S. J., Cashman, K. V., Stewart, R. B., & Smith, I. E. (2007a). Transition from effusive to explosive phases in andesite eruptions—A case-study from the AD1655 eruption of Mt. Taranaki, New Zealand. Journal of Volcanology and Geothermal Research, 161(1), 15-34.

Platz, T., Cronin, S. J., Smith, I. E., Turner, M. B., & Stewart, R. B. (2007b). Improving the reliability of microprobe-based analyses of andesitic glasses for tephra correlation. The Holocene, 17(5), 573-583.

Platz, T., Cronin, S. J., Procter, J. N., Neall, V. E., & Foley, S. F. (2012). Non-explosive, dome-forming eruptions at Mt. Taranaki, New Zealand. Geomorphology, 136(1), 15-30.

Plunkett, G., Coulter, S. E., Ponomareva, V. V., Blaauw, M., Klimaschewski, A., & Hammarlund, D. (2015). Distal tephrochronology in volcanic regions:

challenges and insights from Kamchatkan lake sediments. Global and Planetary Change, 134, 26-40.

Price, R. C., McCulloch, M. T., Smith, I. E. M., & Stewart, R. B. (1992). Pb-Nd-Sr isotopic compositions and trace element characteristics of young volcanic rocks from Egmont Volcano and comparisons with basalts and andesites from the Taupo Volcanic Zone, New Zealand. Geochimica et Cosmochimica Acta, 56(3), 941-953.

Price, R. C., Stewart, R. B., Woodhead, J. D., & Smith, I. E. M. (1999). Petrogenesis of high-K arc magmas: evidence from Egmont volcano, North Island, New Zealand. Journal of Petrology, 40(1), 167-197.

Price, R. C., Gamble, J. A., Smith, I. E., Stewart, R. B., Eggins, S., & Wright, I. C. (2005). An integrated model for the temporal evolution of andesites and rhyolites and crustal development in New Zealand's North Island. Journal of Volcanology and Geothermal Research, 140(1), 1-24.

Price, R. C., Smith, I. E., Stewart, R. B., Gamble, J. A., Gruender, K., & Maas, R. (2016). High-K andesite petrogenesis and crustal evolution: Evidence from mafic and ultramafic xenoliths, Egmont Volcano (Mt. Taranaki) and comparisons with Ruapehu Volcano, North Island, New Zealand. Geochimica et Cosmochimica Acta, 185, 328-357.

Procter, J. N., Cronin, S. J., & Zernack, A. V. (2009). Landscape and sedimentary response to catastrophic debris avalanches, western Taranaki, New Zealand. Sedimentary Geology, 220(3), 271-287.

Procter, J. N., Cronin, S. J., Fuller, I. C., Sheridan, M., Neall, V. E., & Keys, H. (2010). Lahar hazard assessment using Titan2D for an alluvial fan with rapidly changing geomorphology: Whangaehu River, Mt. Ruapehu. Geomorphology, 116(1), 162-174.

Reilly, C., Nicol, A., Walsh, J. J., & Seebeck, H. (2015). Evolution of faulting and plate boundary deformation in the Southern Taranaki Basin, New Zealand. Tectonophysics, 651, 1-18.

Reyment, R. A. (1969). Statistical analysis of some volcanologic data regarded as series of point events. Pure and Applied Geophysics, 74(1), 57-77.

Reyners, M., Eberhart-Phillips, D., Stuart, G., & Nishimura, Y. (2006). Imaging subduction from the trench to 300 km depth beneath the central North Island, New Zealand, with Vp and Vp/Vs. Geophysical Journal International, 165(2), 565-583.

Reyners, M., Eberhart-Phillips, D., & Bannister, S. (2011). Tracking repeated subduction of the Hikurangi Plateau beneath New Zealand. Earth and Planetary Science Letters, 311(1), 165-171.

Rich, C.C., 1959. Late Cenozoic geology of the Manawatu valley, New Zealand. PhD thesis, Massey University, Palmerston North, 188pp.

Rowan, C. J., Roberts, A. P., & Rait, G. J. (2005). Relocation of the tectonic boundary between the Raukumara and Wairoa Domains (East Coast, North Island, New Zealand): implications for the rotation history of the Hikurangi margin. New Zealand Journal of Geology and Geophysics, 48(1), 185-196.

Rowland, J. V., Wilson, C. J., & Gravley, D. M. (2010). Spatial and temporal variations in magma-assisted rifting, Taupo Volcanic Zone, New Zealand. Journal of Volcanology and Geothermal Research, 190(1), 89-108.

Sandiford, A., Alloway, B., & Shane, P. (2001). A 28 000–6600 cal yr record of local and distal volcanism preserved in a paleolake, Auckland, New Zealand. New Zealand Journal of Geology and Geophysics, 44(2), 323-336.

Saucedo, R., Macías, J. L., Gavilanes, J. C., Arce, J. L., Komorowski, J. C., Gardner, J. E., & Valdez-Moreno, G. (2010). Eyewitness, stratigraphy, chemistry, and eruptive dynamics of the 1913 Plinian eruption of Volcán de Colima, México. Journal of Volcanology and Geothermal Research, 191(3), 149-166.

Schaefer, J. M., Denton, G. H., Kaplan, M., Putnam, A., Finkel, R.C., Barrell, D. J., Andersen, B. G., Schwartz, R., Mackintosh, A., Chinn, T., & Schlüchter, C. (2009). High-frequency Holocene glacier fluctuations in New Zealand differ from the northern signature. Science, 324(5927), 622-625.

Shane, P. (2005). Towards a comprehensive distal andesitic tephrostratigraphic framework for New Zealand based on eruptions from Egmont volcano. Journal of Quaternary Science, 20(1), 45-57.

Shane, P., & Hoverd, J. (2002). Distal record of multi-sourced tephra in Onepoto Basin, Auckland, New Zealand: implications for volcanic chronology, frequency and hazards. Bulletin of Volcanology, 64(7), 441-454.

Sherburn, S., & White, R. S. (2005). Crustal seismicity in Taranaki, New Zealand using accurate hypocentres from a dense network. Geophysical Journal International, 162(2), 494-506.

Sherburn, S., & White, R. S. (2006). Tectonics of the Taranaki region, New Zealand: earthquake focal mechanisms and stress axes. New Zealand Journal of Geology and Geophysics, 49(2), 269-279.

Statistics New Zealand (2014). In: http://www.stats.govt.nz/

Stern, T. A., Stratford, W. R., & Salmon, M. L. (2006). Subduction evolution and mantle dynamics at a continental margin: Central North Island, New Zealand. Reviews of Geophysics, 44(4).

Stevens, N. F., Manville, V., & Heron, D. W. (2003). The sensitivity of a volcanic flow model to digital elevation model accuracy: experiments with digitised map contours and interferometric SAR at Ruapehu and Taranaki volcanoes, New Zealand. Journal of Volcanology and Geothermal Research, 119(1), 89-105.

Stewart, R. B., Neall, V. E., Pollok, J. A., & Syers, J. K. (1977). Parent material stratigraphy of an Egmont loam profile, Taranaki, New Zealand. Soil Research, 15(3), 177-190.

Stewart, R. B., & Neall, V. E. (1984). Chronology of palaeoclimatic change at the end of the last glaciation. Nature 311, 47 - 48.

Stewart, R. B., Price, R. C., & Smith, I. E. M. (1996). Evolution of high-K arc magma, Egmont volcano, Taranaki, New Zealand: evidence from mineral chemistry. Journal of Volcanology and Geothermal Research, 74(3), 275-295.

Stewart, C., Johnston, D. M., Leonard, G. S., Horwell, C. J., Thordarson, T., & Cronin, S. J. (2006). Contamination of water supplies by volcanic ashfall: a literature review and simple impact modelling. Journal of Volcanology and Geothermal Research, 158(3), 296-306.

Striewski, B., Shulmeister, J., Augustinus, P. C., & Soderholm, J. (2013). Late Holocene climate variability from Lake Pupuke maar, Auckland, New Zealand. Quaternary Science Reviews, 77, 46-54.

Sutherland, R., Toy, V. G., Townend, J., Cox, S. C., Eccles, J. D., Faulkner, D. R., Prior, D. J., Norris, R. J., Mariani, E., Boulton, C. and Carpenter, B. M. (2012). Drilling reveals fluid control on architecture and rupture of the Alpine fault, New Zealand. Geology, 40(12), 1143-1146.

Taranaki Catchment Commission (1980). Lake Rotokare water management plan. Unpublished report, Taranaki Catchment Commission, Stratford.

Taranaki Regional Council (2014). In: http://www.trc.govt.nz/

Taylor, N. H. (1954) Soils of the North Island of New Zealand (with map of ash showers). N.Z. Soil Bureau Bulletin, 5.

Thompson, C. S. (1981). The climate and weather of the Taranaki region. Ministry of Transport, New Zealand Meteorological Service, Miscellaneous Publication, 115(9).

Tinkler, R. J. (2013). A high resolution record of late quaternary climatic and environmental change in Taranaki, New Zealand: a thesis presented in partial fulfilment of the requirements for the degree of Doctor of Philosophy in Earth Science at Massey University, Palmerston North, New Zealand.

Tonkin, P. J. (1970). The soils of the southeastern sector of Egmont National Park. Earth Science Journal, 4 (1), 36-57.

Topping, W. W. (1972). The Burrell Lapilli Eruptives, Mount Egmont. N.Z. Journal of Geology and Geophysics, 15 (3), 476-90.

Townsend, T. (1998). Paleoseismology of the Waverley Fault Zone and implications for earthquake hazard in South Taranaki, New Zealand. New Zealand Journal of Geology and Geophysics, 41(4), 467-474.

Townsend, D., Vonk, A., & Kamp, P. J. J. (2008). Geology of the Taranaki Area, QMAP 1: 250000 Geological Map. GNS Science, Lower Hutt, New Zealand, 86.

Turner, M. B. (2008). Eruption cycles and magmatic processes at a reawakening volcano, Mt. Taranaki, New Zealand: a thesis presented in partial fulfilment of the requirements for the degree of Doctor of Philosophy in Earth Science at Massey University, Palmerston North, New Zealand.

Turner, M. B., Cronin, S. J., Bebbington, M. S., & Platz, T. (2008a). Developing probabilistic eruption forecasts for dormant volcanoes: a case study from Mt Taranaki, New Zealand. Bulletin of Volcanology, 70(4), 507-515.

Turner, M. B., Cronin, S. J., Stewart, R. B., Bebbington, M., & Smith, I. E. (2008b). Using titanomagnetite textures to elucidate volcanic eruption histories. Geology, 36(1), 31-34.

Turner, M. B., Cronin, S. J., Smith, I. E., Stewart, R. B., & Neall, V. E. (2008c). Eruption episodes and magma recharge events in andesitic systems: Mt Taranaki, New Zealand. Journal of Volcanology and Geothermal Research, 177(4), 1063-1076.

Turner, M. B., Bebbington, M. S., Cronin, S. J., & Stewart, R. B. (2009). Merging eruption datasets: building an integrated Holocene eruptive record for Mt Taranaki, New Zealand. Bulletin of Volcanology, 71(8), 903-918.

Turner, M. B., Cronin, S. J., Bebbington, M. S., Smith, I. E., & Stewart, R. B. (2011a). Integrating records of explosive and effusive activity from proximal and distal sequences: Mt. Taranaki, New Zealand. Quaternary International, 246(1), 364-373.

Turner, M. B., Cronin, S. J., Bebbington, M. S., Smith, I. E., & Stewart, R. B. (2011b). Relating magma composition to eruption variability at andesitic volcanoes: A case study from Mount Taranaki, New Zealand. Geological Society of America Bulletin, 123(9-10), 2005-2015.

Vandergoes, M. J., Hogg, A. G., Lowe, D. J., Newnham, R. M., Denton, G. H., Southon, J., Barrell, D. J., Wilson, C. J., McGlone, M. S., Allan, A. S., & Almond, P. C. (2013). A revised age for the Kawakawa/Oruanui tephra, a key marker for the Last Glacial Maximum in New Zealand. Quaternary Science Reviews, 74, 195-201.

Van Dissen, R., & Yeats, R. S. (1991). Hope fault, Jordan thrust, and uplift of the seaward Kaikoura Range, New Zealand. Geology, 19(4), 393-396.

Vucetich, C. G., & Howorth, R. (1976). Proposed definition of the Kawakawa Tephra, the c. 20 000-years-BP marker horizon in the New Zealand region. New Zealand Journal of Geology and Geophysics, 19(1), 43-50.

Walcott, R. I. (1978). Present tectonics and late Cenozoic evolution of New Zealand. Geophysical Journal International, 52(1), 137-164.

Wallace, R. C. (1987). Mineralogy of the Tokomaru silt loam and the occurrence of cristobalite and tridymite in selected North Island soils. Unpublished PhD thesis, Massey University, Palmerston North, New Zealand.

Wallace, L. M., Beavan, J., McCaffrey, R., & Darby, D. (2004). Subduction zone coupling and tectonic block rotations in the North Island, New Zealand. Journal of Geophysical Research: Solid Earth, 109(B12).

Wallace, L. M., Beavan, J., Bannister, S., & Williams, C. (2012). Simultaneous long-term and short-term slow slip events at the Hikurangi subduction margin, New Zealand: Implications for processes that control slow slip event occurrence, duration, and migration. Journal of Geophysical Research: Solid Earth, 117(B11).

Wellman, H. W. (1962). Holocene of the North Island of New Zealand: a coastal reconnaissance. Transactions of the Royal Society of New Zealand, Geology, 5, 29-99.

Wells, B. (1878). The History of Taranaki: A Standard Work on the History of the Province. Edmondson & Avery.

Wang, T., & Bebbington, M. (2012). Estimating the likelihood of an eruption from a volcano with missing onsets in its record. Journal of Volcanology and Geothermal Research, 243, 14-23.

Whelley, P. L., Newhall, C. G., & Bradley, K. E. (2015). The frequency of explosive volcanic eruptions in Southeast Asia. Bulletin of Volcanology, 77(1), 1-11.

Whitehead, S. J. (1976). Granulometric studies on selected tephra eruptions, North Island, New Zealand. Unpublished Honours Dissertation, lodged in the Library, Massey University, Palmerston North, New Zealand.

Wickman, F. E. (1966). Repose period patterns of volcanoes. I. Volcanic eruptions regarded as random phenomena. Arkiv for Mineralogi och Geologi, 4(4), 291.

Williams, P. W., King, D. N. T., Zhao, J. X., & Collerson, K. D. (2004). Speleothem master chronologies: combined Holocene 18O and 13C records from the North Island of New Zealand and their palaeoenvironmental interpretation. The Holocene, 14(2), 194-208.

Williams, P. W., Neil, H. L., & Zhao, J. X. (2010). Age frequency distribution and revised stable isotope curves for New Zealand speleothems: palaeoclimatic implications. International Journal of Speleology, 39(2), 5.

Wilmshurst, J. M., Eden, D. N., & Froggatt, P. C. (1999). Late Holocene forest disturbance in Gisborne, New Zealand: a comparison of terrestrial and marine pollen records. New Zealand Journal of Botany, 37(3), 523-540.

Wilson, C. J. N., Rogan, A. M., Smith, I. E. M., Northey, D. J., Nairn, I. A., & Houghton, B. F. (1984). Caldera volcanoes of the Taupo volcanic zone, New Zealand. Journal of Geophysical Research: Solid Earth, 89(B10), 8463-8484.

Wilson, C. J. N., Houghton, B. F., McWilliams, M. O., Lanphere, M. A., Weaver, S. D., & Briggs, R. M. (1995). Volcanic and structural evolution of Taupo Volcanic Zone, New Zealand: a review. Journal of Volcanology and Geothermal Research, 68(1), 1-28.

Wilson, C. J. N., Gravley, D. M., Leonard, G. S., & Rowland, J. V. (2009). Volcanism in the central Taupo Volcanic Zone, New Zealand: tempo, styles and controls. Studies in Volcanology: The Legacy of George Walker. Special Publications of IAVCEI, 2, 225-247.

Wilson, T. M., Cole, J. W., Stewart, C., Cronin, S. J., & Johnston, D. M. (2011). Ash storms: impacts of wind-remobilised volcanic ash on rural communities and agriculture following the 1991 Hudson eruption, southern Patagonia, Chile. Bulletin of Volcanology, 73(3), 223-239.

Witham, C. S., Oppenheimer, C., & Horwell, C. J. (2005). Volcanic ash-leachates: a review and recommendations for sampling methods. Journal of Volcanology and Geothermal Research, 141(3), 299-326.

Yokoyama, Y., Lambeck, K., De Deckker, P., Johnston, P., & Fifield, L. K. (2000). Timing of the Last Glacial Maximum from observed sea-level minima. Nature, 406(6797), 713-716.

Zernack, A. V., Procter, J. N., & Cronin, S. J. (2009). Sedimentary signatures of cyclic growth and destruction of stratovolcanoes: a case study from Mt. Taranaki, New Zealand. Sedimentary Geology, 220(3), 288-305.

Zernack, A. V., Cronin, S. J., Neall, V. E., & Procter, J. N. (2011a). A medial to distal volcaniclastic record of an andesite stratovolcano: detailed stratigraphy of the ring-plain succession of south-west Taranaki, New Zealand. International Journal of Earth Sciences, 100(8), 1937-1966.

Zernack, A. V., Price, R. C., Smith, I. E., Cronin, S. J., & Stewart, R. B. (2011b). Temporal evolution of a high-K andesitic magmatic system: Taranaki volcano, New Zealand. Journal of Petrology, egr064.

Zernack, A. V., Cronin, S. J., Bebbington, M. S., Price, R. C., Smith, I. E., Stewart, R. B., & Procter, J. N. (2012). Forecasting catastrophic stratovolcano collapse: a model based on Mount Taranaki, New Zealand. Geology, 40(11), 983-986.

Chapter 2

Methodology

This chapter outlines the methodologies used in this study and identifies and discusses possible limitations of those methods.

2.1 Field study

2.1.1 Field sampling and core processing

Sediment cores were collected during three field expeditions in 2013 and 2014 (Table 2.1). In peatland sites a hydraulic percussion coring system (Fig. 2.1), and at lake sites a hand-operated Livingston piston corer operated from a raft were used for sediment core extraction (Fig. 2.2). The hydraulic percussion coring system consisted of a 1.20 m-long steel core-barrel including a screw-on core-cutter (6 cm in length) and a core-head (14 cm in length) to which various extension rods were attached. The corer is pushed vertically downwards incrementally by one metre and within the core-barrel, a 1 m-long and 6 cm-wide polyvinyl chloride (PVC)-liner collects the penetrated sediments. Due to the corer construction, the first core collected has a total length of 1.06 m, while following cores are of 1-metre length, with 0.94 m of sediment recovered within the PVC-liner and 6 cm within the core-cutter (Fig. 2.1). The steel core-barrel was pushed into the peaty ground using a petrol-driven percussion hammer, and a hydraulic jack was used for extraction. At each peat bog, two sediment cores from two different locations (Fig. 1.9) were extracted to account for local variability in deposition and to provide an overall higher-resolution record. At Midhirst Swamp, deep penetration of sediments was hindered by a thick horizon of large logs, which may indicate a buried forest at this site.

The hand-operated Livingston piston corer contained a 1 m-long and 3.5 cm-width PVC-liner (except R3, see below) with a core-piston at the lower end and the barrel capped by a core-head (Fig. 2.2). The unit was lowered from a floating platform with a succession of 1 m-long extension rods. To protect the corer from unexpected movements caused by water currents and to help evenly and vertically penetrate the lake floor sediments, a steel core-barrel surrounded the PVC-liner. The raft was fixed with ropes to three sides of the lake to provide position stability during coring. Three cores from adjacent sites were extracted from Lake Richmond (Fig. 1.9.) to account for local variability in deposition and to provide an overall higher-resolution record. The PVC-liners of the third Lake Richmond core (R3) were of variable lengths. These were 1.95 m, 1.31 m, 1.48 m, 1.32 m, 1.03 m, and 1.01 m, in sequence.

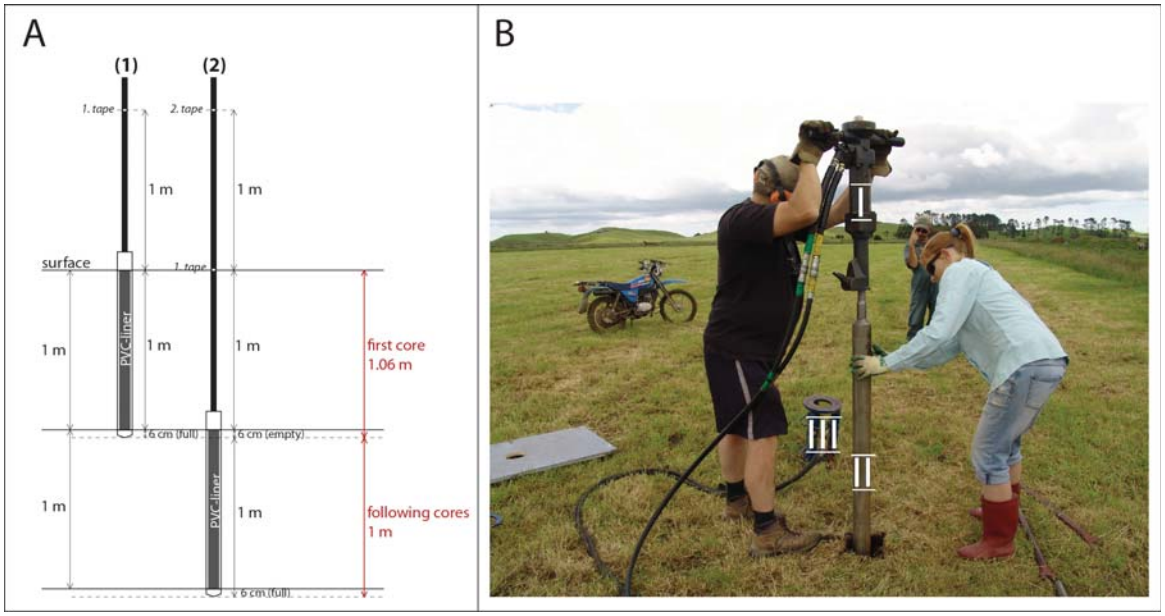

Figure 2. 1 *(A) Illustration of the coring procedure at peat sites, using a percussion coring system. Note (1) that the first core extracted has a total length of 1.06 m, (2) while following cores are of 1-metre lengths with 0.94 m of sediment within the PVC-liner and 6 cm within the core-cutter. (B) Shows the hydraulic percussion coring system used in the field (identified by the Roman numerals in white I, II & III): (I) petrol-driven percussion hammer, (II) steel core-barrel with inserted 1 m-long PVC-liner, and (III) hydraulic jack.*

Table 2. 1 *Field expeditions and recovered sediment cores during this study.*

Coring Location	ID	Coring date (day/month/year)	GPS coordinates	Core length (m)
Midhirst Swamp	M	16/12/2013	S39.28141/E174.29953	4
Tariki Swamp	T1	17-18/12/2013	S39.21578/E174.30089	9
	T2		S39.21452/E174.30473	10
Ngaere Swamp	N1	18-19/12/2013	S39.41066/E174.34425	10
	N2		S39.41513/E174.37073	11
Eltham Swamp	E1	27-28/01/2014	S39.43336/E174.33786	11
	E2		S39.45679/E174.32251	12
Lake Umutekai (swamp site)	U	28/01/2014	S39.08604/E174.13606	9
Lake Richmond	R1	29/01/2014	S39.12243/E174.24001	6
	R2		S39.12261/E174.24031	5
	R3	17/07/2014	S39.12228/E174.23994	8

Note: Core length (penetrated coring depth) differs from the sediment lengths recovered (refer to 2.1.2).

Figure 2. 2 *(A) Shows the raft and the equipment used for coring the lake sediments. (B) Illustrates the jack, which was required to lift Livingston piston-corer from the lake bottom with technician David Feek. The lake shown in both images is Lake Richmond, which was first cored during this study. (C) Diagram from Woodward and Sloss (2013) showing the piston corer components similar to that used during this study, and its coring operation with (1) the corer positioned above the sediment surface and (2-3) subsequently pushed into the soft sediments, while simultaneously keeping the core-cable tight so as to create suction until the desired depth has been penetrated, (4) the corer extracted with the sediments.*

2.1.2 Core shortening

Sediment disturbance, sediment loss, and core shortening during core sampling are all potentially significant issues during coring. These problems are often not addressed in past coring studies and therefore how the core reflects *in-situ* sediment conditions is often not discussed. Accounting correctly for sampling-related modification of sediments is crucial to subsequent depth-related analyses including depth-profiles and sedimentation-rate calculations. The removal of least-disturbed sediment relies strongly upon the sampling method and on the characteristics of the sediments involved. Collecting multiple cores from each location helps understand core-shortening patterns and build more appropriate composite records.

Overall, the main feature observed in all cores recovered during this study was that the cored length of collected sediments was often shorter than the penetration length of the core tube. This can be attributed to sediment shortening, a common process during any type of sediment extraction (e.g., Lebel et al., 1982; Blomqvist, 1985, 1991; Crusius and Anderson, 1991; Morton and White, 1997; Skinner and McCave, 2003; Morton et al., 2005). The shortening is likely a combined result of varying proportions of sediment thinning, bypassing, and compaction. Sediment thinning is caused by friction between the sediment and the liner of the corer, when the partially filled corer begins to exercise pressure just below the mouth of the tube. This depresses and stretches strata immediately below the corer-mouth until they are finally cut and enter the corer-tube. Each layer is normally represented, but depending on their competencies, they may be varying degrees thinner than *in-situ* (e.g., Piggot, 1941; Emery and Dietz, 1941; Nevissi et al., 1989; Glew et al. 2001). Lateral displacement of sediments below the core barrel, or at the cutting edges of the barrel, can contribute to full or partial bypass of sediments and therefore to their total loss from the collected strata (Blomqvist, 1991; Buckley et al., 1994; Morton et al., 2005). This is mainly recognised in density-diverse sequences, where horizons of high-density sediments drive low-density sediments aside as the core barrel penetrates deeper levels. Core shortening is also attributed to physical compaction of peat/sediment, along with air and water content loss. According to Parker and Sills (1990) and Morton and White (1997), core shortening may be variable, reflecting

sediment diversity, or show a systematic increase in the shortening with depth (Fig. 2.3).

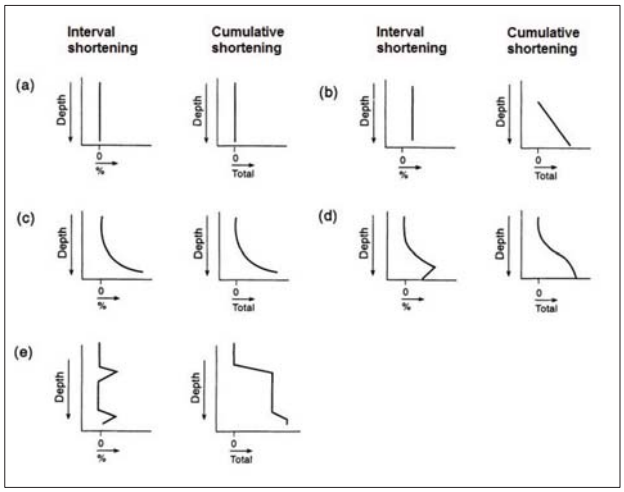

Figure 2. 3 *Diagram from Morton and White (1997) showing core shortening patterns in unconsolidated sediments: (a) no shortening (very rare), (b) uniform shortening (rare), (c) systematic increased shortening (common), (d+e) mixed pattern shortening (very common).*

In the current study, especially in the Tariki Swamp, large tree branches or roots were occasionally encountered. Some sites also contained alternating loam-, mud-, and peat-horizons with differing density and competence. Thus, variable patterns of shortening were observed in this study (Fig. 2.4). Adjusting the entire core lengths by applying a linear correction factor is inappropriate, so here a test was made where each core interval was corrected to the known length of core drive. The adjustment equation used, simplified from Morton and White (1997), is:

$$D_{adj} = D(P/L),$$

where D is the measured depth of the stratigraphic contact in the core barrel, P is the total core-barrel penetration depth, and L is the recovered sediment length.

This is only applicable to core intervals that have small shortening percentages, as at Lake Richmond, where the shortenings are mainly less than 25% (Fig. 2.4). In rare cases where there is a >50% shortening or shortenings are most likely the result of

sediment loss, stretching core intervals to their original penetration lengths would lead to erroneous results (e.g., a 1 cm thick tephra layer would double or more in thickness). For example, the 6-7 m core interval of the Lake Richmond core-3 (R3) shows a ~60% shortening (Fig. 2.4), probably due to a soft peat horizon, sandwiched between firm lake sediments above, and a firm mineral-rich unit below. Age estimations of tephra layers near such horizon must be treated with caution.

Testing of the shortening factor showed that most variations in interpolated tephra ages lie within the normal standard deviation error of the radiocarbon determinations and the sedimentation rates only varied between 0.01 – 0.2 mm/yr. Therefore, during this study no shortening correction factors were applied and depths are reported as shortening depths (s.depth).

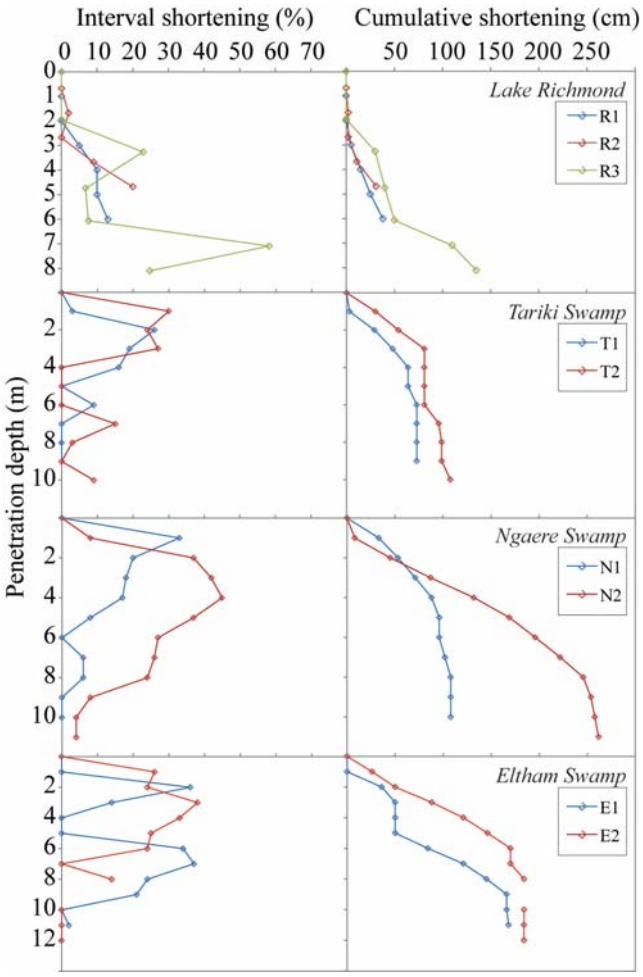

Figure 2. 4 *Interval (%) and cumulative (cm) shortening of individual sediment cores taken during this study.*

2.2 Laboratory procedures

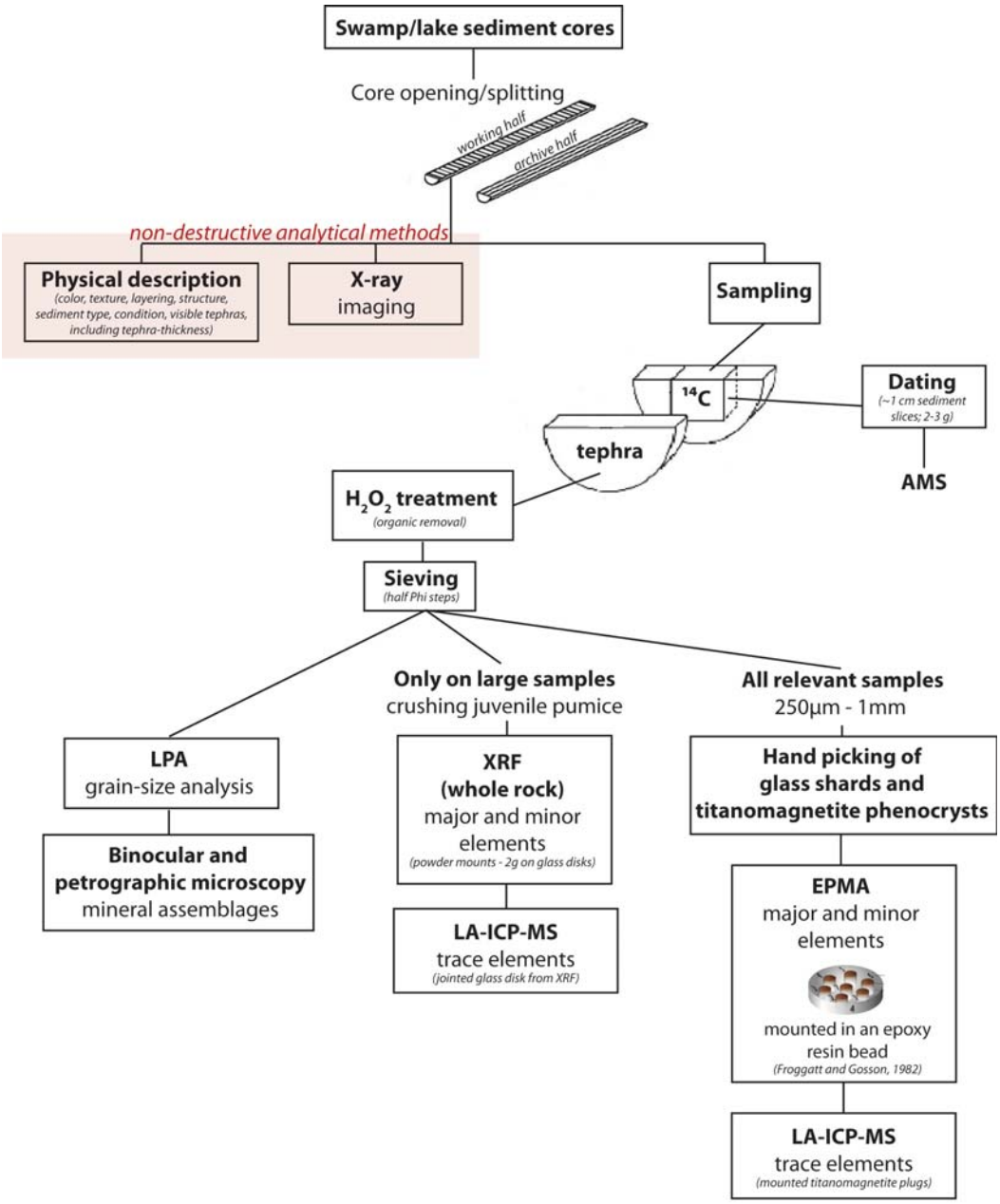

Figure 2. 5 *Flowchart illustrating the methodology that was implemented in this study. Abbreviations for analytical methods as follows: AMS = Accelerator Mass Spectrometry, X-ray = X-radiography, XRD = X-ray diffraction, LPA = Laser Particle Analyser, EPMA = Electron Probe Micro–Analyser, XRF = X-ray fluorescence spectrometry, LA-ICP-MS = laser ablation–inductively coupled plasma–mass spectrometry.*

2.2.1 Sample preparation

All cores were split longitudinally into archived and working halves. The latter were examined visually and imaged using an X-Ray camera at the Institute of Veterinary Animal and Biomedical Sciences, Massey University. The X-radiographs were of high enough resolution and contrast so that tephra/mineral units <0.1 mm in thickness and/or horizons of dispersed tephra/mineral contents could be distinguished from the organic-dominated host sediment/peat. X-Ray images for each core are provided in the electronic appendices. Once located, visually or on the X-Ray images, potential tephra/mineral layers were sampled by slicing those from the core sediments as close as possible to the observed boundaries. The sampled materials were treated with hydrogen peroxide to remove organic matter, and subsequently sieved and examined microscopically (Fig. 2.5). Most of the samples recovered were confirmed to be primary tephras by optical microscopy (well-sorted and angular grain-size characteristics, absence of detrital material) and subsequent geochemical analyses (degree of geochemical homogeneity). A small number of tephras were determined to be 'reworked', as they occur dispersed within non-volcaniclastic horizons (i.e., silt loam, mud) and/or have diverse physical and geochemical characteristics. Tephra samples with enough material of grain-size >63 μm were sub-sampled for geochemical analyses. The nomenclature used for tephras was based on its coring site and tephra number in stratigraphic/age order. For example N1-5 = Ngaere Swamp core1, 5th youngest tephra layer. The same approach was used in composite cores, but the core-number was excluded (see Section 2.2.2). ID-numbers labelled on the individual tephra samples initially taken (sample bags) differ from this nomenclature and need to be checked against the spreadsheet provided within the electronic appendices if used in future studies.

2.2.2 Composite cores

Cores extracted from adjacent locations at the same site differed slightly. In order to obtain the most-complete record possible a composite stratigraphy was established for each site. In the case of Lake Richmond, three cores (R1-R3) were correlated based on stratigraphic position, physical appearance of prominent tephra layers, repetition of

distinctive tephra sequences, and distinct lithological changes. Geochemical correlation was deemed unnecessary, since the three cores recovered were very similar in their physical appearance. For the swamp cores (N1-N2, E1-E2, T1-T2), geochemical evidence from the tephra layers was also required to establish a robust correlation and a composite stratigraphy. Key tephra correlations are given in Chapter 3.

2.2.3 Radiocarbon dating

For radiocarbon dating, slices of bulk sediment up to 1 cm-thick (2-3 g) were collected at regular intervals throughout the cores, normally located immediate below prominent tephra layers, or from horizons where distinct lithological changes occurred. These were analysed by accelerator mass spectrometry (AMS) at the Waikato Radiocarbon Dating Laboratory, Hamilton, New Zealand. All radiocarbon ages are reported as calibrated ages (cal yr BP) with 1σ errors. Calibration was performed using OxCal Version 4.2 (Bronk Ramsey, 2013) and the Southern Hemisphere SHCal13 atmospheric calibration curve (Hogg et al., 2013). A summary of all radiocarbon ages is given in Chapter 3, Table 3.1. and Appendix 1.

In general, radiocarbon dating is based on the occurrence of three natural carbon isotopes: the stable isotopes ^{12}C and ^{13}C, and the unstable (radioactive) isotope ^{14}C. In comparison to both stable isotopes, ^{14}C is extremely rare: 99% of all carbon exists in the form of ^{12}C, 1% as ^{13}C and only 10^{-10} % as ^{14}C. ^{14}C is formed in the upper atmosphere by cosmic rays acting on nitrogen. After organic carbon is rapidly oxidised to CO_2, ^{14}C is taken up by organisms to build up their biomass with the amount accumulated being related to the atmospheric ^{14}C content. After death, ^{14}C accumulation ceases and the ^{14}C decreases by radioactive beta decay at a known constant rate ($ß^-$-decay to ^{14}N; 'old' Libby half-life: $t_{1/2}$ = 5568 yr; Arnold and Libby, 1950 and 'corrected' Oxford half-life: $t_{1/2}$ = 5731 yr; Godwin, 1962).

Therefore, based on the remaining proportion of ^{14}C in a sample, the time elapsed since death, can be calculated. Based on the half-life of radiocarbon, and analytical quality, the dating range extends from the present back to about 55 ka ago. Radiocarbon ages are

reported in years before present (BP), whereby 'Present' is defined as 1950 (Wagner, 1995).

Notwithstanding these principles, radiocarbon dating is affected by significant variations from the parameters explained above, notably:

Atmospheric fluctuations of ^{14}C

By comparing independent dating techniques such as tree ring dating (dendrochronology) to conventional radiocarbon dating methods (Mahaney, 2000) it was shown that there are systematic fluctuations in the amount of ^{14}C in the atmosphere. These were likely caused by cosmic-ray flux variations in the solar system, sunspot activity, or variations in the Earth's magnetic field, over time. Further, the variation in the CO_2 exchange rate between the atmosphere and the ocean, as well as the impact of humans on the atmosphere can cause short-term ^{14}C fluctuations in the atmosphere (e.g., Damon et al., 1978; Bard et al., 1997; Beer, 2000; Scott et al., 2007). Hence, radiocarbon years are not consistent with true calendar years. In order to convert radiocarbon years to calendar years, a calibration must be applied. Standard calibration curves are available for each hemisphere, based on tree-ring, varve and independently dated coral records (McCormack et al., 2004; Reimer et al., 2013; Hogg et al., 2013).

Fractionation of ^{14}C

Organisms generally do not maintain a constant ratio of radiocarbon isotopes throughout their life cycles due to the range of chemical reactions involved in natural biochemical processes. For example, different plant species use varying photosynthetic pathways and therefore fractionate the carbon isotopes differently. Conventional radiocarbon ages are typically corrected for isotope fractionation by normalizing to = -25‰ Pee Dee Belemnite (PDB) or Vienna PDB (VPDB). The international PDB standard carbonate refers to the Cretaceous belemnite formation at Peedee in South Carolina, USA (Keith et al., 1964; Aitken, 1990). This nomenclature has recently been changed to VPDB (Coplen, 1994).

Reservoir effect

There is also variation in the radiocarbon isotopic ratio across different large bodies, or areas, of Earth's surface that have similar response to the presence of CO_2, for example, oceans, lakes, ice/glaciers, forests. One of the most commonly referenced reservoir effects concerns the ocean and lake environments (e.g., Stuiver et al., 1998; Reimer, 2000, 2001). Oceans and some lakes are not in equilibrium with the atmosphere, due to incomplete mixing of CO_2 with surface waters. Fresh water can be very influenced by a catchment geology contacting calcium carbonate (e.g., limestone), with this "old-carbon" causing a shift in the isotope ration and thus apparent radiocarbon age. Reservoir corrections for the world's oceans can be found at the *Marine Reservoir Correction Database* online (CALIB, 2014). Defining the reservoir effect for lakes is more complex and must be determined empirically, ideally against other independent age estimates.

2.2.4 Grain-size

Grain-size analyses were carried out to determine whether tephra layers possessed the well-sorted characteristics of tephra fall units and to understand possible variations in eruption size/eruption column height and wind dispersal direction between units. Tephra samples were wet-sieved through a 63 μm sieve to separate the very fine ash fraction from grains large enough to analyse. The <63 μm (very fine ash) fraction was analysed using a Horiba Partica LA 950V2 Laser Particle Analyser (LPA), at Massey University, while the >63 μm fraction was dry-sieved at half-ϕ intervals. The logarithmic phi (ϕ) scale is a modification of the Wentworth scale after Krumbein and Aberdeen (1937). The two sets of data were combined for analysis using Gradistat Version 8.0 (Blott, 2010). The grain-size data set is available in the electronic appendices.

2.2.5 X-ray diffraction (XRD)

Sediment cores that showed diverse inorganic units were dried and crushed/disaggregated to a fine powder, before being analysed by X-ray diffraction (XRD) using a GBC MMA (mini material analyser) operated with Co K-alpha

radiation, at Massey University. Scans were performed from 3° – 60° 2σ at 2°/min 2σ. The data is summarised within the electronic appendices.

2.2.6 Electron probe micro-analyzer (EPMA)

Major and minor element analysis of single glass shards and titanomagnetite phenocrysts were carried out using a JEOL JXA-840a electron microprobe equipped with a Princeton Gamma Tech Prism 2000 Si(Li) energy dispersive spectrometer (EDS) at Massey University. An accelerating voltage of 15 kV, an 800 pA beam-current, and a 100 seconds acquisition time were used. These conditions along with a defocused beam of 10-20 μm in diameter were used for glass shard analyses to minimize Na-loss. A focused beam (approximately 2-3 μm diameter) was used for titanomagnetite analyses. Titanomagnetite phenocrysts and/or those within glomerocrysts were analysed mainly from the 250-500 μm size fraction. The energy spectrum at the analytical conditions was regularly calibrated using ASTIMEX albite and olivine standards for glass shards, and spinel and rutile for the titanomagnetites. Glass is the most commonly analysed phase for tephrochronology, but titanomagnetite has also been successfully used at many andesitic and rhyolitic volcanoes as discussed in other parts of this thesis. At least 10 analyses per phase per tephra were obtained. Major elements are expressed as oxides and reported in weight per cent (wt%). Glass shard data were normalised to 100% and titanomagnetite data corrected for iron following the procedure of Carmichael (1966). The titanomagnetite and glass shard data (mean ±S.D.) is given in Appendix 2 and 3 (lake-and-peat tephras) and Appendix 5 and 6 (proximal-and-medial tephra units) and as complete data set within the electronic appendices.

Detection limits for electron microprobe analysis are given in Table 2.2. As part of an inter-laboratory EMPA project (64 participating laboratories), basaltic glass was repeatedly analysed and deviations from its accepted composition are listed in Table 2.2 (R. Sims, unpubl. data).

Table 2. 2 *Detection limits of element oxides measured at the electron microprobe (University of Auckland) including the deviation from a reference glass composition.*

	1σ (wt%)	3σ (wt%)	International Round-Robin Inter-lab EPMA project (64 participating labs): Difference to reference values of refused basaltic glass composition
SiO_2	0.11	0.32	-0.18
TiO_2	0.08	0.23	0.12
Al_2O_3	0.06	0.18	-0.05
FeO	0.07	0.20	-0.04
MnO	0.07	0.20	-0.01
MgO	0.07	0.21	0.17
CaO	0.04	0.13	-0.02
Na_2O	0.11	0.32	0.05
K_2O	0.03	0.10	0.02
P_2O_5	0.07	0.20	0.01
SO_3	0.06	0.19	
Cl	0.03	0.08	
Cr_2O_3	0.06	0.17	
NiO	0.10	0.30	

2.2.6.1 Limitations

EPMA is an effective analysis tool, but there are several factors that may influence measured compositions. Some of these include:

1) Instrument failure and instrumental drift, which is monitored for and corrected by repeated standard analyses.
2) Poor polish qualities can lead to a lack of sufficient points to analyse or coating of grains, which can be addressed by re-polishing and re-analysis.
3) Small grains, microlites/impurities within grains and incorrect positioning of the beam, which are usually noted in the analytical totals.
4) Andesitic glass shards are often highly vesicular, and the vesicles are thin-walled, so it can be difficult to find an area >10-20 μm to analyse by a defocused beam.

5) Syn- and post-eruption crystallisation of nanolitic Fe-oxides and microlitic plagioclase often lead to fine-scale heterogeneity of andesitic glass (Best, 2003; Platz et al., 2007). These are difficult to avoid in the large-scale beam areas required for glass analysis.
6) Andesitic tephra hydrates and alters rapidly to allophanic clay and other phases (Lowe, 1986; Alloway et al., 1995), which can influence the major element composition of volcanic glass, resulting in low SiO_2 and high Al_2O_3 contents (Neall, 1977).
7) Exsolved titanomagnetite grains (trellises of ilmenite and magnetite) can lead to heterogeneous titanomagnetite compositions (Turner et al., 2008a).

To avoid most of the listed issues above, EPMA analysis were constantly monitored and the resulting data carefully screened. To minimise the effects of glass and titanomagnetite contamination back-scatter electron imaging and the removal of hybrid data points using the technique of Platz et al. (2007) were applied.

2.2.6.2 Geochemical outliers

Some compositions clearly stood out from the main geochemical groupings and could not be accounted for by the analytical issues described above. These could reflect any of the following factors:

Chemical variation in the magmatic system

1) Assimilation/contamination of xenocrystic or autocrystic titanomagnetites from geochemically different magma reservoirs, the conduit wall, or dome structure as magmas rises and explosively erupts (Stewart et al., 1998).
2) Magma mingling and/or mixing as described by Turner et al. (2008b) based on contrasting titanomagnetite morphologies and Ti-variations in the same eruptive unit. Magma mingling is also observed as banded pumices and zoned phenocrysts (Platz et al., 2007) and in whole-rock major and trace analyses of the general Mt. Taranaki rock suite (Price et al., 1999).

3) Magma recharge episodes may inject geochemically different titanomagnetites from a deeper and hotter magma source to an already existing magma body. Turner et al. (2008b) propose that the upper andesitic magma system of Mt. Taranaki was recharged by magma with similar properties creating cryptic magma mixing results.
4) Titanomagnetite exsolution caused by variations in pressure/temperature and oxidation states in the upper conduit/dome system as described by Turner et al. (2008a). They suggest that magmas that ascended slowly have heterogeneous titanomagnetite compositions while those of magmas that ascended quickly are more homogeneous. Exsolution lamellae are enriched in TiO_2 (up to 30 wt%) compared to the titanomagnetite host (3-6 wt% TiO_2). The scale and degree of the oxidation-induced exsolution may vary greatly (e.g., Haggerty, 1991) and may not always be visible under the electron microprobe leading to heterogeneous compositions.

Contamination due to post-depositional processes and during sample handling

1) Post-depositional processes may cause mixing of tephras and addition of other material from wind or water-borne sources (e.g., Green and Lowe, 1985; de Fontaine et al., 2007). Mixing may also be caused by bioturbation of plant roots and aquatic animals (e.g., Payne and Gehrels, 2010; Payne et al., 2005).
2) Low sedimentation rates and short-intervals between eruptions may also result in co-deposition of tephra with little or no intervening sediment. Very thin, closely spaced tephras are also difficult to extract without cross-contamination.
3) Contamination of samples may also occur during drilling, as material is dragged along the inner walls of the core-liner. Radiocarbon/tephra samples were thus only sampled from the centre of the sediment cores, without material contacting the liner.

2.2.7 X-ray fluorescence (XRF) spectrometry and laser ablation–inductively coupled plasma–mass spectrometry (LA-ICP-MS)

For coarse tephra units, 2 g of cleaned pumice clasts were hand-picked and powdered in a tungsten carbide ring mill. These powders were fused into disks following the Norrish fusion method (Harvey et al., 1973) with a dilution factor of 1:3 (the sample was ignited with a 12:22 lithium tetraborate:lithium metaborate flux). For major elements, the disks were analysed in triplicate using a Panalytical Axios 1 kW wavelength dispersive X-ray fluorescence (XRF) spectrometer at the University of Auckland. Twenty-eight international standards analysed in triplicate were used for calibration. U.S. Geological Survey glass standard BCR-2G was analysed to provide an independent assessment of accuracy and precision. The results for BCR-2G are consistent with the reference values within <1% for elements used in this study, and replicate analyses indicate an analytical precision (2σ) of <1% (mostly ~0.7%).

Whole-lapilli trace element analyses were determined by laser ablation–inductively coupled plasma–mass spectrometry (LA-ICP-MS) at the Australian National University, using an Excimer LPX120 laser and Agilent 7500 series mass spectrometer. The analyses were performed on the XRF discs, following the procedure of Eggins et al. (1998). The NIST 610 glass, analysed after every 15 unknowns, was used as the primary calibration standard, while BCR-2G was analysed to provide an independent assessment of accuracy and precision. The results for BCR-2G are consistent with the reference values within 10% for elements used in this study (mostly ~5%), and replicate analyses indicate an analytical precision (2σ) of ~5% for most elements, except for Zr, Cr, Ni, and Pb (>10%). The data is summarised in Appendix 7.

In addition, spot LA-ICP-MS analyses were performed on titanomagnetite grains mounted, cut and polished in epoxy resin. A ~80 μm spot was used for these analyses, with grains typically >250 μm wide. Ten grains per sample were analysed. A 15 s pre-ablation phase was followed by 30 s of counting, and a 10 s post-ablation phase. The NIST 610 glass was analysed as a standard after each of 10 analyses to monitor drift. EMPA major element data were used to cross-check the LA-ICP-MS results. Replicate

analyses indicate an analytical precision (2σ) of ~5% for all elements. The data is summarised in Appendix 8.

2.3 References

Aitken, M. J. (2014). Science-based dating in archaeology. Routledge.

Alloway, B., Neall, V. E., & Vucetich, C. G. (1995). Late Quaternary (post 28,000 year BP) tephrostratigraphy of northeast and central Taranaki, New Zealand. Journal of the Royal Society of New Zealand, 25(4), 385-458.

Arnold, J. R., & Libby, W. F. (1950). Radiocarbon Dates (September 1, 1950). University of Chicago, Institute for Nuclear Studies.

Bard, E., Raisbeck, G. M., Yiou, F., & Jouzel, J. (1997). Solar modulation of cosmogenic nuclide production over the last millennium: comparison between 14 C and 10 Be records. Earth and Planetary Science Letters, 150(3), 453-462.

Beer, J. (2000). Long-term indirect indices of solar variability. Space Science Reviews, 94(1-2), 53-66.

Best, M.G. (2003). Igneous and metamorphic petrology. Blackwell Science.

Blomqvist, S. (1985). Reliability of core sampling of soft bottom sediment—an in situ study. Sedimentology, 32(4), 605-612.

Blomqvist, S. (1991). Quantitative sampling of soft-bottom sediments: problems and solutions. Marine Ecology Progress Series, 72(3), 295-304.

Blott, S.J. (2010). GRADISTAT ver. 8.0: A grain size distribution and statistics package for the analysis of unconsolidated sediments by sieving or laser granulometer. Kenneth Pye Associates Ltd, UK.

Bronk Ramsey, C. (2013). OxCal 4.2. Web Interface Build, (78).

Buckley, D. E., MacKinnon, W. G., Cranston, R. E., & Christian, H. A. (1994). Problems with piston core sampling: Mechanical and geochemical diagnosis. Marine Geology, 117(1), 95-106.

CALIB (2014) http://calib.qub.ac.uk/marine/

Carmichael, I. S. E. (1966). Iron-titanium oxides of salic volcanic rocks and their associated ferromagnesian silicates. Contributions to Mineralogy and Petrology, 14(1), 36-64.

Coplen, T. B. (1994) Reporting of stable hydrogen, carbon and oxygen isotope abundances. Pure and Applied Chemistry 66, 273-76.

Crusius, J., & Anderson, R. F. (1991). Core compression and surficial sediment loss of lake sediments of high porosity caused by gravity coring. Limnology and Oceanography, 36(5), 1021-1030.

Damon, P. E., Lerman, J. C., & Long, A. (1978). Temporal fluctuations of atmospheric 14C: causal factors and implications. Annual Review of Earth and Planetary Sciences, 6, 457.

de Fontaine, C. S., Kaufman, D. S., Anderson, R. S., Werner, A., Waythomas, C. F., & Brown, T. A. (2007). Late Quaternary distal tephra-fall deposits in lacustrine sediments, Kenai Peninsula, Alaska. Quaternary Research, 68(1), 64-78.

Eggins, S. M., Rudnick, R. L., & McDonough, W. F. (1998). The composition of peridotites and their minerals: a laser-ablation ICP–MS study. Earth and Planetary Science Letters, 154(1), 53-71.

Emery, K. O., & Dietz, R. S. (1941). Gravity coring instrument and mechanics of sediment coring. Geological Society of America Bulletin, 52(10), 1685-1714.

Froggatt, P. C., & Gosson, G. J. (1982). Techniques for the preparation of tephra samples for mineral and chemical analysis and radiometric dating. Department of Geology, Victoria University of Wellington.

Glew, J. R., Smol, J. P., & Last, W. M. (2001). Sediment core collection and extrusion. In: Last, W. M., Smol, J.P. (eds). Tracking environmental change using lake sediments. Springer Netherlands, pp. 73-105.

Green, J. D., & Lowe, D. J. (1985). Stratigraphy and development of c. 17 000 year old Lake Maratoto, North Island, New Zealand, with some inferences about postglacial climatic change. New Zealand Journal of Geology and Geophysics, 28(4), 675-699.

Godwin, H. (1962). Half-life of radiocarbon. Nature, 195.

Haggerty, S. E. (1991). Oxide textures; a mini-atlas. Reviews in Mineralogy and Geochemistry, 25(1), 129-219.

Harvey, P. K., Taylor, D. M., Hendry, R. D., & Bancroft, F. (1973). An accurate fusion method for the analysis of rocks and chemically related materials by X-ray fluorescence spectrometry. X-Ray Spectrometry, 2(1), 33-44.

Hogg, A. G., Hua, Q., Blackwell, P. G., Niu, M., Buck, C. E., Guilderson, T. P., Heaton, T. J., Palmer, J. G., Reimer, P. J., Reimer, R. W., Turney, C. S. M., & Zimmerman, S. R. H. (2013). SHCal13 Southern Hemisphere calibration, 0–50,000 years cal BP. Radiocarbon, 55(4), 1889-1903.

Keith, M. L., Anderson, G. M., & Eichler, R. (1964). Carbon and oxygen isotopic composition of mollusk shells from marine and fresh-water environments. Geochimica et Cosmochimica Acta, 28(10-11), 1757-1786.

Krumbein, W. C., & Aberdeen, E. (1937). The sediments of Barataria Bay. Journal of Sedimentary Research, 7(1).

Lebel, J., Silverberg, N., & Sundby, B. (1982). Gravity core shortening and pore water chemical gradients. Deep Sea Research Part A. Oceanographic Research Papers, 29(11), 1365-1372.

Lowe, D. J. (1986). Controls on the rates of weathering and clay mineral genesis in airfall tephras: a review and New Zealand case study. In: Colam, S. M. & Dethier, D. P. (Eds.), Rates of chemical weathering of rocks and minerals, 265-330. Academic Press, Orlando.

Mahaney, W. C. (Ed.) (2000). Quaternary dating methods (Vol. 7). Elsevier.

McCormack, F. G., Hogg, A. G., Blackwell, P. G., Buck, C. E., Higham, T. F. G., & Reimer, P. J. (2004). SHCal04 Southern Hemisphere calibration, 0–1000 cal BP. Radiocarbon, 46, 1087-1092.

Morton, R. A., & White, W. A. (1997). Characteristics of and corrections for core shortening in unconsolidated sediments. Journal of Coastal Research, 761-769.

Morton, R. A., Bernier, J. C., Barras, J. A., & Ferina, N. F. (2005). Rapid subsidence and historical wetland loss in the Mississippi delta plain: likely causes and future implications. U. S. Geological Survey.

Neall, V. E. (1977). Genesis and weathering of Andosols in Taranaki, New Zealand. Soil Science, 123(6), 400-408.

Nevissi, A. E., Shott, G. J., & Crecelius, E. A. (1989). Comparison of two gravity coring devices for sedimentation rate measurement by 210Pb dating techniques. Hydrobiologia, 179(3), 261-269.

Parker, W. R., & Sills, G. C. (1990). Observation of corer penetration and sample entry during gravity coring. Marine Geological Research, 12(1), 101-107.

Payne, R. J., Kilfeather, A. A., van der Meer, J. J., & Blackford, J. J. (2005). Experiments on the taphonomy of tephra in peat. Suo, 147-156.

Payne, R., & Gehrels, M. (2010). The formation of tephra layers in peatlands: an experimental approach. Catena, 81(1), 12-23.

Piggot, C. S. (1941). Factors involved in submarine core sampling. Geological Society of America Bulletin, 52(10), 1513-1524.

Platz, T., Cronin, S. J., Smith, I. E., Turner, M. B., & Stewart, R. B. (2007). Improving the reliability of microprobe-based analyses of andesitic glasses for tephra correlation. The Holocene, 17(5), 573-583.

Price, R. C., Stewart, R. B., Woodhead, J. D., & Smith, I. E. M. (1999). Petrogenesis of high-K arc magmas: evidence from Egmont volcano, North Island, New Zealand. Journal of Petrology, 40(1), 167-197.

Reimer, P., & Reimer, R. (2000). Marine reservoir correction database. Radiocarbon, 40, 461-463.

Reimer, P. J., & Reimer, R. W. (2001). A marine reservoir correction database and on-line interface. Radiocarbon, 43(2), 461-464.

Reimer, P. J., Bard, E., Bayliss, A., Beck, J. W., Blackwell, P. G., Bronk Ramsey, C., Buck, C. E., Cheng, H., Edwards, R. L., Friedrich, M., Grootes, P. M., Guilderson, T. P., Haflidason, H., Hajdas, I., Hatté, C., Heaton, T. J., Hoffmann, D. L., Hogg, A. G., Hughen, K. A., Kaiser, K. F., Kromer, B., Manning, S. W., Niu, M., Reimer, R. W., Richards, D. A., Scott, E. M., Southon, J. R., Staff, R. A., Turney, C. S. M., & van der Plicht, J. (2013). IntCal13 and Marine13 radiocarbon age calibration curves 0 - 50,000 years cal BP. Radiocarbon 55(4), 1869-1887.

Scott, E. M., Cook, G. T., & Naysmith, P. (2007). Error and uncertainty in radiocarbon measurements. Radiocarbon, 49(2), 427-440.

Stewart, R. B., Price, R. C., & Smith, I. E. M. (1996). Evolution of high-K arc magma, Egmont volcano, Taranaki, New Zealand: evidence from mineral chemistry. Journal of Volcanology and Geothermal Research, 74(3), 275-295.

Turner, M. B., Cronin, S. J., Stewart, R. B., Bebbington, M., & Smith, I. E. (2008a). Using titanomagnetite textures to elucidate volcanic eruption histories. Geology, 36(1), 31-34.

Turner, M. B., Cronin, S. J., Smith, I. E., Stewart, R. B., & Neall, V. E. (2008b). Eruption episodes and magma recharge events in andesitic systems: Mt Taranaki, New Zealand. Journal of Volcanology and Geothermal Research, 177(4), 1063-1076.

Wagner, G. (1995). Altersbestimmung von jungen Gesteinen und Artefakten. Enke, Stuttgart, 277 pp.

Woodward, C. A., & Sloss, C. R. (2013). Coring and augering. Treatise on Geomorphology, 14, 119-137.

Skinner, L. C., & McCave, I. N. (2003). Analysis and modelling of gravity-and piston coring based on soil mechanics. Marine Geology, 199(1), 181-204.

Stuiver, M., Reimer, P. J., Braziunas, T. F. (1998). High-precision radiocarbon age calibration for terrestrial and marine samples. Radiocarbon, 40(3), 1127-51.

Chapter 3

Tephrostratigraphy of lake and peat sediment records from Mt. Taranaki, New Zealand

This chapter comprises a detailed description of the tephra records recovered from lakes and peatlands during this research and the method used to combine those to a composite 30,000-year long eruption history record. It also highlights on possible tephra deposition and preservation issues within single sites and affirms the utility of titanomagnetite phenocrysts as tephra discrimination and correlation tool.

3.1 Introduction

All of chapter 3 is contained within the manuscript: *A 30,000-year high-precision eruption history for the andesitic Mt. Taranaki, North Island, New Zealand* by M. Damaschke, S.J. Cronin, K.A. Holt, M.S. Bebbington, and A. Hogg, which has been published as a Research Paper in *Quaternary Research*. Its format has been altered to match the overall thesis. The contributions of each author are outlined below:

M. Damaschke: Principal investigator
Carried out: Field work
Laboratory work
Analytical work
Geochemical interpretation
Manuscript preparation and writing

S.J. Cronin: Chief Advisor
Aided the study by: Assistance in field work
Discussion of data and interpretations
Editing and discussion of the manuscript

K.A. Holt: Advisor
Aided the study by: Assistance in field work
Editing and discussion of the manuscript

M.S. Bebbington: Statistical advisor
Aided the study by: Creating age-depth models using statistical methods

A. Hogg: Principal of the Waikato Radiocarbon Dating Laboratory
Aided the study by: Radiocarbon dating

3.2 A 30,000-year high-precision eruption history for the andesitic Mt. Taranaki, North Island, New Zealand

Magret Damaschke[1], Shane J. Cronin[1,2], Katherine A. Holt[1], Mark S. Bebbington[1], Alan G. Hogg[3]

[1]*Institute of Agriculture and Environment, Massey University, Private Bag 11222, Palmerston North 4410*

[2]*School of Environment, University of Auckland, Private Bag 92019, Auckland 1142*

[3]*Radiocarbon Dating Laboratory, Waikato University, Private Bag 3105, Hamilton 3240*

3.2.1 Abstract

Tephra layers from 11 sediment cores were examined from a series of closely spaced lake and peat sites, which form an arc around the andesitic stratovolcano Mt. Taranaki, North Island, New Zealand. A new high-resolution composite tephra-deposition record was built, encompassing at least 228 tephra-producing eruptions over the last 30 cal ka BP and providing a basis for understanding variations in magnitude and frequency of explosive volcanism at a typical andesitic volcano. Inter-site correlation and geochemical fingerprinting of almost all tephra layers was achieved using electron microprobe-determined titanomagnetite phenocryst and volcanic glass shard compositions, in conjunction with precise age determination of the tephra layers based on continuous down-core radiocarbon dating. Compositional variation within these data allowed the overall eruption record to be divided into six individual tephra sequences: Tephra Sequence A (0.5 – 3 cal ka BP), B (3 – 4 cal ka BP), C (4 – 9.5 cal ka BP), D (9.5 – 14 cal ka BP), E (14 – 17.5 cal ka BP), and F (23.5 – 30 cal ka BP). This geochemical/stratigraphic division provides a broad basis for widening correlation to incomplete tephra sequences, with confident correlations to specific, distal Mt. Taranaki-derived tephra layers found as far as 270 km from the volcano. Furthermore,

this tephrostratigraphical record is one of the most continuous and detailed for an andesitic stratovolcano. It suggests two general patterns of magmatic evolution, characterised by intricate geochemical variations indicating a complex storage and plumbing system beneath the volcano.

Keywords: Mt. Taranaki; andesitic stratovolcano; tephrochronology; tephra; stratigraphy; titanomagnetite; volcanic glass chemistry; radiocarbon dating; peatland; volcanic hazard

3.2.2 Introduction

Tephra deposits in lake and peat bog environments are often well preserved, due to anoxic, reducing chemical conditions, coupled with effectively continuous accumulation of organic sediments over long time periods. Such preservation is of great value for reconstructing the explosive eruption history of nearby long-lived volcanoes. Such records provide insight into eruption frequency, magnitude, and style (e.g., Lowe, 1988a; Shane and Hoverd, 2002; Shane, 2005; Molloy et al., 2009; Plunkett et al., 2015) and offer the opportunity to determine the time-varying behaviour of complex magmatic systems (e.g., Gamble et al., 1999; Price et al., 1999; Bryant et al., 2003; Gertisser and Keller, 2003; Turner et al., 2011a). However, in order to create reliable volcanic histories, the vagaries of tephra deposition and preservation must be overcome. For instance, changes in the depositional environment, eruption dynamics, and/or variation in direction and intensity of syn-depositional winds, can result in variable accumulation and preservation of tephra over time at any one site (Molloy et al., 2009; Green et al., 2014). To overcome these issues, cores need to be collected at a number of sites around a source, covering as completely as possible the potential variations in tephra dispersal direction. Ideally, a closely spaced arc of sites around a volcano will best capture narrow tephra depositional lobes. Building a robust multiple-site tephra record provides a better understanding of the time-varying magmatic, volcanic and environmental processes, leading to more reliable hazard forecasts.

Mt. Taranaki, a 2518 m-high andesitic stratovolcano located in the Taranaki region, North Island, New Zealand, has erupted multiple times over the past >130 ka (Alloway et al., 2005), distributing ash across the surrounding landscape and at least as far north as the City of Auckland (c. 270 km; Sandiford et al., 2001; Shane, 2005). It is positioned in the middle of an economically significant region of New Zealand, hosting the only producing oil and gas fields, as well as ~25% of the country's dairy farming industry. Thus, Mt. Taranaki poses a considerable threat to New Zealand economically. It also has been dormant for more than a century (Platz et al., 2007), which contributes to an even higher vulnerability, since most people are unaware of the potential devastation of reawakening volcanoes (Gaillard, 2006).

Lake and peat sediment records preserving tephra layers from Mt. Taranaki have been collected during a number of previous studies at single or multiple sites (e.g., Newnham, 1990; Lees and Neall, 1993; McGlone and Neall, 1994; Turner et al., 2008c, 2009, 2011b). Of these, Turner et al., (2008c, 2009, 2011b) focused on obtaining high-resolution tephra records. These studies combined tephra records from Lake Umutekai, NNE of the volcano and Lake Rotokare, ESE of the volcano, together with on-cone stratigraphy to identify 138 eruptions spanning the last 10 ^{14}C ka BP (Turner et al., 2011b). Here we expand on past work, by adding data from four newly cored sites located in an NNE to ESE arc downwind of the prevailing wind directions of Mt. Taranaki (Drost et al., 2007). This new combined record provides a much more comprehensive coverage of the most likely tephra dispersal directions and doubles the length of the existing high-resolution tephrostratigraphy of this region, through generating a sequence covering the last ~30,000 cal yr BP. Geochemical and chronostratigraphic analysis was subsequently used to classify the eruption record into six individual tephra sequences which allow the subdivision of the eruptive history of Taranaki volcano into distinct separate phases.

The use of analyses of accessory minerals, such as titanomagnetite phenocrysts, to discriminate and correlate tephras has been successful in several previous studies (e.g., Kohn, 1970; Cronin et al., 1996; Shane, 1998, 2005; Turner et al., 2008b, 2009, 2011b; Marcaida et al., 2014). Not only are these mineral phases common in andesitic tephras

of Mt. Taranaki (Kohn and Neall, 1973), but also they are highly resistant to post-depositional weathering (Aomine and Wada, 1962), and are easily extractable from very small volumes of tephra by simple magnetic separation. Titanomagnetite compositions usually reflect to individual magmatic conditions (Buddington and Lindsley, 1964; Hill and Roeder, 1974; Frost and Lindsley, 1991; Toplis and Carroll, 1995) and thus can be used in a similar way to compositional fingerprinting of glass. The amount of Ti^{4+} substitution in the iron-oxide spinel structure and to a lesser extent Mg^{2+}, Al^{3+}, and Mn^{2+} (Ghiorso and Sack, 1991) allows geochemical discrimination between titanomagnetites from different magmas. Here we present 12 individual titanomagnetite compositional groups identified in the tephra record established during this study.

Furthermore, whole tephra sequences and/or individual tephra layers were linked to the known distal and proximal record, although precise correlation was often not achievable due to a lack of compositional data from proximal deposits and imprecision regarding chronology. Notably, due to excellent preservation conditions at many of the core sites, this new record reveals several tephra units that have not previously been recognised in exposed soil and cover bed sequences, or in proximal on-cone sequences.

3.2.3 Study sites

Peatlands and lakes occur in several areas on the lower portions of the volcanic ring-plain of Mt. Taranaki, where large debris avalanches and lahar deposits lap up against the deeply dissected and uplifted Tertiary sediments of the hill country to the east (Fig. 1.8). Rapid sediment deposition events from volcanic mass flows have altered or blocked existing stream systems, forming lakes and peatlands. One lake and three peat sites, located 20 to 30 km from Mt. Taranaki's summit, were selected due to their potential for preserving deep sequences of organic deposits and their positions within the known dispersal axis of mapped tephra falls (Alloway et al., 1995). From north to south, the study sites are Lake Richmond (LRi), Tariki Swamp (TS), Ngaere Swamp (NS), and Eltham Swamp (ES) (Fig. 1.8). Data from cores at Lake Umutekai (LU) and Lake Rotokare (LR), obtained by Turner (2008), were re-examined in the present study.

Lake Umutekai lies 25 km NNE of Mt. Taranaki's summit. It is a 0.02 km^2, shallow (<2 m) closed depression on a gently undulating volcaniclastic surface that is ≥170 ka old (Neall, 1979). The surrounding landscape was densely forested throughout the Holocene (McGlone and Neall, 1994). Lake Umutekai has been previously cored for a pollen-based vegetation and climate survey (Newnham, 1990) and more recently by Turner et al. (2008c, 2009, 2011b), who identified 104 tephra layers deposited between c. 1.5 to 10.5 cal ka BP.

Lake Richmond is located 25 km NE of Mt. Taranaki's summit. The lake, which lies within an N-S oriented valley, is interpreted here to have been formed by landslide-damming. It is drained to the north-east by the Mangaonaia Stream and fed by two unnamed streams from the south. The 0.03 km^2 lake, which has not been cored before, has a maximum water depth of 4 m.

Tariki Swamp is located 22 km ENE of Mt. Taranaki's summit. It is bordered by the Manganui River to the west and the anthropogenic Lake Ratapiko to the east. This small, peat-filled basin is abutted to the north by a massive debris avalanche deposit (Okawa Formation, 105 ka BP; Neall and Alloway, 2004). Alteration of drainage by the emplacement of this deposit is interpreted as the cause of peat formation. This peatland has not been successfully cored before and contains many fallen trees within parts of the sequence.

Eltham Swamp and Ngaere Swamp constitute large broad wetlands, which lie 28 km ESE of Mt. Taranaki's summit and are separated from each other by a low, east-west trending ridge of Tertiary mudstone. At 220 m, Ngaere Swamp is 10 m higher than Eltham Swamp. Both are peat-filled basins about 6 km long and 2 km wide. Eltham Swamp is drained by Mangimangi Stream to the south and by Mangawhero Stream to the west. Ngaere Swamp is drained to the north by Ngaere Stream, a tributary of Patea River. These peatlands formed in response to a series of lahar and debris avalanche deposits emplaced between 23-50 ^{14}C ka BP (McGlone and Neall, 1994; Neall and Alloway, 2004; Zernack et al., 2011). These deposits altered the local topography, provided shallow aquitards, and partially blocked the tributary valleys of the eastern hill

country, leading to peat accumulation. Eltham Swamp has been previously investigated by McGlone and Neall (1994) and Tinkler (2013), who undertook pollen-based palaeovegetation investigations. Pollen analyses of peat-cores from this peatland indicate that ~13 ^{14}C ka BP ago the region was mainly open grassland. Shortly after (~12.5 ^{14}C ka BP) there was a rapid transition to a forest-dominated landscape. Today, these peat sites are cleared of their original forest, drained and developed into pasture, which has caused the peatland to subside at least 3 m (McGlone and Neall, 1994).

Lake Rotokare lies approximately 34 km ESE of Mt. Taranaki's summit. This Y-shaped lake was formed by damming of an antecedent valley drainage system following a Holocene landslide (Taranaki Catchment Commission, 1980). It has an area of 0.25 km^2 and a maximum water depth of 12 m. Turner et al. (2009) identified 42 tephra layers dated between c. 0.5 to 7 cal ka BP within sediments of this lake.

3.2.4 Methods

3.2.4.1 Field sampling and core processing

Sediment cores were collected using a hydraulic percussion coring system (peat sites) and a hand-operated Livingston piston corer operated from a raft (lake sites). At each site, two to three closely-spaced cores were collected to check for local depositional variability and to provide an overall higher-resolution record through combining the individual core records to a 'composite' core for each site. All cores were split longitudinally into archived and working halves. The latter were examined visually and imaged using a large-format X-ray density-camera at the Institute of Veterinary Animal and Biomedical Sciences, Massey University. The radiographs allowed identification of tephra units <0.1 mm in thickness and horizons of dispersed tephra particles, which were otherwise difficult to detect by the naked eye. Once located, tephra layers were sampled, treated with hydrogen peroxide to remove organic material, and subsequently sieved and examined microscopically. Most of the mineral layers identified were confirmed to be primary tephras by optical microscopy (well-sorted and angular grain

size characteristics, absence of detrital material) and subsequent geochemical analyses (degree of geochemical homogeneity). A small number of tephras were determined to be 'reworked', as they occur dispersed within non-volcaniclastic horizons (i.e., silt loam, mud) and/or have diverse physical and geochemical characteristics. Tephra samples that yielded sufficient material were sub-sampled for chemical analysis. The nomenclature of individual tephra layers is based on coring site and tephra number in stratigraphic/age order. For example N1-5 = Ngaere Swamp core1, 5th youngest tephra layer. Tephra nomenclature for composite cores excludes the core-number (i.e., N-5).

3.2.4.2 Radiocarbon dating

Samples for radiocarbon age determination comprised slices of bulk sediment up to 1-cm-thick (2-3 g), which were collected at roughly regular intervals throughout the cores. Locations immediately below prominent tephra layers, or horizons where distinct lithological changes occurred, were targeted for sampling. Samples were submitted to the Waikato Radiocarbon Dating Laboratory, Hamilton, New Zealand for accelerator mass spectrometrometry (AMS) radiocarbon dating. All radiocarbon ages are shown in Table 3.1 and are here reported as calibrated ages (cal yr BP) with 1σ errors. Calibration was performed using OxCal Version 4.2 (Bronk Ramsey, 2013) and the Southern Hemisphere SHCal13 atmospheric calibration curve (Hogg et al., 2013). The original reports from the Waikato Radiocarbon Dating Laboratory are attached in Appendix 1.

Table 3. 1 *Radiocarbon ages acquired from lake and peat sediment cores recovered during this study.*

Sample	Lab ID	org. s.depth (cm)	comp. s.depth (cm)	^{14}C age (yr BP)[a]	Calibrated age (cal yr BP)[b]	Dating material[c]
Lake Richmond						
R3-A	Wk39860	39.5	36.5	539±20	524±10	ol
R3-B	Wk39861	126.5	118.5	1735±20	1609±46	ol
R3-C	Wk39862	162.5	167.5	2393±20	2376±45	ol
R1-D	Wk39863	210	210	3055±20	3207±59	ol
R3-E	Wk39864	247.5	260	3641±20	3907±44	ol
R3-F	Wk39865	284.5	303	3946±20	4339±51	ol
R3-G	Wk39866	346.5	370	4875±21	5553±48	ol
R3-H	Wk39867	377	404	6153±22	7002±72	ol
R1-I	Wk39868	464	465	7678±24	8429±34	ol
R3-J	Wk39869	460.5	522	9433±25	10,622±45	ol
R3-K	Wk39870	506.5	568	10,846±32	12,714±17	p
R3-L	Wk39871	608.5	670	12,494±35	14,587±180	p
Tariki Swamp						
T1-A	Wk39127	52	52	2038±26	1955±32	p
T1-C	Wk39128	134.5	134.5	2639±26	2726±52	p-os
T1-F	Wk39129	248	248	3262±26	3440±43	p
T2-C	Wk39135	132.5	248	3263±26	3441±43	os
T1-H	Wk39130	315.5	315.5	5372±28	6105±67	os
T1-I	Wk39131	430.5	430.5	10,184±39	11,789±118	p
T1-J	Wk39132	479.5	479.5	10,353±38	12,133±137	p
T1-L	Wk39133	622.5	635	13,105±50	15,646±126	p
T2-L	Wk39136	749	782.5	14,124±53	17,127±122	os
T1-N	Wk39134	716.5	782.5	14,130±60	17,136±129	os
T2-J	Wk39137	847	880.5	14,334±53	17,404±107	os
Ngaere Swamp						
N1-A	Wk39482	37.5	54.5	2449±25	2461±95	p
N1-C	Wk39483	137.5	199.5	4680±25	5395±52	p
N1-D	Wk39484	221	283	6069±29	6868±53	p
N1-E	Wk39485	273.5	335.5	6315±28	7204±46	p
N1-G	Wk39486	338.5	400.5	7331±29	8098±46	p
N1-I	Wk39487	441.5	503.5	8592±49	9527±37	p
N1-K	Wk39488	536	598	9434±37	10,621±57	p
N1-N	Wk39489	638	700	10,453±37	12,249±111	p
N1-P	Wk39490	689.5	751.5	11,131±40	12,949±71	p

Table 3. 1 *(Continued)*

Eltham Swamp						
E1-B	Wk41024	81.5	81.5	2248±20	2230±49	p
E2-A	Wk41025	50.5	140.5	3406±22	3606±43	p
E2-B	Wk41026	110.5	200.5	5658±26	6385±43	p
E2-C	Wk41027	210.5	300.5	7412±27	8194±70	p
E2-D	Wk41028	254.5	344.5	8728±27	9627±52	p
E2-E	Wk41029	330.5	420.5	9432±28	10,620±48	p
E2-F	Wk41030	428.5	518.5	10,390±33	12,198±118	p
E2-G	Wk41031	508	598	11,610±35	13,396±48	p
E2-H	Wk41032	588.5	678.5	12,763±38	15,152±84	os
E2-I	Wk41033	764.5	854.5	21,152±97	25,454±129	os
E2-J	Wk41034	893	983	23,294±125	27,507±110	os
E2-K	Wk41035	983.5	1073.5	25,663±166	29,807±269	os

[a] *Conventional age (±1σ) based on the Libby half-life of 5568 yr with correction for isotopic fractionation.*

[b] *Mean calibrated age (±1σ) using Oxcal v4.2.4 (Bronk Ramsey, 2013) and the SHCal13 atmospheric curve (Hogg et al., 2013); see Appendix 1 for calibrated age range*

[c] *p=peat, ol=organic-rich lake sediment, os=organic rich sediment (i.e., silt loam, mud), w=wood*

original shortened depth (org. s. depth), composite shortened depth (comp. s. depth)

3.2.4.3 Grain-size and geochemistry

Individual tephra samples were wet-sieved through a 63 μm sieve to separate the very fine ash fraction from grains large enough to analyse. The <63 μm (very fine ash) fraction was analysed using a Horiba Partica LA 950V2 laser particle analyser (LPA) at Massey University. The >63 μm fraction was dry-sieved at half-phi intervals. The logarithmic phi (ϕ) scale is a modification of the Wentworth scale after Krumbein and Aberdeen (1937). The two sets of data were combined for analysis using Gradistat Version 8.0 (Blott, 2010). Appendix 4 shows the bulk grain-size of tephra layers within the composite records.

Major and minor element analysis of single glass shards and titanomagnetite phenocrysts were carried out using a JEOL JXA-840a electron microprobe equipped with a Princeton Gamma Tech Prism 2000 Si(Li) energy dispersive spectrometer (EDS) at Massey University. An accelerating voltage of 15 kV, an 800 pA beam-current, and a 100 seconds acquisition time were used. These conditions along with a 10-20 μm defocused beam were used for glass shard analyses to minimize Na-migration. Syn- and post-eruption crystallisation of nanolitic Fe-oxides and microlitic plagioclase can often lead to fine-scale heterogeneity of the glass (Best, 2003). These are often difficult to avoid using a large diameter electron beam required for glass analysis. To minimise this effect, back-scatter electron imaging and the removal of hybrid data points using the technique of Platz et al. (2007) were applied. A focused beam (approximately 2-3 μm diameter) was used for the titanomagnetite analyses. Titanomagnetite phenocrysts and/or those within glomerocrysts were analysed mainly from the 250-500 μm size fraction. Exsolved titanomagnetite grains (showing trellises of ilmenite and magnetite) show naturally heterogeneous compositions and thus could be avoided using back-scatter electron imaging. The energy spectrum at the analytical conditions was regularly calibrated using a range of ASTIMEX standards appropriate to the compositions of phases analysed. At least 10 analyses of both glass and titanomagnetite were obtained for each tephra. Data points showing obvious contamination were excluded. Major elements are expressed as oxides and reported in weight per cent (wt%). Glass shard data were normalised to 100% and titanomagnetite data corrected for iron following the procedure of Carmichael (1966). The complete dataset is summarized in Appendix 2 and 3.

3.2.4.4 Depth information

Only a handful of studies address the issue of sediment disturbance during core sampling and therefore most do not question how well the core reflects in-situ sediment conditions. This is potentially important for subsequent depth-related analyses, including depth-profiles and accumulation rate calculations. Overall, the main feature observed in all cores recovered during this study was that the collected sediments were

often shorter than the sediment length penetrated by the core tube. This deficit can be attributed to sediment shortening, a combined result of sediment thinning, compaction, and bypassing, which are common processes during any type of sediment extraction (e.g.; Lebel et al., 1982; Blomqvist, 1985, 1991; Crusius and Anderson, 1991; Skinner and McCave, 2003). According to Parker and Sills (1990) and Morton and White (1997), core shortening is not uniformly distributed thought-out the depth of penetration. It is highly likely that a mixed pattern of core shortening occurs, especially if there are variations in sediment strength/coherence down the sequence. In the present study, individual core lengths show total percentages of shortening varying between <10 and 60 %. Hence, adjusting for the entire core lengths by applying a linear correction factor is unsuitable and may lead to erroneous results. In the course of this study, no correction factor was applied and depths are given as shortened depth (s.depth), as this is compatible with the spline-fitting approach to dating and the construction of composite cores described below.

3.2.5 Results

3.2.5.1 Age-depth models

Age-depth models for each sediment core (Fig. 3.1) were created using the calibrated radiocarbon age distributions as a function of s.depth (Table 3.1) and a piecewise cubic Hermite interpolating polynomial fit (Fritsch and Carlson, 1980). The polynomial fitting automatically corrects for the compaction. The tephra layers and other layers that are instantaneously deposited were subtracted (i.e., “event-free” depths) before fitting the polynomial. The core-depth function can be used to assess accumulation rates for each of the core sites and to estimate calendar ages for each tephra represented in the cores (ages are summarized in Appendix 4).

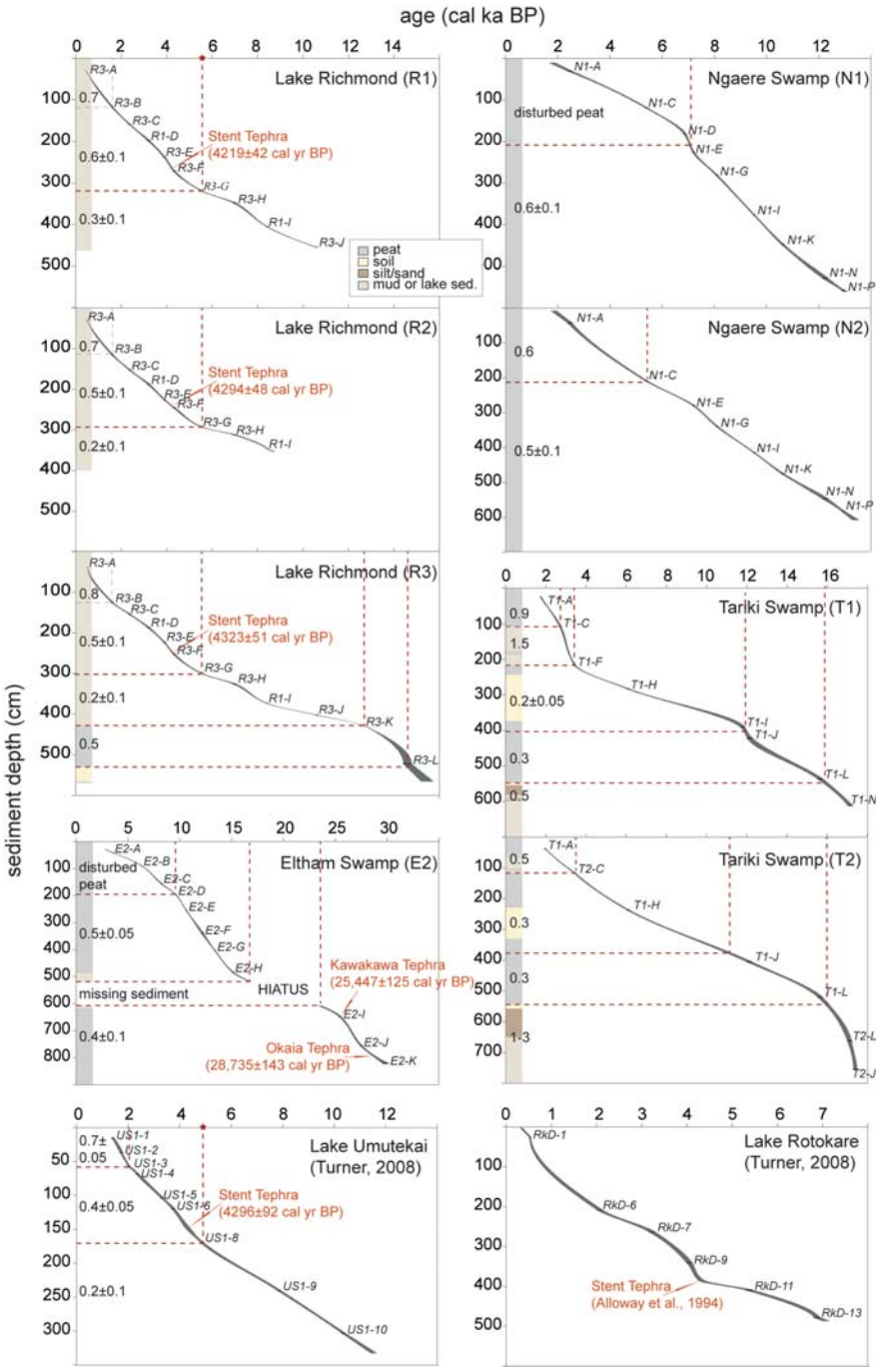

Figure 3. 1 *Age-depth models for lake and peat sediment cores, produced using a piecewise cubic Hermite interpolating polynomial fit (Fritsch and Carlson, 1980). Individual ^{14}C ages are shown as calibrated median probability ages with 1σ errors output by OxCal Version 4.2 (Bronk Ramsey, 2013) (Table 3.1). The s.depths are shown as "event-free" depths. Sediment accumulation rates are given as mm/yr. Brief lithologies are also shown. The red star indicates an accumulation increase around 5-5.5 cal ka BP within Lake Richmond and Lake Umutekai. Three Taupo volcano tephra*

layers are recognised and dated: (1) Stent Tephra (mean age from Lake Richmond: 4279±47 cal yr BP, age from Lake Umutekai: 4296±92 cal yr BP; age from Lake Rotokare: abnormal), (2) Kawakawa Tephra (age from Eltham Swamp: 25,447±125 cal yr BP) and (3) Okaia Tephra (age from Eltham Swamp: 28,735±143 cal yr BP).

3.2.5.2 Core descriptions

Lake Richmond

Three almost identical sediment cores from Lake Richmond were used to assemble a 7.4 m-long composite core, based on stratigraphic position and physical appearances of prominent tephra layers, repetition of obvious tephra sequences, and distinct lithological changes (Fig. 3.2). From c. 15.5 to 12.7 cal ka BP (7.4 to 5.6 m) the sediments mainly consists of horizontally-bedded coarse dark peat, interpreted as a peat bog as a precursor of the open-water lake forming at ~12.7 cal ka BP ago (Fig. 3.2). From c. 15.4 to 14.5 cal ka BP (7.2 to 6.7 m) the peat is interrupted by a distinct pale-yellow silt loam containing dispersed lapilli-sized tephra at the bottom (Ri-130; Fig. 3.2, Appendix 4) and a gradational contact into peat at the top. From c. 12.7 cal ka BP (5.6 m) to the top of the composite core, sediments are mainly composed of finely laminated, organic-rich, grey lake mud. Between c. 12.7 to 5.5 cal ka BP (5.6 to 3.7 m) lake sediments are firmer, denser and tephras are evident as lenses. Above 3.7 m (<5.5 cal ka BP), the accumulation rate increases from c. 0.2 mm/yr^{-1} to 0.5 mm/yr^{-1} (Fig. 3.1) and sediments are more water-saturated and soft. The Lake Richmond record shows the best preservation of very thin tephra layers (<1 mm) out of all the new cores collected during this study. A total of 132 andesitic tephra layers from Mt. Taranaki were distinguished (Fig. 3.2, Appendix 4). The core also contains a 2-cm-thick, pale-grey rhyolitic tephra layer at 2.87 m (mean age 4279±47 cal yr BP; Fig. 3.1), which is here correlated to the widespread, Taupo Volcanic Centre sourced Stent Tephra (also known as unit-Q, 4322±112 cal yr BP; Alloway et al., 1994; Lowe et al., 2013) based on similar age and chemical glass composition.

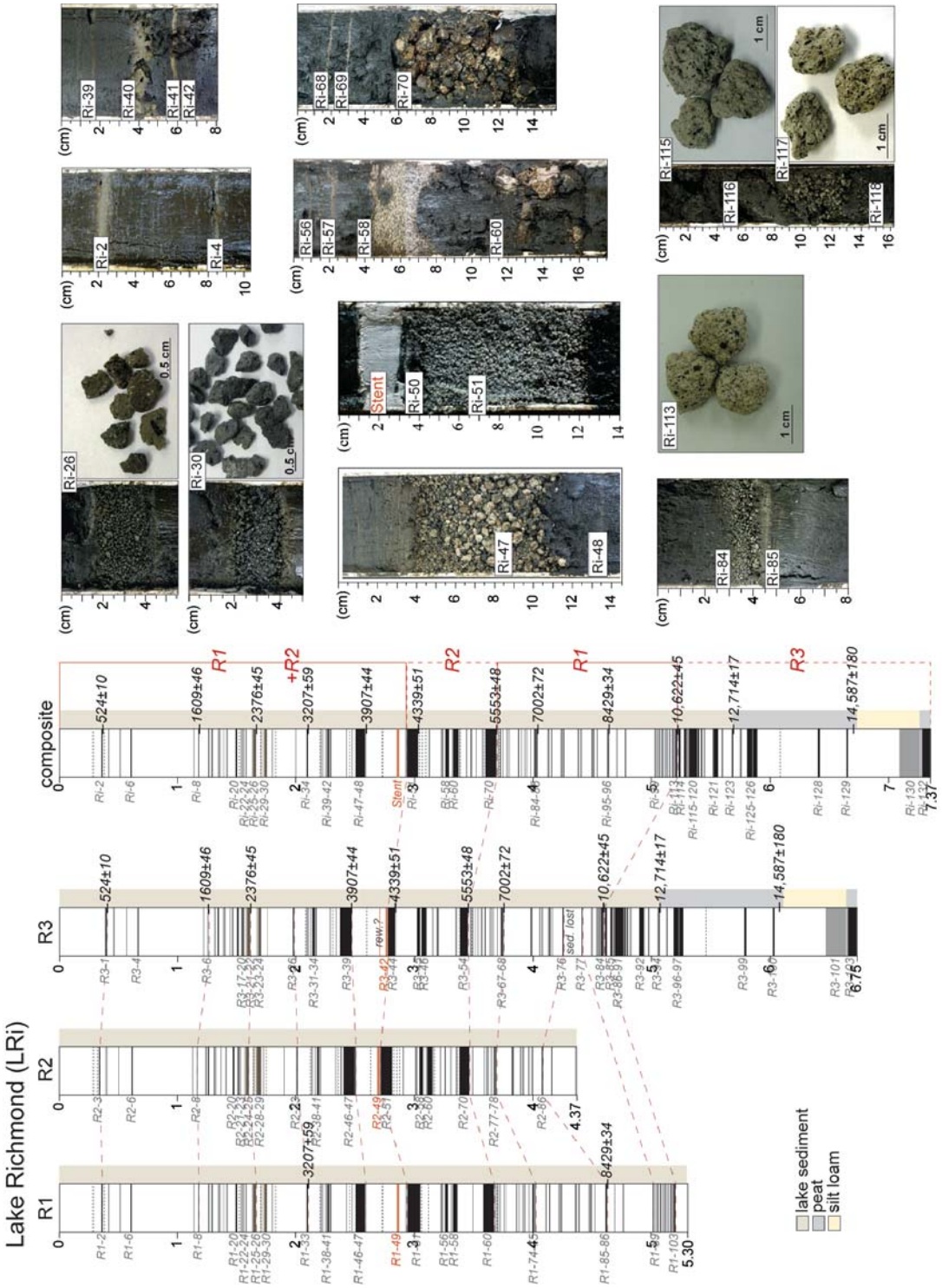

Figure 3. 2 *Lake Richmond sediment cores recovered during this study (R1-R3) and the composite record. Images show prominent tephra layers and their juvenile clast assemblages. Key correlations are marked with dotted red lines and are based on physical characteristics and age. Reworked tephras are abbreviated as 'rew.'. Ages are shown as calibrated ages with 1σ errors (Table 3.1).*

Tariki Swamp

Two sediment cores were correlated based on lithology, radiocarbon ages, geochemical and physical characteristics of prominent tephra layers, to form a 9.3 m-long composite core (Fig. 3.3). The bottom of the composite core consists of dense, dark-grey mud with scattered oxidised vivianite crystals. From c. 17 to 16 cal ka BP (7.8 to 6.6 m) a bedded sequence of alternating medium sand to organic-rich silt/clay layers occurs, capped by a 10-cm-thick, pale-yellow silt loam (Fig. 3.3). This sequence is interpreted as fluvial/alluvial deposits. From c. 16 to 3.4 cal ka BP (6.6 to 2.5 m) the core is mainly composed of dark fibric peat, interrupted by another distinct pale-yellow silt loam at c. 11 to 40 cal ka BP (4.1 to 2.7 m), in which thick roots and root-channels as well occasional large wood fragments occur. Tephra within the silt loam occurs only as grains dispersed throughout mainly fine-grained alluvial material (indicated as "reworked" in Fig. 3.3). At c. 3.4 cal ka BP (2.5 m) the peat accumulation is interrupted by a pale-grey silt to clay bedded unit (Fig. 3.3). This prominent fine-grained horizon contains abundant chironomid head capsules, which indicate standing water. This unit grades into peat at c. 2.7 cal ka BP (1.3 m; Fig. 3.3). The peat of the upper part of the core consists of coarse, horizontally-bedded, plant remains (mostly monocotyledonous) and remains of woody vegetation, including conifers and leaves. Such diverse lithologies suggest considerable variation in depositional conditions at this site, which likely have implications for preservation of tephra. Despite this limitation, the Tariki Swamp record preserves tephra sequences that are not recognised in any of the other sites. A total of 64 Taranaki-derived tephra layers were distinguished within the Tariki Swamp (Fig. 3.3, Appendix 4).

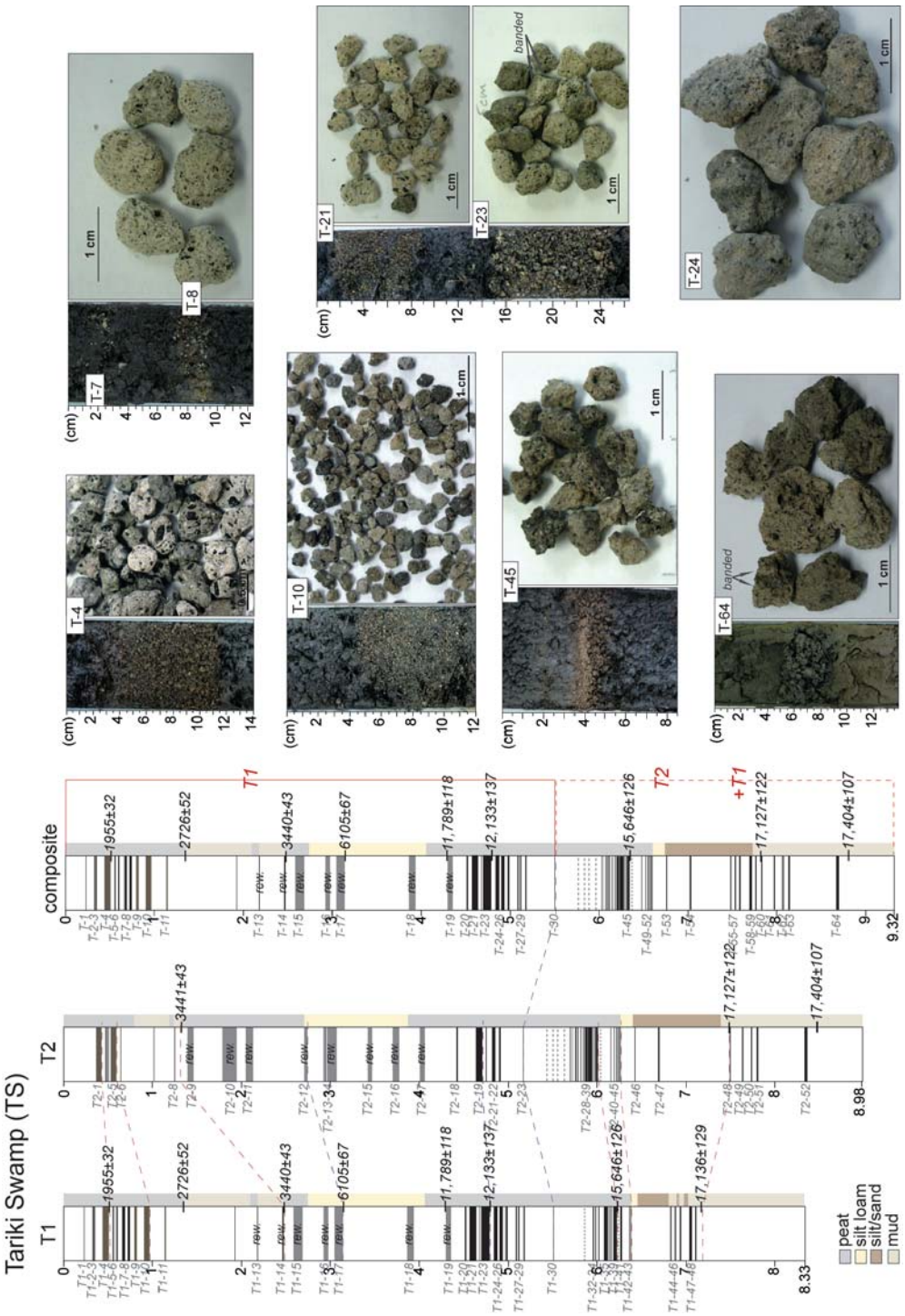

Figure 3. 3 *Tariki Swamp sediment cores recovered during this study (T1-T2) and the composite record. Images show prominent tephra layers and their juvenile clast assemblages. Key correlations are marked with dotted red lines and are based on physical characteristics and age, while dotted purple correlation-lines are additionally based on geochemical characteristics. Reworked tephras are abbreviated as 'rew.'. Ages are shown as calibrated ages with 1σ errors (Table 3.1).*

Ngaere Swamp

A 9.6 m-long composite record from Ngaere Swamp was produced by combining the complete Ngaere Swamp core1 (N1) with the top 1.27 metres of Ngaere Swamp core2 (N2), since the latter preserves more tephra layers <4 cal ka BP (Fig. 3.4). The bottom part of the composite core consists of several bedded units of medium sand grading to silt/clay. These units are interpreted to be fluvial sediments and are capped by individual pale-yellow silt loams containing abundant small roots. At c. 8.7 m a thin peat horizon gradationally grades into another, c. 40-cm-thick, silt loam. The remainder of the core consists entirely of horizontally-bedded fibric peat. Apparent accumulation rates between c. 13.5 to 7 cal ka BP (8 to 3 m; Fig. 3.4) were roughly constant at 0.6 ± 0.1 mm/yr^{-1} (Fig. 3.1). The post-7 cal ka BP accumulation rate was difficult to estimate, because of the presence of water-filled voids and large pieces of wood in the peat sequence. Tephra in this part of the sequence appears displaced and/or dispersed within the peat. The uppermost metre of N2, however, is composed of peat with no obvious disconformities and tephra layers are intact. The composite Ngaere Swamp record includes a total of 68 tephra layers from Mt. Taranaki (Fig. 3.4, Appendix 4).

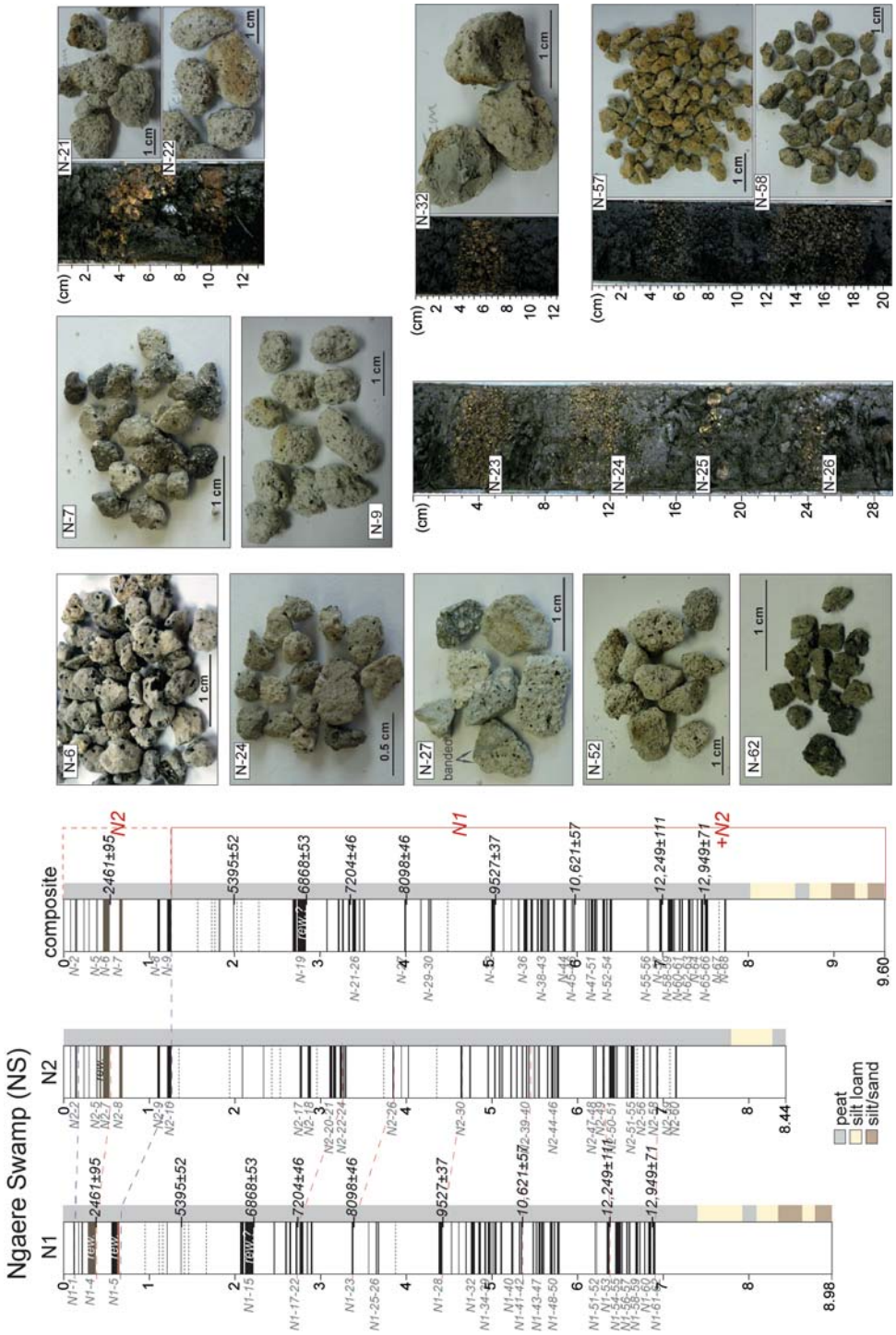

Figure 3. 4 *Ngaere Swamp sediment cores recovered during this study (N1-N2) and the composite record. Images show prominent tephra layers and their juvenile clast assemblages. Key correlations are marked with dotted red lines and are based on physical characteristics and age, while dotted purple correlation-lines are additionally based on geochemical characteristics. Reworked tephras are abbreviated as 'rew.' Ages are shown as calibrated ages with 1σ errors (Table 3.1).*

Eltham Swamp

A 10.95 m-long composite record from Eltham Swamp was produced by combining the whole Eltham Swamp core2 (E2) with the top 1.40 metres of Eltham Swamp core1 (E1), as the latter preserves more tephra layers <4 cal ka BP (Fig. 3.5). From 30 to 23.5 cal ka BP (10.9 to 7.9 m) the record mainly consists of fibric peat, which is interbedded with horizons of yellow to pale-brown fine-grained material interpreted as volcanic loess. Volcanic loess was common during the cold and dry climate conditions of the Last Glacial Maximum in the North Island of New Zealand (Pillans, 1988; Alloway et al., 1992; Lowe et al., 2015). The peat is topped with a 10-cm-thick horizon of dark-grey mud, followed by a metre of missing sediment. This missing section could be interpreted as a void in the coring record caused by a core logging error and/or as an indicator of the presence of thixotropic muddy sands, which could not be captured in the core barrel. Both explanations remain a matter of debate. Around c. 15.3 cal ka BP (7 to 6.8 m) the composite core comprises mud gradually grading upward into peat. A hiatus of ~8000 cal yr BP occurs between the mud at 8 m and 7 m, spanning the missing sediment section (Fig. 3.1). This apparently marks a period of erosion and re-deposition of fluvial sediment at this site. Above 15.1 cal ka BP (6.8 m), peat comprises the remainder of the core (Fig. 3.5). The Eltham Swamp composite core preserves the oldest tephra layers recorded in this study (30-23.5 cal ka BP; Appendix 4). A total of 80 Mt. Taranaki tephra layers were distinguished (Fig. 3.5). Two distinct rhyolitic tephra layers from the Taupo Volcanic Centre were also recognised, based on geochemical correlation using glass major element composition and similar age. A 2.5-cm-thick, pale-white fine ash layer at 8.5 m (25,447±125 cal yr BP), which correlates to the prominent Kawakawa/Oruanui Tephra (25,360±160 cal ka BP; Vandergoes et al., 2013) and a 3-cm-thick, yellow coarse ash to fine lapilli tephra layer at 10.3 m (28,735±143 cal yr BP), which correlates to the Okaia Tephra (28,621±1428 cal yr BP; Lowe et al., 2013).

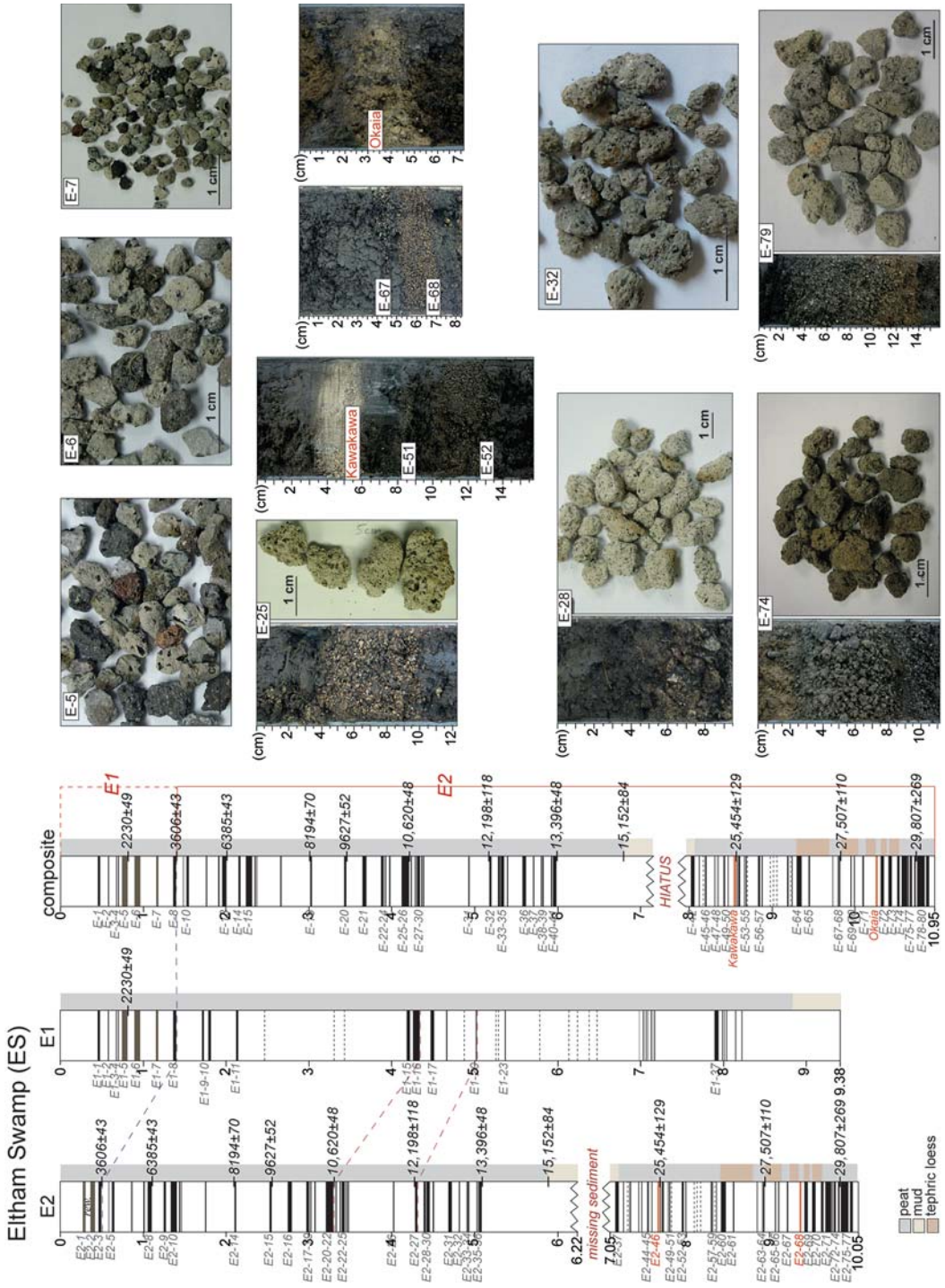

Figure 3. 5 *Eltham Swamp sediment cores recovered during this study (E1-E2) and the composite record. Images show prominent tephra layers and their juvenile clast assemblages. Key correlations are marked with dotted red lines and are based on physical characteristics and age, while dotted purple correlation-lines are additionally based on geochemical characteristics. Reworked tephras are abbreviated as 'rew.' Ages are shown as calibrated ages with 1σ errors (Table 3.1).*

3.2.5.3 Titanomagnetite groups

We analysed titanomagnetite phenocrysts from approximately 200 tephra layers present within the nine newly studied cores (Appendix 2) and reviewed the titanomagnetite-data from two previous cores analysed by Turner (2008). All analyses are presented as bivariate plots of TiO_2 vs. Al_2O_3+MgO, TiO_2 vs. Fe^{3+}, Al_2O_3 vs. MgO, and Fe^{2+} vs. Fe^{3+}, which illustrate the 12 individual titanomagnetite groups at Mt. Taranaki (Fig. 3.6, Table 3.2). The boundaries between the groups were established based on consistent differences in the major element concentrations, which vary between 0.5-1.0 wt% for TiO_2 and Al_2O_3+MgO and less than <0.1 cation proportion for Fe^{2+} and Fe^{3+}. Although most of the tephra layers have homogenous titanomagnetite compositions, some show a distinct bimodality (represented as filled triangles in Fig. 3.6). A few tephra layers have diverse titanomagnetite compositions and therefore cannot be classified into any specific titanomagnetite group (i.e., U-39, Ri-65, Rk-39, N-32, U-83 and U-87; represented as empty triangle in Fig. 3.6).

In general, titanomagnetite TiO_2 contents range from >10 wt% (titanomagnetite group-1), to <7 wt% (titanomagnetite groups-11 and -12) (Fig. 3.6, Table 3.2). Within the entire suite, TiO_2 varies inversely with FeO_{total}, or more precisely with Fe^{3+}. There is only a minor variability in Fe^{2+}, with titanomagnetite group-11 having the lowest Fe^{2+} contents (<1 cation proportion; Fig. 3.6). Al_2O_3+MgO contents range from <4 wt% in titanomagnetite group-10, to >11 wt% in group-11 (Fig. 3.6). The data displays two compositional trends from high-TiO_2 and high-Al_2O_3+MgO contents to low-TiO_2 and low-Al_2O_3+MgO concentrations, represented by titanomagnetite groups-1 to -10, and groups-11 to 12 (Fig. 3.6).

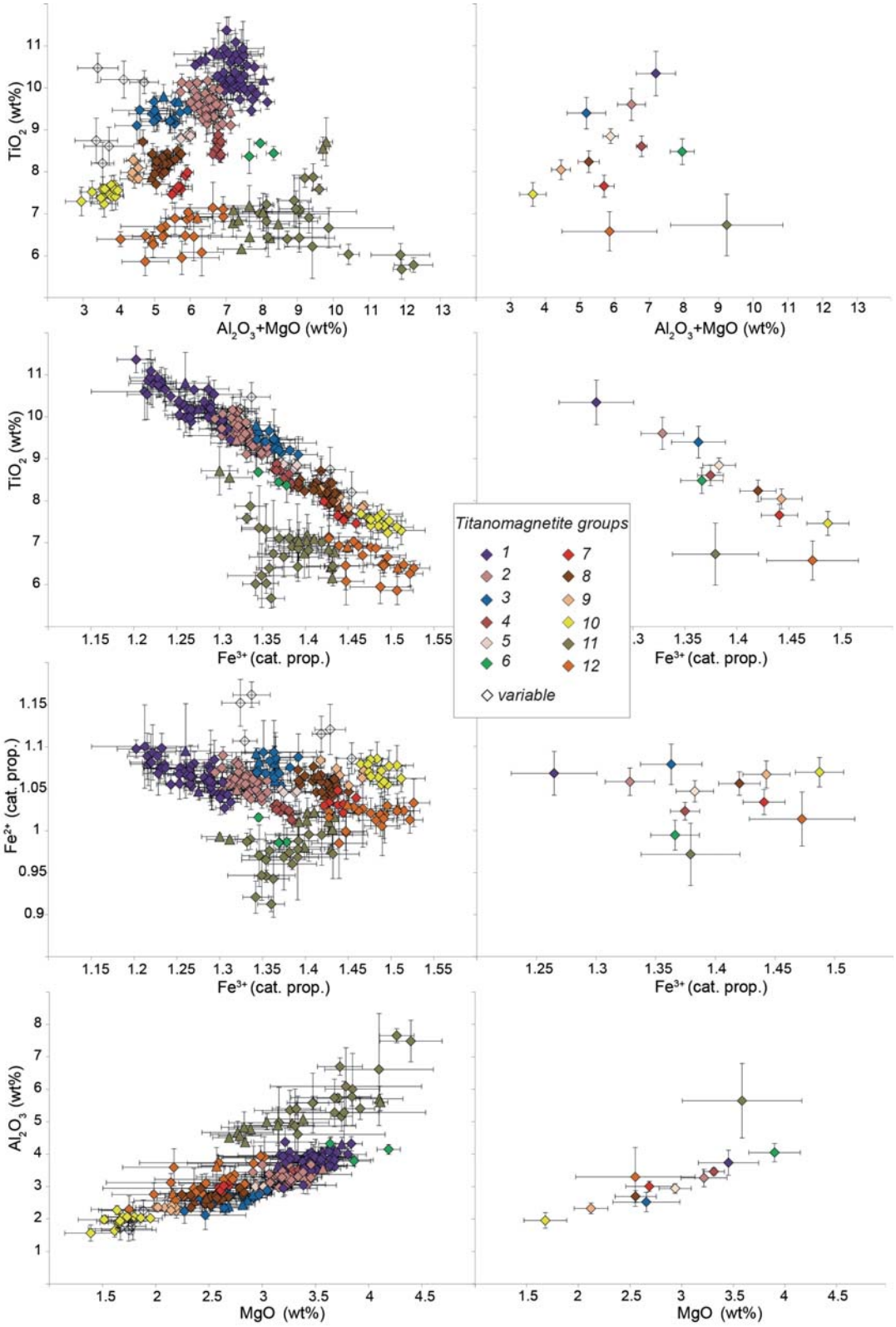

Figure 3. 6 *Compositions of titanomagnetite phenocrysts recognised in lake and peat deposits of Mt. Taranaki (Appendix 2). Each point is the average ±1 standard deviation for each tephra layer (left) and for each titanomagnetite group (right). Twelve*

individual titanomagnetite groups are represented by colours, with empty diamonds indicating variable titanomagnetite compositions that could not be classified to any group. Bimodal titanomagnetite compositions are represented as filled triangles. Analyses in weight percent (wt%) and cation proportion (cat. prop.) calculated on the basis of four oxygen atoms as in Carmichael (1966). Major and minor element compositions of each titanomagnetite group are summarised in Table 3.2.

Table 3. 2 *Compositions of 12 individual titanomagnetite (tm) groups recognised in tephra layers from lake and peat sediment records at Mt Taranaki. Refer also to Figure 3.7. *Additional analyses of grey lapilli tephra layer within the Eltham Swamp core recovered by McGlone and Neall (1994).*

tm group#	1		2		3		4		5		6	
(wt%)	avg.	±S.D.	avg.	±S.D.	avg.	±S.D.	avg.	±S.D.	avg.	±S.D.	avg.	±S.D.
TiO_2	10.34	*0.53*	9.60	*0.38*	9.40	*0.38*	8.60	*0.25*	8.84	*0.17*	8.48	*0.31*
Al_2O_3	3.74	*0.38*	3.27	*0.27*	2.52	*0.30*	3.46	*0.11*	2.94	*0.15*	4.05	*0.28*
FeO_t	76.61	*2.17*	78.85	*1.49*	79.69	*1.53*	78.96	*0.79*	79.84	*1.14*	78.95	*0.70*
MnO	0.93	*0.14*	0.99	*0.18*	1.12	*0.19*	1.05	*0.12*	1.16	*0.13*	0.82	*0.20*
MgO	3.45	*0.29*	3.22	*0.22*	2.66	*0.32*	3.31	*0.10*	2.94	*0.15*	3.90	*0.25*
Al_2O_3+MgO	7.19	*0.57*	6.48	*0.40*	5.18	*0.56*	6.78	*0.15*	5.88	*0.22*	7.95	*0.35*
Total	95.43	*2.02*	96.34	*1.56*	95.83	*1.59*	95.78	*0.94*	96.10	*1.13*	96.57	*0.79*
Number of cations calculated on the basis of four oxygen atoms												
Fe_2O_3	46.17	*2.08*	48.78	*1.19*	49.40	*1.34*	50.31	*0.57*	50.50	*0.99*	50.78	*0.81*
FeO	35.06	*0.86*	34.96	*0.74*	35.20	*0.81*	33.69	*0.53*	34.40	*0.52*	33.26	*0.67*
Total recal	99.92	*2.22*	101.10	*1.67*	100.67	*1.71*	100.68	*0.97*	101.00	*1.17*	101.55	*0.83*
Ti	0.28	*0.02*	0.26	*0.01*	0.26	*0.01*	0.24	*0.01*	0.24	*0.01*	0.23	*0.01*
Al	0.16	*0.02*	0.14	*0.01*	0.11	*0.01*	0.15	*0.00*	0.13	*0.01*	0.17	*0.01*
Fe^{+3}	1.26	*0.04*	1.33	*0.02*	1.36	*0.03*	1.37	*0.01*	1.38	*0.02*	1.37	*0.02*
Fe^{+2}	1.07	*0.03*	1.06	*0.02*	1.08	*0.02*	1.02	*0.01*	1.05	*0.01*	0.99	*0.02*
Mn	0.03	*0.00*	0.03	*0.01*	0.03	*0.01*	0.03	*0.00*	0.04	*0.00*	0.02	*0.01*
Mg	0.19	*0.02*	0.17	*0.01*	0.15	*0.02*	0.18	*0.01*	0.16	*0.01*	0.21	*0.01*
Usp	0.29	*0.02*	0.26	*0.01*	0.26	*0.01*	0.24	*0.01*	0.24	*0.01*	0.23	*0.01*
n-tephra	*55*		*44*		*19*		*9*		*5*		*3*	

Table 3. 2 (*continued)*

7		8		9		10		11		12		grey lapilli*	
avg.	*±S.D.*	avg.	*±S.D.*	avg.	*±S.D.*	avg.	*±S.D.*	avg.	*±S.D.*	avg.	*±S.D.*	avg.	*±S.D.*
7.65	*0.26*	8.23	*0.26*	8.05	*0.24*	7.46	*0.28*	6.73	*0.74*	6.58	*0.47*	10.40	*0.28*
3.01	*0.16*	2.70	*0.18*	2.33	*0.17*	1.96	*0.24*	5.65	*1.15*	3.30	*0.91*	3.43	*0.17*
81.23	*0.91*	80.91	*1.38*	81.32	*1.52*	82.48	*1.50*	77.49	*3.60*	79.71	*2.99*	78.09	*0.33*
1.01	*0.21*	1.04	*0.25*	1.23	*0.25*	1.44	*0.32*	0.61	*0.21*	0.90	*0.26*	0.89	*0.11*
2.69	*0.23*	2.55	*0.20*	2.12	*0.16*	1.68	*0.21*	3.59	*0.58*	2.55	*0.58*	3.55	*0.11*
5.69	*0.29*	5.25	*0.30*	4.45	*0.27*	3.64	*0.38*	9.23	*1.62*	5.85	*1.37*	6.98	*0.24*
96.00	*0.82*	95.83	*1.38*	95.52	*1.29*	95.50	*1.47*	94.54	*3.59*	93.61	*2.84*	96.79	*0.52*
52.56	*0.71*	51.58	*1.16*	51.96	*1.32*	53.32	*1.13*	50.53	*2.53*	52.47	*2.15*	47.51	*0.49*
33.94	*0.59*	34.50	*0.57*	34.56	*0.56*	34.50	*0.80*	32.02	*1.64*	32.50	*1.40*	35.35	*0.39*
101.16	*0.87*	100.90	*1.47*	100.58	*1.42*	100.74	*1.55*	99.50	*3.81*	98.72	*3.02*	101.42	*0.45*
0.21	*0.01*	0.23	*0.01*	0.22	*0.01*	0.21	*0.01*	0.18	*0.02*	0.18	*0.01*	0.28	*0.01*
0.13	*0.01*	0.12	*0.01*	0.10	*0.01*	0.09	*0.01*	0.24	*0.05*	0.15	*0.04*	0.15	*0.01*
1.44	*0.02*	1.42	*0.02*	1.44	*0.02*	1.49	*0.02*	1.38	*0.04*	1.47	*0.04*	1.29	*0.01*
1.03	*0.01*	1.06	*0.01*	1.07	*0.02*	1.07	*0.02*	0.97	*0.04*	1.01	*0.03*	1.06	*0.01*
0.03	*0.01*	0.03	*0.01*	0.04	*0.01*	0.05	*0.01*	0.02	*0.01*	0.03	*0.01*	0.03	*0.00*
0.15	*0.01*	0.14	*0.01*	0.12	*0.01*	0.09	*0.01*	0.19	*0.03*	0.14	*0.03*	0.19	*0.01*
0.21	*0.01*	0.23	*0.01*	0.23	*0.01*	0.21	*0.01*	0.19	*0.02*	0.19	*0.01*	0.28	*0.01*
7		*27*		*7*		*15*		*30*		*20*		*1*	

Note: Titanomagnetite (tm) compositions of individual groups are given as average (avg.) with ±1 standard deviation (±S.D.). n-tephra = number of tephra layers, which have been analysed and classified within the representative group. The complete compositional datasheet with titanomagnetite composition of each tephra layer is summarized in Appendix 2. FeO, Fe_2O_3, cation proportions and Usp (mole fraction ulvöspinel calculated (recal) as in Carmichael (1966).

3.2.5.4 Glass chemistry

Volcanic glass shards from a total of 89 tephra layers present in the cores were analysed (Appendix 3), along with the glass shard-data from previous cores analysed by Turner (2008). Glasses in Mt. Taranaki tephras have a large compositional range, from basalt-andesitic to trachytic and rhyolitic compositions (Figs. 3.7, 3.8). This wide range has been observed before, with andesitic whole rock compositions often having dacitic to rhyolitic glass (Price et al., 2005). K_2O contents of the glasses measured here are mainly >4wt% with the exception of the Manganui Tephra(s), erupted from the parasitic Fanthams Peak vent at around 3 cal yr BP (Fig. 3.7). The lower-alkali glass shard

chemistry of TVZ-derived tephra layers present within the studied cores is also shown for comparison and contrast (Fig. 3.8).

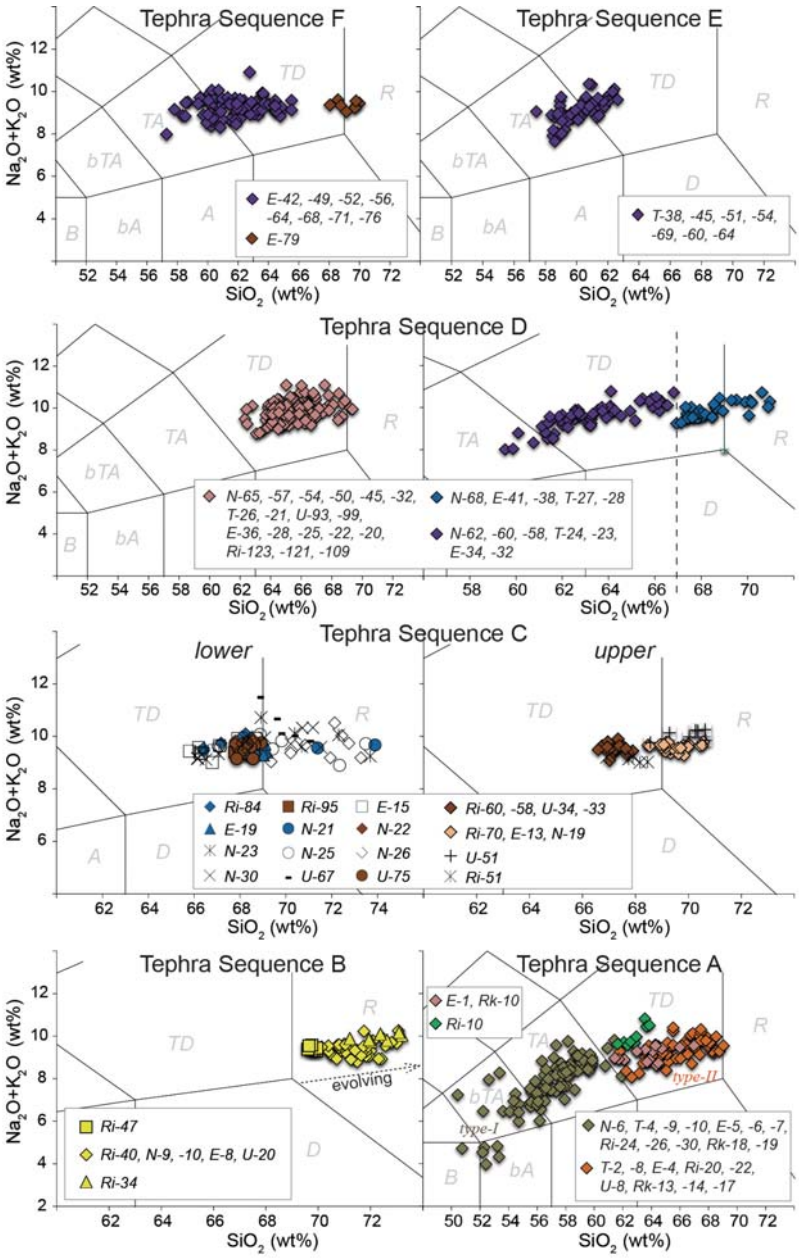

Figure 3. 7 *Glass major element compositions of Tephra Sequences A-F defined in lake and peat sediment cores from Mt. Taranaki (Appendix 3). Normalised analyses are plotted as total alkalis vs. silica with compositional fields of basalt-andesite (bA), basalt-trachyandesite (bTA), trachyandesite (TA), trachydacite (TD) and rhyolite (R). Colours represent the dominant titanomagnetite group of each tephra sequence (refer to Figs. 3.6, 3.9).*

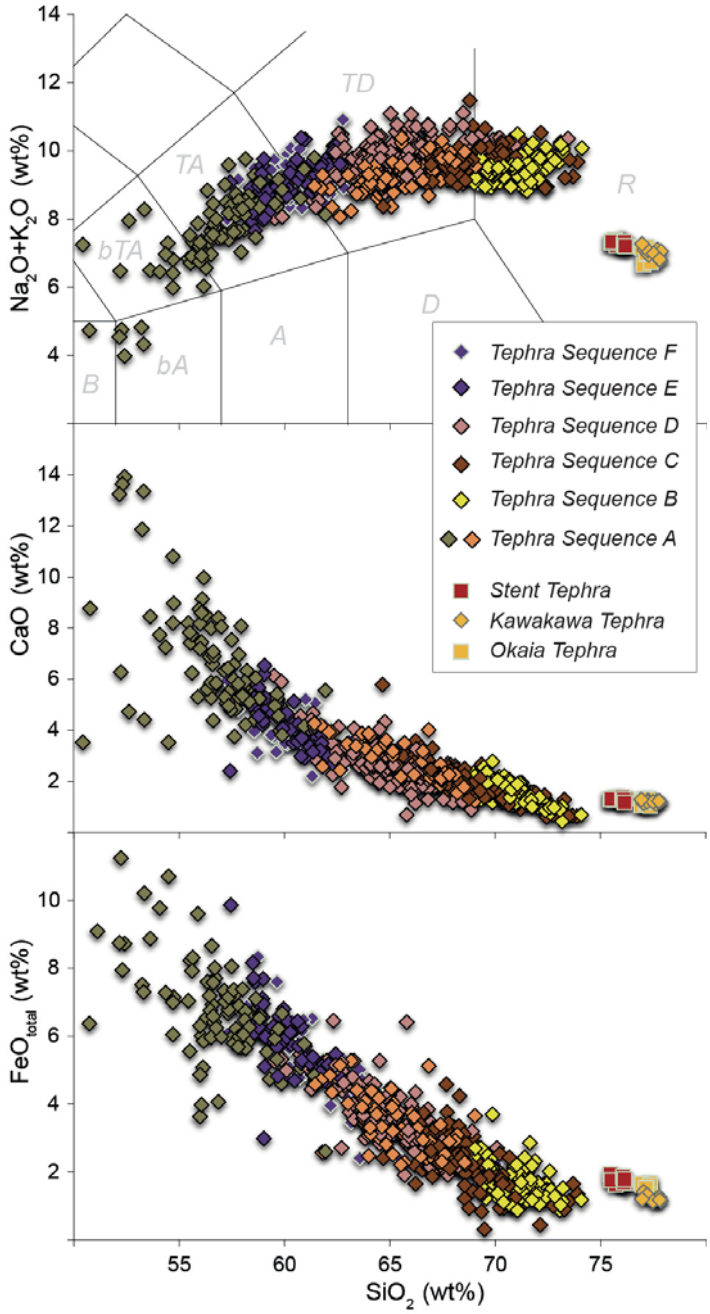

Figure 3. 8 *All glass compositional data from Tephra Sequence A-F summarised on plots of total alkali, FeO_{total}, CaO vs. SiO_2. The Taupo volcano-tephras (i.e., Stent, Kawakawa, Okaia) are also shown. Colours represent the dominant titanomagnetite group of each tephra sequences (refer to Figs. 3.6, 3.9).*

3.2.5.5 Discrimination of tephra sequences

Within the records produced in this study, stratigraphically adjacent tephra layers typically have similar titanomagnetite compositions, which, in conjunction with precise age determination of the tephra layers, enable us to subdivide the whole eruption sequence into six geochemically and stratigraphically distinct tephra sequences (Sequence A-F; Fig. 3.9). The tephra sequences are characterised by their dominant titanomagnetite group (e.g., Tephra Sequence E has titanomagnetite group-1 compositions), but there are a few intercalated tephra layers with aberrant titanomagnetite compositions. Some titanomagnetite compositional groups occur repeatedly through time and therefore occur within several tephra sequences. The suite of the six tephra sequences creates a time-constrained geochemical pattern that is traceable through all sediment cores and therefore enables sequence correlation, even though correlation cannot be extended to the individual tephra bed level (Fig. 3.9). Defined tephra sequences are described in detail below, including their dominant (and subordinate) titanomagnetite compositional groups, their glass chemistry and physical appearance. A summary of the physical, mineralogical, and chemical properties, and ages, of all tephra layers within each composite core is given in the Appendix 4.

Tephra Sequence F (30-23.5 cal ka BP)

Tephra Sequence F is only represented in the Eltham Swamp record and comprises at least 39 Mt. Taranaki tephra layers, which mainly have a group-1 titanomagnetite composition (Figs. 3.6, 3.9, Table 3.2). Most tephra layers of Tephra Sequence F have trachyandesitic to trachydacitic glass compositions, with SiO_2 <65 wt% and FeO_{total} mainly ~4.5 wt% (Figs. 3.7, 3.9). The 9-cm-thick unit E-79 (29,855±274 cal yr BP) is a prominent tephra in this sequence. It comprises bedded, pale-grey to grey, vesicular pumice fragments and grey to reddish brown lithics (Fig. 3.5). This tephra also stands out as compositionally more evolved, with ~69 wt% SiO_2 (Fig. 3.7) and, together with E-78 and -77, has distinctively lower Al_2O_3+MgO and TiO_2 titanomagnetite compositions (titanomagnetite group-8; Figs. 3.6, 3.9, Table 3.2) compared to the dominant titanomagnetite population of the suite. A sequence of tephra layers deposited in palaeolake sediments in the Auckland region, 270 km NNE of Mt. Taranaki (Eg28.9

to Eg23.5, Shane, 2005), are geochemically similar to tephras of Tephra Sequence F described here. In particular the tephra Eg28.9 recognised in the Pukaki Lagoon sediments (Shane, 2005) is a likely distal correlative of E-79 because of its distinctive evolved glass composition underlying a mainly trachyandesitic/dacitic tephra sequence. The occurrence of the Kawakawa/Oruanui Tephra (25,360±160 cal yr BP; Vandergoes et al., 2013) within Tephra Sequence F allows correlation to the Poto Tephra Formation described by Alloway et al. (1995), while tephra layers surrounding the Okaia Tephra (28,621±1428 cal yr BP; Lowe et al., 2013) are correlated to the Tuikonga and Koru Tephra Formations (Alloway et al., 1995), although correlation at the individual bed level is not possible at present.

Tephra Sequence E (17.5 to 14 cal ka BP)

Tephra Sequence E is stratigraphically separated from Tephra Sequence F by a hiatus of c. 6000 cal yr BP (Fig. 3.9). Tephra Sequence E is best represented in the Tariki Swamp record and comprises at least 35 Mt. Taranaki-derived tephra layers, which all have a group-1 titanomagnetite composition (Figs. 3.6, 3.9, Table 3.2). Tephra Sequence E is mainly characterised by dark-grey, medium ash to lapilli, occasionally graded tephra layers (Fig. 3.3, Appendix 4), which have trachyandesitic to trachydacitic glass compositions (59-62 wt% SiO_2) and high FeO_{total} glass contents (>4 wt%; Figs. 3.7, 3.8). The most prominent tephra within this sequence is the 3-cm-thick T-64 (17,397±96 cal yr BP), which is composed of dark-brown to black, scoriaceous, banded medium pumice lapilli, along with common dark-grey altered lithics (Fig. 3.3). Similar physically distinctive tephra layers include a medium ash T-51 (15,960±106 cal yr BP) and a normally graded, lithic-rich, coarse ash T-45 (15,642±123 cal yr BP). Tephra Sequence E is likely correlated to the Kaihouri and Paetahi Tephra Formations (>15 cal ka BP, Alloway et al., 1995). Tephra layers of similar age and composition occur in Auckland's Pukaki Crater (AT203, T19, and AT206; ~15.8 to 17.7 cal ka BP; Sandiford et al., 2001) and the Waikato lakes, Hamilton (Eg13 and Eg14; ~17.5 cal ka BP; Lowe, 1988b).

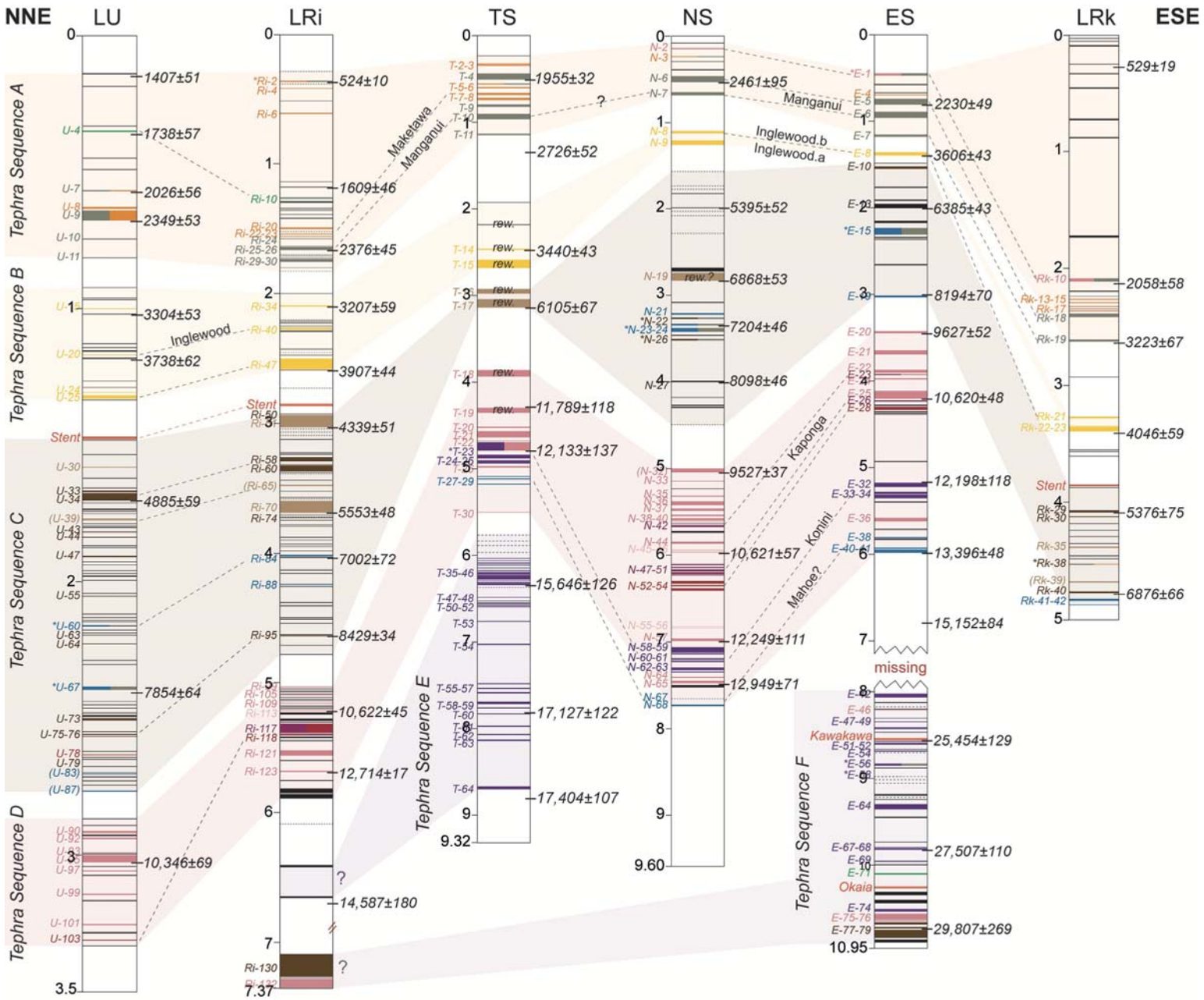

Figure 3. 9 *Summary of sediment cores taken during this study and previous studies of Turner (2008) showing individual tephra layers (thickness and depth of tephra indicated by horizontal bars; titanomagnetite group of each analysed tephra indicated by coloured bars (refer Fig. 3.6, Table 3.2); reworked tephras are abbreviated as 'rew.'), and radiocarbon dating points given in calibrated ages with 1σ errors (Table 3.1 and Turner, 2008). The nomenclature of individual tephra layers is based on their stratigraphic order within the composite core (refer also to Figs. 3.2 to 3.5). Tephra Sequences A-F are indicated by coloured shaded fields. Correlation of individual members and/or groups of members is indicated by black dashed lines and/or described in text. Tephra layers characterised by a bimodal titanomagnetite composition are denoted with an asterisk (refer also to Fig. 3.6). Tephra layers characterised by variable titanomagnetite compositions are denoted with brackets (refer also to Fig. 3.6).*

Tephra Sequence D (14 to 9.5 cal ka BP)

Tephra Sequence D is preserved in most cores, but best represented in the Ngaere Swamp record, which comprises at least 37 Mt. Taranaki-derived tephra layers. It is dominated by tephra layers having a group-2 titanomagnetite composition (Figs. 3.6, 3.9, Table 3.2) and mainly trachydacitic glass shard compositions (Figs. 3.7, 3.8). In general, Tephra Sequence D is characterised by sets of closely-spaced tephra layers indicating eruption within periods of ~50-150 years. The majority of tephras are pale-grey to grey, coarsely-vesicular coarse ash to medium pumice lapilli (Figs. 3.2 to 3.5, Appendix 4). The pumice contains abundant large phenocrysts of mainly clinopyroxene (augite), hornblende, plagioclase, and titanomagnetite. Some tephra layers and/or groups of tephras have titanomagnetite compositions that vary from the dominant suite with group-2 compositions, which enables their discrimination and correlation across the sediment cores taken (Figs. 3.6, 3.9), as described below.

At the base of Tephra Sequence D, tephras N-68 and -67 (correlative to E-41-38 and T-29-27; >13 cal ka BP, Fig. 3.9) are mainly composed of white to pale-grey, pumiceous and crystal-rich coarse ash to fine lapilli (Appendix 4). Their glass compositions are mainly trachydacitic with silica contents around 68 wt%, except for tephras T-27 and T-28, which have variable glass compositions reaching rhyolitic compositions up to 70 wt% SiO_2 (Fig. 3.7). Titanomagnetite compositions are distinctively lower in Al_2O_3+MgO contents (<6 wt%, titanomagnetite group-3; Fig. 3.6, Table 3.2) compared to the dominant titanomagnetite population of Tephra Sequence D. This aberrant tephra group may correlate to two tephra layers recognised in the Pukaki crater-lake, Auckland region (T7 and AT193, Sandiford et al., 2001), based on similar high-silica glass compositions, and may also represent the Mahoe Tephra Formation (~13 cal ka BP) described by Alloway et al. (1995) based on a similar age range. The original informally named ‘Mahoe tephra’ (Franks et al., 1991) is not related to the later defined Mahoe Tephra Formation of Alloway et al. (1995), as shown by physical and compositional differences (latter undertaken by Wallace, 1987). Here it is considered that the original Mahoe tephra of Franks et al., (1991) is more likely to represent a tephra within the Konini Tephra Formation of Alloway et al. (1995).

Tephra layers N-63 to -58 (correlative to E-34-32, and T-25-23; <13 cal ka BP; Fig. 3.9) have trachyandesitic to trachydacitic glass compositions with low silica contents <66 wt% and high FeO_{total} values of ~4 wt% (Figs. 3.7, 3.8), distinctively different from the preceding tephra group described above. Titanomagnetites have high Al_2O_3+MgO and TiO_2 contents (titanomagnetite group-1; Fig. 3.6, Table 3.2). Prominent tephra N-58 (12,370±104 cal yr BP) is a 6-cm-thick, well-bedded, coarse ash to medium lapilli layer composed of grey to dark-grey (yellow coated), vesicular and banded pumice fragments, with up to 50% grey to black and rare reddish dense lithics (Fig. 3.4). These tephra layers N-63 to -58 thus may correlate to the Konini Tephra Formation (~12 cal ka BP; Alloway et al., 1995), which was previously correlated by Alloway et al. (1995) to a grey lapilli-layer dated at ~11,683±207 cal yr BP in the Eltham Swamp record (McGlone and Neall, 1994). In the course of this study, this grey lapilli layer was shown to have consistent group-1 titanomagnetite compositions (Table 3.2). A tephra in the Kaipo bog, 260 km ENE of Mt. Taranaki (anal. 19a, Lowe et al., 1999, 2008), two tephra layers in the Onepoto Basin, Auckland (Eg12.3 and Eg11.7, Shane, 2005) and a tephra in the Pukaki crater-lake, Auckland (AT191, Sandiford et al., 2001) have similar glass compositions and are therefore likely correlatives to tephra layers N-63 to -58 within Tephra Sequence D. Alloway et al. (1995) tentatively correlated one of their Konini tephras (Konini.b) to a tephra layer preserved within sediments of the Waikato lakes (Eg11, Lowe 1988), but geochemistry does not support this correlation, since Eg11 has a distinctively more evolved glass composition than Konini correlatives N-63 to -58. The Konini.b tephra was defined as a regional chronostratigraphic marker horizon for the Pleistocene-Holocene boundary (Lowe et al., 2013).

Younger tephra layers N-54 to -52 (correlative to E-28, parts of Ri-118, and U-103), N-51 to -47 (correlative to E-26 and parts of Ri-117), N-46 to -45 (correlative to Ri-113), and N-42 (correlative to parts of E-23) (Fig. 3.9) show distinctively lower TiO_2 contents (<9 wt%; titanomagnetite groups-7, -5, and -4; Fig. 3.6, Table 3.2). A tephra layer within sediments of the Waikato lakes (Eg9, Lowe 1988) has a titanomagnetite composition similar to N-46 and -45 (~10.6 cal ka BP) and is therefore correlated to Tephra Sequence D. Eg9 as well Eg10 have been previously correlated to the Kaponga

Tephra Formation (~10 cal ka BP; Alloway et al., 1995). Tephra N-32 (9519±36 cal yr BP) is a prominent 5-cm-thick, pale-grey microvesicular pumicious coarse ash (Fig. 3.4). Its titanomagnetite composition is distinctively broad, similar to tephra units U-87 and -83. These units are representative for the transition between Tephra Sequences D to C. While correlation of most of these tephra layers/groups can be made between the different cores, correlation to individual beds at medial sites remains extremely challenging due to many tephra layers having similar characteristics and compositions within the general age range of the Kaponga Tephra Formation (Alloway et al., 1995).

Tephra Sequence C (9.5 to 4 cal ka BP)

Tephra Sequence C is present in all cores including those previously studied by Turner (2008). It is best represented within the Lake Umutekai record, where it includes up to 60 Mt. Taranaki tephra layers (Fig. 3.9). Tephra Sequence C features the thickest and coarsest tephras encountered in this study (Appendix 4). They have predominantly a group-8 titanomagnetite composition, characterised by low Al_2O_3+MgO and TiO_2 contents (5-6 wt% and 8-9 wt%, respectively; Fig. 3.6, Table 3.2). Glass compositions are mainly trachydacitic to rhyolitic, with silica contents >65 wt% (Figs. 3.7, 3.8). A few tephra layers in the lower part of this tephra sequence have higher TiO_2 concentrations (9-10 wt%, titanomagnetite group-3; Fig. 3.6, Table 3.2) and/or a distinct bimodal composition (i.e., titanomagnetite group-3 and -11; Fig. 3.6, Table 3.2). This sequence of tephras allows discrimination between the lower and upper part of Tephra Sequence C.

The lower part of Tephra Sequence C (9.5 to c. 6.8 cal ka BP) includes several lithic-rich and micro-vesicular pumice layers, such as N-21 to -24 (~7.2 cal ka BP). The 2-cm-thick N-27 (8090±46 cal yr BP) is mainly composed of fine to medium pale-grey to grey dense and microvesicular lithic lapilli, some of which are colour-banded (Fig. 3.4, Appendix 4). Some of these tephra units (i.e., N-26, N-22 to -24, U-67, U-60, E-15) have a distinct bimodal titanomagnetite composition (Fig. 3.6, Table 3.2). Their glass composition is mainly trachydacitic (~68 wt% SiO_2), with some showing a broad variation (Fig. 3.7). Based on similar compositional characteristics, tephra Eg7,

recognised in sediments of the Waikato lakes (~6.6 cal ka BP, Lowe, 1988b) is here correlated to the lower part of Tephra Sequence C.

The upper part of Tephra Sequence C (c. 6.8 to 4 cal ka BP) includes a distinctive 7-cm-thick tephra, Ri-70 (5534±48 cal yr BP), composed of pale-grey, vesicular, banded coarse to fine pumice lapilli and rare grey dense lithic lapilli (Fig. 3.2). Its titanomagnetite composition is slightly lower in Al_2O_3+MgO (titanomagnetite group-9; Fig. 3.6, Table 3.2) than to the dominant titanomagnetite population of Tephra Sequence C. Furthermore, its glass composition is high in silica content (~69 wt%, Fig. 3.7) and correspondingly low in FeO_{total} and CaO (Appendix 3). Tephra layers N-19 (6862±53 cal yr BP), E-13 (6366±44 cal yr BP), and Rk-35 (6218±81 cal yr BP) have similar compositional characteristics (Figs. 3.6, 3.7, 3.9). Younger tephras Ri-60 and Ri-58 (4878±46 and 4801±49 cal ka BP, respectively) within the upper part of Tephra Sequence C have homogenous glass compositions with silica contents ~67 wt% (Fig. 3.7). Ri-60 is a 5-cm-thick, pale-grey, highly vesicular pumice lapilli layer with rare altered lithics. Ri-58 is a 3-cm-thick, pale-grey, pumiceous medium ash with rare grey lithics and common free crystals (Fig. 3.2). These tephras correlate across sites to U-34 and -33 (4884±58 and 4839±55 cal yr BP, respectively) based on similar physical and geochemical characteristics. One of the youngest tephra units within the upper part of Tephra Sequence C is Ri-51 (4328±51 cal yr BP), which underlies the Stent Tephra (mean age of 4279±47 cal yr BP; Fig. 3.1). It is an 8.5-cm-thick, well-sorted, pale-grey pumiceous medium ash with abundant free crystals and minor lithics (Fig. 3.4). Its glass contains ~68 wt% SiO_2 (Fig. 3.7). Based on similar composition and stratigraphic position, distal tephra layers Eg-6, -5 and -4 in the Waikato lake sequence (~6 to 4.3 cal ka BP, Lowe, 1988b) are here correlated to the upper part of Tephra Sequence C.

Unfortunately, correlation of individual tephra layers of Tephra Sequence C to any proximal/medial site was not possible, due to age discrepancies in the existing stratigraphic reconstructions of Neall (1972, 1979), Franks et al., (1991) and Alloway et al. (1995).

Tephra Sequence B (4 to 3 cal ka BP)

Tephra Sequence B is preserved in all of the cores, but is most prominent with at least 17 Mt. Taranaki-derived tephra layers in the Lake Richmond and Lake Umutekai records (Fig. 3.9). All tephra layers contain titanomagnetite group-10 composition (Fig. 3.6, Table 3.2). Glass shards have high SiO_2 contents (>69 wt%; Fig. 3.8), with a general trend of increasing silica and potassium concentrations with decreasing age of the tephra units (Fig. 3.7). The oldest tephra layers within Tephra Sequence B include the prominent Ri-47 (3893±46 cal yr BP; Fig. 3.2), an 8-cm-thick, pale-grey to yellow, vesicular, banded, medium ash to pumice lapilli with grey dense and minor red lithic lapilli. The upper 2 cm of this tephra is composed of finely laminated ash (Fig. 3.2). Its stratigraphic position suggests correlation with tephra layers U-25 and Rk-23/-21. However, the physical appearance of the latter tephras (Turner, 2008) suggests closer affinity to younger tephras within Tephra Sequence B, described below. At present, no proximal counterpart has been identified for tephra Ri-47.

The following tephra layers within Tephra Sequence B are composed of pale-grey fine ash, which may host white coarse pumice lapilli (i.e., Ri-40, 3510±45 cal yr BP; Figs. 3.2, 3.9). Pumice clasts have a distinctive finely vesicular texture, and high silica contents (70-72 wt%, Fig. 3.7), with low CaO and FeO_{total} contents (Appendix 3). Similar compositions and physical characteristics are reported for tephra units U-20 (3674±61 cal yr BP), E-8 (3593±43 cal yr BP) and N-9/-8 (3365±65 and 3216±67 cal yr BP, respectively) (Figs. 3.6, 3.7, 3.9, Appendix 4). These tephra layers, as well Rk-23/-21, are correlated to the prominent Inglewood Tephra Formation (~4-3.8 cal ka BP, Alloway et al., 1995). Lapilli tephra N-8 is distinct in that it has a higher lithic content (up to 50%) compared to older tephra N-9, which contains only a few lithics, and both are therefore correlated with Inglewood-b and Inglewood-a, respectively (Alloway et al., 1995). The same observed for correlatives Rk-21 and Rk-23, respectively. Tephra layers T-15 and T-14 appears to be mixtures of Ri-47 and -40, and are therefore considered to be reworked tephra material rather than *in situ* fall units (Fig. 3.9). Alloway et al. (1995) correlated the Inglewood Tephras to two tephra layers preserved within sediments of the Waikato lakes (Eg2 and Eg3, Lowe 1988). However, geochemical evidence obtained in this study does not support this correlation, since Eg2

has a titanomagnetite composition similar to tephra layers recognised in the older Tephra Sequence C.

The youngest tephra layers within Tephra Sequence B (<3.3 cal ka BP) are only found in the Lake Richmond and Lake Umutekai records (Fig. 3.9) and include several thin (<1 cm) pale-grey, fine-ash layers, commonly with orange-stained upper contacts (Fig. 3.2). They have high silica contents of ~72-74 wt% (Fig. 3.7). No proximal/medial counterpart could be distinguished, but these tephra units could be associated with block-and-ash flow events, as past studies have shown that these may travel beyond 15 km from their source at Mt. Taranaki (Platz et al., 2007; Procter et al., 2010).

Tephra Sequence A (3 to 0.5 cal ka BP)

Tephra Sequence A is preserved in all of the cores, but is most prominent in the Lake Richmond record, where it includes up to 32 Mt. Taranaki-derived tephra layers (Fig. 3.9). Tephra sequence A features two physically and compositionally different types of tephra layers (type-I and –II) that are intercalated, as described below.

Type-I tephras are characterised by group-11 titanomagnetite compositions, having the highest Al_2O_3+MgO contents (up to 11 wt%, Fig. 3.6, Table 3.2) seen in this study, as well as low FeO_{total} and MnO contents (<78 wt% and ~0.6 wt%, respectively, Table 3.2). Type-I tephras have basalt-trachyandesitic to trachyandesitic glass compositions (Figs. 3.7, 3.8) with high FeO_{total} (>5 wt%), CaO (>4 wt%) and MgO (>2 wt%) contents (Appendix 3). Physically, type-I tephras feature black to dark-grey microvesicular dense-scoriaceous lapilli to coarse ash, brown microvesicular dense-scoriaceous lapilli to coarse ash with a distinct porphyritic texture, and/or pale-grey to grey microvesicular pumice lapilli to coarse ash with large hornblende phenocrysts and prominent red to purple scoriaceous lapilli (Figs. 3.2 to 3.5, Appendix 4). Most of these tephra layers are repetitively graded and are several centimetres in thickness. The unique morphology, compositions and stratigraphic position indicate these tephras are correlatives of the prominent Manganui Tephra Formation (~3 cal ka BP; Alloway et al., 1995), although single-bed correlation was not possible. However, based on similar physical and compositional characteristics, it is possible to correlate some of these tephra layers

across the sediment cores taken (specifically N-6 to E-5 to Rk-18; N-7 to E-6; Ri-26/25 to T-10; and tentatively E-7 to Rk-19; Fig. 3.9).

Type-II tephras are characterised by a group-12 titanomagnetite composition, having low, and variable Al_2O_3+MgO contents (4-7 wt%) along with constant low TiO_2 contents (<7 wt%; Fig. 3.6, Table 3.2). Type-II tephras have trachydacitic glass compositions (Figs. 3.7, 3.8) and are mainly composed of pale-grey to grey pumiceous lapilli (Fig. 3.3, Appendix 4). The inversely graded tephra Ri-20 (2122±37 cal ka BP), along with T-8 and T-7 (2170±29 and 2118±28 cal ka BP, respectively), correlate to the Maketawa Tephra Formation (Alloway et al., 1995), whereas tephras above prominent Manganui tephra T-4 may correlate to the Curtis Ridge Lapilli (<1.8 ka BP; Turner et al., 2008a). Tephra layers younger than <1 cal ka BP are characterised by several thin (<1 cm) and fine ash beds, from which Ri-2 (517±10 cal yr BP) has a bimodal titanomagnetite composition similar to titanomagnetite groups-11 and -12 (Figs. 3.6, 3.9, Table 3.2).

Within Tephra Sequence A, a prominent tephra in the south-eastern cores (N-2, E-1, Rk-10) has anomalously high TiO_2 contents (>9 wt %, titanomagnetite group-2; Fig. 3.6, Table 3.2). Glass shard compositions are trachydacitic with high FeO_{total} contents (>4 wt%, Fig. 3.7, Appendix 3). Further, a second unusual tephra (Ri-10 and U-4) was recognised with a titanomagnetite group-6 composition (Figs. 3.6, 3.9, Table 3.2). This unit has likewise a trachydacitic glass composition with a high FeO_{total} content (>4 wt%, Appendix 3). As yet, no proximal counterparts for these tephra layers have been identified.

3.2.6 Discussion

3.2.6.1 Correlation using defined tephra sequences

Previous studies at Mt. Taranaki have shown that due to similarities in appearance and bulk composition, as well as ambiguously defined tephra formations, which often comprise multiple units, correlation between individual andesitic tephra layers is a challenging task (e.g., Neall, 1972; Alloway et al., 1995; Cronin et al., 1996; Turner et al., 2009, 2011b; Platz et al., 2007, 2012). Correlation was further complicated by the fact that the sequences studied were incomplete, study sites were far apart, and the degree of chronological control was relatively poor. The new highly detailed tephra record developed in this study has shed new light on andesitic tephra correlations in the Taranaki region. For the first time, packages of physically and geochemically similar tephra layers can be identified as characteristic of specific tephra sequences. This in turn, facilitates more robust correlation between different sites, to derive a composite record encompassing at least 228 tephra layers spanning the last 30 cal ka BP (Fig. 3.10). The total number of tephras, 228 events in the last 30 cal. ka BP, is still an underestimate as not all the sequences are complete but this composite tephra record is one of the most detailed and continuous ever constructed for an andesitic stratovolcano.

Correlation to single sub-aerial (i.e., cover-bed sequences) and on-flank localities is still a challenging task, since little geochemical data from these sites are available at present, and proximal sequences at Mt. Taranaki are very complex, reflecting long and variable eruption sequences (Torres-Orozco et al., 2017). Previously reported proximal tephra correlations are based solely on physical appearance and stratigraphic position, and have been shown in this study to be unreliable. As a consequence of poor age-control and incomplete preservation, unit to unit correlations that are resolved within only hundreds of years from site to site may indeed have several tens of potential correlatives. The data set obtained in this study has already revealed that there are numerous tephra layers from Mt. Taranaki that can be used to correlate these sequences to other key New Zealand Quaternary records.

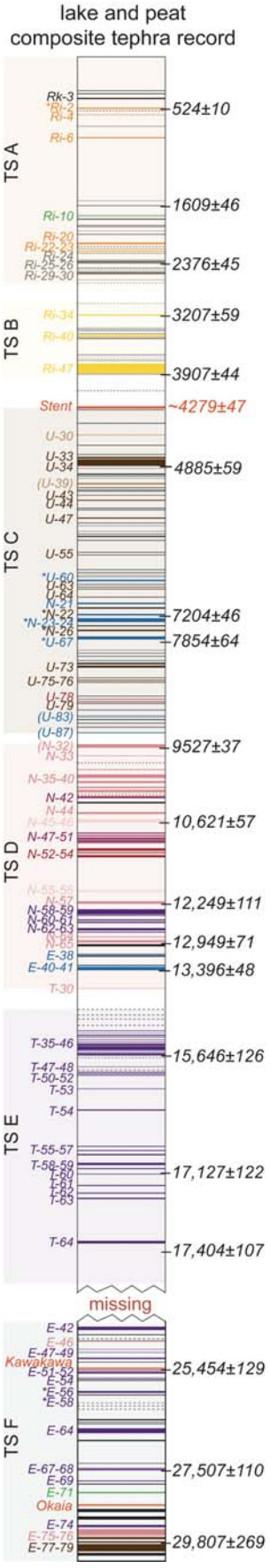

Figure 3. 10 *Lake and peat composite tephra record encompassing at least 228 tephra layers from Mt. Taranaki spanning the last 30 cal ka BP. The composite record has been constructed using the best-preserved and most-complete tephra sequences from single sites (TS = Tephra Sequence presented as colour, refer also to Figs. 3.6, 3.9) and temporal distinct tephra groups, which could be linked to the main sequence.*

3.2.6.2 Tephra deposition/preservation

The primary controls on tephra deposition at any of the studied sites are the eruption behaviour along with wind direction and speed. While the prevailing winds in the North Island were predominantly westerly over at least the past 20 ka BP (e.g., Salinger, 1984; Stewart and Neall, 1984; Drost et al., 2007; Turner et al., 2014), any small-scale transient wind variations, vertical stratification of the wind profile, and/or fluctuations in the eruption column height may lead to tephra being deposited in narrow bands, and thus only in isolated sites. A good example is the prominent Manganui tephra T-4, which was only recognised in the Tariki site (Fig. 3.9). The 7.5-cm-thick, coarse ash to fine lapilli layer shows shower bedding, which suggests a long, pulsating eruption, under strong westerly wind-conditions. A compositionally distinct tephra layer (N-2, E-1, Rk-10) within the upper part of Tephra Sequence A has been only documented in the south-easterly records, suggesting a restricted tephra dispersal of this unknown eruption to the southeast. Furthermore, Inglewood Tephra correlatives Ri-40, N-8 and E-8 are diverse in their bed and grain-size characteristics. Layer Ri-40 consists of a 1 cm thick bimodal tephra bed composed of fine-ash encompassing few fine pumice lapilli (up to 1 cm diameter) in the northeast; while 2.5- to 4-cm-thick tephras N-8 and E-8 comprise only very fine pumice lapilli (<8 mm diameter) in the southeast (Appendix 4). Distribution and grain-size variations suggest that the direction of the plume may have changed from northeast to southeast due to transitioned westerly winds. This is in agreement with recent plume reconstructions of Torres-Orozco et al. (2017), which are based on observations of proximal exposures of the tephra units. Overall, it is critical that comprehensive eruption records are built up from multiple records, ideally in a close arc around a volcano, to understand possible ash-fall dispersal patterns and eruption style changes.

Regarding the deposition site conditions, this study concentrated on wetland areas, which are known to be particularly good preservation sites for tephra falls. Lacustrine sediments were by far the best for continuous and complete preservation of tephra, with <1 mm layers being well preserved (e.g., see references to taphonomy in Lowe, 2011; Payne et al., 2010; Watson et al., 2016). By contrast, tephra layers at the millimetre-

scale are often dispersed within fibrous peat deposits and thus original thicknesses are difficult to estimate. Paludal environments (mainly fens and bogs) have vigorously growing surface vegetation and often deep root systems. These are frequently exposed to surface bioturbation, as well as other common surface processes (e.g., flooding and drying) which strongly influence tephra preservation. Variability of these processes and subtle differences in drainage and vegetation across a large peatland also leads to differences between peat cores taken only 400 m apart (i.e., Tariki Swamp cores; Fig. 3.3). Irregular or diffuse contact of tephra with peat (Appendix 4) reflects deposition on and between vegetation, along with root-bioturbation once buried. Slow peat accumulation rates mean that tephras from several closely timed eruptions are often intermixed. Furthermore, localised variations in sedimentation (e.g., alongside ephemeral stream beds, or at the base of alluvial slopes; Jenny, 1994) and climate-induced sedimentation changes (e.g., increased fluvial activity during wetter interglacial/interstadial periods, or loess/aeolian deposition during cool/dry periods) also play a crucial part in tephra preservation at any site. In all the sites studied, the basal parts of most sediment cores contain an increased non-volcanogenic clastic component, consistent with periglacial processes prevalent during the last glacial to interglacial transition period in New Zealand (~18-12 cal ka BP; Barrell et al., 2013). For all of these reasons, it is important to obtain at least two sediment cores per peatland site to track possible tephra preservation issues and build the most complete composite core possible.

The lacustrine sediment cores recovered during this study show little evidence for bioturbation, mixing of tephras and non-volcanogenic clastic sediments, except for Lake Rotokare, which had periodic influxes of muddy sediment from the steep surrounding Tertiary hill country (Turner et al., 2011b). However, in such sites, tephra can be reworked by bottom currents and/or wave action, as well as washed or blown in from the catchment area (e.g., Fisher and Schmincke, 1984; Green and Lowe, 1985; deFontaine et al., 2007; Watson et al., 2016). Apart from a few possibly reworked units, tephra layers in all three sediment cores taken from that of Lake Richmond were effectively identical. Furthermore, a similar tephrostratigraphy at Lake Umutekai compared to Lake Richmond suggest that tephra deposition rate in both lakes is

reasonably steady (Fig. 3.1). By contrast, Lake Rotokare's variable sedimentation regime has a possible influence on tephra preservation and subsequent age determinations, which should be considered with caution. A distinct doubling of the sedimentation-rate at around 5.5 cal ka BP (Fig. 3.1) was recognised in both the Lake Richmond and Lake Umutekai records. This apparent change in the sedimentation rate potentially reflects either lower compaction, and/or diagenesis of the upper sediments, or a genuine increase in the sedimentation rate in response to increasing rates of organic material supply to the lake in the late Holocene (McGlone et al., 1984; McGlone and Neall, 1994). Some tephra layers in the lower sequence of Lake Richmond were preserved as pockets of tephra (i.e., lenses) rather than discrete tephra layers. Such a mode of preservation could represent stronger water currents caused by higher wind and/or lake-level lowering during dry and cold climate conditions, common during frequent climate fluctuations of the early-mid Holocene (Newnham et al., 1989; Mayewski et al., 2004; Brook et al., 2011).

3.2.6.3 Preliminary implications for Mt. Taranaki's magmatic system

Compositional variations in the titanomagnetite phenocrysts and the glass shards follow two distinct evolutionary trends over time. The first is a change from trachyandesitic glass of Tephra Sequence E to rhyolitic glass of Tephra Sequence B (Fig. 3.8). Correspondingly, titanomagnetite compositions show decreasing Al_2O_3+MgO and TiO_2 abundances and higher FeO_{total}, along with higher Fe^{3+}/Fe^{2+} ratios (Fig. 3.6, Table 3.2). High FeO_{total} contents in glass are associated with lower FeO_{total} contents in the corresponding titanomagnetites. As noted from whole-rock and mineral chemical studies at Mt. Taranaki (Stewart et al., 1996; Price et al., 1999), the glass compositional evolution is likely related to fractionation of clinopyroxene, hornblende, ±plagioclase, which are common mineral phases in this pyroclastic suite. Changes in storage, magma ascent rate and fractionation affect titanomagnetite compositions in a similar way (Hill and Roeder 1974; Tomiya and Takahashi, 2005), reducing Al_2O_3 and MgO contents. Variation in the TiO_2 content of titanomagnetites, however, is more complex and may

relate to a number of processes, both deep and shallow including: (1) temperature and oxygen fugacity variations of magmas (e.g., Buddington and Lindsley, 1964; Hill and Roeder, 1974; Jackson et al., 2003; Annen et al., 2006), (2) variations in the primary magma source, as suggested by previous studies to be at the lower crust (e.g., Stewart et al., 1996; Price et al, 1999; Zernack et al., 2012), and/or (3) a greater compatibility of Ti during early stages of fractional crystallisation.

Some tephra layers, which depart from the overall evolutionary trend described above, show distinctly higher or lower TiO_2 contents in their titanomagnetites, a bimodal titanomagnetite composition, and/or a large range in their glass composition. Such variations probably reflect the polybaric magmatic system of Mt. Taranaki (c.f., Zernack et al., 2012), where different magmas are produced by a combination of fractional crystallisation, crustal melting and assimilation, as well as by magma mixing and/or mingling in a complex mantle-crustal storage system. The lower part of Tephra Sequence C, for example, is composed of two distinct titanomagnetite groups with greatly varying TiO_2 contents, reflecting different oxygen fugacity levels and likely different magma storage levels (Fig. 3.6). Some of these layers include traces of Al_2O_3+MgO-rich titanomagnetites (i.e., titanomagnetite group-11) similar to the more mafic Manganui tephras. This distinct bimodality suggests a period of magma recharge, where less-evolved magma entered the storage system (e.g., Clynne. 1999; Devine et al., 2003; Tomiya and Takahashi, 2005). Another type of bimodality is observed within unit T-23 of Tephra Formation D, where titanomagnetite compositions spread over titanomagnetite groups-1 and 2 (Table 3.2). Such compositional bimodality suggests magma mingling/mixing just shortly prior to or during the eruption, which is consistent with banded pumice and a broad range in glass shard compositions of this unit (Figs. 3.3, 3.7, Appendix 3). In contrast, some tephra layers (i.e., T-5, Ri-117, Ri-118, E-23, U-7, -9; Fig. 3.9) are characterised by a bimodal composition that is more likely caused by contamination rather than any magmatic process, since their bimodal composition is reflected compositions of over- and/or underlying tephra layers or is not documented in compositions for correlative tephras from other cores. In particular, entrainment of material from conduit/vent walls during explosive eruptions, or post-depositional

intermixing of closely spaced tephra layers within the sediment column are most likely contamination causes.

After eruption of Tephra Sequence B, with the most silicic glass composition (including the prominent Inglewood Tephra), a distinct chemical change occurred to more mafic compositions of Tephra Sequence A (Figs. 3.7, 3.9) represented by type-I tephras (Manganui correlatives, titanomagnetite group-11; Fig. 3.6). This change may indicate the beginning of a possible second geochemical trend. Type-I tephras are intercalated with type-II tephras, which are more evolved, but show similar low TiO_2 titanomagnetite concentrations (Fig. 3.6). This affinity of both tephra types may suggest a shared identity where type-II magmas may result from the evolution of type-I magmas and/or may be a product of mixing type-I with older more evolved magmas.

3.2.7 Conclusions

1) The 30,000-year long tephrostratigraphic record constructed in this study is one of the most detailed and continuous for an andesitic stratovolcano. The collection of several sediment cores in a closely spaced arc around the volcano provided the opportunity to sample narrow tephra lobes (deposited under high-wind conditions) and overcome preservation/erosion issues that may be associated with single sites.
2) This approach enabled the building of a detailed composite tephra record, including at least 228 tephra layers, which provides a more complete insight into the explosive eruption history of Mt. Taranaki.
3) Through sampling at a range of locations, this study also records the physical differences in tephra deposition in lacustrine versus paludal environments and highlights the influence of physiographic and sedimentary conditions on tephra preservation.
4) Titanomagnetite phenocrysts in combination with glass analyses, as well as detailed physical observations of the tephra layers and radiocarbon dating provide a robust basis for tephra differentiation and correlation. Packages of physically and compositionally similar tephra layers within a tight chronological

framework were used to define six individual tephra sequences (Tephra Sequence A-F) at Mt. Taranaki. These showed two general pattern of evolution over time at this volcano: (1) Tephra Sequence E to B (17.5 to 3 cal ka BP), and (2) Tephra Sequence A (3 to 0.5 cal ka BP). Additional complex geochemical variations within these broad evolutional trends point to a polybaric magmatic system where fractional crystallisation, crustal melting/assimilation, and magma mingling/mixing take place in a complex storage and plumbing system beneath the volcano.

5) Despite the high-resolution record, correlation of individual beds is not always simple and correlation to on-cone sites is challenging due to poor preservation of proximal deposits and limited compositional data.

3.2.8 Acknowledgements

Magret Damaschke acknowledges the financial support of a Massey Doctoral Scholarship, and the George Mason Trust. All author benefitted from financial support of the Natural Hazards Research Platform, “Living with volcanic risk” programme, funded by the Ministry for Business, Innovation and Employment. We thank David Feek and Dr Alan Palmer for assisting in core extraction and Steve Styger, Gary Comarer, Trevor Jane, John & Jack Newsome, Raymond Foster, Brian Rowlands, Alison Rumball, and family Tamblin for allowing access to their land for sampling. Dr Anja Moebis and Mr Peter Lewis are thanked for their help with electron microprobe and other analytical analyses. We thank Prof Vince Neall for kindly providing samples from previous studies, and Prof Clel Wallace, Prof Bob Stewart and colleague Rafael Torres-Orozco for their helpful discussions. We gratefully acknowledge the helpful review of Prof David Lowe and an anonymous reviewer.

3.2.9 References

Alloway, B. V., Stewart, R. B., Neall, V. E., & Vucetich, C. G. (1992). Climate of the last glaciation in New Zealand, based on aerosolic quartz influx in an andesitic terrain. Quaternary Research, 38, 170-179.

Alloway, B. V., Lowe, D. J., Chan, R. P. K., Eden, D., & Froggatt, P. (1994). Stratigraphy and chronology of the Stent tephra, a c. 4000 year old distal silicic tephra from Taupo Volcanic Centre, New Zealand. New Zealand Journal of Geology and Geophysics, 37(1), 37-47.

Alloway, B. V., Neall, V. E., & Vucetich, C. G. (1995). Late Quaternary (post 28,000 year BP) tephrostratigraphy of northeast and central Taranaki, New Zealand. Journal of the Royal Society of New Zealand, 25, 385-458.

Alloway, B. V., McComb, P., Neall, V. E., Vucetich, C. G., Gibb, J., Sherburn, S., & Stirling, M. (2005). Stratigraphy, age, and correlation of voluminous debris-avalanche events from an ancestral Egmont Volcano: implications for coastal plain construction and regional hazard assessment. Journal of the Royal Society of New Zealand, 35(1-2), 229-267.

Annen, C., Blundy, J. D., & Sparks, R. S. (2006). The genesis of intermediate and silicic magmas in deep crustal hot zones. Journal of Petrology, 47, 505-39.

Aomine, S., & Wada, K. (1962). Differential weathering of volcanic ash and pumice, resulting in formation of hydrated halloysite. American mineralogist, 47, 1024-1048.

Barrell, D. J., Almond, P. C., Vandergoes, M. J., Lowe, D. J., Newnham, R. M., & INTIMATE members (2013). A composite pollen-based stratotype for inter-regional evaluation of climatic events in New Zealand over the past 30,000 years (NZ-INTIMATE project). Quaternary Science Reviews, 74, 4-20.

Best, M.G. (2003). Igneous and metamorphic petrology. Blackwell Science.

Blomqvist, S. (1985). Reliability of core sampling of soft bottom sediment – an in situ study. Sedimentology, 32(4), 605-612.

Blomqvist, S. (1991). Quantitative sampling of soft-bottom sediments: problems and solutions. Marine Ecology Progress Series, 72(3), 295-304.

Blott, S. J. (2010). GRADISTAT ver. 8.0: A grain size distribution and statistics package for the analysis of unconsolidated sediments by sieving or laser granulometer. Kenneth Pye Associates Ltd, UK.

Bronk Ramsey, C. (2013). OxCal 4.2. Web Interface Build (78).

Brook, M. S., Neall, V. E., Stewart, R. B., Dykes, R. C., & Birks, D. L. (2011). Recognition and paleoclimatic implications of late-Holocene glaciation on Mt Taranaki, North Island, New Zealand. The Holocene, 21(7), 1151-1158.

Bryant, C. J., Arculus, R. J., & Eggins, S. M. (2003). The geochemical evolution of the Izu-Bonin arc system: A perspective from tephras recovered by deep-sea drilling. Geochemistry, Geophysics, Geosystems, 4(11).

Buddington, A. F., & Lindsley, D. H. (1964). Iron–titanium oxide minerals and synthetic equivalents. Journal of Petrology, 5(2), 310-357.

Carmichael, I.S.E. (1966). Iron-titanium oxides of salic volcanic rocks and their associated ferromagnesian silicates. Contributions to Mineralogy and Petrology, 14(1), 36-64.

Clynne, M.A. (1999). A complex magma mixing origin for rocks erupted in 1915, Lassen Peak, California. Journal of Petrology, 40(1), 105-132.

Cronin, S. J., Wallace, R. C., & Neall, V. E. (1996). Sourcing and identifying andesitic tephras using major oxide titanomagnetite and hornblende chemistry, Egmont volcano and Tongariro Volcanic Centre, New Zealand. Bulletin of Volcanology, 58, 33-40.

Crusius, J., & Anderson, R. F. (1991). Core compression and surficial sediment loss of lake sediments of high porosity caused by gravity coring. Limnology and Oceanography, 36(5), 1021-1030.

deFontaine, C. S., Kaufman, D. S., Anderson, R. S., Werner, A., Waythomas, C. F., & Brown, T.A. (2007). Late Quaternary distal tephra-fall deposits in lacustrine sediments, Kenai Peninsula, Alaska. Quaternary Research, 68, 64-78.

Devine, J. D., Rutherford, M. J., Norton, G. E., & Young, S. R. (2003). Magma storage region processes inferred from geochemistry of Fe–Ti oxides in andesitic magma, Soufriere Hills Volcano, Montserrat, WI. Journal of Petrology, 44(8), 1375-1400.

Drost, F., Renwick, J., Bhaskaran, B., Oliver, H., & McGregor, J. (2007). A simulation of New Zealand's climate during the Last Glacial Maximum. Quaternary Science Reviews, 26(19), 2505-2525.

Fisher, R., & Schmincke, H. U. (1984). Pyroclastic Rocks. Springer-Verlag, Berlin, p. 472.

Franks, A., Neall, V. E., & Pollock, J. (1991). Soils of Part Eltham County, North Island, New Zealand. DSIR Land Resources Scientific Report No. 14. Lower Hutt, New Zealand. DSIR Land Resources.

Fritsch, F. N., & Carlson, R. E. (1980). Monotone piecewise cubic interpolation. SIAM Journal on Numerical Analysis, 17(2), 238-246.

Frost, B. R., & Lindsley, D. H. (1991). Occurrence of iron–titanium oxides in igneous rocks. Reviews in Mineralogy and Geochemistry, 25(1), 433-468.

Gaillard, J. (2006). Traditional societies in the face of natural hazards: the 1991 Mt. Pinatubo eruption and the Aetas of the Philippines. International Journal of Mass Emergencies and Disasters, 24(1), 5.

Gamble, J. A., Wood, C. P., Price, R. C., Smith, I. E. M., Stewart, R. B., & Waight, T. (1999). A fifty year perspective of magmatic evolution on Ruapehu Volcano, New Zealand: verification of open system behaviour in an arc volcano. Earth and Planetary Science Letters, 170(3), 301-314.

Gertisser, R., & Keller, J. (2003). Temporal variations in magma composition at Merapi Volcano (Central Java, Indonesia): magmatic cycles during the past 2000 years of explosive activity. Journal of Volcanology and Geothermal Research, 123, 1-23.

Ghiorso, M. S., & Sack, R.O. (1991). Thermochemistry of the oxide minerals. Reviews in Mineralogy, 25, 222-264.

Green, J. D., & Lowe, D. J. (1985). Stratigraphy and development of c. 17,000 year old Lake Maratoto, North Island, New Zealand, with some inferences about postglacial climatic change. New Zealand Journal of Geology and Geophysics, 28, 675-699.

Green, R. M., Bebbington, M. S., Cronin, S. J., & Jones, G. (2014). Automated statistical matching of multiple tephra records exemplified using five long maar sequences younger than 75 ka, Auckland, New Zealand. Quaternary Research, 82, 405-419.

Hill, R., & Roeder, P. (1974). The crystallisation of spinel from basaltic liquid as a function of oxygen fugacity. Journal of Geology, 709-729.

Hogg, A. G., Hua, Q., Blackwell, P. G., Niu, M., Buck, C. E., Guilderson, T. P., Heaton, T. J., Palmer, J. G., Reimer, P. J., Reimer, R. W., Turney, C. S. M., & Zimmerman, S. R. H. (2013). SHCal13 Southern Hemisphere calibration, 0-50,000 years cal BP. Radiocarbon 55, 1889-1903.

Jackson, M. D., Cheadle, M. J., & Atherton, M. P. (2003). Quantitative modeling of granitic melt generation and segregation in the continental crust. Journal of Geophysical Research: Solid Earth, 108(B7).

Jenny, H. (1994). Factors of soil formation: a system of quantitative pedology. Courier Corporation.

Kohn, B. P. (1970). Identification of New Zealand tephra-layers by emission spectrographic analysis of their titanomagnetites. Lithos 3, 361-368.

Kohn, B. P., & Neall, V. E. (1973). Identification of late Quaternary tephras for dating Taranaki lahar deposits. New Zealand Journal of Geology and Geophysics, 16, 781-792.

Krumbein, W. C., & Aberdeen, E. (1937). The sediments of Barataria Bay. Journal of Sedimentary Research, 7(1).

Lebel, J., Silverberg, N., & Sundby, B. (1982). Gravity core shortening and pore water chemical gradients. Deep Sea Research Part A. Oceanographic Research Papers, 29(11), 1365-1372.

Lees, C. M., & Neall, V. E. (1993). Vegetation response to volcanic eruptions on Egmont Volcano, New Zealand, during the last 1500 years. Journal of the Royal Society of New Zealand, 23, 91-127.

Lowe, D. J. (1988a). Late Quaternary volcanism in New Zealand: towards an integrated record using distal airfall tephras in lakes and bogs. Journal of Quaternary Science, 3, 111-120.

Lowe, D. J. (1988b). Stratigraphy, age, composition, and correlation of late Quaternary tephras interbedded with organic sediments in Waikato lakes, North Island, New Zealand. New Zealand Journal of Geology and Geophysics, 31, 125-165.

Lowe, D. J. (2011). Tephrochronology and its application: a review. Quaternary Geochronology, 6(2), 107-153. Chicago.

Lowe, D. J., Newnham, R. M., & Ward, C. M. (1999). Stratigraphy and chronology of a 15 ka sequence of multi-sourced silicic tephras in a montane peat bog, eastern North Island, New Zealand. New Zealand Journal of Geology and Geophysics, 42, 565-579.

Lowe, D. J., Shane, P. A. R., Alloway, B. V., & Newnham, R. M. (2008). Fingerprints and age models for widespread New Zealand tephra marker beds erupted since 30,000 years ago: a framework for NZ-INTIMATE. Quaternary Science Reviews, 27, 95-126.

Lowe, D. J., Blaauw, M., Hogg, A. G., & Newnham, R. M. (2013). Ages of 24 widespread tephras erupted since 30,000 years ago in New Zealand, with re-evaluation of the timing and palaeoclimatic implications of the Lateglacial cool episode at Kaipo bog. Quaternary Science Reviews, 74, 170-194.

Lowe, D. J., Tonkin, P. J., Palmer, J., Lanigan, K., & Palmer, A. S. (2015). Dusty horizons. In: Graham, I. (chief editor). A Continent on the Move: New Zealand Geoscience Revealed, 2nd Edition. Geoscience Society of New Zealand with GNS Science, Wellington, GSNZ Miscellaneous Publication, 141, pp. 286-289.

Marcaida, M., Mangan, M. T., Vazquez, J. A., Bursik, M., & Lidzbarski, M. I. (2014). Geochemical fingerprinting of Wilson Creek formation tephra layers (Mono Basin, California) using titanomagnetite compositions. Journal of Volcanology and Geothermal Research, 273, 1-4.

Mayewski, P. A., Rohling, E. E., Stager, J. C., Karlén, W., Maasch, K. A., Meeker, L. D., Meyerson, E. A., Gasse, F., van Kreveld, S., Holmgren, K., & Lee-Thorp, J. (2004). Holocene climate variability. Quaternary research, 62(3), 243-255.

McGlone, M. S., Howorth, R., & Pullar, W. A. (1984). Late Pleistocene stratigraphy, vegetation and climate of the Bay of Plenty and Gisborne regions, New Zealand. New Zealand Journal of Geology and Geophysics, 27(3), 327-350.

McGlone, M. S., & Neall, V. E. (1994). The late Pleistocene and Holocene vegetation history of Taranaki, North Island, New Zealand. New Zealand Journal of Botany 3, 251-269.

Molloy, C., Shane, P., & Augustinus, P. (2009). Eruption recurrence rates in a basaltic volcanic field based on tephra layers in maar sediments: Implications for hazards in the Auckland volcanic field. GSA Bulletin, 121, 1666-1677.

Morton, R. A., & White, W. A. (1997). Characteristics of and corrections for core shortening in unconsolidated sediments. Journal of Coastal Research, 761-769.

Neall, V. E. (1972). Tephrochronology and tephrostratigraphy of western Taranaki (N108-109), New Zealand. New Zealand Journal of Geology and Geophysics, 15, 507-57.

Neall, V. E. (1979). Sheets P19, P20 and P2l New Plymouth, Egmont and Manaia, Geological Map of New Zealand 1:50,000. 3 maps and notes, 36 p. New Zealand Department of Science and Industrial Research, Wellington.

Neall, V. E., & Alloway, B. E. (2004). Quaternary Geological Map of Taranaki. Institute of Natural Resources - Massey University, Soil and Earth Sciences Occasional Publication, No. 4.

Newnham, R. M. (1990). Late Quaternary palynological investigations into the history of vegetation and climate in northern New Zealand. Unpublished PhD thesis, University of Auckland, Auckland, New Zealand.

Newnham, R. M., Lowe, D. J., & Green, J. D. (1989). Palynology, vegetation and climate of the Waikato lowlands, North Island, New Zealand, since c. 18,000 years ago. Journal of the Royal Society of New Zealand, 19(2), 127-150.

Parker, W. R., & Sills, G. C. (1990). Observation of corer penetration and sample entry during gravity coring. In: Marine Geological Surveying and Sampling, Springer Netherlands, pp. 101-107.

Payne, R. J., & Gehrels, M. J. (2010). The formation of tephra layers in peatlands: an experimental approach. Catena, 81, 12-23.

Pillans, B.J. (1988). Loess chronology in Wanganui Basin, New Zealand. In: Eden, D.N., Furkert, R.J. (Eds), Loess-Its Distribution. Geology and Soils, 175-193.

Platz, T., Cronin, S. J., Cashman, K. V., Stewart, R. B., & Smith, I. E. M. (2007). Transitions from effusive to explosive phases in andesite eruptions – A case-study from the AD 1655 eruption of Mt. Taranaki, New Zealand. Journal of Volcanology and Geothermal Research, 161(1), 15-34.

Platz, T., Cronin, S. J., Procter, J. N., Neall, V. E., & Foley, S. F. (2012). Non-explosive dome-forming eruptions at Mt. Taranaki, New Zealand. Geomorphology, 136, 15-30.

Plunkett, G., Coulter, S. E., Ponomareva, V. V., Blaauw, M., Klimaschewski, A., & Hammarlund, D. (2015). Distal tephrochronology in volcanic regions: challenges and insights from Kamchatkan lake sediments. Global and Planetary Change, 134, 26-40.

Price, R. C., Stewart, R. B., Woodhead, J. D., & Smith, I. E. M. (1999). Petrogenesis of high-K arc magmas: evidence from Egmont Volcano, North Island, New Zealand. Journal of Petrology, 40, 167-197.

Price, R. C., Gamble, J. A., Smith, I. E. M., Stewart, R. B., Eggins, S., & Wright, I. C. (2005). An integrated model for the temporal evolution of andesites and rhyolites and crustal development in New Zealand's North Island. Journal of Volcanology and Geothermal Research, 140(1), 1-24.

Procter, J. N., Cronin, S. J., Platz, T., Patra, A., Dalbey, K., Sheridan, M., & Neall, V. E. (2010). Mapping block-and-ash flow hazards based on Titan 2D simulations: a case study from Mt. Taranaki, NZ. Natural Hazards, 53, 483-501.

Salinger, M. J. (1984). New Zealand Climate: the last 5 million years. In: Vogel, J. C. (Ed), Late Cainozoic palaeoclimates of the Southern Hemisphere. Balkema, 131-150, Rotterdam.

Sandiford, A., Alloway, B., & Shane, P. (2001). A 28,000-6600 cal yr record of local and distal volcanism preserved in a palaeolake, Auckland, New Zealand. New Zealand Journal of Geology and Geophysics, 44, 323-336.

Shane, P. (1998). Correlation of rhyolitic pyroclastic eruptive units from the Taupo volcanic zone by Fe–Ti oxide compositional data. Bulletin of Volcanology, 60, 224-38.

Shane, P. (2005). Towards a comprehensive distal andesitic tephrostratigraphic framework for New Zealand based on eruptions from Egmont volcano. Journal of Quaternary Science, 20, 45-57.

Shane, P., & Hoverd, J. (2002). Distal record of multi-sourced tephra in Onepoto Basin, Auckland, New Zealand: Implications for volcanic chronology, frequency, and hazards. Bulletin of Vulcanology, 64, 441-54.

Skinner, L. C., & McCave, I. N. (2003). Analysis and modelling of gravity-and piston coring based on soil mechanics. Marine Geology, 199(1), 181-204.

Stewart, R. B., & Neall, V. E. (1984). Chronology of palaeoclimatic change at the end of the last glaciation. Nature, 311, 47-48.

Stewart, R. B., Price, R. C., & Smith, I. E. (1996). Evolution of high-K arc magma, Egmont volcano, Taranaki, New Zealand: evidence from mineral chemistry. Journal of Volcanology and Geothermal Research, 74, 275-95.

Taranaki Catchment Commission (1980). Lake Rotokare water management plan. Unpublished report, Taranaki Catchment Commission, Stratford, New Zealand.

Tinkler, R. J. (2013). A high resolution record of Late Quaternary climatic and environmental change in Taranaki, New Zealand. Unpublished PhD thesis, Massey University, Palmerston North, New Zealand.

Tomiya, A., & Takahashi, E. (2005). Evolution of the magma chamber beneath Usu Volcano since 1663: a natural laboratory for observing changing phenocryst compositions and textures. Journal of Petrology, 46(12), 2395-2426.

Toplis, M. J., & Carroll, M. R. (1995). An experimental study of the influence of oxygen fugacity on Fe–Ti oxide stability, phase relations, and mineral-melt equilibria in ferro-basaltic systems. Journal of Petrology, 36(5), 1137-1170.

Torres-Orozco, R., Cronin, S. J., Pardo, N., & Palmer, A. S. (2017). New insights into Holocene eruption episodes from proximal deposit sequences at Mt. Taranaki (Egmont), New Zealand. Bulletin of Volcanology, 79(1), 3, DOI: 10.1007/s00445-016-1085-5.

Turner, M. B. (2008). Eruption cycles and magmatic processes at a reawakening volcano, Taranaki, New Zealand. Unpublished PhD thesis, Massey University, Palmerston North, New Zealand.

Turner, M. B., Cronin, S. J., Smith, I. E. M., Stewart, R. B., & Neall, V. E. (2008a). Eruption episodes and magma recharge events in andesitic systems, Mt Taranaki, New Zealand. Journal of Volcanology and Geothermal Research, 177, 1063-1076.

Turner, M. B., Cronin, S. J., Smith, I. E. M., Bebbington, M. S., & Stewart, R. B. (2008b). Using titanomagnetite textures to elucidate volcanic eruption histories. Geology, 36, 31-34.

Turner, M. B, Cronin, S. J., Bebbington, M. S., & Platz, T. (2008c). Developing a probabilistic eruption forecast for dormant volcanos; a case study from Mt Taranaki, New Zealand. Bulletin of Volcanology, 70, 507-515.

Turner, M. B., Bebbington, M. S., Cronin, S. J., & Stewart, R. B. (2009). Merging eruption datasets: towards an integrated Holocene eruptive record of Mount Taranaki, New Zealand. Bulletin of Volcanology, 71, 903-918.

Turner, M. B., Cronin, S. J., Bebbington, M. S., Smith, I. E. M., & Stewart, R. B. (2011a). Relating magma composition with eruption variability at andesitic volcanoes. A case study from Mount Taranaki, New Zealand. Geological Society of America Bulletin, 123, 2005-2015.

Turner, M. B., Cronin, S. J., Bebbington, M. S., Smith, I. E. M., & Stewart, R. B. (2011b). Integrating records of explosive and effusive activity from proximal and distal sequences: Mt. Taranaki, New Zealand. Quaternary International, 246, 364-373.

Turner, R., Moore, S., Pardo, N., Kereszturi, G., Uddstrom, M., Hurst, T., & Cronin, S. (2014). The use of Numerical Weather Prediction and a Lagrangian transport (NAME-III) and dispersion (ASHFALL) models to explain patterns of observed

ash deposition and dispersion following the August 2012 Te Maari, New Zealand eruption. Journal of Volcanology and Geothermal Research, 286, 437-451.

Vandergoes, M. J., Hogg, A. G., Lowe, D. J., Newnham, R. M., Denton, G. H., Southon, J., Barrell, D. J., Wilson, C. J., McGlone, M. S., Allan, A. S., & Almond, P. C. (2013). A revised age for the Kawakawa/Oruanui tephra, a key marker for the Last Glacial Maximum in New Zealand. Quaternary Science Reviews, 74,195-201.

Wallace, R. C. (1987). Mineralogy of the Tokomaru silt loam and the occurrence of cristobalite and tridymite in selected North Island soils. Unpublished PhD thesis, Massey University, Palmerston North, New Zealand.

Watson, E. J., Swindles, G. T., Lawson, I. T., & Savov, I. P. (2016). Do peatlands or lakes provide the most comprehensive distal tephra records? Quaternary Science Reviews, 139, 110-128.

Zernack, A. V., Cronin, S. J., Neall, V. E., & Procter, J. N. (2011). A medial to distal volcaniclastic record of an andesite stratovolcano: Detailed stratigraphy of the ring-plain succession of south-west Taranaki, New Zealand. International Journal of Earth Sciences, 100, 1936-1966.

Zernack, A. V., Price, R. C., Smith, I. E. M., Cronin, S. J., & Stewart, R. B. (2012). Temporal evolution of a high-K andesitic magmatic system: Taranaki Volcano, New Zealand. Journal of Petrology, 53, 325-363.

Chapter 4

A proximal-distal tephra correlation of andesitic tephra deposits from Mt. Taranaki, New Zealand

This chapter links the newly built high-precision tephrostratigraphic record to on-cone stratigraphies to derive a more robust and overall tephrostratigraphy for Mt. Taranaki.

4.1 Chapter synopsis

In Chapter 3 lake and peat tephra records have been used to develop a high-precision tephrostratigraphy for Mt. Taranaki. Titanomagnetite phenocryst and glass shard compositions in conjunction with detailed age determinations of the tephra layers enabled correlation between the individual records to derive the most detailed and complete composite tephra record ever built for an andesitic stratovolcano. The potential of titanomagnetites as differentiation and correlation tool has been proven successful for the andesitic magmas of Mt. Taranaki where effectively identical compositions and physical appearances often hinder individual tephra identification and discrimination. Very little geochemical data is available from past studies and previous correlations were solely based on stratigraphic/age position and mineral assemblages. Having a highly detailed tephra records available will allow testing of correlations and provide the basis for a more robust tephrostratigraphy for Mt. Taranaki. This is not only vital for future studies on tephra dispersal patterns and volcanology studies, but also to other palaeoenvironmental and palaeogeographic studies to the region.

The majority of this chapter is contained within the manuscript: *Unifying tephrostratigraphic approaches to redefine major Holocene marker tephras, Mt. Taranaki, New Zealand* by M. Damaschke, S.J. Cronin, R. Torres-Orozco, and R.C. Wallace, which has been submitted for publication as a Research Paper in *Journal of Volcanology and Geothermal Research.* The contributions of each author are outlined below:

M. Damaschke: Principal investigator
Carried out: Field work
Laboratory work
Analytical work
Geochemical correlation
Manuscript preparation and writing

S.J. Cronin: Chief Advisor
Aided the study by: Editing and discussion of the manuscript

R. Torres-Orozco: Colleague
Aided the study by: Assistance in field work
Providing proximal field data information
Editing and discussion of the manuscript

R.C. Wallace: Advisor
Aided the study by: Providing geochemical data of pyroclastic deposits from the Mangatoki Stream section
Editing and discussion of the manuscript

4.2 Unifying tephrostratigraphic approaches to redefine major Holocene marker tephras, Mt. Taranaki, New Zealand

M. Damaschke[1], S.J. Cronin[1,2], R. Torres-Orozco[1], R.C. Wallace[1]

[1]*Institute of Agriculture and Environment, Massey University, Private Bag 11222, Palmerston North 4410*

[2]*School of Environment, University of Auckland, Private Bag 92019, Auckland 1142*

4.2.1 Abstract

In this study, geochemical fingerprinting of glass shards and titanomagnetite phenocrysts was used to match twenty complex pyroclastic deposits from the flanks of Mt. Taranaki to major tephra fall "marker beds" in medial and distal deposition sites. These correlations hinged upon identifying time-bound compositional changes (a chemostratigraphy) in distal Taranaki tephra-fall sequences preserved in lake and peat sediment records around the volcano. The current work shows that previous soil-stratigraphy based studies led to miscorrelations, because they relied upon radiocarbon dates, a "counting back" approach, and an underestimate of the number of eruptions that actually occurred in any time frame. The new tephrostratigraphy proposed at Mt. Taranaki resulted from stratigraphic rearranging of several earlier-defined units. Some tephra units are older than previously determined (e.g., Waipuku, Tariki, and Mangatoki; ~6 to 9 cal ka BP), while one of the most prominent Taranaki marker tephra deposit, the Korito, is shown to lie stratigraphically above a widespread rhyolitic marker bed from Taupo volcano, the Stent Tephra (also known as unit Q; ~4.3 cal ka BP). Pyroclastic tephra deposits previously dated between ~6 to 4 cal ka BP at a key tephra section, c. 40 km NE of Mt. Taranaki's summit, were misidentified and are now shown to comprise new marker tephra deposits, including the Kokowai (~4.7 cal ka BP), which is a prominent marker horizon on the eastern flanks of the volcano. A new local proximal stratigraphy for <5 cal ka BP tephra units can be well correlated to tephra

layers within distal lake and peat sequences, but the differences between the two records indicates an overall larger number of eruptions have occurred at this volcano than previously thought. This study additionally demonstrates the utility of titanomagnetite chemistry for discrimination and correlation of groups or sequences of tephra deposits – even if unique compositions cannot be identified.

Keywords: Mt. Taranaki; chronostratigraphy; proximal-distal tephra; correlation; marker horizons; titanomagnetite

4.2.2 Introduction

Late Quaternary tephrochronological studies in New Zealand have been extensive over the past 60 years, predominantly within the silicic Taupo Volcanic Zone in the central North Island (Fig. 4.1) (e.g., Vucetich and Pullar, 1969; Froggatt, 1983; Froggatt and Lowe, 1990; Shane, 2000; Gehrels et al., 2006; Lowe et al., 2008; Moebis et al., 2011). In addition, several studies have tried to develop marker horizons derived from the frequently active andesitic stratovolcano Mt. Taranaki in the western North Island (Fig. 4.1) (e.g., Neall, 1972; Kohn and Neall, 1973; Topping, 1974; Franks et al., 1991; Alloway et al., 1995; Turner et al., 2008b, 2009, 2011a, 2011b; Platz et al., 2012). Developing tephrostratigraphies for mafic to intermediate composition volcanoes is challenging, because (1) variations in compositions between individual eruptives are slight, (2) volcanoes of these compositions tend to erupt more frequently and so there is less time to generate unique compositions, and (3) their pyroclastics are rapidly weathered and poorly preserved in oxidising soil environments, particularly in humid areas. Further, intermediate and mafic tephras are notoriously difficult to geochemically analyse with common glass-fingerprinting methods, because their glass is often very thin-walled and contains an abundance of microlites (Best, 2003; Platz et al., 2007b; Lowe, 2011). Crystal-chemical studies are also challenging, due to zoned phenocrysts, presence of xenocrysts and many successive units havin such similar glass and mineral compositions (Cronin et al., 1996a, 1996b). These issues make building a detailed event stratigraphy a challenging task.

The most promising mineral for correlation of andesitic/intermediate tephras over the last few decades has been Fe-Ti oxide minerals, including magnetite, ilmenite, and titanomagnetite (e.g., Kohn, 1970; Lowe, 1988a, 1988b; Cronin et al., 1996a, 1996b; Shane, 1998, 2005; McHenry, 2005; Turner et al., 2008a, 2009, 2011b; Marcaida et al., 2014; Damaschke et al., 2017). Not only are these near-ubiquitous mineral phases in andesitic deposits, but they are also moderately resistant to post-depositional weathering and are easily extractable from tephra deposits by magnetic separation. Furthermore, these minerals are relatively easy to analyse by electron probe micro-analyzer, and are arguably simpler to analyse than glass, because a focused beam can be used under standard operating conditions. Titanomagnetite analyses can, however, be complicated by exsolution, but this, in itself, can be useful for interpreting the thermal history of a grain (Lowe, 1988b, Turner et al., 2008a). Titanomagnetites are common in Mt. Taranaki deposits (Kohn and Neall, 1973), with their mineralogy reflecting a solid-solution between magnetite and ulvöspinel end-members. Their compositions are frequently unique to individual magmatic conditions of differing eruptions sourced from separate magma bodies at different levels within the crust or upper mantle. These relate to variations in host magma chemistry, temperature, and oxygen fugacity (e.g., Buddington and Lindsley, 1964; Hill and Roeder, 1974; Frost and Lindsley, 1991; Ghiorso and Sack, 1991). Hence, titanomagnetites can be used to fingerprint tephra units in a similar way to glass compositions (Shane, 1998). The main chemical signatures are a reflection of the substitution of Mg^{2+} and Al^{3+}, and to lesser extent Mn^{2+} and Cr^{3+}, into the Fe-Ti oxide spinel-structure. These chemical attributes have been used to understand variations in eruption rates over time at Mt. Taranaki (Turner et al., 2011b), and as criteria to help correlate tephra between sites (Green et al., 2016). In more recent work on lake and peat tephra sequences, Damaschke et al. (2017) distinguished twelve compositionally different titanomagnetite groups at Mt. Taranaki, each including several eruptions. While rarely sufficient to identify single unique tephras, these titanomagnetite groups in conjunction with glass compositions, physical properties, and precise age determinations helped define six separate sequences of tephras (designated A-F) collectively including 228 tephra layers erupted over the last ~30 cal ka BP.

In this study, the chemical groupings noted in tephra sequences around Mt. Taranaki were used to re-evaluate older published tephra correlations of major maker beds and to link these to the stratigraphy of newly obtained proximal eruption records (Torres-Orozco et al., 2017). Previous tephrostratigraphies (e.g., Neall, 1972, 1979; Franks et al., 1991; Alloway et al., 1995) have hinged upon identifying large, normally lapilli-dominated units of similar appearance, stratigraphic position and general age. Since precise age constraints are difficult to establish in soil and loess sequences, these approaches can easily lead to miscorrelation between successive authors and hinder the integration of stratigraphic sequences from different locations. Currently there are two separate approaches to tephrostratigraphy at Mt. Taranaki; (1) based on formally named "tephra formations" as defined by a series of workers, culminating in Alloway et al. (1995), and (2) based on a more complex record of individual unnamed tephras that have been extracted from lake and peat cores (e.g., Turner, et al., 2008b, 2009; Damaschke et al., 2017). The second approach has identified many more ash layers than were distinguished in the first approach. Links between multiple records have been made, but need strong age control and understanding of the age errors, along with chemical information (Turner et al., 2009; Green et al., 2016).

The geochemical data set from the present work provides the opportunity to confirm or revise previous correlations and to provide a new robust maker horizon chronology for the region. This data set, with reliable geochemical parameters, will also enable correlations to the eastern and northern North Island (Fig. 4.1) (e.g., Lowe, 1988a, 1988b; Eden and Froggatt, 1996; Sandiford et al., 2001; Shane and Hoverd, 2002) and enhance understanding of the geochronology and climatic variations in these areas. Correlations linking tephra from both proximal and distal locations will also provide the potential to calculate volume and magnitude estimates of the largest eruptions from Mt. Taranaki during the Holocene. Here new titanomagnetite and glass chemistry data are used, along with age determinations, and stratigraphic observations to identify and link 27 marker tephra deposits from flank and ring-plain sites to distal lake and peat tephra sequences at Mt. Taranaki.

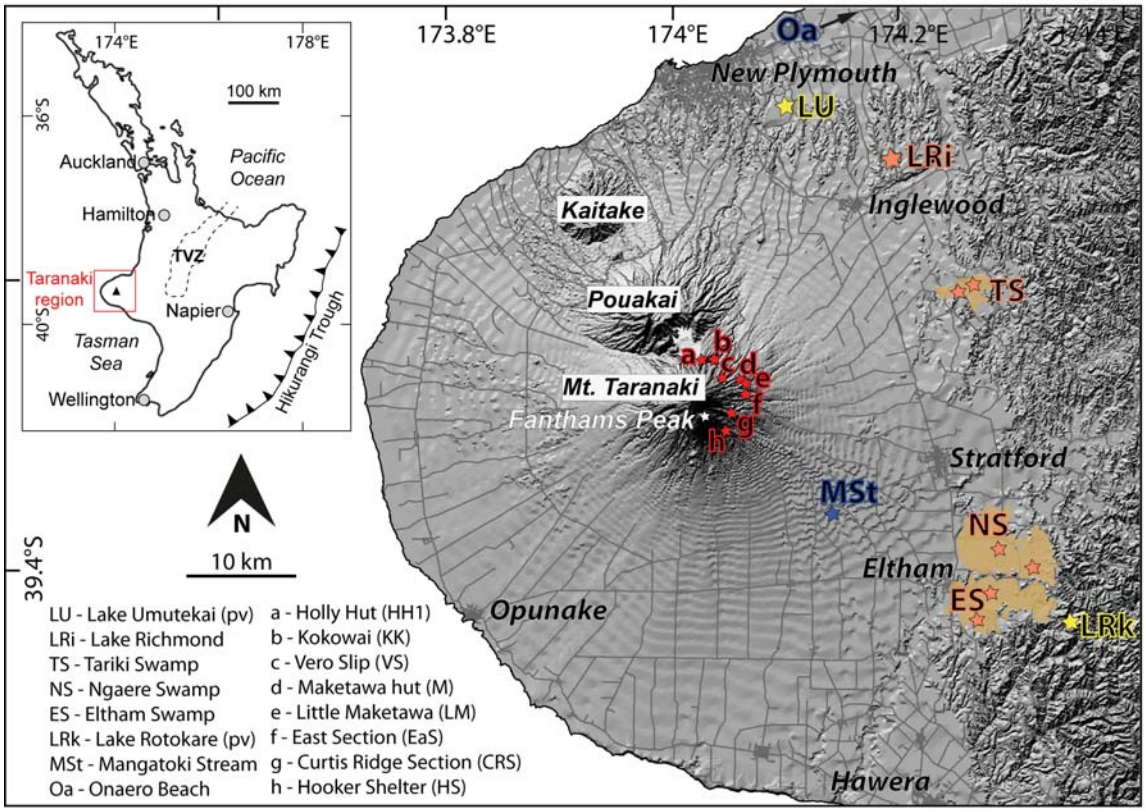

Figure 4. 1 *Location map of the tephra deposition sites in the Taranaki region (pv = previous studied sites by Turner et al., 2008a, 2009), Cape Egmont, western North Island, New Zealand (TVZ = Taupo Volcanic Zone).*

4.2.3 Previous tephrostratigraphy

A simplified summary of the previous tephrostratigraphy at Mt. Taranaki, along with correlation studies, is shown in Figure 4.2. All radiocarbon dates from the literature have been calibrated (cal yr BP) using OxCal Version 4.2 (Bronk Ramsey, 2013) and the Southern Hemisphere SHCal13 (Hogg et al., 2013) atmospheric calibration curve, and are listed in Table 4.1.

The first comprehensive synthesis of the proximal volcanic eruption history of Mt. Taranaki was made by Druce (1966), who identified nine andesitic ash layers, grouped into three formations: (1) Tahurangi Formation (AD 1755), (2) Burrell Formation (AD

1655), and (3) Newall Formation (prior to AD 1604) (Fig. 4.2). Shortly afterwards, Druce's stratigraphy was refined by Tonkin (1970), who studied the influence of these tephras on soil formation in the Dawson Falls region, and Topping (1974), who presented new radiocarbon dates (Table 4.1) and a detailed description of the widespread Burrell tephra, including its deposition and dispersal pattern, which were later revised by Platz et al. (2007a). Cronin et al. (2003) introduced the term 'Maero Eruptive Period' to represent the latest stage of volcanic activity at Mt. Taranaki. It is characterised by 10 eruptive episodes following the eruption of the 1249±157 cal yr BP Kaupokonui tephra (Whitehead, 1976); from oldest to youngest these are: Hooker, Te Popo, Waingongoro, Newall, Waiweranui, Puniho, Burrell, Mangahume, Tahurangi, and Pyramid eruptive episodes (tephrostratigraphy after Platz, 2007; Fig. 4.2, Table 4.1).

Neall (1972) identified widely dispersed tephras in soils surrounding Mt. Taranaki (Fig. 4.2), and identified ten additional ash and lapilli sequences deposited during the last 100 ka. Deposits include the formally named Inglewood and Korito Tephra (p2 and p1, respectively, of Druce, 1966), the Oakura Tephra Formation dated around 7.5 to 8 cal ka BP (Fig. 4.2, Table 4.1), and the Okato Tephra Formation overlying the Saunders Ash, which is considered to be a pyroclastic flow deposit younger than <19 cal ka BP (Neall, 1972). The Carrington Tephras comprise a large group of unnamed tephra deposits separated by buried soils (Neall, 1972; Franks et al., 1991), whereas the Koru tephra represents a widespread marker bed in older pyroclastic deposits (Neall, 1979).

Whitehead (1976) and Franks (1984) subsequently added new data obtained from tephra deposits on the eastern flanks of Mt. Taranaki (Fig. 4.2). Whitehead (1976) formally named the Manganui tephra and the Kaupokonui tephra (p4 of Druce, 1966). For the Manganui tephra, multi-lobed isopachs to the SE, E, and N of the volcano were mapped, implying that the parasitic Fanthams Peak (Fig. 4.2) was the eruption source, rather than the main crater (Whitehead, 1976). A Fanthams Peak origin was later confirmed by detailed studies of deposition on the flanks of the volcano by Turner et al. (2008c) and Torres-Orozco et al. (2017). Franks et al. (1991) mapped several tephra deposits below the prominent Manganui tephra, defining the informally named tephra

units: Mahoe, E1-Konini, E2-Kaponga, E3-Waipuku, E4-Tariki, and E5-Mangatoki (Fig. 4.2), which were tentatively correlated to the previously defined Oakura and Okato Tephra Formations of Neall (1972). During the same time, a sediment core from the Eltham Swamp was recovered (McGlone and Neall, 1994) and tephras encompassed were linked to the tephrostratigraphy of Franks et al. (1991) based on physical properties, stratigraphic position and mineral assemblages (Fig. 4.2).

Alloway et al. (1995) presented a more complete record of the largest and most distinctive Mt. Taranaki tephra marker beds, extending from the pioneering work of Druce (1966), Neall (1972, 1979), and Franks et al. (1991). The study of Alloway et al. (1995) produced a comprehensive synthesis of the post-28 ka record of the marker tephras that could be identified throughout the eastern Taranaki region. This study defined sixteen andesitic tephra formations within three main tephra successions: (1) Manganui to Mahoe Tephra Formation (c. 3 to 15 cal ka BP), (2) Kaihouri to Poto Tephra Formation (c. 15 to 27.5 cal ka BP), and (3) Tuikonga to Waitepuku Tephra Formation (>27.5 cal ka BP) (Fig. 4.2). Many of these formations comprise multiple eruption units, with a total of 76 beds being identified. Distribution information indicated that these tephras were mainly distributed to the north-northeast and south-southeast of the volcano (Lowe, 1986; Alloway et al., 1995). Alloway et al. (1995) provided a chronology for most of the tephra deposits (Table 4.1), from a single key exposure (section 23), where the material that was dated was the peat that was intercalated with the tephra units. Here the Taupo-sourced, silicic, Stent Tephra, also known as unit-Q of post-25 cal ka BP Taupo-eruptive sequences (Wilson, 1993) was also found and dated at 4322±112 cal yr BP (Alloway et al., 1994; Lowe et al., 2013) (Fig. 4.2). The prominent Poto Tephra Formation was documented above the Kawakawa/Oruanui Tephra (Vucetich and Howorth, 1976), which was recently dated at 25,360±160 cal yr BP (Vandergoes et al., 2013). Solely based on age and superpositioning (i.e., occurrence with respect to other deposits), Alloway et al. (1995) tentatively correlated the Taranaki deposits to distal tephra layers that were recognised by Lowe (1988a) in Waikato lake sediments, Hamilton (Fig. 4.2).

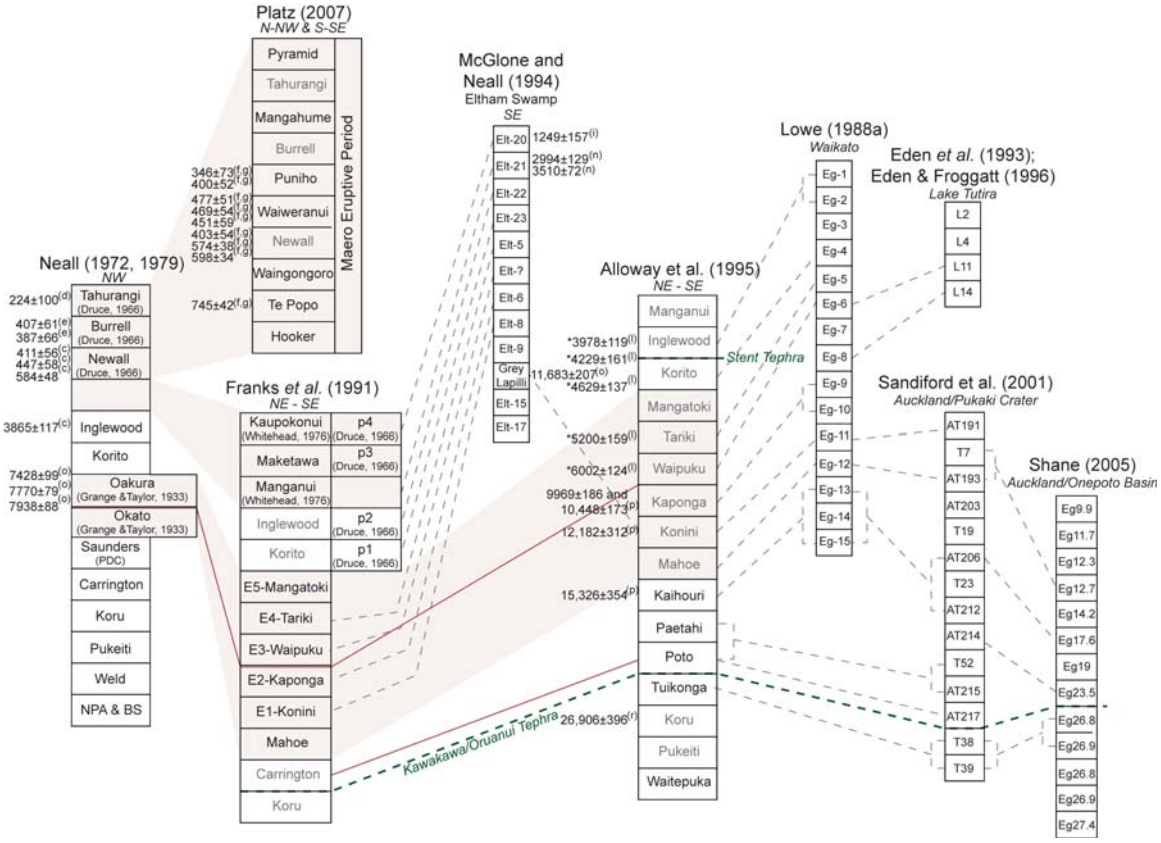

Figure 4. 1 *Brief summary of previous tephrostratigraphic work relating to eruptives of Mt. Taranaki and first correlation attempts solely based on stratigraphic position and physical properties of the deposits. The wide columns represent soil sequence records, whereas the narrow columns represent lake and peatland records. For more detailed information on the relevant tephra correlations (red shaded fields) and minor tephra correlations (dotted grey lines), as well the nomenclature of each deposit, refer to denoted publications. The published ages are re-calibrated using SHCal13 (Hogg et al., 2013), see text and Table 4.1 for details. Ages with asterisks derived from a key section of Alloway et al. (1995) (section 23). PDC = pyroclastic density current, NPA&BS = New Plymouth ashes and buried soils, N = north, S = south, NW = north-west, NE = north-east, SE = south-east.*

Numerous Taranaki-sourced tephra layers have been identified from their chemical composition in distal lake and maar sediments around Auckland City (e.g., Lake Pupuke, Onepoto Basin, Pukaki Lagoon, Orakei Basin, Hopua Crater) (Fig. 4.1), some

270 km N-NW from the source (Sandiford et al., 2001; Shane and Hoverd, 2002; Shane, 2005; Molloy et al., 2009). Correlation of those tephra layers to the Alloway et al. (1995) medial tephrostratigraphy was based on stratigraphic position and age (Fig. 4.2), although the authors recognised that these correlations were provisional due to the lack of compositional data to match distal deposits to source.

Table 4. 1 *Current proximal tephrostratigraphy and relevant radiocarbon dates at Mt Taranaki.*

Tephra unit	Lab ID[1]	Age (yr BP)[2]	Calibrated age (cal yr BP)[3]	Sample location	Mate-rial[4]	Age Ref[5]	Comments
Pyramid		90				(a)	AD 1860
		150				(a)	AD 1800
Tahurangi		195				(b)	AD 1755
	NZ5593	<250				(c)	
	NZ721	249±55	224±100	Cardiff Road	w	(d)	Lahar
Mangahume							No data available
Burrell	NZ63	400±60	407±61	SE flank	c	(e)	Maori oven buried by Burrell
	NZ64	360±60	387±66	SE flank	c	(e)	Maori oven buried by Burrell
Puniho	Wk11590	305±39	346±73	Pyramid Stream	c	(f,g)	
	Wk11593	382±39	400±52	Stony River	c	(f,g)	
Waiweranui	Wk11591	475±42	477±51	Pyramid Stream	c	(f,g)	
	Wk11584	468±42	469±54	Maero Stream	c	(f,g)	
	Wk11589	453±43	451±59	Pyramid Stream	c	(f,g)	
Newall	NZ720	439±55	431±62	Puniho Hut	l	(d)	Between Newall Ash &
	NZ941	404±44	411±56	Saunders Road	c	(c)	Lapilli
	NZ1141	447±40	447±58	Stony River	c	(c)	Beneath river alluvium
	Wk11585	387±43	403±54	Maero Stream	c	(f,g)	
	Wk11594	605±42	574±38	Stony River	c	(f,g)	PDC within Newall
	Wk11592	649±46	598±34	Pyramid Stream	c	(f,g)	
	NZ1256	620±74	584±48	Maero Stream	c	(c)	
Waingongoro	NZ1561	453±55	443±63	Waingongoro section	c	(h)	Maori oven buried by Newall
Te Popo	Wk11586	878±39	745±42	Maero Stream	c	(f,g)	BAF
	Wk2378	970±40	842±48	Stony River	w	(c)	Diamicton beneath Newall
Hooker	Wk16391	1130±34	995±39	Little Maketawa Stream	c	(f,g)	PDC between MG and Te Popo
Kaupokonui	NZ6508	1390±150	1249±157	Potaema Swamp	p	(i)	
Manganui G							No data available
Curtis Ridge							No data available
Manganui F	Wk16390	1739±35	1617±50	Little Maketawa Stream	c	(j)	PDC below MF
Maketawa II	Wk16392	1989±45	1901±59	Little Maketawa Stream	c	(j)	PDC between Maketawa II-I
	NZ3886	1934±70	1833±86	Stratford Mtn Rd	c	(k,l)	PDC between Maketawa II-I
Maketawa I	Wk39445	2223±25	2217±60	Maketawa hut	c	(m)	Maketawa I
	Wk19168	2277±39	2241±57	York track	w	(m)	Maketawa I
	Wk16397	2217±36	2202±71	North Egmont Rd	c	(j)	PDC below Maketawa I
Manganui A-E	NZ3139	3320±60	3510±72	Ahukawakawa Swamp	p	(n)	Below scoriacous lapilli layer
	NZ3423	2890±100	2994±129	Ahukawakawa Swamp	p	(n)	Above scoriacous lapilli layer
	Wk19169	2515±38	2561±98	Kaupokonui Stream	w	(m)	PDC below MC

Table 4.1 *(continued)*

	Wk39446	2946±25	3042±57	Maketawa hut	c	(m)	PDC below MA and above Upper Inglewood
Upper Inglewood	NZ3353	3610±80	3865±117	Norfolk Rd	w	(c)	Below Ngatoro Formation
	Wk16393	3102±37	3267±60	North Egmont	c	(j)	
	Wk39436	3115±25	3284±48	Holly Hut (HH1)	c	(m)	
Lower Inglewood	Wk39437	3180±29	3350±53	Camphouse	c	(m)	
IgF-I							No data available
Korito	Wk16395	3362±37	3547±55	Okahu Stream	c	(j)	PDC within Korito
Kapuni-B	Wk1031	3690±80	3978±119	Onaero Beach	p	(l)	Revised in this study
Kapuni-A							No data available
KkF-I, -II							No data available
Kokowai	Wk39440	4213±25	4712±69	Kokowai (KK)	c	(m)	Layer-4
	Wk39439	4140±25	4634±95	Kokowai (KK)	c	(m)	Layer-7
	Wk16396	4429±45	4984±103	Okahu Stream	c	(j)	PDC below Kokowai
	Wk1033	4150±100	4629±137	Onaero Beach	p	(l)	Revised in this study
Tw-I to -XI	Wk1034	4590±100	5200±159	Onaero Beach	p	(l)	Revised in this study
	Wk1035	5260±90	6002±124	Onaero Beach	p	(l)	Revised in this study
Mangatoki							No data available
Tariki	NZ1781	6570±110	7428±99	Middletons Bay	w	(o)	Within Opua Formation
	NZ1144	6970±76	7770+79	Waiweranui Stream	w	(o)	Below Kahui Drebris Flow
	NZ1142	7160±80	7938±88	Warea River	w	(o)	Below Kahui Drebris Flow
Waipuku	Wk19166	7913±62	8720±121	Wilkies Pool	s	(j)	Sample M06-64, see this study
Kaponga	NZ7986	8947±130	9969±186	Egmont Rd	c	(p)	
	NZ5409	9280±130	10,448±173	Durham Rd	p	(p)	
Konini	NZ5410	10,450±200	12,182±312	Durham Rd	p	(p)	
	NZ3153	10,150±100	11,683±207	Eltham Swamp core	p	(o)	Within gray lapilli bed
Mahoe							No data available
Kaihouri	NZ5411	12,900±200	15,326±354	Durham Rd		(p)	
Paetahi							No data available
Poto			25,360±160	Mangatu Stream and Taurewa south		(q)	Dated Kawakawa Tephra
Tuikonga							No data available
Koru	Wk1516	22,700±400	26,906±396	Omahina Rd	c	(r)	
Pukeiti							No data available
Waitepuka							No data available

[1] Rafter (NZ) and Waikato (Wk) radiocarbon dating laboratories
[2]All conventional radiocarbon ages in years before present (yr BP) ±1 standard deviation, are based on the old half-life (Libby half- life of 5568 years), and are not corrected for secular effects.
[3]Radiocarbon ages were calibrated (mean calibrated age ±1σ) using OxCal Version 4.2 (Bronk Ramsey, 2013) and the Southern Hemisphere SHCal13 (Hogg et al., 2013) atmospheric calibration curve.
[4]Material dated: c=charcoal, p=peat, l=leaves and w=wood
[5]Age references as followed:(a) Platz (2007), (b) Druce (1966), (c) Neall (1972, 1979, 1999), (d) Grant-Taylor and Rafter (1971), (e) Grant-Taylor and Rafter (1963), (f) Cronin et al. (2003), (g) Turner et al. (2008b), (h) Topping (1974), (i) Neall and Jansen (1984), (j) Turner (2008), (k) Franks et al. (1991), (l) Alloway et al. (1995), (m) Torres-Orozco et al. (2017), (n) McGlone et al. (1988), (o) McGlone and Neall (1994), (p) Alloway et al. (1992), (q) Vandergoes et al. (2013), (r) Pillans et al. (1993).
**BAF – Block and Ash flow, PDC – pyroclastic density current*

4.2.4 Sites and samples

4.2.4.1 Flank localities (proximal)

Twenty tephra units were sampled (only their fall deposits) from eight proximal sites on the upper, north- to south-eastern flanks of Mt. Taranaki (Fig. 4.1, Table 4.2). For a detailed description of those deposits see Torres-Orozco et al. (2017).

4.2.4.2 Ring-plain localities (medial)

Section 23 and section 25 of Alloway et al. (1994, 1995) at the Waitara Onaero Bay, were revisited during this study. While the latter has been destroyed by a landslide, two pyroclastic deposits above (aS) and below (bS) the distinctive Taupo-sourced Stent Tephra at the beach-cliff exposure of section 23 (here referred to as Onaero Beach section; Fig. 4.1), c. 0.4 km west of Sutton Road, were sampled. These beds consist of dispersed weathered fine pumice lapilli scattered within soil and peat.

A further prominent medial key site considered was the Mangatoki Stream section of Franks (1984) and Franks et al. (1991), c. 13 km south-east of Mt. Taranaki's summit (Fig. 4.1). Nine tephra units from this site were geochemically analysed by Wallace (1987), with the data integrated into the present study (Table 4.2).

Table 4. 2 *The marker tephra units from Mt. Taranaki analysed in the current study.*

Tephra unit	Flank sites (Torres-Orozco et al., 2017)	Mangatoki Stream section (Franks et al., 1991)
Burrell	x	
Te Popo	x	
Kaupokonui	x	
Manganui G	x	
Curtis Ridge	x	
Manganui F	x	
Maketawa II	x	
Maketawa I	x	
Manganui A-E	x	x
Upper Inglewood	x	x
Lower Inglewood	x	
Korito	x	
Kapuni-B	x	
Kapuni-A	x	
Kokowai	x	
Tw-I	x	
E5-Mangatoki		x
E4-Tariki		x
E3-Waipuku		x
E2-Kaponga		x
E1-Konini		x
Mahoe		x
Layer-256*		x

*Note: *Tephra ID according to Wallace (1987) = unnamed ash-layer of the Carrington tephra unit overlying the Taupo-derived Kawakawa/Oruanui Tephra (Franks et al., 1991).*

4.2.5 Methods

Pumice lapilli from proximal and medial sites were handpicked, washed and gently crushed. Titanomagnetite phenocrysts were extracted by a hand-magnet and glass shards were handpicked using an optical microscope. All samples were mounted in epoxy resin and polished using conventional methods. Major and minor element analyses of single glass shards and titanomagnetite phenocrysts were carried out using a JEOL JXA-840a electron microprobe equipped with a Princeton Gamma Tech Prism 2000 Si(Li) EDS X-ray detector at Massey University. An accelerating voltage of 15 kV, an 800 pA beam-current, and a 100 seconds live time count were used. A 10-20 µm defocused beam was used for glass shard analyses to minimize sodium loss (Froggatt,

1983). Syn- and post-eruption crystallisation of nanolitic Fe-oxides and microlitic plagioclase can often lead to fine-scale heterogeneity of the glass (Best, 2003). These are often difficult to avoid in the large-scale beam areas required for glass analysis. To minimise this effect, back-scatter electron imaging and the removal of hybrid data points using the technique of Platz et al. (2007b) were applied. A focused beam (approximately 2-3 µm diameter) was used for the titanomagnetite analyses. Titanomagnetite phenocrysts and/or those within glomerocrysts were analysed, mainly from the 250-500 µm size fraction. Exsolved titanomagnetite grains with trellises of ilmenite and magnetite have heterogeneous compositions and were avoided by use of back-scatter electron imaging. The analytical conditions were regularly calibrated using a range of ASTIMEX standards (manufactured by Astimex Scientific Limited, Toronto, Ontario, Canada) appropriate to the compositions of glass and titanomagnetite being analysed. At least 10 analyses per phase per tephra were obtained. Data points showing obvious contamination were excluded. Major elements are expressed as oxides and reported in weight per cent (wt%). Glass shard data were normalised to 100% and titanomagnetite data corrected for iron following the procedure of Carmichael (1966). The titanomagnetite and glass shard data (mean±S.D.) is given in Appendix 5 and Appendix 6, respectively.

The nomenclature for individual lake and peat tephra layers was adopted from the previous work of Damaschke et al. (2017) and is based on the coring site and tephra number in stratigraphic/age order. For example N-5 = Ngaere Swamp core, 5th youngest tephra layer. The nomenclature for proximal deposits varies between different works. In older tephrostratigraphies of Mt. Taranaki (Neall, 1972; Alloway et al., 1995), the term “Tephra Formation” was used to describe a formally named tephra and/or a set of tephra deposits, which is/are separated above and below by buried soil horizons indicating a period of minimal deposition or low eruptive activity. ‘Tephra’ stands hereby for all unconsolidated pyroclastic material irrespective of their origin or nature of emplacement (Thorarinsson, 1974, Howorth, 1975; Schmid, 1981; Froggatt and Lowe, 1990). In recent works, terminologies as that of eruptive episode (Cronin et al., 2003; Platz et al., 2007a, 2012) or bed-set constituted by single or multiple layers (Torres-Orozco et al., 2017) were used, since the criteria for defining formations could

not be achieved. Those detailed works distinguished between fallout, pyroclastic density current, block-and-ash flow and/or their longitudinal and lateral transformations into epiclastic (i.e., lahar) deposits. Because the current study integrated pyroclastic deposits of both terminologies a simplified term “tephra unit” was adopted.

4.2.6 Results

4.2.6.1 Titanomagnetite and glass chemistry of proximal deposits on the flanks

Fallout layers of tephra units Tw-I, Kokowai and Kapuni-A have similar titanomagnetite compositions, characterised by moderately low Al_2O_3+MgO and moderately high TiO_2 contents (~5 wt% and 8 wt%, respectively; Fig. 4.3, Appendix 5) corresponding to group-8 of the titanomagnetite compositional groups identified in Mt. Taranaki lake and peat tephras by Damaschke et al. (2017) (Table 4.3). Kokowai and Kapuni-A have trachydacitic glass compositions with ~67 wt% SiO_2 (Fig. 4.4, Appendix 6).

Titanomagnetite compositions of younger units including the Kapuni-B, Korito, Lower and Upper Inglewood have distinctively lower Al_2O_3+MgO and TiO_2 contents (~3-4 wt% and 7-8 wt%, respectively; Fig. 4.3, Appendix 5) corresponding to group-10 titanomagnetites (Table 4.3). All contain glass with high silica contents of 69-70 wt% for the Kapuni-B and 70-72 wt% for the Lower and Upper Inglewood (Fig. 4.4, Appendix 6). Glass of the Korito tephra unit is unusual in that it has a wide spread in silica concentrations (69-71 wt%; Fig. 4.4, Appendix 6).

Titanomagnetites of the Manganui tephra units (MA-MG), sourced from Fanthams Peak (a parasitic vent), have high Al_2O_3+MgO (8-12 wt%), low TiO_2 (6-7 wt%), and low Fe^{2+} contents (<1 cat. prop.; Fig. 4.3) corresponding to group-11 titanomagnetites (Table 4.3). Each individual Manganui tephra unit has a slightly different titanomagnetite composition. Unit MC has the highest Al_2O_3+MgO contents recognised

(~11.5 wt%), while MD, one of the largest-volume units, has a large compositional spread (Fig. 4.5, Appendix 5). The glass composition of most Manganui tephra units is dominantly trachyandesitic (Fig. 4.4, Appendix 6).

Tephra units of Maketawa I and II, Curtis Ridge, and Burrell (all believed to be sourced from the summit crater of Mt. Taranaki) have distinctively lower Al_2O_3+MgO (<6 wt%) and comparatively low TiO_2 titanomagnetite contents (6-7 wt%; Fig. 4.3) corresponding to group-12 titanomagnetites (Table 4.3). Their glass compositions are mainly trachydacitic, with Burrell having ~65 wt% SiO_2 and Curtis Ridge having ~68 wt% SiO_2 (Fig. 4.4).

Kaupokonui and Te Popo tephra units, however, are unique in that they are compositionally different from the units described in this sequence. Titanomagnetite compositions of the Kaupokonui have high TiO_2 contents (~9 wt%; Fig. 4.3, Appendix 5) similar to group-2 titanomagnetites (Table 4.3). Glass from the Kaupokonui is trachydacitic with low SiO_2 (62-63 wt%) and high FeO_{total} (~4 wt%) contents (Fig. 4.4, Appendix 6). The Te Popo has titanomagnetite composition similar to that of older units of Lower and Upper Inglewood, but with slightly higher MgO contents (>2 wt%; Fig. 4.3) corresponding to group-9 titanomagnetites (Table 4.3). It contains glass compositions with relatively high silica contents (~69.5 wt%; Fig. 4.4).

Table 4. 3 *Summary of the titanomagnetite groups defined by Damaschke et al. (2017) and associated proximal and medial deposits analysed in the current study.*

Titano-magnetite	Colour code	Main characteristics	Tephra Sequence	Flank and ring-plain deposits
Group 1	purple	Highest TiO_2 (10-11 wt%), lowest Fe^{3+} (<1.3 cat. prop.), moderately high Al_2O_3+MgO (6-8 wt%)	D, **E**, **F**	Mahoe = Konini*, Poto (Layer-256)
Group 2	pink	High TiO_2 (9-10 wt%), moderately high Al_2O_3+MgO (6-7 wt%), with MgO >3 wt%	A, **D**, F	Kaupokonui
Group 3	blue	High TiO_2 (9-10 wt%), moderately low Al_2O_3+MgO (5-6 wt%), with MgO <3 wt%	C, D	Tariki (upper&mid)
Group 4	dark pink	Moderately high Al_2O_3+MgO (6.5-7 wt%), moderately high TiO_2 (8-9 wt%)	D	Kaponga
Group 5	light pink	Moderately low Al_2O_3+MgO (5.5-6 wt%), moderately high TiO_2 (8-9 wt%)	D	
Group 6	green	High Al_2O_3+MgO (~8 wt%), with high MgO (>3.5 wt%), low Fe^{2+} (~1 cat. prop.)	A, F	
Group 7	red	Moderately low TiO_2 (7-8 wt%), moderately low Al_2O_3+MgO (5-6 wt%)	C, D	Waipuku
Group 8	brown	Moderately high TiO_2 (8-9 wt%), moderately low Al_2O_3+MgO (5-6 wt%)	**C**, F	Kapuni-A, Kokowai, Tw-I, Mangatoki, Tariki (lower)
Group 9	beige	Moderately high TiO_2 (~8 wt%), moderately low Al_2O_3+MgO (4-5 wt%), with MgO >2 wt%	A, C	Te Popo
Group 10	yellow	Lowest Al_2O_3+MgO (3-4 wt%), with MgO <2 wt%, moderately low TiO_2 (7-8 wt%), high Fe^{3+} (>1.45 cat. prop.)	**B**	Upper and Lower Inglewood, Korito, Kapuni-B
Group 11	khaki	Highest Al_2O_3+MgO (7-12 wt%), with highest Al_2O_3 (>4 wt%), low TiO_2 (~6-7 wt%), lowest Fe^{2+} (<1 cat. prop.)	**A**, C	Manganui A-G
Group 12	orange	Broad Al_2O_3+MgO (4-7 wt%), low TiO_2 (~6-7 wt%), high Fe^{3+} (>1.45 cat. prop.)	A	Burrell, Curtis Ridge, Maketawa (I and II)

*Note: Tephra sequences that are bold-highlighted represent sequences dominated by the representative titanomagnetite group. The age range of each tephra sequence is as followed: Tephra Sequence A (0.5-3 cal. ka B.P.), B (3-4 cal. ka B.P.), C (4-9.5 cal. ka B.P.), D (9.5-14 cal. ka B.P.), E (14-17.5 cal. ka B.P.), and F (23.5-30 cal. ka B.P.). *Mahoe (Franks et al., 1991) = Konini (Alloway et al., 1995) (refer to text).*

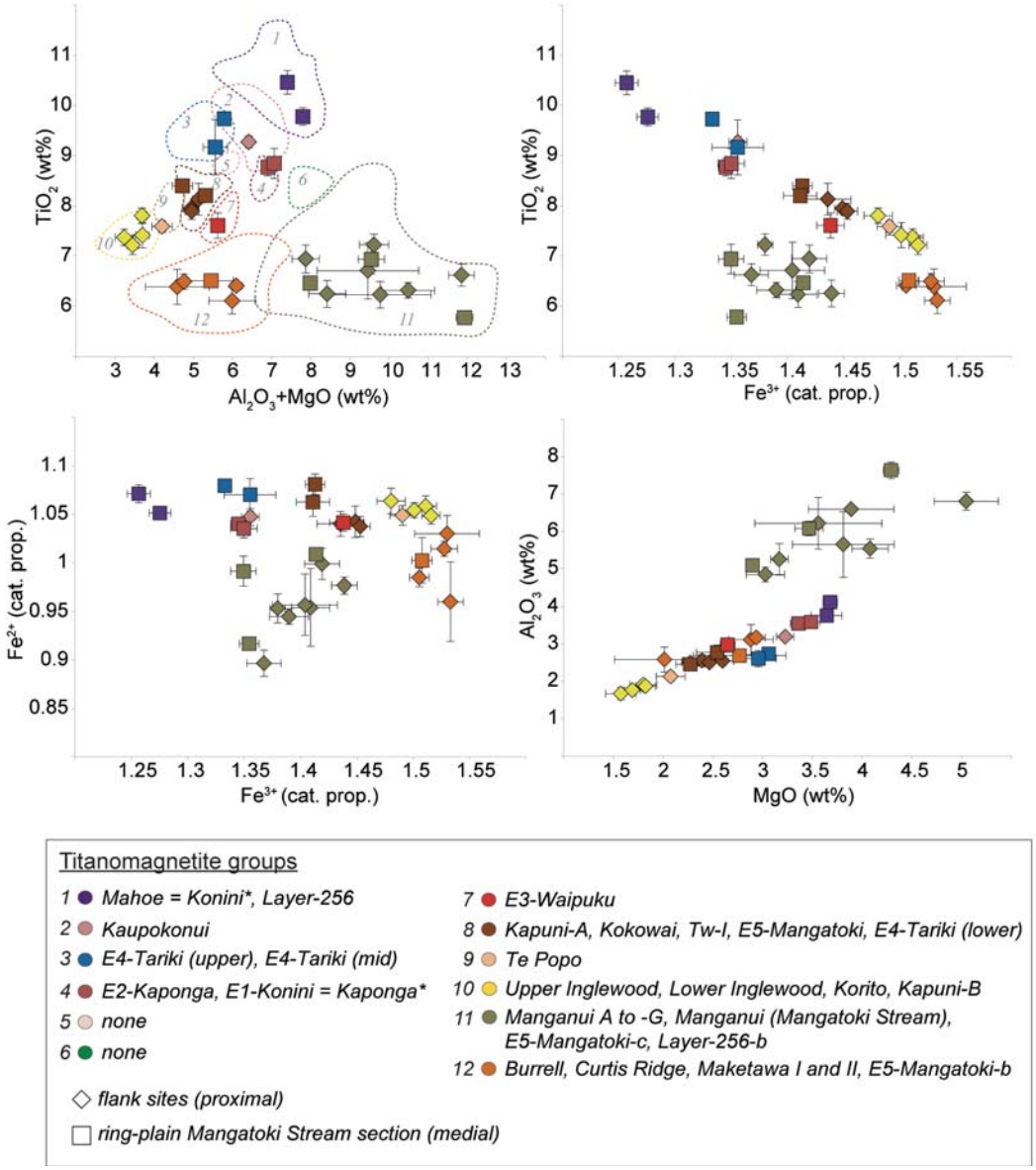

Figure 4. 2 *Compositions of titanomagnetite phenocrysts from flank and ring-plain tephra deposits analysed in the current study. Each point is the average ±1 standard deviation for each tephra unit. Each dotted field (numbered from 1-12) and colour represent an individual titanomagnetite group defined by Damaschke et al. (2017) and summarised in Table 4.3. Bi- and multi-modal titanomagnetite compositions are indicated by additional letters "-b" and "-c" after the sample name. *E1-Konini and Mahoe (Franks et al., 1991) = Kaponga and Konini (Alloway et al., 1995) (refer to text. Analyses in weight percent (wt%) and cation proportion (cat. prop.) calculated on the basis of four oxygen atoms as in Carmichael (1966). All data is summarized in Appendix 5.*

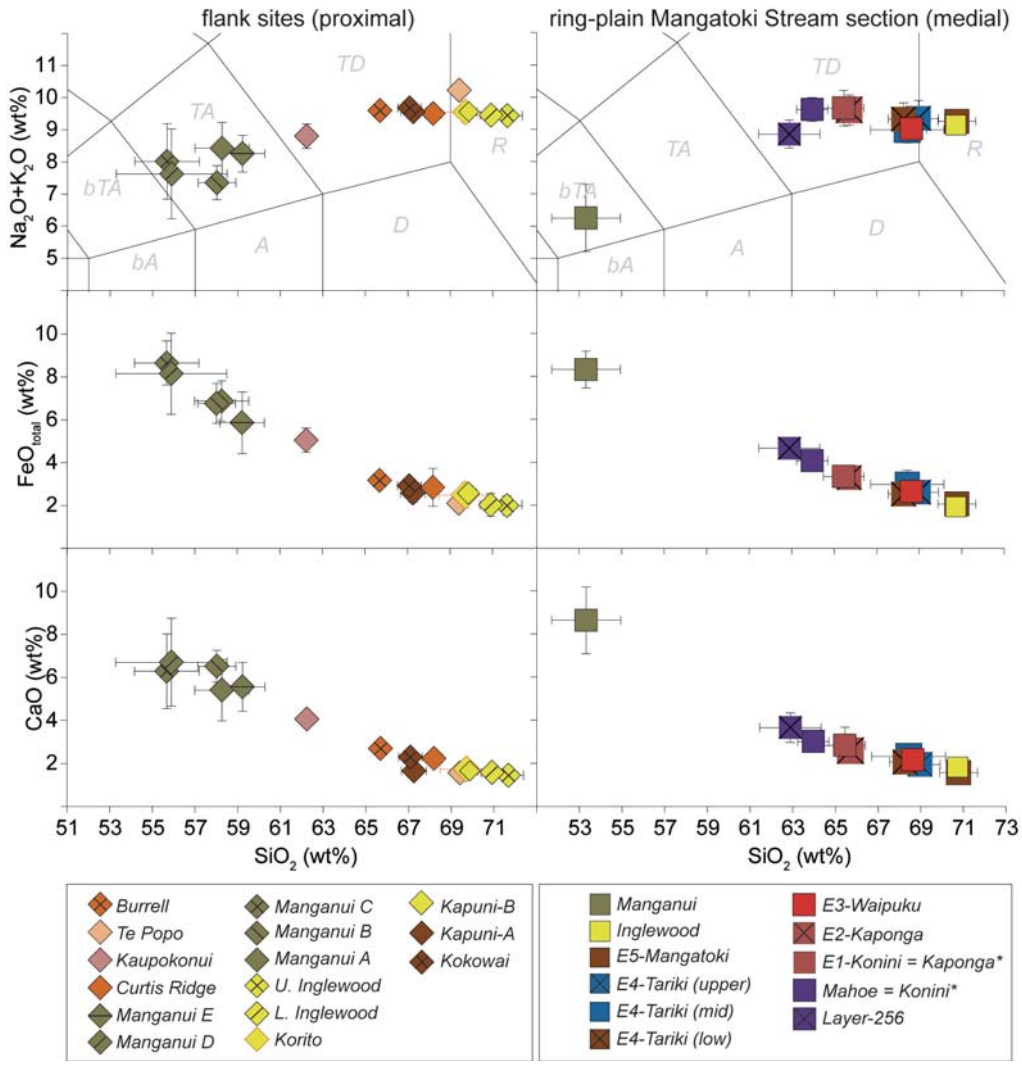

Figure 4. 3 *Glass chemistry of the flank and ring-plain tephra deposits analysed in the current study. Normalised analyses are plotted as total alkalis, FeO_{total}, and CaO vs. silica. The compositional fields (after Le Bas et al., 1986) of basalt-andesite (bA), basalt-trachyandesite (bTA), trachyandesite (TA), trachydacite (TD) and rhyolite (R) are also shown. Each point is the average ±1 standard deviation for each tephra unit. Colours represent the titanomagnetite composition of each sample (refer to Fig. 4.3, Table 4.3). *E1-Konini and Mahoe (Franks et al., 1991) = Kaponga and Konini (Alloway et al., 1995) (refer to text). All data is summarized in Appendix 6.*

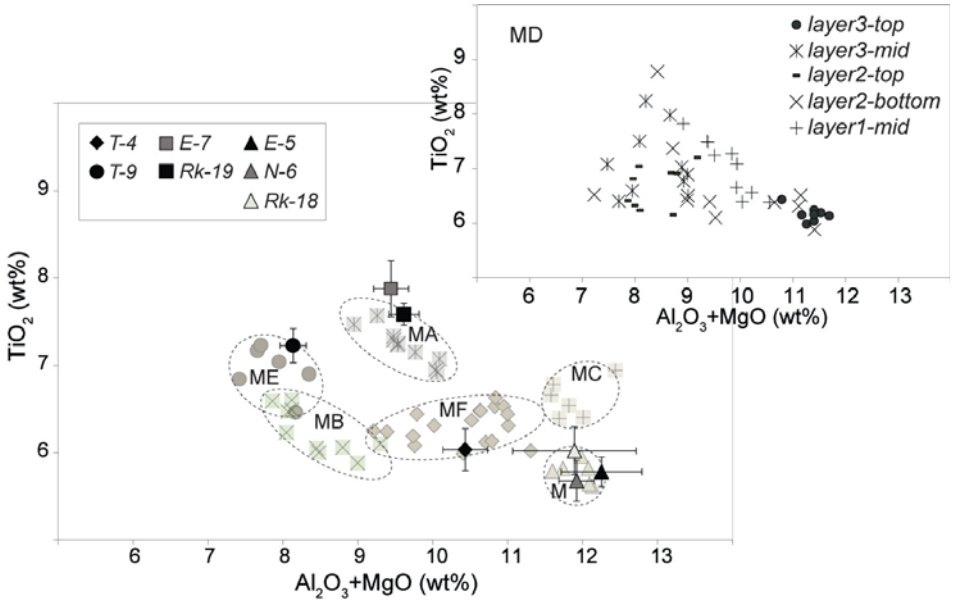

Figure 4. 4 *Electron microprobe-determined titanomagnetite composition of the Manganui tephra units (MA-MF) and single Manganui tephra unit (M) from the Mangatoki Stream section shown as compositional fields and correlative lake and peat tephra layers shown as average points with ±1 standard deviation. Note the large compositional variability of Manganui D.*

4.2.6.2 Onaero Beach section

Geochemical analyses of tephra deposits at the Onaero Beach section were challenging, because the glass was extremely weathered. However, titanomagnetite compositions could be reliably determined. The main titanomagnetite compositions of tephra unit bS contain low Al_2O_3+MgO and TiO_2 contents (Fig. 4.6, Appendix 5), and they are most similar to Kokowai and Kapuni-A tephra units and therefore similar to group-8 titanomagnetites (Table 4.3).

The dominant titanomagnetite composition of tephra unit aS has distinctively low TiO_2 contents (Fig. 4.6), similar to the compositions of Kapuni-B, Korito, Upper and Lower Inglewood, Maketawa (I and II) and Manganui tephra units and, hence, corresponds to group-10, -11, and -12 titanomagnetites (Table 4.3).

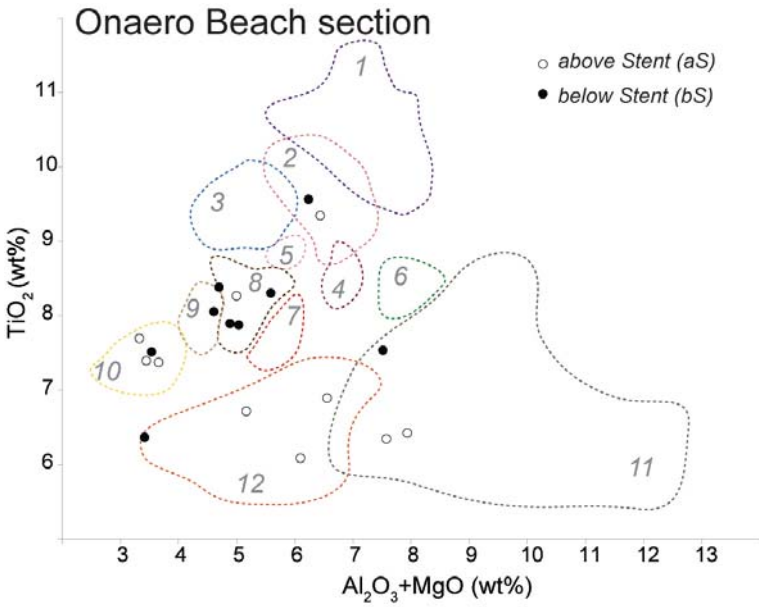

Figure 4. 5 *Electron microprobe-determined compositions of titanomagnetite phenocrysts from the pyroclastic deposits at the Onaero Beach section (section-23; Alloway et al., 1995). Each dotted field (1-12) and colour represent an individual titanomagnetite group defined by Damaschke et al. (2017) summarised in Table 4.3.*

4.2.6.3 Mangatoki Stream section

Titanomagnetites from Layer-256 (Carrington tephra unit) overlying the Taupo-sourced Kawakawa/Oruanui Tephra, and the younger Mahoe tephra unit have extremely high Al_2O_3+MgO and TiO_2 (7-8 and 9-11 wt%, respectively) and low Fe^{3+} (<1.3 cat. prop.) contents (Fig. 4.3, Appendix 5) corresponding to group-1 titanomagnetites (Table 4.3). Both tephra units have a trachydacitic glass composition with low silica (62-65 wt%) and high FeO_{total} (~4 wt%) contents (Fig. 4.4, Appendix 6).

The younger E1-Konini and E2-Kaponga tephra units have titanomagnetites with moderately high Al_2O_3+MgO and TiO_2 contents (~7 wt% and 9 wt%, respectively; Fig. 4.3) corresponding to group-4 titanomagnetites (Table 4.3) and glass silica contents between 65-66 wt% (Fig. 4.4).

The E3-Waipuku titanomagnetites have distinctively lower Al_2O_3+MgO and TiO_2 contents (~5-6 wt% and 7-8 wt%, respectively; Fig. 4.3, Appendix 5) corresponding to group-7 titanomagnetites (Table 4.3) and moderately high glass silica contents between 68-69 wt% (Fig. 4.4, Appendix 6).

The thickest deposit in this outcrop was described as the E4-Tariki tephra unit, and was subdivided into lower, mid and upper layer (Wallace, 1987; Franks et al., 1991). Titanomagnetites from the lower layer have TiO_2 contents (~8 wt%; Fig. 4.3) similar to group-8 titanomagnetites (Table 4.3), whereas the upper layer has a slightly higher TiO_2 content (~9-10 wt% TiO_2) similar to that of group-3 titanomagnetites (Table 4.3). The middle layer of the E4-Tariki tephra unit has compositional characteristics of both titanomagnetite groups. The glass composition of the lower and upper layers is trachydacitic (68-69 wt% SiO_2), while the mid layer contains a broad range in silica (67-70 wt%) (Fig. 4.4).

The E5-Mangatoki tephra unit contains high-silica glass (70-71 wt%; Fig. 4.4), with most titanomagnetites having moderately low Al_2O_3+MgO contents (~5 wt%; Fig. 4.3) corresponding to group-8 titanomagnetites (Table 4.3). Some titanomagnetite grains within the same unit, however, contain Al_2O_3+MgO concentrations similar to those of group-11 and -12 titanomagnetites (Fig. 4.3).

The Inglewood tephra unit at this site has a high-silica glass composition (70-71 wt%; Fig. 4.4, Appendix 6), whereas the younger Manganui tephra unit is basalt-trachyandesitic with high FeO_{total} (>6wt %), MgO (~4 wt%) and CaO (~8 wt%) contents. The Manganui tephra unit has high Al_2O_3+MgO titanomagnetite concentrations (~12 wt%, Fig. 4.3, Appendix 5) corresponding to group-11 titanomagnetites.

4.2.7 Discussion

4.2.7.1 Correlating proximal and medial deposits with dated tephra sequences from lake and peat records

Damaschke et al. (2017) defined a chemostratigraphic framework of six geochemically and stratigraphically different tephra sequences (TS A-F) from Mt. Taranaki, within lake and peat records, dating back to 30 cal ka BP. This framework was achieved by using time-varying titanomagnetite (and glass) compositions of the individual tephra sequences and a tight chronological framework from continuous down-core radiocarbon dating. Using this framework enables the patchy medial tephra formations of Franks et al. (1991) and Alloway et al. (1995) to be better integrated and helps to link the new discoveries from the proximal flank deposits of Turner (2008) and Torres-Orozco et al. (2017) to the tephra sequences of the high-resolution composite lake-and-peat record (Fig. 4.7). In turn, these integrations have helped resolve several stratigraphic problems and miscorrelations and now provide a more robust tephrostratigraphy of the explosive products of the largest eruptions known from Mt. Taranaki. Franks et al. (1991) and earlier tephrostratigraphic work applied informal unit names, hence the formal tephra names introduced by Alloway et al. (1995) were adopted, and subsequently revised, in this study.

Waitepuka, Pukeiti, Koru, Tuikonga, Poto – Tephra Sequence F (30-23.5 cal ka BP)

Layer-256 within the Carrington tephra unit above the Kawakawa/Oruanui Tephra at the Mangatoki Stream section (Franks et al., 1991) has a similar geochemical composition to thast of tephra layers E-49 to E-47 recognised above the Kawakawa/Oruanui Tephra within Tephra Sequence F of the detailed composite lake-and-peat record (~25 cal ka BP; Fig. 4.7). According to their stratigraphic position, all are correlated to the Poto Tephra Formation (Alloway et al., 1995). Older tephra formations, including the Tuikonga, Koru, Pukeiti and Waitepuka, likely correlate to the remainder of Tephra Sequence F, based on their stratigraphic position (Fig. 4.7). However, a lack of geochemical data on these deposits from proximal sites makes confirmation of this match and single-bed correlation impossible.

Paetahi, Kaihouri – Tephra Sequence E (17.5-14 cal ka BP)

No proximal or medial tephra deposits that can be related directly to individual tephra layers in Tephra Sequence E have been found. As with the older units, these sequences were presumably eroded from proximal areas by debris avalanches or ice and slope-wash erosion, during the Last Glacial Maximum period. This period was known to have caused intense physical weathering and the widespread formation of loess and sand deposits in medial areas (e.g., Alloway et al., 1992; Pillans et al., 1993; Eden and Hammong, 2003). Solely based on stratigraphic position and age estimates (Table 4.1), the Paetahi (6 tephra beds) and Kaihouri (8 tephra beds) Tephra Formations (Alloway et al., 1995) are correlated to Tephra Sequence E, which encompasses numerous tephra layers in the composite lake-and-peat record (Fig. 4.7).

Mahoe, Konini, Kaponga – Tephra Sequence D (14-9.5 cal ka BP)

Miscorrelation of the Mahoe tephra of Franks et al. (1991) and the Mahoe Tephra Formation studied by Alloway et al. (1995) was identified by Damaschke et al. (2017), who recognised that the eruptives had different lithological and geochemical characteristics. Here, it is suggested that the “Mahoe” tephra of Franks et al., (1991) is more likely to represent a tephra within the Konini Tephra Formation of Alloway et al. (1995), while the Alloway et al. (1995) Mahoe Tephra Formation likely correspond to three unnamed tephra deposits below the Franks et al.’s (1991) “Mahoe” tephra (Fig. 4.7). Hence, the informally named “E1-Konini” tephra of Franks et al. (1991) is here revised to the Kaponga Tephra Formation of Alloway et al. (1995) and should not be confused with the formally defined Konini Tephra Formation introduced by Alloway et al. (1995).

On the basis of similar titanomagnetite compositions (i.e., group-1 titanomagnetites; Fig. 4.3) and a low-silica, high-iron glass composition (Fig. 4.4), the “Mahoe” tephra of Franks et al. (1991) and therefore the Konini Tephra Formation of Alloway et al. (1995) are correlated to tephra layers N-63 to N-58 within Tephra Sequence D of the composite lake-and-peat record (Fig. 4.7). The age of c. 12,182±312 cal yr BP of the Konini Tephra Formation (Alloway et al., 1995; Table 4.1) is in good agreement with ages

obtained for the correlative lake and peat tephra groups (~12.5 cal ka BP; Fig. 4.7). The Mahoe Tephra Formation of Alloway et al. (1995) is tentatively correlated via stratigraphic position to tephra layers E-41 to E-38, which are characterised by group-3 titanomagnetites (Table 4.3) and are ~13.3 cal ka BP in age (Fig. 4.7). In addition to these recognised units, the composite lake-and-peat record also contains a further unrecognised sequence of tephras with differing chemical compositions (i.e., group-2 and -5 titanomagnetites) intercalating with the here re-defined Konini and Mahoe tephra units (i.e., T-30, N-65 to N-64, and N-57 to N-55; Fig. 4.7).

Younger tephra units, E1-Konini and E2-Kaponga of Franks et al. (1991), were both linked to beds within the formally named Kaponga Tephra Formation of Alloway et al. (1995). E1 and E2 have a unique titanomagnetite composition (i.e., group-4 titanomagnetites; Fig. 4.3) and can therefore be correlated to tephra layers N-51 to N-47 (~10.9 cal ka BP) and tephra N-42 (~10.2 cal ka BP) within Tephra Sequence D of the composite lake-and-peat record (Fig. 4.7). The lake and peat sequence ages for the correlatives match well with the suggested age range of 9.9 to 10.5 cal ka B.P for the Kaponga Tephra Formation (Alloway et al., 1995; Table 4.1). Previously the Kaponga Tephra Formation comprised a closely spaced set of at least 10 ash and lapilli beds, whereas now it is clear, from the composite lake-and-peat record, that at least 23 tephra layers (with differing compositions) were formed during this period of eruptions.

Waipuku, Tariki, Mangatoki, Kokowai, Kapuni-A – Tephra Sequence C (9.5-4 cal ka BP)

The Franks et al., (1991) E3-Waipuku tephra has a unique titanomagnetite composition (i.e., group-7 titanomagnetites; Fig. 4.3), which can be correlated with a single tephra layer U-78 (8810±59 cal ka BP) within the lower part of Tephra Sequence C of the composite lake-and-peat record (Fig. 4.7). It also chemically matches with a dated tephra deposit (M06-64, 8720±121 cal yr BP) recognised in previously studied proximal flank outcrops of Turner (2008). Both ages are in good agreement. The E4-Tariki tephra of Franks et al. (1991) is geochemically variable (i.e., group-3 and -8 titanomagnetites; Fig. 4.3), with the compositional variation corresponding to discrete physical

beds/stratifications within the unit. The two distinctively different compositions of E4 represent individual tephra layers (i.e., U-76 to U-60) within the lower part of Tephra Sequence C of the composite lake-and-peat record (~8.5 to 6.8 cal ka BP; Fig. 4.7). E4-Tariki is therefore correlated to this sequence and can be considered as an amalgamation of several closely spaced eruptions with two different titanomagnetite fingerprints.

The overlying E5-Mangatoki tephra of Franks et al. (1991) is characterised by a multimodal titanomagnetite composition (group-8, -11, and -12 titanomagnetites; Fig. 4.3) and high-silica glass shard composition with a broad range in silica contents (Fig. 4.4). The overall compositional character of E5-Mangatoki also suggests correlation to the lower part of the Tephra Sequence C of the composite lake-and-peat record (Fig. 4.7), although single bed correlation is not possible due to the many tephra layers with similar compositional fingerprints in this particular sequence. Alloway et al. (1995) recognised 8 tephra units within their Tariki and Mangatoki Tephra Formations, but now it is clear that at least 25 tephra layers were deposited in these periods of eruptions, based on the composite lake-and-peat record.

According to Franks et al. (1991), E3-Waipuku, E4-Tariki, and E5-Mangatoki tephras were correlated to the north-westerly mapped Oakura Tephra Formation dated between ~7.5 to 8 cal ka BP (Neall, 1972, 1979; Fig. 4.2, Table 4.1). This age range matches well with ages obtained for correlative tephra deposits in the composite lake-and-peat record (~9.5 to 6.8 cal ka BP; Fig. 4.7). However, ages presented by Alloway et al. (1995) for the same tephras mismatch and are more than 2000 cal yr BP younger (Figs. 4.2, 4.7). Alloway et al. (1995) derived most of their ages for this series of tephra units from the Onaero Beach section, ~40 km north-east of the studied key-sections, such as at the Mangatoki Stream. At this beach-cliff exposure, tephra occurred as dispersed and strongly weathered fine lapilli, as observed for tephra units aS and bS. Both dispersed tephra units have extremely broad titanomagnetite compositions (Fig. 4.6), most likely a result of mixing of tephras from multiple closely spaced eruptions in a vegetated soil sequence. Hence, single pyroclastic deposits are extremely difficult to differentiate and to correlate back to ring-plain successions. Therefore, it is suggested that Alloway et al. (1995) miscorrelated the Waipuku, Tariki and Mangatoki Tephra Formations to the

Onaero Beach section and thus these units are considerably older than previously described (Fig. 4.7). The stratigraphic revision suggested here is strongly supported by the new geochemical evidence, but also explains the anomalously large age-gap (up to 4 cal ka) noted between the Kaponga and Waipuku Tephra Formations within the older Alloway et al. (1995) composite stratigraphy.

The ages (and compositions) of tephra deposits at the beach sections are more likely related to units within the upper part of Tephra Sequence C (i.e., Ri-70, Ri-60 and Ri-58) and possibly some units in the younger Tephra Sequence B (i.e., Ri-47) of the composite lake-and-peat record (Fig. 4.7). The dominant titanomagnetite composition of tephra unit bS is corresponding to group-8 titanomagnetites, which is represented by Tephra Sequence C, while tephra unit aS compositions include group-10, -11, and -12 titanomagnetites, which are represented by younger Tephra Sequence B and A (Figs. 4.6, 4.7, Table 4.3). The age of 4229±161 cal yr BP obtained directly below the Stent Tephra at the Onaero Beach section (Alloway et al., 1995; Table 4.1) is in good agreement with the mean calibrated age of 4279±47 cal yr BP for the Stent Tephra within the composite lake-and-peat record (Fig. 4.7).

The youngest part of Taranaki's proximal tephrostratigraphy is best preserved in the newly mapped flank depositional sites of Torres-Orozco et al. (2017). The thickest deposits identified correspond to the Kokowai tephra unit, which has similar physical and geochemical characteristics to tephras Ri-60 and Ri-58 (correlatives of U-34 and U-35) within the upper part of Tephra Sequence C of the composite lake-and-peat record (Fig. 4.7). Tephra Ri-60 represents hereby the lower, and Ri-58 the upper fall deposit of the Kokowai tephra unit (layer-4 and layer-7, respectively). Existing ages for the lower and upper Kokowai (4712±69 and 4634±95 cal yr BP, respectively; Table 4.1) are in good agreement with age determinations for the correlative lake tephras (4878±46 and 4801±49 cal yr BP, respectively; Fig. 4.7). The younger Kapuni-A tephra unit, has a similar geochemical fingerprint to the prominent Kokowai tephra unit (Figs. 4.3, 4.4). It may correlate to a thin ash layer, Ri-50, within the upper part of Tephra Sequence C, but several tephra layers occur above the Kokowai tephra unit and below the prominent Stent Tephra in the composite lake-and-peat record (Fig. 4.7).

Kapuni-B, Korito, Inglewood – Tephra Sequence B (4-3 cal ka BP)

Tephras including Kapuni-B, Korito, Lower and Upper Inglewood all have a group-10 titanomagnetite composition (Fig. 4.3), which is representative of Tephra Sequence B of the composite lake-and-peat record (Fig. 4.7, Table 4.3). Kapuni-B correlates stratigraphically and geochemically to a single tephra layer Ri-47 (~3.9 cal ka BP, Fig. 4.7). The Korito tephra, however, could not be correlated with any lake and peat tephra layer, because it has a broad, nonspecific, range in glass silica contents, not observed in any chemically analysed lake or peat tephra layer (Fig. 4.4). It may be that it is only represented as fine and thin ash-layer in the composite lake-and-peat record. In addition, detailed field observation of the Korito tephra (Torres-Orozco et al., 2017) show that deposits of this eruption were small in volume and thus likely restricted to proximal areas. Hence, Alloway et al. (1995) miscorrelated the Korito tephra with a tephra deposit below the Stent Tephra at the Onaero Beach section (Fig. 4.7). This recognition of the miscorrelation is supported by the differing titanomagnetite composition of the Korito compared to the bS tephra unit (Figs. 4.3, 4.6). This latter tephra unit is more likely to represent the widespread Kokowai tephra, based on a similar titanomagnetite fingerprint, age estimation (4629±137 cal yr BP, Alloway et al., 1995; Fig. 4.7, Table 4.1), and its position below the Stent Tephra. For the same reasons, the distal correlative Eg-4 in the Waikato lake sediments (Lowe, 1988a) is most likely also a correlative to the Kokowai tephra rather than the Korito tephra. According to its group-10 titanomagnetite fingerprint, the Korito tephra is here revised to be stratigraphically located above the prominent rhyolitic Stent Tephra.

Upper and Lower Inglewood (~3.3 cal yr BP; Table 4.1) are readily recognisable tephra deposit within Tephra Formation B, since they have highly-evolved glass compositions (Fig. 4.4) and a finely vesicular texture. They are widely dispersed and tephra layers Ri-40, U-20, N-9 to N-8, E-8, and Rk-23 to Rk-21 (~3.6 cal ka BP) are correlatives within the composite lake-and-peat records (Fig. 4.7). The apparent age discrepancy of c. 300 cal yr BP between proximal flank and distal lake-and-peat sites Inglewood tephra deposits is most likely a result of dating different materials with variable inbuilt ages (i.e., charcoal vs. peat), as well as the result of a different place of radiocarbon sample extraction (below or above deposits vs. within deposits).

Manganui, Maketawa (I and II), Curtis Ridge, Kaupokonui, Te Popo, Burrell – Tephra Sequence A (3-0.5 cal ka BP)

The Manganui tephra units, MA to MG, as well as the single Manganui tephra unit from the Mangatoki Stream section (Franks et al., 1991) have, among all tephras, the least-evolved glass compositions seen at Mt. Taranaki (Fig. 4.4) and a group-11 titanomagnetite composition (Fig. 4.3, Table 4.3). These are correlated to type-I tephra layers (Damaschke et al., 2017) within Tephra Sequence A of the composite lake-and-peat record (i.e., Ri-32 to Ri-24 correlatives to E-7 to E-5, and T-11 to T-9; Fig. 4.7). The ages of the lower Manganui tephra units, MA to ME, of 3042±57 to 2561±98 cal yr BP (Fig. 4.7, Table 4.1) are in good agreement with ages obtained for correlative lake and peat tephras (~3 to 2.3 cal ka BP; Fig. 4.7). However, the approximate age for the MF tephra unit of 1615±50 cal yr BP (Fig. 4.7, Table 4.1) is significantly younger than the age of 1955±32 cal yr BP documented for its correlative peat tephra layer T-4, possibly for the same reasons as stated above, since physical and geochemical characteristics (Fig. 4.5) as well distinct stratigraphic position above the Maketawa tephra units (I and II) (Fig. 4.7) match very well.

Correlation of individual Manganui tephra units to the lake and peat records, like that of MF, was only realisable for a few tephras. This is mainly a consequence of most Manganui titanomagnetites having a broad compositional range (Figs. 4.3, 4.4, 4.5). Variable compositions may be caused by (1) pre- and/or syn-eruptive mingling/mixing of different Manganui magmas, (2) crustal assimilation, (3) contamination due to vent and conduit erosion during eruption, (4) post-depositional mixing of tephra from closely spaced Manganui eruptions, and/or (5) as in case of MD, a compositionally stratified nature (layer1 to layer3, Fig. 4.5). MD, one of the largest-volume Manganui eruptive events, which encompasses at least 3 eruptive pulses (Torres-Orozco et al., 2017), is here correlated with lake and peat tephra layers Ri-26, T-10, N-7, and E-6 based on thickness, physical appearance and stratigraphic position, since titanomagnetite compositions are of limited use.

Single tephra layer T-9 has a similar titanomagnetite fingerprint to that of ME (Fig. 4.5), but is here only correlated tentatively. Based on similar physical characteristics, MB is

tentatively correlated with a single tephra layer, Ri-30, within the Lake Richmond record. The oldest Manganui unit, MA, is correlated to tephras Rk-19 and E-7 from the composite lake-and-peat record based on stratigraphic position and similar titanomagnetite compositions (Fig. 4.5). The Manganui tephra unit at the Mangatoki Stream key-section (Franks et al., 1991) has a high Al_2O_3+MgO titanomagnetite composition (~12 wt%; Fig. 4.5) similar to that of the south-easterly dispersed tephras, N-6, E-5, and Rk-18 (~2.2 cal ka BP; Fig. 4.7). Unfortunately, this distinct fingerprint was not recognised in on-cone Manganui deposits. However, according to Torres-Orozco et al. (2017), several lahar deposits occur above the prominent MD and, hence, their erosive nature during emplacement may explain the absence of this particular Manganui unit in proximal localities. Thus, this Manganui tephra unit at the Mangatoki Stream section and correlatives in the composite lake-and-peat record may be still part of MD, or represent an additional tephra unit younger than MD.

The Manganui tephra units are intercalated with the Maketawa (I and II) and Curtis Ridge tephra units, which have lower Al_2O_3+MgO, but similar distinctively low TiO_2 titanomagnetite concentrations (group-12 titanomagnetites; Fig. 4.3, Table 4.3). Compositionally similar tephra layers, described as type-II tephras (Damaschke et al., 2017), are recognised within Tephra Sequence A in the composite lake-and-peat record (i.e., Ri-23 to Ri-20, T-8 to T-5, T-3 to T-2, E-4; Fig. 4.7). The ages obtained for the Maketawa tephra units (I and II) of 2217±60 to 1833±86 cal yr BP (Table 4.1) are in good agreement with ages obtained for correlative tephras within the composite lake-and-peat record (~2.1 to ~1.8 cal ka BP; Fig. 4.7).

The unique geochemical fingerprint of the Kaupokonui tephra unit is similar to that of south-easterly lake and peat tephra layers E-1, N-2 and Rk-10 within Tephra Sequence A (Damaschke et al., 2017; Fig. 4.7). However, the suggested age of the Kaupokonui of 1249±157 cal yr BP by Neall and Jansen (1984) in previous studies (Table 4.1) is noticeably younger than the ages obtained for the lake and peat correlatives (~1.5 to 2 cal ka BP). It is conspicuous that lake and peat sequence ages vary greatly, possibly caused by the position of these tephras within the top-metre of sediment where ages had to be extrapolated, except for Rk-10 in the Lake Rotokare core, where all ages in

general seem to be inconsistent with the overall age observations, likely due to a strongly varying background sedimentation regime of fault-related landslide deposition (Tuner et al., 2011b).

Tephra units younger than 1 cal ka BP, including the Te Popo (~745 cal yr BP, Table 1) and the Burrell (AD 1655), could not be recognised in the upper parts of the composite lake-and-peat record, or may only be preserved as fine ash-layers within Tephra Sequence A.

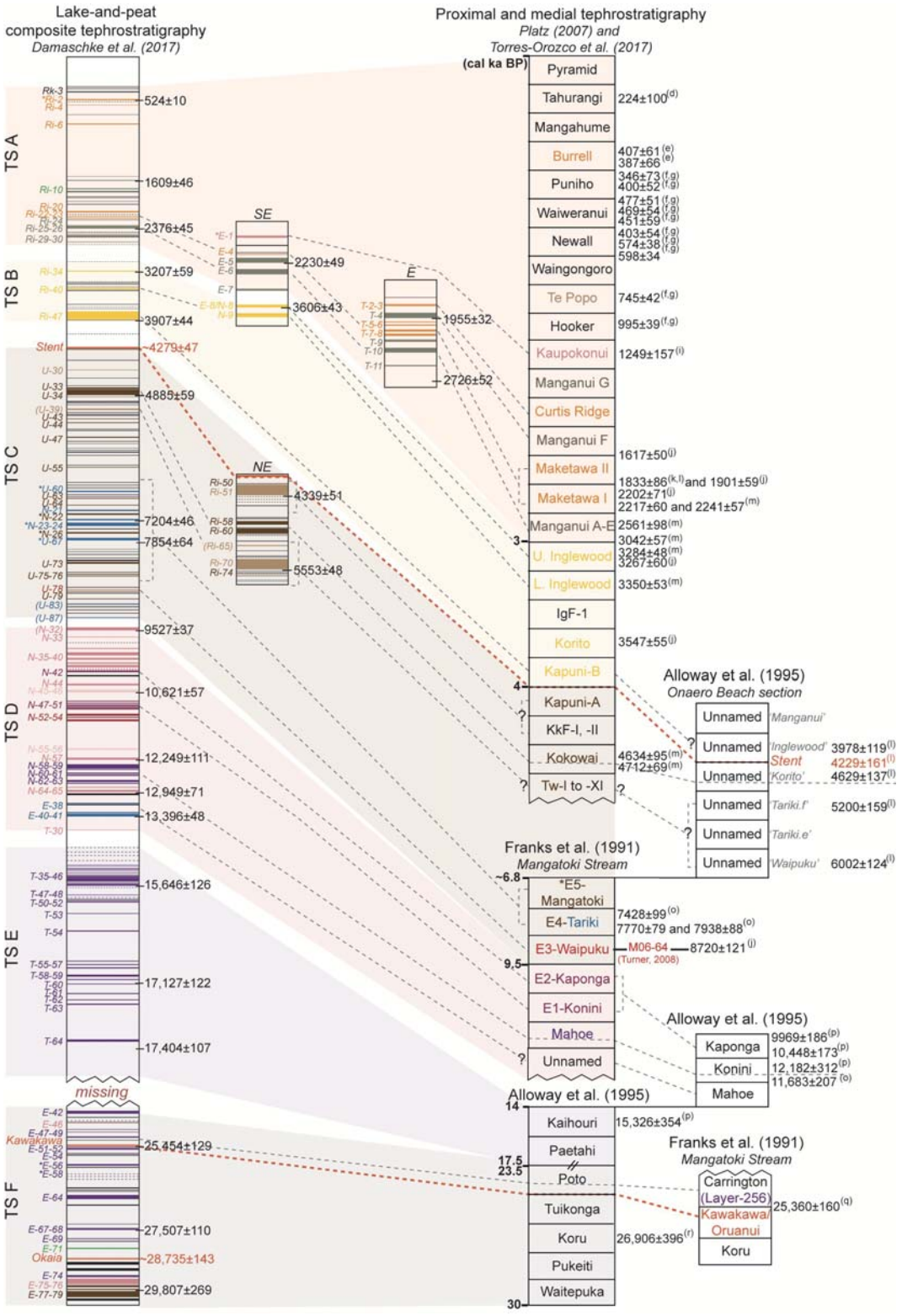

Figure 4. 6 *Representation of the links between lake and peat tephra sequences, and proximal and medial tephra successions on Mt. Taranaki. Each coloured line in the lake and peat column and coloured names in the medial and proximal column indicate the titanomagnetite composition (i.e., group) of the respective tephra deposit (refer to Fig. 4.3, Table 4.3). Asterisks indicate bi- or multimodal titanomagnetite compositions. The coloured bands that link the columns indicate Tephra Sequences (TS A-F) characterised by their dominant titanomagnetite group. Dotted lines highlight specific correlations (refer to text). Age references are according to Table 4.1 and ages for the lake-and-peat composite record after Chapter 3. Note the previous stratigraphy of Alloway et al. (1995) at the Onaero Beach section (grey-coloured names), which has been revised in the current study.*

4.2.7.2 Implications for andesitic tephra correlation

The establishment of a robust regional tephrostratigraphy depends upon anchoring by well-constrained stratigraphic marker beds. Uniquely identifiable units are difficult to find at mafic to intermediate composition volcanoes, like Mt. Taranaki, where pumices and glass shards are often rapidly weathered (e.g., Kirkman and McHardy, 1980; Lowe, 1986; Hodder et al., 1991; Alloway et al., 1995; Churchman and Lowe, 2012) and intense erosion occurs on high and steep edifices, e.g., during the Last Glacial Maximum (Pillans et al., 1993; Shane, 2000). Further, at stratovolcanoes erosion and superposition of tephra sequences occurs during repeated emplacement of debris avalanches and/or massive block-and-ash flows (Cortés et al., 2010; Zernack et al., 2011). The correlation of tephra units from disparate subaerial sites is also made difficult for mafic and intermediate tephras, because varying degrees of oxidation and weathering between different depositional sites mask textures and bedding characteristics. Furthermore, the general petrological and geochemical complexity of andesitic tephra and the lack of systematic compositional analyses on proximal deposits has hampered their detailed identification and discrimination for decades (e.g., Kohn and Neall, 1973; Froggatt and Rodgers, 1990; Cronin et al., 1996a, 1996b; Shane, 2005; Donoghue et al., 2007; Platz et al., 2007b; Shane et al., 2008; Ponomareva et al., 2015).

The method presented in this study has enabled a disparate set of data old and new to be integrated. Stratigraphically controlled and often well-dated continuous tephra sequences deposited in distal lacustrine and/or paludal environments allow identification of geochemically distinctive sequences of tephras that collectively could be marker “packages”. With good time-constraints, these packages can be correlated to proximal tephra units. This approach could be applied at similar volcanoes such as the highly active Merapi volcano (Indonesia), where older pyroclastic sequences hold a fuller eruptive history than could be gleaned from historical records (Andreastuti et al., 2000; Voight et al., 2000; Gertisser et al., 2012), or for example at the San Martin volcano within the Tuxtla Volcanic Field (Mexico), where rapid weathering blurs

preservation of isolated or individual tephra units (Espíndola et al., 2010). Another well-known example is the andesitic Shiveluch volcano in Kamchatka, which has produced numerous compositionally similar Holocene tephras and complex proximal stratigraphic sequences (Ponomareva et al., 2007, 2011, 2015).

Multiple studies utilise glass geochemistry to correlate between diverse types and locations of pyroclastic deposits. In continental margin and island arc mafic-intermediate systems, magmas are produced by a series of processes that lead to repeated similar compositions (e.g., Smith and Leeman, 1987; Price et al., 1992, 1999; Smith et al., 1997; Gamble et al., 1999). In particular, magmas sourced from flux-melting of the mantle wedge are subsequently modified by stalling, often at the base of the crust, before rising into independent or coalescing reservoirs in mid-crustal depths, before eruption (e.g., Devine et al., 2003; Annen et al., 2006; Price et al., 2012; Zernack et al., 2011; Adam et al., 2016). This processing leads to many eruptions that preserve evidence for mixed crystal assemblages (Stewart et al., 1996), and magma mingling and mixing before eruption (e.g., Price et al., 2005; Shane et al., 2008; Innocenti et al., 2013). As a result of these processes, it is understandable that unique tephra compositions are rarely formed (and hence the term 'fingerprint' was described as a misnomer in such circumstances by Lowe, 2011, p.120), and that many mineral phases are unlikely to be diagnostic for individual eruptions. For example, feldspars and pyroxenes typically to crystallize at a range of pressures and depths, with most growth occurring in mid-crustal reservoirs, where considerable mixing and mingling occurs. Glass chemistry is often the most defining character of eruptions since it represents the residual melt or the melt fraction that carries the magma to the surface. However, it has been shown that andesitic and basaltic glass can also be compositionally highly heterogeneous (e.g., Shane, 2005; Humphreys et al., 2010; Ponomareva et al., 2015) and often contain syn- and post-eruption crystallisations of nanolitic Fe-oxides and microlitic plagioclase (Best, 2003; Martel and Poussineau, 2007; Platz et al., 2007b; Humphreys et al., 2009). At this stage, Fe-Ti oxides have proven to be the most useful diagnostic tool in that they form early in the crystallisation sequence of magmas (Neall et al., 1986; Stewart et al., 1996) and are barely influenced by pre- and post-eruption processes and may thus record original melt compositions. Reconnaissance studies of

Marcaida et al. (2014), Damaschke et al. (2017) and those of the current study have demonstrated that titanomagnetite compositions, when combined with detailed geochronological data, are unique for individual tephra groups and/or sequences, which can operate as well-constrained stratigraphic marker horizons.

Irrespective of the approach taken, with such a large number of eruptions at most active stratovolcanoes around the world, identifying single tephras based on unique characteristics will always yield only a limited number of marker units. Here it is shown that even if unique compositions are rare, it is possible to identify periods that have fairly distinctive characteristics. These periods, tephra sequences, can be an extremely useful aid in the correlation of tephra layers from stratovolcanoes.

4.2.8 Conclusions

The results presented here help resolve stratigraphic uncertainties that challenged researchers attempting to correlate ash sequences around Mt. Taranaki. It has been demonstrated that the Korito tephra unit is stratigraphically located above the widespread Taupo-sourced Stent Tephra and compositionally related to the younger Upper and Lower Inglewood tephra units. Previously defined tephra units, including the Waipuku, Tariki and Mangatoki, are of older stratigraphic positions and ages (~6.8 to 9.5 cal yr BP) than hitherto assumed. Previously dated pyroclastic deposits between ~6 to 4 cal ka BP at the Onaero Beach section, 40 km north-east of Mt. Taranaki's summit, are considered to represent new tephra deposits, which can be partly associated with newly-studied and stratigraphically younger flank deposits including the Tw-I to -XI, Kokowai, Kapuni-A and Kapuni-B tephra units. The Kokowai tephra unit (~4.7 cal ka BP) is one of the most useful chronostratigraphic marker horizons identified in this study, because it is widely dispersed and has distinctive physical and geochemical characteristics.

The development of a chemostratigraphic framework provides an opportunity to link distinct geochemically and stratigraphically different tephra sequences and add refined age definitions to individual tephra layers and/or groups, which then can act as

chronostratigraphic marker horizons. This process is not only essential for future studies on tephra dispersal patterns and/or eruption volume and column height calculations, but also to future hazard assessments at Mt. Taranaki. There remain a great number of deposits recognised in the lake and peat records that cannot be correlated to previous and newly described proximal and medial sequences. The identification of many new tephra units show how much more frequently active Mt. Taranaki has been over the last ~30,000 years.

Most importantly this study shows that improving the tephrostratigraphy around long-lived volcanic areas hinges upon building a detailed "master" record of eruptions. While identifying unique compositions to match single tephra layers has been the goal of many past studies, here it is shown that if this is possible, identifying a chemostratigraphy or a time-variable chemical pattern can be the next best thing. Unique compositional patterns, sequences, or cycles can help identify sequences of tephras of similar chemistry – aiding correlations to one or two of these that may be preserved in wider-spread areas or off typical dispersal axes. It must, however, be recognised that the chemical sequences in some cases repeat, so that accurate dating is still required to identify which of the cycles an unknown tephra is correlated to.

4.2.9 Acknowledgements

MD and RTO acknowledge the financial support of Massey Doctoral Scholarships, and the George Mason Trust. Dr Anja Moebis and Mr Peter Lewis are thanked for their help with electron microprobe and other analytical analyses. SJC acknowledges support from the project "Quantifying exposure to multiple volcanic hazards" of the New Zealand Platform for Natural Hazards Research. We gratefully acknowledge the helpful review of Prof David Lowe and Dario Pedrazzi.

4.2.10 References

Adam, J., Turner, S., & Rushmer, T. (2016). The genesis of silicic arc magmas in shallow crustal cold zones. Lithos, 264, 472-494.

Alloway, B. V., McGlone, M. S., Neall, V. E., & Vucetich, C. G. (1992). The role of Egmont-sourced tephra in evaluating the paleoclimatic correspondence between the bio-and soil-stratigraphic records of central Taranaki, New Zealand. Quaternary international, 13, 187-194.

Alloway, B., Lowe, D. J., Chan, R. P. K., Eden, D., & Froggatt, P. (1994). Stratigraphy and chronology of the Stent tephra, a c. 4000 year old distal silicic tephra from Taupo Volcanic Centre, New Zealand. New Zealand journal of geology and geophysics, 37(1), 37-47.

Alloway, B., Neall, V. E., & Vucetich, C. G. (1995). Late Quaternary (post 28,000 year BP) tephrostratigraphy of northeast and central Taranaki, New Zealand. Journal of the Royal Society of New Zealand, 25(4), 385-458.

Andreastuti, S. D., Alloway, B. V., & Smith, I. E. M. (2000). A detailed tephrostratigraphic framework at Merapi Volcano, Central Java, Indonesia: implications for eruption predictions and hazard assessment. Journal of Volcanology and Geothermal Research, 100(1), 51-67.

Annen, C., Blundy, J. D., & Sparks, R. S. J. (2006). The genesis of intermediate and silicic magmas in deep crustal hot zones. Journal of Petrology, 47(3), 505-539.

Best, M.G. (2003). Igneous and metamorphic petrology. Blackwell Science.

Bronk Ramsey, C. (2013). OxCal 4.2. Web Interface Build, (78).

Buddington, A. F., & Lindsley, D. H. (1964). Iron-titanium oxide minerals and synthetic equivalents. Journal of petrology, 5(2), 310-357.

Carmichael, I. S. E., & Nicholls, J. (1966). Iron-titanium oxides of salic volcanic rocks and their associated ferromagnesian silicates. Contributions to Mineralogy and Petrology, 14(1), 36-64.

Churchman, J., & Lowe, D. J. (2012). Alteration, formation, and occurrence of minerals in soils. CRC Press.

Cortés, A., Macías, J. L., Capra, L., & Garduño-Monroy, V. H. (2010). Sector collapse of the SW flank of Volcán de Colima, México: The 3600yr BP La Lumbre–Los Ganchos debris avalanche and associated debris flows. Journal of Volcanology and Geothermal Research, 197(1), 52-66.

Cronin, S. J., Neall, V. E., Stewart, R. B., & Palmer, A. S. (1996a). A multiple-parameter approach to andesitic tephra correlation, Ruapehu volcano, New Zealand. Journal of volcanology and geothermal research, 72(3), 199-215.

Cronin, S. J., Wallace, R. C., & Neall, V. E. (1996b). Sourcing and identifying andesitic tephras using major oxide titanomagnetite and hornblende chemistry, Egmont volcano and Tongariro Volcanic Centre, New Zealand. Bulletin of Volcanology, 58(1), 33-40.

Cronin, S. J., Stewart, R. B., Neall, V. E., Platz, T., & Gaylord, D. (2003). The AD1040 to present Maero Eruptive Period of Egmont Volcano, Taranaki, New Zealand. Geol Soc NZ Misc Publ A, 116, 43.

Damaschke, M., Cronin, S. J., Holt, K. A., Bebbington, M. S., & Hogg, A. G. (2017). A 30,000 yr high-precision eruption history for the andesitic Mt. Taranaki, North Island, New Zealand. Quaternary Research, 1-23. DOI:10.1017/qua.2016.11

Devine, J. D., Rutherford, M. J., Norton, G. E., & Young, S. R. (2003). Magma storage region processes inferred from geochemistry of Fe–Ti oxides in andesitic magma, Soufriere Hills Volcano, Montserrat, WI. Journal of Petrology, 44(8), 1375-1400.

Donoghue, S. L., Vallance, J., Smith, I. E., & Stewart, R. B. (2007). Using geochemistry as a tool for correlating proximal andesitic tephra: case studies from Mt Rainier (USA) and Mt Ruapehu (New Zealand). Journal of Quaternary Science, 22(4), 395-410.

Druce, A. P. (1966). Tree-ring dating of recent volcanic ash and lapilli, Mt Egmont. New Zealand journal of botany, 4(1), 3-41.

Eden, D. N., Froggatt, P. C., Trustrum, N. A., & Page, M. J. (1993). A multiple-source Holocene tephra sequence from Lake Tutira, Hawke's Bay, New Zealand. New Zealand journal of geology and geophysics, 36(2), 233-242.

Eden, D. N., & Froggatt, P. C. (1996). A 6500-year-old history of tephra deposition recorded in the sediments of Lake Tutira, eastern North Island, New Zealand. Quaternary international, 34, 55-64.

Eden, D. N., & Hammond, A. P. (2003). Dust accumulation in the New Zealand region since the last glacial maximum. Quaternary science reviews, 22(18), 2037-2052.

Espíndola, J. M., Zamora-Camacho, A., Godinez, M. L., Schaaf, P., & Rodríguez, S. R. (2010). The 1793 eruption of San Martín Tuxtla volcano, Veracruz, Mexico. Journal of Volcanology and Geothermal Research, 197(1), 188-208.

Franks, A. M. (1984). Soils of Eltham county and the tephrochronology of central Taranaki: a thesis presented in partial fulfilment of the requirements for the degree of Doctor of Philosophy in Soil Science (Doctoral dissertation, Massey University).

Franks, A., Neall, V. E., & Pollock, J. (1991). Soils of Eltham County, North Island, New Zealand. DSIR Land Resources Scientific Report No. 14. Lower Hutt, New Zealand. DSIR Land Resources.

Froggatt, P. C. (1983). Toward a comprehensive Upper Quaternary tephra and ignimbrite stratigraphy in New Zealand using electron microprobe analysis of glass shards. Quaternary research, 19(2), 188-200.

Froggatt, P. C., & Lowe, D. J. (1990). A review of late Quaternary silicic and some other tephra formations from New Zealand: their stratigraphy, nomenclature, distribution, volume, and age. New Zealand journal of geology and geophysics, 33(1), 89-109.

Froggatt, P. C., & Rogers, G. M. (1990). Tephrostratigraphy of high-altitude peat bogs along the axial ranges, North Island, New Zealand. New Zealand journal of geology and geophysics, 33(1), 111-124.

Frost, B. R., & Lindsley, D. H. (1991). Occurrence of iron-titanium oxides in igneous rocks. Reviews in Mineralogy and geochemistry, 25(1), 433-468.

Gamble, J. A., Wood, C. P., Price, R. C., Smith, I. E. M., Stewart, R. B., & Waight, T. (1999). A fifty year perspective of magmatic evolution on Ruapehu Volcano, New Zealand: verification of open system behaviour in an arc volcano. Earth and Planetary Science Letters, 170(3), 301-314.

Gehrels, M. J., Lowe, D. J., Hazell, Z. J., & Newnham, R. M. (2006). A continuous 5300-yr Holocene cryptotephrostratigraphic record from northern New Zealand and implications for tephrochronology and volcanic hazard assessment. The Holocene, 16(2), 173-187.

Gertisser, R., Charbonnier, S. J., Keller, J., & Quidelleur, X. (2012). The geological evolution of Merapi volcano, Central Java, Indonesia. Bulletin of volcanology, 74(5), 1213-1233.

Ghiorso, M. S., & Sack, O. (1991). Fe-Ti oxide geothermometry: thermodynamic formulation and the estimation of intensive variables in silicic magmas. Contributions to Mineralogy and Petrology, 108(4), 485-510.

Grant-Taylor, T. L., & Rafter, T. A. (1963). New Zealand natural radiocarbon measurements IV. American Journal of Science.

Grant-Taylor, T. L., & Rafter, T. A. (1971). New Zealand radiocarbon age measurements—6. New Zealand Journal of Geology and Geophysics, 14(2), 364-402.

Green, R. M., Bebbington, M. S., Jones, G., Cronin, S. J., & Turner, M. B. (2016). Estimation of tephra volumes from sparse and incompletely observed deposit thicknesses. Bulletin of Volcanology, 78(4), 1-18.

Hill, R., & Roeder, P. (1974). The crystallisation of spinel from basaltic liquid as a function of oxygen fugacity. The Journal of Geology, 709-729.

Hodder, A. P. W., De Lange, P. J., & Lowe, D. J. (1991). Dissolution and depletion of ferromagnesian minerals from Holocene tephra layers in an acid bog, New

Zealand, and implications for tephra correlation. Journal of Quaternary science, 6(3), 195-208.

Hogg, A. G., Hua, Q., Blackwell, P. G., Niu, M., Buck, C. E., Guilderson, T. P., Heaton, T. J., Palmer, J. G., Reimer, P. J., Reimer, R. W., Turney, C. S. M., & Zimmerman, S. R. H. (2013). SHCal13 Southern Hemisphere calibration, 0–50,000 years cal BP. Radiocarbon, 55(4), 1889-1903.

Howorth, R. (1975). New formations of late Pleistocene tephras from the Okataina volcanic centre, New Zealand. New Zealand journal of geology and geophysics, 18(5), 683-712.

Humphreys, M. C., Christopher, T., & Hards, V. (2009). Microlite transfer by disaggregation of mafic inclusions following magma mixing at Soufrière Hills volcano, Montserrat. Contributions to Mineralogy and Petrology, 157(5), 609-624.

Humphreys, M. C. S., Edmonds, M., Christopher, T., & Hards, V. (2010). Magma hybridisation and diffusive exchange recorded in heterogeneous glasses from Soufrière Hills Volcano, Montserrat. Geophysical Research Letters, 37(19).

Innocenti, S., del Marmol, M. A., Voight, B., Andreastuti, S., & Furman, T. (2013). Textural and mineral chemistry constraints on evolution of Merapi Volcano, Indonesia. Journal of Volcanology and Geothermal Research, 261, 20-37.

Kirkman, J. H., & McHardy, W. J. (1980). A comparative study of the morphology, chemical composition and weathering of rhyolitic and andesitic glass. Clay minerals, 15(2), 165-173.

Kohn, B. P. (1970). Identification of New Zealand tephralayers by emission spectrographic analysis of their titanomagnetites. Lithos, 3(4), 361-368.

Kohn, B. P., & Neall, V. E. (1973). Identification of late Quaternary tephras for dating Taranaki lahar deposits. New Zealand journal of geology and geophysics, 16(3), 781-792.

Lowe, D. J. (1986). Controls on the rates of weathering and clay mineral genesis in airfall tephras: a review and New Zealand case study. In: Colam, S. M. & Dethier, D. P. (Eds.), Rates of chemical weathering of rocks and minerals, 265-330. Academic Press, Orlando.

Lowe, D. J. (1988). Stratigraphy, age, composition, and correlation of late Quaternary tephras interbedded with organic sediments in Waikato lakes, North Island, New Zealand. New Zealand journal of geology and geophysics, 31(2), 125-165.

Lowe, D. J., Shane, P. A., Alloway, B. V., & Newnham, R. M. (2008). Fingerprints and age models for widespread New Zealand tephra marker beds erupted since 30,000 years ago: a framework for NZ-INTIMATE. Quaternary Science Reviews, 27(1), 95-126.

Lowe, D. J., Blaauw, M., Hogg, A. G., & Newnham, R. M. (2013). Ages of 24 widespread tephras erupted since 30,000 years ago in New Zealand, with re-evaluation of the timing and palaeoclimatic implications of the Lateglacial cool episode recorded at Kaipo bog. Quaternary Science Reviews, 74, 170-194.

Marcaida, M., Mangan, M. T., Vazquez, J. A., Bursik, M., & Lidzbarski, M. I. (2014). Geochemical fingerprinting of Wilson Creek formation tephra layers (Mono Basin, California) using titanomagnetite compositions. Journal of Volcanology and Geothermal Research, 273, 1-14.

Martel, C., & Poussineau, S. (2007). Diversity of eruptive styles inferred from the microlites of Mt Pelée andesite (Martinique, Lesser Antilles). Journal of Volcanology and Geothermal Research, 166(3), 233-254.

McGlone, M. S., Neall, V. E., & Clarkson, B. D. (1988). The effect of recent volcanic events and climatic changes on the vegetation of Mt Egmont (Mt Taranaki), New Zealand. New Zealand journal of botany, 26(1), 123-144.

McGlone, M. S., & Neall, V. E. (1994). The late Pleistocene and Holocene vegetation history of Taranaki, North Island, New Zealand. New Zealand journal of botany, 32(3), 251-269.

McHenry, L. J. (2005). Phenocryst composition as a tool for correlating fresh and altered tephra, Bed I, Olduvai Gorge, Tanzania. Stratigraphy, 2(2), 101-115.

Moebis, A., Cronin, S. J., Neall, V. E., & Smith, I. E. (2011). Unravelling a complex volcanic history from fine-grained, intricate Holocene ash sequences at the Tongariro Volcanic Centre, New Zealand. Quaternary International, 246(1), 352-363.

Molloy, C., Shane, P., & Augustinus, P. (2009). Eruption recurrence rates in a basaltic volcanic field based on tephra layers in maar sediments: implications for hazards in the Auckland volcanic field. Geological Society of America Bulletin, 121(11-12), 1666-1677.

Neall, V. E. (1972). Tephrochronology and tephrostratigraphy of western Taranaki (N108–109), New Zealand. New Zealand journal of geology and geophysics, 15(4), 507-557.

Neall, V. E. (1979). Geological Map of New Zealand 1: 50,000 Sheet P19, P20, & P21: New Plymouth, Egmont and Manaia. New Zealand Geological Survey, Department of Scientific and Industrial Research.

Neall, V. E. (1999). Stony River at the Blue Rata Reserve. Report to the Taranaki Regional Council, Taranaki, p 13.

Neall, V. E., & Jansen, H. S. (1984). Anomalous radiocarbon dates from Mt Egmont. Programme and Abstracts, Geological Society of New Zealand Conference. Geological Society of New Zealand Miscellaneous Publication 31A.

Neall, V. E., Stewart, R. B., & Smith, I. E. M. (1986). History and petrology of the Taranaki volcanoes. Royal Society of New Zealand Bulletin, 23, 251-263.

Pillans, B., McGlone, M., Palmer, A., Mildenhall, D., Alloway, B., & Berger, G. (1993). The Last Glacial Maximum in central and southern North Island, New Zealand: a paleoenvironmental reconstruction using the Kawakawa Tephra Formation as a chronostratigraphic marker. Palaeogeography, palaeoclimatology, palaeoecology, 101(3), 283-304.

Platz, T. (2007). Understanding aspects of andesitic dome-forming eruptions through the last 1000 yr of volcanism at Mt. Taranaki, New Zealand: a dissertation presented in partial fulfilment of the requirements for the degree of Doctor of Philosophy in Earth Science, Massey University, Palmerston North, New Zealand.

Platz, T., Cronin, S. J., Cashman, K. V., Stewart, R. B., & Smith, I. E. (2007a). Transition from effusive to explosive phases in andesite eruptions—A case-study from the AD1655 eruption of Mt. Taranaki, New Zealand. Journal of volcanology and geothermal research, 161(1), 15-34.

Platz, T., Cronin, S. J., Smith, I. E., Turner, M. B., & Stewart, R. B. (2007b). Improving the reliability of microprobe-based analyses of andesitic glasses for tephra correlation. The Holocene, 17(5), 573-583.

Platz, T., Cronin, S. J., Procter, J. N., Neall, V. E., & Foley, S. F. (2012). Non-explosive, dome-forming eruptions at Mt. Taranaki, New Zealand. Geomorphology, 136(1), 15-30.

Ponomareva, V., Kyle, P., Pevzner, M., Sulerzhitsky, L., & Hartman, M. (2007). Holocene eruptive history of Shiveluch volcano, Kamchatka Peninsula, Russia. Volcanism and subduction: the Kamchatka region, 263-282.

Ponomareva, V., Portnyagin, M., Blaauw, M., Pevzner, M., & Kyle, P. R. (2011, December). Variations of glass composition in the Holocene tephra of Shiveluch volcano (Kamchatka): applications for magmatic history and tephrochronology. In AGU Fall Meeting Abstracts (Vol. 1, p. 2585).

Ponomareva, V., Portnyagin, M., Pevzner, M., Blaauw, M., Kyle, P., & Derkachev, A. (2015). Tephra from andesitic Shiveluch volcano, Kamchatka, NW Pacific: chronology of explosive eruptions and geochemical fingerprinting of volcanic glass. International Journal of Earth Sciences, 104(5), 1459-1482.

Price, R. C., McCulloch, M. T., Smith, I. E. M., & Stewart, R. B. (1992). Pb-Nd-Sr isotopic compositions and trace element characteristics of young volcanic rocks from Egmont Volcano and comparisons with basalts and andesites from the Taupo Volcanic Zone, New Zealand. Geochimica et cosmochimica acta, 56(3), 941-953.

Price, R. C., Stewart, R. B., Woodhead, J. D., & Smith, I. E. M. (1999). Petrogenesis of high-K arc magmas: evidence from Egmont volcano, North Island, New Zealand. Journal of Petrology, 40(1), 167-197.

Price, R. C., Gamble, J. A., Smith, I. E., Stewart, R. B., Eggins, S., & Wright, I. C. (2005). An integrated model for the temporal evolution of andesites and rhyolites and crustal development in New Zealand's North Island. Journal of Volcanology and Geothermal Research, 140(1), 1-24.

Price, R. C., Gamble, J. A., Smith, I. E., Maas, R., Waight, T., Stewart, R. B., & Woodhead, J. (2012). The anatomy of an Andesite volcano: a time–stratigraphic study of andesite petrogenesis and crustal evolution at Ruapehu Volcano, New Zealand. Journal of Petrology, egs050.

Sandiford, A., Alloway, B., & Shane, P. (2001). A 28 000–6600 cal yr record of local and distal volcanism preserved in a paleolake, Auckland, New Zealand. New Zealand Journal of Geology and Geophysics, 44(2), 323-336.

Schmid, R. (1981). Descriptive nomenclature and classification of pyroclastic deposits and fragments: Recommendations of the IUGS Subcommission on the Systematics of Igneous Rocks. Geology, 9(1), 41-43.

Shane, P. (1998). Correlation of rhyolitic pyroclastic eruptive units from the Taupo volcanic zone by Fe–Ti oxide compositional data. Bulletin of Volcanology, 60(3), 224-238.

Shane, P. (2000). Tephrochronology: a New Zealand case study. Earth-Science Reviews, 49(1), 223-259.

Shane, P. (2005). Towards a comprehensive distal andesitic tephrostratigraphic framework for New Zealand based on eruptions from Egmont volcano. Journal of Quaternary Science, 20(1), 45-57.

Shane, P., & Hoverd, J. (2002). Distal record of multi-sourced tephra in Onepoto Basin, Auckland, New Zealand: implications for volcanic chronology, frequency and hazards. Bulletin of Volcanology, 64(7), 441-454.

Shane, P., Doyle, L. R., & Nairn, I. A. (2008). Heterogeneous andesite–dacite ejecta in 26–16.6 ka pyroclastic deposits of Tongariro Volcano, New Zealand: the product of multiple magma-mixing events. Bulletin of Volcanology, 70(4), 517-536.

Smith, D. R., & Leeman, W. P. (1987). Petrogenesis of Mount St. Helens dacitic magmas. Journal of Geophysical Research, 92, 10313.

Smith, I. E., Worthington, T. J., Price, R. C., & Gamble, J. A. (1997). Primitive magmas in arc-type volcanic associations: examples from the southwest Pacific. Canadian Mineralogist, 35, 257-274.

Stewart, R. B., Price, R. C., & Smith, I. E. M. (1996). Evolution of high-K arc magma, Egmont volcano, Taranaki, New Zealand: evidence from mineral chemistry. Journal of Volcanology and Geothermal Research, 74(3), 275-295.

Thorarinsson, S. (1974). The Terms Teprha and Tephrochronology. World Bibliography and Index of Quaternary Tephrochronology. edited by JA Westgate and CM Gold, 1-528.

Thorarinsson, S. (1949). Some tephrochronological contributions to the volcanology and glaciology of Iceland. Geografiska Annaler, 31, 239-256.

Tonkin, P. J. (1970). The soils of the southeastern sector of Egmont National Park.

Topping, W. W. (1974). A 1480 AD Maori oven from Mount Egmont, New Zealand. New Zealand Journal of Science, 17, 119-122.

Torres-Orozco, R., Cronin, S. J., Pardo, N., & Palmer, A. S. (2017). New insights into Holocene eruption episodes from proximal deposit sequences at Mt. Taranaki (Egmont), New Zealand. Bulletin of Volcanology, 79(1), 3. DOI: 10.1007/s00445-016-1085-5.

Turner, M. B. (2008). Eruption cycles and magmatic processes at a reawakening volcano, Mt. Taranaki, New Zealand: a thesis presented in partial fulfilment of the requirements for the degree of Doctor of Philosophy in Earth Science at Massey University, Palmerston North, New Zealand.

Turner, M. B., Cronin, S. J., Stewart, R. B., Bebbington, M., & Smith, I. E. (2008a). Using titanomagnetite textures to elucidate volcanic eruption histories. Geology, 36(1), 31-34.

Turner, M. B., Cronin, S. J., Bebbington, M. S., & Platz, T. (2008b). Developing probabilistic eruption forecasts for dormant volcanoes: a case study from Mt Taranaki, New Zealand. Bulletin of Volcanology, 70(4), 507-515.

Turner, M. B., Cronin, S. J., Smith, I. E., Stewart, R. B., & Neall, V. E. (2008c). Eruption episodes and magma recharge events in andesitic systems: Mt Taranaki, New Zealand. Journal of Volcanology and Geothermal Research, 177(4), 1063-1076.

Turner, M. B., Bebbington, M. S., Cronin, S. J., & Stewart, R. B. (2009). Merging eruption datasets: building an integrated Holocene eruptive record for Mt Taranaki, New Zealand. Bulletin of volcanology, 71(8), 903-918.

Turner, M. B., Cronin, S. J., Bebbington, M. S., Smith, I. E., & Stewart, R. B. (2011a). Integrating records of explosive and effusive activity from proximal and distal sequences: Mt. Taranaki, New Zealand. Quaternary International, 246(1), 364-373.

Turner, M. B., Cronin, S. J., Bebbington, M. S., Smith, I. E., & Stewart, R. B. (2011b). Relating magma composition to eruption variability at andesitic volcanoes: A

case study from Mount Taranaki, New Zealand. Geological Society of America Bulletin, 123(9-10), 2005-2015.

Vandergoes, M. J., Hogg, A. G., Lowe, D. J., Newnham, R. M., Denton, G. H., Southon, J., Barrell, D. J., Wilson, C. J., McGlone, M. S., Allan, A. S., & Almond, P. C. (2013). A revised age for the Kawakawa/Oruanui tephra, a key marker for the Last Glacial Maximum in New Zealand. Quaternary Science Reviews, 74, 195-201.

Voight, B., Constantine, E. K., Siswowidjoyo, S., & Torley, R. (2000). Historical eruptions of Merapi volcano, central Java, Indonesia, 1768–1998. Journal of Volcanology and Geothermal Research, 100(1), 69-138.

Vucetich, C. T., & Pullar, W. A. (1969). Stratigraphy and chronology of late Pleistocene volcanic ash beds in central North Island, New Zealand. New Zealand journal of geology and geophysics, 12(4), 784-837.

Vucetich, C. G., & Howorth, R. (1976). Proposed definition of the Kawakawa Tephra, the c. 20,000-years-BP marker horizon in the New Zealand region. New Zealand journal of geology and geophysics 19(1), 43-50.

Wallace, R. C. (1987). Mineralogy of the Tokomaru silt loam and the occurrence of cristobalite and tridymite in selected North Island soils. Unpublished PhD thesis, Massey University, Palmerston North.

Whitehead, S. J. (1976). Granulometric studies on selected tephra eruptions, North Island, New Zealand. Unpublished Honours Dissertation, lodged in the Library, Massey University, Palmerston North, New Zealand.

Zernack, A. V., Cronin, S. J., Neall, V. E., & Procter, J. N. (2011). A medial to distal volcaniclastic record of an andesite stratovolcano: detailed stratigraphy of the ring-plain succession of south-west Taranaki, New Zealand. International Journal of Earth Sciences, 100(8), 1937-1966.

Chapter 5

Probabilistic eruption forecasting using a multi-site high-resolution tephra record from Mt. Taranaki, New Zealand

This chapter illustrates how stratigraphic data is combined to build the most complete and un-biased data sets for developing models of eruption frequency and ultimately forecasts of eruption probability. It extends from single-site to multiple-location records in order to capture a wider range of tephra dispersal directions, variations in eruption sizes/styles, and account for variable tephra preservation and/or depositional issues. The approach taken highlights some of the key components of statistical merging procedures to compile a record of the eruption frequency of Mt. Taranaki than in past attempts

5.1 Chapter synopsis

In Chapter 3 a high-resolution tephrostratigraphy was built from deposits within six lake and peat sites surrounding Mt. Taranaki, spanning an arc from northeast to southeast of the volcano, which are downwind of the most common tephra dispersal directions. This record forms one of the most detailed and continuous eruption history records available for an andesitic stratovolcano. Due to slow and continuous accumulation of organic-rich sediment, minimal erosion and slow weathering, very thin and fine-grained tephra falls are well preserved. Such continuously accumulating environments allowed age-depth relationships to be built by using multiple radiocarbon dated horizons and depth, to interpolate age estimates for each tephra. The latter were used, in conjunction with

detailed physical and geochemical observations, to correlate between different records, as well as, in the last chapter, to units on the cone. In this following chapter 5, a statistical approach is used to build a more complete image of the true eruption history of Mt. Taranaki than hitherto constructed. The use of multiple sites not only provides evidence of tephras that are distributed over wider areas, but also captures data from tephra that have been preserved in narrow dispersal lobes and so maybe missed in studies of single sites. Once a reliable multi-site record was constructed, the temporal distributions of tephras were used to generate accurate time-varying eruption frequency estimates and apply volcanic hazard models to estimate future eruption probabilities.

All of chapter 5 is contained within the manuscript: *Using multi-site tephra records to develop volcanic eruption frequency models and hazard estimates, Mt. Taranaki, New Zealand* by M. Damaschke, S.J. Cronin and M.S. Bebbington, which has been submitted as a Research paper to *Bulletin of Volcanology*. Its format has been altered to match that of the overall thesis.

The contributions of each author are outlined below:

M. Damaschke: Principal investigator

Carried out: Manual merging
Geochemical correlations, which were fitted into the statistical models
Manuscript preparation and writing

S.J. Cronin: Chief Advisor

Aided the study by: Discussion of data and interpretations
Editing and discussion of the manuscript

M.S. Bebbington: Statistical advisor

Aided the study by: Application of statistical methods (e.g., merging algorithm, probabilistic eruption forecast modelling)
Discussion of data and interpretations
Editing and discussion of the manuscript

5.2 Using multi-site tephra records to develop volcanic eruption frequency models and hazard estimates, Mt. Taranaki, New Zealand

Magret Damaschke[1], Shane J. Cronin[1,2], Mark S. Bebbington[1]

[1]*Institute of Agriculture and Environment, Massey University, Private Bag 11222, Palmerston North 4410*

[2]*School of Environment, University of Auckland, Private Bag 92019, Auckland 1142*

5.2.1 Abstract

Robust time-varying volcanic hazard assessments are difficult to develop, because they rely entirely upon knowing a complete and extensive eruptive activity record. Missing events in eruption records are likely endemic in many volcanic areas, due to erosion of tephra. Difficulties in matching tephras with similar compositions using classical tephra correlation methods can lead to underestimation or overestimation of eruption numbers. Further, records with many tens of events spanning long time periods, while necessary for accurate modelling, are rare, particularly from sites in multiple directions downwind of a volcano. Here we examine the sensitivity of probabilistic hazard estimates in the context of a suite of several new high-resolution tephra records located around Mt. Taranaki, New Zealand. Previous estimates have been made using only single, or two correlated tephra records. In this study, data from six individual tephra records (including those of previous studies) from lake and peat sites are used as they provide a substantially longer record and cover of ~120^{o} downwind of the volcano. The new data confirm a previously identified cyclical pattern of changing eruption frequency. The recurrence interval is bimodal, with the primary mode having a mean of ~65 years. The secondary mode, where centuries separate eruptions, accounts for only 2% of reposes, but has not disappeared with the inclusion of additional eruptions from the new records, providing strong evidence that it is a real phenomenon. The new data also demonstrate that one of the two records (Lake Rotokare) used in earlier works had a "old-carbon"

effect on age determinations, resulting in shifted age estimates, and hence duplication and an artificially high eruption frequency, in the combined record. New modelled time-varying frequency estimates suggest a 33-42% probability of an explosive eruption from Mt. Taranaki in the next 50 years, which is significantly lower than suggested by previous studies. Overall, this paper outlines possible pitfalls during merging procedures and their consequences in subsequent hazard assessments to derive a more reliable probabilistic eruption forecast for andesitic Mt. Taranaki.

Keywords: tephra; tephrostratigraphy; probabilistic eruption forecasting; Mt Taranaki; merging algorithm; hazard

5.2.2 Introduction

Improving hazard assessments with accurate probabilistic forecasts is a significant responsibility of volcanologists because of the increasing population densities around volcanoes over the last century (Small and Naumann 2001). An unexpected large-scale eruption may cause a volcanic disasters (e.g., Krakatau 1882; Self and Rampino 1981; Mt. Pelee 1902; Tanguy 1994), but even small-scale eruptions, like that of Ruapehu (New Zealand) in 1995-1996 (Johnston et al. 2000), could impact greatly on our increasingly more technological societies. Long-term dormant volcanoes pose a significant compounding risk, because they are often underestimated by their inhabitants. For example, Pinatubo was dormant for 650 years prior to its devastating 1991 eruption (Dartevelle et al. 2002; Gaillard 2006). Even with an increasing understanding of volcanic systems, many mafic to intermediate volcanoes with irregular eruption patterns and styles remain inexplicably diverse and poorly predictable (e.g., Miyaji 1988; Scandone et al. 1993; Melnik and Sparks 1999; Andreastuti et al. 2000). Robust eruption forecasts at many volcanoes are hindered by a lack of well-documented volcanic histories. Event records that are long and detailed enough to enable identification of fundamental eruption recurrence patterns are rare. Here an example of a highly detailed eruption event record from Mt. Taranaki is examined in order to improve volcanic eruption forecasting.

Mt. Taranaki is an andesitic stratovolcano located in the western North Island of New Zealand (Fig. 5.1), and has remained dormant for ~200 years (Platz et al. 2012). Its recorded volcanic activity covers a period of over 170,000 years, based on extensively studied mass flow and tephra deposits on its flanks and ring-plain (Alloway et al. 1995, 2005; Turner et al. 2008, 2009, 2011a; Zernack et al. 2009, 2011). Alloway et al. (1995) determined an eruption frequency of one event per 330 years, based on proximal, post-32 ka deposits. This was considered a minimum, because it was biased toward larger magnitude and coarser-grained fall deposits. Frequency estimates of Taranaki tephras were also made based on ashes preserved within distal lacustrine sediments (e.g., Waikato lakes (Hamilton), one event per 1.1 kyr; Lowe 1988; Auckland palaeolakes, one event per 1.4 kyr; Shane 2005; Molloy et al. 2009). These also highly underestimate the volcanic activity since they only include the larger magnitude events that disperse ash up to 270 km and in a narrow specific wind direction (to the NNE). The first high-resolution tephrochronological studies at this volcano (Turner et al. 2008, 2009) identified that a simple average eruption rate did not well describe the observed activity. Instead there was quite regular eruption frequency cycle over time, with a ~1500 year periodicity. Time-variability was significant, with a five-fold difference in the annual eruptive frequency of Mt. Taranaki over the past ~10 ka BP. Using a tephra record from sediments at Lake Umutekai north-east of the vent (Fig. 5.1), Turner et al. (2008) estimated a 37-48% chance of an eruption from this volcano in the next 50 years. After adding data from a second tephra record, south-east of the volcano (Lake Rotokare), some of the apparent gaps in the original eruption record were “filled”, leading Turner et al. (2009) to raise the 50 year probability for an eruption to 52-59%.

In this study, a longer period of volcanic history (~30,000 cal yr BP) for Mt. Taranaki was assembled over a wider area of tephra dispersal by adding four new lake and peat tephra records (Damaschke et al. 2017a; Fig. 5.1). The distribution of these sampling sites around a ~120^{o} northeast-southeast arc downwind of the volcano provides the opportunity to track a range of tephra dispersal patterns and also evaluate tephra preservation biases and variations between sites. Expanding the composite two site record to a multiple-site site record makes the overall eruption history record more representative and inclusive of the actual eruptive behaviour, providing a more robust

basis for improved probabilistic hazard forecasts. Nevertheless, combining sequences from more than one site must be conducted with care, to avoid over- or under-inflating the true eruption frequency, because individual andesitic tephra bed correlation based on physical and chemical characteristics remains challenging (Cronin et al. 1996; Donoghue et al. 2007; Damaschke et al. 2017a, 2017b). Statistical methods for correlating multiple records using radiocarbon age and stratigraphy models exist (Turner et al. 2009; Green et al. 2014), but the quality of the result depends on the accuracy of age determinations. Particularly difficult is the matching of near-contemporaneous tephras, as well as situations where the sedimentation regime trapping tephra deposits is discontinuous, or highly variable between sites. These issues are addressed in this study so as to strengthen future probabilistic assessment methods and revise current eruption probabilities at Mt. Taranaki.

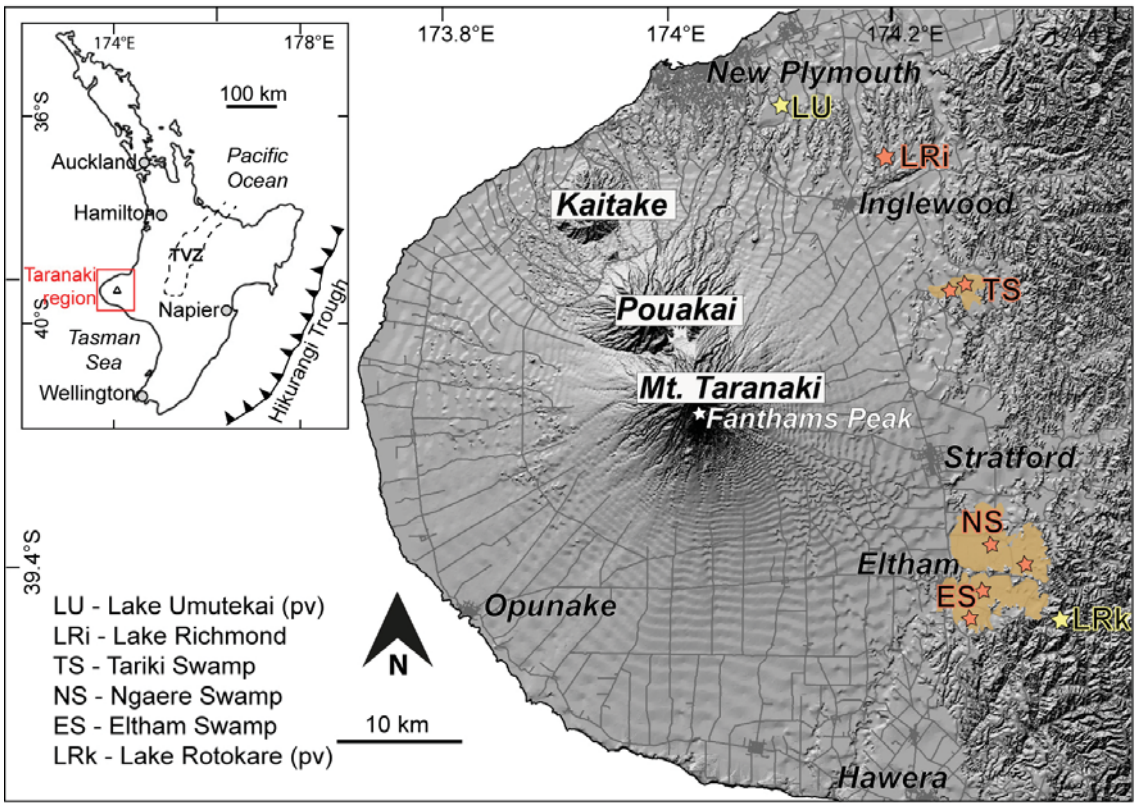

Figure 5. 1 *Location map of the tephra deposition sites (pv = previous studied sites by Turner et al. 2008, 2009), Cape Egmont, western North Island, New Zealand. TVZ = Taupo Volcanic Zone*

5.2.3 Eruption frequency

5.2.3.1 Single records

Tephras recovered in lake and peat sediment cores surrounding Mt. Taranaki are our basis for understanding eruption rates. The time frame encapsulated by the records and the number of tephra layers preserved is not uniform throughout time (Fig. 5.2). Analysing those records using a Gaussian kernel smoother (Silverman 1984, 1986; Wand and Jones 1994) with a bandwidth of 100 years, estimates were made of the overall annual eruption rates over time – as indicated by each single site (Fig. 5.2A). The lake sediments examined here preserve the highest number of tephra deposits over most time frames. However, integration across all sites is important, because one or two sites are likely to have little chance of recording all tephra falls due to variable wind and tephra dispersal patterns (Carey and Sparks 1986) and/or variations in eruption style and magnitude (Woods 1995; Bursik 1998).

At Lake Richmond 129 Taranaki eruptions were recorded with an average interval of 113 years, similar to that found at Lake Umutekai (111 years). Both lakes show similar cycling patterns of ~1000-1500 year-long intervals with particularly high rates of tephra deposition (HRTD) centred at ~0.5, 2, 3.5, 5, 7, 8.5, 10.5, and 12.5 cal ka BP (indicated by numbers 1-8 in Figure 5.2A), separated by periods of low rates of tephra deposition (LRTD) and/or a lack of tephra deposition (both indicated by letters A-H in Figure 5.2B). Older variations in the rate of tephra deposition are documented within the Tariki Swamp record only (HRTD intervals-9 and -10 at ~15 and 17 cal ka BP, respectively, separated by LRTD interval-I at ~16.5 cal ka BP; Figs. 5.2A, B).

The HRTD interval-1 (~0.5 cal ka BP; Fig. 5.2A) is only recognised in the Lake Richmond and Lake Rotokare cores, because most of the peatlands have been drained and developed into pasture causing oxidation, mixing and loss of the upper ~1 m of sediment. In Lake Umutekai, uncompacted suspended material at the top of the sediment core was lost during extraction (Turner 2008). HRTD interval-1 is preceded

by a distinct period of ~700 years where no tephra deposition is observed (A; Fig. 5.2B).

The HRTD interval-2 (~2 cal ka BP) is recognised in all sediment cores, but is most prominent within the Lake Richmond record (0.028 units per year; Fig. 5.2A). HRTD interval-2 was generated by eruptions from two vents; mafic eruptions from Fanthams Peak (1966 m elevation on the southern flanks of the volcano) producing the Manganui tephras, which intercalate with more silicic units (e.g., Maketawa tephras) from the summit vent of the 2518 m Mt. Taranaki (Damaschke et al. 2017b; Torres-Orozco et al. 2017). The preceding HRTD interval-3 (~3.5 cal ka BP) only encompasses tephras from the summit vent, including the prominent and widespread Inglewood tephra unit. It is noteworthy that the HRTD intervals-2 and -3 within the Lake Rotokare record contain tephras that are ~300-500 years older than their apparent age determinations of their tephra correlatives (Fig. 5.2A).

The HRTD interval-4 (~5 cal ka BP; Fig. 5.2A) is best observed within Lake Richmond and Lake Umutekai, because during this time interval discontinuous peat accumulation hinders complete tephra preservation within the peat records. The HRTD interval-5 (~7 cal ka BP; Fig. 5.2A), however, is also prominent within the Ngaere Swamp, and so expands the length of this phase of high rates of tephra deposition to ~1000 years. The preceding HRTD interval-6 (~8.5 cal ka BP; Fig. 5.2A) is most prominent within Lake Umutekai, which preserves tephra layers not recognised/preserved within the rest of the tephra records (i.e., U-78 to U-87, ~9-9.4 cal ka BP; Damaschke et al. 2017a).

The HRTD interval-7 (~10.5 cal ka BP; Fig. 5.2A) is noted within most records, except Tariki Swamp (section of disturbed sediment) and Lake Rotokare (too short). A tephra deposition rate of up to 0.02 units per year is recorded for this interval. The HRTD interval-8 (~12.5 cal ka BP; Fig. 5.2A) appears to be time-transgressive (e.g., Tariki Swamp vs. Ngaere Swamp). This probably results from large age errors, because a distinct geochemical fingerprint of this tephra sequence suggests that this interval is correlatable between sites. The HRTD interval-8 is separated from HRTD interval-9 (~15 cal ka BP) by a period of non-tephra deposition lasting >500 years (H; Fig. 5.2B).

The HRTD intervals-9 and -10 (~17 cal ka BP) are only documented within the Tariki Swamp tephra record, because none of the other sequences cover this time interval in detail.

It is clear from these data that multiple tephra records can help to reveal a more robust and complete eruption frequency from a volcano. Site-specific gaps, overlaps and/or offsets in the rate of tephra deposition can be recognised between locations. However, it must be remembered, that, although this NE-SE sampling arc is downwind for the prevailing winds, it does only cover about 120^{o} around the eastern side of volcano and is likely missing eruptive events dispersed to the unfavourable upwind direction to the south and west, as well as, effusive events with minor or no associated falls. Hence, the frequency data are, at this stage, an underrepresentation and any synthesis of them only a best-estimate of reality. A number of different methods of combining multiple eruption deposits and sequences into a single record of eruption events are described below.

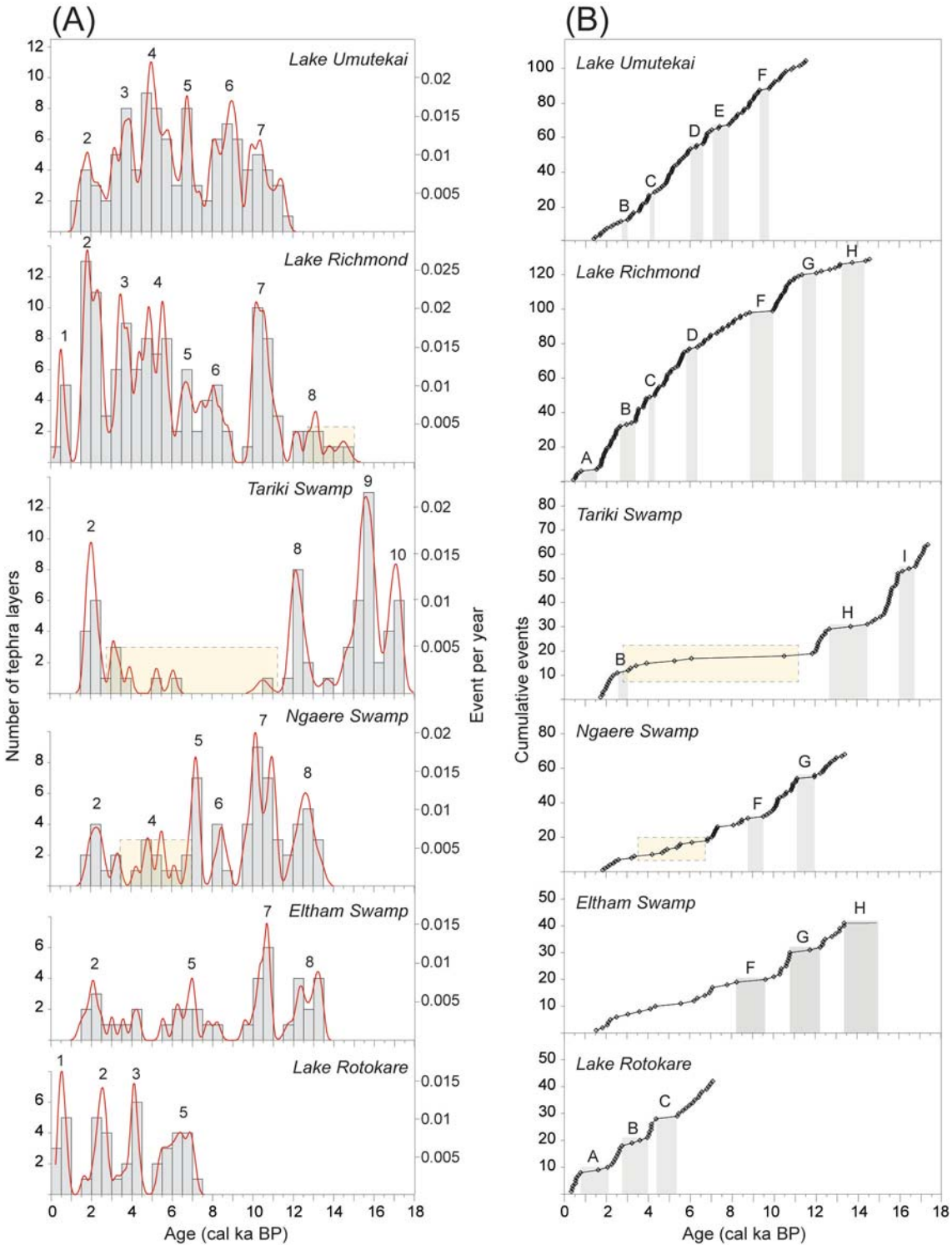

Figure 5. 2 *(A) The rates of deposition of tephras within lake and peat sequences recovered from six different localities at Mt. Taranaki (age data from Damaschke et al. 2017a) presented as histograms of tephras deposited over 500 year intervals (left axis, grey columns), and annual tephra deposition rates generated using a Gaussian kernel*

smoother (Silverman 1984, 1986; Wand and Jones 1994, 1995) with a 100-year bandwidth (right axis, red line). Numbers indicate intervals during which particularly high rates of tephra deposition occurred. (B) Cumulative deposition of the same tephra units. Letters indicate periods of low rates of tephra deposition and/or no deposition. Yellow coloured fields represent disturbed or oxidised/dried sediment horizons.

5.2.3.2 Merged records

A first-order composite stratigraphic record can be created by conventional manual matching of core segments based on visual properties of units or sets of units, ideally between the most continuous tephra deposition horizons from each site. This is reinforced by recognising some temporally and geochemically distinct tephra groups that can be correlated to each other. A manually-merged composite record for Mt. Taranaki constructed in this way (Damaschke et al. 2017a) comprises ~228 tephra layers spanning the last 30 cal ka BP. The quality of this eruption record varies over the entire period, with the older part particularly compromised by a break in deposition within the core that covers it (e.g., Eltham Swamp). As a first-order estimate of eruption frequency, the manually-merged composite tephra record is thus most reliable only in the post-17.5 cal ka BP part. This record includes ~189 tephra layers yielding a crude estimated average interval between ash-falls of 92 years (0.011 tephra deposition events per year, Fig. 5.3A).

A second means of matching tephra sequences between sites involves a statistical matching procedure (Green et al. 2014). This uses a matching algorithm based on interpolated age determinations of tephra layers at each site, with the stratigraphic-order constrained. Other factors, such as geochemistry, can be used to force or prohibit specific tephra matches, which has consequences for any correlations made for units stratigraphically above or below the geochemically-matched units. Details of these constraints are further described below. For Mt. Taranaki, the resulting statistically-combined record comprises ~272 tephra layers spanning the last 30 cal ka BP and ~231 tephra layers within the continuous sequences younger than 17.5 cal ka BP (Fig. 5.3B).

The latter implies an average ash-fall frequency of one event per 75 years (0.013 tephra deposition events per year).

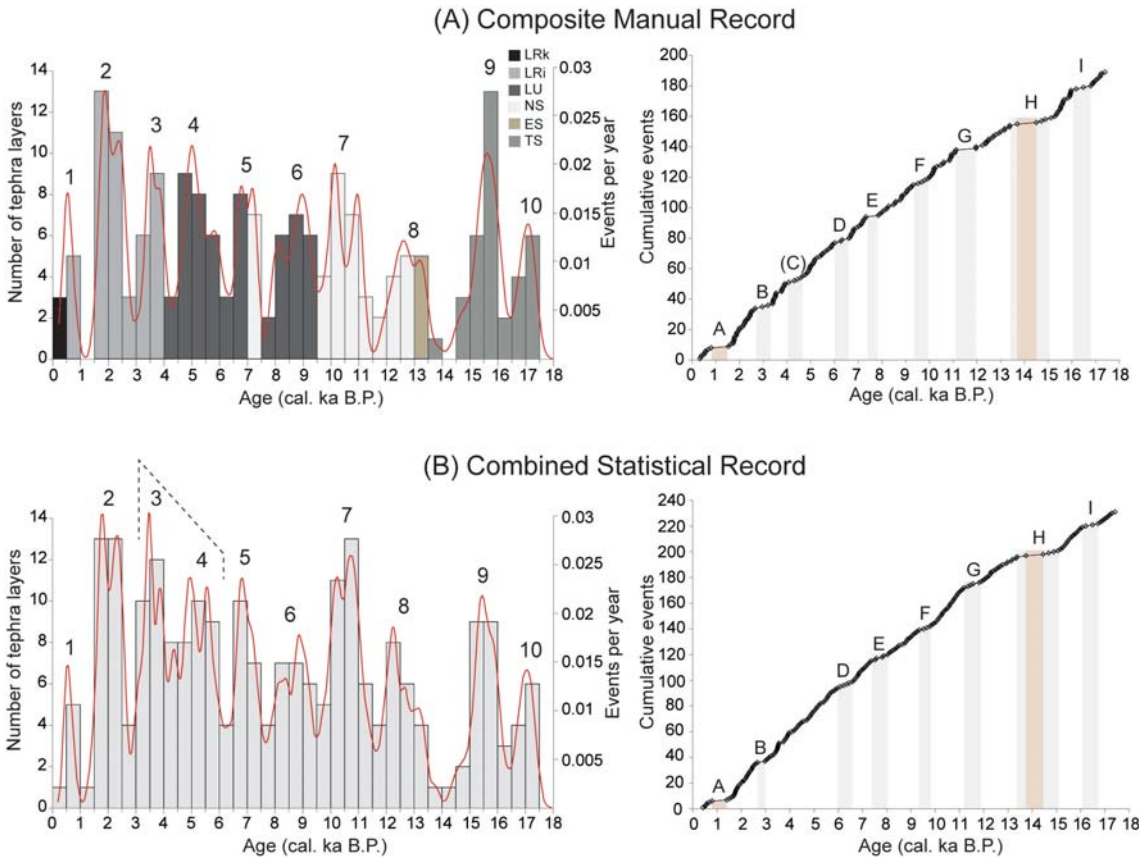

Figure 5. 3 *Variation in the deposition rate of tephra layers across all sites analysed presented as histograms of tephras deposited over 500 year intervals (left axis, columns), and annual tephra deposition rates generated using a Gaussian kernel smoother (Silverman 1984, 1986; Wand and Jones 1994) with a 100-year bandwidth (right axis, red line). Cumulative deposition rates are also shown. Two different matching models are presented: (A) A manually-merged composite record with conservative traditional stratigraphic matching, based on tephra appearance (individual and patterns) and geochemical matches; and (B) a statistically-combined record developed using a matching algorithm (following the approach of Green et al. 2014). Numbers indicate periods of high rates of tephra deposition and letters indicate periods where tephra deposition rates were low including two quiescence periods (A and H; marked as red-shaded fields) (refer to text). Note: HRTD intervals-3 and -4 may*

indicate one long-lasting high-frequency interval, since no repose times >200 years are recorded within this particular period (dotted line). LRk = Lake Rotokare, LRi = Lake Richmond, LU = Lake Umutekai, NS = Ngaere Swamp, ES = Eltham Swamp, TS = Tariki Swamp.

The composite manual approach provides a conservative estimate of event frequency, because only tephra sequences of single sites are merged, and this mostly avoids the possibility of doubling-up of closely timed events. Where strong winds prevail (common in New Zealand) tephras may be dispersed in very narrow lobes (e.g., Ruapehu 1995 and 1996 eruptions, Cronin et al. 2003; Te Maari eruption 2012; Turner et al. 2014). In such cases, a single site is unlikely to capture a record of all eruptions. A good example of this is documented at ~4.3 cal ka BP where the stratigraphically matched record (based on the Lake Umutekai sequence) misses tephra deposits recorded elsewhere (i.e., Lake Richmond) implying an erroneous long period of low tephra deposition rates (C; Fig. 5.3A), which is not present within the statistically-combined record (Fig. 5.3B).

A preliminary attempt at producing a statistically-combined record in order to cross-check the age determinations was conducted using solely the probability distributions developed for each determined tephra age and associated age error, i.e., without forcing any matches due to similar geochemistry and/or tephra packages. Individual ages were estimated using a piecewise cubic Hermitian interpolating polynomial (Fritsch and Carlson 1980) for each sediment record. The polynomial fitting between dated levels models sedimentation rates, which may vary down-core, and depends both on the intervals between dates and the shape of the function above and below the dated levels. While this is necessarily an approximation, sudden changes in sediment accumulation rates and erosion processes may not be captured in age-depth relationships (Telford et al. 2004; Blaauw 2010). A possible example of this is the temporal offset of HRTD intervals-2 and -3 in the Lake Rotokare record compared to the rest of the frequency records (Figs. 5.2, 5.4). Detailed geochemical analyses of encompassed tephras by Damaschke et al. (2017a) within those particular intervals allowed for their correlation

between sites, and consequently demonstrated that the estimated tephra ages in the Lake Rotokare record were inconsistent with the other records and probably problematic. Hence, at least one of the ^{14}C determinations on which these were based must have been inaccurate. Here it is suggested that these ages are contaminated by an "old carbon effect", by which ancient carbon derived from carbonate sediments from the lake catchments, or other sources, caused a shift in the carbon isotope ratio and thus in the apparent radiocarbon age (e.g., Keaveney and Reimer 2012; Philippsen 2013; Hart 2014). Lake Rotokare is unique amongst the sites studied here in being a landslide-dammed lake within a steep valley set in Tertiary-aged calcareous mudstone and sandstone. Turner (2008) recorded frequent landslide deposition into this lake and the tephra layers are intercalated with the mud-rich landslide debris. Thus, the inaccurate chronology for the Lake Rotokare record means that in cannot be used in the statistical matching process. The Rotokare dates could be included after detailed in-core correlation adjustments, but given the observed haphazard nature of the offsets, this would require the addition of further correlative cores beyond those used in this study. Hence, the entire Lake Rotokare record was excluded from further statistical matching procedures below.

Another example, which may have an impact on subsequent statistical merging procedures, is that of a highly variable background sedimentation regime, such as occurs around some horizons within the Tariki Swamp record (Fig. 5.2). Tariki Swamp sediments contain thick silt loams in which tephra deposits are diffuse and reworked (Damaschke et al. 2017a), thus accurate age determinations are problematic. Such poor age estimates within these horizons produce a degree of randomness in the record that adds a source of 'noise' to the matching procedure. For this reason, the affected parts of the Tariki Swamp record (e.g., 3 – 12 cal ka BP) were also excluded from further statistical matching.

The results from the preliminary statistical run demonstrated the need for additional (geochemical) constraints on the statistical matching procedure (cf., Turner et al. 2009; Green et al. 2014) to derive the best possible solution. These constraints can work either way; tephras with incompatible compositions will not be allowed to match, and tephras

that, for observational reasons, are considered a certain correlation (Damaschke et al. 2017a; Table 5.1), will be matched regardless of the age distributions. Geochemical fingerprinting (i.e., chemical constraints) frequently involve the analysis of minerals and glasses, however, at mafic to intermediate composition volcanoes, unique compositions are rarely produced and hence sufficient discrimination between single tephra deposits within continuous tephra sequences is almost impossible. Therefore, only a few geochemically fixed points (Table 5.1) were applied to the records presented. In addition, a number of tephra deposits could not be constrained by their compositions, since these did not provide enough material for subsequent geochemical analysis. Re-running the matching algorithm after applying the constraints discussed above produced a solution that is currently considered to represent the most reliable eruption record of Mt. Taranaki (Fig. 5.3B).

Although the manual and statistical merged eruption records vary slightly in detail, they show a similar pattern of cyclic variation in the eruption frequency over time (Fig. 5.3A, B). Cyclicity was also recognised in earlier studies by Turner et al. (2008, 2009, 2011b). The current data indicates ten periods of high tephra deposition/eruption frequency, each lasting ~1000-1500 years. These are separated by eight periods of low eruption frequency, including two intervals of >500 years with no tephra deposition (A and H, ~1 cal ka BP and ~14 cal ka BP, respectively; Fig. 5.3A, B), which may indicate two significant quiescence periods at Mt. Taranaki. Further, it appears that the two HRTD intervals-3 and -4 (from 6 to 3 cal ka BP) point to a single continuous high-activity period, since no >200 yr repose intervals occur (Fig. 5.3B). Over this 3000 year HRTD interval there is an average ash-fall frequency of one event per 52 years (0.019 events per year).

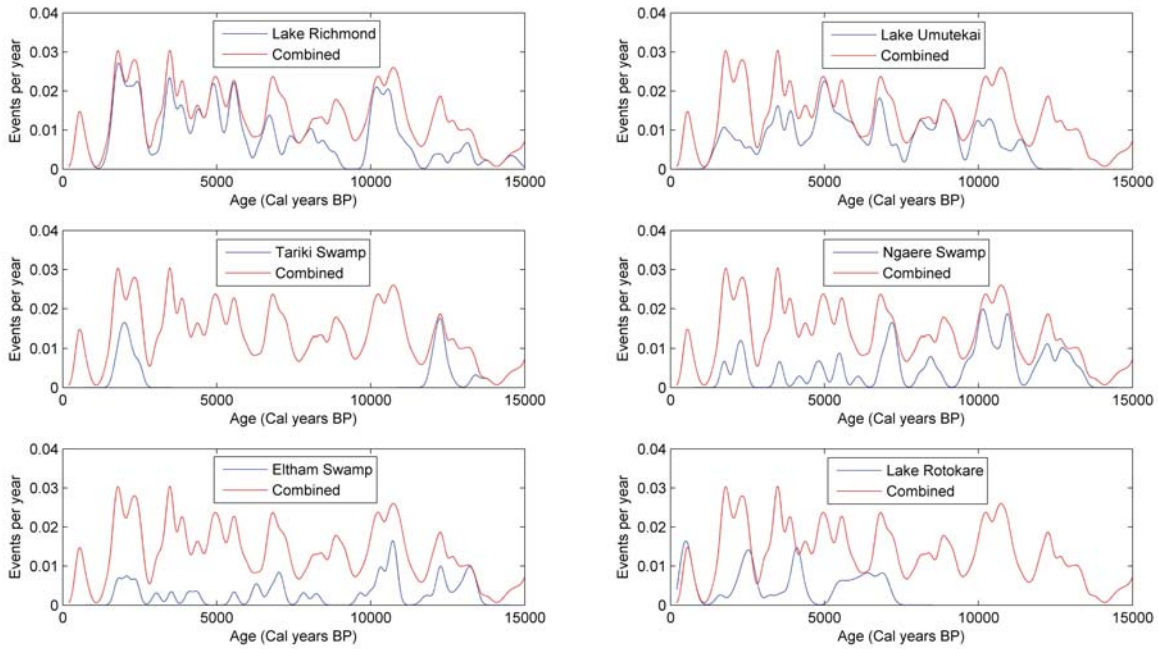

Figure 5. 4 *Annual tephra deposition rates of each single record in comparison with the statistically-combined record. Rates are generated using a Gaussian kernel smoother (Silverman 1984, 1986; Wand and Jones 1994) with a 100-year bandwidth. Note the offset of the Lake Rotokare events.*

Table 5. 1 *Correlations used in the merging algorithm (c.f., Green et al. 2014). They are based on the physical and geochemical characteristics of the tephras, as well as, on their stratigraphic position and age constraints (implemented by Damaschke et al. 2017a).*

Correlation pairs	Lake Umutekai	Lake Richmond	Tariki Swamp	Ngaere Swamp	Eltham Swamp
1	U-4	Ri-10			
2				N-2	E-1
3				N-6	E-5
4		Ri-26	T-10	N-7	E-6
5	U-20	Ri-40		N-8	E-8
6	U-25	Ri-47			
7	U-34	Ri-60			
8	U-39	Ri-65			
9	U-60	Ri-84			
10				N-42	E-23
11		Ri-113		N-46	
12		Ri-121	T-21	N-57	
13			T-23	N-58	E-32
14			T-29	N-68	E-41

5.2.4 Hazard modelling

5.2.4.1 Temporal models

There are many types of statistical models that can be used to model eruption histories. The simplest approach, used mainly when little data are available is a Poisson process (Wickman 1966; De la Cruz-Reyna 1991), where repose-intervals are described by an exponential (memory-less) distribution. Hence the rate of volcanic eruptions $\lambda(t)$ is a constant λ independent of time t. The probability of an eruption onset occurring in a short time interval $(t,t+\Delta)$ is approximately $\lambda\Delta$, and thus λ can be thought of as the instantaneous rate of occurrence.

A memory-less repose assumption does not fit when repose intervals are more complex and variable over time (Wickman 1966; Bebbington and Lai 1996a). Hence, Bebbington and Lai (1996a) introduced the Weibull renewal model. A renewal process depends on the inter-event time τ, rather than on the absolute time t. The inter-event times are independent and identically distributed according to a known probability density function $f(\tau)$. Hence, the time to the next event is dependent on the time since the last event (e.g., Reyment 1969; Bebbington and Lai 1996a; Bebbington 2010). The occurrence rate of a renewal process is given by:

$\lambda(t) = \frac{f(t-s)}{1-F(t-s)}$, with $t - s = \tau$ as the elapsed repose time, hence,

$\lambda(\tau) = \frac{f(\tau)}{1-F(\tau)}$,

where the most recent event occurred at time $s < t$, and $f(\tau) = F(\tau)'$ is the renewal density function. Marzocchi and Bebbington (2012) summarised a large number of renewal distribution functions used in volcanology, but that used here is the Weibull distribution, where:

$f(\tau) = \alpha(\beta\tau)^{\alpha-1} \exp[-(\beta\tau)^{\alpha}]$, $\alpha,\beta > 0$,

with α and β being shape and scale parameters, respectively.

If α = 1, the Weibull distribution reduces to an exponential distribution; if α < 1 the model is 'over-dispersed', or shows clustering behaviour; and if α > 1 the model corresponds to a periodic distribution with a mode at $\tau = (1 / \beta)(1 - 1 / \alpha)^{1/\alpha}$. The Weibull renewal process has been successfully fitted to historical eruption data from a large number of volcanoes (e.g., Bebbington and Lai 1996a, 1996b; Cronin et al. 2001; Watt et al. 2007; Dzierma and Wehrmann 2010).

However, when the distribution of inter-event times is bimodal, a mixture of Weibull distributions may be more appropriate (Jiang and Murthy 1995, 1998; Turner et al., 2008):

$$f(\tau) = p\alpha_1\beta_1{}^{\alpha 1}\tau^{\alpha 1-1} \exp[-(\beta_1\tau)^{\alpha 1}] + (1-p)\alpha_2\beta_2{}^{\alpha 2}\tau^{\alpha 2-1} \exp[-(\beta_2\tau)^{\alpha 2}] ,$$

where $0 < p < 1$ is the mixing proportion, and modes are at $\tau = (1 - 1 / \alpha_1)^{1/\alpha 1} / \beta_1$ and $\tau = (1 - 1 / \alpha_2)^{1/\alpha 2} / \beta_2$. Given any density function $f(\tau)$ and underlying inter-event times τ, the parameters can be estimated by maximizing the log-likelihood:

$$\log L(\tau) = [1 - F(\tau^*)] \prod_{i=1}^{n-1} f(\tau_i),$$

where τ* is the elapsed repose time since the last event and $\tau_1,\ldots, \tau_n$ are the inter-event times. Turner et al. (2008) used a Monte Carlo simulation to model uncertainties associated with event ages. To determine the start of the observation period is effectively impossible here, hence, observation is normally assumed to start at the first recorded onset.

The method of moments or least squares are alternative techniques to estimate the parameters of a given distribution (Press et al. 1992; Bebbington and Lai 1996b; Boudt et al. 2011). A more serious issue than the parameter values is that of which distribution

should be used. Distributions with more parameters, if they include a nested simpler model (for example, the exponential distribution contained in the Weibull) will always fit better. However, the more parameters used in any model, the higher the likelihood of overfitting. To evaluate which model best balances this bias-variance trade-off, the Akaike Information Criterion (AIC; Akaike 1977) can be applied, which measures the goodness of fit using:

$$AIC = -2\log L + 2k,$$

where k is the number of parameters and logL is the log-likelihood of the model. The model with the lower AIC value is favoured. Given any two estimated models, a difference of 1.5 – 2 in the AIC value is usually considered as significant (Akaike 1977).

5.2.4.2 Probabilistic eruption forecasting

The three models described above: (1) the exponential, (2) the Weibull renewal, and (3) the mixture of Weibulls renewal, were applied to the final statistically-combined data set obtained in this study to estimate the probability of a future tephra-producing eruption. The Tahurangi eruption, dated by dendrochronology at AD1755, is the last recorded significant tephra fall (Druce 1966). However, the summit dome was emplaced and partly collapsed after this. As estimated by Platz et al. (2012), the last eruption of Mt. Taranaki, thus most likely occurred between AD1785 and AD1820. This age range was incorporated as the last event in the statistical probability modelling below.

The estimated parameters and average log-likelihoods are shown in Table 5.2. Only inter-events from the final statistically-merged record <14.5 cal ka BP were fitted, noting that the older sequence cannot be used since it is only from single sites (i.e., Tariki Swamp). Combining multiple core and single core records would lead to inhomogeneous data. The single-site records would contribute longer intervals, because missing events are not filled in from another record, and hence artificially inflate the

secondary mode. In total, 200 events span the last ~14.5 cal ka BP in the statistical merged record. A Monte Carlo simulation was run with n=100 (i.e., 19,900 sampled inter-event times) to derive the fitted densities shown in Figure 5.5. In a slight update from previous procedures (Turner et al. 2008, 2009), this study used calibrated calendar ages applying OxCal Version 4.2 (Bronk Ramsey 2013) and the Southern Hemisphere SHCal13 atmospheric calibration curve (Hogg et al. 2013).

Table 5. 2 *Fitted parameters and average log-likelihoods for the models tested for both of the last explosive eruptions of Mt. Taranaki at AD1785 and AD1820.*

Model	Last event AD1785				Last event AD1820			
	Parameters	Modes	logL	AIC	Parameters	Modes	logL	AIC
Poisson process	$\lambda = 0.0134$	0	-1046.4	2094.7	$\lambda = 0.0134$	0	-1046.4	2094.7
Weibull renewal process	$\alpha = 0.9901$ $\beta = 0.0136$	0	-1044.1	2092.2	$\alpha = 0.9922$ $\beta = 0.0136$	0	-1043.6	2091.2
Mixture of Weibulls renewal process	$\alpha_1 = 1.1206$ $\beta_1 = 0.0147$ $\alpha_2 = 3.7393$ $\beta_2 = 0.0016$ $p = 0.9819$	9.31 573.70	-1037.8	**2085.5**	$\alpha_1 = 1.1188$ $\beta_1 = 0.0147$ $\alpha_2 = 3.9236$ $\beta_2 = 0.0016$ $p = 0.9834$	9.20 587.00	-1037.4	**2084.7**

Note: AIC = Akaike Information Criterion (Akaike, 1977); logL = log-likelihood

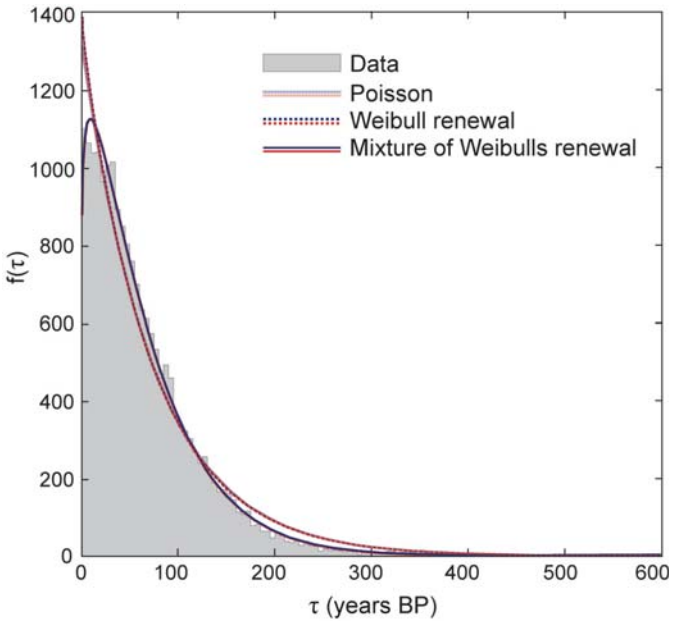

Figure 5. 5 *Histogram of 19,900 sampled inter-event times based on Monte Carlo simulations of the new statistically-merged Mt. Taranaki eruption record. Curves show the different densities fitted for this data set with AD1785 (red) and AD1820 (blue) as last volcanic activity events.*

The best fit for the distribution of modelled inter-event periods was achieved by the mixture of Weibulls model according to the AIC statistic (Table 5.2). The Poisson process is less well suited because event times are systematically variable. The Weibull renewal distribution has $\alpha < 1$ implying clustering behaviour. In this case, α is almost = 1, thus the result is very similar to a simple Poisson process (indicated by dotted and dashed lines almost overlying; Figs. 5.5, 5.6). The mixtures distribution includes a strong primary mode at inter-event times of ~9 years and a secondary mode at inter-event times of ~580 years (Table 5.2). This overall pattern is similar in form to that found in previous studies of Turner et al. (2008, 2009), but with a much more refined outcome indicated by increased α and p values (with p = 1 corresponding to a simple unimodal Weibull distribution; Table 5.2). The primary short repose mode, with a mean repose of ~65 years, accounts now for 98% of interval times compared to 75-96% in previous studies, while the secondary long repose mode reduces to only 2% compared to 25-4% in previous studies. The increase in the long repose interval mode to ~580

years compared to ~165 and ~210 years in previous work (Turner et al. 2008, 2009; Fig. 5.7B) is striking. This implies that activity at Mt. Taranaki is overall more frequent than previously detected, but that the long repose periods represent actual long breaks where tephra-producing eruptions are not occurring, rather than an incomplete explosive-eruption data set.

The probability of no eruption in the next t years, given that the most recent event occurred at T years ago, is:

$$\Pr(\tau > T + t | \tau > T) = \frac{\int_{T+t}^{\infty} f(\tau) d\tau}{\int_{T}^{\infty} f(\tau) d\tau}.$$

Assuming that the last eruption event occurred between AD1785 to AD1820, the probability of an eruption within the next 50 years is 33-42%, based on the best fitting mixture of Weibulls model (Fig. 5.6A). This is significantly different to the results of previous probability models using only two records, which suggested a 52-59% chance of an eruption within the next 50 years (Turner et al. 2009; Fig. 5.7A). Plotting the annual eruption probability progression (Fig. 5.6B), the preferred mixture of Weibulls model indicates that a high-probability peak occurred at approximately AD1900 with an annual eruption probability of ~0.016 (1.6 %) and a low-probability trough is expected in the future around AD2200 with an annual eruption probability of ~0.003 (0.3%). Assuming the most recent eruption was between AD1785 and AD1820 the current annual eruption probability is estimated at 0.01 to 0.013 (1% to 1.3%; Fig. 5.6B). In both scenarios the high-probability peak has just been passed, indicating that the likelihood of a long repose is steadily increasing. As a result we areproceeding towards a low-probability trough, decreasing the probability of a future eruption within the short to medium term future.

These results contrast strongly with previous estimates made by Turner et al. (2009) (Fig. 5.7), who estimated a current annual eruption rate of 0.016 (1.6%) with the trough occurring earlier (i.e., after 210 years in the two core merged record). This subtle difference in the position of the secondary mode of inter-event times (trough), strongly

affects the eruption probability progression of Turner et al. (2008, 2009) compared with the findings in this study (Fig. 5.7B). Turner et al. (2009) used the Lake Rotokare record to fill in potential gaps within the Lake Umutekai record. As revealed in this study, the Lake Rotokare record is strongly, but non-systematically, biased in its age estimates. This led to apparent infill of long intervals, and possibly an over-inflating of the true frequency, and hence the differences in forecast eruption probability detailed above.

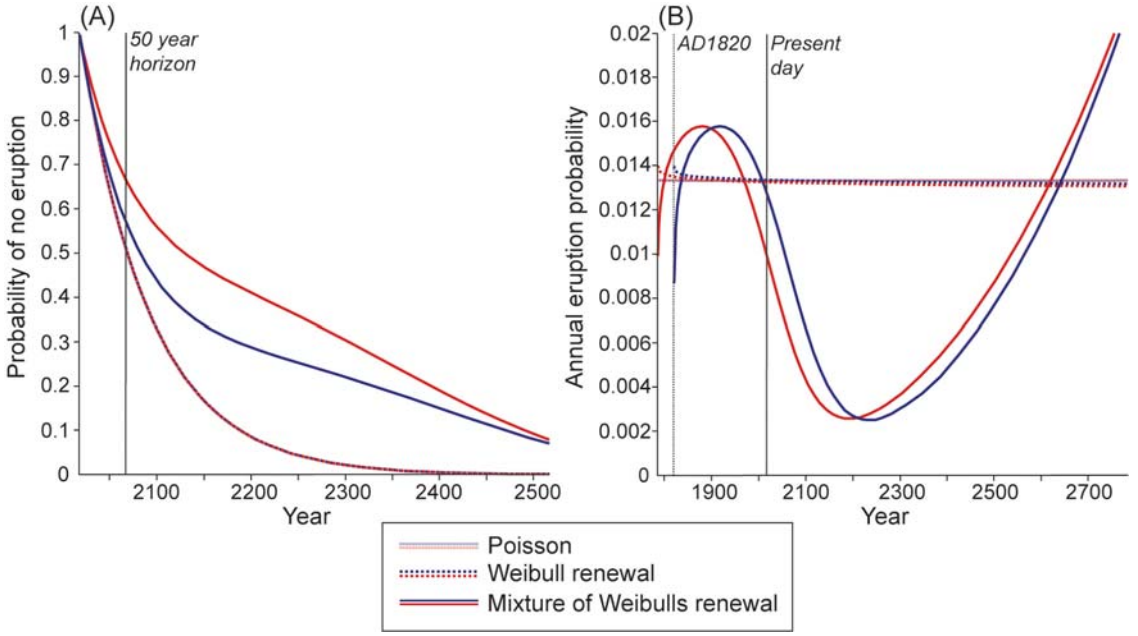

Figure 5. 6 *(A) Probabilities of no eruption of Mt. Taranaki occurring over future time periods, based on three models of inter-event distributions with AD1785 (red) and AD1820 (blue) as last volcanic activity events. (B) Annual eruption probabilities estimated for Mt. Taranaki, assuming the last volcanic activity event was at AD1785 (red) and AD1820 (blue). Note: The Weibull renewal distribution is similar to a simple Poisson process..*

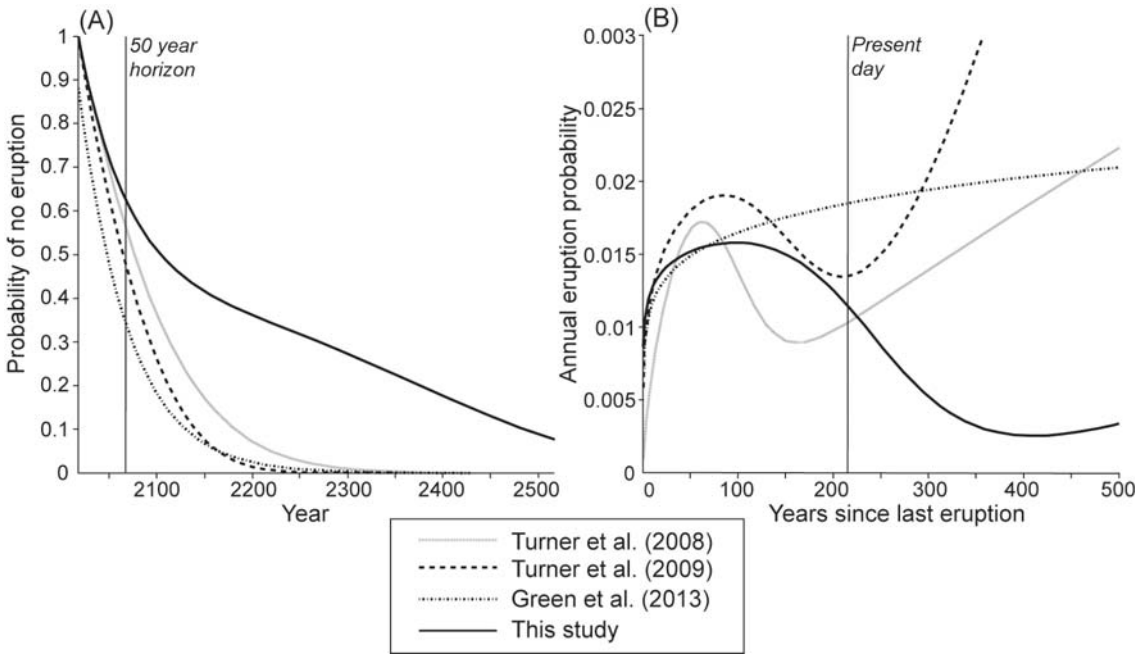

Figure 5. 7 *(A) Probabilities of no eruption at Mt. Taranaki occurring over future time periods, based on the inter-event distribution constructed in each previous paper and for the statistically-combined record built in this study, with AD1800 (compromise date between AD1785 and AD1820) as last volcanic activity events. (B) Annual eruption probabilities of Mt. Taranaki estimated for different records proposed in previous studies and for the statistically-combined record built in this study, assuming the last volcanic activity event was at AD1800..*

5.2.5 Discussion and conclusions

Long and complete chronological eruption records from volcanoes are fundamental to robust probabilistic hazard models. In this case, tephra deposition was used as a proxy for eruptions, although it is clear that this will not capture very small-scale events (with only proximal deposits), nor effusive-only events. Putting this limitation aside, tephra-forming eruptions are the most hazardous to surrounding populations and tracking at least this type of behaviour is a good way of understanding overall volcanic behaviour. To build robust tephra records at any volcano, methods to extend from single-site to multiple-location stratigraphies are needed to capture a range of possible tephra

dispersal directions, variations in eruption sizes/styles, and account for variable tephra preservation and/or depositional issues. Good age determinations for tephras strongly rely upon a stable sedimentation background regime. In this study, one of the sites (Lake Rotokare) was discovered to have a distinctive old-carbon effect within its radiocarbon ages. It was not possible to isolate this in previous two-record combinations (Turner et al. 2009), as it was not possible to conduct the sort of cross-validation performed above (i.e., either record could have been at fault). However, with several new sites in this study, the clear non-conformity of this record with the others was obvious. In other sites, parts of the records are disturbed, but with enough sites to bridge these gaps, a good overall coverage can be achieved through subsequent merging procedures.

It has also been confirmed that incorporating geochemical constraints is far more reliable for indicating incompatible matches, rather than forcing direct match-links, although the latter decrease computation time (for this exercise, on the order of 2-3 days on an Intel i7 3.4GHz desktop) enormously. Hence, a balanced approach in the use of geochemical covariates within the statistical merging procedures is suggested. Distinct titanomagnetite compositional groups for packages of tephras identified in earlier studies (Damaschke et al. 2017a) were useful to inform some correlations, but currently the matching algorithm is not sensitive to the compositional patterns. Additional independent tools are needed to improve the correlation of tephras between multiple sites.

Probabilistic assessments of volcanic recurrence at other volcanic sites have been carried out, but due to the greater difficulties of assembling a complete record at polygenetic volcanoes, many studies have focussed on monogenetic volcanic fields and caldera or rift-zone volcanoes (e.g., Yucca Mountain region, Conner and Hill 1995; Ho and Smith 1997, 1998; Conner et al. 2000; Springerville volcanic field, Arizona, Condit and Connor 1996; Taveuni volcano, Fiji, Cronin et al. 2001; Auckland volcanic field, Molloy et al. 2009; Bebbington and Cronin 2011). These tend to have far more erratic temporal variation compared to long-lived subduction-related stratovolcanoes, where periods of high-frequency activity have been conjectured to alternate with atypical

longer periods of quiescence (Wadge 1982). Further, many studies have been made using short (c. 200-400 year) eruption records at individual volcanoes, a number of which have been shown to exhibit cyclic patterns on the order of decades to centuries (Bebbington 2010). A singular example of a longer, relatively complete record, is Mt. Vesuvius (Scandone et al. 1993), which appears to have a well-defined eruption cycle, where each cycle is initiated by a large (sub-Plinian to Plinian) eruption, similar to the behaviour of Mt. Taranaki postulated by Turner et al. (2011b).

According to this study, Mt. Taranaki exhibits strong cyclic patterns in event frequency, with an apparent long secondary mode in the repose time distribution, which may have implications for its magmatic system. Those longer inter-event intervals may correspond to longer feeding pulses of magma (replenishment) between bursts of activity (Turner et al. 2011b) and/or may be associated with distinct tectonic regime processes, such as changes in the regional crustal stress triggering magma movement into the crust (cf., Walter et al. 2007; Watt et al. 2009; Caricchi et al. 2014). Regular gravitational loading and unloading of the volcano due to regular collapse and re-growth cycles (seen at Mt. Taranaki; Zernack et al. 2012) modifies the stress-field at depth and could suppress or enhance magma ascent rates and/or dyke propagation (e.g., Pinel and Jaupart 2000; Muller et al. 2001; McGovern et al. 2013). Suppression phases could lead to periods of low-activity and be terminated due to unloading of the volcano by large debris avalanche events (Manconi et al. 2009; Pinel and Albino 2013). At Mt. Taranaki two major debris avalanches are reported during the time frame investigated in this study (e.g., ~14 cal ka BP Motumate debris avalanche, and ~7.5 cal ka BP Opua debris avalanche; Zernack et al. 2011). It is unclear if the earlier load/collapse cycle had any influence because it is at the beginning of the robust combined record. The window of the 7.5 cal ka BP terminating growth/collapse cycle is, however, captured in the new record, but clear pre/post-collapse variability is not immediately obvious because shorter-period variability seems to dominate.

To fit the long tailed/bimodal inter-event distributions recorded here, the mixture of Weibulls renewal model was proven to be the most suitable fit. An estimate of 33-42% probability of an eruption occurring within the next 50 years was made. This is a

reduction in the estimated probability of an eruption in the near future compared to previous work. There is now stronger evidence that we are in a 'long' repose, which are now less frequent, but longer, than previously supposed. The apparent cyclicity proposed in previous studies is traceable throughout the new record, but there seem to appear periods within the usual variability, particularly 3 to 6 cal ka BP, where there are no repose times >200 years, and hence the distinction between peak and trough is slightly blurred.

These findings reinforce the importance of complete and accurate data sets, which are highly desirable for subsequent merging procedures and, thus, accurate and realistic eruption probability forecasts. If this can be implemented at any such 're-awakening' volcano like that of Mt. Taranaki, more reliable hazard assessments can be made.

5.2.6 Acknowledgements

MD acknowledges the support of a Massey University Doctoral Scholarship, and a Auckland University supplementary scholarship. MD also would like to thank Prof Clel Wallace (Massey University) for thorough review of this manuscript. SJC and MB are supported by the NZ Natural Hazards Research Platform project, "Quantifying exposure to specific and multiple volcanic hazards".

5.2.7 References

Akaike, H. (1977). An extension of the method of maximum likelihood and the Stein's problem. Annals of the Institute of Statistical Mathematics, 29(1), 153-164.

Alloway, B., Neall, V. E., & Vucetich, C. G. (1995). Late Quaternary (post 28,000 year BP) tephrostratigraphy of northeast and central Taranaki, New Zealand. Journal of the Royal Society of New Zealand, 25(4), 385-458.

Alloway, B., McComb, P., Neall, V., Vucetich, C., Gibb, J., Sherburn, S., & Stirling, M. (2005). Stratigraphy, age, and correlation of voluminous debris-avalanche events from an ancestral Egmont Volcano: implications for coastal plain construction and regional hazard assessment. Journal of the Royal Society of New Zealand, 35(1-2), 229-267.

Andreastuti, S. D., Alloway, B. V., & Smith, I. E. M. (2000). A detailed tephrostratigraphic framework at Merapi Volcano, Central Java, Indonesia: implications for eruption predictions and hazard assessment. Journal of Volcanology and Geothermal Research, 100(1), 51-67.

Bebbington, M. S. (2010). Trends and clustering in the onsets of volcanic eruptions. Journal of Geophysical Research: Solid Earth, 115(B1).

Bebbington, M. S., & Lai, C. D. (1996a). On nonhomogeneous models for volcanic eruptions. Mathematical Geology, 28(5), 585-600.

Bebbington, M. S., & Lai, C. D. (1996b). Statistical analysis of New Zealand volcanic occurrence data. Journal of Volcanology and Geothermal Research, 74(1), 101-110.

Bebbington, M. S., & Cronin, S. J. (2011). Spatio-temporal hazard estimation in the Auckland Volcanic Field, New Zealand, with a new event-order model. Bulletin of Volcanology, 73(1), 55-72.

Blaauw, M. (2010). Methods and code for 'classical'age-modelling of radiocarbon sequences. Quaternary Geochronology, 5(5), 512-518.

Boudt, K., Caliskan, D., & Croux, C. (2011). Robust explicit estimators of Weibull parameters. Metrika, 73(2), 187-209.

Bronk Ramsey, C. (2013). OxCal 4.2. Web Interface Build (78).

Bursik, M. (1998). Tephra dispersal. Geological Society, London, Special Publications, 145(1), 115-144.

Carey, S., & Sparks, R. S. J. (1986). Quantitative models of the fallout and dispersal of tephra from volcanic eruption columns. Bulletin of Volcanology, 48(2-3), 109-125.

Caricchi, L., Annen, C., Blundy, J., Simpson, G., & Pinel, V. (2014). Frequency and magnitude of volcanic eruptions controlled by magma injection and buoyancy. Nature Geoscience, 7(2), 126-130.

Condit, C. D., & Connor, C. B. (1996). Recurrence rates of volcanism in basaltic volcanic fields: An example from the Springerville volcanic field, Arizona. Geological Society of America Bulletin, 108(10), 1225-1241.

Connor, C. B., & Hill, B. E. (1995). Three nonhomogeneous Poisson models for the probability of basaltic volcanism: application to the Yucca Mountain region, Nevada. Journal of Geophysical Research: Solid Earth, 100(B6), 10107-10125.

Connor, C. B., Stamatakos, J. A., Ferrill, D. A., Hill, B. E., Ofoegbu, G. I., Conway, F. M., Sagar, B., & Trapp, J. (2000). Geologic factors controlling patterns of small-volume basaltic volcanism: Application to a volcanic hazards assessment at Yucca Mountain, Nevada. Journal of Geophysical Research: Solid Earth, 105(B1), 417-432.

Cronin, S. J., Neall, V. E., Stewart, R. B., & Palmer, A. S. (1996). A multiple-parameter approach to andesitic tephra correlation, Ruapehu volcano, New Zealand. Journal of Volcanology and Geothermal Research, 72(3), 199-215.

Cronin, S. J., Bebbington, M., & Lai, C. (2001). A probabilistic assessment of eruption recurrence on Taveuni volcano, Fiji. Bulletin of Volcanology, 63(4), 274-288.

Cronin, S. J., Neall, V. E., Lecointre, J. A., Hedley, M. J., & Loganathan, P. (2003). Environmental hazards of fluoride in volcanic ash: a case study from Ruapehu volcano, New Zealand. Journal of Volcanology and Geothermal Research, 121(3), 271-291.

Damaschke, M., Cronin, S. J., Holt, K. A., Bebbington, M. S., & Hogg, A. G. (2017a). A 30,000 yr high-precision eruption history for the andesitic Mt. Taranaki, North Island, New Zealand. Quaternary Research, 1-23. DOI:10.1017/qua.2016.11

Damaschke, M., Cronin, S. J., Torres-Orozco, R., Wallace, R. C. (2017b). Unifying tephrostratigraphic approaches to redefine major Holocene marker tephras, Mt. Taranaki, New Zealand. Journal of Volcanology and Geothermal Research, doi:10.1016/j.jvolgeores.2017.02.021.

Dartevelle, S., Ernst, G. G., Stix, J., & Bernard, A. (2002). Origin of the Mount Pinatubo climactic eruption cloud: Implications for volcanic hazards and atmospheric impacts. Geology, 30(7), 663-666.

De la Cruz-Reyna, S. (1991). Poisson-distributed patterns of explosive eruptive activity. Bulletin of Volcanology, 54(1), 57-67.

Donoghue, S. L., Vallance, J., Smith, I. E., & Stewart, R. B. (2007). Using geochemistry as a tool for correlating proximal andesitic tephra: case studies from Mt Rainier (USA) and Mt Ruapehu (New Zealand). Journal of Quaternary Science, 22(4), 395-410.

Druce, A. P. (1966). Tree-ring dating of recent volcanic ash and lapilli, Mt Egmont. New Zealand Journal of Botany, 4(1), 3-41.

Dzierma, Y., & Wehrmann, H. (2010). Eruption time series statistically examined: Probabilities of future eruptions at Villarrica and Llaima Volcanoes, Southern Volcanic Zone, Chile. Journal of Volcanology and Geothermal Research, 193(1), 82-92.

Fritsch, F. N., & Carlson, R. E. (1980). Monotone piecewise cubic interpolation. SIAM Journal on Numerical Analysis, 17(2), 238-246.

Gaillard, J. (2006). Traditional societies in the face of natural hazards: the 1991 Mt. Pinatubo eruption and the Aetas of the Philippines. International Journal of Mass Emergencies and Disasters, 24(1), 5.

Green, R. M., Bebbington, M. S., Cronin, S. J., & Jones, G. (2014). Automated statistical matching of multiple tephra records exemplified using five long maar

sequences younger than 75ka, Auckland, New Zealand. Quaternary Research, 82(2), 405-419.

Hart, J. P. (2014). A model for calculating freshwater reservoir offsets on AMS-dated charred, encrusted cooking residues formed from varying resources. Radiocarbon, 56(3), 981-9.

Ho, C. H., & Smith, E. I. (1997). Volcanic hazard assessment incorporating expert knowledge: application to the Yucca Mountain region, Nevada, USA. Mathematical Geology, 29(5), 615-627.

Ho, C. H., & Smith, E. I. (1998). A spatial-temporal/3-D model for volcanic hazard assessment: application to the Yucca Mountain region, Nevada. Mathematical Geology, 30(5), 497-510.

Hogg, A. G., Hua, Q., Blackwell, P. G., Niu, M., Buck, C. E., Guilderson, T. P., Heaton, T. J., Palmer, J. G., Reimer, P. J., Reimer, R. W., Turney, C. S. M., & Zimmerman, S. R. H. (2013). SHCal13 Southern Hemisphere calibration, 0-50,000 years cal BP. Radiocarbon 55, 1889-1903.

Jiang, R., & Murthy, D. N. P. (1995). Reliability modeling involving two Weibull distributions. Reliability Engineering & System Safety, 47(3), 187-198.

Jiang, R., & Murthy, D. N. P. (1998). Mixture of Weibull distributions—parametric characterization of failure rate function. Applied Stochastic Models and Data Analysis, 14(1), 47-65.

Johnston, D. M., Houghton, B. F., Neall, V. E., Ronan, K. R., & Paton, D. (2000). Impacts of the 1945 and 1995–1996 Ruapehu eruptions, New Zealand: an example of increasing societal vulnerability. Geological Society of America Bulletin, 112(5), 720-726.

Keaveney, E. M., & Reimer, P. J. (2012). Understanding the variability in freshwater radiocarbon reservoir offsets: a cautionary tale. Journal of Archaeological Science, 39(5), 1306-1316.

Lowe, D. J. (1988). Stratigraphy, age, composition, and correlation of late Quaternary tephras interbedded with organic sediments in Waikato lakes, North Island, New Zealand. New Zealand Journal of Geology and Geophysics, 31(2), 125-165.

Manconi, A., Longpré, M. A., Walter, T. R., Troll, V. R., & Hansteen, T. H. (2009). The effects of flank collapses on volcano plumbing systems. Geology, 37(12), 1099-1102.

Marzocchi, W., & Zaccarelli, L. (2006). A quantitative model for the time-size distribution of eruptions. Journal of Geophysical Research: Solid Earth, 111(B4).

Marzocchi, W., & Bebbington, M. S. (2012). Probabilistic eruption forecasting at short and long time scales. Bulletin of Volcanology, 74(8), 1777-1805.

McGovern, P. J., Rumpf, M. E., & Zimbelman, J. R. (2013). The influence of lithospheric flexure on magma ascent at large volcanoes on Venus. Journal of Geophysical Research: Planets, 118(11), 2423-2437.

Melnik, O., & Sparks, R. S. J. (1999). Nonlinear dynamics of lava dome extrusion. Nature, 402(6757), 37-41.

Miyaji, N. (1988). History of younger Fuji volcano. Journal of the Geological Society of Japan, 94(6), 433-452.

Molloy, C., Shane, P., & Augustinus, P. (2009). Eruption recurrence rates in a basaltic volcanic field based on tephra layers in maar sediments: implications for hazards in the Auckland volcanic field. Geological Society of America Bulletin, 121(11-12), 1666-1677.

Muller, J. R., Ito, G., & Martel, S. J. (2001). Effects of volcano loading on dike propagation in an elastic half-space. Journal of Geophysical Research: Solid Earth, 106(B6), 11101-11113.

Philippsen, B. (2013). The freshwater reservoir effect in radiocarbon dating. Heritage Science, 1(1), 1.

Pinel, V., & Jaupart, C. (2000). The effect of edifice load on magma ascent beneath a volcano. Philosophical Transactions of the Royal Society of London A: Mathematical, Physical and Engineering Sciences, 358(1770), 1515-1532.

Pinel, V., & Albino, F. (2013). Consequences of volcano sector collapse on magmatic storage zones: Insights from numerical modeling. Journal of Volcanology and Geothermal Research, 252, 29-37.

Platz, T., Cronin, S. J., Procter, J. N., Neall, V. E., & Foley, S. F. (2012). Non-explosive, dome-forming eruptions at Mt. Taranaki, New Zealand. Geomorphology, 136(1), 15-30.

Press, W. H., Teukolsky, S. A., Vetterling, W. T., & Flannery, B. P. (1992). Numerical Recipies in C.

Reyment, R. A. (1969). Statistical analysis of some volcanologic data regarded as series of point events. Pure and Applied Geophysics, 74(1), 57-77.

Scandone, R., Giacomelli, L., & Gasparini, P. (1993). Mount Vesuvius: 2000 years of volcanological observations. Journal of Volcanology and Geothermal Research, 58(1), 5-25.

Self, S., & Rampino, M. R. (1981). The 1883 eruption of Krakatau. Nature, 294, 699-704.

Shane, P. (2005). Towards a comprehensive distal andesitic tephrostratigraphic framework for New Zealand based on eruptions from Egmont volcano. Journal of Quaternary Science, 20(1), 45-57.

Silverman, B. W. (1984). Spline smoothing: the equivalent variable kernel method. The Annals of Statistics, 898-916.

Silverman, B. W. (1986). Density Estimation for Statistics and Data Analysis (Vol. 26). CRC press.

Small, C., & Naumann, T. (2001). The global distribution of human population and recent volcanism. Global Environmental Change Part B: Environmental Hazards, 3(3), 93-109.

Tanguy, J. C. (1994). The 1902–1905 eruptions of Montagne Pelée, Martinique: anatomy and retrospection. Journal of Volcanology and Geothermal Research, 60(2), 87-107.

Telford, R. J., Heegaard, E., & Birks, H. J. B. (2004). All age–depth models are wrong: but how badly? Quaternary Science Reviews, 23(1), 1-5.

Torres-Orozco, R., Cronin, S. J., Pardo, N., & Palmer, A. S. (2017). New insights into Holocene eruption episodes from proximal deposit sequences at Mt. Taranaki (Egmont), New Zealand. Bulletin of Volcanology, 79(1), 3.

Turner, M. B. (2008). Eruption cycles and magmatic processes at a reawakening volcano, Mt. Taranaki, New Zealand. Unpublished PhD Thesis, INR, Massey University, New Zealand.

Turner, M. B., Cronin, S. J., Bebbington, M. S., & Platz, T. (2008). Developing probabilistic eruption forecasts for dormant volcanoes: a case study from Mt Taranaki, New Zealand. Bulletin of Volcanology, 70(4), 507-515.

Turner, M. B., Bebbington, M. S., Cronin, S. J., & Stewart, R. B. (2009). Merging eruption datasets: building an integrated Holocene eruptive record for Mt Taranaki, New Zealand. Bulletin of Volcanology, 71(8), 903-918.

Turner, M. B., Cronin, S. J., Bebbington, M. S., Smith, I. E., & Stewart, R. B. (2011a). Integrating records of explosive and effusive activity from proximal and distal sequences: Mt. Taranaki, New Zealand. Quaternary International, 246(1), 364-373.

Turner, M. B., Cronin, S. J., Bebbington, M. S., Smith, I. E., & Stewart, R. B. (2011b). Relating magma composition to eruption variability at andesitic volcanoes: A case study from Mount Taranaki, New Zealand. Geological Society of America Bulletin, 123(9-10), 2005-2015.

Turner, R., Moore, S., Pardo, N., Kereszturi, G., Uddstrom, M., Hurst, T., & Cronin, S. (2014). The use of Numerical Weather Prediction and a Lagrangian transport (NAME-III) and dispersion (ASHFALL) models to explain patterns of observed ash deposition and dispersion following the August 2012 Te Maari, New Zealand eruption. Journal of Volcanology and Geothermal Research, 286, 437-451.

Wadge, G. (1982). Steady state volcanism: evidence from eruption histories of polygenetic volcanoes. Journal of Geophysical Research: Solid Earth, 87(B5), 4035-4049.

Walter, T. R., Wang, R., Zimmer, M., Grosser, H., Lühr, B., & Ratdomopurbo, A. (2007). Volcanic activity influenced by tectonic earthquakes: static and dynamic stress triggering at Mt. Merapi. Geophysical Research Letters, 34(5).

Wand, M. P., & Jones, M. C. (1994). Kernel smoothing. CRC Press.

Watt, S. F. L., Mather, T. A., & Pyle, D. M. (2007). Vulcanian explosion cycles: Patterns and predictability. Geology, 35(9), 839-842.

Watt, S. F., Pyle, D. M., & Mather, T. A. (2009). The influence of great earthquakes on volcanic eruption rate along the Chilean subduction zone. Earth and Planetary Science Letters, 277(3), 399-407.

Wickman, F. E. (1966). Repose period patterns of volcanoes. I. Volcanic eruptions regarded as random phenomena. Arkiv for Mineralogi och Geologi, 4(4), 291.

Woods, A. W. (1995). The dynamics of explosive volcanic eruptions. Reviews of geophysics, 33(4), 495-530.

Zernack, A. V., Procter, J. N., & Cronin, S. J. (2009). Sedimentary signatures of cyclic growth and destruction of stratovolcanoes: a case study from Mt. Taranaki, New Zealand. Sedimentary Geology, 220(3), 288-305.

Zernack, A. V., Cronin, S. J., Neall, V. E., & Procter, J. N. (2011). A medial to distal volcaniclastic record of an andesite stratovolcano: detailed stratigraphy of the ring-plain succession of south-west Taranaki, New Zealand. International Journal of Earth Sciences, 100(8), 1937-1966.

Zernack, A. V., Cronin, S. J., Bebbington, M. S., Price, R. C., Smith, I. E., Stewart, R. B., & Procter, J. N. (2012). Forecasting catastrophic stratovolcano collapse: A model based on Mount Taranaki, New Zealand. Geology, 40(11), 983-986.

Chapter 6

Geochemical variation of tephras from Mt. Taranaki, New Zealand: Implications for magma evolution

This chapter aims to explore the geochemical variations recognised within a series of tephras within lake and peatland sequences, using these to provide a window into time-varying magma evolution. Titanomagnetite variations indicate gradual changes in a deep crustal magma feeding system, overprinted by periodic variations that are the basis of chemostratigraphy. Intense microlite crystallisation shortly prior to eruption has greatly impacted on glass compositions. Additional whole-lapilli major and trace element analyses highlight possible magma stratification within the conduit.

6.1 Chapter synopsis

In the previous chapters, titanomagnetite compositions were shown to be the most useful tool for andesitic tephra discrimination and correlations at the Mt. Taranaki andesitic stratovolcanoes. The Mt. Taranaki titanomagnetites have distinct compositional signatures that were used to define twelve individual compositional groups on the basis of varying TiO_2, Al_2O_3, MgO, and FeO concentrations (Chapter 3; Damaschke et al., 2017a). Most of these titanomagnetite groups fall into specific, temporally-constrained, tephra sequences within the sediments that were collected: Tephra Sequence A (0.5 – 3 cal ka BP) dominated by group-11 and -12 titanomagnetites, B (3 – 4 cal ka BP) dominated by group-10 titanomagnetites, C (4 – 9.5 cal ka BP) dominated by group-8 and -3 titanomagnetites, D (9.5 – 14 cal ka BP)

dominated by group-2 titanomagnetites, E (14 – 17.5 cal ka BP) dominated by group-1 titanomagnetites, and F (23.5 – 30 cal ka BP) dominated by group-1 titanomagnetites (see also Table 4.3). In this chapter, the relationship of this time-varying compositional pattern to the underlying magmatic system is investigated, with additional information from glass and whole-lapilli chemistry, to investigate andesitic magma generation, storage and evolution at Mt. Taranaki.

6.2 Introduction

The application of distal tephra deposits to understanding magmatic systems is an interesting extension from conventional petrological and whole-rock geochemical studies, because tephra sequences add a high-resolution temporal perspective. Direct comparison of tephra records to on-volcano studies needs care, however, due to the lack of sufficient material available for whole-rock analyses, or possible risks of distal tephra being contaminated with xenogeneic material. It is known that the atmospheric sorting of particles of different density and aerodynamics (i.e., different minerals, vs. glass shards or platy minerals such as biotite) may divert bulk sample compositions away from that of an average erupted magma (Spark et al., 1992; Braitseva et al., 1997). Furthermore, tephra-producing phases within an eruption may only be a short-lived part of a whole eruptive episode and involve magma evolved to different volatile and whole-rock composition compared to effusive phases (Shane et al., 2008, 2013). For these reasons, many petrological and geochemical studies of distal tephra deposits focus on analysis of micro-sized glass shard compositions including their trace element ratios (e.g., Shane and Smith, 2000; Pearce et al., 2002; Albert et al., 2012; Ponomareva et al., 2015; Tomlinson et al., 2015) to obtain information about the volcanic source and possible late-stage magmatic conditions of a volcano. Matrix glass compositions may be challenging for understanding parental melts, since glass is a residual melt fraction after extensive magma crystallisation (Price et al., 2005; Blundy and Cashman, 2008). For this reason, many distal tephra layers are also difficult to link back to their specific volcano (e.g., Preece et al., 2000; Bourne et al., 2010; Óladóttir et al., 2011). An alternative approach is to use the chemistry of minerals in tephra deposits, because

mineral assemblages and compositions can also be used as unique correlation tools and/or in petrological and geochemical studies where these can reflect on their host melts (e.g., Romick et al., 1992; Devine et al., 2003; Shane, 1998; Shane et al., 2003, 2008; Turner et al., 2008a, 2011; Smith et al., 2011). Further, minerals are often more resistant to post-depositional weathering than associated glass. However, because transport and depositional processes can fractionate crystal components towards distal sites, not all mineral phases may be present in far-travelled ejecta.

Despite all of these limitations, distal tephra deposits are often the only source-material available for reconstructing complete volcanic eruption histories and, hence, to gain insights into the magmatic evolution of their source volcanoes. This is particularly true for volcanoes where outcrops in subaerial proximal/medial sites are incomplete due to erosion and/or superposition (Chapter 4; Damaschke et al., 2017b). Mt. Taranaki, for example, has collapsed on at least 14 occasions over the last 170 ka (Zernack et al., 2011), so that the upper part of the cone (>1400 m) only exposes rock sequences that are <10 ka old and mainly tephra units of <5 ka (Torres-Orozco et al., 2017). In such cases, distal tephra records can significantly extend our understanding of the long-term geochemical evolution of a volcanic-magmatic system. Furthermore, tephras often provide long, and well-time-constrained records with closely spaced sampling points, because they are preserved within continuous sedimentation environments that can be independently dated (e.g., marine/lacustrine/paludal sites; Shane et al., 2006; Allan et al., 2008; Gehrels et al., 2008; Gudmundsdóttir et al., 2012; Wulf et al., 2012). In many cases, long tephra records have been used to understand volcanic evolution (e.g., Paterne et al., 1988; Romick et al., 1992; Shane and Hoverd, 2002), the conditions of magma generation (e.g., Lee et al., 1995; Bryant et al., 1999, 2003; Straub et al., 2015), or temporal variations in magma source properties (e.g., Clift et al., 2003, 2005; Erlund et al., 2010; Turner et al., 2008a, 2011).

In this chapter, the high-precision tephrochronological record recovered from lake and peatland environments surrounding the andesitic stratovolcano Mt. Taranaki (North Island, New Zealand) (Chapter 3; Fig. 3.10; Damaschke et al., 2017a) is used to investigate time-related compositional variations. Insights gained from this, are used to

develop an understanding of the processes that might drive magma rise, fractionation, evolution and eruption. Whole-lapilli chemistry data, along with compositions of single glass shards and titanomagnetite phenocrysts were used in these studies.

6.2.1 Andesitic volcanism

One of the most enduring debates in igneous petrology is that of the origin and evolution of intermediate magmas, mainly those linked to subduction processes (Gill, 1981; Thorpe 1982). Intermediate magmas in subduction settings are generally considered to be derived from melts of mantle wedge material, fluxed by volatiles driven off by dehydration and metasomatism of a descending slab (e.g., Hawkesworth et al., 1979; Gill, 1981; Arculus and Powell, 1986; McCulloch and Gamble, 1991; Brenan et al., 1995; Kessel et al., 2005). A range of discussion points, and complications, with this process chiefly involve (1) variations in mantle fertility, (2) volatiles and the sediment cargo in the slab, and (3) major modification and assimilation of magmas as they pause in the lithospheric mantle or lower crust (e.g., Davidson et al., 2005; Price et al., 2005; 2012; Annen et al., 2006; Solano et al., 2012). Typical modification processes include: incomplete crystallisation of basaltic material (Annen and Sparks, 2002; Prouteau and Scaillet, 2003); dehydration partial melting of earlier intruded basalts (Smith and Leeman, 1987; Annen and Sparks, 2002; Price et al., 2005); partial melting of older crustal rocks by intrusion or underplating of mantle-derived basaltic magma (e.g., Hildreth and Moorbath, 1988; DePaolo et al., 1992; Petford and Atherton, 1996; Reubi and Blundy, 2009); fractional crystallisation (FC) and/or assimilation fractional crystallisation (AFC) (Bowen, 1928; Gill, 1981; Kuno, 1968; Grove and Kitzler, 1986; Grove et al., 2003); and magma mixing (e.g., Eichelberger 1978; Tepley et al., 2000; Turner et al., 2008a).

In the case of Mt Taranaki, intermediate magmas, ranging from basalt to high-silica andesitic eruptives, are derived from a multiple-stage (polybaric) magmatic system (Stewart et al., 1996; Price et al., 1999, 2005, 2016; Gruender et al., 2010; Zernack et al., 2012a). In general, it has been argued that hydrous, oxidised, and high-Mg basaltic parental magmas are generated in the mantle wedge by fluxing of fluid from the

subducted slab. The most primitive compositions are represented in mafic magmas from the early Mt. Taranaki eruptives (Zernack et al., 2012a) and peridotite xenoliths (Price et al., 2016). Mantle-derived magmas are thought to accumulate at the mantle-crust boundary due to density limits, forming a gradually evolving 'hot-zone' (after Annen et al., 2006). This is augmented by repeated intrusion of primitive mantle-melts (underplating), which raises the geothermal gradient and allows partial melting of the amphibolitised lower crust. Partial melting of the amphibole-bearing lower crust further gives rise to the formation of high-K magmas (Stewart et al., 1996). Over time, these magmas rise and stall at various levels in the ~35 km-thick crust (Sherburn and White, 2005; Sherburn et al., 2006; Stern et al., 2006), where they are further modified by FC, AFC and/or mixing with resident magmas. This process has eventually produced a vertically zoned plumbing and magma storage system beneath Mt. Taranaki (Price et al., 1999; 2016; Zernack et al., 2012a). Magma storage depth(s) at Mt. Taranaki are mainly estimated on the basis of amphibole thermobarometry (Gruender et al., 2010; Price et al., 2016). Sherburn et al. (2006) tomographically imaged what is believed to be a 10 km deep, 5 km wide solidified magmatic root system beneath Mt. Taranaki. However, evidence for a discrete liquid magma body could not be found, possibly due to the 5 km resolution of the model that would not detect dispersed small-scale magma reservoirs.

6.2.2 Previous petrographic and geochemical work at Mt. Taranaki

Petrological and geochemical studies of Mt. Taranaki are mainly based on lava and pyroclastic successions on the current edifice (Price et al., 1992, 1999; Stewart et al., 1996; Platz et al., 2007a; Turner et al., 2008a, 2011). Additionally, lava clasts within large debris avalanche deposits emplaced over the last 170 ka (Zernack et al., 2011) and complex xenolith assemblages contained in Mt. Taranaki's eruptives (Gruender et al., 2010; Price et al., 2016) have also been used.

According to the classification scheme of Gill (1981), Mt. Taranaki lavas range in composition from medium- to high-K basalts to andesites and trachyandesites (Neall et al., 1986; Price et al., 1992, 1999; Stewart et al., 1996). They mainly have low abundances of MgO, Ni and Cr, indicating advanced evolution from primitive arc-magma characteristics (Price et al., 1992). It has also been noted that magmas erupted have become progressively enriched in potassium over time (Price et al., 1999; Zernack et al., 2011). This is typical within volcanic arc and back-arc volcanism/magmatism (e.g., Foden and Varne, 1980; Nicholls and Whitford, 1983; Edwards et al., 1991; Gertisser and Keller, 2003; Turner et al., 2003). Mt. Taranaki eruptives have distinctively higher K_2O abundances than the andesites of Mt. Ruapehu and Mt. Tongariro in the Taupo Volcanic Zone (TVZ) (Price et al., 1999; 2005) allowing them to be distinguished from TVZ material (Cronin et al., 1996; Shane, 2005). Mt. Taranaki's lavas are generally porphyritic with up to 55% phenocrysts and glomerocrysts, which are dominated by plagioclase, clinopyroxene, titanomagnetite, hornblende, with minor olivine and rare orthopyroxene, ilmenite, apatite and phlogopite (Stewart et al., 1996; Price et al., 1999; Zernack et al., 2012a).

Trace element characteristics of Mt. Taranaki's eruptives have subduction-related arc-signatures with high concentrations of Rb, K, and light rare earth elements (LREE) relative to Zr, Y, and heavy rare earth elements (HREE); depletion of Ta and Nb relative to K; and enrichment of Pb relative to Ce (Price et al., 1999; Zernack et al., 2012a). Isotope studies illustrate a narrow compositional range of $^{87}Sr/^{86}Sr$ ratio (mean=0.70457±22 at 1σ), $^{143}Nd/^{144}Nd$ ratio (mean=0.51285±3 at 1σ), and $^{206}Pb/^{204}Pb$ ratio (range=18.729 to 18.889) (Price et al., 1992, 1999).

6.2.3 Basement geology and xenoliths

Mt. Taranaki overlies Cretaceous to Tertiary sedimentary rocks of the Taranaki Basin and the upper crust (down to 6 km; Collen et al., 1985; King and Thrasher, 1996), while the deeper basement (6-14 km) is interpreted to comprise calc-alkaline plutonic and metamorphic rocks of the Median Batholith (Mortimer et al., 1997; Townsend et al., 2008). The deeper rocks are inferred to mainly comprise diorites, gabbros and granitoid

rocks containing occasionally significant modal biotite (Muir et al., 1998; Gruender et al., 2010; Price et al., 2011, 2016). The xenolith suites from Mt. Taranaki include sedimentary, plutonic and metamorphic rocks from the underlying basement, but are dominated by 80% cognate igneous rocks linked to the magmatic system of Mt. Taranaki (Gruender et al., 2010; Price et al., 2016). The igneous xenoliths (and autoliths) include gabbroic and ultramafic rocks, which represent cumulates generated during FC and AFC processes within various levels of the plumbing system, along with restites derived from partial melting of an amphibolitic crust, and metasomatised mantle/crustal materials.

6.3 Methods

For lapilli-bearing tephra units in the sediment cores of this study, 2 g of cleaned pumice lapilli were handpicked and powdered in a tungsten carbide ring mill. These powders were fused into disks following the Norrish fusion method (Harvey et al., 1973) with a dilution factor of 1:3 (the sample was ignited with a 12:22 lithium tetraborate:lithium metaborate flux). For major elements, the disks were analysed in triplicate using a Panalytical Axios 1 kW wavelength dispersive X-ray fluorescence (XRF) spectrometer at the University of Auckland. Twenty-eight international standards analysed in triplicate were used for calibration. U.S. Geological Survey glass standard BCR-2G was analysed to provide an independent assessment of accuracy and precision. The results for BCR-2G are consistent with the reference values within <1% for elements used in this study, and replicate analyses indicate an analytical precision (2σ) of <1% (mostly ~0.7%).

Whole-lapilli trace element analyses were determined by laser ablation–inductively coupled plasma–mass spectrometry (LA-ICP-MS) at the Australian National University, using an Excimer LPX120 laser and Agilent 7500 series mass spectrometer. The analyses were performed on the XRF discs, following the procedure of Eggins et al. (1998). The NIST 610 glass, analysed after every 15 unknowns, was used as the primary calibration standard, while BCR-2G was analysed to provide an independent

assessment of accuracy and precision. The results for BCR-2G are consistent with the reference values within 10% for elements used in this study (mostly ~5%), and replicate analyses indicate an analytical precision (2σ) of ~5% for most elements, except for Zr, Cr, Ni, and Pb (>10%). Whole-lapilli major and trace element data is summarised in Appendix 7.

In addition, spot LA-ICP-MS analyses were performed on titanomagnetite grains mounted, cut and polished in epoxy resin. A ~80 μm spot was used for these analyses, with grains typically >250 μm wide. Ten grains per sample were analysed. A 15 s pre-ablation phase was followed by 30 s of counting, and a 10 s post-ablation phase. The NIST 610 glass was analysed as a standard after each of 10 analyses to monitor drift. EMPA major element data were used to cross-check the LA-ICP-MS results. Replicate analyses indicate an analytical precision (2σ) of ~5% for all elements. LA-ICP-MS results are summarised in Appendix 8.

Major and minor element analysis of single glass shards and titanomagnetite phenocrysts were carried out using a JEOL JXA-840a electron microprobe equipped with a Princeton Gamma Tech Prism 2000 Si(Li) energy dispersive spectrometer (EDS) at Massey University. An accelerating voltage of 15 kV, an 800 pA beam-current, and a 100 seconds acquisition time were used. These conditions along with a 10-20 μm defocused beam were used for glass shard analyses to minimize Na-migration. Syn- and post-eruption crystallisation of nanolitic Fe-oxides and microlitic plagioclase can often lead to fine-scale heterogeneity of the glass (Best, 2003). These are often difficult to avoid using a large diameter electron beam required for glass analysis. To minimise this effect, back-scatter electron imaging and the removal of hybrid data points using the technique of Platz et al. (2007b) were applied. A focused beam (approximately 2-3 μm diameter) was used for the titanomagnetite analyses. Titanomagnetite phenocrysts and/or those within glomerocrysts were analysed mainly from the 250-500 μm size fraction. Exsolved titanomagnetite grains (showing trellises of ilmenite and magnetite), show naturally heterogeneous compositions and thus could be avoided using back-scatter electron imaging. The energy spectrum at the analytical conditions was regularly calibrated using a range of ASTIMEX standards appropriate to the compositions of

phases analysed. At least 10 analyses of both glass and titanomagnetite were obtained for each tephra. Data points showing obvious contamination were excluded. Major elements are expressed as oxides and reported in weight per cent (wt%). Glass shard data were normalised to 100% and titanomagnetite data corrected for iron following the procedure of Carmichael (1966). The complete electron microprobe-determined data set is summarised in the printed and electronic appendices.

The nomenclature for individual lake and peat tephra layers is based on the coring site and tephra number in stratigraphic/age order. For example N-5 = Ngaere Swamp core, 5th youngest tephra layer. Individual tephra sequences are described in detail in Chapter 3 and include Tephra Sequence E (17.5-14 cal ka BP), D (14-9.5 cal ka BP), C (9.5-4 cal ka BP), B (4-3 cal ka BP) and A (3-0.5 cal ka BP).

6.4 Results

6.4.1 Whole-lapilli compositions

In total, 59 tephra layers were analysed for their whole-lapilli (fresh, juvenile pumice clasts) major and trace elements. Whole-lapilli compositions range from subalkaline medium-K to high-K basalts, basaltic-andesites, basaltic-trachyandesites and trachyandesites (Figs. 6.1, 6.2). SiO_2 abundances of ~51 wt% occur in the least evolved tephra samples, particularly those of the Manganui tephras (i.e., Ri-26, Ri-30, T-4, T-10, N-6, E-5, E-6, E-7; Fig. 1), which were erupted from the parasitic Fanthams Peak cone (~3 cal ka BP). Highest silica units, up to ~61 wt% include the prominent Inglewood tephra unit (i.e., Ri-40, E-8, N-8/9; Fig. 6.1). The gradual enrichment in potassium over time cited in previous studies (Price et al., 1999; Zernack et al., 2012a) is also observed in the whole-lapilli analyses of this study with the youngest tephra, Ri-6 (<1 cal ka BP), having the highest K_2O content (~3.5 wt%; Fig. 6.2).

Figure 6.2 shows the major element abundances of each tephra sequence using silica variation diagrams. Representative data for each analysed tephra are given in Appendix 7. Conventional patterns of evolution are observed with TiO_2, MgO, Fe_2O_3(t), and CaO concentrations decreasing with increasing SiO_2, whereas Na_2O and K_2O abundances increase (Fig. 6.2). Tephra Sequence F and E as well as the Manganui tephras have the highest TiO_2, MgO, Fe_2O_3(t) and CaO, and the lowest Na_2O and K_2O abundances compared with Tephra Sequence B and A. The same patterns occur with the trace elements, and with the incompatible elements such as Rb, Ba, Zr, and Hf in that they increase with increasing SiO_2 (Fig. 6.2), while V, Ti, and Cu decrease. These data fit well with previous whole-rock analyses of lava flows, lava blocks, pyroclastic flow and fall deposits (Price et al., 1999; Turner et al., 2011; Zernack et al., 2012a; Torres-Orozco et al., in review; Fig. 6.2). However, it is conspicuous that some of the tephras show different levels of major and trace element abundances with mirroring trends, but systematically lower Fe_2O_3(t), MnO, K_2O and V, along with higher CaO, Al_2O_3 and Sr (encompassed by the ellipsoids in Fig. 6.2).

Normalised trace element patterns (Sun and McDonough, 1989) of each tephra sequence in Figure 6.3 show typical characteristics of subduction-related magmas (e.g., Pearce, 1982; McCulloch and Gamble, 1991; Rudnick and Gao, 2003; Kelemen et al., 2005) with enriched incompatible large ion lithophile elements (LILE) including U, Th, and Pb relative to the normal mid-ocean ridge basalts (N-MORB), and enriched light rare earth elements (LREE) relative to heavy rare earth elements (HREE). Elements such as Nb, Ta, and Ti show distinct negative anomalies, with Nb and Ta being strongly depleted relative to K, and Ce relative to Pb and Sr. The chondrite-normalised rare earth element (REE) plots show a flat pattern for the HREE (Er-Lu), while the LREE (La-Eu) slightly increase toward La (Fig. 6.3). Furthermore, no Eu anomalies are observed for the Mt. Taranaki tephras. These patterns arise from the immobility vs mobility of those elements within the mantle wedge where fluids or melts are infiltrated from the subducted slab (e.g., Gill, 1981; Pearce, 1982; Sun and McDonough, 1989; McCulloch and Gamble, 1991). Tephras younger than <1 cal ka BP, Tephra Sequence B, and C show a stronger subduction signature than the less-evolved samples of Tephra Sequence

E and the Manganui tephras, with slightly greater enrichment of LILE over high field strength elements (HFSE) and N-MORB.

Although the overall compositional variations in the trace element patterns between the different tephra sequences are minor, some elements are conspicuously variable. In general, the younger Tephra Sequences A and B show slightly higher concentrations of LILE (excluding Sr), HFSE (excluding Ti) and LREE (La, Ce, Pr, Nd) compared with the older Tephra Sequences E, F, and the Manganui tephras. A strong depletion in Ti in more evolved compositions of Tephra Sequence B and A is recognised, whereas Tephra Sequences E, F, and the Manganui tephras have a closer affinity to N-MORB Ti abundances (Fig. 6.3). Zr and Hf show small negative anomalies towards N-MORB compositions in the Manganui tephras and in Tephra Sequence F, E, and D, compared with the Tephra Sequence C, B, and the single tephra Ri-6 (Fig. 6.3). In all tephra sequences, a slight positive anomaly in Nd is recorded.

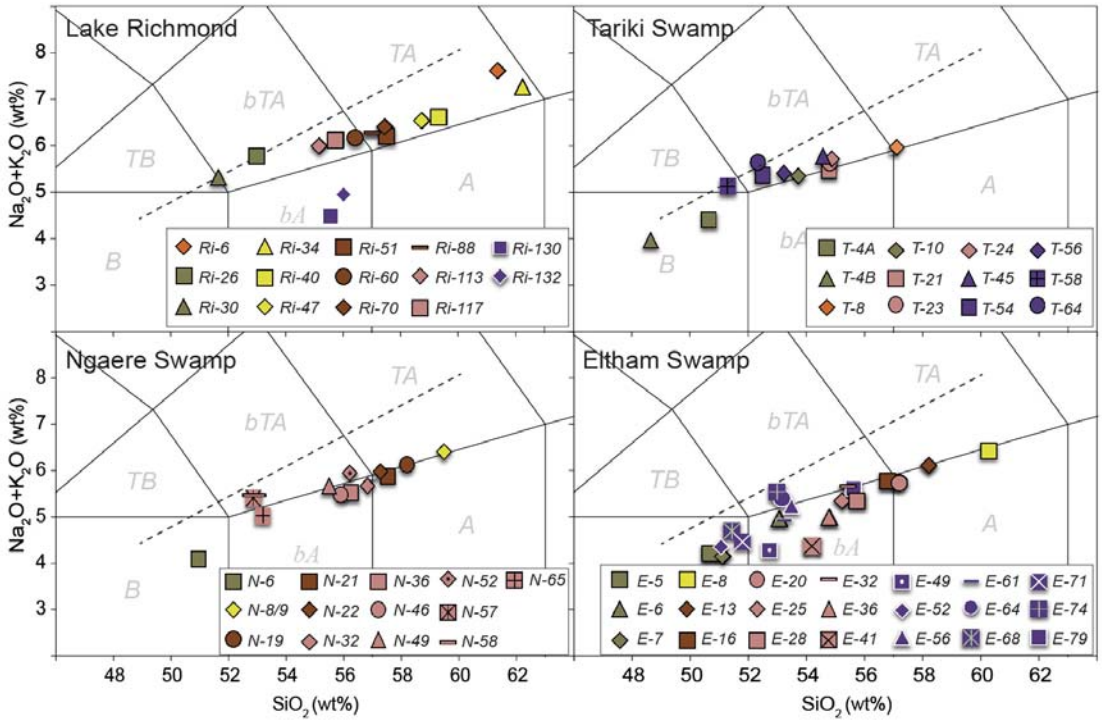

Figure 6. 1 *Total Alkalis vs. Silica (TAS) diagram (Le Bas et al., 1986) for the Mt. Taranaki whole-lapilli samples analysed from lake and peatland tephras recovered in this study (Appendix 7). Compositional fields are basalt (B), basalt-andesite (bA), andesite (A), trachybasalt (TB), basalt-trachyandesite (bTA), and trachyandesite (TA). All analyses are on a water-free basis. Colours represent the titanomagnetite group of each tephra sample (refer also to Fig. 6.8 and Chapter 3). Dotted line represents the alkaline/subalkaline compositional boundary.*

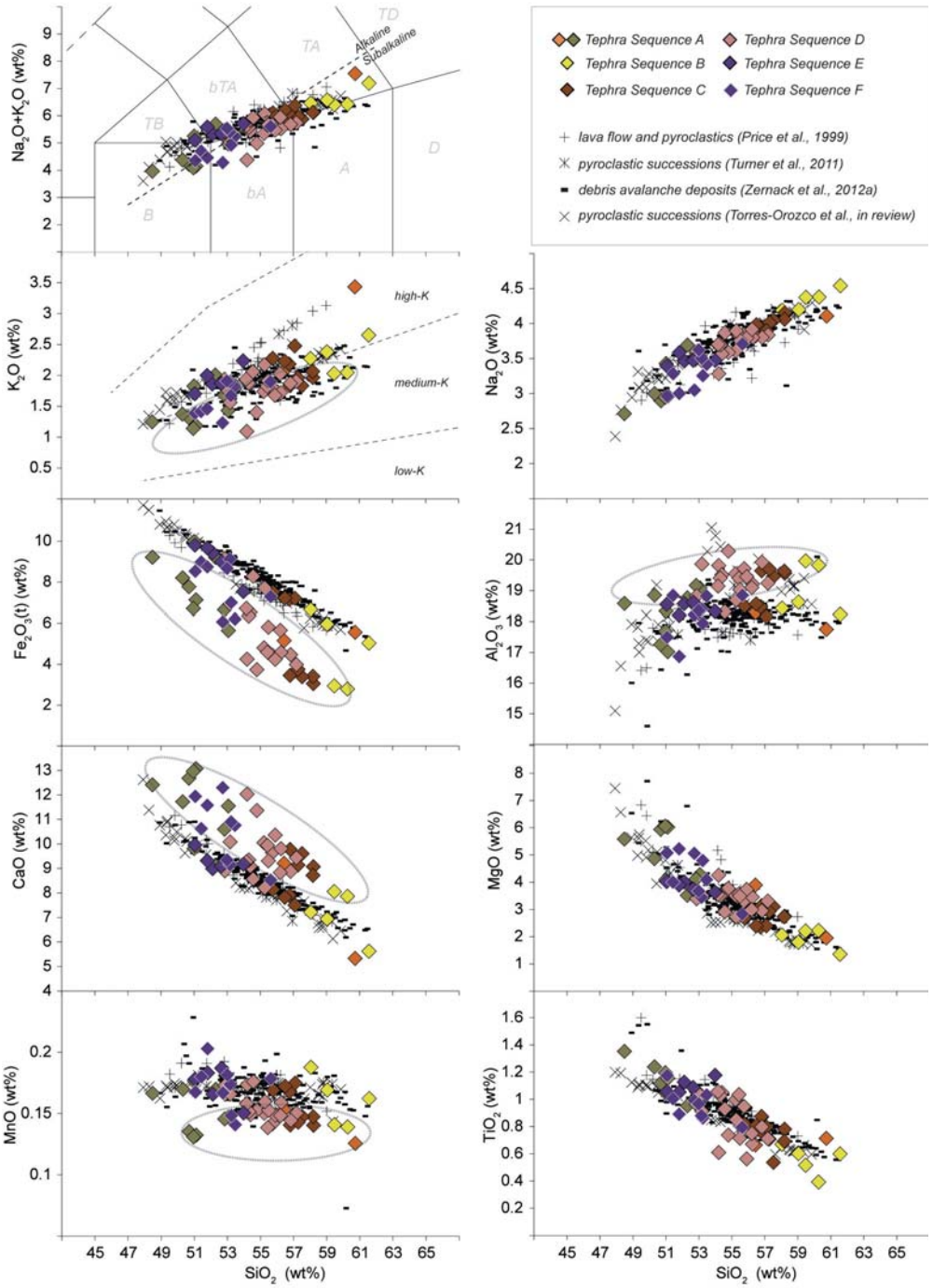

Figure 6. 2 *Total Alkalis vs. Silica (TAS) diagram (Le Bas et al., 1986) and selected SiO_2 variation diagrams (with K_2O v.s SiO_2 after LeMaitre et al., 2002) illustrating variation in the whole-lapilli major and trace elements for the Mt. Taranaki tephra sequences (A-F) from the lake and peat cores (Chapter 3). Whole-rock analyses of lava flows, pyroclastic flows and fall deposits (references as in figure) are also shown for comparison. All analyses are on a water-free basis with total iron presented as Fe_2O_3.*

Compositional fields are basalt (B), basalt-andesite (bA), andesite (A), dacite (D), trachybasalt (TB), basalt-trachyandesite (bTA), trachyandesite (TA), and trachydacite (TD). Dotted ellipsoids indicate contrasting whole-lapilli sample compositions (referred to in the text).

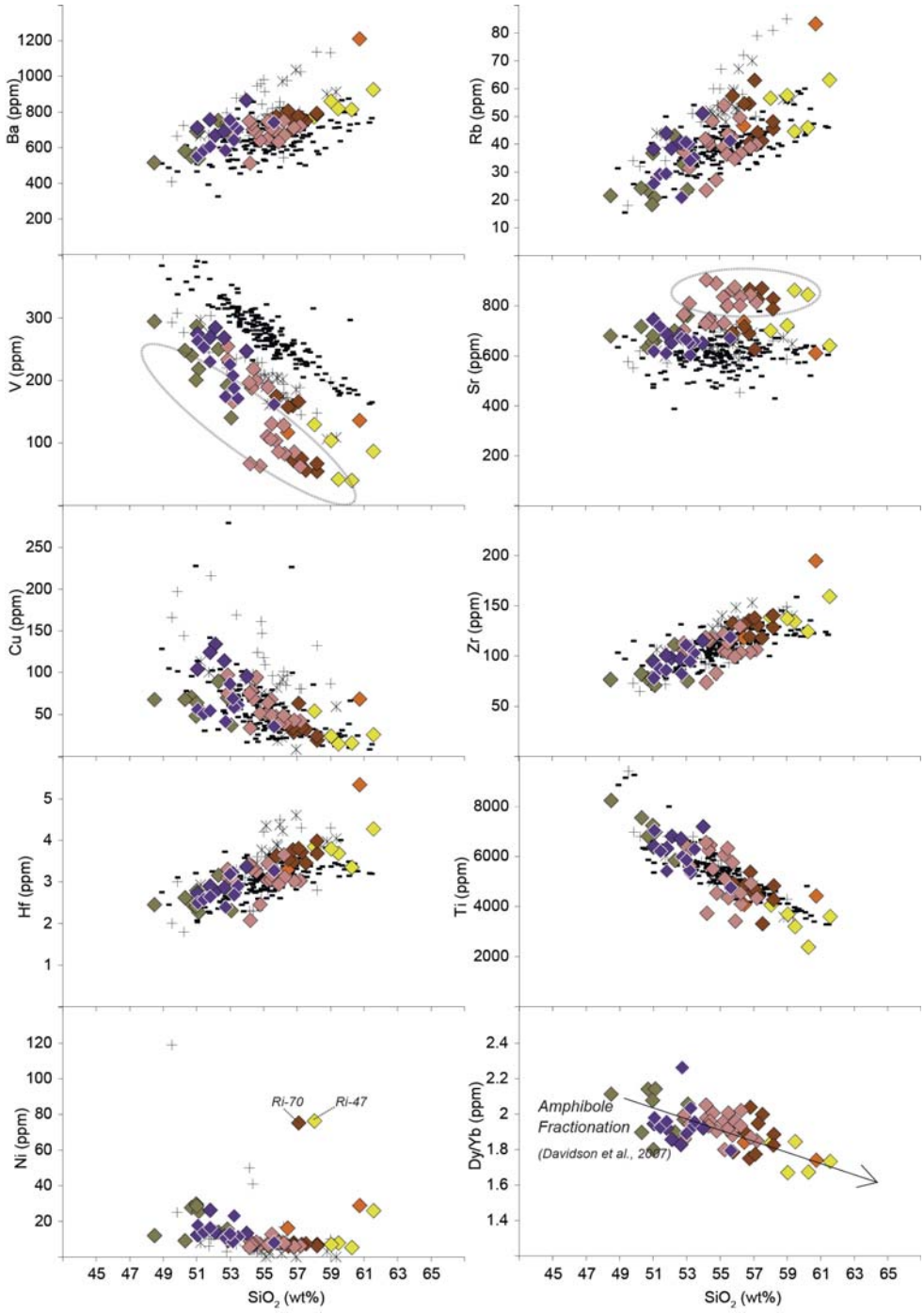

Figure 6.2 *(continued)*

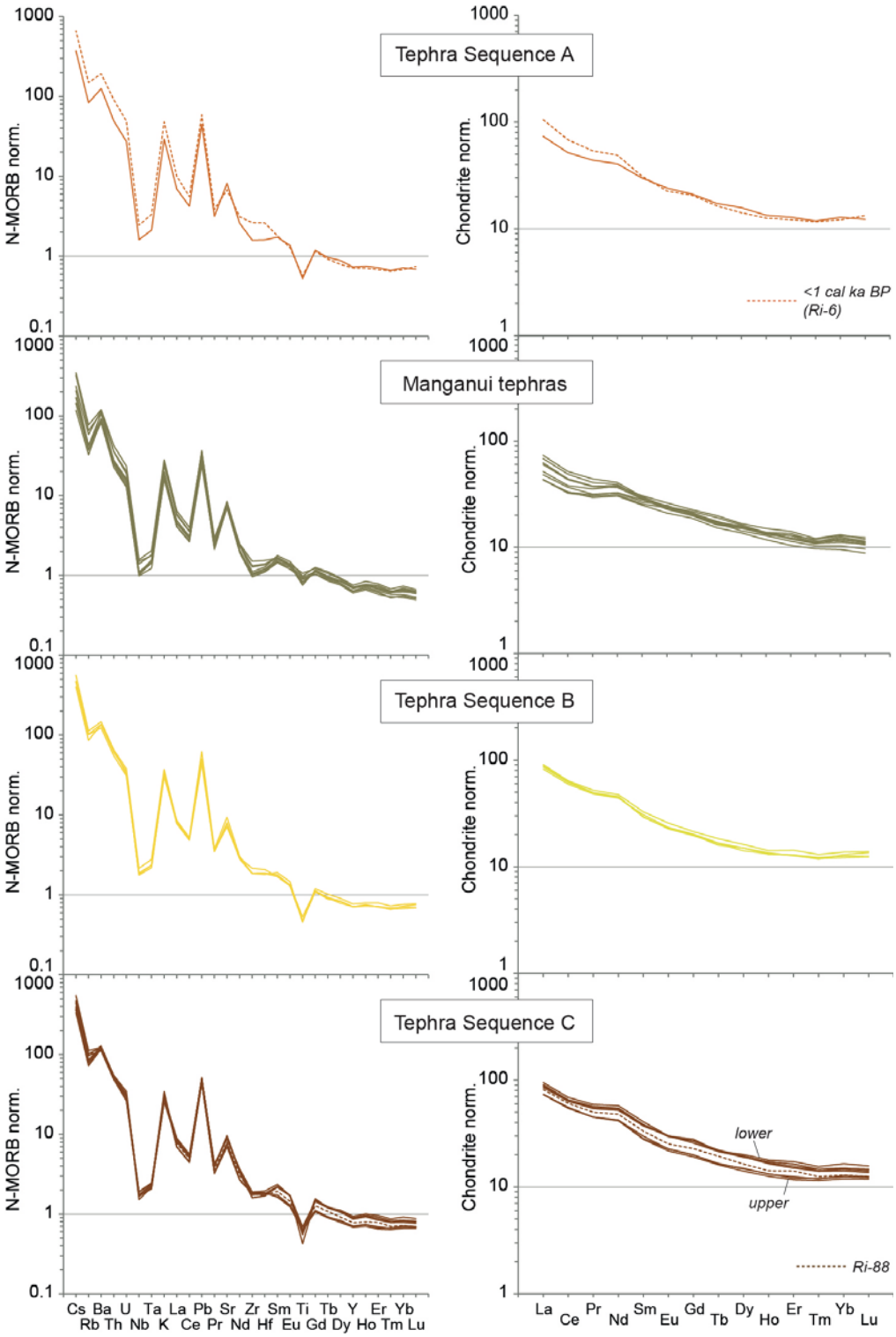

Figure 6. 3 *Normalised trace element diagrams for the Mt. Taranaki whole-lapilli samples with the normalised values from Sun and McDonough (1989). Individual tephra samples are classified within their tephra sequence (A-F) represented by different colours (see Chapter 3).*

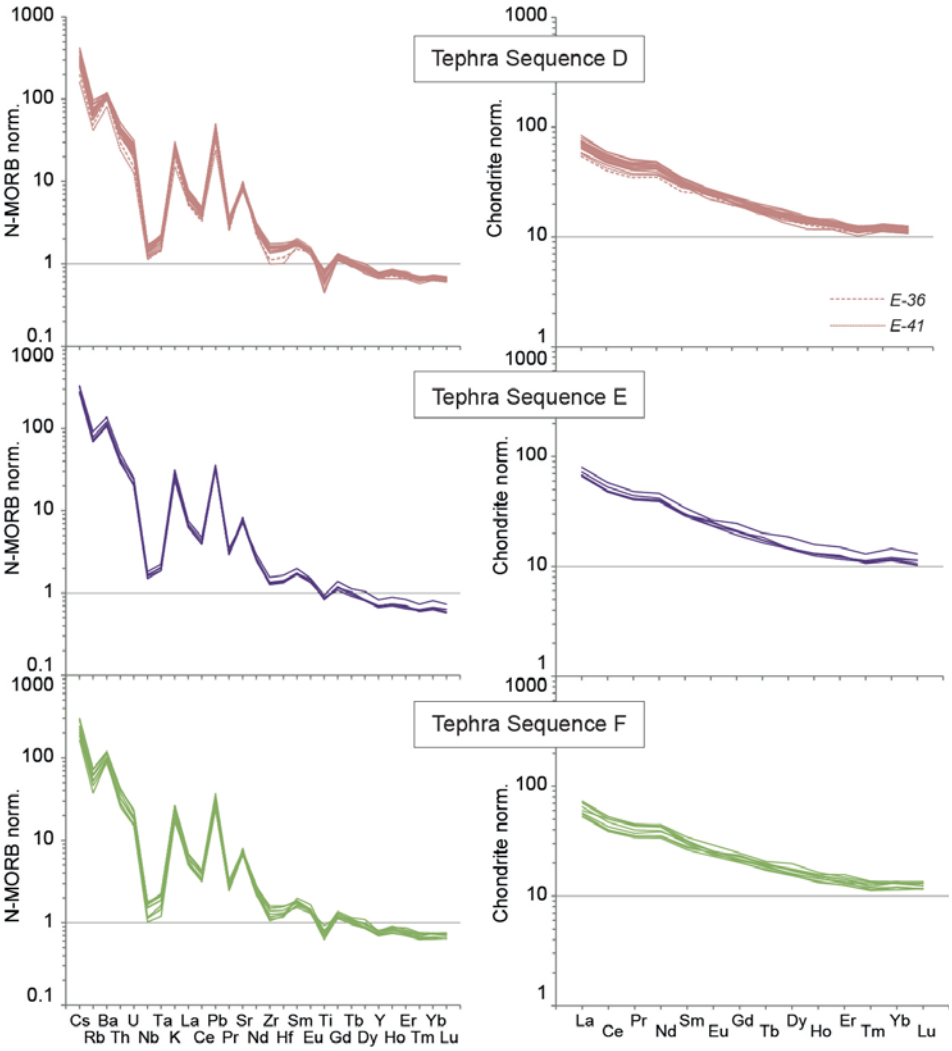

Figure 6.3 *(continued)*

6.4.2 Glass shard compositions

Glass shard analyses were reported from distal and proximal tephra layers in Chapter 3 and 4 (Damaschke et al., 2017a, 2017b). Glasses exhibit well-defined trends of decreasing $FeO_{(t)}$, TiO_2, CaO, and MgO contents with increasing SiO_2 (Fig. 6.4). Alkali contents increase from 6 to 9.5 wt% within the less evolved samples (<63 wt% SiO_2) and plateau at their highest alkali levels between 63 and 72.5 wt% SiO_2. Overall, the main glass trends observed are similar to whole-lapilli compositional patterns.

6.4.3 Titanomagnetite compositions

Titanomagnetite analyses were assembled from distal and proximal tephra layers in Chapter 3 and 4 (Damaschke et al., 2017a, 2017b). TiO_2 contents range from >10 wt% (group-1 titanomagnetites) to <7 wt% (group-11 and group-12 titanomagnetites) (Fig. 6.5). Within the entire suite, TiO_2 varies inversely with Fe^{3+}. There is only a minor variability in Fe^{2+}, with group-11 titanomagnetites having the lowest Fe^{2+} contents (<1 cation proportion; Fig. 6.5). MgO contents range from 5 wt% (group-11 titanomagnetites) to <2 wt% (group-10 titanomagnetites). Al_2O_3 follows the trend of MgO; while group-11 titanomagnetites have the highest Al_2O_3 abundances (4-8 wt%).

Overall, the data displays two compositional trends from high-TiO_2, high-Al_2O_3, high-MgO and low-Fe^{3+} contents to low-TiO_2, low-Al_2O_3, low-MgO and high-Fe^{3+} concentrations, represented by titanomagnetite groups-1 to -10, and groups-11 to -12 (Fig. 6.5). Within these overall compositional trends, secondary trends within each titanomagnetite group are evident. This is best demonstrated within the Fe^{2+} vs Fe^{3+} variation diagram, where major titanomagnetite groups (e.g., groups -1, -2, -8, and -10) decrease in Fe^{2+} with increasing Fe^{3+} contents. This produces a step-wise variation from group-1 titanomagnetites through to group-10 titanomagnetites. Group-11 and group-12 titanomagnetites do not trend in a similar way.

Furthermore, 42 selected tephra samples were analysed for their titanomagnetite minor and trace elements using laser ablation–inductively coupled plasma–mass spectrometry

(LA-ICP-MS) (Figure 6.6; Appendix 8). LA-ICP-MS has rarely been used to fingerprint titanomagnetites despite indications that it could be very useful (Nadoll and Koenig, 2011). Between 10 and 20 grains were ablated per sample. The ablation spot size used was between 60-80 μm in order to provide good signal to noise ratios, but this also meant that any small inclusions of glass or apatite or other silicate phases generated strong impacts on the compositions. These were filtered out by removing analyses with spurious Si, Ca or P contents. Some analyses were greatly variable within the same tephra sample, possibly caused by co-existing pyroxene and magnetite or ilmenite and magnetite. The most reliable elements analysed and those that are compatible with titanomagnetite (cf., Nadol and Koenig, 2011) were found to be V, Co, S, Sc, Ga, Ni, and Ge. Many of these would replace Mg, but elements such as vanadium are interesting since these can occupy a number of spots within the spinel-structure due having multiple potential valence states. This suite of elements, which are mainly known as compatible elements in silicate system, follow the same pattern in showing highest concentrations in the least-evolved titanomagnetites and lowest in the more-evolved titanomagnetites (following Mg; Fig. 6.6). Analyses against the average glass and whole-rock silica concentrations from the same tephras, these data show a consistent pattern with evolutionary state.

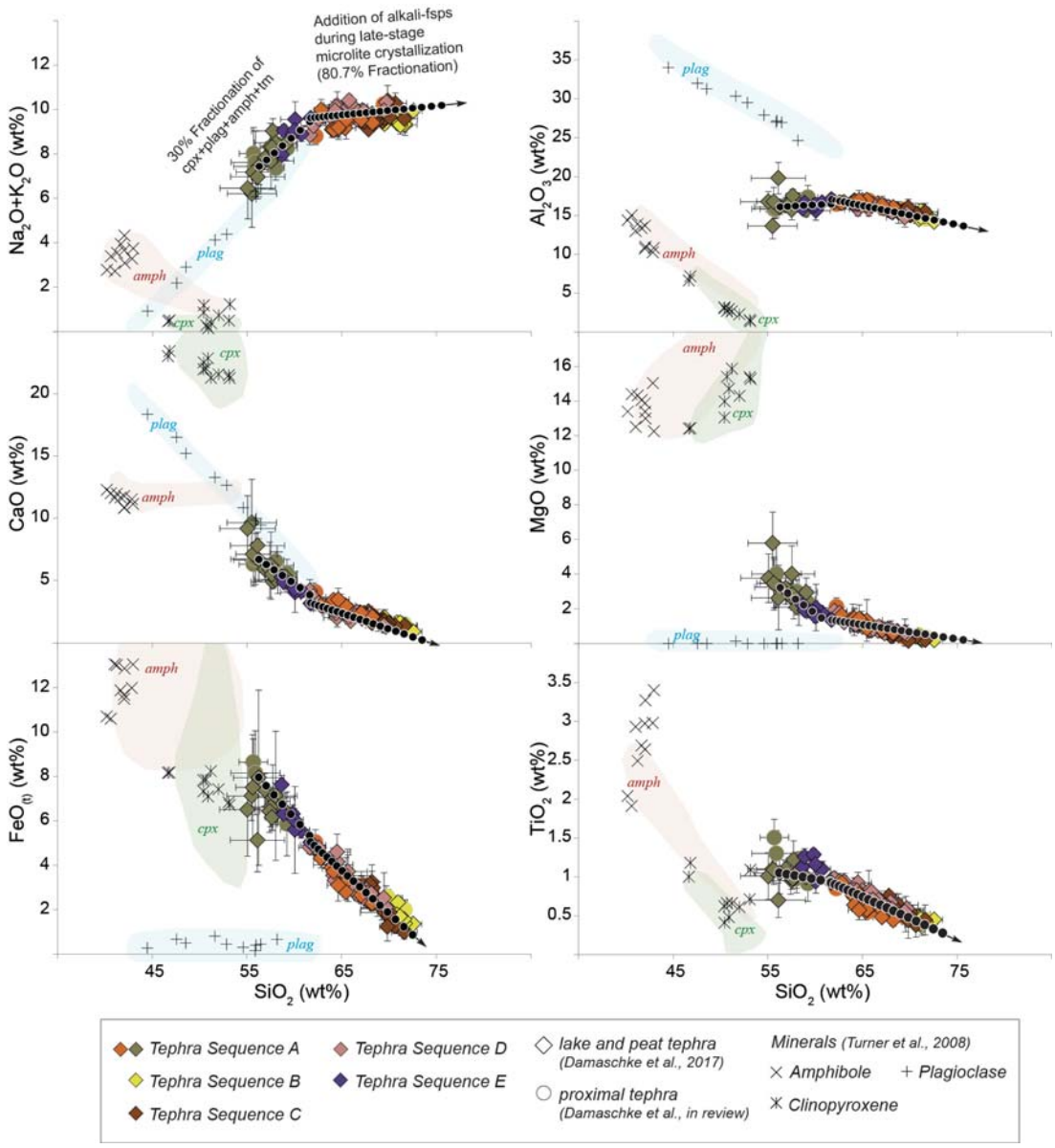

Figure 6. 4 *Glass compositional variations of the alkalis, Al_2O_3, CaO, MgO, FeO, and TiO_2 vs. SiO_2 abundances for the Mt. Taranaki distal and proximal tephras (compiled in Chapters 3 and 4; Damaschke et al. 2017a, 2017b) compared with model fractional crystallisation paths represented by the series of black spots, which mark 5% crystallisation steps (see Table 6.2). All analyses are normalised to 100% and each point is the average ±1 standard deviation for each tephra sample. FeO is determined as total iron. Also shown are the compositions of common mineral phases (plag = plagioclase, amph = amphibole, cpx = clinopyroxene) in Mt. Taranaki volcanic rocks (Turner et al., 2008a) and xenoliths (coloured shaded fields that correspond to their respective minerals; Gruender, 2006, Gruender et al., 2010).*

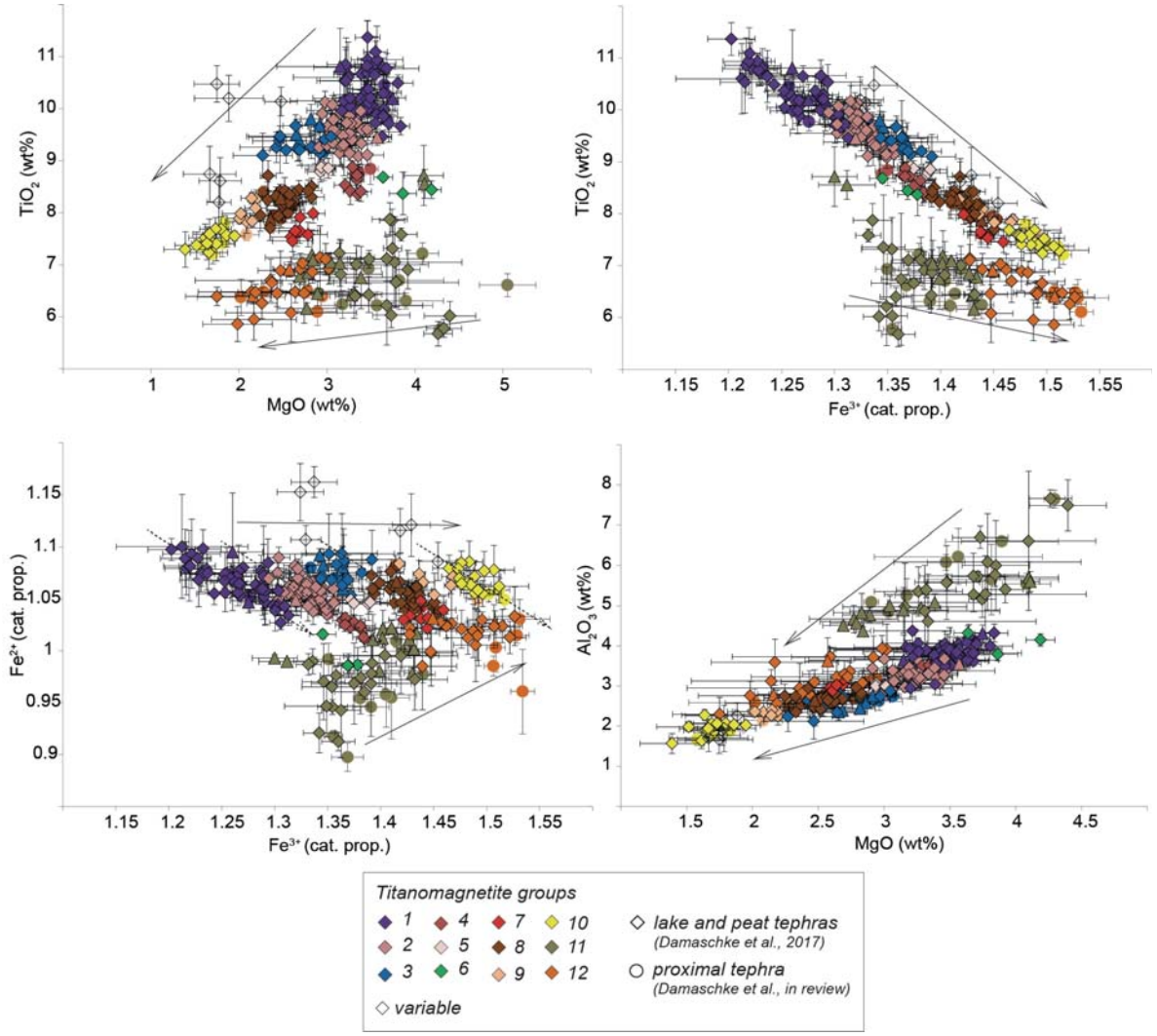

Figure 6. 5 *Titanomagnetite compositional variations of MgO and Fe^{3+} vs. TiO_2, Fe^{2+} vs. Fe^{3+}, and Al_2O_3 vs. MgO abundances for the Mt. Taranaki distal and proximal tephras (compiled in Chapters 3 and 4; Damaschke et al. 2017a, 2017b). All analyses are in weight percent and the cation proportion (cat. prop.) is calculated on the basis of four oxygen atoms as in Carmichael (1966). Each point is the average ±1 standard deviation for each tephra sample. Two compositional trends are highlighted by solid arrows alongside the plotted trends, and secondary trends are indicated by dotted arrows (refer to text, 6.5.3.2).*

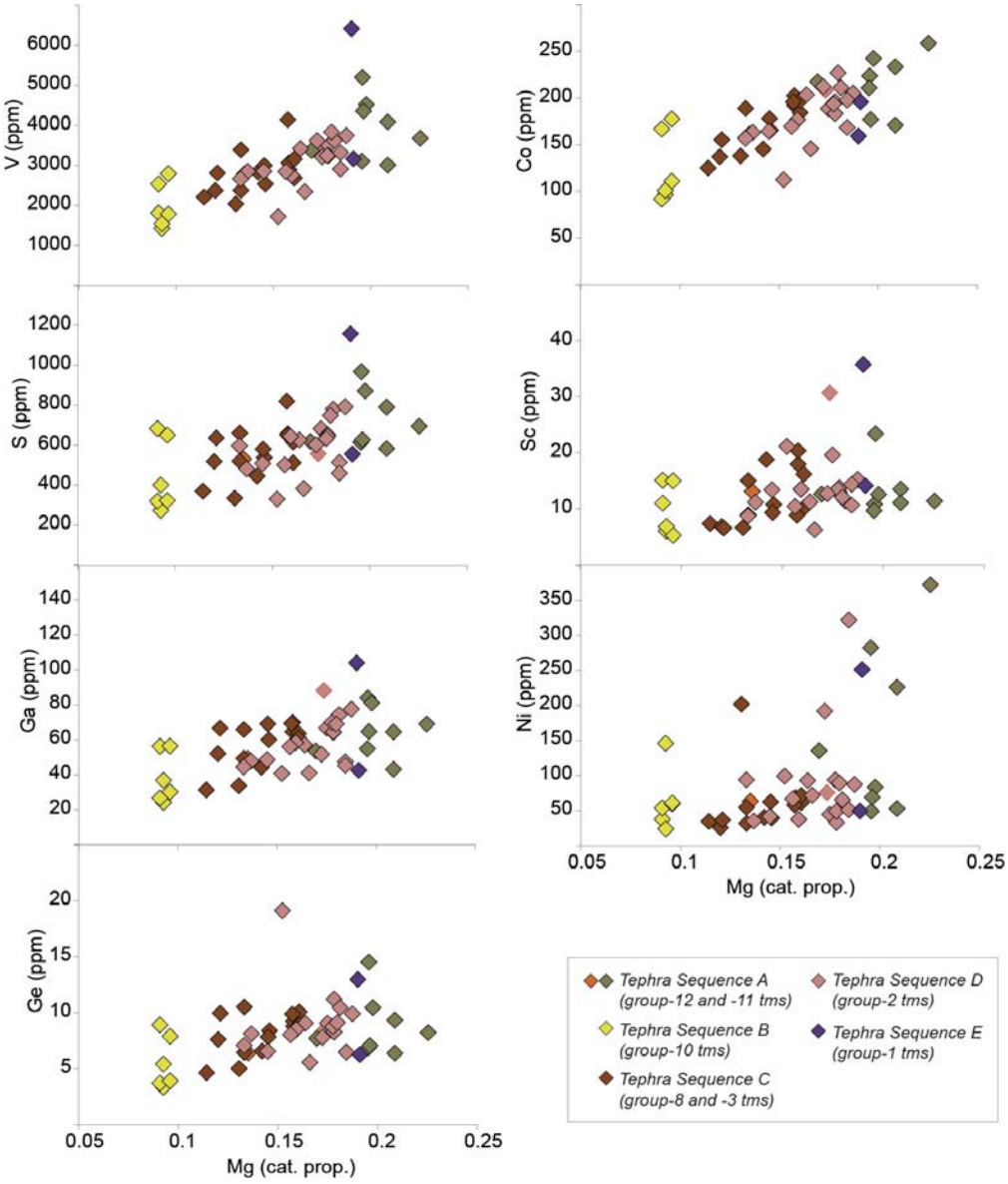

Figure 6. 6 *Minor and trace element titanomagnetite variation as function of Mg abundances (latter is based on microprobe data) for Mt. Taranaki lake and peatland tephra layers. All analyses are in parts per million (ppm) with Mg as cation proportion (cat. prop.) calculated on the basis of four oxygen atoms as in Carmichael (1966). Colours represent different tephra sequences and their respective dominant titanomagnetite group (see Chapter 3).*

6.4.4 Temporal variation of whole-lapilli, glass shard, and titanomagnetite compositions

The high-resolution composite record built in Chapter 3 (Fig. 3.10) was used to plot a time-series of the main geochemical trends (age determinations as in Chapter 3; Damaschke et al., 2017a). While the entire record is ~30 cal ka BP-long and encompasses ~228 tephra layers, it is most continuous post-17.5 cal ka BP. To complete the youngest suite, which was difficult to capture in distal lakes and peats, the chemistry of prominent proximal fall units was added (e.g., Burrell, Te Popo, Kaupokonui, Maketawa tephra units; Turner et al., 2011; Damaschke et al., in 2017b; Torres-Orozco et al., in review), as well as, Fanthams Peak (parasitic vent) and summit whole-rock lava compositions (Stewart et al., 1996; Price et al., 1992, 1999).

6.4.4.1 Whole-lapilli and glass shard compositional variations

Figure 6.7 combines the whole-lapilli and glass analyses and both show similar trends over time (Fig. 6.7). With time, SiO_2 contents of whole-lapilli and glass compositions of Tephra Sequence E to B (17.5 to 3 cal ka BP) increase, while $FeO_{(t)}$, MgO, CaO, and TiO_2 abundances decrease. At 3 cal ka BP, represented by the start of Tephra Sequence A (Manganui tephras), a significant change in composition is documented, with SiO_2 contents abruptly decreasing and $FeO_{(t)}$, MgO, CaO, and TiO_2 abundances increasing. Al_2O_3 abundances within the whole-lapilli and the glass compositions are more or less constant throughout all the tephra sequences, with exception of the Manganui tephras and Fanthams Peak lavas <3 cal ka BP, which have highly variable whole-lapilli compositions (Fig. 6.7). The trends seen in Na_2O and K_2O are different between whole-lapilli and glass compositions. While the alkalis in the whole-lapilli dataset increase slightly over time (except Manganui, intercalating Maketawa tephras and the Fanthams Peak lavas), no significant time-related changes are observed for the alkalis within the glass (Fig. 6.7). Tephra samples and summit lava bulk-compositions younger than 1 cal ka BP have the highest potassium abundances (>2.5 wt%) and noticeably lower and

variable MnO contents (Appendix 7). Nevertheless, the abrupt compositional change at 3 cal ka BP is recognizable in both, the whole-lapilli and glass alkali compositions.

6.4.4.2 Titanomagnetite compositional variations

While whole-lapilli and glass shard analyses display only broad compositional variation trends over time, titanomagnetite compositional variations display more nuanced trends, as a consequence of more tephras being analysed.

The TiO_2, Al_2O_3, and MgO abundances decrease from Tephra Sequence E (<17.5 cal ka BP) to Tephra Sequence B (>3 cal ka BP), while Fe^{3+} increases (Fig. 6.8). Tephra Sequence B is characterised by distinctively elevated MnO contents (>1.5 wt%; Appendix 2). At 3 cal ka BP, represented by the start of Tephra Sequence A, a significant change in composition occurs within the titanomagnetites, with Al_2O_3 and MgO contents much higher and Fe^{3+} contents lower. TiO_2 appears less affected.

Several small-scale variations occur within the overall decreasing TiO_2 trend. For example, at c. 11 to 9 cal BP (part of Tephra Sequence D) TiO_2 rise from ~7 to 10 wt%; Fig. 6.8A), before dropping back to ~8 wt%. Fe^{3+} contents mirror this observation (Fig. 6.8B). TiO_2 contents within the lower part of Tephra Sequence C (8-6.5 cal ka BP) alternate between ~8 to ~9.5 wt% with intercalating group-3 and group-8 titanomagnetites (Fig. 6.5). Some of these tephras are also characterised by bimodal compositions, including a sub-population having ~6-7 wt% TiO_2 and high Al_2O_3 contents (~4-5 wt%) (indicated by dashed ellipsoids in Fig. 6.8A, C). Low Al_2O_3 and MgO contents occur in some tephra layers with distinctively variable titanomagnetite compositions, e.g., at 9.5 cal ka BP (at the transition between Tephra Sequence D and C) and at ~5 cal ka BP (tephra U-39/Ri-65) (Fig. 6.8C, D).

The oldest tephra sequence (TS F) is characterised by broadly increasing TiO_2 and decreasing Fe^{3+} contents from ~ 30 to 26 cal ka BP, with little variation in both for samples <26 cal ka BP (except single tephra E-46, group-2 titanomagnetites, ~24.2 cal

ka BP). There is also an obvious bimodality in sample E-56 and E-58 (~26 cal ka BP; Fig. 6.8A, C).

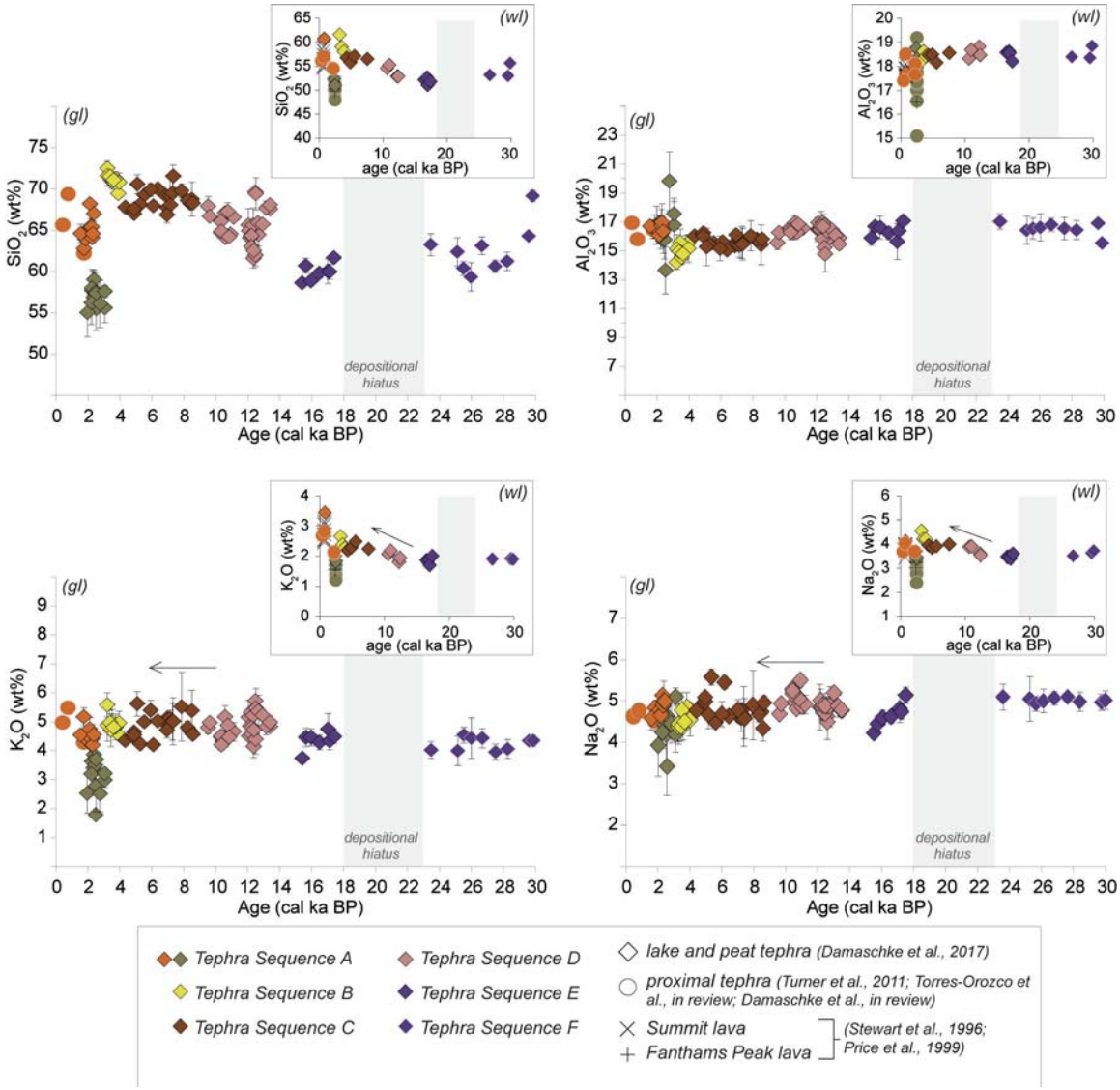

Figure 6. 7 *Time-series glass (gl) and whole-lapilli (wl) compositional trends observed within distal and proximal tephra deposits of Mt. Taranaki. Bulk-analyses of young lava flows, including the Summit and Fanthams Peak lavas (Stewart et al., 1996; Price et al., 1999), are also shown so as to complete the youngest time-frame of emplacement. All analyses are on a water-free basis with total iron as Fe_2O_3 in bk, and FeO in gl. Each point is the average ±1 standard deviation for each tephra layer within the gl. Note: Tephra Sequence F is stratigraphically separated from the rest of the tephra sequences by a ~6000 cal yr BP depositional hiatus (for more information see Chapter 3).*

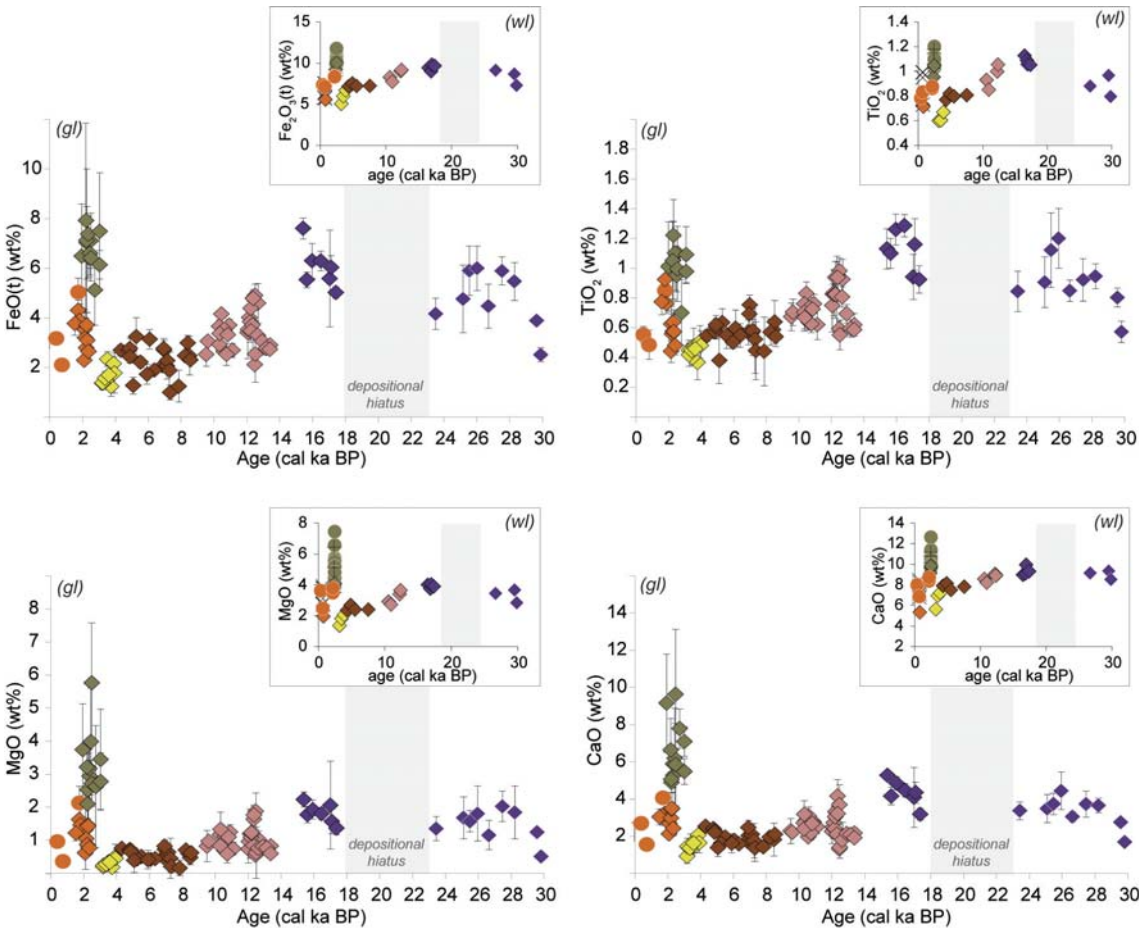

Figure 6.7 *(continued)*

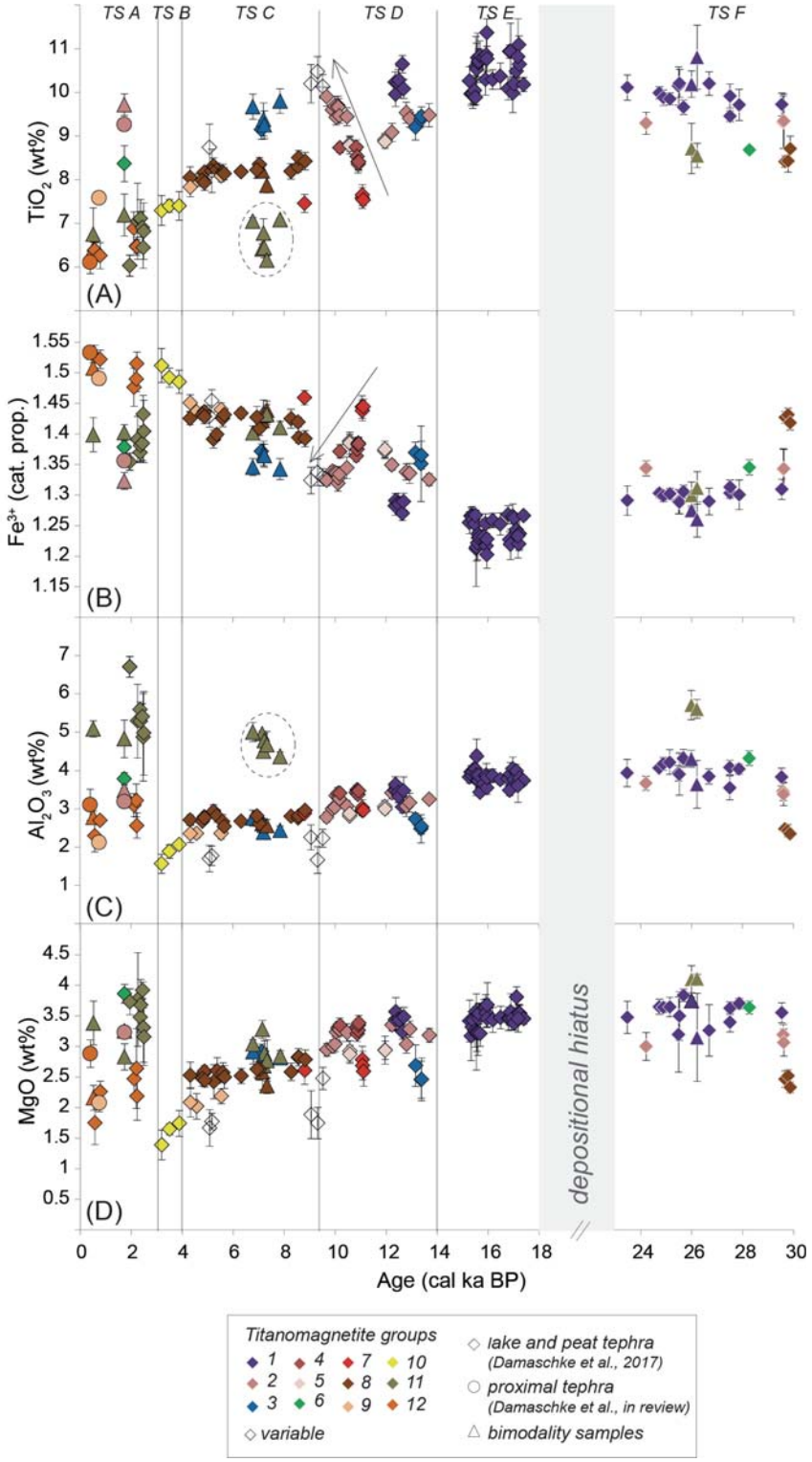

Figure 6. 8 *Time-series titanomagnetite compositional trends observed within distal and proximal tephra deposits of Mt. Taranaki. All analyses are weight percent and cation proportion (cat. prop.) is calculated on the basis of four oxygen atoms as in Carmichael (1966). Each tephra (each point = average +1 standard deviation) is*

indicated by its respective tm-group (see colour). Only tephras from the composite record are shown (Chapter 3 and 4). Triangles represent tephras with bimodal compositions. (sub-population is indicated by ellipsoid; referred to in text). Note: Tephra Sequence F is stratigraphically separated from the rest of the tephra sequences by a ~6000 cal yr BP depositional hiatus (for more information see Chapter 3).

6.5 Discussion

6.5.1 Contrasting whole-lapilli compositions

A compositional difference of up to 2 wt% in several major elements between some tephra samples is noticed between the easterly and south-easterly sites of Tariki, Eltham and Ngaere, vs. north-easterly sites such as Lake Richmond (Fig. 6.2). In particular the major oxides affected include Fe_2O_3(t), CaO, K_2O, Al_2O_3 and MnO. Also minor elements such as V and Sr follow the same pattern. These samples also differ from lava, debris avalanche and pyroclastic whole-rock data sets from other studies (e.g., Price et al., 1999; Turner et al., 2011; Zernack et al., 2012a; Torres-Orozco et al., in review).

The differences in compositions are unlikely to be related to reductive dissolution processes, because glass compositions are not affected, yet volcanic glass is metastable and is generally the first phase to be chemically altered in settings such as anaerobic and acid peat bogs. It is inferred that the variation in these bulk compositions are related to variations in the mineral contents of the samples, and/or changes in the bulk magma composition. The whole rock data represents the weighted average of the heterogeneous crystal cargo and host melt. Considering Fe_2O_3(t), CaO, and Al_2O_3 are major oxides in plagioclase and pyroxene, which in turn are major phenocryst phases within the Mt. Taranaki rock suite, it is likely that the variation in the whole-lapilli composition could result from different modal proportions of these phases within the analysed lapilli fragments. Variation of these crystal proportions and variability in the bulk magma composition may arise from a stratified magma within the conduit.

A physical and/or chemical vertically zoned magma within the conduit prior eruption is not unusual at highly explosive volcanoes, such as Mt. Taranaki, where several complex sub-surface conditions and processes occur (e.g., concentrations of dissolved volatiles, bubbles and crystals; Pinkerton and Stevenson, 1992; Hess and Dingwell, 1996; Manga et al., 1998; Stevenson et al., 1998; conduit width, conduit shear processes or influx of external water; Barberi et al., 1989; Massol et al., 2001; Rust et al., 2003). During the course of a single eruption the eruption style (effusive vs. explosive) can shift abruptly (e.g., Houghton et al. 2004; Platz et al., 2007a; Shea et al., 2012), which can be associated with changes in magma composition (e.g., Lirer et al. 1973; Sigurdsson et al. 1982). Each eruption phase or pulse may correspond to individual layers within the conduit.

The compositional heterogeneities seen within some of the whole-lapilli samples may be a reflection of such stratified magma conduits where the upper, lowest-density, gas-rich layers may have different modal proportions of plagioclase ± pyroxene compared with deeper levels in the conduit. The selective dispersal of these components during subsequent eruption may occur, depending on the variability in height of an eruption column, in relation to different wind speeds and directions at different elevations. This may explain the east to south-east vs. north-east variations in composition. The gas-charged upper conduit magmas are more likely to produce the highest eruption columns, thus reaching stratospheric levels, where it is dispersed by high-level, predominantly westerly, winds (Salinger, 1984; Drost et al., 2007; Chappell, 2014) and/or the lateral expansion of an ash plume. The largest eruptions at Mt. Taranaki easily exceed 20 km in column height during their paroxysmal phases (Torres-Orozco et al., in review). By contrast, the northerly sites may have received tephra from pre- or post-climactic phases and/or from ash falls from the general column direction. Torres-Orozco et al. (in review), studying proximal sites also noted a wide range in compositions between the climactic-phase lapilli, and the samples deposited before or after.

A good example of this phenomenon is the Upper Inglewood eruption and its corresponding distal ash fall deposits (tephra Ri-40 in the north-easterly and tephra N-8

and E-8 in the south-easterly sites). All are diverse in their bed and grain-size characteristics (Chapter 3), and whole-lapilli compositions of the north-easterly site overlaps with the main proximal Inglewood whole-rock compositions, but the south-easterly sites units show predominantly higher CaO and lower Fe_2O_3(t) abundances than are seen in proximal sites (Table 1). Detailed eruption plume reconstructions of Torres-Orozco et al. (in review), show that the main Upper Inglewood plume was directed towards the north-east, but later as it grew in height it was then dispersed to the east by the constant high-level winds.

Table 6. 1 *Whole-lapilli composition for Upper Inglewood distal and proximal tephras.*

(wt%)	E-8	N-8	Ri-40	Upper Inglewood (proximal)*								
SiO_2	60.27	59.48	59.05	58.93	58.01	57.65	58.76	59.39	58.74	56.61	58.55	58.50	59.86
Al_2O_3	19.83	19.96	18.63	18.54	18.97	19.62	19.16	19.40	19.14	20.04	19.04	19.37	18.55
Fe_2O_3(t)	**2.79**	**2.94**	**5.96**	**6.01**	**6.23**	**5.77**	**6.16**	**5.83**	**6.08**	**6.97**	**6.47**	**6.05**	**5.68**
MgO	2.23	2.20	1.80	1.88	2.03	2.18	1.79	1.91	1.80	2.22	1.79	1.84	1.71
CaO	**7.86**	**8.06**	**6.94**	**6.95**	**7.28**	**7.66**	**6.58**	**6.13**	**6.69**	**7.26**	**6.58**	**6.76**	**6.45**
Na_2O	4.38	4.37	4.20	4.22	4.15	4.20	4.17	3.91	4.15	3.92	4.15	4.13	4.30
K_2O	2.05	2.03	2.38	2.38	2.22	1.97	2.31	2.34	2.32	1.80	2.36	2.27	2.43
TiO_2	0.39	0.52	0.60	0.62	0.65	0.59	0.62	0.66	0.62	0.73	0.63	0.63	0.60
P_2O_5	0.06	0.30	0.29	0.29	0.30	0.19	0.29	0.30	0.29	0.29	0.27	0.28	0.26
MnO	0.14	0.14	0.17	0.17	0.17	0.16	0.16	0.14	0.17	0.16	0.17	0.17	0.17

*Note: *proximal data from Torres-Orozco et al. (in review)*

6.5.2 Fractionation trends

Quantitative modelling of geochemical variations in major and trace element data for Mt. Taranaki andesites was recognised to be problematic in several previous studies (Stewart et al., 1996; Price et al., 1999, 2016; Zernack et al., 2012a). Compositions were shown to be poorly representative of simple liquid lines of ascent and hence are not solely controlled by simple crystal-melt fractionation (Eichelberger, 2006). It was suggested that these andesitic compositions were resulting from rising melts carrying crystals from a range of reservoir depths and derived by a number of processes, including FC (e.g., Bowen, 1928; Gill, 1981; Gamble et al., 1990; Grove et al., 2003), AFC (e.g., Grove and Kinzler, 1986; Graham and Hackett, 1987), and/or magma mingling/mixing (e.g., Eichelberger, 1978; Clynne, 1999; Tepley et al., 2000).

Mt. Taranaki's isotopic fingerprint (it has less evolved isotopic compositions; Price et al., 1999; Zernack et al., 2012a) is not consistent with extensive assimilation of older crust. The assimilant believed to be involved in AFC processes at Mt. Taranaki are granodiorite, diorite, and granitic rocks of the Median Batholith (emplacement ages ranging from Carboniferous to Early Cretaceous; Mortimer et al., 1999; Gruender et al., 2010; Price et al., 2016), which have similar geochemical compositions to rocks derived from within Mt. Taranaki's own magmatic system. This similarity is due to the Median Batholith representing the plutonic component of a long-lived subduction-related magmatic system (Price et al., 2011). The xenolith suite from the crustal section of Mt. Taranaki does not exhibit the typical degree of arc maturity (Gruender et al., 2010), since it is young (~170 ka; Zernack et al., 2011) and situated away from the main arc in a rear arc setting. Unless there is a great isotope and/or trace element contrast between magma and assimilant (like that of Ruapehu, Taupo Volcanic Zone; Graham and Hackett, 1987), AFC will not leave a recognizable imprint on the chemistry of magmas (DePaolo, 1981; Powell, 1984).

Compositional trends seen at Mt. Taranaki, therefore, could be explainable by FC and mixing/mingling as the main evolutionary processes. Here tephra compositions are used to model possible fractionation trends in Mt. Taranaki tephra data (Fig. 6.4, Table 6.2). The modelling was carried out with glass shard compositions, because they represent the last melt fraction shortly prior to eruption. One of the less-evolved Manganui samples (E-5; Table 6.2) was used as the mafic end member (note that this is likely to be a poor estimate of the mafic end member, since it is itself already relatively evolved and derived from a different vent – nevertheless, it represents the most mafic composition seen in the suite examined in this study). The first model involving clinopyroxene – amphibole – plagioclase – titanomagnetite crystal fractionation provides a reasonable fit for the major element chemistry of all samples <63 wt% SiO_2, with T-64 acting as the daughter composition (Table 6.2). In the second model, with sample T-64 as the parent, alkali-feldspar (sanidine/orthoclase) fractionation is required to gain the fractionating assemblages to derive constant alkali compositions with increasing SiO_2 contents, with Ri-34 acting as the daughter composition (Fig. 6.4).

While the modelling here suggests alkali feldspars are required as fractionating phases for the most evolved compositions (i.e., Tephra Sequence D, C, B, type-II of A), neither sanidine nor orthoclase is seen within the phenocryst assemblages of the tephra samples, but these phases may be present as microlites. Microlite growth during melt ascent at the onset of eruption is a common process in trachydacitic melt compositions, where equally more-evolved mineral phases start to form (Cashman, 1992; Blundy and Cashman, 2001; Genareau et al., 2007). The process of microlite crystallisation is not fractional crystallisation *sensu stricto*, because the crystals are not physically removed from the melt. However, slow diffusion between Ca-Al, Na-Si, and that of Na and K implies that equilibration is not achieved before eruption and glasses may be evolved from their original melt composition. Furthermore, heterogeneous conduit conditions may also favour some fractionation of microlites by the development of different viscosity domains associated with diverse rates of gas-supply and cross-conduit temperature fluctuations caused by solidification and heat transfer to conduit walls during magma ascent (c.f., Costa et al., 2007; Shea et al., 2012).

Table 6. 2 *Fractional crystallisation modelling of tephra chemistry at Mt. Taranaki.*

	Parent	Daughter observed	Daughter calculated	Mineral phases (30% Fractionation) *Turner et al. (2008a); Damaschke et al. (2017a)*				
	E-5	*T-64*						
Glass major elements (wt%)				Cpx (33%)	Plag 1 (22%)	Plag 2 (11%)	Amph (21%)	Tm (13%)
SiO_2	56.26	61.72	61.62	50.68	44.49	58.20	40.63	
Al_2O_3	16.11	17.05	16.42	2.67	34.01	24.62	15.00	7.92
$FeO_{(total)}$	7.94	5.03	5.31	7.85	0.27	0.66	10.60	78.36
MgO	3.23	1.38	1.27	15.40			14.40	4.33
CaO	6.64	3.18	3.78	22.02	18.34	7.27	12.00	
Na_2O	4.25	5.15	5.25	0.28	0.72	6.29	2.47	
K_2O	3.19	4.47	4.19	0.00	0.20	1.55	0.92	
TiO_2	1.05	0.92	0.93	0.66			1.91	5.78
P_2O_5	0.67	0.30	0.91					
MnO	0.31	0.21	0.34	0.25			0.46	0.56

Table 6.2 *(continued)*

	Parent *T-64*	Daughter observed *Ri-34*	Daughter calculated	Mineral phases (80.7% Fractionation) *Deer et al. (1992); Stewart et al. (1996); Turner et al. (2008a); Damaschke et al. (2017a)*						
Glass major elements (wt%)				Sanidine (43%)	Orthoclase (18%)	Cpx (3%)	Plag (18%)	Amph (9%)	Tm (8%)	Ilm (1%)
SiO_2	61.72	72.58	72.52	67.27	63.66	53.18	44.49	42.03		
Al_2O_3	17.05	14.19	14.41	18.35	19.54	1.36	34.01	10.72	3.74	0.21
$FeO_{(total)}$	5.03	1.36	0.85	0.92	0.10	6.71	0.27	11.67	75.52	51.23
MgO	1.38	0.21	0.48			15.27		13.87	3.45	2.63
CaO	3.18	0.92	0.45	0.15	0.50	21.26	18.34	10.82		0.14
Na_2O	5.15	4.39	7.72	6.45	0.80	1.23	0.72	2.56		
K_2O	4.47	5.56	2.34	7.05	15.60	0.00	0.20	1.10		
TiO_2	0.92	0.45	0.33			1.09		2.97	10.18	39.2
P_2O_5	0.30	-0.07	0.72							
MnO	0.21	0.09	0.31			0.31		0.61	0.92	1.08

Note: Cpx = clinopyroxene, Plag = plagioclase, Amph = amphibole, Tm = titanomagnetite, Ilm = ilmenite

According to Figure 6.9, if fractional crystallisation is the mechanism for chemical change, then it not only occurred at shallow depths characterised by microlite crystallisation, but also in deeper magma storage levels, since glass compositional variations correlate with those of the titanomagnetites. The strong correlation of MgO-whole-lapilli vs. MgO-titanomagnetite compositions (Fig. 6.9) also gives strong weight to this assumption. Stewart et al. (1996) described two titanomagnetite populations, one as inclusions within or clustered near magnesian olivine and clinopyroxene, indicating coeval and hence early crystallisation, and the other as small euhedral microphenocrysts. The titanomagnetites analysed in this study, derive mainly from phenocrysts (250-500 μm), glomerocrysts and/or inclusions within phenocrysts. Their compositions differ from the groundmass titanomagnetites described by Stewart et al. (1996) and are therefore believed to correspond to the first-formed titanomagnetite population. Stewart et al. (1996) used titanomagnetite-ilmenite pairs to estimate fO_2 conditions for the early formed titanomagnetites (ulvospinel), which were consistent with mantle and/or deep crustal source regions. Therefore, it is considered here that titanomagnetites analysed in this study crystallised at deep crustal levels. Temperature and pressure studies on amphibole (Stewart et al., 1996; Price et al., 2016) illustrate that it crystallised at various crustal levels and forms an important mineral phase in the evolution of Mt. Taranaki magmas. Decreasing Dy/Yb compositional trends within the

whole-lapilli dataset in this study indicates the presence and fractionation of amphibole (Fig. 6.2; c.f., Davidson et al., 2007).

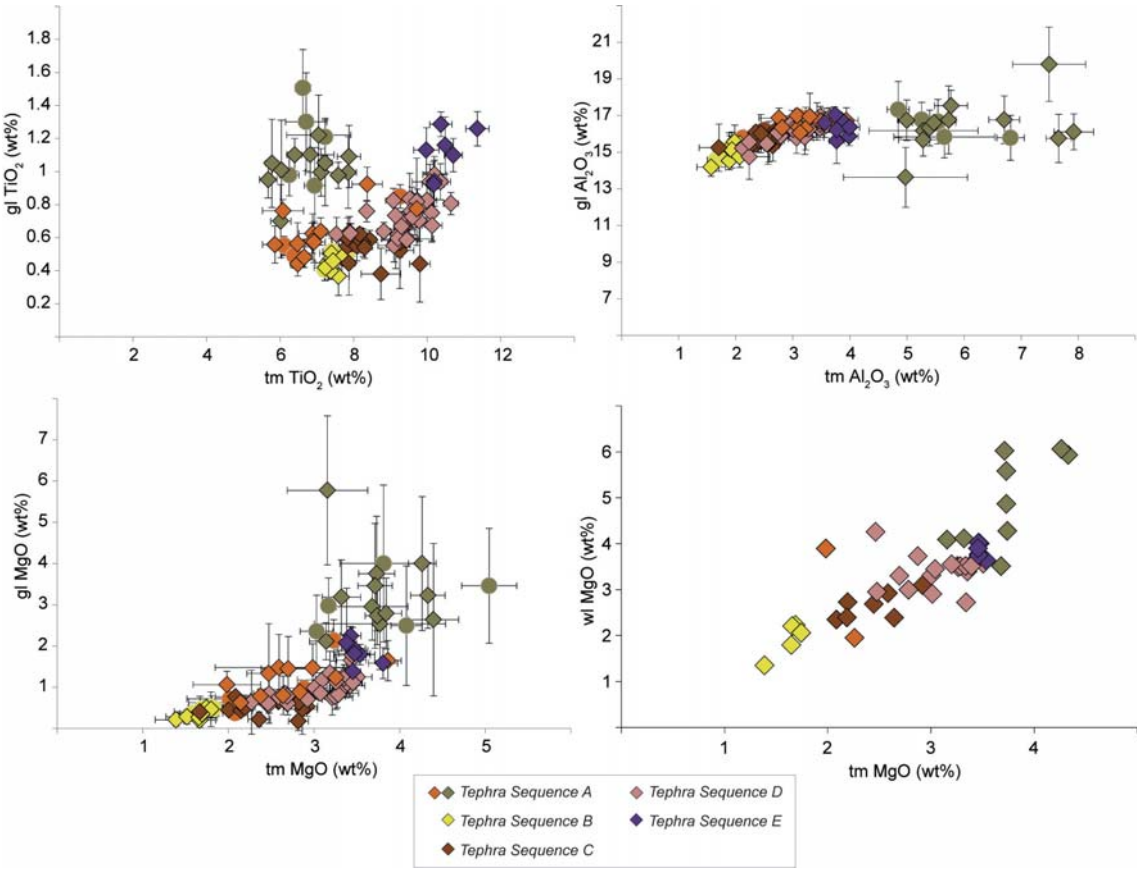

Figure 6. 9 *Major element glass (gl) vs. titanomagnetite (tm) abundances, and MgO whole-lapilli (wl) vs. MgO titanomagnetite (tm) abundances for Mt. Taranaki tephras. Diamonds represent lake and peat tephras (Damaschke et al., 2017a) and circles represent proximal tephra deposits (Damaschke et al., 2017b).*

6.5.3 Compositional variations: Implication for Mt. Taranaki's magmatic system

6.5.3.1 Whole-lapilli and glass trends

Fractional crystallisation models indicate that the glass compositional dataset does not represent original melt compositions, because significant late-stage microlite crystallisation occurred, typically pushing the residual glass compositions into dacitic or rhyolitic fields. Thus glass contrasts with the whole-lapilli chemistry which shows the alkali content increasing over time. In the glass, compositions are buffered (except for Manganui tephras and Fanthams Peak lava), probably by crystallisation of alkali-rich groundmass phases (such as alkali feldspars) in the final phases before and during eruption. An increasing K_2O content with time within the whole-lapilli analyses (highest content in Ri-6, Burrell, and Te Popo, <1 cal ka BP; Fig. 6.7) parallels that observed in previous studies of lava and debris avalanche samples (e.g., Stewart et al., 1996; Price et al., 1999; 2016; Zernack et al., 2012a). From inception of volcanism at Mt. Taranaki >170 ka, the gradual potassium enrichment is thought to reflect a progressive intrusion of basaltic magma into the lower crust (underplating), first forming and then breaking down metasomatised amphibole-rich intrusions (Foden and Green, 1992; Stewart et al., 1996). Over time, this formed a lower-crustal hot zone (c.f., Annnen et al., 2006). Progressively lower degrees of partial melting of the mantle source could also explain this change, but this would produce gradually smaller magma volumes, which is incompatible with the semi-continuous volumetric eruption rate seen at the volcano (Zernack et al., 2012b).

Using whole-lapilli compositions to model parental melt compositions is problematic if they contain many antecrysts or xenocrysts, such as postulated for most Mt. Taranaki rocks (Higgins, 1996; Platz et al., 2007a; Turner et al., 2008a, 2011; Martin, 2012). Petrological studies on these suites have shown complex sieved crystal textures and zoned textures, mainly within plagioclase and pyroxene, indicating many episodes of growth and stalling of those mineral phases within multiple depths and pressures during

rise to eruption, including within temporary mid-crustal reservoirs (often modelled between 6-10 km depth; Platz et al., 2007a; Turner et al., 2008a; Martin, 2012). With magma passing through these zones, there is also likely mixing and mingling with various generations of intrusion. This would lead to the large spread in plagioclase compositions observed and the occurrence of glomerocrysts in many samples. According to Price et al. (2005), 80% of Mt. Taranaki's xenoliths are cognate and formed as mafic to gabbroic cumulates within the magmatic system. Geothermobarometry on amphibole crystals within those cognate xenoliths indicate a crystallisation depth range of 3-21 km for group-1, 17-30 km for group-2 and 11-30 km for group-3 xenoliths (Price et al., 2016).

In summary, the magmas forming the Mt. Taranaki eruptions discussed here originate from mantle partial melts modified within a lower crustal hot zone or those originating from this zone (c.f., Annen et al., 2006), where restite, cumulate and/or wall-rock materials can be easily incorporated. A complex polybaric magma storage, recharge and mixing system then modifies these magmas to varying degrees during ascent (c.f., Turner et al., 2008a; Price et al., 2005, 2012; Zernack et al., 2012a).

6.5.3.2 Titanomagnetite trends

The formation and behaviour of titanomagnetites within magma storage and plumbing systems is as yet poorly understood. Titanomagnetite (solid-solution between magnetite and ulvöspinel) compositions can be formed under a range of pressures, temperatures and oxygen fugacities (fO_2) (e.g., Buddington and Lindsley, 1964; Hill and Roeder 1974; Spencer and Lindsley, 1981; Frost and Lindsley, 1991; Ghiorso and Sack, 1991; Toplis and Carroll, 1995; Tomiya and Takahashi, 2005). Some experimental investigators have documented that increasing temperature at constant fO_2 or decreasing fO_2 at constant temperature results in an increase in TiO_2 contents within the titanomagnetite structure (Frost and Lindsley, 1991; Devine et al., 2003). In contrast, the behaviour of MgO and Al_2O_3 is dependent on the actual source composition and crystallisation stage of the surrounding magma (Tomiya and Takahashi, 2005). Abundant amphibole ± pyroxene ± olivine crystallisation could lead to a decrease of

MgO and to a lesser extent Al_2O_3 within the melt and thus would therefore be less available for subsequent titanomagnetite crystallisation.

Further, Turner et al. (2008b) has shown that under relative slow cooling and oxidising condition, such as dome-forming processes, titanomagnetites may exsolve and solid-state migration of Ti may occur (Buddington and Lindsley, 1964). The exsolution of titanomagnetite grains will form trellises of ilmenite and magnetite, which have extremely increased TiO_2 contents (up to 30 wt%; Turner et al., 2008b) compared to their host and hence are readily recognised not only by resulting heterogeneous compositions, but often under backscatter electron imaging during analysis due to highly contrasting exsolved lamina. Such grains were excluded from the analyses of this study. Solid-state migration of some components, e.g., Ti may occur relatively rapidly under some conditions, leaving no exsolution signatures, however, the timescales of rise and eruption of the Mt. Taranaki samples analysed here are considered to be too short for such processes to occur.

As mentioned above, titanomagnetites analysed probably fractionated within the deep crust, and hence, compositional trends observed over time (Figs. 6.5, 6.7) may reflect recharge processes and ongoing evolution of a magma complex at deep crustal levels (e.g., hot zone, c.f., Annen et al., 2006). The overall decreasing trend of TiO_2, MgO and Al_2O_3 abundances from Tephra Sequence E (group-1 titanomagnetites) to B (group-10 titanomagnetites), from 17.5 to 3 cal ka BP (Figs. 6.5, 6.7), may indicate a progressively evolving and cooling magma source region (hot-zone). However, small-scale variations in magmas erupted over time (seen in the small-scale variations of titanomagnetite compositions; Fig. 6.7) show that there were spatially separate magma zones active within the overall source region. These zones erupted magmas (i.e., magma batches) successively, at times with considerable overlap during transitions from one to the next. Some batches were erupted over long periods (e.g., group-1, -2, -3, -8 titanomagnetites) while others were erupted in only brief intervals (e.g., group-10, -4, -5 titanomagnetites) (Fig. 6.8). Secondary trends observed within each titanomagnetite group (e.g., each magma batch; Fig. 6.5), show that each magma batch was spatially isolated and underwent systematic internal evolution parallel with possibly neighbouring source

regions. These within-batch variations may also reflect changing magma compositions during stalling in shallow crustal storage and magma ascent. Titanomagnetite bimodalities, for example seen for several tephra layers within the lower Tephra Sequence C (8-6.5 cal ka BP), likely point to distinct mixing events between batches. The sub-population involved in this bimodality has similar compositions to younger Manganui eruptives with higher Al_2O_3 and lower TiO_2 contents (Fig. 6.8) and may therefore represent a less-evolved, more hydrous magma recharging and mixing with more-evolved batches (group-8 and -3 titanomagnetites).

The overall evolutional trend from 17.5 to 3 cal ka BP is in agreement with whole-lapilli and glass compositional trends (Fig. 6.7). Zernack et al. (2012a) postulated several evolving time-series trends within sequences of debris avalanche deposits (<170 ka). These were observed as separate linear evolutionary trends within rock suites erupted over ~10-30 kyr-long episodes of regrowth after major edifice collapse events (see
Fig. 7 in Zernack et al., 2012a). The observed evolutional trend in tephras of this study may thus represent one such magmatic regrowth cycle since the largest debris avalanche known from Mt. Taranaki, the ~25 ka Pungarehu Debris Avalanche (Zernack et al., 2011).

The occurrence of a significant increase in MgO and Al_2O_3 with constant low TiO_2 contents at 3 cal ka BP at the beginning of Tephra Sequence A (i.e., Manganui tephras; Fig. 6.8) is a distinctive change. This may indicate 1) a different magma source region or 2) a significant recharge event of hotter, more hydrous, and less-crystalline magma. Notably this eruption sequence was sourced from a new vent, the Fanthams Peak on southern Mt. Taranaki and not the summit region. It intercalates with group-12 titanomagnetite tephras (from the summit), which show similar low TiO_2 contents, but slightly more increased Al_2O_3 and MgO contents (Fig. 6.8). This implies that latter tephras may represent the evolved member of the Manganui magmas, possibly forming a new evolutional trend.

Possible triggers for this shift may be diverse, such as a shift in the tectonic regime allowing dyke propagation and/or initiation, such as movement of the Inglewood Fault, which is known to have ruptured near this time (Hull, 1994), or it may represent underlying magmatic processes such as recharge events or migration of the source region within a lower crustal hot zone (c.f., Turner et al., 2008a; Kent et al., 2010).

6.5.3.3 An exploratory study of the use of LA-ICP-MS techniques to fingerprint titanomagnetites

Most of the previous studies on Fe-Ti oxides employed electron microprobe (EMP) analysis, which measures a limited number of major and minor elements such as Mg, Al, Ca, Ti, V, Cr and Mn with a relatively high detection limit of ~0.01 wt% and a small beam diameter of normally <5 μm (e.g., Beaudoin and Dupuis, 2009; Dare et al., 2012; Marcaida et al., 2014). More recent studies focused on laser ablation–inductively coupled plasma–mass spectrometry (LA-ICP-MS), which allowed in-situ measurement of a larger number of minor and trace elements with relatively low detection limit of ~1 ppm (e.g., Nadoll and Koenig, 2011; Dare et al., 2014; Liu et al., 2015). This requires larger spot sizes, which means inhomogeneities in titianomagnetite grains first need to be understood. Following this, the behaviour of these elements within the complex iron-oxide spinel structure remains poorly understood. The likelihood of substitution depends on many parameters including the similarity of the ionic radii and the valence of the cations, oxygen fugacity, magma composition, and temperature (Buddington and Lindsley, 1964, Frost and Lindsley, 1991, Goldschmidt, 1937, Lindsley, 1991 and Toplis and Carroll, 1995).

The data in this study demonstrates that the minor and trace element compositions of titanomagnetites appear to give an indication of the stage of differentiation of the liquid from which the minerals crystallized. Less-evolved titanomagnetites (e.g., group-1, -2, and -11 titanomagnetites) contain a greater amount of V, Co, S, Sc, Ga, Ni, and Ge than titanomagnetites that are more-evolved (e.g., group-10 titanomagnetites) and formed at later stages of differentiation (Fig. 6.6). Hence, compositional trends observed for those elements appear to fall into the same evolutionary trends seen for the major elements

above and may reflect on the concentration of those elements in the host melt and/or different partitioning of the elements between melt and crystal controlled by magma condition as well as temperature and oxygen fugacity during magma evolution.

6.6 Conclusions

Detailed geochemical observations of a 30,000 cal yr BP-long sequence of tephra deposits were used to investigate time-related compositional variation at Mt. Taranaki, and infer processes that drive magma rise, fractionation, evolution and eruption.

Whole-lapilli major and trace element analyses have highlighted that most of the easterly to south-easterly dispersed tephra layers have compositions contrasting to their equivalent-aged units dispersed to the north-east, as well as to the overall bulk-compositions observed in previous studies on lavas, debris avalanches and proximal pyroclastic deposits. This is explained by eruption of a stratified magma reservoir, which holds greater modal proportions of plagioclase and lower proportions of pyroxene within low-density, gas-rich upper conduit regions. During the most explosive phases of eruptions, when plumes reach the stratospheric jet-stream the lowest-density pumice is thus dispersed by high-level predominantly westerly winds.

Glass shard compositions are overprinted by late-stage alkali-rich microlite crystallisation, pushing the residual glass compositions into dacitic or rhyolitic fields. In contrast to whole-lapilli compositions, which show increasing alkali contents, particular potassium, with time. This is consistent with previous observations, where a K_2O-enrichment is believed to stem from the systematically underplated lower crust and hence greater incorporation of amphibole-bearing phases.

Titanomagnetite analyses showed two consistent evolutional trends. The first trend from 17.5 to 3 cal ka BP is believed to reflect on a progressively evolving and cooling magma source (hot-zone) with multiple, spatially separated magma source regions forming, each generating magma batches with unique titanomagnetite compositions

(e.g., group-1 to group-10 titanomagnetites). At 3 cal ka BP a significant shift towards less-evolved compositions occurs, with the prominent Manganui eruptions sourced from Fanthams Peak as the initial events intercalating with slightly more evolved andesitic deposits sourced from the main vent. This shift is believed to represent a different magma source and thus could reflect a significant recharge event or indicate the beginning of migration of the magma-supply system below the volcano. The direction of its migration (to the SSE) is consistent with the overall age-spatial trend of volcanism of the Taranaki Volcanic Lineament.

6.7 References

Albert, P. G., Tomlinson, E. L., Smith, V. C., Di Roberto, A., Todman, A., Rosi, M., Marani, M., Muller, W., & Menzies, M. A. (2012). Marine-continental tephra correlations: volcanic glass geochemistry from the Marsili Basin and the Aeolian Islands, Southern Tyrrhenian Sea, Italy. Journal of Volcanology and Geothermal Research, 229, 74-94.

Allan, A. S., Baker, J. A., Carter, L., & Wysoczanksi, R. J. (2008). Reconstructing the Quaternary evolution of the world's most active silicic volcanic system: insights from an~ 1.65 Ma deep ocean tephra record sourced from Taupo Volcanic Zone, New Zealand. Quaternary Science Reviews, 27(25), 2341-2360.

Annen, C., & Sparks, R. S. J. (2002). Effects of repetitive emplacement of basaltic intrusions on thermal evolution and melt generation in the crust. Earth and Planetary Science Letters, 203(3), 937-955.

Annen, C., Blundy, J. D., & Sparks, R. S. J. (2006). The genesis of intermediate and silicic magmas in deep crustal hot zones. Journal of Petrology, 47(3), 505-539.

Arculus, R. J., & Powell, R. (1986). Source component mixing in the regions of arc magma generation. Journal of Geophysical Research: Solid Earth, 91(B6), 5913-5926.

Barberi, F., Cioni, R., Rosi, M., Santacroce, R., Sbrana, A., & Vecci, R. (1989). Magmatic and phreatomagmatic phases in explosive eruptions of Vesuvius as deduced by grain-size and component analysis of the pyroclastic deposits. Journal of Volcanology and Geothermal Research, 38(3-4), 287-307.

Beaudoin, G., & Dupuis, C. (2009). Iron-oxide trace element fingerprinting of mineral deposit types. Exploring for iron oxide copper–gold deposits: Canada and global analogues. GAC Short Course Notes, 107-121.

Best, M.G. (2003). Igneous and Metamorphic Petrology. Blackwell Science.

Blundy, J., & Cashman, K. (2001). Ascent-driven crystallisation of dacite magmas at Mount St Helens, 1980–1986. Contributions to Mineralogy and Petrology, 140(6), 631-650.

Blundy, J., & Cashman, K. (2008). Petrologic reconstruction of magmatic system variables and processes. Reviews in Mineralogy and Geochemistry, 69(1), 179-239.

Bourne, A. J., Lowe, J. J., Trincardi, F., Asioli, A., Blockley, S. P. E., Wulf, S., Matthews, I.P., Piva, A., & Vigliotti, L. (2010). Distal tephra record for the last ca 105,000 years from core PRAD 1-2 in the central Adriatic Sea: implications for marine tephrostratigraphy. Quaternary Science Reviews, 29(23), 3079-3094.

Bowen, N. L. (1928). Evolution of the igenous rocks. Princeton University Press, Princeton, New Jersey.

Braitseva, O. A., Ponomareva, V. V., Sulerzhitsky, L. D., Melekestsev, I. V., & Bailey, J. (1997). Holocene key-marker tephra layers in Kamchatka, Russia. Quaternary Research, 47(2), 125-139.

Brenan, J. M., Shaw, H. F., Ryerson, F. J., & Phinney, D. L. (1995). Mineral-aqueous fluid partitioning of trace elements at 900 C and 2.0 GPa: Constraints on the trace element chemistry of mantle and deep crustal fluids. Geochimica et Cosmochimica Acta, 59(16), 3331-3350.

Bryant, C. J., Arculus, R. J., & Eggins, S. M. (1999). Laser ablation–inductively coupled plasma–mass spectrometry and tephras: a new approach to understanding arc-magma genesis. Geology, 27(12), 1119-1122.

Bryant, C. J., Arculus, R. J., & Eggins, S. M. (2003). The geochemical evolution of the Izu-Bonin arc system: A perspective from tephras recovered by deep-sea drilling. Geochemistry, Geophysics, Geosystems, 4(11).

Buddington, A. F., & Lindsley, D. H. (1964). Iron–titanium oxide minerals and synthetic equivalents. Journal of Petrology, 5(2), 310-357.

Carmichael, I. S. E. (1966). Iron-titanium oxides of salic volcanic rocks and their associated ferromagnesian silicates. Contributions to Mineralogy and Petrology, 14(1), 36-64.

Cashman, K. V. (1992). Groundmass crystallisation of Mount St. Helens dacite, 1980–1986: a tool for interpreting shallow magmatic processes. Contributions to Mineralogy and Petrology, 109(4), 431-449.

Chappell, P. R. (2014). The climate and weather of Taranaki. 2nd edition, NIWA Science and Technology Series, 64.

Clift, P. D., Layne, G. D., Najman, Y. M., Kopf, A., Shimizu, N., & Hunt, J. (2003). Temporal evolution of boron flux in the NE Japan and Izu arcs measured by ion

microprobe from the forearc tephra record. Journal of Petrology, 44(7), 1211-1236.

Clift, P. D., Chan, L. H., Blusztajn, J., Layne, G. D., Kastner, M., & Kelly, R. K. (2005). Pulsed subduction accretion and tectonic erosion reconstructed since 2.5 Ma from the tephra record offshore Costa Rica. Geochemistry, Geophysics, Geosystems, 6(9).

Collen, J. D., Neall, V. E., & Johnston, J. H. (1985). Sandstone xenoliths in the Pungarehu Formation, western Taranaki, New Zealand: implications for petroleum exploration. Journal of the Royal Society of New Zealand, 15(2), 201-212.

Costa, A., Melnik, O., & Sparks, R. S. J. (2007). Controls of conduit geometry and wallrock elasticity on lava dome eruptions. Earth and Planetary Science Letters, 260(1), 137-151.

Cronin, S. J., Wallace, R. C., & Neall, V. E. (1996). Sourcing and identifying andesitic tephras using major oxide titanomagnetite and hornblende chemistry, Egmont volcano and Tongariro Volcanic Centre, New Zealand. Bulletin of Volcanology, 58(1), 33-40.

Damaschke, M., Cronin, S. J., Holt, K. A., Bebbington, M. S., & Hogg, A. G. (2017a). A 30,000 yr high-precision eruption history for the andesitic Mt. Taranaki, North Island, New Zealand. Quaternary Research, 1-23. DOI:10.1017/qua.2016.11

Damaschke, M., Cronin, S. J., Torres-Orozco, R., Wallace, R. C. (2017b). Unifying tephrostratigraphic approaches to redefine major Holocene marker tephras, Mt. Taranaki, New Zealand. Journal of Volcanology and Geothermal Research, doi:10.1016/j.jvolgeores.2017.02.021.

Dare, S. A., Barnes, S. J., & Beaudoin, G. (2012). Variation in trace element content of magnetite crystallized from a fractionating sulfide liquid, Sudbury, Canada: implications for provenance discrimination. Geochimica et Cosmochimica Acta, 88, 27-50.

Dare, S. A., Barnes, S. J., Beaudoin, G., Méric, J., Boutroy, E., & Potvin-Doucet, C. (2014). Trace elements in magnetite as petrogenetic indicators. Mineralium Deposita, 49(7), 785-796.

Davidson, J. P., Hora, J. M., Garrison, J. M., & Dungan, M. A. (2005). Crustal forensics in arc magmas. Journal of Volcanology and Geothermal Research, 140(1), 157-170.

Davidson, J. P., Turner, S., Handley, H., Macpherson, C., & Dosseto, A. (2007). Amphibole “sponge” in arc crust?. Geology, 35(9), 787-790.

Deer, W. A., Howie, R. A., & Zussman, J. (1992). An introduction to the rock-forming minerals (Vol. 696). London: Longman.

DePaolo, D. J. (1981). Trace element and isotopic effects of combined wallrock assimilation and fractional crystallisation. Earth and Planetary Science Letters, 53(2), 189-202.

DePaolo, D. J., Perry, F. V., & Baldridge, W. S. (1992). Crustal versus mantle sources of granitic magmas: a two-parameter model based on Nd isotopic studies. Geological Society of America Special Papers, 272, 439-446.

Devine, J. D., Rutherford, M. J., Norton, G. E., & Young, S. R. (2003). Magma storage region processes inferred from geochemistry of Fe–Ti oxides in andesitic magma, Soufriere Hills Volcano, Montserrat, WI. Journal of Petrology, 44(8), 1375-1400.

Drost, F., Renwick, J., Bhaskaran, B., Oliver, H., & McGregor, J. (2007). A simulation of New Zealand's climate during the Last Glacial Maximum. Quaternary Science Reviews, 26(19), 2505-2525.

Edwards, C., Menzies, M., & Thirlwall, M. (1991). Evidence from Muriah, Indonesia, for the interplay of supra-subduction zone and intraplate processes in the genesis of potassic alkaline magmas. Journal of Petrology, 32(3), 555-592.

Eggins, S. M., Rudnick, R. L., & McDonough, W. F. (1998). The composition of peridotites and their minerals: a laser-ablation ICP–MS study. Earth and Planetary Science Letters, 154(1), 53-71.

Eichelberger, J. C. (1978). Andesitic volcanism and crustal evolution. Nature, 275, 21-27.

Eichelberger, J. C., Izbekov, P. E., & Browne, B. L. (2006). Bulk chemical trends at arc volcanoes are not liquid lines of descent. Lithos, 87(1), 135-154.

Erlund, E. J., Cashman, K. V., Wallace, P. J., Pioli, L., Rosi, M., Johnson, E., & Granados, H. D. (2010). Compositional evolution of magma from Parícutin Volcano, Mexico: the tephra record. Journal of Volcanology and Geothermal Research, 197(1), 167-187.

Foden, J. D., & Varne, R. (1980). The petrology and tectonic setting of Quaternary—Recent volcanic centres of Lombok and Sumbawa, Sunda arc. Chemical Geology, 30(3), 201-226.

Foden, J. D., & Green, D. H. (1992). Possible role of amphibole in the origin of andesite: some experimental and natural evidence. Contributions to Mineralogy and Petrology, 109(4), 479-493.

Frost, B. R., & Lindsley, D. H. (1991). Occurrence of iron-titanium oxides in igneous rocks. Reviews in Mineralogy and Geochemistry, 25(1), 433-468.

Gamble, J. A., Smith, I. E., Graham, I. J., Kokelaar, B. P., Cole, J. W., Houghton, B. F., & Wilson, C. J. (1990). The petrology, phase relations and tectonic setting of basalts from the Taupo Volcanic Zone, New Zealand and the Kermadec Island

Arc-Havre Trough, SW Pacific. Journal of Volcanology and Geothermal Research, 43(1-4), 253-270.

Gehrels, M. J., Newnham, R. M., Lowe, D. J., Wynne, S., Hazell, Z. J., & Caseldine, C. (2008). Towards rapid assay of cryptotephra in peat cores: review and evaluation of various methods. Quaternary International, 178(1), 68-84.

Genareau, K., Hervig, R., & Clarke, A. (2007). Geochemical variations in late-stage growth of volcanic phenocrysts revealed by SIMS depth-profiling. American Mineralogist, 92(8-9), 1374-1382.

Gertisser, R., & Keller, J. (2003). Temporal variations in magma composition at Merapi Volcano (Central Java, Indonesia): magmatic cycles during the past 2000 years of explosive activity. Journal of Volcanology and Geothermal Research, 123(1), 1-23.

Ghiorso, M. S., & Sack, O. (1991). Fe-Ti oxide geothermometry: thermodynamic formulation and the estimation of intensive variables in silicic magmas. Contributions to Mineralogy and Petrology, 108(4), 485-510.

Gill, J. (1981). Orogenic andesites and plate tectonics. Springer-Verlag, Berlin, p. 390.

Goldschmidt, V. M. (1937). The principles of distribution of chemical elements in minerals and rocks. The seventh Hugo Müller Lecture, delivered before the Chemical Society on March 17th, 1937. Journal of the Chemical Society (Resumed), 655-673.

Graham, I. J., & Hackett, W. R. (1987). Petrology of calc-alkaline lavas from Ruapehu Volcano and related vents, Taupo Volcanic Zone, New Zealand. Journal of Petrology, 28(3), 531-567.

Grove, T. L., & Kinzler, R. J. (1986). Petrogenesis of andesites. Annual Review of Earth and Planetary Sciences 14, 417-454.

Grove, T. L., Elkins-Tanton, L. T., Parman, S. W., Chatterjee, N., Müntener, O., & Gaetani, G. A. (2003). Fractional crystallisation and mantle-melting controls on calc-alkaline differentiation trends. Contributions to Mineralogy and Petrology, 145(5), 515-533.

Gruender, K. (2006). Petrography and mineral chemistry of a xenolith suite from Mt. Taranaki, New Zealand: Insights into the sub-volcanic lithosphere of an arc volcano. Unpublished Diploma thesis. Johannes-Gutenberg-Universität Mainz, Bundesrepublik Deutschland.

Gruender, K., Stewart, R. B., & Foley, S. (2010). Xenoliths from the sub-volcanic lithosphere of Mt Taranaki, New Zealand. Journal of Volcanology and Geothermal Research, 190(1), 192-202.

Gudmundsdóttir, E. R., Larsen, G., & Eiríksson, J. (2012). Tephra stratigraphy on the North Icelandic shelf: extending tephrochronology into marine sediments off North Iceland. Boreas, 41(4), 719-734.

Harvey, P. K., Taylor, D. M., Hendry, R. D., & Bancroft, F. (1973). An accurate fusion method for the analysis of rocks and chemically related materials by X-ray fluorescence spectrometry. X-Ray Spectrometry, 2(1), 33-44.

Hawkesworth, C. J., Norry, M. J., Roddick, J. C., Baker, P. E., Francis, P. W., & Thorpe, R. S. (1979). 143Nd/144Nd, 87Sr/86Sr, and incompatible element variations in calc-alkaline andesites and plateau lavas from South America. Earth and Planetary Science Letters, 42(1), 45-57.

Hess, K. U., & Dingwell, D. D. (1996). Viscosities of hydrous leucogranitic melts: A non-Arrhenian model. American Mineralogist, 81(9-10), 1297-1300.

Higgins, M. D. (1996). Crystal size distributions and other quantitative textural measurements in lavas and tuff from Egmont volcano (Mt. Taranaki), New Zealand. Bulletin of Volcanology, 58(2), 194-204.

Hildreth, W., & Moorbath, S. (1988). Crustal contributions to arc magmatism in the Andes of central Chile. Contributions to Mineralogy and Petrology, 98(4), 455-489.

Hill, R., & Roeder, P. (1974). The crystallisation of spinel from basaltic liquid as a function of oxygen fugacity. Journal of Geology, 709-729.

Houghton, B. F., Wilson, C. J. N., Del Carlo, P., Coltelli, M., Sable, J. E., & Carey, R. (2004). The influence of conduit processes on changes in style of basaltic Plinian eruptions: Tarawera 1886 and Etna 122 BC. Journal of Volcanology and Geothermal Research, 137(1), 1-14.

Hull, A. G. (1994). Past earthquake timing and magnitude along the Inglewood Fault, Taranaki, New Zealand. Bulletin of the New Zealand National Society for Earthquake Engineering, 27(2), 155Á162.

Kelemen, P. B., Hanghøj, K., & Greene, A. R. (2003). One view of the geochemistry of subduction-related magmatic arcs, with an emphasis on primitive andesite and lower crust. Treatise on Geochemistry, 3, 593-659.

Kessel, R., Schmidt, M. W., Ulmer, P., & Pettke, T. (2005). Trace element signature of subduction-zone fluids, melts and supercritical liquids at 120–180 km depth. Nature, 437(7059), 724-727.

King, P. R., & Thrasher, G. P. (1996). Cretaceous Cenozoic geology and petroleum systems of the Taranaki Basin, New Zealand (Vol. 2). Institute of Geological & Nuclear Sciences.

Kuno, H. (1968). Differentiation of basalt magmas. Basalts, 2(3), 623-688.

Le Bas, M. J., Le Maitre, R. W., Streckeisen, A., & Zanettin, B. (1986). A chemical classification of volcanic rocks based on the total alkali-silica diagram. Journal of Petrology, 27(3), 745-750.

Lee, J., Stern, R. J., & Bloomer, S. H. (1995). Forty million years of magmatic evolution in the Mariana arc: The tephra glass record. Journal of Geophysical Research: Solid Earth, 100(B9), 17671-17687.

Le Maitre, R. W., Streckeisen, A., Zanettin, B., Le Bas, M. J., Bonin, B., Bateman, P., Bellieni, G., Dudek, A., Efremova, S., Keller, J., & Lameyre, J. (2002). Igneous rocks: A classification and glossary of terms; Recommendations of the International Union of Geological Sciences. In Subcommission on the Systematics of Igneous rocks. Cambridge University Press.

Lindsley, D. H. (1991). Experimental studies of oxide minerals. Reviews in Mineralogy and Geochemistry, 25(1), 69-106.

Lirer, L., Pescatore, T., Booth, B., & Walker, G. P. (1973). Two plinian pumice-fall deposits from Somma-Vesuvius, Italy. Geological Society of America Bulletin, 84(3), 759-772.

Liu, P. P., Zhou, M. F., Chen, W. T., Gao, J. F., & Huang, X. W. (2015). In-situ LA-ICP-MS trace elemental analyses of magnetite: Fe–Ti–(V) oxide-bearing mafic–ultramafic layered intrusions of the Emeishan Large Igneous Province, SW China. Ore Geology Reviews, 65, 853-871.

Manga, M., Castro, J., Cashman, K. V., & Loewenberg, M. (1998). Rheology of bubble-bearing magmas. Journal of Volcanology and Geothermal Research, 87(1), 15-28.

Marcaida, M., Mangan, M. T., Vazquez, J. A., Bursik, M., & Lidzbarski, M. I. (2014). Geochemical fingerprinting of Wilson Creek formation tephra layers (Mono Basin, California) using titanomagnetite compositions. Journal of Volcanology and Geothermal Research, 273, 1-14.

Martin, S. A. (2012). Crystal Specific Constraints on Subvolcanic Processes Preceding Eruptions at Mt Taranaki, New Zealand. Unpublished Master thesis, Victoria University of Wellington, New Zealand.

Massol, H., Jaupart, C., & Pepper, D. (2001). Ascent and decompression of viscous vesicular magma in a volcanic conduit. Journal of Geophysical Research-Solid Earth, 106(B8), 16223.

McCulloch, M. T., & Gamble, J. A. (1991). Geochemical and geodynamical constraints on subduction zone magmatism. Earth and Planetary Science Letters, 102(3-4), 358-374.

Mortimer, N., Tulloch, A. J., & Ireland, T. R. (1997). Basement geology of Taranaki and Wanganui Basins, New Zealand. New Zealand Journal of Geology and Geophysics, 40(2), 223-236.

Mortimer, N., Gans, P., Calvert, A., & Walker, N. (1999). Geology and thermochronometry of the east edge of the Median Batholith (Median Tectonic

Zone): a new perspective on Permian to Cretaceous crustal growth of New Zealand. Island Arc, 8(3), 404-425.

Muir, R. J., Ireland, T. R., Weaver, S. D., Bradshaw, J. D., Evans, J. A., Eby, G. N., & Shelley, D. (1998). Geochronology and geochemistry of a Mesozoic magmatic arc system, Fiordland, New Zealand. Journal of the Geological Society, 155(6), 1037-1053.

Nadoll, P., & Koenig, A. E. (2011). LA-ICP-MS of magnetite: methods and reference materials. Journal of Analytical Atomic Spectrometry, 26(9), 1872-1877.

Neall, V. E., Stewart, R. B., & Smith, I. E. M. (1986). History and petrology of the Taranaki volcanoes. Royal Society of New Zealand Bulletin, 23, 251-263.

Nicholls, I. A., & Whitford, D. J. (1983). Potassium-rich volcanic rocks of the Muriah complex, Java, Indonesia: products of multiple magma sources?. Journal of Volcanology and Geothermal Research, 18(1-4), 337-359.

Óladóttir, B. A., Sigmarsson, O., Larsen, G., & Devidal, J. L. (2011). Provenance of basaltic tephra from Vatnajökull subglacial volcanoes, Iceland, as determined by major-and trace-element analyses. The Holocene, 21(7), 1037-1048.

Paterne, M., Guichard, F., & Labeyrie, J. (1988). Explosive activity of the South Italian volcanoes during the past 80,000 years as determined by marine tephrochronology. Journal of Volcanology and Geothermal Research, 34(3), 153-172.

Pearce, J. A. (1982). Trace element characteristics of lavas from destructive plate boundaries. Andesites, 8, 525-548.

Pearce, N. J., Eastwood, W. J., Westgate, J. A., & Perkins, W. T. (2002). Trace-element composition of single glass shards in distal Minoan tephra from SW Turkey. Journal of the Geological Society, 159(5), 545-556.

Petford, N., & Atherton, M. (1996). Na-rich partial melts from newly underplated basaltic crust: the Cordillera Blanca Batholith, Peru. Journal of Petrology, 37(6), 1491-1521.

Pillans, B., McGlone, M., Palmer, A., Mildenhall, D., Alloway, B., & Berger, G. (1993). The Last Glacial Maximum in central and southern North Island, New Zealand: a paleoenvironmental reconstruction using the Kawakawa Tephra Formation as a chronostratigraphic marker. Palaeogeography, Palaeoclimatology, Palaeoecology, 101(3), 283-304.

Pinkerton, H., & Stevenson, R. J. (1992). Methods of determining the rheological properties of magmas at sub-liquidus temperatures. Journal of Volcanology and Geothermal Research, 53(1-4), 47-66.

Platz, T., Cronin, S. J., Cashman, K. V., Stewart, R. B., & Smith, I. E. (2007a). Transition from effusive to explosive phases in andesite eruptions—A case-

study from the AD1655 eruption of Mt. Taranaki, New Zealand. Journal of Volcanology and Geothermal Research, 161(1), 15-34.

Platz, T., Cronin, S. J., Smith, I. E., Turner, M. B., & Stewart, R. B. (2007b). Improving the reliability of microprobe-based analyses of andesitic glasses for tephra correlation. The Holocene, 17(5), 573-583.

Ponomareva, V., Portnyagin, M., Pevzner, M., Blaauw, M., Kyle, P., & Derkachev, A. (2015). Tephra from andesitic Shiveluch volcano, Kamchatka, NW Pacific: chronology of explosive eruptions and geochemical fingerprinting of volcanic glass. International Journal of Earth Sciences, 104(5), 1459-1482.

Powell, R. (1984). Inversion of the assimilation and fractional crystallisation (AFC) equations; characterization of contaminants from isotope and trace element relationships in volcanic suites. Journal of the Geological Society, 141(3), 447-452.

Preece, S. J., Westgate, J. A., Alloway, B. V., & Milner, M. W. (2000). Characterization, identity, distribution, and source of late Cenozoic tephra beds in the Klondike district of the Yukon, Canada. Canadian Journal of Earth Sciences, 37(7), 983-996.

Price, R. C., McCulloch, M. T., Smith, I. E. M., & Stewart, R. B. (1992). Pb-Nd-Sr isotopic compositions and trace element characteristics of young volcanic rocks from Egmont Volcano and comparisons with basalts and andesites from the Taupo Volcanic Zone, New Zealand. Geochimica et Cosmochimica Acta, 56(3), 941-953.

Price, R. C., Stewart, R. B., Woodhead, J. D., & Smith, I. E. M. (1999). Petrogenesis of high-K arc magmas: evidence from Egmont volcano, North Island, New Zealand. Journal of Petrology, 40(1), 167-197.

Price, R. C., Gamble, J. A., Smith, I. E., Stewart, R. B., Eggins, S., & Wright, I. C. (2005). An integrated model for the temporal evolution of andesites and rhyolites and crustal development in New Zealand's North Island. Journal of Volcanology and Geothermal Research, 140(1), 1-24.

Price, R., Spandler, C., Arculus, R., & Reay, A. (2011). The Longwood igneous complex, Southland, New Zealand: a Permo-Jurassic, intra-oceanic, subduction-related, I-type batholithic complex. Lithos, 126(1), 1-21.

Price, R. C., Gamble, J. A., Smith, I. E., Maas, R., Waight, T., Stewart, R. B., & Woodhead, J. (2012). The anatomy of an Andesite volcano: a time–stratigraphic study of andesite petrogenesis and crustal evolution at Ruapehu Volcano, New Zealand. Journal of Petrology, egs050.

Price, R. C., Smith, I. E., Stewart, R. B., Gamble, J. A., Gruender, K., & Maas, R. (2016). High-K andesite petrogenesis and crustal evolution: Evidence from mafic and ultramafic xenoliths, Egmont Volcano (Mt. Taranaki) and

comparisons with Ruapehu Volcano, North Island, New Zealand. Geochimica et Cosmochimica Acta, 185, 328-357.

Prouteau, G., & Scaillet, B. (2003). Experimental constraints on the origin of the 1991 Pinatubo dacite. Journal of Petrology, 44(12), 2203-2241.

Reubi, O., & Blundy, J. (2009). A dearth of intermediate melts at subduction zone volcanoes and the petrogenesis of arc andesites. Nature, 461(7268), 1269-1273.

Romick, J. D., Kay, S. M., & Kay, R. W. (1992). The influence of amphibole fractionation on the evolution of calc-alkaline andesite and dacite tephra from the central Aleutians, Alaska. Contributions to Mineralogy and Petrology, 112(1), 101-118.

Rudnick, R. L., & Gao, S. (2003). Composition of the continental crust. Treatise on Geochemistry, 3, 659.

Rust, A. C., Manga, M., & Cashman, K. V. (2003). Determining flow type, shear rate and shear stress in magmas from bubble shapes and orientations. Journal of Volcanology and Geothermal Research, 122(1), 111-132.

Salinger, M. J. (1984). New Zealand Climate: the last 5 million years. In: Vogel, J. C. (Ed), Late Cainozoic palaeoclimates of the Southern Hemisphere. Balkema, 131-150, Rotterdam.

Smith, D. R., & Leeman, W. P. (1987). Petrogenesis of Mount St. Helens dacitic magmas. Journal of Geophysical Research, 92, 10313.

Smith, V. C., Pearce, N. J., Matthews, N. E., Westgate, J. A., Petraglia, M. D., Haslam, M., Lane, C.S., Korisettar, R., & Pal, J. N. (2011). Geochemical fingerprinting of the widespread Toba tephra using biotite compositions. Quaternary International, 246(1), 97-104.

Shane, P. (2000). Tephrochronology: a New Zealand case study. Earth-Science Reviews, 49(1), 223-259.

Shane, P., Black, T., Eggins, S., & Westgate, J. (1998). Late Miocene marine tephra beds: recorders of rhyolitic volcanism in North Island, New Zealand. New Zealand Journal of Geology and Geophysics, 41(2), 165-178.

Shane, P., & Smith, I. (2000). Geochemical fingerprinting of basaltic tephra deposits in the Auckland Volcanic Field. New Zealand Journal of Geology and Geophysics, 43(4), 569-577.

Shane, P., & Hoverd, J. (2002). Distal record of multi-sourced tephra in Onepoto Basin, Auckland, New Zealand: implications for volcanic chronology, frequency and hazards. Bulletin of Volcanology, 64(7), 441-454.

Shane, P., Smith, V., & Nairn, I. (2003). Biotite composition as a tool for the identification of Quaternary tephra beds. Quaternary Research, 59(2), 262-270.

Shane, P., Sikes, E. L., & Guilderson, T. P. (2006). Tephra beds in deep-sea cores off northern New Zealand: implications for the history of Taupo Volcanic Zone, Mayor Island and White Island volcanoes. Journal of Volcanology and Geothermal Research, 154(3), 276-290.

Shane, P., Nairn, I. A., Martin, S. B., & Smith, V. C. (2008). Compositional heterogeneity in tephra deposits resulting from the eruption of multiple magma bodies: implications for tephrochronology. Quaternary International, 178(1), 44-53.

Shane, P., Gehrels, M., Zawalna-Geer, A., Augustinus, P., Lindsay, J., & Chaillou, I. (2013). Longevity of a small shield volcano revealed by crypto-tephra studies (Rangitoto volcano, New Zealand): change in eruptive behavior of a basaltic field. Journal of Volcanology and Geothermal Research, 257, 174-183.

Shea, T., Gurioli, L., & Houghton, B. F. (2012). Transitions between fall phases and pyroclastic density currents during the AD 79 eruption at Vesuvius: building a transient conduit model from the textural and volatile record. Bulletin of Volcanology, 74(10), 2363-2381.

Sherburn, S., & White, R. S. (2005). Crustal seismicity in Taranaki, New Zealand using accurate hypocentres from a dense network. Geophysical Journal International, 162(2), 494-506.

Sherburn, S., White, R. S., & Chadwick, M. (2006). Three-dimensional tomographic imaging of the Taranaki volcanoes, New Zealand. Geophysical Journal International, 166(2), 957-969.

Sigurdsson, H., Carey, S., Cornell, W., & Pescatore, T. (1985). The eruption of Vesuvius in AD 79. National Geographic Research, 1(3), 332-387.

Solano, J. M. S., Jackson, M. D., Sparks, R. S. J., Blundy, J. D., & Annen, C. (2012). Melt segregation in deep crustal hot zones: a mechanism for chemical differentiation, crustal assimilation and the formation of evolved magmas. Journal of Petrology, 53(10), 1999-2026.

Sparks, R. S. J., Bursik, M. I., Ablay, G. J., Thomas, R. M. E., & Carey, S. N. (1992). Sedimentation of tephra by volcanic plumes. Part 2: controls on thickness and grain-size variations of tephra fall deposits. Bulletin of Volcanology, 54(8), 685-695.

Spencer, K. J., & Lindsley, D. H. (1981). A solution model for coexisting iron-titanium oxides. American Mineralogist, 66(11-12), 1189-1201.

Stern, T. A., Stratford, W. R., & Salmon, M. L. (2006). Subduction evolution and mantle dynamics at a continental margin: Central North Island, New Zealand. Reviews of Geophysics, 44(4).

Stevenson, R. J., Bagdassarov, N. S., Dingwell, D. B., & Romano, C. (1998). The influence of trace amounts of water on the viscosity of rhyolites. Bulletin of Volcanology, 60(2), 89-97.

Stewart, R. B., Price, R. C., & Smith, I. E. M. (1996). Evolution of high-K arc magma, Egmont volcano, Taranaki, New Zealand: evidence from mineral chemistry. Journal of Volcanology and Geothermal Research, 74(3), 275-295.

Straub, S. M., Woodhead, J. D., & Arculus, R. J. (2015). Temporal evolution of the Mariana Arc: Mantle wedge and subducted slab controls revealed with a tephra perspective. Journal of Petrology, egv005.

Sun, S. S., & McDonough, W. S. (1989). Chemical and isotopic systematics of oceanic basalts: implications for mantle composition and processes. Geological Society, London, Special Publications, 42(1), 313-345.

Tepley, F. J., Davidson, J. P., Tilling, R. I., & Arth, J. G. (2000). Magma mixing, recharge and eruption histories recorded in plagioclase phenocrysts from El Chichon Volcano, Mexico. Journal of Petrology, 41(9), 1397-1411.

Thorpe, R. S. (1982). Andesites: Orogenic Andesites and Related Rocks. New York, Wiley, 724 pp.

Tomiya, A., & Takahashi, E. (2005). Evolution of the magma chamber beneath Usu Volcano since 1663: a natural laboratory for observing changing phenocryst compositions and textures. Journal of Petrology, 46(12), 2395-2426.

Tomlinson, E. L., Smith, V. C., Albert, P. G., Aydar, E., Civetta, L., Cioni, R., Çubukçu, E., Gertisser, R., Isaia, R., Menzies, M.A., & Orsi, G. (2015). The major and trace element glass compositions of the productive Mediterranean volcanic sources: tools for correlating distal tephra layers in and around Europe. Quaternary Science Reviews, 118, 48-66.

Toplis, M. J., & Carroll, M. R. (1995). An experimental study of the influence of oxygen fugacity on Fe-Ti oxide stability, phase relations, and mineral—melt equilibria in ferro-basaltic systems. Journal of Petrology, 36(5), 1137-1170.

Torres-Orozco, R., Cronin, S. J., Pardo, N., & Palmer, A. S. (2017). New insights into Holocene eruption episodes from proximal deposit sequences at Mt. Taranaki (Egmont), New Zealand. Bulletin of Volcanology, 79(1), 3, DOI: 10.1007/s00445-016-1085-5.

Torres-Orozco, R., Cronin, S. J., Damaschke, M., & Pardo, N. (in review). Diverse dynamics of Holocene mafic-intermediate Plinian eruptions at Mt. Taranaki (Egmont), New Zealand. Bulletin of Volcanology, XX, XX-XX.

Townsend, D., Vonk, A., & Kamp, P. J. J. (2008). Geology of the Taranaki Area, QMAP 1: 250000 Geological Map. GNS Science, Lower Hutt, New Zealand, 86.

Turner, S., Foden, J., George, R., Evans, P., Varne, R., Elburg, M., & Jenner, G. (2003). Rates and processes of potassic magma evolution beneath Sangeang Api volcano, East Sunda arc, Indonesia. Journal of Petrology, 44(3), 491-515.

Turner, M. B., Cronin, S. J., Smith, I. E., Stewart, R. B., & Neall, V. E. (2008a). Eruption episodes and magma recharge events in andesitic systems: Mt Taranaki, New Zealand. Journal of Volcanology and Geothermal Research, 177(4), 1063-1076.

Turner, M. B., Cronin, S. J., Stewart, R. B., Bebbington, M., & Smith, I. E. (2008b). Using titanomagnetite textures to elucidate volcanic eruption histories. Geology, 36(1), 31-34.

Turner, M. B., Cronin, S. J., Bebbington, M. S., Smith, I. E., & Stewart, R. B. (2011). Relating magma composition to eruption variability at andesitic volcanoes: A case study from Mount Taranaki, New Zealand. Geological Society of America Bulletin, 123(9-10), 2005-2015.

Wulf, S., Keller, J., Paterne, M., Mingram, J., Lauterbach, S., Opitz, S., Sottili, G., Giaccio, B., Albert, P.G., Satow, C., & Tomlinson, E. L. (2012). The 100–133 ka record of Italian explosive volcanism and revised tephrochronology of Lago Grande di Monticchio. Quaternary Science Reviews, 58, 104-123.

Zernack, A. V., Cronin, S. J., Neall, V. E., & Procter, J. N. (2011). A medial to distal volcaniclastic record of an andesite stratovolcano: detailed stratigraphy of the ring-plain succession of south-west Taranaki, New Zealand. International Journal of Earth Sciences, 100(8), 1937-1966.

Zernack, A. V., Price, R. C., Smith, I. E., Cronin, S. J., & Stewart, R. B. (2012a). Temporal evolution of a high-K andesitic magmatic system: Taranaki volcano, New Zealand. Journal of Petrology, 53(2), 325-363.

Zernack, A. V., Cronin, S. J., Bebbington, M. S., Price, R. C., Smith, I. E., Stewart, R. B., & Procter, J. N. (2012b). Forecasting catastrophic stratovolcano collapse: A model based on Mount Taranaki, New Zealand. Geology, 40(11), 983-986.

Chapter 7

Conclusions and future work

7.1 Conclusions

Tephra deposits are now routinely identified and used as isochronous horizons for correlating terrestrial, lacustrine, paludal, marine, and ice-core records over wide distances. They are thus a very important tool for many scientific disciplines including stratigraphy, sedimentology, volcanology (including volcanic hazard assessments), glaciology, archaeology, palaeo-environmental studies and climatology.

The principle aim of this study was to improve the completeness of, and extend the length of, the eruption history records of Mt. Taranaki, covering the Late Pleistocene to Holocene. The study resulted in a new high-resolution tephrostratigraphy and chronological framework, constructed from tephra sequences recovered from several lakes and peatlands situated downwind of the volcano (Chapter 3). Challenges of tephra preservation and narrow tephra dispersal-lobes were overcome by collecting a number of tephra records in sites spaced around a 120^{o} arc, spanning NE-SE of Mt. Taranaki. This approach, in combination with detailed geochemical studies and precise age determinations of the tephra layers, enabled the construction of a high-precision tephra record dating back to 30,000 cal yr BP, including at least 272 discrete tephra layers. Further, six distinct chemo-stratigraphic tephra sequences were recognised: A (0.5 – 3 cal ka BP), B (3 – 4 cal ka BP), C (4 – 9.5 cal ka BP), D (9.5 – 14 cal ka BP), E (14 – 17.5 cal ka BP), and F (23.5 – 30 cal ka BP). This is one of the most detailed and continuous tephra records ever built for an andesitic stratovolcano.

Using this tephrochronology, along with geochemical matching, incomplete and poorly age-constrained proximal and medial cover-bed sequences were correlated across a wide range of sites (Chapter 4). The results helped to resolve several stratigraphic

uncertainties and past correlation discrepancies. Marker tephra deposits including the Waipuku, Tariki, and Mangatoki were shown to be older (~6.8 to 9.5 cal yr BP) than hitherto inferred. Also, previously dated pyroclastic deposits between ~6 to 4 cal ka BP at a beach-cliff exposure, 40 km north-east of Mt. Taranaki's summit, were shown to represent new tephra deposits, which were associated with newly-studied flank deposits, including the Kokowai tephra unit (~4.7 cal ka BP), prominent east of the volcano.

In chapters 3 and 4, titanomagnetite compositions were shown to be a powerful discrimination and correlation tool, although only distinct tephra groups and/or packages of tephras could be uniquely identified. In fulfilment of the third objective of this project, the statistically dated sequence of tephras and their geochemical fingerprints were used to identify compositional changes through time (Chapter 6). The first compositional trend observed within whole-lapilli, glass, and titanomagnetite compositions shows that the overall magma source region was undergoing continuous evolution from 17.5 to 3 cal ka BP. This source region was found to be a deep-crustal magma source, akin to a hot-zone model (c.f., Annen et al., 2006). Production of progressively more evolved magmas over this time resulted from cooling and crystallisation of this magma source. Small-scale variations in magmas erupted over time (seen in the titanomagnetite groups) show that there were spatially separate magma zones active within the overall source region (hot-zone). These zones erupted magmas (i.e., batches) successively, at times with considerable overlap during transitions from one to the next. At 3 cal ka BP a significant shift towards less-evolved compositions was signalled by the appearance of the prominent Manganui eruptives sourced from the parasitic Fanthams Peak vent on the southern flank of Mt. Taranaki. This may imply a new magma source region or a significant recharge event, of hotter, more hydrous, and less-crystalline magma. The Manganui tephras intercalate with more evolved tephras from the summit vent and may be geochemically related to each other based on the geochemical evidence presented in Chapter 6; generating a possible second evolutionary trend. Within both overall evolutionary trends, small-scale variations are much more complex and may point to various processes taking place in the magma source, and/or storage, and/or plumbing regions.

During synthesis of the whole-lapilli chemistry data it became apparent that some major and trace elements differ from the overall observed composition related to previous whole-rock analyses of lava, debris avalanche and pyroclastic deposits (e.g., Price et al., 1999; Turner et al., 2008, 2011; Zernack et al., 2012; Torres-Orozco et al., in review). This probably indicates the eruption of a density-stratified magma reservoir, with the lowest-density, gas-rich components being erupted during climactic phases, and so being the only ones penetrating high enough into the stratosphere to be dispersed by high-level jet-stream winds to the east.

In Chapter 5 it was demonstrated that robust probabilistic hazard models, particularly in their structure, strongly rely upon long and complete chronological eruption records. Tephra which would otherwise be missed due to variations in tephra dispersal directions, eruption sizes/styles, and variable tephra preservation and/or depositional issues can only be detected if multiple-site records are available. By following this approach a significant offset within Lake Rotokare's tephra age determinations was identified. It is inferred that this is caused by "old"-carbon contaminating original radiocarbon dates. This had been unnoticeable in earlier studies of Turner et al. (2009), and had led to a falsely-high probabilistic eruption hazard assessment (50-59% chance of eruption over 50 years). In the present study, additional sites allowed the Lake Rotokare record to be excluded, providing a new, more reliable, eruption probability model for Mt. Taranaki. The new time-varying frequency estimates suggest a lower probability for a new eruption at Mt. Taranaki over the next 50 years of 33-42%. Further, the model conforms that the repose distribution observed at Mt. Taranaki is bimodal, with a primary mode that accounts for 98% of interval times with a modal recurrence interval of ~9 years – and an average interval of ~65 years. Around 2% of eruptions are preceded by very long intervals, described by a diffuse secondary mode of ~580 years, which is much longer than previously noted. With the new robust data set this long mode can now be considered real, rather than due to missing data.

7.2 Future work

The outcome of this study added important new knowledge to the volcanic eruption history of Mt. Taranaki and to its complex stratigraphy. Only a well-defined tephrostratigraphic record can give further insights into eruption frequency and underlying magmatic processes. It is recognised that this work is only one milestone along the way to a better understanding of andesitic stratovolcanoes and the risk they pose. Upon completion of this work, the following suggestions and ideas are raised for future studies:

1) The north-east to south-east section of Mt. Taranaki, including lakes and peatlands, has been studied in detail and several tephra deposits were mapped and correlated. However, even though the predominant wind direction over the Last Glacial to Holocene was mainly westerly (Salinger, 1984; Stewart and Neall, 1984; Drost et al., 2007), it can be expected that several ash falls would have been distributed to the west. It is therefore recommended that the western flank and/or ring-plain of Mt. Taranaki be searched to identify locations and environments where tephra might be preserved. Ideally, a deep-sea drilling program on the western off-shore regions of Mt. Taranaki could be favourable, if stable depo-centres can be identified in this very active coastal setting. This would not only greatly supplement the overall eruption record, but also strengthen probabilistic eruption forecasts.

2) In Chapter 4 several new tephra deposits dated between 6 to 4 cal ka BP were identified within beach-cliff exposures at the north-eastern end of Taranaki coast. This time-frame is particularly poorly constrained within the medial/proximal stratigraphy and will need further attention in future studies. Lake and peat tephra records show that several tephras that were sourced from large-scale eruptions were deposited during this particular time-frame. Further, the period between 17.5 and 23.5 cal ka BP, appears to be occupied by a ~6000 year-long depositional hiatus in the records of this study. This period should also

be targeted in new coring studies at alternative sites to determine how many ashes are missing and extend the record.

3) The role of andesitic tephra deposits as stratigraphic marker horizon has been generally, underestimated due to their complex and effectively identical chemistry over time. This study has demonstrated that specific tephra groups (packages) with distinct geochemical characteristics (particularly titanomagnetite compositions) can be used to correlate between sites. Future studies are encouraged to link Mt. Taranaki tephra deposits found elsewhere (e.g., distal sites, like that of Waikato; Lowe, 1988, or Auckland; Sandiford et al., 2001; Shane, 2005) to this newly presented andesitic tephra framework to establish an overall comprehensive link between the well-constrained rhyolitic and the emerging andesitic tephrochronology of New Zealand.

4) The improved eruption frequency record for Mt. Taranaki (Chapter 5) needs to be further investigated in order to test some of the hypotheses proposed in this study and to investigate the relationship to underlying magmatic and/or tectonic processes. What causes the observed cyclicity in the frequency? Turner et al. (2011) hypothesize that variations within the frequency are synchronous with compositional variations within the magma as reflected in MgO contents of titanomagnetites. With more data available in this study, these coexisting trends were not as clear. Periodic high and low phases of volcanic activity may alternatively correlate with the underlying crustal stress regime; where changes may enable dyke initiation and propagation, which in turn may occur over regular intervals. At Mt. Taranaki geophysical studies have been rare (e.g., Sherburn and White, 2005; Sherburn et al., 2006; Stern et al., 2006; Stagpoole and Nicol, 2008) and future such studies are here recommended.

5) The magmatic evolution of Mt. Taranaki has only been briefly investigated within this study based on variations within whole-lapilli, glass and titanomagnetite compositions. Titanomagnetites were of particular interest since

these showed specific, time-related trends of variations of chemistry, which are broadly consistent with the documented glass and whole-lapilli trends documented in this study. A major focus in future studies could involve the integration of titanomagnetite trace element analysis and/or analysis of glassy melt inclusions in phenocrysts to quantify physiochemical conditions of magma evolution at depth, and during ascent, to eruption (e.g., Wallace, 2005; Blundy and Cashman, 2008; Johnson et al., 2008).

6) Two parallel and currently independent sets of studies have been carried out at Mt. Taranaki and many similar volcanoes, that on the effusive record, vs. that of explosive, pyroclastic deposits. Integration of these two records is essential for understanding volumetric eruption rates and to gain a full understanding of the magma system. Integration, however, is very difficult due to the lack of full lava flow exposure for long stratigraphies on the volcano and problematic age-determinations. It is here suggested that the titanomagnetite-group chemistry approach could be used to relate tephras and lavas, at least for the last ~14 ka effusive units known to be exposed on the current Mt. Taranaki edifice. A unified effusive and explosive eruption record will provide a better eruption frequency record and a clearer understanding of the magmatic-system-drivers at re-awakening andesitic volcanoes.

7.3 References

Annen, C., Blundy, J. D., & Sparks, R. S. J. (2006). The genesis of intermediate and silicic magmas in deep crustal hot zones. Journal of Petrology, 47(3), 505-539.

Blundy, J., & Cashman, K. (2008). Petrologic reconstruction of magmatic system variables and processes. Reviews in Mineralogy and Geochemistry, 69(1), 179-239.

Drost, F., Renwick, J., Bhaskaran, B., Oliver, H., & McGregor, J. (2007). A simulation of New Zealand's climate during the Last Glacial Maximum. Quaternary Science Reviews, 26(19), 2505-2525.

Johnson, E. R., Wallace, P. J., Cashman, K. V., Granados, H. D., & Kent, A. J. (2008). Magmatic volatile contents and degassing-induced crystallisation at Volcán

Jorullo, Mexico: Implications for melt evolution and the plumbing systems of monogenetic volcanoes. Earth and Planetary Science Letters, 269(3), 478-487.

Price, R. C., Stewart, R. B., Woodhead, J. D., & Smith, I. E. M. (1999). Petrogenesis of high-K arc magmas: evidence from Egmont volcano, North Island, New Zealand. Journal of Petrology, 40(1), 167-197.

Salinger, M. J. (1984). New Zealand Climate: the last 5 million years. In: Vogel, J. C. (Ed), Late Cainozoic palaeoclimates of the Southern Hemisphere. Balkema, 131-150, Rotterdam.

Sandiford, A., Alloway, B., & Shane, P. (2001). A 28 000–6600 cal yr record of local and distal volcanism preserved in a paleolake, Auckland, New Zealand. New Zealand Journal of Geology and Geophysics, 44(2), 323-336.

Shane, P. (2005). Towards a comprehensive distal andesitic tephrostratigraphic framework for New Zealand based on eruptions from Egmont volcano. Journal of Quaternary Science, 20(1), 45-57.

Sherburn, S., & White, R. S. (2005). Crustal seismicity in Taranaki, New Zealand using accurate hypocentres from a dense network. Geophysical Journal International, 162(2), 494-506.

Sherburn, S., & White, R. S. (2006). Tectonics of the Taranaki region, New Zealand: earthquake focal mechanisms and stress axes. New Zealand Journal of Geology and Geophysics, 49(2), 269-279.

Stagpoole, V., & Nicol, A. (2008). Regional structure and kinematic history of a large subduction back thrust: Taranaki Fault, New Zealand. Journal of Geophysical Research: Solid Earth, 113(B1).

Stern, T. A., Stratford, W. R., & Salmon, M. L. (2006). Subduction evolution and mantle dynamics at a continental margin: Central North Island, New Zealand. Reviews of Geophysics, 44(4).

Stewart, R. B., & Neall, V. E. (1984). Chronology of palaeoclimatic change at the end of the last glaciation. Nature, 311, 47-48.

Torres-Orozco, R., Cronin, S. J., Damaschke, M., & Pardo, N. (in review). Diverse dynamics of Holocene mafic-intermediate Plinian eruptions at Mt. Taranaki (Egmont), New Zealand. Bulletin of Volcanology, XX, XX-XX.

Turner, M. B., Cronin, S. J., Smith, I. E., Stewart, R. B., & Neall, V. E. (2008). Eruption episodes and magma recharge events in andesitic systems: Mt Taranaki, New Zealand. Journal of Volcanology and Geothermal Research, 177(4), 1063-1076.

Turner, M. B., Bebbington, M. S., Cronin, S. J., & Stewart, R. B. (2009). Merging eruption datasets: building an integrated Holocene eruptive record for Mt Taranaki, New Zealand. Bulletin of volcanology, 71(8), 903-918.

Turner, M. B., Cronin, S. J., Bebbington, M. S., Smith, I. E., & Stewart, R. B. (2011). Relating magma composition to eruption variability at andesitic volcanoes: A

case study from Mount Taranaki, New Zealand. Geological Society of America Bulletin, 123(9-10), 2005-2015.

Wallace, P. J. (2005). Volatiles in subduction zone magmas: concentrations and fluxes based on melt inclusion and volcanic gas data. Journal of Volcanology and Geothermal Research, 140(1), 217-240.

Zernack, A. V., Price, R. C., Smith, I. E., Cronin, S. J., & Stewart, R. B. (2012). Temporal evolution of a high-K andesitic magmatic system: Taranaki volcano, New Zealand. Journal of Petrology, 53(2), 325-363.

List of appendices

Printed appendices

Electronic appendices (on DVD)

Digital Copy of Thesis

Radiographs of each sediment core

Spreadsheet "Tephra ID vs tephra number (nb)"

Grain-size data

X-ray powder diffraction (XRD) data

Electron probe micro-analyzer (EPMA) data

Glass shard data from lake and peat sediment records
Titanomagnetite data from lake and peat sediment records
Glass shard data from proximal and medial sites
Titanomagnetite data from proximal and medial sites

X-ray fluorescence spectrometry (XRF) and Laser ablation–inductively coupled plasma–mass spectrometry (LA-ICP-MS) data

Whole-lapilli major and trace elements from lake and peat sediment records
Titanomagnetite minor and trace elements from lake and peat sediment records

Appendix 1 *Radiocarbon age determination reports for each coring site using accelerator mass spectrometrometry (AMS) performed by the Waikato Radiocarbon Laboratory, Hamilton.*

THE UNIVERSITY OF WAIKATO
Te Whare Wānanga o Waikato

Private Bag 3105
Hamilton,
New Zealand.
Ph +64 7 838 4278
email c14@waikato.ac.nz

Wednesday, 10 September 20

Radiocarbon Dating Laboratory

Report on Radiocarbon Age Determination for Wk- 39860

Submitter	M Damaschke
Submitter's Code	R-A
Site & Location	Lake Richmond, Taranaki, New Zealand
Sample Material	Lake muds, Gyttja, Clays
Physical Pretreatment	Visible contaminants removed.
Chemical Pretreatment	Sample washed in hot HCl, rinsed and treated with multiple hot NaOH washes. The NaOH insoluble fraction was treated with hot HCl, filtered, rinsed and dried.

$D^{14}C$	-64.8 ± 2.4 ‰
$F^{14}C\%$	93.5 ± 0.2 %
Result	**539 ± 20 BP**

(AMS measurement)

Comments

Please note: Because of the small size of this sample, the Carbon-13 stable isotope value ($\delta^{13}C$) was measured on prepared graphite using the AMS spectrometer. The radiocarbon date has therefore been corrected for isotopic fractionation. However the AMS-measured $\delta^{13}C$ value can differ from the $\delta^{13}C$ of the original material and it is therefore not shown.

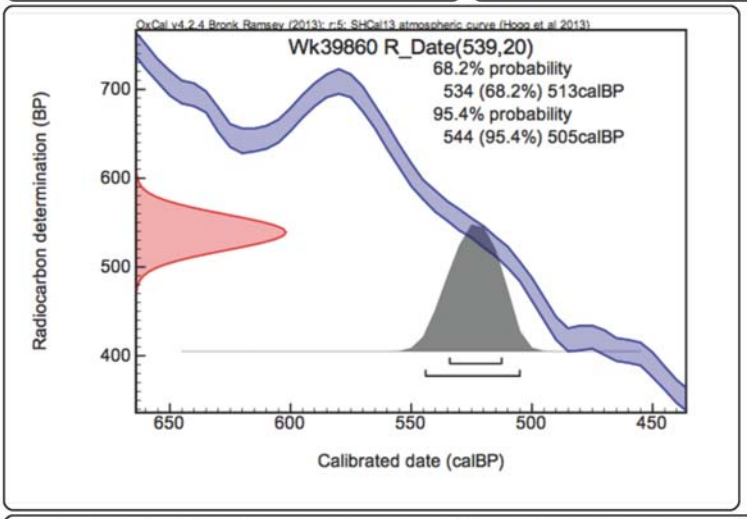

- Explanation of the calibrated Oxcal plots can be found at the Oxford Radiocarbon Accelerator Unit's calibration web pages (http://c14.arch.ox.ac.uk/embed.php?File=explanation.php)
- Result is *Conventional Age or Percent Modern Carbon (pMC)* following Stuiver and Polach, 1977, Radiocarbon 19, 355-363. This is based on the Libby half-life of 5568 yr with correction for isotopic fractionation applied. This age is normally quoted in publications and must include the appropriate error term and Wk number.
- Quoted errors are 1 standard deviation due to counting statistics multiplied by an experimentally determined Laboratory Error Multiplier.
- The isotopic fractionation, $\delta^{13}C$, is expressed as ‰ wrt PDB and is measured on sample CO_2.
- $F^{14}C\%$ is also known as *Percent Modern Carbon (pMC)*.

AG Hogg

THE UNIVERSITY OF
WAIKATO
Te Whare Wānanga o Waikato

Private Bag 3105
Hamilton,
New Zealand.
Ph +64 7 838 4278
email c14@waikato.ac.nz

Radiocarbon Dating Laboratory

Wednesday, 10 September 20

Report on Radiocarbon Age Determination for Wk- 39861

Submitter	M Damaschke
Submitter's Code	R-B
Site & Location	Lake Richmond, Taranaki, New Zealand
Sample Material	Lake muds, Gyttja, Clays
Physical Pretreatment	Visible contaminants removed.
Chemical Pretreatment	Sample washed in hot HCl, rinsed and treated with multiple hot NaOH washes. The NaOH insoluble fraction was treated with hot HCl, filtered, rinsed and dried.

$D^{14}C$	-194.2 ±	2.0 ‰
$F^{14}C$%	80.6 ±	0.2 %
Result	**1735 ± 20 BP**	

(AMS measurement)

Comments

Please note: Because of the small size of this sample, the Carbon-13 stable isotope value ($\delta^{13}C$) was measured on prepared graphite using the AMS spectrometer. The radiocarbon date has therefore been corrected for isotopic fractionation. However the AMS-measured $\delta^{13}C$ value can differ from the $\delta^{13}C$ of the original material and it is therefore not shown.

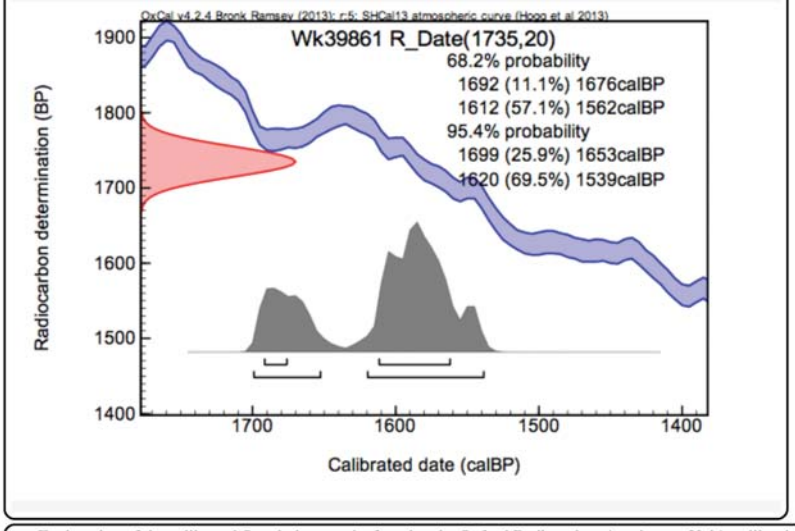

- Explanation of the calibrated Oxcal plots can be found at the Oxford Radiocarbon Accelerator Unit's calibration web pages (http://c14.arch.ox.ac.uk/embed.php?File=explanation.php)
- Result is *Conventional Age or Percent Modern Carbon (pMC)* following Stuiver and Polach, 1977, Radiocarbon 19, 355-363. This is based on the Libby half-life of 5568 yr with correction for isotopic fractionation applied. This age is normally quoted in publications and must include the appropriate error term and Wk number.
- Quoted errors are 1 standard deviation due to counting statistics multiplied by an experimentally determined Laboratory Error Multiplier.
- The isotopic fractionation, $\delta^{13}C$, is expressed as ‰ wrt PDB and is measured on sample CO_2.
- $F^{14}C$% is also known as *Percent Modern Carbon (pMC)*.

AG Hogg

THE UNIVERSITY OF
WAIKATO
Te Whare Wānanga o Waikato

Private Bag 3105
Hamilton,
New Zealand.
Ph +64 7 838 4278
email c14@waikato.ac.nz

Wednesday, 10 September 20

Radiocarbon Dating Laboratory

Report on Radiocarbon Age Determination for Wk- 39862

Submitter	M Damaschke
Submitter's Code	R-C
Site & Location	Lake Richmond, Taranaki, New Zealand
Sample Material	Lake muds, Gyttja, Clays
Physical Pretreatment	Visible contaminants removed.
Chemical Pretreatment	Sample washed in hot HCl, rinsed and treated with multiple hot NaOH washes. The NaOH insoluble fraction was treated with hot HCl, filtered, rinsed and dried.

$D^{14}C$	-257.6 ±	1.8 ‰
$F^{14}C$%	74.2 ±	0.2 %
Result	**2393 ± 20 BP**	

(AMS measurement)

Comments

Please note: Because of the small size of this sample, the Carbon-13 stable isotope value ($\delta^{13}C$) was measured on prepared graphite using the AMS spectrometer. The radiocarbon date has therefore been corrected for isotopic fractionation. However the AMS-measured $\delta^{13}C$ value can differ from the $\delta^{13}C$ of the original material and it is therefore not shown.

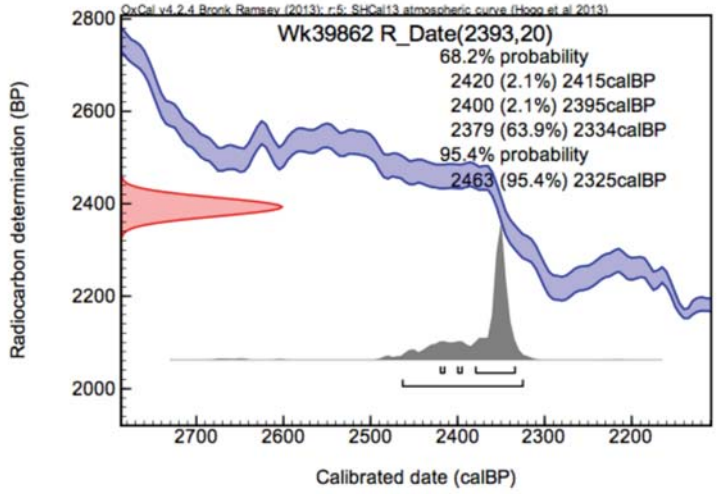

- Explanation of the calibrated Oxcal plots can be found at the Oxford Radiocarbon Accelerator Unit's calibration web pages (http://c14.arch.ox.ac.uk/embed.php?File=explanation.php)
- Result is *Conventional Age or Percent Modern Carbon (pMC)* following Stuiver and Polach, 1977, Radiocarbon 19, 355-363. This is based on the Libby half-life of 5568 yr with correction for isotopic fractionation applied. This age is normally quoted in publications and must include the appropriate error term and Wk number.
- Quoted errors are 1 standard deviation due to counting statistics multiplied by an experimentally determined Laboratory Error Multiplier.
- The isotopic fractionation, $\delta^{13}C$, is expressed as ‰ wrt PDB and is measured on sample CO_2.
- $F^{14}C$% is also known as *Percent Modern Carbon (pMC)*.

AG Hogg

THE UNIVERSITY OF
WAIKATO
Te Whare Wānanga o Waikato

Private Bag 3105
Hamilton,
New Zealand.
Ph +64 7 838 4278
email c14@waikato.ac.nz

Wednesday, 10 September 20

Radiocarbon Dating Laboratory

Report on Radiocarbon Age Determination for Wk- 39863

Submitter	M Damaschke
Submitter's Code	R-D
Site & Location	Lake Richmond, Taranaki, New Zealand
Sample Material	Lake muds, Gyttja, Clays
Physical Pretreatment	Visible contaminants removed.
Chemical Pretreatment	Sample washed in hot HCl, rinsed and treated with multiple hot NaOH washes. The NaOH insoluble fraction was treated with hot HCl, filtered, rinsed and dried.

$D^{14}C$	-316.3 ±	1.7 ‰
$F^{14}C\%$	68.4 ±	0.2 %
Result	**3055 ± 20 BP**	

(AMS measurement)

Comments

Please note: Because of the small size of this sample, the Carbon-13 stable isotope value ($\delta^{13}C$) was measured on prepared graphite using the AMS spectrometer. The radiocarbon date has therefore been corrected for isotopic fractionation. However the AMS-measured $\delta^{13}C$ value can differ from the $\delta^{13}C$ of the original material and it is therefore not shown.

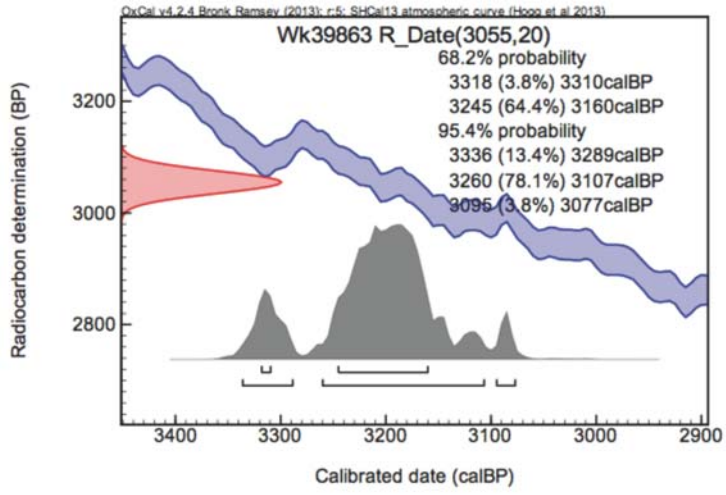

- Explanation of the calibrated Oxcal plots can be found at the Oxford Radiocarbon Accelerator Unit's calibration web pages (http://c14.arch.ox.ac.uk/embed.php?File=explanation.php)
- Result is *Conventional Age or Percent Modern Carbon (pMC)* following Stuiver and Polach, 1977, Radiocarbon 19, 355-363. This is based on the Libby half-life of 5568 yr with correction for isotopic fractionation applied. This age is normally quoted in publications and must include the appropriate error term and Wk number.
- Quoted errors are 1 standard deviation due to counting statistics multiplied by an experimentally determined Laboratory Error Multiplier.
- The isotopic fractionation, $\delta^{13}C$, is expressed as ‰ wrt PDB and is measured on sample CO_2.
- $F^{14}C\%$ is also known as *Percent Modern Carbon (pMC)*.

AG Hogg

THE UNIVERSITY OF
WAIKATO
Te Whare Wānanga o Waikato

Private Bag 3105
Hamilton,
New Zealand.
Ph +64 7 838 4278
email c14@waikato.ac.nz

Wednesday, 10 September 20

Radiocarbon Dating Laboratory

Report on Radiocarbon Age Determination for Wk- 39864

Submitter	M Damaschke
Submitter's Code	R-E
Site & Location	Lake Richmond, Taranaki, New Zealand
Sample Material	Lake muds, Gyttja, Clays
Physical Pretreatment	Visible contaminants removed.
Chemical Pretreatment	Sample washed in hot HCl, rinsed and treated with multiple hot NaOH washes. The NaOH insoluble fraction was treated with hot HCl, filtered, rinsed and dried.

$D^{14}C$	-364.4 ±	1.6 ‰
$F^{14}C\%$	63.6 ±	0.2 %
Result	**3641 ± 20 BP**	

(AMS measurement)

Comments

Please note: Because of the small size of this sample, the Carbon-13 stable isotope value ($\delta^{13}C$) was measured on prepared graphite using the AMS spectrometer. The radiocarbon date has therefore been corrected for isotopic fractionation. However the AMS-measured $\delta^{13}C$ value can differ from the $\delta^{13}C$ of the original material and it is therefore not shown.

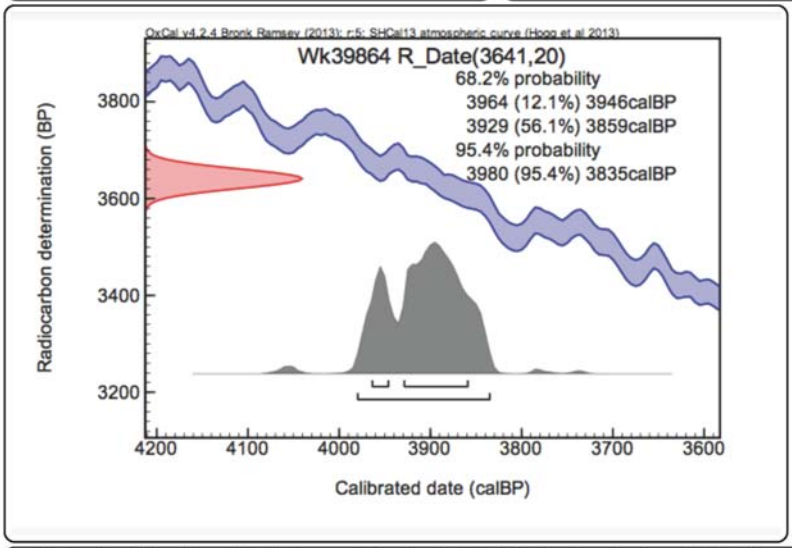

- Explanation of the calibrated Oxcal plots can be found at the Oxford Radiocarbon Accelerator Unit's calibration web pages (http://c14.arch.ox.ac.uk/embed.php?File=explanation.php)
- Result is *Conventional Age or Percent Modern Carbon (pMC)* following Stuiver and Polach, 1977, Radiocarbon 19, 355-363. This is based on the Libby half-life of 5568 yr with correction for isotopic fractionation applied. This age is normally quoted in publications and must include the appropriate error term and Wk number.
- Quoted errors are 1 standard deviation due to counting statistics multiplied by an experimentally determined Laboratory Error Multiplier.
- The isotopic fractionation, $\delta^{13}C$, is expressed as ‰ wrt PDB and is measured on sample CO_2.
- $F^{14}C\%$ is also known as *Percent Modern Carbon (pMC)*.

AG Hogg

THE UNIVERSITY OF
WAIKATO
Te Whare Wānanga o Waikato

Private Bag 3105
Hamilton,
New Zealand.
Ph +64 7 838 4278
email c14@waikato.ac.nz

Radiocarbon Dating Laboratory

Wednesday, 10 September 20

Report on Radiocarbon Age Determination for Wk- 39865

Submitter	M Damaschke
Submitter's Code	R-F
Site & Location	Lake Richmond, Taranaki, New Zealand
Sample Material	Lake muds, Gyttja, Clays
Physical Pretreatment	Visible contaminants removed.
Chemical Pretreatment	Sample washed in hot HCl, rinsed and treated with multiple hot NaOH washes. The NaOH insoluble fraction was treated with hot HCl, filtered, rinsed and dried.

$D^{14}C$	-388.1 ±	1.5 ‰
$F^{14}C\%$	61.2 ±	0.1 %
Result	**3946 ± 20 BP**	

(AMS measurement)

Comments

Please note: Because of the small size of this sample, the Carbon-13 stable isotope value ($\delta^{13}C$) was measured on prepared graphite using the AMS spectrometer. The radiocarbon date has therefore been corrected for isotopic fractionation. However the AMS-measured $\delta^{13}C$ value can differ from the $\delta^{13}C$ of the original material and it is therefore not shown.

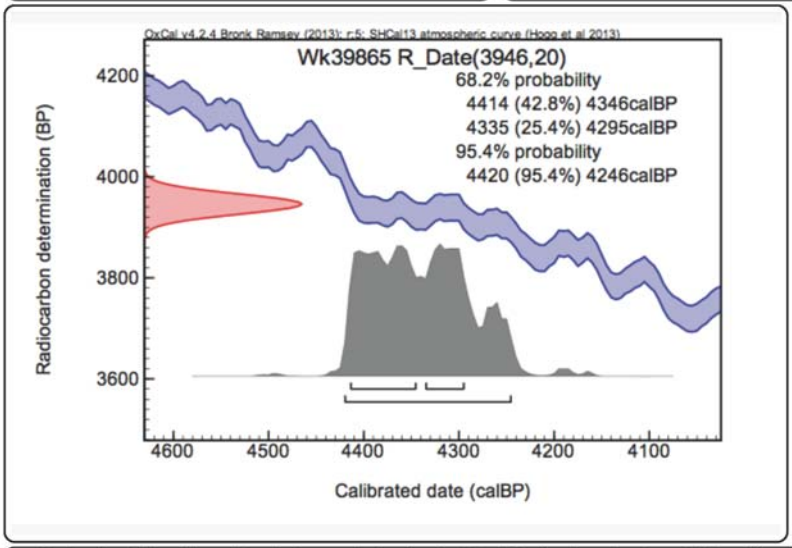

- Explanation of the calibrated Oxcal plots can be found at the Oxford Radiocarbon Accelerator Unit's calibration web pages (http://c14.arch.ox.ac.uk/embed.php?File=explanation.php)
- Result is *Conventional Age or Percent Modern Carbon (pMC)* following Stuiver and Polach, 1977, Radiocarbon 19, 355-363. This is based on the Libby half-life of 5568 yr with correction for isotopic fractionation applied. This age is normally quoted in publications and must include the appropriate error term and Wk number.
- Quoted errors are 1 standard deviation due to counting statistics multiplied by an experimentally determined Laboratory Error Multiplier.
- The isotopic fractionation, $\delta^{13}C$, is expressed as ‰ wrt PDB and is measured on sample CO_2.
- $F^{14}C\%$ is also known as *Percent Modern Carbon (pMC)*.

AG Hogg

THE UNIVERSITY OF
WAIKATO
Te Whare Wānanga o Waikato

Private Bag 3105
Hamilton,
New Zealand.
Ph +64 7 838 4278
email c14@waikato.ac.nz

Wednesday, 10 September 20

Radiocarbon Dating Laboratory

Report on Radiocarbon Age Determination for Wk- 39866

Submitter	M Damaschke
Submitter's Code	R-G
Site & Location	Lake Richmond, Taranaki, New Zealand
Sample Material	Lake muds, Gyttja, Clays
Physical Pretreatment	Visible contaminants removed.
Chemical Pretreatment	Sample washed in hot HCl, rinsed and treated with multiple hot NaOH washes. The NaOH insoluble fraction was treated with hot HCl, filtered, rinsed and dried.

$D^{14}C$	-455.0 ±	1.4 ‰
$F^{14}C\%$	54.5 ±	0.1 %
Result	**4875 ± 21 BP**	

(AMS measurement)

Comments

Please note: Because of the small size of this sample, the Carbon-13 stable isotope value ($\delta^{13}C$) was measured on prepared graphite using the AMS spectrometer. The radiocarbon date has therefore been corrected for isotopic fractionation. However the AMS-measured $\delta^{13}C$ value can differ from the $\delta^{13}C$ of the original material and it is therefore not shown.

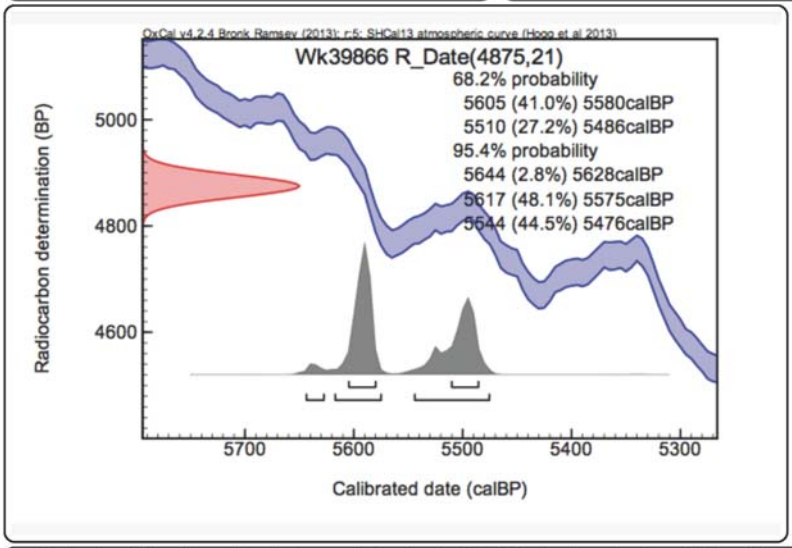

- Explanation of the calibrated Oxcal plots can be found at the Oxford Radiocarbon Accelerator Unit's calibration web pages (http://c14.arch.ox.ac.uk/embed.php?File=explanation.php)
- Result is *Conventional Age or Percent Modern Carbon (pMC)* following Stuiver and Polach, 1977, Radiocarbon 19, 355-363. This is based on the Libby half-life of 5568 yr with correction for isotopic fractionation applied. This age is normally quoted in publications and must include the appropriate error term and Wk number.
- Quoted errors are 1 standard deviation due to counting statistics multiplied by an experimentally determined Laboratory Error Multiplier.
- The isotopic fractionation, $\delta^{13}C$, is expressed as ‰ wrt PDB and is measured on sample CO_2.
- $F^{14}C\%$ is also known as *Percent Modern Carbon (pMC)*.

AG Hogg

THE UNIVERSITY OF
WAIKATO
Te Whare Wānanga o Waikato

Private Bag 3105
Hamilton,
New Zealand.
Ph +64 7 838 4278
email c14@waikato.ac.nz

Radiocarbon Dating Laboratory

Wednesday, 10 September 20

Report on Radiocarbon Age Determination for Wk- 39867

Submitter	M Damaschke
Submitter's Code	R-H
Site & Location	Lake Richmond, Taranaki, New Zealand
Sample Material	Lake muds, Gyttja, Clays
Physical Pretreatment	Visible contaminants removed.
Chemical Pretreatment	Sample washed in hot HCl, rinsed and treated with multiple hot NaOH washes. The NaOH insoluble fraction was treated with hot HCl, filtered, rinsed and dried.

$D^{14}C$	-535.1 ±	1.3 ‰
$F^{14}C\%$	46.5 ±	0.1 %
Result	**6153 ± 22 BP**	

(AMS measurement)

Comments

Please note: Because of the small size of this sample, the Carbon-13 stable isotope value ($\delta^{13}C$) was measured on prepared graphite using the AMS spectrometer. The radiocarbon date has therefore been corrected for isotopic fractionation. However the AMS-measured $\delta^{13}C$ value can differ from the $\delta^{13}C$ of the original material and it is therefore not shown.

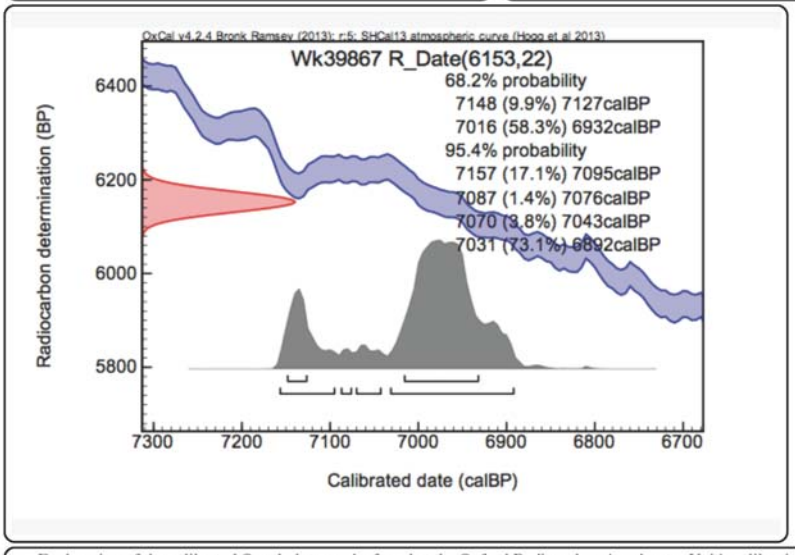

- Explanation of the calibrated Oxcal plots can be found at the Oxford Radiocarbon Accelerator Unit's calibration web pages (http://c14.arch.ox.ac.uk/embed.php?File=explanation.php)
- Result is *Conventional Age or Percent Modern Carbon (pMC)* following Stuiver and Polach, 1977, Radiocarbon 19, 355-363. This is based on the Libby half-life of 5568 yr with correction for isotopic fractionation applied. This age is normally quoted in publications and must include the appropriate error term and Wk number.
- Quoted errors are 1 standard deviation due to counting statistics multiplied by an experimentally determined Laboratory Error Multiplier.
- The isotopic fractionation, $\delta^{13}C$, is expressed as ‰ wrt PDB and is measured on sample CO_2.
- $F^{14}C\%$ is also known as *Percent Modern Carbon (pMC)*.

AG Hogg

THE UNIVERSITY OF
WAIKATO
Te Whare Wānanga o Waikato

Private Bag 3105
Hamilton,
New Zealand.
Ph +64 7 838 4278
email c14@waikato.ac.nz

Wednesday, 10 September 20

Radiocarbon Dating Laboratory

Report on Radiocarbon Age Determination for Wk- 39868

Submitter	M Damaschke
Submitter's Code	R-I
Site & Location	Lake Richmond, Taranaki, New Zealand
Sample Material	Lake muds, Gyttja, Clays
Physical Pretreatment	Visible contaminants removed.
Chemical Pretreatment	Sample washed in hot HCl, rinsed and treated with multiple hot NaOH washes. The NaOH insoluble fraction was treated with hot HCl, filtered, rinsed and dried.

$D^{14}C$	-615.5 ±	1.2 ‰
$F^{14}C\%$	38.5 ±	0.1 %
Result	**7678 ± 24 BP**	

(AMS measurement)

Comments

Please note: Because of the small size of this sample, the Carbon-13 stable isotope value ($\delta^{13}C$) was measured on prepared graphite using the AMS spectrometer. The radiocarbon date has therefore been corrected for isotopic fractionation. However the AMS-measured $\delta^{13}C$ value can differ from the $\delta^{13}C$ of the original material and it is therefore not shown.

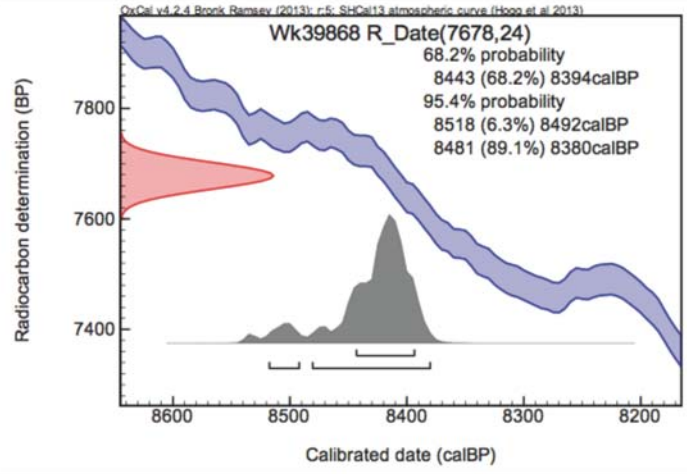

- Explanation of the calibrated Oxcal plots can be found at the Oxford Radiocarbon Accelerator Unit's calibration web pages (http://c14.arch.ox.ac.uk/embed.php?File=explanation.php)
- Result is *Conventional Age or Percent Modern Carbon (pMC)* following Stuiver and Polach, 1977, Radiocarbon 19, 355-363. This is based on the Libby half-life of 5568 yr with correction for isotopic fractionation applied. This age is normally quoted in publications and must include the appropriate error term and Wk number.
- Quoted errors are 1 standard deviation due to counting statistics multiplied by an experimentally determined Laboratory Error Multiplier.
- The isotopic fractionation, $\delta^{13}C$, is expressed as ‰ wrt PDB and is measured on sample CO_2.
- $F^{14}C\%$ is also known as *Percent Modern Carbon (pMC)*.

AG Hogg

THE UNIVERSITY OF
WAIKATO
Te Whare Wānanga o Waikato

Private Bag 3105
Hamilton,
New Zealand.
Ph +64 7 838 4278
email c14@waikato.ac.nz

Radiocarbon Dating Laboratory

Wednesday, 10 September 20

Report on Radiocarbon Age Determination for Wk- 39869

Submitter	M Damaschke
Submitter's Code	R-J
Site & Location	Lake Richmond, Taranaki, New Zealand
Sample Material	Lake muds, Gyttja, Clays
Physical Pretreatment	Visible contaminants removed.
Chemical Pretreatment	Sample washed in hot HCl, rinsed and treated with multiple hot NaOH washes. The NaOH insoluble fraction was treated with hot HCl, filtered, rinsed and dried.

$D^{14}C$	-690.9 ±	1.0 ‰
$F^{14}C\%$	30.9 ±	0.1 %
Result	**9433 ± 25 BP**	

(AMS measurement)

Comments

Please note: Because of the small size of this sample, the Carbon-13 stable isotope value ($\delta^{13}C$) was measured on prepared graphite using the AMS spectrometer. The radiocarbon date has therefore been corrected for isotopic fractionation. However the AMS-measured $\delta^{13}C$ value can differ from the $\delta^{13}C$ of the original material and it is therefore not shown.

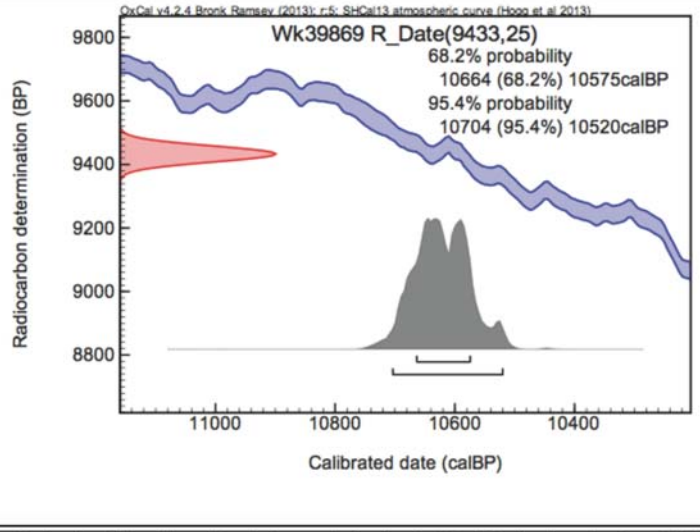

- Explanation of the calibrated Oxcal plots can be found at the Oxford Radiocarbon Accelerator Unit's calibration web pages (http://c14.arch.ox.ac.uk/embed.php?File=explanation.php)
- Result is *Conventional Age or Percent Modern Carbon (pMC)* following Stuiver and Polach, 1977, Radiocarbon 19, 355-363. This is based on the Libby half-life of 5568 yr with correction for isotopic fractionation applied. This age is normally quoted in publications and must include the appropriate error term and Wk number.
- Quoted errors are 1 standard deviation due to counting statistics multiplied by an experimentally determined Laboratory Error Multiplier.
- The isotopic fractionation, $\delta^{13}C$, is expressed as ‰ wrt PDB and is measured on sample CO_2.
- $F^{14}C\%$ is also known as *Percent Modern Carbon (pMC)*.

AG Hogg

THE UNIVERSITY OF
WAIKATO
Te Whare Wānanga o Waikato

Private Bag 3105
Hamilton,
New Zealand.
Ph +64 7 838 4278
email c14@waikato.ac.nz

Wednesday, 10 September 20

Radiocarbon Dating Laboratory

Report on Radiocarbon Age Determination for Wk- 39870

Submitter	M Damaschke
Submitter's Code	R-K
Site & Location	Lake Richmond, Taranaki, New Zealand
Sample Material	Peat
Physical Pretreatment	Visible contaminants removed.
Chemical Pretreatment	Sample washed in hot HCl, rinsed and treated with multiple hot NaOH washes. The NaOH insoluble fraction was treated with hot HCl, filtered, rinsed and dried.

$D^{14}C$	-740.8 ±	1.1 ‰
$F^{14}C\%$	25.9 ±	0.1 %
Result	**10,846 ± 32 BP**	

(AMS measurement)

Comments

Please note: Because of the small size of this sample, the Carbon-13 stable isotope value ($\delta^{13}C$) was measured on prepared graphite using the AMS spectrometer. The radiocarbon date has therefore been corrected for isotopic fractionation. However the AMS-measured $\delta^{13}C$ value can differ from the $\delta^{13}C$ of the original material and it is therefore not shown.

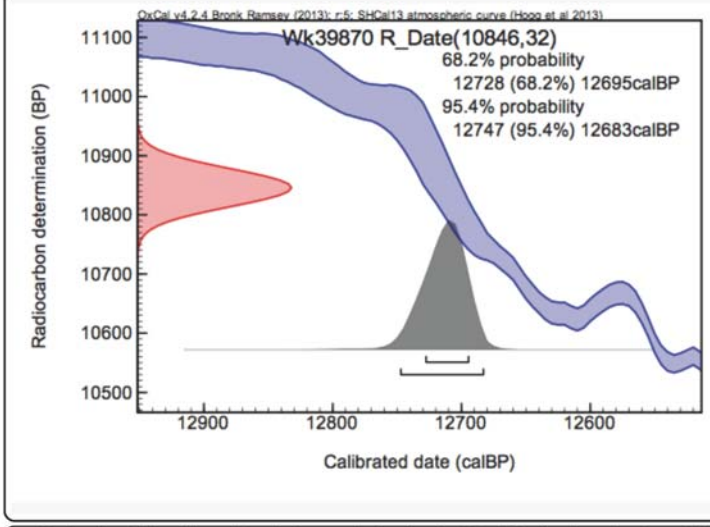

- Explanation of the calibrated Oxcal plots can be found at the Oxford Radiocarbon Accelerator Unit's calibration web pages (http://c14.arch.ox.ac.uk/embed.php?File=explanation.php)
- Result is *Conventional Age or Percent Modern Carbon (pMC)* following Stuiver and Polach, 1977, Radiocarbon 19, 355-363. This is based on the Libby half-life of 5568 yr with correction for isotopic fractionation applied. This age is normally quoted in publications and must include the appropriate error term and Wk number.
- Quoted errors are 1 standard deviation due to counting statistics multiplied by an experimentally determined Laboratory Error Multiplier.
- The isotopic fractionation, $\delta^{13}C$, is expressed as ‰ wrt PDB and is measured on sample CO_2.
- $F^{14}C\%$ is also known as *Percent Modern Carbon (pMC)*.

AG Hogg

THE UNIVERSITY OF
WAIKATO
Te Whare Wānanga o Waikato

Private Bag 3105
Hamilton,
New Zealand.
Ph +64 7 838 4278
email c14@waikato.ac.nz

Radiocarbon Dating Laboratory

Wednesday, 10 September 20

Report on Radiocarbon Age Determination for Wk- 39871

Submitter	M Damaschke
Submitter's Code	R-L
Site & Location	Lake Richmond, Taranaki, New Zealand
Sample Material	Peat
Physical Pretreatment	Visible contaminants removed.
Chemical Pretreatment	Sample washed in hot HCl, rinsed and treated with multiple hot NaOH washes. The NaOH insoluble fraction was treated with hot HCl, filtered, rinsed and dried.

$D^{14}C$	-788.9 ±	0.9 ‰
$F^{14}C\%$	21.1 ±	0.1 %
Result	**12,494 ± 35 BP**	

(AMS measurement)

Comments

Please note: Because of the small size of this sample, the Carbon-13 stable isotope value ($\delta^{13}C$) was measured on prepared graphite using the AMS spectrometer. The radiocarbon date has therefore been corrected for isotopic fractionation. However the AMS-measured $\delta^{13}C$ value can differ from the $\delta^{13}C$ of the original material and it is therefore not shown.

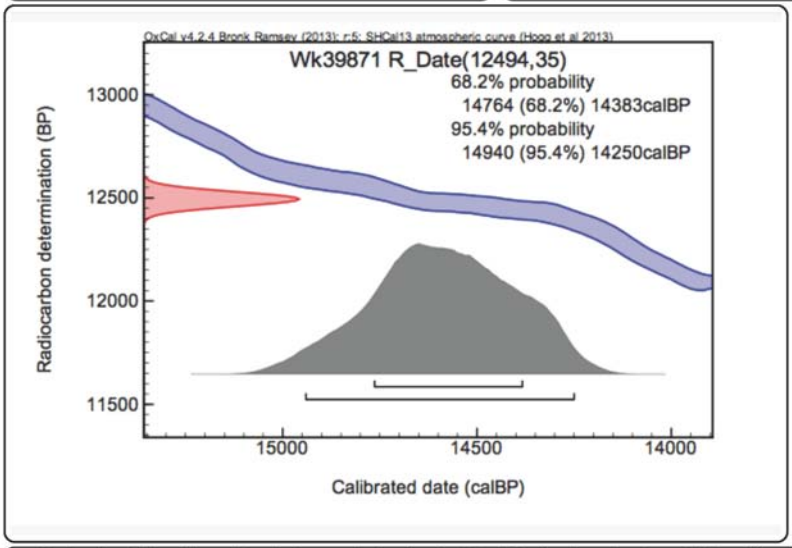

- Explanation of the calibrated Oxcal plots can be found at the Oxford Radiocarbon Accelerator Unit's calibration web pages (http://c14.arch.ox.ac.uk/embed.php?File=explanation.php)
- Result is *Conventional Age or Percent Modern Carbon (pMC)* following Stuiver and Polach, 1977, Radiocarbon 19, 355-363. This is based on the Libby half-life of 5568 yr with correction for isotopic fractionation applied. This age is normally quoted in publications and must include the appropriate error term and Wk number.
- Quoted errors are 1 standard deviation due to counting statistics multiplied by an experimentally determined Laboratory Error Multiplier.
- The isotopic fractionation, $\delta^{13}C$, is expressed as ‰ wrt PDB and is measured on sample CO_2.
- $F^{14}C\%$ is also known as *Percent Modern Carbon (pMC)*.

AG Hogg

THE UNIVERSITY OF
WAIKATO
Te Whare Wānanga o Waikato

Private Bag 3105
Hamilton,
New Zealand.
Ph +64 7 838 4278
email c14@waikato.ac.nz

Monday, 16 June 2014

Radiocarbon Dating Laboratory

Report on Radiocarbon Age Determination for Wk- 39127

Submitter	M Damaschke
Submitter's Code	T1-A
Site & Location	Tariki Swamp, Taranaki, New Zealand
Sample Material	Peat
Physical Pretreatment	Visible contaminants removed.
Chemical Pretreatment	Sample washed in hot HCl, rinsed and treated with multiple hot NaOH washes. The NaOH insoluble fraction was treated with hot HCl, filtered, rinsed and dried.

$D^{14}C$	-224.1 ±	2.5 ‰
$F^{14}C$%	77.6 ±	0.2 %
Result	**2038 ± 26 BP**	

(AMS measurement)

Comments

Please note: Because of the small size of this sample, the Carbon-13 stable isotope value ($\delta^{13}C$) was measured on prepared graphite using the AMS spectrometer. The radiocarbon date has therefore been corrected for isotopic fractionation. However the AMS-measured $\delta^{13}C$ value can differ from the $\delta^{13}C$ of the original material and it is therefore not shown.

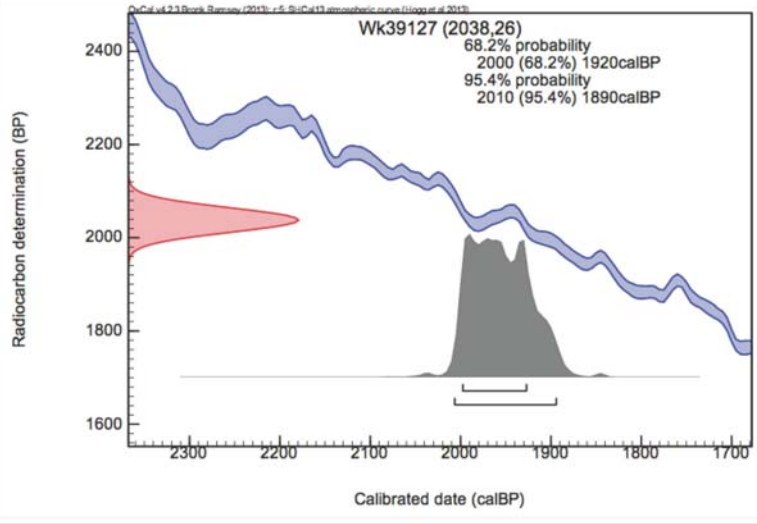

- Explanation of the calibrated Oxcal plots can be found at the Oxford Radiocarbon Accelerator Unit's calibration web pages (http://c14.arch.ox.ac.uk/embed.php?File=explanation.php)
- Result is *Conventional Age or Percent Modern Carbon (pMC)* following Stuiver and Polach, 1977, Radiocarbon 19, 355-363. This is based on the Libby half-life of 5568 yr with correction for isotopic fractionation applied. This age is normally quoted in publications and must include the appropriate error term and Wk number.
- Quoted errors are 1 standard deviation due to counting statistics multiplied by an experimentally determined Laboratory Error Multiplier.
- The isotopic fractionation, $\delta^{13}C$, is expressed as ‰ wrt PDB and is measured on sample CO_2.
- $F^{14}C$% is also known as *Percent Modern Carbon (pMC)*.

THE UNIVERSITY OF
WAIKATO
Te Whare Wānanga o Waikato

Private Bag 3105
Hamilton,
New Zealand.
Ph +64 7 838 4278
email c14@waikato.ac.nz

Monday, 16 June 2014

Radiocarbon Dating Laboratory

Report on Radiocarbon Age Determination for Wk- 39128

Submitter	M Damaschke
Submitter's Code	T1-C
Site & Location	Tariki Swamp, Taranaki, New Zealand
Sample Material	Peat/organic mud
Physical Pretreatment	Visible contaminants removed.
Chemical Pretreatment	Sample washed in hot HCl, rinsed and treated with multiple hot NaOH washes. The NaOH insoluble fraction was treated with hot HCl, filtered, rinsed and dried.

$D^{14}C$	-280.0 ±	2.3 ‰
$F^{14}C\%$	72.0 ±	0.2 %
Result	**2639 ± 26 BP**	

(AMS measurement)

Comments

Please note: Because of the small size of this sample, the Carbon-13 stable isotope value ($\delta^{13}C$) was measured on prepared graphite using the AMS spectrometer. The radiocarbon date has therefore been corrected for isotopic fractionation. However the AMS-measured $\delta^{13}C$ value can differ from the $\delta^{13}C$ of the original material and it is therefore not shown.

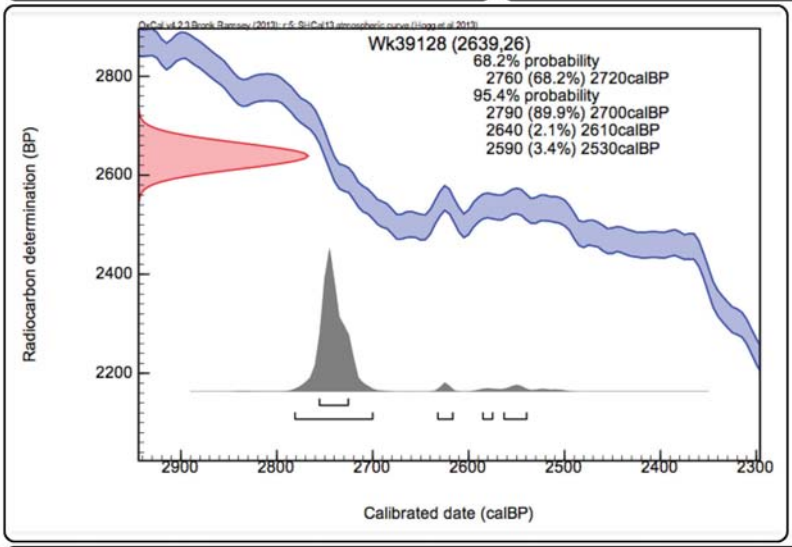

- Explanation of the calibrated Oxcal plots can be found at the Oxford Radiocarbon Accelerator Unit's calibration web pages (http://c14.arch.ox.ac.uk/embed.php?File=explanation.php)
- Result is *Conventional Age or Percent Modern Carbon (pMC)* following Stuiver and Polach, 1977, Radiocarbon 19, 355-363. This is based on the Libby half-life of 5568 yr with correction for isotopic fractionation applied. This age is normally quoted in publications and must include the appropriate error term and Wk number.
- Quoted errors are 1 standard deviation due to counting statistics multiplied by an experimentally determined Laboratory Error Multiplier.
- The isotopic fractionation, $\delta^{13}C$, is expressed as ‰ wrt PDB and is measured on sample CO_2.
- $F^{14}C\%$ is also known as *Percent Modern Carbon (pMC)*.

THE UNIVERSITY OF
WAIKATO
Te Whare Wānanga o Waikato

Private Bag 3105
Hamilton,
New Zealand.
Ph +64 7 838 4278
email c14@waikato.ac.nz

Monday, 16 June 2014

Radiocarbon Dating Laboratory

Report on Radiocarbon Age Determination for Wk- 39129

Submitter	M Damaschke
Submitter's Code	T1-F
Site & Location	Tariki Swamp, Taranaki, New Zealand
Sample Material	Peat
Physical Pretreatment	Visible contaminants removed.
Chemical Pretreatment	Sample washed in hot HCl, rinsed and treated with multiple hot NaOH washes. The NaOH insoluble fraction was treated with hot HCl, filtered, rinsed and dried.

$D^{14}C$	-333.7 ±	2.1 ‰
$F^{14}C$%	66.6 ±	0.2 %
Result	**3262 ± 26 BP**	

(AMS measurement)

Comments

Please note: Because of the small size of this sample, the Carbon-13 stable isotope value ($\delta^{13}C$) was measured on prepared graphite using the AMS spectrometer. The radiocarbon date has therefore been corrected for isotopic fractionation. However the AMS-measured $\delta^{13}C$ value can differ from the $\delta^{13}C$ of the original material and it is therefore not shown.

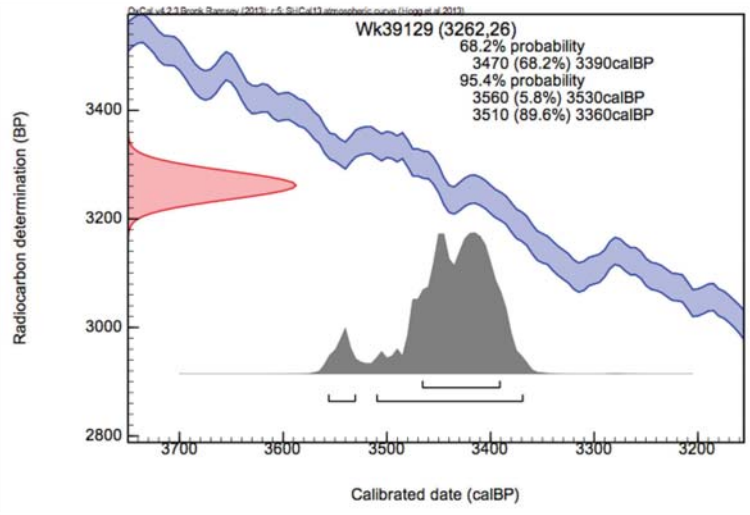

- Explanation of the calibrated Oxcal plots can be found at the Oxford Radiocarbon Accelerator Unit's calibration web pages (http://c14.arch.ox.ac.uk/embed.php?File=explanation.php)
- Result is *Conventional Age or Percent Modern Carbon (pMC)* following Stuiver and Polach, 1977, Radiocarbon 19, 355-363. This is based on the Libby half-life of 5568 yr with correction for isotopic fractionation applied. This age is normally quoted in publications and must include the appropriate error term and Wk number.
- Quoted errors are 1 standard deviation due to counting statistics multiplied by an experimentally determined Laboratory Error Multiplier.
- The isotopic fractionation, $\delta^{13}C$, is expressed as ‰ wrt PDB and is measured on sample CO_2.
- $F^{14}C$% is also known as *Percent Modern Carbon (pMC)*.

THE UNIVERSITY OF
WAIKATO
Te Whare Wānanga o Waikato

Private Bag 3105
Hamilton,
New Zealand.
Ph +64 7 838 4278
email c14@waikato.ac.nz

Monday, 16 June 2014

Radiocarbon Dating Laboratory

Report on Radiocarbon Age Determination for Wk- 39130

Submitter	M Damaschke
Submitter's Code	T1-H
Site & Location	Tariki Swamp, Taranaki, New Zealand
Sample Material	Soil, organics
Physical Pretreatment	Visible contaminants removed.
Chemical Pretreatment	Sample washed in hot HCl, rinsed and treated with multiple hot NaOH washes. The NaOH insoluble fraction was treated with hot HCl, filtered, rinsed and dried.

$D^{14}C$	-487.7 ±	1.8 ‰
$F^{14}C\%$	51.2 ±	0.2 %
Result	**5372 ± 28 BP**	

(AMS measurement)

Comments

Please note: Because of the small size of this sample, the Carbon-13 stable isotope value ($\delta^{13}C$) was measured on prepared graphite using the AMS spectrometer. The radiocarbon date has therefore been corrected for isotopic fractionation. However the AMS-measured $\delta^{13}C$ value can differ from the $\delta^{13}C$ of the original material and it is therefore not shown.

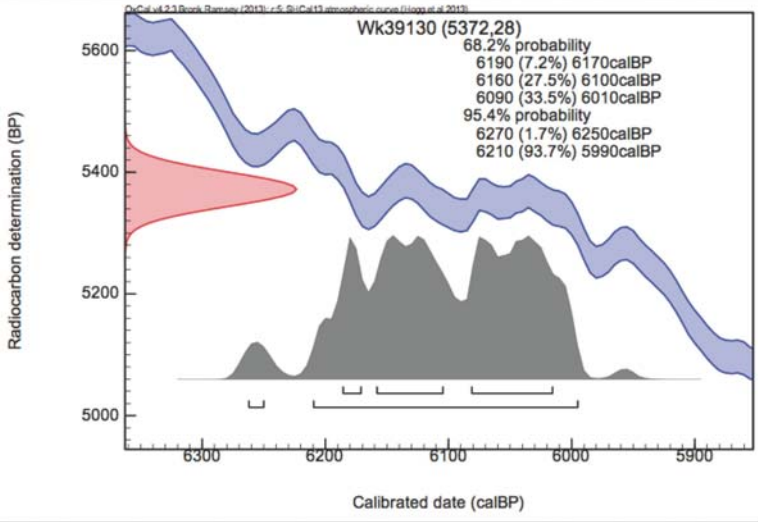

- Explanation of the calibrated Oxcal plots can be found at the Oxford Radiocarbon Accelerator Unit's calibration web pages (http://c14.arch.ox.ac.uk/embed.php?File=explanation.php)
- Result is *Conventional Age or Percent Modern Carbon (pMC)* following Stuiver and Polach, 1977, Radiocarbon 19, 355-363. This is based on the Libby half-life of 5568 yr with correction for isotopic fractionation applied. This age is normally quoted in publications and must include the appropriate error term and Wk number.
- Quoted errors are 1 standard deviation due to counting statistics multiplied by an experimentally determined Laboratory Error Multiplier.
- The isotopic fractionation, $\delta^{13}C$, is expressed as ‰ wrt PDB and is measured on sample CO_2.
- $F^{14}C\%$ is also known as *Percent Modern Carbon (pMC)*.

THE UNIVERSITY OF
WAIKATO
Te Whare Wānanga o Waikato

Private Bag 3105
Hamilton,
New Zealand.
Ph +64 7 838 4278
email c14@waikato.ac.nz

Monday, 16 June 2014

Radiocarbon Dating Laboratory

Report on Radiocarbon Age Determination for Wk- 39131

Submitter	M Damaschke
Submitter's Code	T1-I
Site & Location	Tariki Swamp, Taranaki, New Zealand
Sample Material	Peat
Physical Pretreatment	Visible contaminants removed.
Chemical Pretreatment	Sample washed in hot HCl, rinsed and treated with multiple hot NaOH washes. The NaOH insoluble fraction was treated with hot HCl, filtered, rinsed and dried.

$D^{14}C$	-718.5 ±	1.4 ‰
$F^{14}C$%	28.1 ±	0.1 %
Result	**10,184 ± 39 BP**	

(AMS measurement)

Comments

Please note: Because of the small size of this sample, the Carbon-13 stable isotope value ($\delta^{13}C$) was measured on prepared graphite using the AMS spectrometer. The radiocarbon date has therefore been corrected for isotopic fractionation. However the AMS-measured $\delta^{13}C$ value can differ from the $\delta^{13}C$ of the original material and it is therefore not shown.

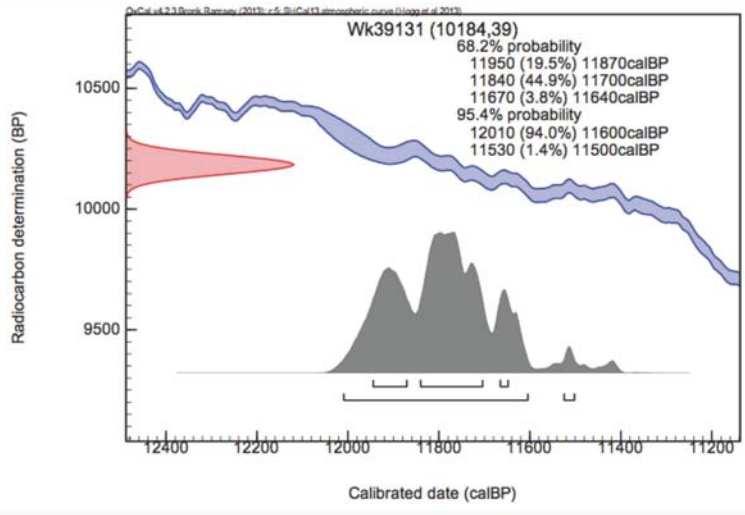

- Explanation of the calibrated Oxcal plots can be found at the Oxford Radiocarbon Accelerator Unit's calibration web pages (http://c14.arch.ox.ac.uk/embed.php?File=explanation.php)
- Result is *Conventional Age or Percent Modern Carbon (pMC)* following Stuiver and Polach, 1977, Radiocarbon 19, 355-363. This is based on the Libby half-life of 5568 yr with correction for isotopic fractionation applied. This age is normally quoted in publications and must include the appropriate error term and Wk number.
- Quoted errors are 1 standard deviation due to counting statistics multiplied by an experimentally determined Laboratory Error Multiplier.
- The isotopic fractionation, $\delta^{13}C$, is expressed as ‰ wrt PDB and is measured on sample CO_2.
- $F^{14}C$% is also known as *Percent Modern Carbon (pMC)*.

THE UNIVERSITY OF WAIKATO
Te Whare Wānanga o Waikato

Private Bag 3105
Hamilton,
New Zealand.
Ph +64 7 838 4278
email c14@waikato.ac.nz

Monday, 16 June 2014

Radiocarbon Dating Laboratory

Report on Radiocarbon Age Determination for Wk- 39132

Submitter	M Damaschke
Submitter's Code	T1-J
Site & Location	Tariki Swamp, Taranaki, New Zealand
Sample Material	Peat
Physical Pretreatment	Visible contaminants removed.
Chemical Pretreatment	Sample washed in hot HCl, rinsed and treated with multiple hot NaOH washes. The NaOH insoluble fraction was treated with hot HCl, filtered, rinsed and dried.

$D^{14}C$	-724.4 ±	1.3 ‰
$F^{14}C\%$	27.6 ±	0.1 %
Result	**10,353 ± 38 BP**	

(AMS measurement)

Comments

Please note: Because of the small size of this sample, the Carbon-13 stable isotope value ($\delta^{13}C$) was measured on prepared graphite using the AMS spectrometer. The radiocarbon date has therefore been corrected for isotopic fractionation. However the AMS-measured $\delta^{13}C$ value can differ from the $\delta^{13}C$ of the original material and it is therefore not shown.

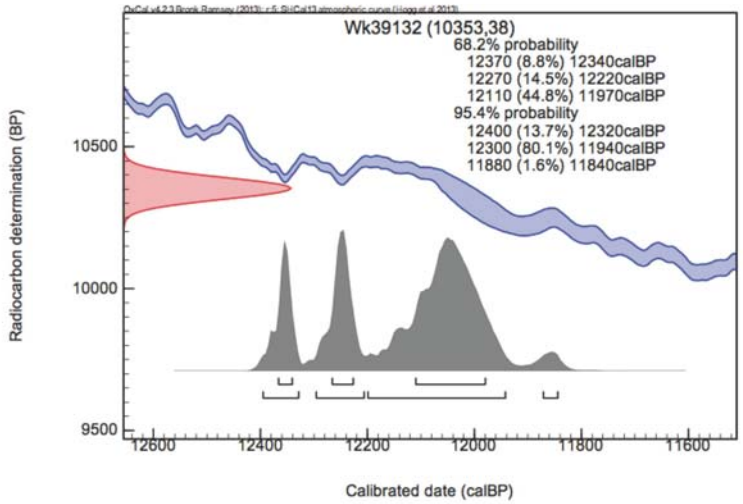

- Explanation of the calibrated Oxcal plots can be found at the Oxford Radiocarbon Accelerator Unit's calibration web pages (http://c14.arch.ox.ac.uk/embed.php?File=explanation.php)
- Result is *Conventional Age or Percent Modern Carbon (pMC)* following Stuiver and Polach, 1977, Radiocarbon 19, 355-363. This is based on the Libby half-life of 5568 yr with correction for isotopic fractionation applied. This age is normally quoted in publications and must include the appropriate error term and Wk number.
- Quoted errors are 1 standard deviation due to counting statistics multiplied by an experimentally determined Laboratory Error Multiplier.
- The isotopic fractionation, $\delta^{13}C$, is expressed as ‰ wrt PDB and is measured on sample CO_2.
- $F^{14}C\%$ is also known as *Percent Modern Carbon (pMC)*.

THE UNIVERSITY OF
WAIKATO
Te Whare Wānanga o Waikato

Private Bag 3105
Hamilton,
New Zealand.
Ph +64 7 838 4278
email c14@waikato.ac.nz

Monday, 16 June 2014

Radiocarbon Dating Laboratory

Report on Radiocarbon Age Determination for Wk- 39133

Submitter	M Damaschke
Submitter's Code	T1-L
Site & Location	Tariki Swamp, Taranaki, New Zealand
Sample Material	Peat
Physical Pretreatment	Visible contaminants removed.
Chemical Pretreatment	Sample washed in hot HCl, rinsed and treated with multiple hot NaOH washes. The NaOH insoluble fraction was treated with hot HCl, filtered, rinsed and dried.

$D^{14}C$	-804.3 ±	1.2 ‰
$F^{14}C\%$	19.6 ±	0.1 %
Result	**13,105 ± 50 BP**	

(AMS measurement)

Comments

Please note: Because of the small size of this sample, the Carbon-13 stable isotope value ($\delta^{13}C$) was measured on prepared graphite using the AMS spectrometer. The radiocarbon date has therefore been corrected for isotopic fractionation. However the AMS-measured $\delta^{13}C$ value can differ from the $\delta^{13}C$ of the original material and it is therefore not shown.

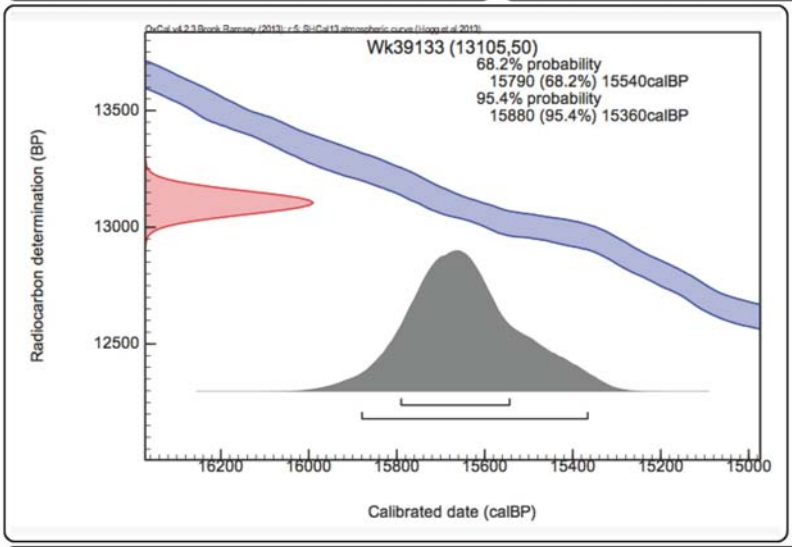

- Explanation of the calibrated Oxcal plots can be found at the Oxford Radiocarbon Accelerator Unit's calibration web pages (http://c14.arch.ox.ac.uk/embed.php?File=explanation.php)
- Result is *Conventional Age or Percent Modern Carbon (pMC)* following Stuiver and Polach, 1977, Radiocarbon 19, 355-363. This is based on the Libby half-life of 5568 yr with correction for isotopic fractionation applied. This age is normally quoted in publications and must include the appropriate error term and Wk number.
- Quoted errors are 1 standard deviation due to counting statistics multiplied by an experimentally determined Laboratory Error Multiplier.
- The isotopic fractionation, $\delta^{13}C$, is expressed as ‰ wrt PDB and is measured on sample CO_2.
- $F^{14}C\%$ is also known as *Percent Modern Carbon (pMC)*.

THE UNIVERSITY OF
WAIKATO
Te Whare Wānanga o Waikato

Private Bag 3105
Hamilton,
New Zealand.
Ph +64 7 838 4278
email c14@waikato.ac.nz

Monday, 16 June 2014

Radiocarbon Dating Laboratory

Report on Radiocarbon Age Determination for Wk- 39134

Submitter	M Damaschke
Submitter's Code	T1-N
Site & Location	Tariki Swamp, Taranaki, New Zealand
Sample Material	Organic mud
Physical Pretreatment	Visible contaminants removed.
Chemical Pretreatment	Sample washed in hot HCl, rinsed and treated with multiple hot NaOH washes. The NaOH insoluble fraction was treated with hot HCl, filtered, rinsed and dried.

$D^{14}C$	-827.8 ±	1.3 ‰
$F^{14}C\%$	17.2 ±	0.1 %
Result	**14,130 ± 60 BP**	

(AMS measurement)

Comments

Please note: Because of the small size of this sample, the Carbon-13 stable isotope value ($\delta^{13}C$) was measured on prepared graphite using the AMS spectrometer. The radiocarbon date has therefore been corrected for isotopic fractionation. However the AMS-measured $\delta^{13}C$ value can differ from the $\delta^{13}C$ of the original material and it is therefore not shown.

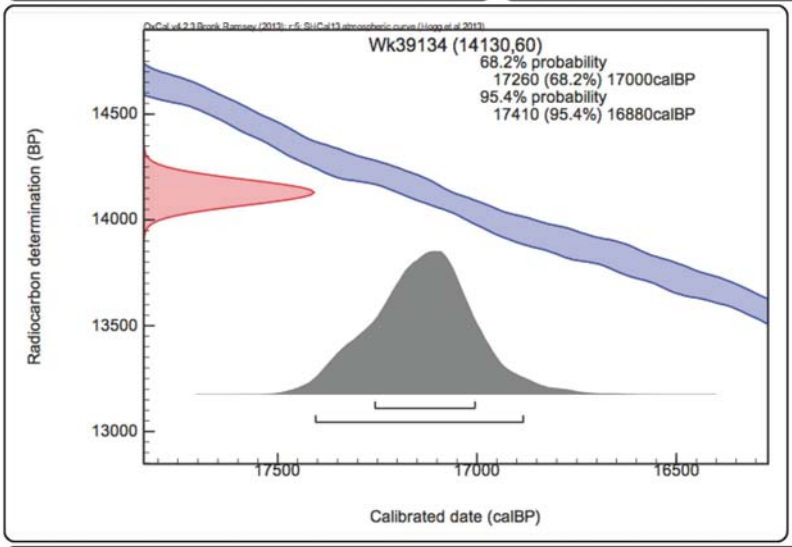

- Explanation of the calibrated Oxcal plots can be found at the Oxford Radiocarbon Accelerator Unit's calibration web pages (http://c14.arch.ox.ac.uk/embed.php?File=explanation.php)
- Result is *Conventional Age or Percent Modern Carbon (pMC)* following Stuiver and Polach, 1977, Radiocarbon 19, 355-363. This is based on the Libby half-life of 5568 yr with correction for isotopic fractionation applied. This age is normally quoted in publications and must include the appropriate error term and Wk number.
- Quoted errors are 1 standard deviation due to counting statistics multiplied by an experimentally determined Laboratory Error Multiplier.
- The isotopic fractionation, $\delta^{13}C$, is expressed as ‰ wrt PDB and is measured on sample CO_2.
- $F^{14}C\%$ is also known as *Percent Modern Carbon (pMC)*.

THE UNIVERSITY OF
WAIKATO
Te Whare Wānanga o Waikato

Private Bag 3105
Hamilton,
New Zealand.
Ph +64 7 838 4278
email c14@waikato.ac.nz

Monday, 16 June 2014

Radiocarbon Dating Laboratory

Report on Radiocarbon Age Determination for Wk- 39135

Submitter	M Damaschke
Submitter's Code	T2-C
Site & Location	Tariki Swamp, Taranaki, New Zealand
Sample Material	Organic mud
Physical Pretreatment	Visible contaminants removed.
Chemical Pretreatment	Sample washed in hot HCl, rinsed and treated with multiple hot NaOH washes. The NaOH insoluble fraction was treated with hot HCl, filtered, rinsed and dried.

$D^{14}C$	-333.8 ±	2.2 ‰
$F^{14}C\%$	66.6 ±	0.2 %
Result	**3263 ± 26 BP**	

(AMS measurement)

Comments

Please note: Because of the small size of this sample, the Carbon-13 stable isotope value ($\delta^{13}C$) was measured on prepared graphite using the AMS spectrometer. The radiocarbon date has therefore been corrected for isotopic fractionation. However the AMS-measured $\delta^{13}C$ value can differ from the $\delta^{13}C$ of the original material and it is therefore not shown.

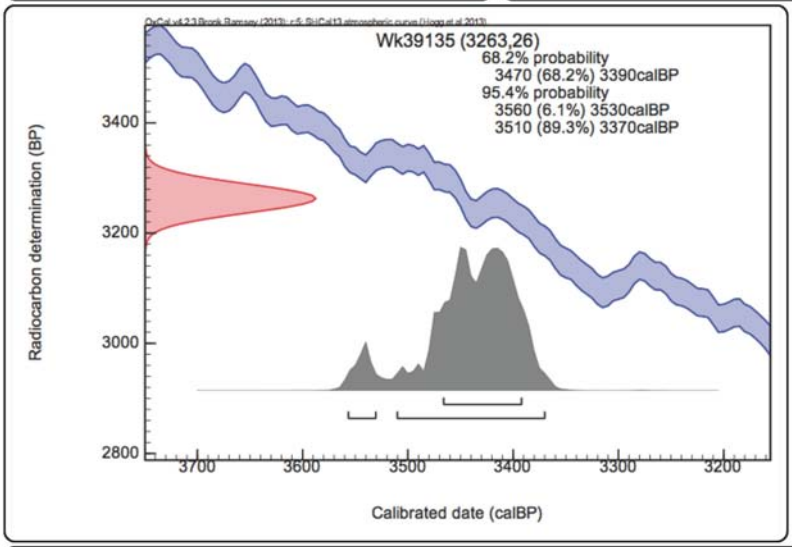

- Explanation of the calibrated Oxcal plots can be found at the Oxford Radiocarbon Accelerator Unit's calibration web pages (http://c14.arch.ox.ac.uk/embed.php?File=explanation.php)
- Result is *Conventional Age or Percent Modern Carbon (pMC)* following Stuiver and Polach, 1977, Radiocarbon 19, 355-363. This is based on the Libby half-life of 5568 yr with correction for isotopic fractionation applied. This age is normally quoted in publications and must include the appropriate error term and Wk number.
- Quoted errors are 1 standard deviation due to counting statistics multiplied by an experimentally determined Laboratory Error Multiplier.
- The isotopic fractionation, $\delta^{13}C$, is expressed as ‰ wrt PDB and is measured on sample CO_2.
- $F^{14}C\%$ is also known as *Percent Modern Carbon (pMC)*.

THE UNIVERSITY OF WAIKATO
Te Whare Wānanga o Waikato

Private Bag 3105
Hamilton,
New Zealand.
Ph +64 7 838 4278
email c14@waikato.ac.nz

Monday, 16 June 2014

Radiocarbon Dating Laboratory

Report on Radiocarbon Age Determination for Wk- 39136

Submitter	M Damaschke
Submitter's Code	T2-L
Site & Location	Tariki Swamp, Taranaki, New Zealand
Sample Material	Clay
Physical Pretreatment	Visible contaminants removed.
Chemical Pretreatment	Sample washed in hot HCl, rinsed and treated with multiple hot NaOH washes. The NaOH insoluble fraction was treated with hot HCl, filtered, rinsed and dried.

$D^{14}C$	-827.7 ±	1.1 ‰
$F^{14}C\%$	17.2 ±	0.1 %
Result	**14,124 ± 53 BP**	

(AMS measurement)

Comments

Please note: Because of the small size of this sample, the Carbon-13 stable isotope value ($\delta^{13}C$) was measured on prepared graphite using the AMS spectrometer. The radiocarbon date has therefore been corrected for isotopic fractionation. However the AMS-measured $\delta^{13}C$ value can differ from the $\delta^{13}C$ of the original material and it is therefore not shown.

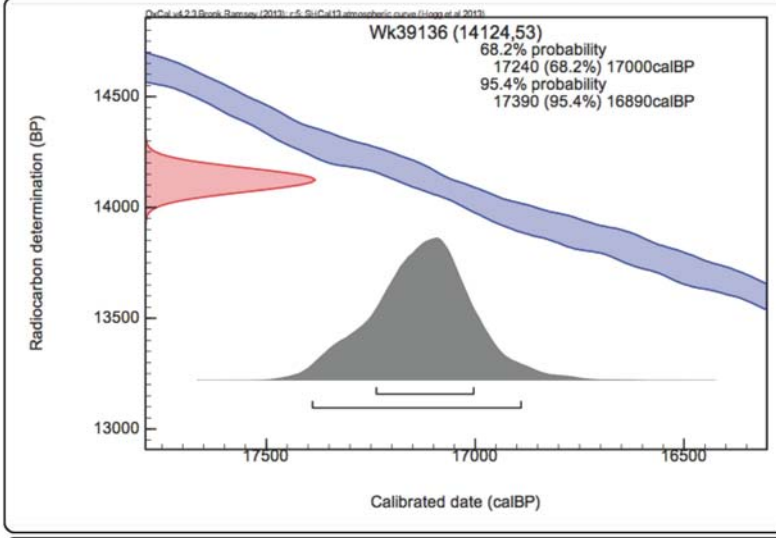

- Explanation of the calibrated Oxcal plots can be found at the Oxford Radiocarbon Accelerator Unit's calibration web pages (http://c14.arch.ox.ac.uk/embed.php?File=explanation.php)
- Result is *Conventional Age or Percent Modern Carbon (pMC)* following Stuiver and Polach, 1977, Radiocarbon 19, 355-363. This is based on the Libby half-life of 5568 yr with correction for isotopic fractionation applied. This age is normally quoted in publications and must include the appropriate error term and Wk number.
- Quoted errors are 1 standard deviation due to counting statistics multiplied by an experimentally determined Laboratory Error Multiplier.
- The isotopic fractionation, $\delta^{13}C$, is expressed as ‰ wrt PDB and is measured on sample CO_2.
- $F^{14}C\%$ is also known as *Percent Modern Carbon (pMC)*.

THE UNIVERSITY OF
WAIKATO
Te Whare Wānanga o Waikato

Private Bag 3105
Hamilton,
New Zealand.
Ph +64 7 838 4278
email c14@waikato.ac.nz

Monday, 16 June 2014

Radiocarbon Dating Laboratory

Report on Radiocarbon Age Determination for Wk- 39137

Submitter	M Damaschke
Submitter's Code	T2-J
Site & Location	Tariki Swamp, Taranaki, New Zealand
Sample Material	Clay=silt
Physical Pretreatment	Visible contaminants removed.
Chemical Pretreatment	Sample washed in hot HCl, rinsed and treated with multiple hot NaOH washes. The NaOH insoluble fraction was treated with hot HCl, filtered, rinsed and dried.

$D^{14}C$	-832.1 ±	1.1 ‰
$F^{14}C\%$	16.8 ±	0.1 %
Result	**14,334 ± 53 BP**	

(AMS measurement)

Comments

Please note: Because of the small size of this sample, the Carbon-13 stable isotope value ($\delta^{13}C$) was measured on prepared graphite using the AMS spectrometer. The radiocarbon date has therefore been corrected for isotopic fractionation. However the AMS-measured $\delta^{13}C$ value can differ from the $\delta^{13}C$ of the original material and it is therefore not shown.

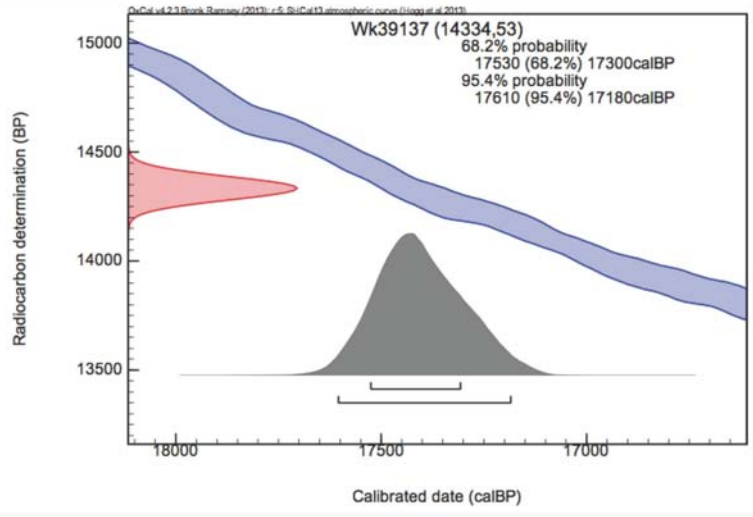

- Explanation of the calibrated Oxcal plots can be found at the Oxford Radiocarbon Accelerator Unit's calibration web pages (http://c14.arch.ox.ac.uk/embed.php?File=explanation.php)
- Result is *Conventional Age or Percent Modern Carbon (pMC)* following Stuiver and Polach, 1977, Radiocarbon 19, 355-363. This is based on the Libby half-life of 5568 yr with correction for isotopic fractionation applied. This age is normally quoted in publications and must include the appropriate error term and Wk number.
- Quoted errors are 1 standard deviation due to counting statistics multiplied by an experimentally determined Laboratory Error Multiplier.
- The isotopic fractionation, $\delta^{13}C$, is expressed as ‰ wrt PDB and is measured on sample CO_2.
- $F^{14}C\%$ is also known as *Percent Modern Carbon (pMC)*.

THE UNIVERSITY OF
WAIKATO
Te Whare Wānanga o Waikato

Private Bag 3105
Hamilton,
New Zealand.
Ph +64 7 838 4278
email c14@waikato.ac.nz

Monday, 4 August 2014

Radiocarbon Dating Laboratory

Report on Radiocarbon Age Determination for Wk- 39482

Submitter	M Damaschke
Submitter's Code	N1-A
Site & Location	Ngaere Swamp, Taranaki, New Zealand
Sample Material	Peat
Physical Pretreatment	Visible contaminants removed.
Chemical Pretreatment	Sample washed in hot HCl, rinsed and treated with multiple hot NaOH washes. The NaOH insoluble fraction was treated with hot HCl, filtered, rinsed and dried.

$D^{14}C$	-262.8 ±	2.3 ‰
$F^{14}C\%$	73.7 ±	0.2 %
Result	**2449 ± 25 BP**	

(AMS measurement)

Comments

Please note: Because of the small size of this sample, the Carbon-13 stable isotope value ($\delta^{13}C$) was measured on prepared graphite using the AMS spectrometer. The radiocarbon date has therefore been corrected for isotopic fractionation. However the AMS-measured $\delta^{13}C$ value can differ from the $\delta^{13}C$ of the original material and it is therefore not shown.

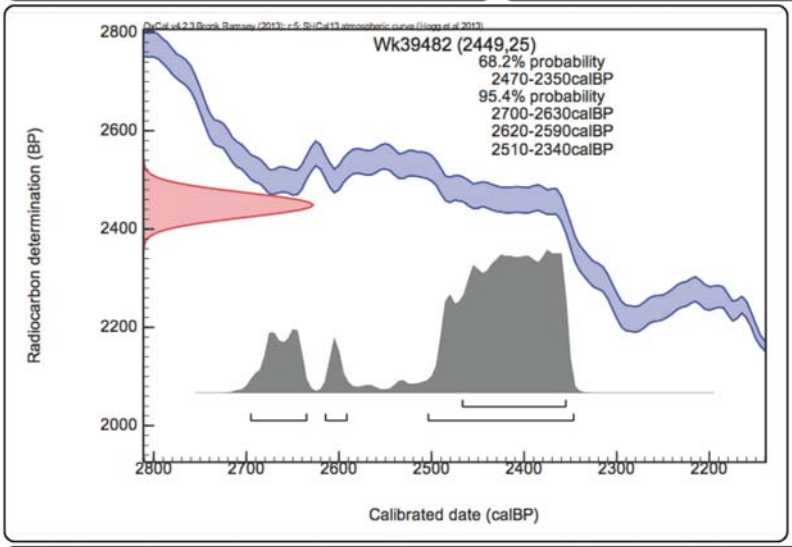

- Explanation of the calibrated Oxcal plots can be found at the Oxford Radiocarbon Accelerator Unit's calibration web pages (http://c14.arch.ox.ac.uk/embed.php?File=explanation.php)
- Result is *Conventional Age or Percent Modern Carbon (pMC)* following Stuiver and Polach, 1977, Radiocarbon 19, 355-363. This is based on the Libby half-life of 5568 yr with correction for isotopic fractionation applied. This age is normally quoted in publications and must include the appropriate error term and Wk number.
- Quoted errors are 1 standard deviation due to counting statistics multiplied by an experimentally determined Laboratory Error Multiplier.
- The isotopic fractionation, $\delta^{13}C$, is expressed as ‰ wrt PDB and is measured on sample CO_2.
- $F^{14}C\%$ is also known as *Percent Modern Carbon (pMC)*.

THE UNIVERSITY OF
WAIKATO
Te Whare Wānanga o Waikato

Private Bag 3105
Hamilton,
New Zealand.
Ph +64 7 838 4278
email c14@waikato.ac.nz

Monday, 4 August 2014

Radiocarbon Dating Laboratory

Report on Radiocarbon Age Determination for Wk- 39483

Submitter	M Damaschke
Submitter's Code	N1-C
Site & Location	Ngaere Swamp, Taranaki, New Zealand
Sample Material	Peat
Physical Pretreatment	Visible contaminants removed.
Chemical Pretreatment	Sample washed in hot HCl, rinsed and treated with multiple hot NaOH washes. The NaOH insoluble fraction was treated with hot HCl, filtered, rinsed and dried.

$D^{14}C$	-441.6 ±	1.7 ‰
$F^{14}C\%$	55.8 ±	0.2 %
Result	**4680 ± 25 BP**	

(AMS measurement)

Comments

Please note: Because of the small size of this sample, the Carbon-13 stable isotope value ($\delta^{13}C$) was measured on prepared graphite using the AMS spectrometer. The radiocarbon date has therefore been corrected for isotopic fractionation. However the AMS-measured $\delta^{13}C$ value can differ from the $\delta^{13}C$ of the original material and it is therefore not shown.

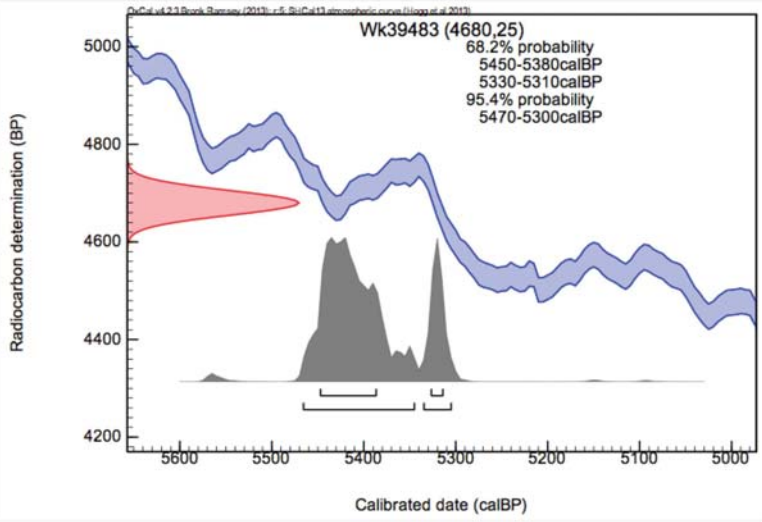

- Explanation of the calibrated Oxcal plots can be found at the Oxford Radiocarbon Accelerator Unit's calibration web pages (http://c14.arch.ox.ac.uk/embed.php?File=explanation.php)
- Result is *Conventional Age or Percent Modern Carbon (pMC)* following Stuiver and Polach, 1977, Radiocarbon 19, 355-363. This is based on the Libby half-life of 5568 yr with correction for isotopic fractionation applied. This age is normally quoted in publications and must include the appropriate error term and Wk number.
- Quoted errors are 1 standard deviation due to counting statistics multiplied by an experimentally determined Laboratory Error Multiplier.
- The isotopic fractionation, $\delta^{13}C$, is expressed as ‰ wrt PDB and is measured on sample CO_2.
- $F^{14}C\%$ is also known as *Percent Modern Carbon (pMC)*.

THE UNIVERSITY OF
WAIKATO
Te Whare Wānanga o Waikato

Private Bag 3105
Hamilton,
New Zealand.
Ph +64 7 838 4278
email c14@waikato.ac.nz

Monday, 4 August 2014

Radiocarbon Dating Laboratory

Report on Radiocarbon Age Determination for Wk- 39484

Submitter	M Damaschke
Submitter's Code	N1-D
Site & Location	Ngaere Swamp, Taranaki, New Zealand
Sample Material	Peat
Physical Pretreatment	Visible contaminants removed.
Chemical Pretreatment	Sample washed in hot HCl, rinsed and treated with multiple hot NaOH washes. The NaOH insoluble fraction was treated with hot HCl, filtered, rinsed and dried.

$D^{14}C$	-530.2 ±	1.7 ‰
$F^{14}C\%$	47.0 ±	0.2 %
Result	**6069 ± 29 BP**	

(AMS measurement)

Comments

Please note: Because of the small size of this sample, the Carbon-13 stable isotope value ($\delta^{13}C$) was measured on prepared graphite using the AMS spectrometer. The radiocarbon date has therefore been corrected for isotopic fractionation. However the AMS-measured $\delta^{13}C$ value can differ from the $\delta^{13}C$ of the original material and it is therefore not shown.

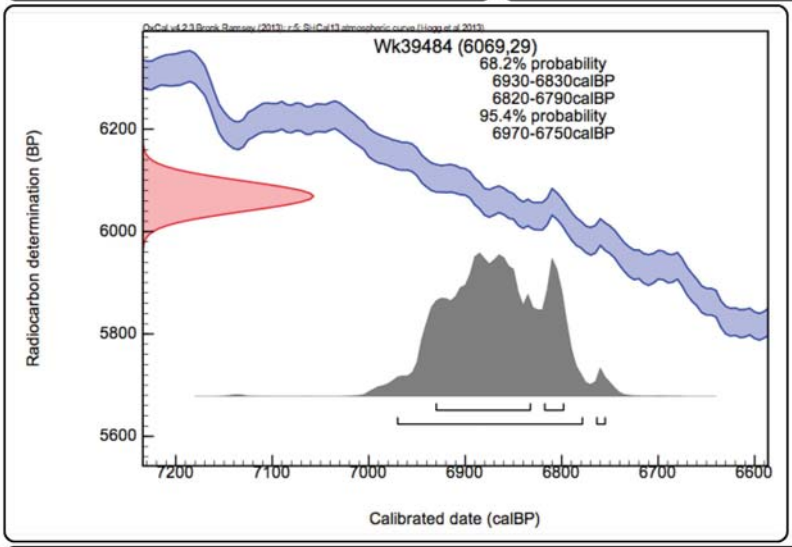

- Explanation of the calibrated Oxcal plots can be found at the Oxford Radiocarbon Accelerator Unit's calibration web pages (http://c14.arch.ox.ac.uk/embed.php?File=explanation.php)
- Result is *Conventional Age or Percent Modern Carbon (pMC)* following Stuiver and Polach, 1977, Radiocarbon 19, 355-363. This is based on the Libby half-life of 5568 yr with correction for isotopic fractionation applied. This age is normally quoted in publications and must include the appropriate error term and Wk number.
- Quoted errors are 1 standard deviation due to counting statistics multiplied by an experimentally determined Laboratory Error Multiplier.
- The isotopic fractionation, $\delta^{13}C$, is expressed as ‰ wrt PDB and is measured on sample CO_2.
- $F^{14}C\%$ is also known as *Percent Modern Carbon (pMC)*.

THE UNIVERSITY OF
WAIKATO
Te Whare Wānanga o Waikato

Private Bag 3105
Hamilton,
New Zealand.
Ph +64 7 838 4278
email c14@waikato.ac.nz

Monday, 4 August 2014

Radiocarbon Dating Laboratory

Report on Radiocarbon Age Determination for Wk- 39485

Submitter	M Damaschke
Submitter's Code	N1-E
Site & Location	Ngaere Swamp, Taranaki, New Zealand
Sample Material	Peat
Physical Pretreatment	Visible contaminants removed.
Chemical Pretreatment	Sample washed in hot HCl, rinsed and treated with multiple hot NaOH washes. The NaOH insoluble fraction was treated with hot HCl, filtered, rinsed and dried.

$D^{14}C$	-544.4 ±	1.6 ‰
$F^{14}C\%$	45.6 ±	0.2 %
Result	**6315 ± 28 BP**	

(AMS measurement)

Comments

Please note: Because of the small size of this sample, the Carbon-13 stable isotope value ($\delta^{13}C$) was measured on prepared graphite using the AMS spectrometer. The radiocarbon date has therefore been corrected for isotopic fractionation. However the AMS-measured $\delta^{13}C$ value can differ from the $\delta^{13}C$ of the original material and it is therefore not shown.

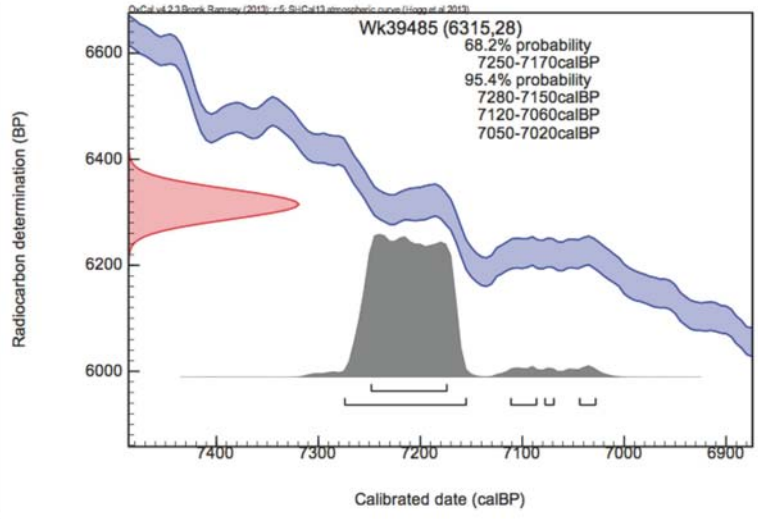

- Explanation of the calibrated Oxcal plots can be found at the Oxford Radiocarbon Accelerator Unit's calibration web pages (http://c14.arch.ox.ac.uk/embed.php?File=explanation.php)
- Result is *Conventional Age or Percent Modern Carbon (pMC)* following Stuiver and Polach, 1977, Radiocarbon 19, 355-363. This is based on the Libby half-life of 5568 yr with correction for isotopic fractionation applied. This age is normally quoted in publications and must include the appropriate error term and Wk number.
- Quoted errors are 1 standard deviation due to counting statistics multiplied by an experimentally determined Laboratory Error Multiplier.
- The isotopic fractionation, $\delta^{13}C$, is expressed as ‰ wrt PDB and is measured on sample CO_2.
- $F^{14}C\%$ is also known as *Percent Modern Carbon (pMC)*.

THE UNIVERSITY OF
WAIKATO
Te Whare Wānanga o Waikato

Private Bag 3105
Hamilton,
New Zealand.
Ph +64 7 838 4278
email c14@waikato.ac.nz

Monday, 4 August 2014

Radiocarbon Dating Laboratory

Report on Radiocarbon Age Determination for Wk- 39486

Submitter	M Damaschke
Submitter's Code	N1-G
Site & Location	Ngaere Swamp, Taranaki, New Zealand
Sample Material	Peat
Physical Pretreatment	Visible contaminants removed.
Chemical Pretreatment	Sample washed in hot HCl, rinsed and treated with multiple hot NaOH washes. The NaOH insoluble fraction was treated with hot HCl, filtered, rinsed and dried.

$D^{14}C$	-598.5 ±	1.5 ‰
$F^{14}C\%$	40.1 ±	0.1 %
Result	**7331 ± 29 BP**	

(AMS measurement)

Comments

Please note: Because of the small size of this sample, the Carbon-13 stable isotope value ($\delta^{13}C$) was measured on prepared graphite using the AMS spectrometer. The radiocarbon date has therefore been corrected for isotopic fractionation. However the AMS-measured $\delta^{13}C$ value can differ from the $\delta^{13}C$ of the original material and it is therefore not shown.

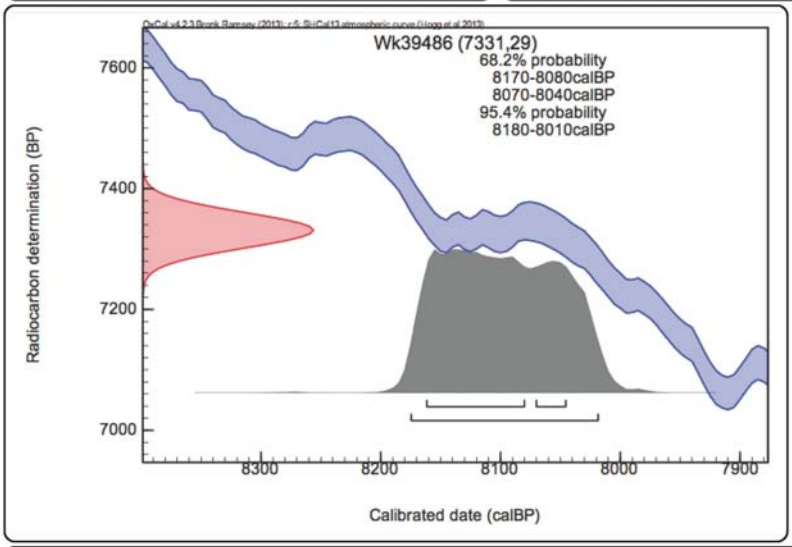

- Explanation of the calibrated Oxcal plots can be found at the Oxford Radiocarbon Accelerator Unit's calibration web pages (http://c14.arch.ox.ac.uk/embed.php?File=explanation.php)
- Result is *Conventional Age or Percent Modern Carbon (pMC)* following Stuiver and Polach, 1977, Radiocarbon 19, 355-363. This is based on the Libby half-life of 5568 yr with correction for isotopic fractionation applied. This age is normally quoted in publications and must include the appropriate error term and Wk number.
- Quoted errors are 1 standard deviation due to counting statistics multiplied by an experimentally determined Laboratory Error Multiplier.
- The isotopic fractionation, $\delta^{13}C$, is expressed as ‰ wrt PDB and is measured on sample CO_2.
- $F^{14}C\%$ is also known as *Percent Modern Carbon (pMC)*.

THE UNIVERSITY OF
WAIKATO
Te Whare Wānanga o Waikato

Private Bag 3105
Hamilton,
New Zealand.
Ph +64 7 838 4278
email c14@waikato.ac.nz

Monday, 4 August 2014

Radiocarbon Dating Laboratory

Report on Radiocarbon Age Determination for Wk- 39487

Submitter	M Damaschke
Submitter's Code	N1-I
Site & Location	Ngaere Swamp, Taranaki, New Zealand
Sample Material	Peat
Physical Pretreatment	Visible contaminants removed.
Chemical Pretreatment	Sample washed in hot HCl, rinsed and treated with multiple hot NaOH washes. The NaOH insoluble fraction was treated with hot HCl, filtered, rinsed and dried.

$D^{14}C$	-656.8 ±	2.1 ‰
$F^{14}C\%$	34.3 ±	0.2 %
Result	**8592 ± 49 BP**	

(AMS measurement)

Comments

Please note: Because of the small size of this sample, the Carbon-13 stable isotope value ($\delta^{13}C$) was measured on prepared graphite using the AMS spectrometer. The radiocarbon date has therefore been corrected for isotopic fractionation. However the AMS-measured $\delta^{13}C$ value can differ from the $\delta^{13}C$ of the original material and it is therefore not shown.

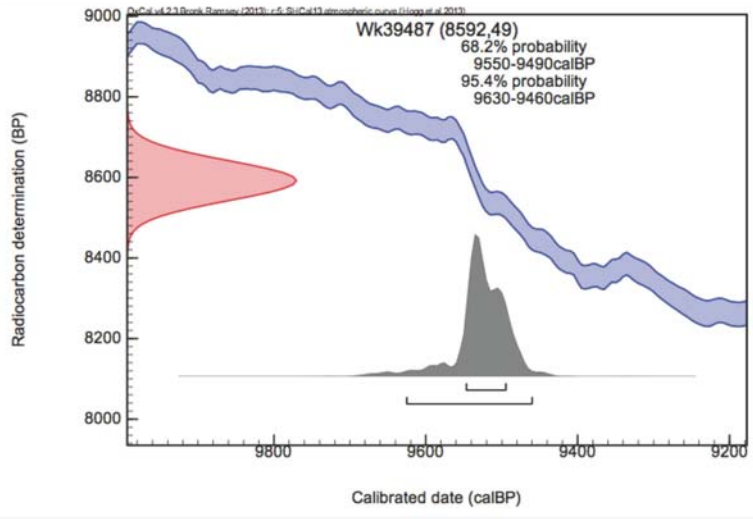

- Explanation of the calibrated Oxcal plots can be found at the Oxford Radiocarbon Accelerator Unit's calibration web pages (http://c14.arch.ox.ac.uk/embed.php?File=explanation.php)
- Result is *Conventional Age or Percent Modern Carbon (pMC)* following Stuiver and Polach, 1977, Radiocarbon 19, 355-363. This is based on the Libby half-life of 5568 yr with correction for isotopic fractionation applied. This age is normally quoted in publications and must include the appropriate error term and Wk number.
- Quoted errors are 1 standard deviation due to counting statistics multiplied by an experimentally determined Laboratory Error Multiplier.
- The isotopic fractionation, $\delta^{13}C$, is expressed as ‰ wrt PDB and is measured on sample CO_2.
- $F^{14}C\%$ is also known as *Percent Modern Carbon (pMC)*.

THE UNIVERSITY OF
WAIKATO
Te Whare Wānanga o Waikato

Private Bag 3105
Hamilton,
New Zealand.
Ph +64 7 838 4278
email c14@waikato.ac.nz

Monday, 4 August 2014

Radiocarbon Dating Laboratory

Report on Radiocarbon Age Determination for Wk- 39488

Submitter	M Damaschke
Submitter's Code	N1-K
Site & Location	Ngaere Swamp, Taranaki, New Zealand
Sample Material	Peat
Physical Pretreatment	Visible contaminants removed.
Chemical Pretreatment	Sample washed in hot HCl, rinsed and treated with multiple hot NaOH washes. The NaOH insoluble fraction was treated with hot HCl, filtered, rinsed and dried.

$D^{14}C$	-691.0 ±	1.4 ‰
$F^{14}C\%$	30.9 ±	0.1 %
Result	**9434 ± 37 BP**	

(AMS measurement)

Comments

Please note: Because of the small size of this sample, the Carbon-13 stable isotope value ($\delta^{13}C$) was measured on prepared graphite using the AMS spectrometer. The radiocarbon date has therefore been corrected for isotopic fractionation. However the AMS-measured $\delta^{13}C$ value can differ from the $\delta^{13}C$ of the original material and it is therefore not shown.

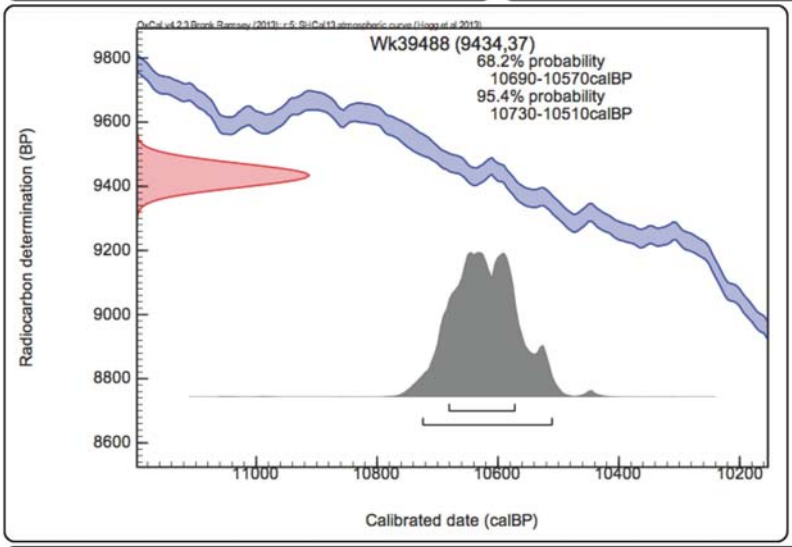

- Explanation of the calibrated Oxcal plots can be found at the Oxford Radiocarbon Accelerator Unit's calibration web pages (http://c14.arch.ox.ac.uk/embed.php?File=explanation.php)
- Result is *Conventional Age or Percent Modern Carbon (pMC)* following Stuiver and Polach, 1977, Radiocarbon 19, 355-363. This is based on the Libby half-life of 5568 yr with correction for isotopic fractionation applied. This age is normally quoted in publications and must include the appropriate error term and Wk number.
- Quoted errors are 1 standard deviation due to counting statistics multiplied by an experimentally determined Laboratory Error Multiplier.
- The isotopic fractionation, $\delta^{13}C$, is expressed as ‰ wrt PDB and is measured on sample CO_2.
- $F^{14}C\%$ is also known as *Percent Modern Carbon (pMC)*.

THE UNIVERSITY OF
WAIKATO
Te Whare Wānanga o Waikato

Private Bag 3105
Hamilton,
New Zealand.
Ph +64 7 838 4278
email c14@waikato.ac.nz

Monday, 4 August 2014

Radiocarbon Dating Laboratory

Report on Radiocarbon Age Determination for Wk- 39489

Submitter	M Damaschke
Submitter's Code	N1-N
Site & Location	Ngaere Swamp, Taranaki, New Zealand
Sample Material	Peat
Physical Pretreatment	Visible contaminants removed.
Chemical Pretreatment	Sample washed in hot HCl, rinsed and treated with multiple hot NaOH washes. The NaOH insoluble fraction was treated with hot HCl, filtered, rinsed and dried.

$D^{14}C$	-727.8 ±	1.2 ‰
$F^{14}C$%	27.2 ±	0.1 %
Result	**10,453 ± 37 BP**	

(AMS measurement)

Comments

Please note: Because of the small size of this sample, the Carbon-13 stable isotope value ($\delta^{13}C$) was measured on prepared graphite using the AMS spectrometer. The radiocarbon date has therefore been corrected for isotopic fractionation. However the AMS-measured $\delta^{13}C$ value can differ from the $\delta^{13}C$ of the original material and it is therefore not shown.

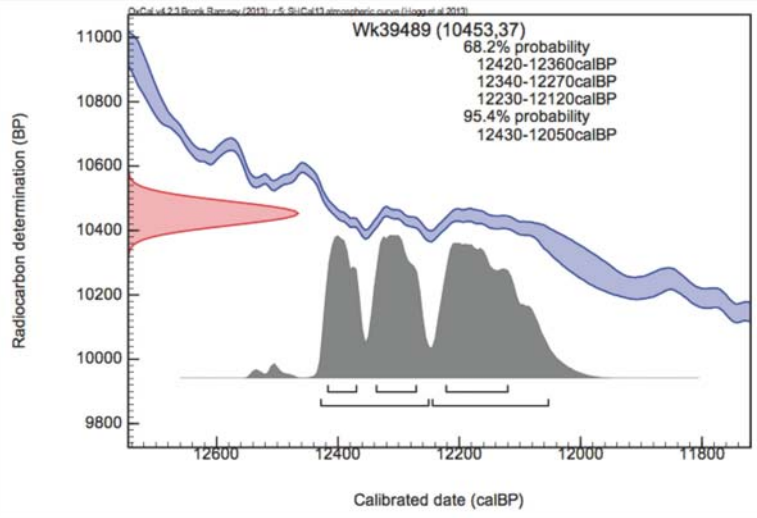

- Explanation of the calibrated Oxcal plots can be found at the Oxford Radiocarbon Accelerator Unit's calibration web pages (http://c14.arch.ox.ac.uk/embed.php?File=explanation.php)
- Result is *Conventional Age or Percent Modern Carbon (pMC)* following Stuiver and Polach, 1977, Radiocarbon 19, 355-363. This is based on the Libby half-life of 5568 yr with correction for isotopic fractionation applied. This age is normally quoted in publications and must include the appropriate error term and Wk number.
- Quoted errors are 1 standard deviation due to counting statistics multiplied by an experimentally determined Laboratory Error Multiplier.
- The isotopic fractionation, $\delta^{13}C$, is expressed as ‰ wrt PDB and is measured on sample CO_2.
- $F^{14}C$% is also known as *Percent Modern Carbon (pMC)*.

THE UNIVERSITY OF
WAIKATO
Te Whare Wānanga o Waikato

Private Bag 3105
Hamilton,
New Zealand.
Ph +64 7 838 4278
email c14@waikato.ac.nz

Monday, 4 August 2014

Radiocarbon Dating Laboratory

Report on Radiocarbon Age Determination for Wk- 39490

Submitter	M Damaschke
Submitter's Code	N1-P
Site & Location	Ngaere Swamp, Taranaki, New Zealand
Sample Material	Peat
Physical Pretreatment	Visible contaminants removed.
Chemical Pretreatment	Sample washed in hot HCl, rinsed and treated with multiple hot NaOH washes. The NaOH insoluble fraction was treated with hot HCl, filtered, rinsed and dried.

$D^{14}C$	-749.9 ±	1.3 ‰
$F^{14}C\%$	25.0 ±	0.1 %
Result	**11,131 ± 40 BP**	

(AMS measurement)

Comments

Please note: Because of the small size of this sample, the Carbon-13 stable isotope value ($\delta^{13}C$) was measured on prepared graphite using the AMS spectrometer. The radiocarbon date has therefore been corrected for isotopic fractionation. However the AMS-measured $\delta^{13}C$ value can differ from the $\delta^{13}C$ of the original material and it is therefore not shown.

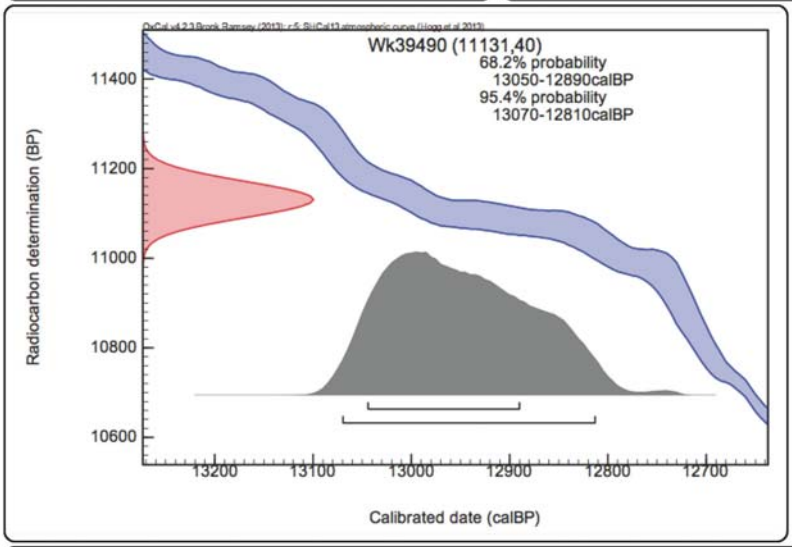

- Explanation of the calibrated Oxcal plots can be found at the Oxford Radiocarbon Accelerator Unit's calibration web pages (http://c14.arch.ox.ac.uk/embed.php?File=explanation.php)
- Result is *Conventional Age or Percent Modern Carbon (pMC)* following Stuiver and Polach, 1977, Radiocarbon 19, 355-363. This is based on the Libby half-life of 5568 yr with correction for isotopic fractionation applied. This age is normally quoted in publications and must include the appropriate error term and Wk number.
- Quoted errors are 1 standard deviation due to counting statistics multiplied by an experimentally determined Laboratory Error Multiplier.
- The isotopic fractionation, $\delta^{13}C$, is expressed as ‰ wrt PDB and is measured on sample CO_2.
- $F^{14}C\%$ is also known as *Percent Modern Carbon (pMC)*.

THE UNIVERSITY OF
WAIKATO
Te Whare Wānanga o Waikato

Private Bag 3105
Hamilton,
New Zealand.
Ph +64 7 838 4278
email c14@waikato.ac.nz

Thursday, 19 March 2015

Radiocarbon Dating Laboratory

Report on Radiocarbon Age Determination for Wk- 41024

Submitter	M Damaschke
Submitter's Code	E1-B
Site & Location	Eltham Swamp, Taranaki, New Zealand
Sample Material	Peat
Physical Pretreatment	Visible contaminants removed.
Chemical Pretreatment	Sample washed in hot HCl, rinsed and treated with multiple hot NaOH washes. The NaOH insoluble fraction was treated with hot HCl, filtered, rinsed and dried.

$D^{14}C$	-244.1 ±	1.9 ‰
$F^{14}C$%	75.6 ±	0.2 %
Result	**2248 ± 20 BP**	

(AMS measurement)

Comments

Please note: The Carbon-13 stable isotope value ($\delta^{13}C$) was measured on prepared graphite using the AMS spectrometer. The radiocarbon date has therefore been corrected for isotopic fractionation. However the AMS-measured $\delta^{13}C$ value can differ from the $\delta^{13}C$ of the original material and it is therefore not shown.

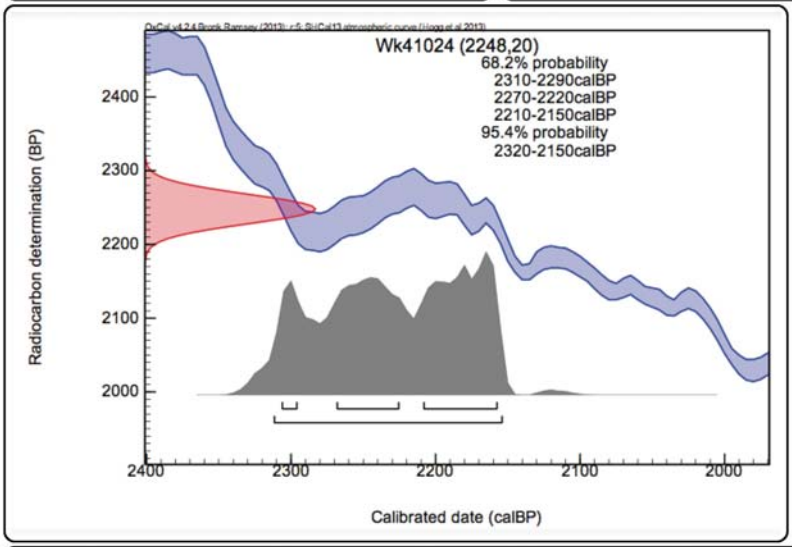

- Explanation of the calibrated Oxcal plots can be found at the Oxford Radiocarbon Accelerator Unit's calibration web pages (http://c14.arch.ox.ac.uk/embed.php?File=explanation.php)
- Result is *Conventional Age or Percent Modern Carbon (pMC)* following Stuiver and Polach, 1977, Radiocarbon 19, 355-363. This is based on the Libby half-life of 5568 yr with correction for isotopic fractionation applied. This age is normally quoted in publications and must include the appropriate error term and Wk number.
- Quoted errors are 1 standard deviation due to counting statistics multiplied by an experimentally determined Laboratory Error Multiplier.
- The isotopic fractionation, $\delta^{13}C$, is expressed as ‰ wrt PDB and is measured on sample CO_2.
- $F^{14}C$% is also known as *Percent Modern Carbon (pMC)*.

THE UNIVERSITY OF
WAIKATO
Te Whare Wānanga o Waikato

Private Bag 3105
Hamilton,
New Zealand.
Ph +64 7 838 4278
email c14@waikato.ac.nz

Thursday, 19 March 2015

Radiocarbon Dating Laboratory

Report on Radiocarbon Age Determination for Wk- 41025

Submitter	M Damaschke
Submitter's Code	E2-A
Site & Location	Eltham Swamp, Taranaki, New Zealand
Sample Material	Peat
Physical Pretreatment	Visible contaminants removed.
Chemical Pretreatment	Sample washed in hot HCl, rinsed and treated with multiple hot NaOH washes. The NaOH insoluble fraction was treated with hot HCl, filtered, rinsed and dried.

$D^{14}C$	-345.6 ±	1.7 ‰
$F^{14}C\%$	65.4 ±	0.2 %
Result	**3406 ± 22 BP**	

(AMS measurement)

Comments

Please note: The Carbon-13 stable isotope value ($\delta^{13}C$) was measured on prepared graphite using the AMS spectrometer. The radiocarbon date has therefore been corrected for isotopic fractionation. However the AMS-measured $\delta^{13}C$ value can differ from the $\delta^{13}C$ of the original material and it is therefore not shown.

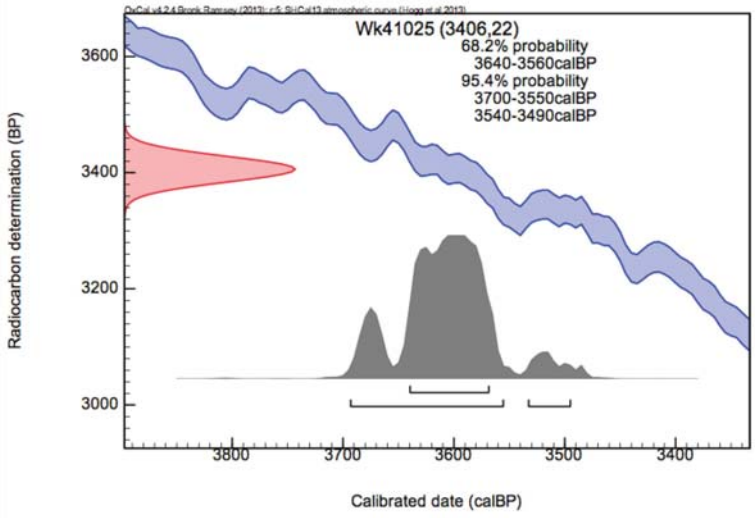

- Explanation of the calibrated Oxcal plots can be found at the Oxford Radiocarbon Accelerator Unit's calibration web pages (http://c14.arch.ox.ac.uk/embed.php?File=explanation.php)
- Result is *Conventional Age or Percent Modern Carbon (pMC)* following Stuiver and Polach, 1977, Radiocarbon 19, 355-363. This is based on the Libby half-life of 5568 yr with correction for isotopic fractionation applied. This age is normally quoted in publications and must include the appropriate error term and Wk number.
- Quoted errors are 1 standard deviation due to counting statistics multiplied by an experimentally determined Laboratory Error Multiplier.
- The isotopic fractionation, $\delta^{13}C$, is expressed as ‰ wrt PDB and is measured on sample CO_2.
- $F^{14}C\%$ is also known as *Percent Modern Carbon (pMC)*.

THE UNIVERSITY OF
WAIKATO
Te Whare Wānanga o Waikato

Private Bag 3105
Hamilton,
New Zealand.
Ph +64 7 838 4278
email c14@waikato.ac.nz

Thursday, 19 March 2015

Radiocarbon Dating Laboratory

Report on Radiocarbon Age Determination for Wk- 41026

Submitter	M Damaschke
Submitter's Code	E2-B
Site & Location	Eltham Swamp, Taranaki, New Zealand
Sample Material	Peat
Physical Pretreatment	Visible contaminants removed.
Chemical Pretreatment	Sample washed in hot HCl, rinsed and treated with multiple hot NaOH washes. The NaOH insoluble fraction was treated with hot HCl, filtered, rinsed and dried.

$D^{14}C$	-505.5 ±	1.6 ‰
$F^{14}C\%$	49.4 ±	0.2 %
Result	**5658 ± 26 BP**	

(AMS measurement)

Comments

Please note: The Carbon-13 stable isotope value ($\delta^{13}C$) was measured on prepared graphite using the AMS spectrometer. The radiocarbon date has therefore been corrected for isotopic fractionation. However the AMS-measured $\delta^{13}C$ value can differ from the $\delta^{13}C$ of the original material and it is therefore not shown.

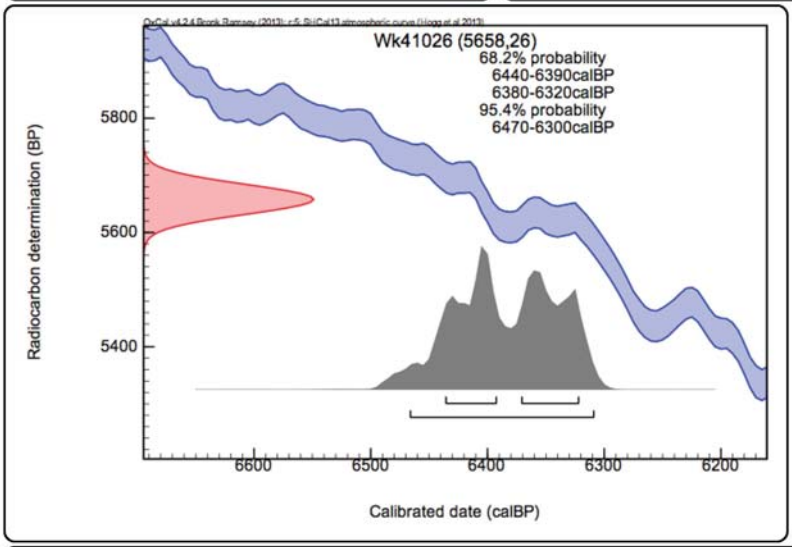

- Explanation of the calibrated Oxcal plots can be found at the Oxford Radiocarbon Accelerator Unit's calibration web pages (http://c14.arch.ox.ac.uk/embed.php?File=explanation.php)
- Result is *Conventional Age or Percent Modern Carbon (pMC)* following Stuiver and Polach, 1977, Radiocarbon 19, 355-363. This is based on the Libby half-life of 5568 yr with correction for isotopic fractionation applied. This age is normally quoted in publications and must include the appropriate error term and Wk number.
- Quoted errors are 1 standard deviation due to counting statistics multiplied by an experimentally determined Laboratory Error Multiplier.
- The isotopic fractionation, $\delta^{13}C$, is expressed as ‰ wrt PDB and is measured on sample CO_2.
- $F^{14}C\%$ is also known as *Percent Modern Carbon (pMC)*.

THE UNIVERSITY OF WAIKATO
Te Whare Wānanga o Waikato

Private Bag 3105
Hamilton,
New Zealand.
Ph +64 7 838 4278
email c14@waikato.ac.nz

Thursday, 19 March 2015

Radiocarbon Dating Laboratory

Report on Radiocarbon Age Determination for Wk- 41027

Submitter	M Damaschke
Submitter's Code	E2-C
Site & Location	Eltham Swamp, Taranaki, New Zealand
Sample Material	Peat
Physical Pretreatment	Visible contaminants removed.
Chemical Pretreatment	Sample washed in hot HCl, rinsed and treated with multiple hot NaOH washes. The NaOH insoluble fraction was treated with hot HCl, filtered, rinsed and dried.

$D^{14}C$	-602.5 ±	1.3 ‰
$F^{14}C\%$	39.7 ±	0.1 %
Result	**7412 ± 27 BP**	

(AMS measurement)

Comments
Please note: The Carbon-13 stable isotope value ($\delta^{13}C$) was measured on prepared graphite using the AMS spectrometer. The radiocarbon date has therefore been corrected for isotopic fractionation. However the AMS-measured $\delta^{13}C$ value can differ from the $\delta^{13}C$ of the original material and it is therefore not shown.

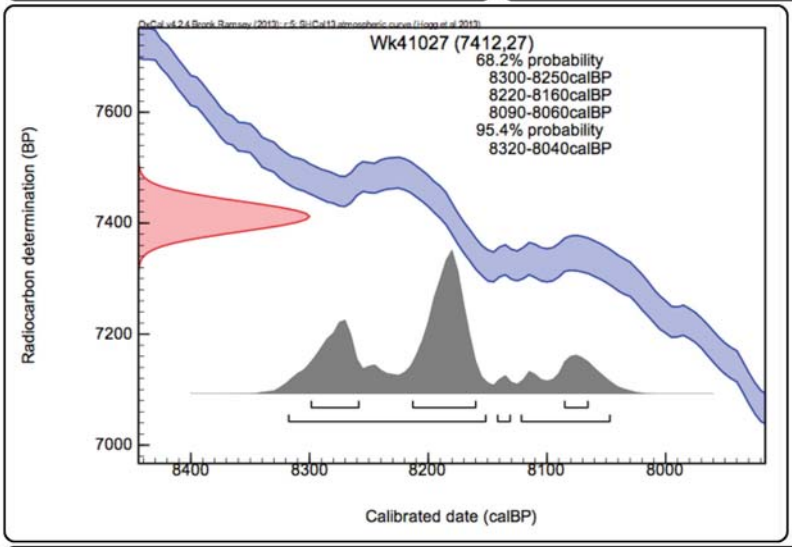

- Explanation of the calibrated Oxcal plots can be found at the Oxford Radiocarbon Accelerator Unit's calibration web pages (http://c14.arch.ox.ac.uk/embed.php?File=explanation.php)
- Result is *Conventional Age or Percent Modern Carbon (pMC)* following Stuiver and Polach, 1977, Radiocarbon 19, 355-363. This is based on the Libby half-life of 5568 yr with correction for isotopic fractionation applied. This age is normally quoted in publications and must include the appropriate error term and Wk number.
- Quoted errors are 1 standard deviation due to counting statistics multiplied by an experimentally determined Laboratory Error Multiplier.
- The isotopic fractionation, $\delta^{13}C$, is expressed as ‰ wrt PDB and is measured on sample CO_2.
- $F^{14}C\%$ is also known as *Percent Modern Carbon (pMC)*.

THE UNIVERSITY OF
WAIKATO
Te Whare Wānanga o Waikato

Private Bag 3105
Hamilton,
New Zealand.
Ph +64 7 838 4278
email c14@waikato.ac.nz

Thursday, 19 March 2015

Radiocarbon Dating Laboratory

Report on Radiocarbon Age Determination for Wk- 41028

Submitter	M Damaschke
Submitter's Code	E2-D
Site & Location	Eltham Swamp, Taranaki, New Zealand
Sample Material	Peat
Physical Pretreatment	Visible contaminants removed.
Chemical Pretreatment	Sample washed in hot HCl, rinsed and treated with multiple hot NaOH washes. The NaOH insoluble fraction was treated with hot HCl, filtered, rinsed and dried.

$D^{14}C$	-662.6 ±	1.1 ‰
$F^{14}C$%	33.7 ±	0.1 %
Result	**8728 ± 27 BP**	

(AMS measurement)

Comments

Please note: The Carbon-13 stable isotope value ($\delta^{13}C$) was measured on prepared graphite using the AMS spectrometer. The radiocarbon date has therefore been corrected for isotopic fractionation. However the AMS-measured $\delta^{13}C$ value can differ from the $\delta^{13}C$ of the original material and it is therefore not shown.

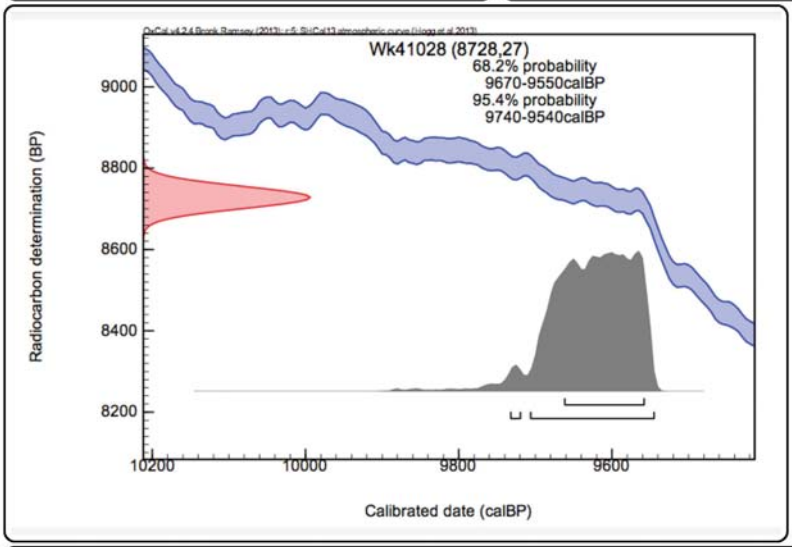

- Explanation of the calibrated Oxcal plots can be found at the Oxford Radiocarbon Accelerator Unit's calibration web pages (http://c14.arch.ox.ac.uk/embed.php?File=explanation.php)
- Result is *Conventional Age or Percent Modern Carbon (pMC)* following Stuiver and Polach, 1977, Radiocarbon 19, 355-363. This is based on the Libby half-life of 5568 yr with correction for isotopic fractionation applied. This age is normally quoted in publications and must include the appropriate error term and Wk number.
- Quoted errors are 1 standard deviation due to counting statistics multiplied by an experimentally determined Laboratory Error Multiplier.
- The isotopic fractionation, $\delta^{13}C$, is expressed as ‰ wrt PDB and is measured on sample CO_2.
- $F^{14}C$% is also known as *Percent Modern Carbon (pMC)*.

THE UNIVERSITY OF WAIKATO
Te Whare Wānanga o Waikato

Private Bag 3105
Hamilton,
New Zealand.
Ph +64 7 838 4278
email c14@waikato.ac.nz

Thursday, 19 March 2015

Radiocarbon Dating Laboratory

Report on Radiocarbon Age Determination for Wk- 41029

Submitter	M Damaschke
Submitter's Code	E2-E
Site & Location	Eltham Swamp, Taranaki, New Zealand
Sample Material	Peat
Physical Pretreatment	Visible contaminants removed.
Chemical Pretreatment	Sample washed in hot HCl, rinsed and treated with multiple hot NaOH washes. The NaOH insoluble fraction was treated with hot HCl, filtered, rinsed and dried.

$D^{14}C$	-690.9 ±	1.1 ‰
$F^{14}C\%$	30.9 ±	0.1 %
Result	**9432 ± 28 BP**	

(AMS measurement)

Comments

Please note: The Carbon-13 stable isotope value ($\delta^{13}C$) was measured on prepared graphite using the AMS spectrometer. The radiocarbon date has therefore been corrected for isotopic fractionation. However the AMS-measured $\delta^{13}C$ value can differ from the $\delta^{13}C$ of the original material and it is therefore not shown.

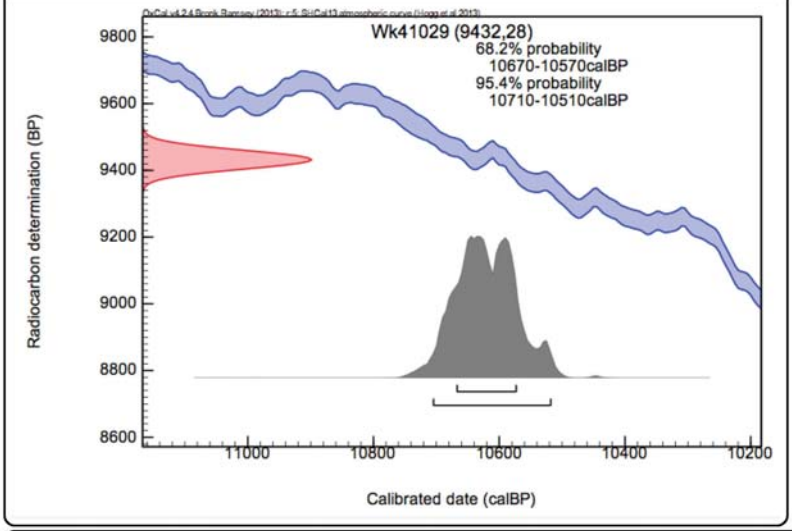

- Explanation of the calibrated Oxcal plots can be found at the Oxford Radiocarbon Accelerator Unit's calibration web pages (http://c14.arch.ox.ac.uk/embed.php?File=explanation.php)
- Result is *Conventional Age or Percent Modern Carbon (pMC)* following Stuiver and Polach, 1977, Radiocarbon 19, 355-363. This is based on the Libby half-life of 5568 yr with correction for isotopic fractionation applied. This age is normally quoted in publications and must include the appropriate error term and Wk number.
- Quoted errors are 1 standard deviation due to counting statistics multiplied by an experimentally determined Laboratory Error Multiplier.
- The isotopic fractionation, $\delta^{13}C$, is expressed as ‰ wrt PDB and is measured on sample CO_2.
- $F^{14}C\%$ is also known as *Percent Modern Carbon (pMC)*.

THE UNIVERSITY OF
WAIKATO
Te Whare Wānanga o Waikato

Private Bag 3105
Hamilton,
New Zealand.
Ph +64 7 838 4278
email c14@waikato.ac.nz

Thursday, 19 March 2015

Radiocarbon Dating Laboratory

Report on Radiocarbon Age Determination for Wk- 41030

Submitter	M Damaschke
Submitter's Code	E2-F
Site & Location	Eltham Swamp, Taranaki, New Zealand
Sample Material	Peat
Physical Pretreatment	Visible contaminants removed.
Chemical Pretreatment	Sample washed in hot HCl, rinsed and treated with multiple hot NaOH washes. The NaOH insoluble fraction was treated with hot HCl, filtered, rinsed and dried.

$D^{14}C$	-725.7 ±	1.1 ‰
$F^{14}C$%	27.4 ±	0.1 %
Result	**10,390 ± 33 BP**	

(AMS measurement)

Comments

Please note: The Carbon-13 stable isotope value ($\delta^{13}C$) was measured on prepared graphite using the AMS spectrometer. The radiocarbon date has therefore been corrected for isotopic fractionation. However the AMS-measured $\delta^{13}C$ value can differ from the $\delta^{13}C$ of the original material and it is therefore not shown.

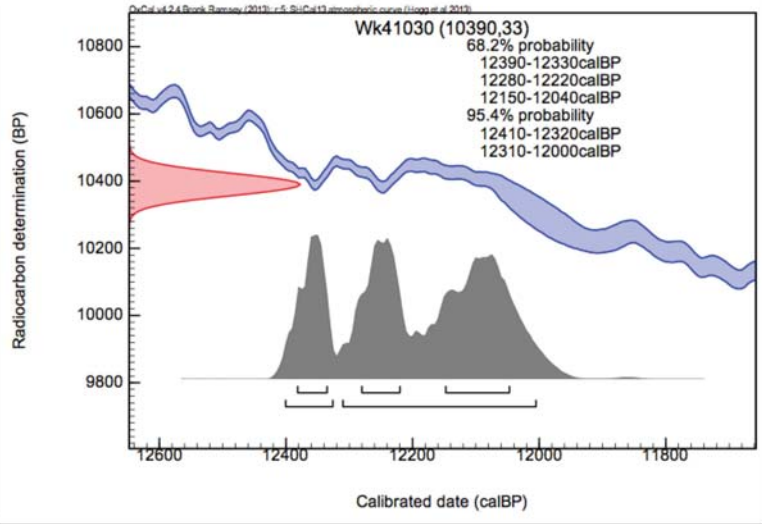

- Explanation of the calibrated Oxcal plots can be found at the Oxford Radiocarbon Accelerator Unit's calibration web pages (http://c14.arch.ox.ac.uk/embed.php?File=explanation.php)
- Result is *Conventional Age or Percent Modern Carbon (pMC)* following Stuiver and Polach, 1977, Radiocarbon 19, 355-363. This is based on the Libby half-life of 5568 yr with correction for isotopic fractionation applied. This age is normally quoted in publications and must include the appropriate error term and Wk number.
- Quoted errors are 1 standard deviation due to counting statistics multiplied by an experimentally determined Laboratory Error Multiplier.
- The isotopic fractionation, $\delta^{13}C$, is expressed as ‰ wrt PDB and is measured on sample CO_2.
- $F^{14}C$% is also known as *Percent Modern Carbon (pMC)*.

THE UNIVERSITY OF
WAIKATO
Te Whare Wānanga o Waikato

Private Bag 3105
Hamilton,
New Zealand.
Ph +64 7 838 4278
email c14@waikato.ac.nz

Thursday, 19 March 2015

Radiocarbon Dating Laboratory

Report on Radiocarbon Age Determination for Wk- 41031

Submitter	M Damaschke
Submitter's Code	E2-G
Site & Location	Eltham Swamp, Taranaki, New Zealand
Sample Material	Peat
Physical Pretreatment	Visible contaminants removed.
Chemical Pretreatment	Sample washed in hot HCl, rinsed and treated with multiple hot NaOH washes. The NaOH insoluble fraction was treated with hot HCl, filtered, rinsed and dried.

$D^{14}C$	-764.3 ±	1.0 ‰
$F^{14}C\%$	23.6 ±	0.1 %
Result	**11,610 ± 35 BP**	

(AMS measurement)

Comments

Please note: The Carbon-13 stable isotope value ($\delta^{13}C$) was measured on prepared graphite using the AMS spectrometer. The radiocarbon date has therefore been corrected for isotopic fractionation. However the AMS-measured $\delta^{13}C$ value can differ from the $\delta^{13}C$ of the original material and it is therefore not shown.

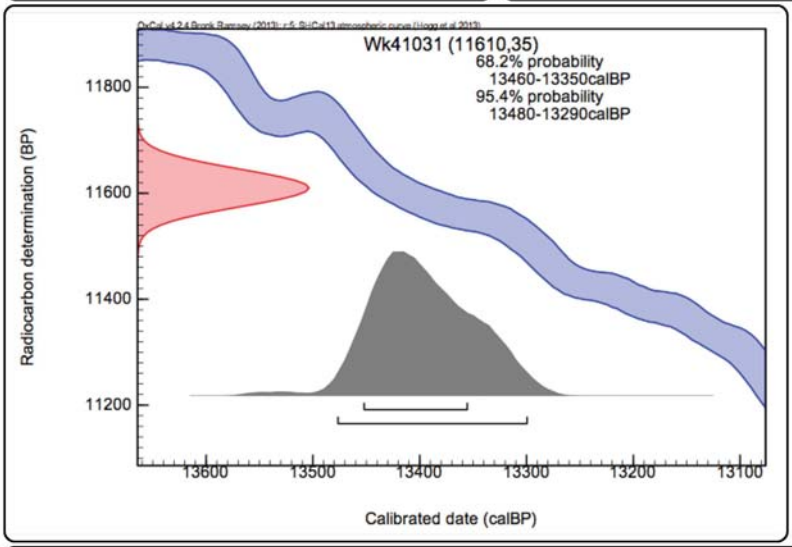

- Explanation of the calibrated Oxcal plots can be found at the Oxford Radiocarbon Accelerator Unit's calibration web pages (http://c14.arch.ox.ac.uk/embed.php?File=explanation.php)
- Result is *Conventional Age or Percent Modern Carbon (pMC)* following Stuiver and Polach, 1977, Radiocarbon 19, 355-363. This is based on the Libby half-life of 5568 yr with correction for isotopic fractionation applied. This age is normally quoted in publications and must include the appropriate error term and Wk number.
- Quoted errors are 1 standard deviation due to counting statistics multiplied by an experimentally determined Laboratory Error Multiplier.
- The isotopic fractionation, $\delta^{13}C$, is expressed as ‰ wrt PDB and is measured on sample CO_2.
- $F^{14}C\%$ is also known as *Percent Modern Carbon (pMC)*.

THE UNIVERSITY OF
WAIKATO
Te Whare Wānanga o Waikato

Private Bag 3105
Hamilton,
New Zealand.
Ph +64 7 838 4278
email c14@waikato.ac.nz

Thursday, 19 March 2015

Radiocarbon Dating Laboratory

Report on Radiocarbon Age Determination for Wk- 41032

Submitter	M Damaschke
Submitter's Code	E2-H
Site & Location	Eltham Swamp, Taranaki, New Zealand
Sample Material	Organic rich sediment
Physical Pretreatment	Visible contaminants removed.
Chemical Pretreatment	Sample washed in hot HCl, rinsed and treated with multiple hot NaOH washes. The NaOH insoluble fraction was treated with hot HCl, filtered, rinsed and dried.

$D^{14}C$	-795.8 ±	1.0 ‰
$F^{14}C$%	20.4 ±	0.1 %
Result	**12,763 ± 38 BP**	

(AMS measurement)

Comments

Please note: The Carbon-13 stable isotope value ($\delta^{13}C$) was measured on prepared graphite using the AMS spectrometer. The radiocarbon date has therefore been corrected for isotopic fractionation. However the AMS-measured $\delta^{13}C$ value can differ from the $\delta^{13}C$ of the original material and it is therefore not shown.

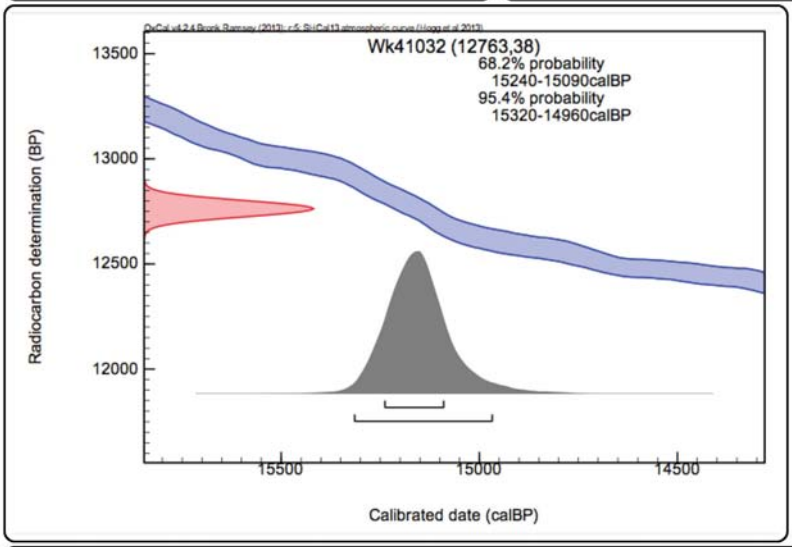

- Explanation of the calibrated Oxcal plots can be found at the Oxford Radiocarbon Accelerator Unit's calibration web pages (http://c14.arch.ox.ac.uk/embed.php?File=explanation.php)
- Result is *Conventional Age or Percent Modern Carbon (pMC)* following Stuiver and Polach, 1977, Radiocarbon 19, 355-363. This is based on the Libby half-life of 5568 yr with correction for isotopic fractionation applied. This age is normally quoted in publications and must include the appropriate error term and Wk number.
- Quoted errors are 1 standard deviation due to counting statistics multiplied by an experimentally determined Laboratory Error Multiplier.
- The isotopic fractionation, $\delta^{13}C$, is expressed as ‰ wrt PDB and is measured on sample CO_2.
- $F^{14}C$% is also known as *Percent Modern Carbon (pMC)*.

THE UNIVERSITY OF
WAIKATO
Te Whare Wānanga o Waikato

Private Bag 3105
Hamilton,
New Zealand.
Ph +64 7 838 4278
email c14@waikato.ac.nz

Thursday, 19 March 2015

Radiocarbon Dating Laboratory

Report on Radiocarbon Age Determination for Wk- 41033

Submitter	M Damaschke
Submitter's Code	E2-I
Site & Location	Eltham Swamp, Taranaki, New Zealand
Sample Material	Organic rich sediment
Physical Pretreatment	Visible contaminants removed.
Chemical Pretreatment	Sample washed in hot HCl, rinsed and treated with multiple hot NaOH washes. The NaOH insoluble fraction was treated with hot HCl, filtered, rinsed and dried.

$D^{14}C$	-928.1 ±	0.9 ‰
$F^{14}C\%$	7.2 ±	0.1 %
Result	**21,152 ± 97 BP**	

(AMS measurement)

Comments

Please note: The Carbon-13 stable isotope value ($\delta^{13}C$) was measured on prepared graphite using the AMS spectrometer. The radiocarbon date has therefore been corrected for isotopic fractionation. However the AMS-measured $\delta^{13}C$ value can differ from the $\delta^{13}C$ of the original material and it is therefore not shown.

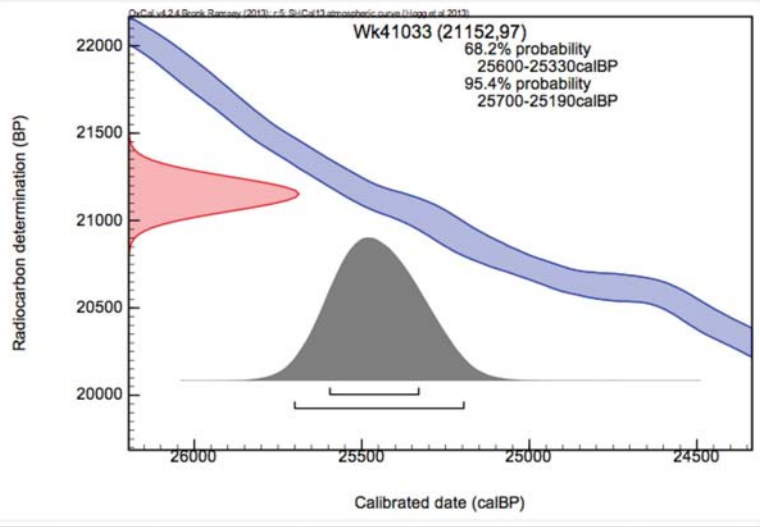

- Explanation of the calibrated Oxcal plots can be found at the Oxford Radiocarbon Accelerator Unit's calibration web pages (http://c14.arch.ox.ac.uk/embed.php?File=explanation.php)
- Result is *Conventional Age or Percent Modern Carbon (pMC)* following Stuiver and Polach, 1977, Radiocarbon 19, 355-363. This is based on the Libby half-life of 5568 yr with correction for isotopic fractionation applied. This age is normally quoted in publications and must include the appropriate error term and Wk number.
- Quoted errors are 1 standard deviation due to counting statistics multiplied by an experimentally determined Laboratory Error Multiplier.
- The isotopic fractionation, $\delta^{13}C$, is expressed as ‰ wrt PDB and is measured on sample CO_2.
- $F^{14}C\%$ is also known as *Percent Modern Carbon (pMC)*.

THE UNIVERSITY OF
WAIKATO
Te Whare Wānanga o Waikato

Private Bag 3105
Hamilton,
New Zealand.
Ph +64 7 838 4278
email c14@waikato.ac.nz

Thursday, 19 March 2015

Radiocarbon Dating Laboratory

Report on Radiocarbon Age Determination for Wk- 41034

Submitter	M Damaschke
Submitter's Code	E2-J
Site & Location	Eltham Swamp, Taranaki, New Zealand
Sample Material	Organic rich sediment
Physical Pretreatment	Visible contaminants removed.
Chemical Pretreatment	Sample washed in hot HCl, rinsed and treated with multiple hot NaOH washes. The NaOH insoluble fraction was treated with hot HCl, filtered, rinsed and dried.

$D^{14}C$	-945.0 ±	0.9 ‰
$F^{14}C\%$	5.5 ±	0.1 %
Result	**23,294 ± 125 BP**	

(AMS measurement)

Comments

Please note: The Carbon-13 stable isotope value ($\delta^{13}C$) was measured on prepared graphite using the AMS spectrometer. The radiocarbon date has therefore been corrected for isotopic fractionation. However the AMS-measured $\delta^{13}C$ value can differ from the $\delta^{13}C$ of the original material and it is therefore not shown.

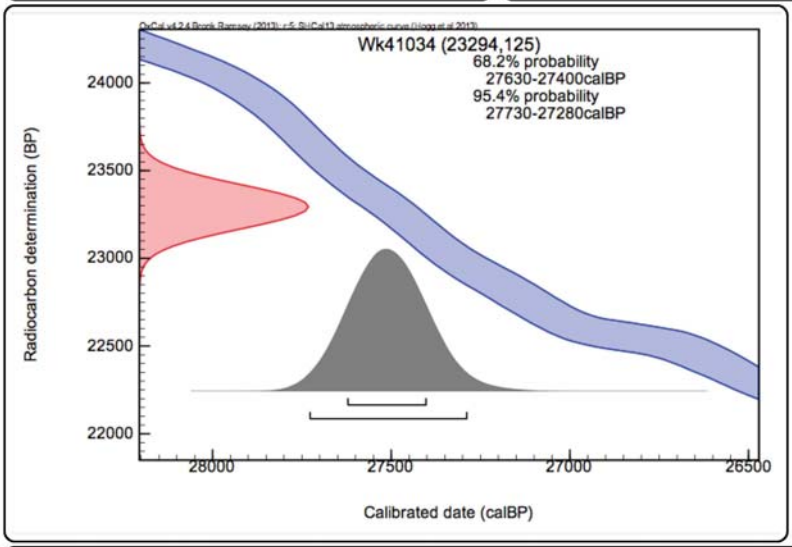

- Explanation of the calibrated Oxcal plots can be found at the Oxford Radiocarbon Accelerator Unit's calibration web pages (http://c14.arch.ox.ac.uk/embed.php?File=explanation.php)
- Result is *Conventional Age or Percent Modern Carbon (pMC)* following Stuiver and Polach, 1977, Radiocarbon 19, 355-363. This is based on the Libby half-life of 5568 yr with correction for isotopic fractionation applied. This age is normally quoted in publications and must include the appropriate error term and Wk number.
- Quoted errors are 1 standard deviation due to counting statistics multiplied by an experimentally determined Laboratory Error Multiplier.
- The isotopic fractionation, $\delta^{13}C$, is expressed as ‰ wrt PDB and is measured on sample CO_2.
- $F^{14}C\%$ is also known as *Percent Modern Carbon (pMC)*.

THE UNIVERSITY OF
WAIKATO
Te Whare Wānanga o Waikato

Private Bag 3105
Hamilton,
New Zealand.
Ph +64 7 838 4278
email c14@waikato.ac.nz

Thursday, 19 March 2015

Radiocarbon Dating Laboratory

Report on Radiocarbon Age Determination for Wk- 41035

Submitter	M Damaschke
Submitter's Code	E2-K
Site & Location	Eltham Swamp, Taranaki, New Zealand
Sample Material	Organic rich sediment
Physical Pretreatment	Visible contaminants removed.
Chemical Pretreatment	Sample washed in hot HCl, rinsed and treated with multiple hot NaOH washes. The NaOH insoluble fraction was treated with hot HCl, filtered, rinsed and dried.

$D^{14}C$	-959.0 ±	0.8 ‰
$F^{14}C\%$	4.1 ±	0.1 %
Result	**25,663 ± 166 BP**	

(AMS measurement)

Comments

Please note: The Carbon-13 stable isotope value ($\delta^{13}C$) was measured on prepared graphite using the AMS spectrometer. The radiocarbon date has therefore been corrected for isotopic fractionation. However the AMS-measured $\delta^{13}C$ value can differ from the $\delta^{13}C$ of the original material and it is therefore not shown.

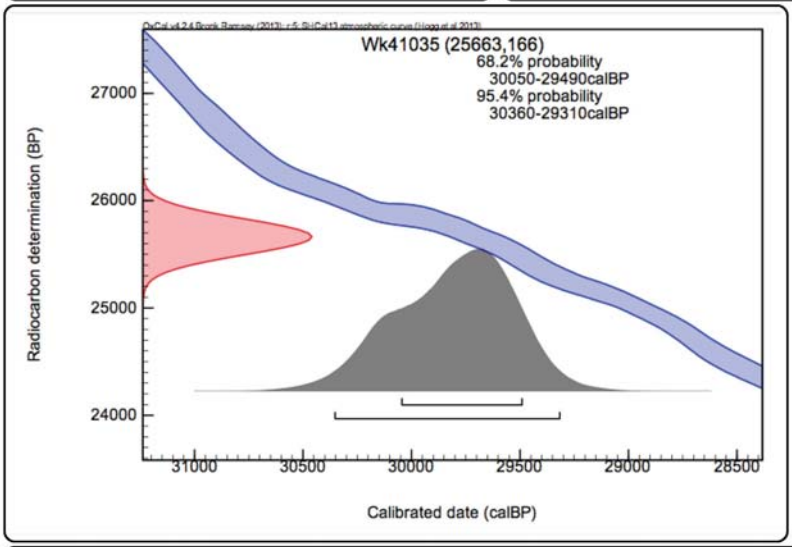

- Explanation of the calibrated Oxcal plots can be found at the Oxford Radiocarbon Accelerator Unit's calibration web pages (http://c14.arch.ox.ac.uk/embed.php?File=explanation.php)
- Result is *Conventional Age or Percent Modern Carbon (pMC)* following Stuiver and Polach, 1977, Radiocarbon 19, 355-363. This is based on the Libby half-life of 5568 yr with correction for isotopic fractionation applied. This age is normally quoted in publications and must include the appropriate error term and Wk number.
- Quoted errors are 1 standard deviation due to counting statistics multiplied by an experimentally determined Laboratory Error Multiplier.
- The isotopic fractionation, $\delta^{13}C$, is expressed as ‰ wrt PDB and is measured on sample CO_2.
- $F^{14}C\%$ is also known as *Percent Modern Carbon (pMC)*.

Appendix 2 *Electron microprobe-determined titanomagnetite compositions of tephra layers from lake and peatland cores recovered during this study. Refer also to Figure 3.6.*

Sample#	N-2		N-3		N-6		N-7		N-9		N-19		N-21	
Tm-group	2		12/11		11		11		10		9		3	
(wt%)	avg.	±S.D.	avg.	±S.D.	avg.	±S.D.	avg.	±S.D.	avg.	±S.D.	avg.	±S.D.	avg.	±S.D.
TiO_2	9.24	*0.16*	6.93	*0.30*	5.68	*0.23*	7.31	*0.61*	7.24	*0.31*	8.26	*0.17*	9.15	*0.22*
Al_2O_3	3.32	*0.11*	3.91	*0.63*	7.66	*0.22*	5.17	*0.45*	1.93	*0.20*	2.24	*0.21*	2.65	*0.11*
FeO_t	78.42	*0.77*	79.01	*2.08*	76.60	*0.48*	74.90	*2.41*	81.33	*1.60*	80.43	*0.26*	78.50	*1.00*
MnO	1.01	*0.16*	0.94	*0.15*	0.52	*0.11*	0.75	*0.13*	1.65	*0.24*	1.57	*0.21*	1.25	*0.13*
MgO	3.19	*0.16*	3.02	*0.39*	4.26	*0.16*	3.74	*0.10*	1.66	*0.21*	2.19	*0.10*	2.92	*0.12*
Al_2O_3+MgO	6.51	*0.22*	6.93	*0.94*	11.92	*0.24*	8.91	*0.47*	3.59	*0.38*	4.44	*0.29*	5.57	*0.22*
Total	95.64	*1.06*	94.83	*0.59*	95.31	*0.65*	92.56	*2.42*	94.43	*1.85*	95.11	*0.54*	94.76	*1.18*
Fe_2O_3	49.00	*0.74*	52.13	*1.21*	50.94	*0.60*	48.60	*1.91*	53.00	*1.08*	51.42	*0.35*	49.34	*0.72*
FeO	34.33	*0.24*	32.11	*1.53*	30.76	*0.32*	31.17	*1.12*	33.63	*0.74*	34.17	*0.40*	34.10	*0.51*
Total recal	100.39	*1.05*	99.60	*1.19*	100.31	*0.68*	97.32	*2.60*	99.54	*1.88*	100.16	*0.51*	99.57	*1.22*
Ti	0.25	*0.01*	0.19	*0.01*	0.15	*0.01*	0.20	*0.02*	0.20	*0.01*	0.23	*0.00*	0.25	*0.01*
Al	0.14	*0.00*	0.17	*0.03*	0.32	*0.01*	0.23	*0.02*	0.09	*0.01*	0.10	*0.01*	0.12	*0.00*
Fe^{+3}	1.34	*0.01*	1.44	*0.03*	1.36	*0.02*	1.35	*0.03*	1.50	*0.02*	1.43	*0.01*	1.37	*0.01*
Fe^{+2}	1.05	*0.01*	0.99	*0.04*	0.91	*0.01*	0.97	*0.02*	1.06	*0.01*	1.06	*0.01*	1.05	*0.01*
Mn	0.03	*0.01*	0.03	*0.00*	0.02	*0.00*	0.02	*0.00*	0.05	*0.01*	0.05	*0.01*	0.04	*0.00*
Mg	0.17	*0.01*	0.17	*0.02*	0.23	*0.01*	0.21	*0.01*	0.09	*0.01*	0.12	*0.00*	0.16	*0.01*
Usp	0.25	*0.00*	0.19	*0.01*	0.15	*0.01*	0.21	*0.02*	0.21	*0.01*	0.23	*0.01*	0.26	*0.01*
n	*14*		*11*		*19*		*11*		*22*		*10*		*7*	

Sample#	N-22		N-22b		N-23		N-23b		N-24		N-24b		N-26	
Tm-group	8		11		3		11		3		11		8	
(wt%)	avg.	±S.D.	avg.	±S.D.	avg.	±S.D.	avg.	±S.D.	avg.	±S.D.	avg.	±S.D.	avg.	±S.D.
TiO_2	8.20	*0.11*	6.42	*0.11*	9.38	*0.38*	6.78	*0.33*	9.26	*0.32*	6.45	*0.24*	7.87	*0.17*
Al_2O_3	2.62	*0.08*	4.95	*0.07*	2.39	*0.15*	4.51	*0.10*	2.58	*0.12*	4.78	*0.18*	2.57	*0.16*
FeO_t	79.82	*0.53*	78.88	*0.64*	79.38	*0.93*	80.47	*0.37*	78.64	*0.74*	79.45	*0.84*	80.12	*0.85*
MnO	1.35	*0.11*	0.61	*0.20*	1.22	*0.10*	0.71	*0.05*	1.30	*0.17*	0.58	*0.12*	1.30	*0.09*
MgO	2.58	*0.29*	3.28	*0.15*	2.68	*0.17*	2.69	*0.16*	2.86	*0.11*	2.89	*0.21*	2.36	*0.13*
Al_2O_3+MgO	5.20	*0.29*	8.23	*0.11*	5.08	*0.27*	7.20	*0.06*	5.44	*0.16*	7.67	*0.38*	4.93	*0.04*
Total	94.89	*0.76*	94.28	*0.56*	95.43	*0.86*	95.17	*0.81*	94.93	*1.11*	94.60	*1.15*	94.48	*0.71*
Fe_2O_3	51.18	*0.66*	52.05	*0.43*	49.43	*0.83*	52.32	*0.43*	49.18	*0.78*	51.94	*0.58*	51.49	*0.81*
FeO	33.77	*0.58*	32.04	*0.35*	34.90	*0.51*	33.38	*0.76*	34.38	*0.57*	32.72	*0.64*	33.79	*0.44*
Total recal	99.98	*0.71*	99.47	*0.61*	100.37	*0.82*	100.45	*0.70*	99.84	*1.04*	99.60	*1.19*	99.62	*0.81*
Ti	0.23	*0.00*	0.18	*0.00*	0.26	*0.01*	0.19	*0.01*	0.26	*0.01*	0.18	*0.01*	0.22	*0.01*
Al	0.11	*0.00*	0.21	*0.00*	0.10	*0.01*	0.19	*0.00*	0.11	*0.01*	0.21	*0.01*	0.11	*0.01*
Fe^{+3}	1.42	*0.01*	1.43	*0.01*	1.37	*0.02*	1.43	*0.02*	1.36	*0.02*	1.43	*0.01*	1.44	*0.02*
Fe^{+2}	1.04	*0.02*	0.98	*0.01*	1.07	*0.01*	1.02	*0.02*	1.06	*0.01*	1.00	*0.02*	1.05	*0.01*
Mn	0.04	*0.00*	0.02	*0.01*	0.04	*0.00*	0.02	*0.00*	0.04	*0.01*	0.02	*0.00*	0.04	*0.00*
Mg	0.14	*0.02*	0.18	*0.01*	0.15	*0.01*	0.15	*0.01*	0.16	*0.00*	0.16	*0.01*	0.13	*0.01*
Usp	0.23	*0.00*	0.18	*0.00*	0.26	*0.01*	0.19	*0.01*	0.26	*0.01*	0.18	*0.01*	0.22	*0.01*
n	*7*		*3*		*14*		*2*		*6*		*6*		*6*	

Sample#	N-26b		N-32		N-33		N-35		N-36		N-37		N-38	
Tm-group	11		variable		2		2		2		2		2	
(wt%)	avg.	±S.D.	avg.	±S.D.	avg.	±S.D.	avg.	±S.D.	avg.	±S.D.	avg.	±S.D.	avg.	±S.D.
TiO_2	6.16	*0.11*	10.14	*0.27*	9.90	*0.22*	9.60	*0.08*	9.69	*0.21*	9.43	*0.17*	9.70	*0.22*
Al_2O_3	4.67	*0.34*	2.24	*0.23*	2.79	*0.13*	3.00	*0.12*	3.05	*0.12*	3.35	*0.12*	3.41	*0.15*
FeO_t	78.11	*2.27*	78.63	*0.65*	78.16	*1.06*	79.01	*0.52*	79.50	*0.68*	78.68	*0.74*	78.46	*0.42*
MnO	0.63	*0.07*	1.24	*0.10*	1.23	*0.15*	1.18	*0.06*	1.08	*0.06*	1.04	*0.11*	1.06	*0.16*
MgO	2.77	*0.34*	2.48	*0.18*	2.95	*0.10*	3.00	*0.11*	3.04	*0.12*	3.24	*0.14*	3.31	*0.09*
Al_2O_3+MgO	7.44	*0.68*	4.71	*0.40*	5.73	*0.23*	6.00	*0.14*	6.09	*0.23*	6.59	*0.21*	6.72	*0.17*
Total	92.84	*2.67*	95.08	*0.74*	95.31	*0.86*	96.11	*0.60*	96.66	*0.55*	96.15	*0.71*	96.18	*0.55*
Fe_2O_3	51.08	*2.09*	47.68	*0.49*	47.95	*0.62*	48.93	*0.53*	49.15	*0.49*	48.97	*0.61*	48.46	*0.41*
FeO	32.15	*0.41*	35.73	*0.50*	35.02	*0.56*	34.98	*0.23*	35.28	*0.41*	34.62	*0.33*	34.85	*0.38*
Total recal	97.94	*2.85*	99.73	*0.72*	100.07	*0.99*	100.92	*0.63*	101.45	*0.64*	100.90	*0.80*	100.97	*0.58*
Ti	0.17	*0.00*	0.28	*0.01*	0.27	*0.00*	0.26	*0.00*	0.26	*0.01*	0.26	*0.00*	0.26	*0.01*
Al	0.20	*0.01*	0.10	*0.01*	0.12	*0.01*	0.13	*0.00*	0.13	*0.01*	0.14	*0.00*	0.15	*0.01*
Fe^{+3}	1.43	*0.02*	1.33	*0.01*	1.32	*0.01*	1.34	*0.01*	1.34	*0.01*	1.34	*0.01*	1.32	*0.01*
Fe^{+2}	1.00	*0.02*	1.11	*0.01*	1.07	*0.01*	1.06	*0.01*	1.07	*0.01*	1.05	*0.01*	1.05	*0.01*
Mn	0.02	*0.00*	0.04	*0.00*	0.04	*0.00*	0.04	*0.00*	0.03	*0.00*	0.03	*0.00*	0.03	*0.00*
Mg	0.15	*0.01*	0.14	*0.01*	0.16	*0.01*	0.16	*0.01*	0.16	*0.01*	0.17	*0.01*	0.18	*0.00*
Usp	0.18	*0.01*	0.28	*0.01*	0.28	*0.00*	0.26	*0.00*	0.27	*0.01*	0.26	*0.00*	0.27	*0.01*
n	*3*		*9*		*6*		*9*		*8*		*10*		*10*	

Appendix 2 *(continued)*

Sample#	N-39		N-40		N-42		N-44		N-45		N-46		N-47	
Tm-group	2		2		4		2		5		5		4	
(wt%)	avg.	±S.D.	avg.	±S.D.	avg.	±S.D.	avg.	±S.D.	avg.	±S.D.	avg.	±S.D.	avg.	±S.D.
TiO_2	9.66	*0.19*	9.46	*0.17*	8.73	*0.11*	9.44	*0.20*	8.82	*0.18*	8.78	*0.19*	8.75	*0.17*
Al_2O_3	3.29	*0.20*	3.26	*0.15*	3.42	*0.08*	3.08	*0.15*	2.81	*0.09*	2.88	*0.11*	3.43	*0.13*
FeO_t	78.86	*0.48*	78.45	*0.86*	78.58	*0.58*	78.52	*0.63*	79.69	*0.33*	79.54	*0.58*	78.39	*0.44*
MnO	1.02	*0.11*	1.07	*0.13*	1.08	*0.11*	1.07	*0.13*	1.16	*0.11*	1.27	*0.09*	1.02	*0.17*
MgO	3.29	*0.12*	3.27	*0.19*	3.34	*0.08*	3.23	*0.15*	2.93	*0.17*	2.87	*0.15*	3.32	*0.08*
Al_2O_3+MgO	6.58	*0.32*	6.54	*0.26*	6.76	*0.10*	6.30	*0.27*	5.74	*0.18*	5.75	*0.24*	6.75	*0.10*
Total	96.26	*0.45*	95.95	*1.05*	95.38	*0.45*	95.50	*0.56*	95.67	*0.45*	95.70	*0.55*	95.28	*0.50*
Fe_2O_3	48.85	*0.40*	48.84	*0.57*	50.02	*0.56*	48.94	*0.75*	50.48	*0.39*	50.37	*0.90*	49.64	*0.40*
FeO	34.91	*0.31*	34.50	*0.56*	33.57	*0.16*	34.48	*0.27*	34.27	*0.42*	34.21	*0.40*	33.72	*0.31*
Total recal	101.20	*0.44*	100.73	*1.06*	100.31	*0.50*	100.29	*0.60*	100.62	*0.41*	100.63	*0.57*	100.07	*0.52*
Ti	0.26	*0.01*	0.26	*0.00*	0.24	*0.00*	0.26	*0.01*	0.24	*0.00*	0.24	*0.01*	0.24	*0.00*
Al	0.14	*0.01*	0.14	*0.01*	0.15	*0.00*	0.13	*0.01*	0.12	*0.00*	0.12	*0.00*	0.15	*0.01*
Fe^{+3}	1.33	*0.01*	1.33	*0.01*	1.37	*0.01*	1.34	*0.02*	1.39	*0.01*	1.38	*0.02*	1.36	*0.01*
Fe^{+2}	1.05	*0.01*	1.05	*0.01*	1.02	*0.01*	1.05	*0.01*	1.05	*0.01*	1.05	*0.02*	1.03	*0.01*
Mn	0.03	*0.00*	0.03	*0.00*	0.03	*0.00*	0.03	*0.00*	0.04	*0.00*	0.04	*0.00*	0.03	*0.01*
Mg	0.18	*0.01*	0.18	*0.01*	0.18	*0.00*	0.18	*0.01*	0.16	*0.01*	0.16	*0.01*	0.18	*0.01*
Usp	0.26	*0.01*	0.26	*0.00*	0.24	*0.00*	0.26	*0.01*	0.24	*0.01*	0.24	*0.01*	0.24	*0.01*
n	*6*		*9*		*8*		*8*		*8*		*10*		*8*	

Sample#	N-48		N-49		N-50		N-51		N-52		N-53		N-54	
Tm-group	4		4		4		4		7		7		7	
(wt%)	avg.	±S.D.	avg.	±S.D.	avg.	±S.D.	avg.	±S.D.	avg.	±S.D.	avg.	±S.D.	avg.	±S.D.
TiO_2	8.53	*0.12*	8.42	*0.26*	8.36	*0.12*	8.41	*0.20*	7.58	*0.24*	7.65	*0.24*	7.53	*0.12*
Al_2O_3	3.50	*0.13*	3.38	*0.13*	3.48	*0.09*	3.48	*0.09*	2.97	*0.12*	3.04	*0.21*	2.97	*0.09*
FeO_t	78.91	*0.47*	78.43	*0.32*	78.49	*0.69*	78.70	*0.46*	80.31	*0.55*	80.61	*0.37*	80.85	*0.63*
MnO	1.07	*0.11*	1.06	*0.11*	1.00	*0.08*	1.07	*0.13*	1.11	*0.08*	1.07	*0.05*	1.19	*0.17*
MgO	3.21	*0.12*	3.27	*0.08*	3.35	*0.11*	3.38	*0.12*	2.78	*0.22*	2.69	*0.24*	2.59	*0.24*
Al_2O_3+MgO	6.71	*0.15*	6.64	*0.17*	6.83	*0.12*	6.86	*0.19*	5.75	*0.31*	5.72	*0.33*	5.56	*0.22*
Total	95.56	*0.54*	94.99	*0.31*	95.24	*0.54*	95.38	*0.61*	95.20	*0.47*	95.47	*0.40*	95.58	*0.56*
Fe_2O_3	50.18	*0.47*	50.16	*0.52*	50.41	*0.32*	50.49	*0.57*	52.27	*0.67*	52.18	*0.49*	52.42	*0.43*
FeO	33.75	*0.28*	33.29	*0.32*	33.13	*0.57*	33.26	*0.23*	33.28	*0.34*	33.66	*0.34*	33.69	*0.58*
Total recal	100.45	*0.55*	99.86	*0.36*	100.08	*0.70*	100.32	*0.66*	100.30	*0.49*	100.58	*0.38*	100.70	*0.55*
Ti	0.23	*0.00*	0.23	*0.01*	0.23	*0.00*	0.23	*0.01*	0.21	*0.01*	0.21	*0.01*	0.21	*0.00*
Al	0.15	*0.01*	0.15	*0.00*	0.15	*0.00*	0.15	*0.00*	0.13	*0.00*	0.13	*0.01*	0.13	*0.00*
Fe^{+3}	1.37	*0.01*	1.38	*0.01*	1.39	*0.01*	1.38	*0.01*	1.44	*0.02*	1.44	*0.02*	1.44	*0.01*
Fe^{+2}	1.03	*0.01*	1.02	*0.01*	1.01	*0.01*	1.01	*0.01*	1.02	*0.01*	1.03	*0.01*	1.03	*0.02*
Mn	0.03	*0.00*	0.03	*0.00*	0.03	*0.00*	0.03	*0.00*	0.03	*0.00*	0.03	*0.00*	0.04	*0.01*
Mg	0.17	*0.01*	0.18	*0.00*	0.18	*0.01*	0.18	*0.01*	0.15	*0.01*	0.15	*0.01*	0.14	*0.01*
Usp	0.24	*0.00*	0.23	*0.01*	0.23	*0.00*	0.23	*0.01*	0.21	*0.01*	0.21	*0.01*	0.21	*0.00*
n	*8*		*10*		*8*		*8*		*10*		*9*		*9*	

Sample#	N-55		N-56		N-57		N-58		N-59		N-60		N-61	
Tm-group	5		5		2		1		1		1		1	
(wt%)	avg.	±S.D.	avg.	±S.D.	avg.	±S.D.	avg.	±S.D.	avg.	±S.D.	avg.	±S.D.	avg.	±S.D.
TiO_2	8.91	*0.14*	8.87	*0.15*	9.08	*0.21*	10.23	*0.23*	9.96	*0.28*	10.20	*0.32*	10.28	*0.32*
Al_2O_3	3.07	*0.16*	3.00	*0.13*	3.43	*0.16*	3.48	*0.13*	3.64	*0.20*	3.43	*0.26*	3.33	*0.15*
FeO_t	79.35	*0.67*	79.02	*0.72*	78.61	*0.36*	76.67	*0.34*	76.60	*0.38*	77.02	*0.72*	76.63	*0.26*
MnO	1.14	*0.11*	1.19	*0.14*	1.04	*0.20*	0.96	*0.14*	1.04	*0.12*	0.96	*0.17*	1.19	*0.12*
MgO	2.94	*0.23*	2.94	*0.15*	3.35	*0.10*	3.44	*0.17*	3.57	*0.23*	3.45	*0.18*	3.43	*0.13*
Al_2O_3+MgO	6.01	*0.14*	5.94	*0.21*	6.78	*0.15*	6.92	*0.27*	7.21	*0.42*	6.88	*0.41*	6.75	*0.17*
Total	95.83	*0.73*	95.46	*0.54*	95.90	*0.23*	95.03	*0.54*	95.02	*0.39*	95.27	*0.59*	95.13	*0.63*
Fe_2O_3	49.96	*0.71*	49.88	*0.61*	49.43	*0.34*	46.57	*0.62*	47.00	*0.55*	46.88	*0.89*	46.69	*0.40*
FeO	34.39	*0.55*	34.14	*0.45*	34.13	*0.23*	34.76	*0.48*	34.31	*0.65*	34.84	*0.43*	34.62	*0.34*
Total recal	100.64	*0.81*	100.28	*0.65*	100.73	*0.32*	99.61	*0.58*	99.67	*0.38*	99.88	*0.72*	99.74	*0.48*
Ti	0.24	*0.00*	0.24	*0.00*	0.25	*0.01*	0.28	*0.01*	0.27	*0.01*	0.28	*0.01*	0.28	*0.01*
Al	0.13	*0.01*	0.13	*0.01*	0.15	*0.01*	0.15	*0.01*	0.16	*0.01*	0.15	*0.01*	0.14	*0.01*
Fe^{+3}	1.37	*0.01*	1.37	*0.01*	1.35	*0.01*	1.28	*0.02*	1.29	*0.01*	1.29	*0.02*	1.28	*0.01*
Fe^{+2}	1.05	*0.02*	1.05	*0.01*	1.04	*0.01*	1.06	*0.02*	1.05	*0.02*	1.06	*0.02*	1.06	*0.01*
Mn	0.04	*0.00*	0.04	*0.00*	0.03	*0.01*	0.03	*0.00*	0.03	*0.00*	0.03	*0.01*	0.04	*0.00*
Mg	0.16	*0.01*	0.16	*0.01*	0.18	*0.01*	0.19	*0.01*	0.19	*0.01*	0.19	*0.01*	0.19	*0.01*
Usp	0.25	*0.01*	0.25	*0.00*	0.25	*0.01*	0.28	*0.01*	0.27	*0.01*	0.28	*0.01*	0.28	*0.01*
n	*6*		*9*		*8*		*9*		*10*		*10*		*6*	

Appendix 2 *(continued)*

Sample#	N-62		N-63		N-64		N-65		N-67		N-68		E-1	
Tm-group	1		1		2		2		3		3		2	
(wt%)	avg.	±S.D.	avg.	±S.D.	avg.	±S.D.	avg.	±S.D.	avg.	±S.D.	avg.	±S.D.	avg.	±S.D.
TiO_2	10.65	*0.20*	10.08	*0.22*	9.54	*0.24*	9.40	*0.20*	9.26	*0.22*	9.22	*0.23*	9.72	*0.25*
Al_2O_3	3.06	*0.16*	3.48	*0.36*	3.07	*0.27*	3.17	*0.25*	2.72	*0.14*	2.79	*0.15*	3.49	*0.06*
FeO_t	76.47	*0.36*	76.44	*0.59*	78.06	*0.59*	77.53	*0.66*	79.26	*0.35*	79.49	*1.38*	79.66	*0.64*
MnO	1.13	*0.12*	1.14	*0.15*	1.20	*0.10*	1.08	*0.11*	1.15	*0.05*	1.11	*0.11*	1.00	*0.10*
MgO	3.24	*0.12*	3.48	*0.16*	3.04	*0.15*	3.28	*0.13*	2.82	*0.11*	2.66	*0.11*	3.26	*0.08*
Al_2O_3+MgO	6.30	*0.22*	6.96	*0.51*	6.11	*0.21*	6.45	*0.33*	5.54	*0.23*	5.45	*0.24*	6.74	*0.12*
Total	94.95	*0.40*	94.85	*0.46*	95.16	*0.68*	94.81	*0.73*	95.51	*0.52*	96.31	*0.81*	97.51	*0.62*
Fe_2O_3	45.93	*0.49*	46.79	*0.53*	48.46	*0.53*	48.31	*0.51*	49.39	*0.53*	49.63	*0.37*	49.18	*0.68*
FeO	35.14	*0.39*	34.34	*0.38*	34.46	*0.44*	34.06	*0.42*	34.82	*0.41*	34.83	*1.38*	35.41	*0.32*
Total recal	99.45	*0.35*	99.48	*0.42*	99.91	*0.73*	99.54	*0.70*	100.41	*0.40*	100.81	*0.84*	102.24	*0.59*
Ti	0.29	*0.01*	0.28	*0.01*	0.26	*0.01*	0.26	*0.00*	0.26	*0.01*	0.25	*0.01*	0.26	*0.01*
Al	0.13	*0.01*	0.15	*0.02*	0.13	*0.01*	0.14	*0.01*	0.12	*0.01*	0.12	*0.01*	0.15	*0.00*
Fe^{+3}	1.27	*0.01*	1.29	*0.01*	1.34	*0.01*	1.34	*0.02*	1.36	*0.02*	1.36	*0.01*	1.32	*0.01*
Fe^{+2}	1.08	*0.01*	1.05	*0.01*	1.06	*0.01*	1.05	*0.01*	1.07	*0.01*	1.06	*0.04*	1.06	*0.01*
Mn	0.04	*0.00*	0.04	*0.00*	0.04	*0.00*	0.03	*0.00*	0.04	*0.00*	0.03	*0.00*	0.03	*0.00*
Mg	0.18	*0.01*	0.19	*0.01*	0.17	*0.01*	0.18	*0.01*	0.15	*0.01*	0.14	*0.01*	0.17	*0.00*
Usp	0.30	*0.01*	0.28	*0.01*	0.26	*0.01*	0.26	*0.01*	0.26	*0.01*	0.26	*0.01*	0.26	*0.01*
n	*9*		*5*		*14*		*8*		*5*		*9*		*6*	

Sample#	E-1b		E-4		E-5		E-6		E-7		E-8		E-10	
Tm-group	11		12		11		11		11		10		8	
(wt%)	avg.	±S.D.	avg.	±S.D.	avg.	±S.D.	avg.	±S.D.	avg.	±S.D.	avg.	±S.D.	avg.	±S.D.
TiO_2	7.19	*0.48*	6.48	*0.20*	5.78	*0.17*	7.85	*0.22*	7.87	*0.32*	7.44	*0.19*	7.70	*0.24*
Al_2O_3	4.83	*0.48*	3.13	*0.28*	7.92	*0.35*	5.47	*0.38*	5.73	*0.13*	2.07	*0.21*	2.70	*0.32*
FeO_t	80.80	*0.42*	81.93	*0.65*	78.36	*0.69*	78.40	*0.58*	78.74	*0.61*	82.76	*0.77*	81.70	*0.85*
MnO	0.74	*0.26*	1.16	*0.07*	0.56	*0.06*	0.74	*0.20*	0.78	*0.13*	1.61	*0.20*	1.12	*0.25*
MgO	2.83	*0.22*	2.14	*0.61*	4.33	*0.20*	3.74	*0.14*	3.71	*0.20*	1.69	*0.20*	2.35	*0.27*
Al_2O_3+MgO	7.66	*0.70*	5.27	*0.54*	12.25	*0.54*	9.21	*0.31*	9.44	*0.23*	3.76	*0.37*	5.05	*0.38*
Total	96.71	*0.48*	95.69	*0.78*	97.59	*0.29*	96.86	*0.42*	97.23	*0.41*	96.25	*0.75*	95.87	*0.52*
Fe_2O_3	51.96	*0.61*	54.11	*1.28*	52.19	*0.22*	50.15	*0.70*	50.26	*0.73*	53.82	*0.66*	52.75	*0.58*
FeO	34.05	*0.53*	33.24	*0.72*	31.39	*0.53*	33.28	*0.52*	33.51	*0.36*	34.33	*0.54*	34.24	*0.45*
Total recal	101.76	*0.31*	100.92	*0.89*	102.64	*0.31*	101.72	*0.55*	102.12	*0.49*	101.49	*0.85*	101.20	*0.61*
Ti	0.19	*0.01*	0.18	*0.01*	0.15	*0.00*	0.21	*0.01*	0.21	*0.01*	0.21	*0.01*	0.21	*0.01*
Al	0.20	*0.02*	0.14	*0.01*	0.32	*0.01*	0.23	*0.02*	0.24	*0.01*	0.09	*0.01*	0.12	*0.01*
Fe^{+3}	1.40	*0.01*	1.49	*0.02*	1.36	*0.01*	1.34	*0.02*	1.34	*0.02*	1.49	*0.01*	1.45	*0.01*
Fe^{+2}	1.02	*0.02*	1.02	*0.03*	0.91	*0.02*	0.99	*0.02*	0.99	*0.01*	1.06	*0.01*	1.05	*0.01*
Mn	0.02	*0.01*	0.04	*0.00*	0.02	*0.00*	0.02	*0.01*	0.02	*0.00*	0.05	*0.01*	0.03	*0.01*
Mg	0.15	*0.01*	0.12	*0.03*	0.22	*0.01*	0.20	*0.01*	0.20	*0.01*	0.09	*0.01*	0.13	*0.01*
Usp	0.20	*0.01*	0.18	*0.00*	0.15	*0.01*	0.21	*0.01*	0.21	*0.01*	0.21	*0.01*	0.22	*0.01*
n	*3*		*4*		*6*		*7*		*10*		*9*		*6*	

Sample#	E-15		E-15b		E-19		E-20		E-21		E-22		E-23	
Tm-group	3		11		3		2		2		2		2	
(wt%)	avg.	±S.D.	avg.	±S.D.	avg.	±S.D.	avg.	±S.D.	avg.	±S.D.	avg.	±S.D.	avg.	±S.D.
TiO_2	9.51	*0.29*	6.85	*0.25*	9.26	*0.29*	9.65	*0.30*	9.97	*0.23*	9.57	*0.43*	9.15	*0.26*
Al_2O_3	2.35	*0.21*	4.57	*0.12*	2.64	*0.13*	3.01	*0.26*	3.43	*0.25*	3.31	*0.15*	3.33	*0.22*
FeO_t	79.57	*0.89*	80.75	*0.38*	80.31	*0.84*	79.00	*0.90*	79.96	*0.96*	79.42	*1.43*	80.54	*0.84*
MnO	1.17	*0.12*	0.77	*0.27*	1.16	*0.11*	1.05	*0.14*	1.04	*0.13*	1.05	*0.13*	1.10	*0.18*
MgO	2.65	*0.22*	2.79	*0.20*	2.42	*0.41*	3.01	*0.15*	3.23	*0.21*	3.10	*0.29*	3.15	*0.17*
Al_2O_3+MgO	5.01	*0.37*	7.36	*0.22*	5.06	*0.47*	6.01	*0.37*	6.66	*0.40*	6.41	*0.33*	6.47	*0.34*
Total	95.53	*0.92*	96.16	*0.42*	96.36	*1.00*	96.15	*1.24*	98.23	*1.21*	96.90	*1.47*	97.81	*0.64*
Fe_2O_3	49.34	*0.74*	52.52	*0.40*	49.74	*1.21*	48.82	*0.77*	49.13	*0.67*	49.11	*1.28*	50.53	*0.91*
FeO	35.17	*0.64*	33.49	*0.62*	35.55	*0.89*	35.07	*0.49*	35.75	*0.58*	35.23	*0.64*	35.08	*0.40*
Total recal	100.43	*0.95*	101.22	*0.39*	101.24	*1.10*	100.91	*1.23*	102.94	*1.29*	101.70	*1.51*	102.75	*0.76*
Ti	0.26	*0.01*	0.19	*0.01*	0.25	*0.01*	0.26	*0.01*	0.27	*0.00*	0.26	*0.01*	0.25	*0.01*
Al	0.10	*0.01*	0.19	*0.00*	0.11	*0.01*	0.13	*0.01*	0.14	*0.01*	0.14	*0.01*	0.14	*0.01*
Fe^{+3}	1.36	*0.01*	1.43	*0.01*	1.36	*0.02*	1.34	*0.01*	1.31	*0.01*	1.33	*0.03*	1.36	*0.02*
Fe^{+2}	1.08	*0.02*	1.01	*0.02*	1.08	*0.03*	1.07	*0.02*	1.06	*0.01*	1.06	*0.02*	1.05	*0.01*
Mn	0.04	*0.00*	0.02	*0.01*	0.04	*0.00*	0.03	*0.00*	0.03	*0.00*	0.03	*0.00*	0.03	*0.01*
Mg	0.15	*0.01*	0.15	*0.01*	0.13	*0.02*	0.16	*0.01*	0.17	*0.01*	0.17	*0.02*	0.17	*0.01*
Usp	0.27	*0.01*	0.19	*0.01*	0.26	*0.01*	0.27	*0.01*	0.27	*0.00*	0.26	*0.01*	0.25	*0.01*
n	*9*		*4*		*11*		*14*		*14*		*18*		*6*	

Appendix 2 *(continued)*

Sample#	E-23b		E-24		E-25		E-26		E-28		E-32		E-33	
Tm-group	4		2		2		4		7		1		1	
(wt%)	avg.	±S.D.	avg.	±S.D.	avg.	±S.D.	avg.	±S.D.	avg.	±S.D.	avg.	±S.D.	avg.	±S.D.
TiO_2	8.64	*0.25*	9.26	*0.16*	9.14	*0.13*	8.88	*0.12*	7.91	*0.25*	10.08	*0.48*	10.29	*0.22*
Al_2O_3	3.49	*0.04*	3.44	*0.17*	3.65	*0.11*	3.50	*0.06*	3.17	*0.20*	3.52	*0.14*	3.62	*0.11*
FeO_t	80.41	*0.37*	80.38	*1.11*	80.41	*0.42*	80.07	*0.26*	81.39	*0.64*	78.02	*0.96*	78.15	*0.57*
MnO	0.98	*0.05*	1.12	*0.15*	1.07	*0.09*	1.05	*0.16*	1.10	*0.11*	1.00	*0.14*	0.95	*0.12*
MgO	3.34	*0.08*	2.91	*0.17*	3.26	*0.11*	3.29	*0.11*	2.69	*0.20*	3.51	*0.17*	3.68	*0.11*
Al_2O_3+MgO	6.83	*0.04*	6.35	*0.20*	6.91	*0.20*	6.79	*0.14*	5.87	*0.13*	7.03	*0.26*	7.30	*0.15*
Total	97.23	*0.37*	97.62	*0.90*	98.05	*0.75*	97.21	*0.36*	96.67	*0.65*	96.64	*0.60*	96.87	*0.50*
Fe_2O_3	51.31	*0.41*	49.99	*1.01*	50.47	*0.45*	50.71	*0.22*	52.46	*0.48*	47.69	*1.88*	47.84	*0.78*
FeO	34.24	*0.43*	35.40	*0.36*	35.00	*0.30*	34.44	*0.19*	34.19	*0.52*	35.11	*0.92*	35.11	*0.30*
Total recal	102.27	*0.32*	102.46	*0.97*	102.94	*0.76*	102.10	*0.27*	101.81	*0.69*	101.28	*0.73*	101.56	*0.60*
Ti	0.23	*0.01*	0.25	*0.01*	0.24	*0.00*	0.24	*0.00*	0.22	*0.01*	0.27	*0.01*	0.28	*0.01*
Al	0.15	*0.00*	0.15	*0.01*	0.15	*0.00*	0.15	*0.00*	0.14	*0.01*	0.15	*0.01*	0.15	*0.00*
Fe^{+3}	1.38	*0.01*	1.35	*0.02*	1.35	*0.01*	1.37	*0.01*	1.43	*0.01*	1.29	*0.05*	1.29	*0.01*
Fe^{+2}	1.02	*0.01*	1.06	*0.01*	1.04	*0.01*	1.03	*0.01*	1.03	*0.01*	1.06	*0.03*	1.05	*0.01*
Mn	0.03	*0.00*	0.03	*0.00*	0.03	*0.00*	0.03	*0.00*	0.03	*0.00*	0.03	*0.00*	0.03	*0.00*
Mg	0.18	*0.00*	0.16	*0.01*	0.17	*0.01*	0.18	*0.01*	0.15	*0.01*	0.19	*0.01*	0.20	*0.01*
Usp	0.23	*0.01*	0.25	*0.01*	0.25	*0.00*	0.24	*0.00*	0.22	*0.01*	0.28	*0.02*	0.28	*0.01*
n	*4*		*9*		*6*		*10*		*7*		*8*		*9*	

Sample#	E-34		E-36		E-38		E-40		E-41		E-42		E-46	
Tm-group	1		2		3		3		3		1		2	
(wt%)	avg.	±S.D.	avg.	±S.D.	avg.	±S.D.	avg.	±S.D.	avg.	±S.D.	avg.	±S.D.	avg.	±S.D.
TiO_2	10.36	*0.27*	9.55	*0.17*	9.20	*0.30*	9.38	*0.18*	9.45	*0.21*	10.11	*0.29*	9.29	*0.25*
Al_2O_3	3.50	*0.25*	3.38	*0.20*	2.74	*0.15*	2.48	*0.37*	2.55	*0.20*	3.94	*0.36*	3.67	*0.19*
FeO_t	78.14	*0.49*	78.64	*0.97*	80.03	*0.68*	79.60	*3.58*	80.82	*1.36*	79.49	*0.85*	81.25	*0.91*
MnO	1.04	*0.15*	1.10	*0.11*	1.09	*0.11*	1.16	*0.10*	1.18	*0.05*	0.92	*0.12*	1.03	*0.11*
MgO	3.45	*0.21*	3.46	*0.38*	2.69	*0.34*	2.46	*0.30*	2.46	*0.35*	3.48	*0.26*	3.00	*0.23*
Al_2O_3+MgO	6.94	*0.41*	6.84	*0.20*	5.43	*0.47*	4.94	*0.65*	5.01	*0.49*	7.42	*0.56*	6.68	*0.32*
Total	96.97	*0.60*	97.28	*0.45*	96.20	*0.83*	95.81	*3.08*	96.99	*1.21*	98.33	*1.19*	98.52	*1.01*
Fe_2O_3	47.46	*0.44*	48.42	*1.30*	49.96	*0.99*	48.95	*3.78*	50.01	*1.44*	48.55	*1.11*	50.49	*0.62*
FeO	35.43	*0.43*	35.07	*0.36*	35.08	*0.61*	35.55	*0.32*	35.82	*0.67*	35.80	*0.64*	35.82	*0.42*
Total recal	101.61	*0.66*	101.93	*0.42*	101.11	*0.92*	100.53	*3.69*	101.84	*1.39*	103.02	*1.15*	103.54	*1.03*
Ti	0.28	*0.01*	0.26	*0.01*	0.25	*0.01*	0.26	*0.01*	0.26	*0.01*	0.27	*0.01*	0.25	*0.01*
Al	0.15	*0.01*	0.14	*0.01*	0.12	*0.01*	0.11	*0.01*	0.11	*0.01*	0.16	*0.01*	0.15	*0.01*
Fe^{+3}	1.28	*0.01*	1.30	*0.04*	1.37	*0.02*	1.35	*0.06*	1.37	*0.02*	1.29	*0.02*	1.34	*0.01*
Fe^{+2}	1.06	*0.01*	1.05	*0.01*	1.07	*0.02*	1.09	*0.04*	1.09	*0.02*	1.06	*0.02*	1.06	*0.01*
Mn	0.03	*0.00*	0.03	*0.00*	0.03	*0.00*	0.04	*0.00*	0.04	*0.00*	0.03	*0.00*	0.03	*0.00*
Mg	0.18	*0.01*	0.18	*0.02*	0.15	*0.02*	0.13	*0.01*	0.13	*0.02*	0.18	*0.01*	0.16	*0.01*
Usp	0.28	*0.01*	0.28	*0.03*	0.26	*0.01*	0.27	*0.03*	0.26	*0.01*	0.27	*0.01*	0.25	*0.01*
n	*7*		*5*		*12*		*8*		*10*		*9*		*10*	

Sample#	E-47		E-48		E-49		E-51		E-52		E-54		E-56	
Tm-group	1		1		1		1		1		1		1	
(wt%)	avg.	±S.D.	avg.	±S.D.	avg.	±S.D.	avg.	±S.D.	avg.	±S.D.	avg.	±S.D.	avg.	±S.D.
TiO_2	9.99	*0.14*	9.88	*0.18*	9.85	*0.14*	10.15	*0.44*	10.21	*0.32*	9.66	*0.17*	10.19	*0.30*
Al_2O_3	4.07	*0.08*	4.18	*0.17*	4.22	*0.32*	3.94	*0.20*	3.91	*0.55*	4.32	*0.22*	4.31	*0.21*
FeO_t	80.23	*0.36*	80.00	*0.53*	80.03	*0.42*	79.91	*0.61*	79.37	*0.75*	79.60	*0.56*	79.18	*0.58*
MnO	0.95	*0.13*	0.92	*0.11*	0.94	*0.09*	0.92	*0.11*	0.95	*0.17*	0.95	*0.08*	0.93	*0.06*
MgO	3.65	*0.12*	3.64	*0.09*	3.64	*0.16*	3.20	*0.61*	3.50	*0.40*	3.84	*0.10*	3.75	*0.06*
Al_2O_3+MgO	7.72	*0.16*	7.82	*0.22*	7.87	*0.25*	7.13	*0.81*	7.41	*0.93*	8.16	*0.21*	8.06	*0.24*
Total	99.04	*0.49*	99.01	*0.61*	98.90	*0.51*	98.37	*0.66*	98.12	*0.53*	98.60	*0.55*	98.74	*0.59*
Fe_2O_3	49.49	*0.43*	49.30	*0.44*	49.40	*0.45*	48.44	*0.94*	48.40	*0.62*	49.51	*0.57*	48.32	*0.36*
FeO	35.70	*0.29*	35.64	*0.31*	35.58	*0.29*	36.33	*1.33*	35.82	*0.75*	35.05	*0.24*	35.70	*0.47*
Total recal	103.91	*0.53*	103.87	*0.55*	103.78	*0.54*	103.14	*0.66*	102.91	*0.53*	103.50	*0.59*	103.42	*0.64*
Ti	0.26	*0.00*	0.26	*0.00*	0.26	*0.00*	0.27	*0.01*	0.27	*0.01*	0.25	*0.00*	0.27	*0.01*
Al	0.17	*0.00*	0.17	*0.01*	0.17	*0.01*	0.16	*0.01*	0.16	*0.02*	0.18	*0.01*	0.18	*0.01*
Fe^{+3}	1.30	*0.01*	1.30	*0.01*	1.30	*0.01*	1.29	*0.02*	1.29	*0.02*	1.31	*0.01*	1.28	*0.01*
Fe^{+2}	1.04	*0.01*	1.04	*0.01*	1.04	*0.01*	1.08	*0.04*	1.06	*0.03*	1.03	*0.01*	1.05	*0.01*
Mn	0.03	*0.00*	0.03	*0.00*	0.03	*0.00*	0.03	*0.00*	0.03	*0.01*	0.03	*0.00*	0.03	*0.00*
Mg	0.19	*0.01*	0.19	*0.00*	0.19	*0.01*	0.17	*0.03*	0.18	*0.02*	0.20	*0.00*	0.20	*0.00*
Usp	0.26	*0.00*	0.26	*0.00*	0.26	*0.00*	0.27	*0.01*	0.27	*0.01*	0.26	*0.01*	0.27	*0.01*
n	*9*		*10*		*8*		*8*		*7*		*9*		*6*	

Appendix 2 *(continued)*

Sample#	E-56b		E-58		E-58b		E-64		E-67		E-68		E-69	
Tm-group	11		1		11		1		1		1		1	
(wt%)	avg.	±S.D.	avg.	±S.D.	avg.	±S.D.	avg.	±S.D.	avg.	±S.D.	avg.	±S.D.	avg.	±S.D.
TiO_2	8.72	*0.58*	10.81	*0.73*	8.56	*0.28*	10.20	*0.27*	9.92	*0.28*	9.46	*0.12*	9.71	*0.36*
Al_2O_3	5.71	*0.38*	3.65	*0.62*	5.61	*0.25*	3.85	*0.20*	3.56	*0.32*	4.09	*0.19*	4.05	*0.14*
FeO_t	78.37	*0.50*	79.27	*0.78*	78.88	*0.89*	79.85	*0.54*	78.67	*0.34*	78.66	*0.32*	78.45	*0.24*
MnO	0.82	*0.10*	0.93	*0.16*	0.63	*0.29*	0.98	*0.18*	0.97	*0.14*	0.94	*0.18*	0.79	*0.23*
MgO	4.10	*0.22*	3.15	*0.72*	4.11	*0.07*	3.26	*0.42*	3.40	*0.16*	3.63	*0.10*	3.70	*0.09*
Al_2O_3+MgO	9.81	*0.18*	6.80	*1.25*	9.72	*0.18*	7.12	*0.49*	6.95	*0.43*	7.72	*0.26*	7.75	*0.16*
Total	97.94	*0.52*	98.20	*0.63*	98.17	*0.02*	98.46	*0.37*	96.93	*0.53*	97.05	*0.29*	97.07	*0.31*
Fe_2O_3	49.37	*0.66*	47.14	*1.44*	49.96	*0.96*	48.46	*0.96*	48.26	*0.46*	48.90	*0.39*	48.47	*0.86*
FeO	33.94	*0.19*	36.85	*1.60*	33.92	*0.03*	36.24	*0.87*	35.25	*0.30*	34.66	*0.30*	34.84	*0.70*
Total recal	102.83	*0.36*	102.80	*0.65*	103.18	*0.05*	103.17	*0.39*	101.65	*0.47*	101.86	*0.30*	101.89	*0.28*
Ti	0.23	*0.01*	0.29	*0.02*	0.22	*0.01*	0.27	*0.01*	0.27	*0.01*	0.25	*0.00*	0.26	*0.01*
Al	0.24	*0.02*	0.15	*0.03*	0.23	*0.01*	0.16	*0.01*	0.15	*0.01*	0.17	*0.01*	0.17	*0.01*
Fe^{+3}	1.30	*0.02*	1.26	*0.03*	1.31	*0.03*	1.29	*0.02*	1.30	*0.01*	1.31	*0.01*	1.30	*0.02*
Fe^{+2}	0.99	*0.00*	1.10	*0.06*	0.99	*0.00*	1.07	*0.03*	1.06	*0.01*	1.03	*0.01*	1.04	*0.02*
Mn	0.02	*0.00*	0.03	*0.00*	0.02	*0.01*	0.03	*0.01*	0.03	*0.00*	0.03	*0.01*	0.02	*0.01*
Mg	0.21	*0.01*	0.17	*0.04*	0.21	*0.00*	0.17	*0.02*	0.18	*0.01*	0.19	*0.01*	0.20	*0.00*
Usp	0.23	*0.02*	0.29	*0.02*	0.23	*0.00*	0.27	*0.01*	0.27	*0.01*	0.26	*0.00*	0.26	*0.01*
n	*4*		*8*		*2*		*10*		*7*		*8*		*4*	

Sample#	E-71		E-74		E-75		E-76		E-77		E-78		E-79	
Tm-group	6		1		2		2		8		8		8	
(wt%)	avg.	±S.D.	avg.	±S.D.	avg.	±S.D.	avg.	±S.D.	avg.	±S.D.	avg.	±S.D.	avg.	±S.D.
TiO_2	8.68	*0.07*	9.72	*0.26*	9.32	*0.61*	9.34	*0.63*	8.42	*0.13*	8.43	*0.25*	8.71	*0.29*
Al_2O_3	4.32	*0.18*	3.84	*0.23*	3.47	*0.25*	3.39	*0.30*	2.48	*0.09*	2.43	*0.16*	2.35	*0.10*
FeO_t	79.06	*0.45*	78.78	*0.40*	79.55	*0.83*	79.82	*0.82*	81.76	*0.36*	81.66	*0.24*	81.48	*0.58*
MnO	0.85	*0.10*	0.98	*0.06*	1.03	*0.11*	1.04	*0.11*	1.29	*0.15*	1.33	*0.12*	1.42	*0.19*
MgO	3.64	*0.11*	3.55	*0.16*	3.19	*0.17*	3.06	*0.22*	2.47	*0.14*	2.52	*0.10*	2.33	*0.09*
Al_2O_3+MgO	7.96	*0.17*	7.39	*0.35*	6.66	*0.31*	6.45	*0.43*	4.94	*0.13*	4.95	*0.22*	4.68	*0.13*
Total	96.75	*0.36*	97.11	*0.76*	96.82	*0.34*	96.90	*0.49*	96.66	*0.33*	96.71	*0.45*	96.55	*0.87*
Fe_2O_3	50.06	*0.50*	48.73	*0.59*	49.63	*1.26*	49.63	*1.23*	52.22	*0.41*	52.32	*0.34*	51.69	*0.42*
FeO	34.02	*0.17*	34.93	*0.53*	34.90	*0.49*	35.17	*0.45*	34.77	*0.28*	34.58	*0.33*	34.97	*0.32*
Total recal	101.69	*0.37*	101.98	*0.74*	101.78	*0.39*	101.83	*0.51*	101.88	*0.38*	101.81	*0.42*	101.65	*0.84*
Ti	0.23	*0.00*	0.26	*0.01*	0.25	*0.02*	0.25	*0.02*	0.23	*0.00*	0.23	*0.01*	0.24	*0.01*
Al	0.18	*0.01*	0.16	*0.01*	0.15	*0.01*	0.14	*0.01*	0.11	*0.00*	0.10	*0.01*	0.10	*0.00*
Fe^{+3}	1.35	*0.01*	1.31	*0.02*	1.34	*0.03*	1.34	*0.03*	1.43	*0.01*	1.43	*0.01*	1.42	*0.01*
Fe^{+2}	1.02	*0.00*	1.04	*0.02*	1.05	*0.01*	1.06	*0.02*	1.06	*0.01*	1.05	*0.01*	1.07	*0.01*
Mn	0.03	*0.00*	0.03	*0.00*	0.03	*0.00*	0.03	*0.00*	0.04	*0.00*	0.04	*0.00*	0.04	*0.01*
Mg	0.19	*0.01*	0.19	*0.01*	0.17	*0.01*	0.16	*0.01*	0.13	*0.01*	0.14	*0.01*	0.13	*0.00*
Usp	0.24	*0.00*	0.26	*0.01*	0.25	*0.02*	0.25	*0.02*	0.23	*0.00*	0.23	*0.01*	0.24	*0.01*
n	*10*		*8*		*9*		*9*		*8*		*10*		*9*	

Sample#	T-2		T-3		T-4		T-5		T-5b		T-6		T-7	
Tm-group	12		12		11		12		11		12		12	
(wt%)	avg.	±S.D.	avg.	±S.D.	avg.	±S.D.	avg.	±S.D.	avg.	±S.D.	avg.	±S.D.	avg.	±S.D.
TiO_2	6.08	*0.56*	6.45	*0.58*	6.03	*0.24*	5.95	*0.40*	5.80	*0.17*	6.45	*0.25*	6.70	*0.41*
Al_2O_3	3.73	*0.23*	3.36	*0.23*	6.70	*0.27*	3.59	*0.58*	6.90	*0.41*	2.79	*0.58*	2.95	*0.61*
FeO_t	72.97	*1.46*	74.70	*1.79*	73.33	*1.92*	78.66	*0.92*	74.50	*1.28*	77.43	*0.76*	77.79	*3.46*
MnO	0.80	*0.11*	0.87	*0.18*	0.49	*0.09*	0.86	*0.32*	0.47	*0.13*	0.98	*0.12*	0.89	*0.31*
MgO	2.59	*0.74*	2.74	*0.21*	3.73	*0.21*	2.17	*0.48*	3.79	*0.45*	2.43	*0.39*	2.36	*0.86*
Al_2O_3+MgO	6.32	*0.61*	6.10	*0.41*	10.43	*0.30*	5.76	*1.04*	10.68	*0.65*	5.23	*0.85*	5.31	*1.25*
Total	86.66	*1.16*	88.85	*1.92*	90.70	*2.12*	91.67	*0.83*	91.72	*1.26*	90.36	*0.60*	91.32	*3.06*
Fe_2O_3	48.01	*0.75*	49.11	*1.63*	47.98	*1.30*	51.87	*0.85*	49.17	*0.62*	51.21	*0.42*	50.87	*2.59*
FeO	29.77	*0.90*	30.51	*0.79*	30.15	*0.79*	31.98	*0.75*	30.26	*0.99*	31.35	*0.56*	32.02	*1.76*
Total recal	91.38	*1.26*	93.59	*2.17*	95.38	*2.23*	96.75	*0.84*	96.59	*1.28*	95.43	*0.65*	96.29	*3.30*
Ti	0.18	*0.02*	0.19	*0.02*	0.17	*0.01*	0.17	*0.01*	0.16	*0.01*	0.19	*0.01*	0.19	*0.01*
Al	0.18	*0.01*	0.16	*0.01*	0.30	*0.01*	0.16	*0.02*	0.30	*0.01*	0.13	*0.03*	0.13	*0.03*
Fe^{+3}	1.45	*0.02*	1.45	*0.02*	1.35	*0.01*	1.49	*0.04*	1.37	*0.01*	1.49	*0.01*	1.47	*0.05*
Fe^{+2}	1.00	*0.03*	1.00	*0.02*	0.95	*0.01*	1.02	*0.03*	0.94	*0.03*	1.01	*0.02*	1.03	*0.05*
Mn	0.03	*0.00*	0.03	*0.01*	0.02	*0.00*	0.03	*0.01*	0.01	*0.00*	0.03	*0.00*	0.03	*0.01*
Mg	0.15	*0.04*	0.16	*0.01*	0.21	*0.01*	0.12	*0.03*	0.21	*0.03*	0.14	*0.02*	0.14	*0.05*
Usp	0.19	*0.01*	0.20	*0.02*	0.17	*0.01*	0.17	*0.01*	0.16	*0.01*	0.19	*0.01*	0.20	*0.01*
n	*7*		*7*		*17*		*6*		*5*		*6*		*8*	

Appendix 2 *(continued)*

Sample#	T-8		T-9		T-10		T-11		T-14		T-15		T-16	
Tm-group	12		11		11		11		10		10		9	
(wt%)	avg.	±S.D.	avg.	±S.D.	avg.	±S.D.	avg.	±S.D.	avg.	±S.D.	avg.	±S.D.	avg.	±S.D.
TiO_2	5.86	*0.34*	7.22	*0.19*	6.40	*0.19*	6.22	*0.76*	7.37	*0.26*	7.68	*0.23*	7.89	*0.10*
Al_2O_3	2.76	*0.35*	5.00	*0.14*	5.40	*0.19*	5.74	*0.57*	1.98	*0.12*	2.07	*0.18*	2.36	*0.13*
FeO_t	76.41	*1.23*	80.09	*3.09*	70.55	*0.71*	69.07	*3.22*	85.26	*0.70*	84.62	*0.66*	83.77	*0.51*
MnO	1.03	*0.14*	0.81	*0.15*	0.56	*0.15*	0.56	*0.12*	1.31	*0.13*	1.26	*0.18*	1.03	*0.15*
MgO	1.98	*0.39*	3.14	*0.19*	3.32	*0.23*	3.68	*0.41*	1.52	*0.25*	1.80	*0.08*	2.00	*0.14*
Al_2O_3+MgO	4.74	*0.65*	8.14	*0.17*	8.72	*0.37*	9.42	*0.78*	3.50	*0.31*	3.87	*0.20*	4.37	*0.09*
Total	88.56	*1.06*	96.79	*3.40*	86.57	*0.80*	85.74	*3.22*	97.88	*0.58*	97.64	*0.49*	97.23	*0.43*
Fe_2O_3	50.57	*0.65*	51.85	*2.53*	45.61	*0.52*	45.11	*2.49*	55.24	*0.98*	54.68	*0.99*	53.82	*0.60*
FeO	30.91	*0.79*	33.44	*0.89*	29.50	*0.37*	28.48	*1.39*	35.55	*0.67*	35.42	*0.47*	35.34	*0.35*
Total recal	93.57	*1.11*	101.84	*3.55*	91.09	*0.83*	90.13	*3.50*	103.24	*0.65*	103.15	*0.57*	102.59	*0.48*
Ti	0.17	*0.01*	0.19	*0.00*	0.19	*0.00*	0.19	*0.02*	0.20	*0.01*	0.21	*0.01*	0.22	*0.00*
Al	0.13	*0.02*	0.21	*0.01*	0.25	*0.01*	0.27	*0.03*	0.08	*0.00*	0.09	*0.01*	0.10	*0.01*
Fe^{+3}	1.51	*0.02*	1.39	*0.02*	1.36	*0.02*	1.35	*0.04*	1.51	*0.02*	1.49	*0.02*	1.47	*0.01*
Fe^{+2}	1.02	*0.02*	1.00	*0.01*	0.98	*0.01*	0.95	*0.03*	1.08	*0.02*	1.07	*0.01*	1.07	*0.01*
Mn	0.03	*0.00*	0.02	*0.00*	0.02	*0.01*	0.02	*0.00*	0.04	*0.00*	0.04	*0.01*	0.03	*0.00*
Mg	0.12	*0.02*	0.17	*0.01*	0.20	*0.01*	0.22	*0.02*	0.08	*0.01*	0.10	*0.00*	0.11	*0.01*
Usp	0.18	*0.01*	0.20	*0.01*	0.19	*0.00*	0.19	*0.02*	0.20	*0.01*	0.21	*0.01*	0.21	*0.00*
n	*7*		*10*		*9*		*18*		*7*		*8*		*6*	

Sample#	T-17		T-18		T-19		T-20		T-21		T-22		T-23	
Tm-group	9		2		2		2		2		2		1	
(wt%)	avg.	±S.D.	avg.	±S.D.	avg.	±S.D.	avg.	±S.D.	avg.	±S.D.	avg.	±S.D.	avg.	±S.D.
TiO_2	7.84	*0.11*	9.28	*0.37*	9.87	*0.16*	9.33	*0.40*	9.73	*0.25*	9.53	*0.19*	9.99	*0.26*
Al_2O_3	2.40	*0.16*	3.37	*0.24*	3.16	*0.21*	3.24	*0.12*	3.31	*0.17*	3.34	*0.15*	3.58	*0.22*
FeO_t	83.51	*0.45*	80.99	*0.50*	80.29	*0.57*	76.94	*0.85*	78.21	*2.48*	77.06	*0.80*	76.43	*2.16*
MnO	1.09	*0.09*	0.73	*0.10*	0.82	*0.07*	1.09	*0.12*	1.04	*0.09*	1.05	*0.06*	0.98	*0.13*
MgO	2.15	*0.13*	3.16	*0.17*	3.26	*0.19*	3.39	*0.12*	3.34	*0.16*	3.25	*0.24*	3.39	*0.17*
Al_2O_3+MgO	4.55	*0.27*	6.53	*0.39*	6.42	*0.26*	6.63	*0.19*	6.65	*0.21*	6.59	*0.31*	6.97	*0.31*
Total	97.29	*0.26*	97.68	*0.63*	97.67	*0.57*	94.35	*0.76*	95.98	*2.62*	94.85	*1.00*	94.75	*2.17*
Fe_2O_3	53.80	*0.33*	50.51	*0.63*	49.53	*0.73*	48.12	*1.06*	48.37	*1.84*	47.48	*0.95*	46.59	*1.55*
FeO	35.10	*0.25*	35.54	*0.50*	35.72	*0.40*	33.63	*0.38*	34.69	*0.93*	34.34	*0.63*	34.51	*0.92*
Total recal	102.56	*0.30*	102.74	*0.62*	102.56	*0.57*	98.96	*0.78*	100.70	*2.82*	99.37	*1.04*	99.26	*2.38*
Ti	0.21	*0.00*	0.25	*0.01*	0.27	*0.00*	0.26	*0.01*	0.27	*0.01*	0.26	*0.01*	0.28	*0.01*
Al	0.10	*0.01*	0.14	*0.01*	0.13	*0.01*	0.14	*0.01*	0.14	*0.01*	0.14	*0.01*	0.16	*0.01*
Fe^{+3}	1.47	*0.01*	1.36	*0.01*	1.33	*0.02*	1.34	*0.02*	1.32	*0.02*	1.31	*0.02*	1.29	*0.02*
Fe^{+2}	1.06	*0.01*	1.06	*0.02*	1.07	*0.02*	1.04	*0.01*	1.05	*0.01*	1.06	*0.02*	1.06	*0.01*
Mn	0.03	*0.00*	0.02	*0.00*	0.02	*0.00*	0.03	*0.00*	0.03	*0.00*	0.03	*0.00*	0.03	*0.00*
Mg	0.12	*0.01*	0.17	*0.01*	0.17	*0.01*	0.19	*0.01*	0.18	*0.01*	0.18	*0.01*	0.19	*0.01*
Usp	0.21	*0.00*	0.25	*0.01*	0.27	*0.00*	0.26	*0.01*	0.27	*0.01*	0.27	*0.01*	0.28	*0.01*
n	*7*		*9*		*6*		*6*		*27*		*9*		*34*	

Sample#	T-23b		T-24		T-25		T-26		T-27		T-28		T-29	
Tm-group	2		1		1		2		3		3		3	
(wt%)	avg.	±S.D.	avg.	±S.D.	avg.	±S.D.	avg.	±S.D.	avg.	±S.D.	avg.	±S.D.	avg.	±S.D.
TiO_2	9.60	*0.24*	10.54	*0.34*	10.66	*0.30*	9.72	*0.43*	9.47	*0.71*	9.10	*0.43*	9.20	*0.25*
Al_2O_3	3.17	*0.11*	2.95	*0.26*	3.04	*0.26*	3.21	*0.33*	2.12	*0.44*	2.24	*0.37*	2.44	*0.19*
FeO_t	78.37	*2.82*	79.07	*2.70*	78.44	*2.81*	76.19	*0.85*	78.35	*0.97*	80.19	*2.05*	80.65	*2.32*
MnO	1.08	*0.13*	0.99	*0.18*	1.00	*0.22*	1.06	*0.14*	1.11	*0.14*	1.25	*0.18*	1.22	*0.13*
MgO	3.07	*0.15*	3.20	*0.32*	3.39	*0.31*	3.27	*0.25*	2.47	*0.38*	2.27	*0.33*	2.54	*0.26*
Al_2O_3+MgO	6.24	*0.18*	6.14	*0.54*	6.43	*0.51*	6.48	*0.54*	4.59	*0.77*	4.51	*0.61*	4.98	*0.34*
Total	95.56	*3.02*	97.16	*2.68*	96.85	*2.68*	93.82	*0.86*	93.90	*0.81*	95.34	*2.43*	96.51	*2.35*
Fe_2O_3	48.40	*2.04*	47.81	*2.22*	47.47	*2.05*	46.86	*0.97*	48.32	*1.46*	50.03	*1.85*	50.42	*1.74*
FeO	34.82	*0.99*	36.05	*1.06*	35.73	*1.10*	34.03	*0.58*	34.87	*1.05*	35.17	*0.85*	35.29	*0.98*
Total recal	100.26	*3.23*	101.85	*2.92*	101.43	*2.92*	98.42	*0.95*	98.63	*0.86*	100.23	*2.62*	101.42	*2.58*
Ti	0.26	*0.01*	0.29	*0.01*	0.29	*0.01*	0.27	*0.01*	0.27	*0.02*	0.25	*0.01*	0.25	*0.01*
Al	0.14	*0.01*	0.12	*0.01*	0.13	*0.01*	0.14	*0.01*	0.09	*0.02*	0.10	*0.01*	0.10	*0.01*
Fe^{+3}	1.33	*0.02*	1.29	*0.03*	1.29	*0.02*	1.31	*0.02*	1.36	*0.03*	1.39	*0.02*	1.38	*0.02*
Fe^{+2}	1.06	*0.01*	1.08	*0.02*	1.08	*0.02*	1.06	*0.02*	1.09	*0.04*	1.09	*0.03*	1.08	*0.02*
Mn	0.03	*0.00*	0.03	*0.01*	0.03	*0.01*	0.03	*0.00*	0.04	*0.00*	0.04	*0.01*	0.04	*0.00*
Mg	0.17	*0.01*	0.17	*0.02*	0.18	*0.02*	0.18	*0.01*	0.14	*0.02*	0.12	*0.02*	0.14	*0.01*
Usp	0.27	*0.01*	0.29	*0.02*	0.29	*0.01*	0.27	*0.01*	0.27	*0.02*	0.25	*0.01*	0.25	*0.01*
n	*12*		*19*		*9*		*18*		*12*		*17*		*15*	

Appendix 2 *(continued)*

Sample#	T-30		T-35		T-36		T-37		T-38		T-39		T-40	
Tm-group	2		1		1		1		1		1		1	
(wt%)	avg.	±S.D.	avg.	±S.D.	avg.	±S.D.	avg.	±S.D.	avg.	±S.D.	avg.	±S.D.	avg.	±S.D.
TiO_2	9.48	*0.27*	10.26	*0.32*	9.96	*0.26*	9.99	*0.25*	9.98	*0.35*	10.05	*0.35*	9.88	*0.17*
Al_2O_3	3.26	*0.10*	3.84	*0.16*	3.96	*0.17*	3.89	*0.18*	3.99	*0.16*	4.06	*0.13*	4.04	*0.11*
FeO_t	76.44	*0.95*	75.74	*0.40*	75.54	*0.39*	75.28	*0.27*	75.05	*0.41*	75.00	*0.53*	74.84	*0.60*
MnO	1.00	*0.13*	0.71	*0.10*	0.79	*0.13*	0.85	*0.09*	0.71	*0.08*	0.85	*0.09*	0.78	*0.08*
MgO	3.18	*0.11*	3.42	*0.34*	3.17	*0.40*	3.32	*0.07*	3.43	*0.12*	3.26	*0.27*	3.57	*0.09*
Al_2O_3+MgO	6.44	*0.19*	7.26	*0.43*	7.13	*0.46*	7.21	*0.21*	7.41	*0.21*	7.32	*0.33*	7.61	*0.12*
Total	93.76	*1.07*	94.47	*0.58*	93.84	*0.33*	93.64	*0.35*	93.57	*0.44*	93.65	*0.53*	93.46	*0.59*
Fe_2O_3	47.25	*0.60*	45.33	*0.74*	45.36	*0.55*	45.28	*0.42*	45.17	*0.72*	44.88	*0.68*	45.42	*0.47*
FeO	33.92	*0.56*	34.95	*0.72*	34.72	*0.77*	34.54	*0.27*	34.41	*0.51*	34.61	*0.66*	33.97	*0.26*
Total recal	98.09	*1.21*	98.87	*0.47*	98.15	*0.41*	98.02	*0.48*	97.95	*0.45*	97.96	*0.43*	97.86	*0.59*
Ti	0.27	*0.01*	0.28	*0.01*	0.28	*0.01*	0.28	*0.01*	0.28	*0.01*	0.28	*0.01*	0.28	*0.01*
Al	0.14	*0.00*	0.17	*0.01*	0.17	*0.01*	0.17	*0.01*	0.17	*0.01*	0.18	*0.01*	0.18	*0.00*
Fe^{+3}	1.33	*0.01*	1.25	*0.02*	1.27	*0.01*	1.26	*0.01*	1.26	*0.02*	1.25	*0.02*	1.27	*0.01*
Fe^{+2}	1.06	*0.01*	1.08	*0.02*	1.08	*0.03*	1.07	*0.01*	1.07	*0.01*	1.07	*0.02*	1.05	*0.00*
Mn	0.03	*0.00*	0.02	*0.00*	0.02	*0.00*	0.03	*0.00*	0.02	*0.00*	0.03	*0.00*	0.02	*0.00*
Mg	0.18	*0.01*	0.19	*0.02*	0.18	*0.02*	0.18	*0.00*	0.19	*0.01*	0.18	*0.01*	0.20	*0.01*
Usp	0.27	*0.01*	0.29	*0.01*	0.28	*0.01*	0.28	*0.01*	0.28	*0.01*	0.28	*0.01*	0.28	*0.00*
n	*12*		*8*		*9*		*6*		*9*		*8*		*7*	

Sample#	T-41		T-42		T-43		T-44		T-45		T-46		T-47	
Tm-group	1		1		1		1		1		1		1	
(wt%)	avg.	±S.D.	avg.	±S.D.	avg.	±S.D.	avg.	±S.D.	avg.	±S.D.	avg.	±S.D.	avg.	±S.D.
TiO_2	10.60	*0.68*	10.53	*0.60*	10.79	*0.56*	10.68	*0.32*	10.71	*0.25*	10.84	*0.34*	10.80	*0.17*
Al_2O_3	3.89	*0.53*	4.38	*0.44*	3.74	*0.34*	3.74	*0.18*	3.88	*0.15*	3.44	*0.11*	3.66	*0.09*
FeO_t	74.31	*1.39*	74.79	*0.48*	74.42	*0.51*	74.98	*0.67*	74.89	*0.59*	74.80	*0.47*	74.81	*0.65*
MnO	0.78	*0.09*	0.90	*0.15*	1.00	*0.06*	0.90	*0.06*	0.90	*0.08*	0.94	*0.08*	0.90	*0.11*
MgO	3.24	*0.62*	3.22	*0.29*	3.22	*0.37*	3.46	*0.23*	3.54	*0.17*	3.21	*0.21*	3.64	*0.13*
Al_2O_3+MgO	7.13	*0.65*	7.59	*0.49*	6.96	*0.56*	7.20	*0.27*	7.42	*0.30*	6.65	*0.23*	7.29	*0.17*
Total	93.48	*0.82*	94.32	*0.45*	93.63	*0.33*	94.20	*0.49*	94.37	*0.70*	93.59	*0.57*	94.30	*0.78*
Fe_2O_3	43.31	*2.61*	43.84	*0.99*	43.64	*1.01*	44.49	*1.15*	44.43	*0.89*	43.95	*0.60*	44.42	*0.66*
FeO	35.34	*1.21*	35.34	*0.78*	35.15	*0.97*	34.95	*0.48*	34.91	*0.40*	35.25	*0.61*	34.84	*0.36*
Total recal	97.62	*1.09*	98.50	*0.44*	97.83	*0.31*	98.48	*0.59*	98.65	*0.66*	97.82	*0.62*	98.54	*0.85*
Ti	0.30	*0.02*	0.29	*0.02*	0.30	*0.02*	0.30	*0.01*	0.30	*0.01*	0.30	*0.01*	0.30	*0.00*
Al	0.17	*0.02*	0.19	*0.02*	0.16	*0.01*	0.16	*0.01*	0.17	*0.01*	0.15	*0.00*	0.16	*0.00*
Fe^{+3}	1.21	*0.06*	1.22	*0.02*	1.22	*0.03*	1.24	*0.03*	1.23	*0.02*	1.23	*0.02*	1.23	*0.01*
Fe^{+2}	1.10	*0.05*	1.09	*0.03*	1.09	*0.03*	1.08	*0.02*	1.07	*0.02*	1.10	*0.02*	1.07	*0.01*
Mn	0.02	*0.00*	0.03	*0.00*	0.03	*0.00*	0.03	*0.00*	0.03	*0.00*	0.03	*0.00*	0.03	*0.00*
Mg	0.18	*0.03*	0.18	*0.02*	0.18	*0.02*	0.19	*0.01*	0.19	*0.01*	0.18	*0.01*	0.20	*0.01*
Usp	0.31	*0.04*	0.30	*0.02*	0.31	*0.02*	0.30	*0.01*	0.30	*0.01*	0.31	*0.01*	0.30	*0.01*
n	*8*		*6*		*6*		*7*		*9*		*17*		*8*	

Sample#	T-48		T-50		T-51		T-52		T-53		T-54		T-55	
Tm-group	1		1		1		1		1		1		1	
(wt%)	avg.	±S.D.	avg.	±S.D.	avg.	±S.D.	avg.	±S.D.	avg.	±S.D.	avg.	±S.D.	avg.	±S.D.
TiO_2	10.29	*0.36*	10.86	*0.53*	11.37	*0.31*	10.77	*0.29*	10.29	*0.23*	10.37	*0.30*	10.09	*0.26*
Al_2O_3	3.86	*0.12*	3.89	*0.30*	3.56	*0.17*	3.82	*0.21*	3.87	*0.17*	3.77	*0.13*	3.79	*0.17*
FeO_t	74.75	*0.32*	74.25	*0.42*	74.24	*0.70*	74.58	*0.57*	75.73	*0.38*	75.49	*0.82*	75.56	*0.84*
MnO	0.96	*0.12*	0.90	*0.12*	0.91	*0.08*	0.95	*0.09*	0.88	*0.07*	0.94	*0.17*	0.87	*0.17*
MgO	3.64	*0.20*	3.55	*0.23*	3.46	*0.14*	3.68	*0.36*	3.43	*0.20*	3.47	*0.18*	3.45	*0.19*
Al_2O_3+MgO	7.50	*0.31*	7.43	*0.47*	7.02	*0.25*	7.50	*0.48*	7.31	*0.31*	7.24	*0.29*	7.24	*0.32*
Total	93.77	*0.17*	93.86	*0.40*	93.97	*0.51*	94.21	*0.58*	94.51	*0.37*	94.57	*0.76*	94.12	*0.71*
Fe_2O_3	45.09	*0.60*	43.73	*0.78*	43.13	*0.90*	44.33	*0.74*	45.49	*0.45*	45.30	*0.80*	45.66	*0.68*
FeO	34.18	*0.55*	34.91	*0.78*	35.42	*0.27*	34.69	*0.75*	34.80	*0.45*	34.73	*0.29*	34.48	*0.49*
Total recal	98.20	*0.20*	98.11	*0.45*	98.12	*0.58*	98.48	*0.61*	98.89	*0.38*	98.92	*0.78*	98.55	*0.79*
Ti	0.29	*0.01*	0.30	*0.01*	0.32	*0.01*	0.30	*0.01*	0.28	*0.01*	0.29	*0.01*	0.28	*0.01*
Al	0.17	*0.01*	0.17	*0.01*	0.16	*0.01*	0.17	*0.01*	0.17	*0.01*	0.16	*0.01*	0.16	*0.01*
Fe^{+3}	1.25	*0.02*	1.22	*0.02*	1.20	*0.02*	1.23	*0.02*	1.26	*0.01*	1.25	*0.02*	1.27	*0.01*
Fe^{+2}	1.06	*0.02*	1.08	*0.03*	1.10	*0.01*	1.07	*0.03*	1.07	*0.01*	1.07	*0.01*	1.06	*0.01*
Mn	0.03	*0.00*	0.03	*0.00*	0.03	*0.00*	0.03	*0.00*	0.03	*0.00*	0.03	*0.01*	0.03	*0.01*
Mg	0.20	*0.01*	0.20	*0.01*	0.19	*0.01*	0.20	*0.02*	0.19	*0.01*	0.19	*0.01*	0.19	*0.01*
Usp	0.29	*0.01*	0.30	*0.01*	0.32	*0.01*	0.30	*0.01*	0.29	*0.01*	0.29	*0.01*	0.28	*0.01*
n	*9*		*9*		*16*		*15*		*9*		*7*		*9*	

Appendix 2 *(continued)*

Sample#	T-56		T-57		T-58		T-59		T-60		T-61		T-62	
Tm-group	1		1		1		1		1		1		1	
(wt%)	avg.	±S.D.	avg.	±S.D.	avg.	±S.D.	avg.	±S.D.	avg.	±S.D.	avg.	±S.D.	avg.	±S.D.
TiO_2	10.94	*0.15*	10.94	*0.65*	9.98	*0.45*	10.19	*0.16*	10.49	*0.16*	10.82	*0.87*	11.09	*0.20*
Al_2O_3	3.49	*0.14*	3.91	*0.30*	4.06	*0.30*	3.77	*0.13*	4.00	*0.17*	3.61	*0.44*	3.72	*0.10*
FeO_t	74.65	*0.42*	75.03	*0.26*	75.82	*0.56*	75.56	*0.43*	75.07	*0.56*	74.97	*0.88*	74.83	*0.36*
MnO	0.84	*0.12*	0.86	*0.10*	0.94	*0.16*	1.03	*0.11*	0.87	*0.12*	0.96	*0.09*	0.89	*0.07*
MgO	3.46	*0.11*	3.57	*0.30*	3.46	*0.14*	3.38	*0.12*	3.81	*0.17*	3.46	*0.22*	3.55	*0.14*
Al_2O_3+MgO	6.95	*0.21*	7.48	*0.58*	7.52	*0.41*	7.15	*0.20*	7.80	*0.33*	7.07	*0.62*	7.27	*0.21*
Total	93.79	*0.46*	94.68	*0.52*	94.84	*0.53*	94.34	*0.50*	94.53	*0.83*	94.14	*0.63*	94.50	*0.42*
Fe_2O_3	43.95	*0.60*	44.19	*0.99*	45.93	*0.76*	45.52	*0.42*	45.12	*0.72*	44.39	*1.54*	44.08	*0.48*
FeO	35.09	*0.23*	35.27	*1.00*	34.49	*0.38*	34.60	*0.28*	34.47	*0.16*	35.03	*0.83*	35.17	*0.33*
Total recal	98.06	*0.47*	98.94	*0.34*	99.22	*0.54*	98.73	*0.50*	98.94	*0.84*	98.50	*0.73*	98.74	*0.38*
Ti	0.31	*0.01*	0.30	*0.02*	0.27	*0.01*	0.28	*0.01*	0.29	*0.00*	0.30	*0.03*	0.31	*0.01*
Al	0.15	*0.01*	0.17	*0.01*	0.17	*0.01*	0.16	*0.01*	0.17	*0.01*	0.16	*0.02*	0.16	*0.00*
Fe^{+3}	1.23	*0.01*	1.22	*0.02*	1.27	*0.02*	1.26	*0.01*	1.24	*0.02*	1.23	*0.04*	1.22	*0.01*
Fe^{+2}	1.09	*0.01*	1.08	*0.03*	1.06	*0.01*	1.07	*0.01*	1.06	*0.01*	1.08	*0.03*	1.08	*0.01*
Mn	0.03	*0.00*	0.03	*0.00*	0.03	*0.01*	0.03	*0.00*	0.03	*0.00*	0.03	*0.00*	0.03	*0.00*
Mg	0.19	*0.01*	0.19	*0.02*	0.19	*0.01*	0.19	*0.01*	0.21	*0.01*	0.19	*0.01*	0.19	*0.01*
Usp	0.31	*0.00*	0.30	*0.02*	0.28	*0.01*	0.29	*0.00*	0.29	*0.01*	0.30	*0.03*	0.31	*0.01*
n	*6*		*8*		*7*		*10*		*6*		*9*		*9*	

Sample#	T-63		T-64		Ri-2		Ri-2b		Ri-4		Ri-6		Ri-10	
Tm-group	1		1		12		11		12		12		6	
(wt%)	avg.	±S.D.	avg.	±S.D.	avg.	±S.D.	avg.	±S.D.	avg.	±S.D.	avg.	±S.D.	avg.	±S.D.
TiO_2	10.65	*0.50*	10.18	*0.16*	6.41	*0.16*	6.76	*0.60*	6.39	*0.18*	6.26	*0.30*	8.37	*0.41*
Al_2O_3	3.81	*0.13*	3.74	*0.12*	2.79	*0.16*	5.08	*0.21*	2.30	*0.42*	2.70	*0.11*	3.79	*0.16*
FeO_t	74.88	*0.35*	75.52	*0.22*	82.10	*0.34*	78.86	*0.90*	82.08	*1.64*	82.39	*0.30*	78.49	*0.72*
MnO	0.85	*0.15*	0.92	*0.12*	1.12	*0.18*	0.76	*0.10*	1.23	*0.17*	1.17	*0.13*	0.97	*0.15*
MgO	3.54	*0.13*	3.45	*0.09*	2.16	*0.20*	3.39	*0.36*	1.75	*0.36*	2.26	*0.17*	3.86	*0.15*
Al_2O_3+MgO	7.35	*0.24*	7.20	*0.14*	4.95	*0.21*	8.47	*0.30*	4.05	*0.66*	4.96	*0.14*	7.65	*0.21*
Total	94.04	*0.38*	94.10	*0.27*	95.02	*0.48*	95.54	*0.52*	94.85	*0.69*	95.44	*0.31*	95.97	*0.78*
Fe_2O_3	44.52	*0.88*	45.59	*0.24*	54.27	*0.25*	51.52	*1.15*	54.40	*1.02*	54.98	*0.67*	50.84	*0.81*
FeO	34.82	*0.61*	34.49	*0.19*	33.26	*0.25*	32.50	*0.42*	33.14	*1.06*	32.92	*0.42*	32.74	*0.60*
Total recal	98.36	*0.40*	98.53	*0.25*	100.39	*0.49*	100.53	*0.62*	99.86	*1.17*	100.76	*0.32*	100.90	*0.77*
Ti	0.30	*0.01*	0.28	*0.00*	0.18	*0.00*	0.18	*0.02*	0.18	*0.01*	0.17	*0.01*	0.23	*0.01*
Al	0.17	*0.01*	0.16	*0.00*	0.12	*0.01*	0.22	*0.01*	0.10	*0.02*	0.12	*0.00*	0.16	*0.01*
Fe^{+3}	1.24	*0.02*	1.27	*0.01*	1.51	*0.01*	1.40	*0.03*	1.53	*0.02*	1.52	*0.02*	1.38	*0.02*
Fe^{+2}	1.07	*0.02*	1.06	*0.00*	1.03	*0.01*	0.98	*0.02*	1.03	*0.03*	1.01	*0.02*	0.99	*0.02*
Mn	0.03	*0.00*	0.03	*0.00*	0.03	*0.01*	0.02	*0.00*	0.04	*0.01*	0.04	*0.00*	0.03	*0.00*
Mg	0.19	*0.01*	0.19	*0.01*	0.12	*0.01*	0.18	*0.02*	0.10	*0.02*	0.12	*0.01*	0.21	*0.01*
Usp	0.30	*0.01*	0.28	*0.00*	0.18	*0.00*	0.19	*0.02*	0.18	*0.01*	0.18	*0.01*	0.23	*0.01*
n	*8*		*9*		*5*		*4*		*7*		*7*		*15*	

Sample#	Ri-20		Ri-22		Ri-23		Ri-24		Ri-25		Ri-26		Ri-27	
Tm-group	12		12		12		11		11		11		11	
(wt%)	avg.	±S.D.	avg.	±S.D.	avg.	±S.D.	avg.	±S.D.	avg.	±S.D.	avg.	±S.D.	avg.	±S.D.
TiO_2	6.89	*0.38*	6.48	*0.20*	6.47	*0.15*	7.05	*0.87*	7.11	*0.17*	7.11	*0.43*	6.91	*0.37*
Al_2O_3	3.10	*0.30*	3.22	*0.43*	2.57	*0.33*	5.29	*0.96*	5.59	*0.20*	5.28	*0.43*	5.41	*0.34*
FeO_t	81.37	*0.76*	81.57	*0.89*	82.51	*0.61*	79.47	*1.77*	78.42	*0.45*	78.67	*0.74*	78.33	*1.25*
MnO	1.12	*0.13*	1.01	*0.17*	1.20	*0.20*	0.71	*0.18*	0.69	*0.12*	0.72	*0.17*	0.66	*0.08*
MgO	2.47	*0.26*	2.64	*0.65*	2.19	*0.39*	3.77	*0.77*	3.48	*0.25*	3.68	*0.42*	3.92	*0.14*
Al_2O_3+MgO	5.57	*0.40*	5.86	*1.02*	4.75	*0.71*	9.06	*1.60*	9.07	*0.08*	8.96	*0.46*	9.33	*0.31*
Total	95.34	*0.42*	95.44	*0.55*	95.50	*0.24*	96.72	*1.42*	95.67	*0.63*	95.98	*0.24*	95.75	*0.99*
Fe_2O_3	53.47	*1.04*	54.12	*0.68*	54.71	*0.45*	52.08	*1.98*	50.68	*0.32*	51.27	*0.84*	51.40	*1.27*
FeO	33.26	*0.59*	32.87	*0.92*	33.28	*0.37*	32.60	*1.35*	32.82	*0.36*	32.54	*0.48*	32.08	*0.39*
Total recal	100.60	*0.43*	100.73	*0.54*	100.84	*0.19*	101.87	*1.59*	100.67	*0.65*	101.00	*0.24*	100.74	*0.99*
Ti	0.19	*0.01*	0.18	*0.01*	0.18	*0.00*	0.19	*0.03*	0.19	*0.00*	0.19	*0.01*	0.19	*0.01*
Al	0.13	*0.01*	0.14	*0.02*	0.11	*0.01*	0.22	*0.04*	0.24	*0.01*	0.22	*0.02*	0.23	*0.01*
Fe^{+3}	1.48	*0.03*	1.49	*0.02*	1.51	*0.02*	1.39	*0.04*	1.37	*0.01*	1.38	*0.03*	1.38	*0.03*
Fe^{+2}	1.02	*0.02*	1.01	*0.04*	1.02	*0.02*	0.97	*0.05*	0.99	*0.01*	0.97	*0.02*	0.96	*0.01*
Mn	0.03	*0.00*	0.03	*0.01*	0.04	*0.01*	0.02	*0.01*	0.02	*0.00*	0.02	*0.01*	0.02	*0.00*
Mg	0.14	*0.01*	0.14	*0.03*	0.12	*0.02*	0.20	*0.04*	0.19	*0.01*	0.20	*0.02*	0.21	*0.01*
Usp	0.19	*0.01*	0.18	*0.01*	0.18	*0.00*	0.19	*0.03*	0.19	*0.01*	0.20	*0.01*	0.19	*0.01*
n	*7*		*7*		*9*		*19*		*9*		*9*		*6*	

Appendix 2 *(continued)*

Sample#	Ri-29		Ri-30		Ri-34		Ri-40		Ri-47		Ri-50		Ri-51	
Tm-group	11		11		10		10		10		8		9	
(wt%)	avg.	±S.D.	avg.	±S.D.	avg.	±S.D.	avg.	±S.D.	avg.	±S.D.	avg.	±S.D.	avg.	±S.D.
TiO_2	6.44	*0.47*	6.82	*0.65*	7.30	*0.34*	7.40	*0.15*	7.40	*0.33*	8.05	*0.24*	7.83	*0.22*
Al_2O_3	4.87	*1.14*	4.98	*1.09*	1.57	*0.25*	1.89	*0.18*	2.07	*0.10*	2.71	*0.14*	2.35	*0.23*
FeO_t	80.02	*1.17*	79.54	*1.23*	82.80	*0.49*	82.43	*0.34*	82.48	*0.38*	80.72	*0.68*	81.40	*0.94*
MnO	0.83	*0.25*	0.74	*0.17*	2.04	*0.29*	1.82	*0.14*	1.53	*0.16*	1.33	*0.07*	1.37	*0.11*
MgO	3.31	*0.57*	3.16	*0.47*	1.39	*0.24*	1.65	*0.09*	1.74	*0.21*	2.53	*0.22*	2.09	*0.24*
Al_2O_3+MgO	8.18	*1.61*	8.13	*1.44*	2.96	*0.45*	3.54	*0.17*	3.81	*0.17*	5.24	*0.32*	4.44	*0.41*
Total	96.08	*0.40*	95.75	*0.80*	95.63	*0.56*	95.75	*0.45*	95.67	*0.57*	95.88	*0.46*	95.96	*0.68*
Fe_2O_3	52.97	*0.79*	51.72	*1.47*	54.04	*0.88*	53.58	*0.51*	53.41	*0.58*	51.75	*0.46*	52.40	*0.46*
FeO	32.36	*0.68*	33.00	*0.99*	34.17	*0.49*	34.21	*0.45*	34.42	*0.45*	34.16	*0.38*	34.25	*0.73*
Total recal	101.23	*0.37*	100.81	*0.74*	100.90	*0.57*	100.98	*0.42*	100.93	*0.57*	100.88	*0.50*	100.86	*0.67*
Ti	0.17	*0.01*	0.19	*0.02*	0.20	*0.01*	0.21	*0.00*	0.21	*0.01*	0.22	*0.01*	0.22	*0.01*
Al	0.21	*0.05*	0.21	*0.04*	0.07	*0.01*	0.08	*0.01*	0.09	*0.00*	0.12	*0.01*	0.10	*0.01*
Fe^{+3}	1.43	*0.03*	1.40	*0.05*	1.51	*0.03*	1.49	*0.02*	1.49	*0.02*	1.43	*0.01*	1.45	*0.01*
Fe^{+2}	0.97	*0.03*	1.00	*0.03*	1.06	*0.02*	1.06	*0.01*	1.06	*0.01*	1.05	*0.01*	1.05	*0.02*
Mn	0.03	*0.01*	0.02	*0.01*	0.06	*0.01*	0.06	*0.00*	0.05	*0.00*	0.04	*0.00*	0.04	*0.00*
Mg	0.18	*0.03*	0.17	*0.02*	0.08	*0.01*	0.09	*0.01*	0.10	*0.01*	0.14	*0.01*	0.11	*0.01*
Usp	0.18	*0.01*	0.19	*0.02*	0.21	*0.01*	0.21	*0.01*	0.21	*0.01*	0.23	*0.00*	0.22	*0.01*
n	*10*		*20*		*8*		*9*		*9*		*7*		*10*	

Sample#	Ri-58		Ri-60		Ri-65		Ri-70		Ri-74		Ri-84		Ri-88	
Tm-group	8		8		variable		9		8		3		3	
(wt%)	avg.	±S.D.	avg.	±S.D.	avg.	±S.D.	avg.	±S.D.	avg.	±S.D.	avg.	±S.D.	avg.	±S.D.
TiO_2	7.99	*0.14*	7.93	*0.18*	8.20	*0.50*	8.09	*0.14*	8.14	*0.14*	9.65	*0.23*	9.67	*0.22*
Al_2O_3	2.68	*0.07*	2.77	*0.11*	1.78	*0.26*	2.36	*0.15*	2.55	*0.11*	2.67	*0.18*	2.34	*0.13*
FeO_t	80.80	*0.57*	81.04	*0.26*	82.24	*0.56*	81.37	*0.39*	80.78	*0.41*	79.52	*0.48*	80.34	*0.61*
MnO	1.34	*0.10*	1.32	*0.14*	1.47	*0.14*	1.29	*0.10*	1.45	*0.14*	1.23	*0.11*	1.31	*0.11*
MgO	2.47	*0.12*	2.45	*0.11*	1.77	*0.14*	2.19	*0.12*	2.50	*0.19*	2.91	*0.13*	2.64	*0.14*
Al_2O_3+MgO	5.15	*0.12*	5.21	*0.19*	3.55	*0.32*	4.55	*0.22*	5.05	*0.27*	5.58	*0.24*	4.98	*0.22*
Total	96.08	*0.67*	96.09	*0.35*	95.94	*0.70*	95.58	*0.35*	95.71	*0.52*	96.27	*0.75*	96.76	*0.56*
Fe_2O_3	52.00	*0.41*	51.97	*0.46*	52.32	*0.73*	51.96	*0.51*	51.89	*0.44*	49.16	*0.59*	49.67	*0.40*
FeO	34.02	*0.69*	34.28	*0.28*	35.17	*0.63*	34.62	*0.22*	34.09	*0.38*	35.28	*0.42*	35.65	*0.53*
Total recal	100.96	*0.44*	101.14	*0.37*	101.05	*0.69*	100.72	*0.38*	100.84	*0.52*	101.19	*0.78*	101.61	*0.55*
Ti	0.22	*0.00*	0.22	*0.00*	0.23	*0.01*	0.22	*0.00*	0.22	*0.00*	0.26	*0.01*	0.26	*0.01*
Al	0.12	*0.00*	0.12	*0.00*	0.08	*0.01*	0.10	*0.01*	0.11	*0.00*	0.11	*0.01*	0.10	*0.01*
Fe^{+3}	1.43	*0.01*	1.43	*0.01*	1.45	*0.02*	1.44	*0.01*	1.43	*0.01*	1.34	*0.01*	1.36	*0.01*
Fe^{+2}	1.04	*0.02*	1.05	*0.01*	1.09	*0.02*	1.07	*0.01*	1.05	*0.01*	1.07	*0.01*	1.08	*0.01*
Mn	0.04	*0.00*	0.04	*0.00*	0.05	*0.00*	0.04	*0.00*	0.04	*0.00*	0.04	*0.00*	0.04	*0.00*
Mg	0.13	*0.01*	0.13	*0.01*	0.10	*0.01*	0.12	*0.01*	0.14	*0.01*	0.16	*0.01*	0.14	*0.01*
Usp	0.22	*0.00*	0.22	*0.01*	0.23	*0.01*	0.23	*0.01*	0.23	*0.00*	0.27	*0.01*	0.27	*0.01*
n	*10*		*10*		*8*		*8*		*10*		*7*		*10*	

Sample#	Ri-95		Ri-99		Ri-105		Ri-109		Ri-113		Ri-117		Ri-117b	
Tm-group	8		2		2		2		5		4		7	
(wt%)	avg.	±S.D.	avg.	±S.D.	avg.	±S.D.	avg.	±S.D.	avg.	±S.D.	avg.	±S.D.	avg.	±S.D.
TiO_2	8.44	*0.18*	10.12	*0.21*	9.91	*0.14*	9.59	*0.20*	8.85	*0.19*	8.72	*0.19*	8.14	*0.11*
Al_2O_3	2.68	*0.10*	2.79	*0.15*	2.97	*0.12*	3.47	*0.12*	3.00	*0.14*	3.52	*0.13*	3.17	*0.08*
FeO_t	80.60	*0.43*	79.36	*0.37*	79.04	*0.46*	78.92	*0.38*	81.31	*1.24*	79.24	*0.56*	80.35	*0.59*
MnO	1.27	*0.14*	1.14	*0.04*	1.09	*0.06*	1.03	*0.13*	1.06	*0.12*	1.07	*0.11*	1.13	*0.15*
MgO	2.68	*0.12*	2.98	*0.11*	3.16	*0.12*	3.40	*0.10*	3.01	*0.09*	3.34	*0.06*	2.77	*0.19*
Al_2O_3+MgO	5.36	*0.17*	5.77	*0.25*	6.13	*0.16*	6.87	*0.19*	6.01	*0.15*	6.86	*0.16*	5.95	*0.16*
Total	96.14	*0.51*	96.83	*0.54*	96.59	*0.56*	96.97	*0.48*	97.59	*1.31*	96.25	*0.90*	95.87	*0.98*
Fe_2O_3	51.47	*0.49*	48.45	*0.52*	48.59	*0.51*	48.89	*0.59*	51.55	*1.09*	50.31	*0.43*	51.34	*0.40*
FeO	34.29	*0.33*	35.76	*0.32*	35.32	*0.34*	34.92	*0.41*	34.93	*0.44*	33.97	*0.32*	34.16	*0.43*
Total recal	101.14	*0.52*	101.53	*0.54*	101.38	*0.61*	101.71	*0.53*	102.54	*1.28*	101.23	*0.86*	100.96	*1.02*
Ti	0.23	*0.00*	0.28	*0.01*	0.27	*0.00*	0.26	*0.01*	0.24	*0.00*	0.24	*0.00*	0.22	*0.00*
Al	0.12	*0.00*	0.12	*0.01*	0.13	*0.00*	0.15	*0.01*	0.13	*0.01*	0.15	*0.01*	0.14	*0.00*
Fe^{+3}	1.41	*0.01*	1.32	*0.01*	1.32	*0.01*	1.32	*0.01*	1.39	*0.02*	1.37	*0.01*	1.41	*0.01*
Fe^{+2}	1.05	*0.01*	1.08	*0.01*	1.07	*0.01*	1.05	*0.01*	1.05	*0.01*	1.03	*0.01*	1.04	*0.01*
Mn	0.04	*0.00*	0.04	*0.00*	0.03	*0.00*	0.03	*0.00*	0.03	*0.00*	0.03	*0.00*	0.03	*0.00*
Mg	0.15	*0.01*	0.16	*0.01*	0.17	*0.01*	0.18	*0.01*	0.16	*0.00*	0.18	*0.00*	0.15	*0.01*
Usp	0.23	*0.01*	0.28	*0.01*	0.27	*0.01*	0.26	*0.01*	0.24	*0.01*	0.24	*0.01*	0.23	*0.00*
n	*9*		*7*		*8*		*9*		*10*		*9*		*5*	

Appendix 2 *(continued)*

Sample#	Ri-118		Ri-118b		Ri-121		Ri-123		Ri-130		Ri-132	
Tm-group	7		4		2		2		8		2	
(wt%)	avg.	*±S.D.*	avg.	*±S.D.*	avg.	*±S.D.*	avg.	*±S.D.*	avg.	*±S.D.*	avg.	*±S.D.*
TiO_2	7.98	*0.19*	8.79	*0.12*	10.12	*0.15*	10.17	*0.30*	7.95	*0.30*	9.82	*0.24*
Al_2O_3	3.09	*0.14*	3.46	*0.07*	2.98	*0.25*	3.07	*0.29*	2.76	*0.29*	3.23	*0.14*
FeO_t	80.89	*0.25*	79.62	*0.45*	80.12	*1.11*	79.25	*1.12*	81.72	*0.36*	78.93	*0.50*
MnO	1.14	*0.14*	1.03	*0.05*	1.01	*0.09*	1.06	*0.12*	1.14	*0.12*	1.05	*0.09*
MgO	2.84	*0.13*	3.14	*0.06*	3.21	*0.24*	3.42	*0.17*	2.25	*0.12*	3.26	*0.19*
Al_2O_3+MgO	5.93	*0.17*	6.61	*0.08*	6.20	*0.37*	6.49	*0.43*	5.00	*0.31*	6.49	*0.28*
Total	96.36	*0.25*	96.71	*0.63*	97.90	*1.22*	97.54	*1.11*	96.27	*0.33*	96.75	*0.57*
Fe_2O_3	52.13	*0.55*	50.11	*0.32*	49.21	*1.26*	48.85	*1.05*	52.17	*0.51*	48.58	*0.49*
FeO	33.98	*0.42*	34.53	*0.17*	35.84	*0.37*	35.29	*0.64*	34.79	*0.30*	35.22	*0.33*
Total recal	101.50	*0.31*	101.48	*0.59*	102.69	*1.35*	102.22	*1.17*	101.35	*0.39*	101.48	*0.53*
Ti	0.22	*0.00*	0.24	*0.00*	0.27	*0.01*	0.27	*0.01*	0.22	*0.01*	0.27	*0.01*
Al	0.13	*0.01*	0.15	*0.00*	0.13	*0.01*	0.13	*0.01*	0.12	*0.01*	0.14	*0.01*
Fe^{+3}	1.42	*0.01*	1.36	*0.00*	1.32	*0.02*	1.32	*0.02*	1.43	*0.01*	1.32	*0.01*
Fe^{+2}	1.03	*0.01*	1.04	*0.00*	1.07	*0.02*	1.06	*0.02*	1.06	*0.01*	1.06	*0.01*
Mn	0.03	*0.00*	0.03	*0.00*	0.03	*0.00*	0.03	*0.00*	0.04	*0.00*	0.03	*0.00*
Mg	0.15	*0.01*	0.17	*0.00*	0.17	*0.01*	0.18	*0.01*	0.12	*0.01*	0.18	*0.01*
Usp	0.22	*0.00*	0.24	*0.00*	0.27	*0.01*	0.28	*0.01*	0.22	*0.01*	0.27	*0.01*
n	*7*		*3*		*15*		*18*		*18*		*8*	

Note: Titanomagnetite compositions of individual groups are given as average (avg.) with 1 standard deviation (±S.D.), based on n (number of analyses per tephra).
Tephra layers denoted with 'b' are bimodal (refer to Chapter 3).
FeO, Fe_2O_3, cation proportions and Usp (mole fraction ulvöspinel) calculated as in Carmichael (1966). The complete compositional datasheet is available within the electronic appendices.

Appendix 3 *Electron microprobe-determined glass shard compositions of tephra layers from lake and peatland cores recovered during this study. Refer also to Figure 3.7.*

Tephra nb#	Ri-10		Ri-20		Ri-22		Ri-24		Ri-26		Ri-30		Ri-34	
(wt%)	avg.	±S.D.	avg.	±S.D.	avg.	±S.D.	avg.	±S.D.	avg.	±S.D.	avg.	±S.D.	avg.	±S.D.
SiO_2	62.83	*0.75*	65.46	*1.64*	67.10	*1.26*	57.73	*2.29*	59.05	*1.16*	55.51	*2.61*	72.58	*0.88*
Al_2O_3	16.61	*0.51*	16.36	*0.65*	16.29	*1.16*	16.17	*0.51*	15.68	*0.89*	13.63	*1.63*	14.19	*0.50*
TiO_2	0.92	*0.10*	0.62	*0.12*	0.56	*0.13*	1.22	*0.24*	1.00	*0.14*	1.10	*0.18*	0.45	*0.07*
FeO_{total}	4.31	*0.42*	3.54	*0.81*	2.89	*0.62*	7.05	*1.47*	6.44	*0.81*	7.12	*1.11*	1.36	*0.21*
MnO	0.15	*0.13*	0.18	*0.09*	0.14	*0.07*	0.30	*0.14*	0.30	*0.09*	0.37	*0.10*	0.09	*0.15*
MgO	1.64	*0.49*	1.33	*1.21*	0.80	*0.47*	2.53	*1.11*	2.95	*0.81*	5.77	*1.81*	0.21	*0.15*
CaO	3.03	*0.42*	2.70	*0.57*	2.22	*0.51*	4.89	*0.55*	5.27	*0.66*	9.63	*3.49*	0.92	*0.38*
Na_2O	4.84	*0.17*	4.73	*0.33*	4.67	*0.36*	4.62	*0.27*	4.59	*0.31*	3.43	*0.71*	4.39	*0.36*
K_2O	5.15	*0.31*	4.65	*0.48*	4.89	*0.52*	4.42	*0.48*	3.86	*0.50*	2.79	*0.90*	5.56	*0.41*
Cl	0.34	*0.06*	0.30	*0.09*	0.24	*0.16*	0.38	*0.16*	0.33	*0.07*	0.25	*0.11*	0.29	*0.12*
Anal diff [a]	0.17	*0.15*	0.13	*0.16*	0.20	*0.11*	0.70	*0.20*	0.53	*0.12*	0.40	*0.21*	-0.04	*0.15*
Total (anal)	97.83		98.94		98.21		99.36		99.13		99.55		98.34	
n	*9*		*19*		*9*		*8*		*9*		*9*		*8*	

Tephra nb#	Ri-40		Ri-47		Stent		Ri-51		Ri-58		Ri-60		Ri-70	
(wt%)	avg.	±S.D.	avg.	±S.D.	avg.	±S.D.	avg.	±S.D.	avg.	±S.D.	avg.	±S.D.	avg.	±S.D.
SiO_2	70.98	*0.95*	69.50	*0.51*	75.89	*0.28*	67.84	*0.59*	67.39	*0.36*	67.07	*0.29*	69.33	*0.38*
Al_2O_3	14.53	*0.49*	15.47	*0.19*	13.04	*0.11*	16.01	*0.22*	16.15	*0.13*	16.23	*0.13*	15.54	*0.18*
TiO_2	0.48	*0.12*	0.50	*0.11*	0.22	*0.05*	0.55	*0.04*	0.57	*0.05*	0.60	*0.08*	0.55	*0.09*
FeO_{total}	2.33	*0.29*	2.15	*0.27*	1.77	*0.09*	2.70	*0.23*	2.69	*0.08*	2.77	*0.41*	2.21	*0.22*
MnO	0.12	*0.12*	0.13	*0.10*	0.07	*0.06*	0.20	*0.08*	0.20	*0.09*	0.19	*0.10*	0.13	*0.04*
MgO	0.36	*0.14*	0.50	*0.10*	0.18	*0.05*	0.77	*0.04*	0.73	*0.05*	0.72	*0.07*	0.52	*0.09*
CaO	1.44	*0.42*	2.07	*0.20*	1.31	*0.06*	2.54	*0.14*	2.41	*0.10*	2.30	*0.08*	1.95	*0.08*
Na_2O	4.39	*0.32*	4.81	*0.14*	4.30	*0.06*	4.78	*0.14*	4.98	*0.17*	5.00	*0.08*	4.49	*0.09*
K_2O	4.97	*0.44*	4.55	*0.10*	2.97	*0.03*	4.34	*0.07*	4.49	*0.07*	4.64	*0.07*	4.98	*0.08*
Cl	0.29	*0.07*	0.36	*0.05*	0.23	*0.03*	0.41	*0.04*	0.41	*0.04*	0.40	*0.04*	0.36	*0.05*
Anal diff [a]	0.12	*0.20*	-0.04	*0.11*	*0.01*	*0.18*	-0.12	*0.12*	-0.02	*0.13*	0.07	*0.30*	-0.07	*0.17*
Total (anal)	98.62		96.29		102.30		97.65		98.40		98.39		98.50	
n	*11*		*10*		*10*		*5*		*6*		*8*		*10*	

Tephra nb#	Ri-84		Ri-95		Ri-109		Ri-121		Ri-123		Ri-132		T-2	
(wt%)	avg.	±S.D.	avg.	±S.D.	avg.	±S.D.	avg.	±S.D.	avg.	±S.D.	avg.	±S.D.	avg.	±S.D.
SiO_2	67.80	*0.82*	68.30	*0.32*	64.56	*0.40*	65.68	*1.99*	64.53	*1.41*	71.58	*0.61*	63.97	*0.60*
Al_2O_3	15.65	*0.30*	15.52	*0.13*	16.31	*0.37*	16.46	*0.82*	15.78	*0.84*	14.67	*0.68*	16.66	*0.83*
TiO_2	0.75	*0.07*	0.59	*0.06*	0.83	*0.08*	0.75	*0.18*	0.92	*0.13*	0.51	*0.06*	0.76	*0.07*
FeO_{total}	2.70	*0.39*	2.99	*0.30*	4.16	*0.15*	3.41	*1.05*	4.60	*0.80*	2.04	*0.20*	3.90	*0.66*
MnO	0.15	*0.06*	0.14	*0.10*	0.22	*0.07*	0.15	*0.12*	0.17	*0.11*	0.10	*0.12*	0.20	*0.07*
MgO	0.73	*0.13*	0.61	*0.05*	1.31	*0.07*	0.75	*0.43*	1.04	*0.25*	0.43	*0.11*	1.48	*0.80*
CaO	2.03	*0.30*	1.89	*0.10*	2.85	*0.25*	2.26	*0.66*	2.03	*0.72*	1.95	*0.35*	3.22	*0.28*
Na_2O	4.65	*0.15*	4.74	*0.11*	4.97	*0.14*	4.86	*0.55*	4.87	*0.49*	4.68	*0.21*	4.70	*0.27*
K_2O	5.11	*0.13*	4.66	*0.13*	4.33	*0.21*	5.14	*0.59*	5.33	*0.57*	3.75	*0.20*	4.41	*0.17*
Cl	0.32	*0.06*	0.40	*0.06*	0.33	*0.06*	0.19	*0.24*	0.37	*0.04*	0.35	*0.07*	0.32	*0.07*
Anal diff [a]	0.10	*0.14*	0.16	*0.12*	0.15	*0.17*	0.26	*0.32*	0.36	*0.16*	-0.09	*0.22*	0.38	*0.17*
Total (anal)	99.11		99.18		98.99		99.00		99.17		95.52		97.62	
n	*10*		*9*		*5*		*10*		10		*5*		*9*	

Tephra nb#	T-4		T-8		T-9		T-10		T-14		T-15		T-16	
(wt%)	avg.	±S.D.	avg.	±S.D.	avg.	±S.D.	avg.	±S.D.	avg.	±S.D.	avg.	±S.D.	avg.	±S.D.
SiO_2	55.06	*2.93*	65.34	*1.13*	58.04	*2.26*	56.88	*0.94*	71.19	*0.97*	70.86	*1.12*	68.21	*0.53*
Al_2O_3	16.77	*1.30*	16.87	*0.54*	16.74	*1.11*	16.32	*0.97*	15.57	*0.91*	15.14	*0.97*	15.43	*0.40*
TiO_2	1.01	*0.30*	0.56	*0.11*	1.05	*0.26*	1.10	*0.10*	0.40	*0.05*	0.48	*0.10*	0.63	*0.09*
FeO_{total}	6.51	*2.10*	3.19	*0.62*	7.13	*2.91*	7.39	*0.74*	1.47	*0.32*	1.77	*0.82*	3.24	*0.77*
MnO	0.32	*0.11*	0.17	*0.11*	0.32	*0.12*	0.31	*0.08*	0.11	*0.10*	0.13	*0.16*	0.07	*0.08*
MgO	3.76	*1.39*	1.06	*0.32*	2.12	*0.45*	3.18	*0.90*	0.28	*0.18*	0.47	*0.42*	0.45	*0.09*
CaO	9.16	*2.64*	3.03	*0.47*	5.06	*0.41*	5.89	*0.86*	1.59	*0.53*	1.64	*0.53*	1.61	*0.24*
Na_2O	3.93	*0.75*	4.70	*0.14*	4.87	*0.30*	4.43	*0.24*	4.79	*0.43*	4.56	*0.40*	5.59	*0.19*
K_2O	2.52	*0.68*	4.47	*0.33*	3.63	*0.34*	3.40	*0.40*	4.69	*0.56*	4.94	*0.39*	4.22	*0.08*
Cl	0.25	*0.06*	0.36	*0.05*	0.38	*0.10*	0.34	*0.09*	0.19	*0.13*	0.22	*0.10*	0.32	*0.05*
Anal diff [a]	0.72	*0.44*	0.25	*0.10*	0.67	*0.08*	0.75	*0.19*	-0.27	*0.24*	-0.21	*0.57*	0.23	*0.10*
Total (anal)	98.06		95.17		97.49		98.80		97.87		98.18		100.25	
n	*7*		*8*		*10*		*9*		*15*		*9*		*5*	

Appendix 3 *(continued)*

Tephra nb#	T-17		T-21		T-23		T-24		T-26		T-27		T-28	
(wt%)	avg.	±S.D.	avg.	±S.D.	avg.	±S.D.	avg.	±S.D.	avg.	±S.D.	avg.	±S.D.	avg.	±S.D.
SiO_2	68.01	*0.45*	65.01	*0.19*	64.12	*2.08*	64.39	*1.42*	65.67	*2.05*	69.70	*0.52*	69.48	*1.96*
Al_2O_3	15.62	*0.29*	16.92	*0.10*	16.47	*0.63*	16.45	*0.37*	15.81	*0.94*	15.22	*0.23*	14.76	*1.23*
TiO_2	0.60	*0.12*	0.83	*0.07*	0.84	*0.15*	0.83	*0.16*	0.82	*0.26*	*0.59*	*0.05*	*0.55*	*0.10*
FeO_{total}	3.14	*0.39*	3.53	*0.20*	4.02	*0.76*	3.85	*0.83*	3.72	*1.01*	*2.11*	*0.15*	*2.53*	*1.13*
MnO	0.19	*0.09*	0.16	*0.13*	0.17	*0.10*	0.17	*0.08*	0.15	*0.08*	0.11	*0.12*	0.14	*0.14*
MgO	0.43	*0.08*	0.98	*0.06*	1.21	*0.75*	1.10	*0.23*	0.86	*0.36*	*0.56*	*0.05*	*0.64*	*0.78*
CaO	1.77	*0.14*	2.49	*0.13*	2.73	*0.88*	2.41	*0.49*	2.11	*0.58*	1.31	*0.08*	1.41	*0.60*
Na_2O	5.46	*0.15*	5.02	*0.27*	4.85	*0.29*	4.82	*0.15*	4.94	*0.26*	*4.64*	*0.12*	*4.50*	*0.42*
K_2O	4.19	*0.13*	4.49	*0.14*	4.84	*0.55*	5.31	*0.39*	5.20	*0.59*	*5.70*	*0.12*	*5.45*	*0.68*
Cl	0.32	*0.04*	0.42	*0.03*	0.36	*0.06*	0.34	*0.05*	0.31	*0.09*	*0.35*	*0.04*	*0.28*	*0.10*
Anal diff [a]	0.27	*0.15*	0.15	*0.14*	0.41	*0.22*	0.33	*0.16*	0.41	*0.40*	-0.30	*0.19*	0.25	*0.25*
Total (anal)	100.50		101.33		97.87		96.76		97.32		95.70		95.41	
n	*5*		*10*		*11*		*9*		*14*		*7*		*10*	

Tephra nb#	T-38		T-45		T-51		T-54		T-59		T-60		T-64	
(wt%)	avg.	±S.D.	avg.	±S.D.	avg.	±S.D.	avg.	±S.D.	avg.	±S.D.	avg.	±S.D.	avg.	±S.D.
SiO_2	58.67	*0.21*	60.75	*0.88*	58.90	*0.37*	59.84	*0.61*	60.08	*1.52*	60.03	*0.92*	61.72	*0.54*
Al_2O_3	15.87	*0.51*	16.67	*0.26*	16.60	*0.79*	16.22	*0.44*	15.62	*1.23*	16.36	*0.47*	17.05	*0.21*
TiO_2	1.13	*0.14*	1.10	*0.10*	1.26	*0.10*	1.29	*0.07*	0.94	*0.15*	1.16	*0.17*	0.92	*0.09*
FeO_{total}	7.63	*0.43*	5.55	*0.32*	6.31	*0.71*	6.31	*0.40*	5.60	*1.95*	6.04	*0.49*	5.03	*0.23*
MnO	0.24	*0.08*	0.23	*0.08*	0.18	*0.08*	0.23	*0.12*	0.24	*0.14*	0.21	*0.07*	0.21	*0.08*
MgO	2.25	*0.22*	1.79	*0.25*	1.94	*0.29*	1.82	*0.19*	2.07	*1.33*	1.58	*0.38*	1.38	*0.20*
CaO	5.28	*0.26*	4.16	*0.47*	4.85	*0.35*	4.47	*0.36*	4.09	*1.62*	4.35	*0.57*	3.18	*0.31*
Na_2O	4.23	*0.13*	4.45	*0.20*	4.60	*0.18*	4.63	*0.16*	4.83	*0.34*	4.74	*0.18*	5.15	*0.19*
K_2O	3.73	*0.15*	4.45	*0.31*	4.45	*0.29*	4.27	*0.25*	4.73	*0.54*	4.33	*0.31*	4.47	*0.23*
Cl	0.34	*0.08*	0.33	*0.06*	0.28	*0.05*	0.34	*0.06*	0.51	*0.12*	0.41	*0.05*	0.50	*0.05*
Anal diff [a]	0.63	*0.14*	0.53	*0.13*	0.62	*0.13*	0.59	*0.13*	1.30	*1.71*	0.79	*0.23*	0.38	*0.13*
Total (anal)	97.49		101.28		98.04		97.85		97.49		98.35		101.98	
n	*5*		*8*		*8*		*7*		*8*		*9*		*10*	

Tephra nb#	N-6		N-8		N-9		N-19		N-21		N-22		N-23	
(wt%)	avg.	±S.D.	avg.	±S.D.	avg.	±S.D.	avg.	±S.D.	avg.	±S.D.	avg.	±S.D.	avg.	±S.D.
SiO_2	57.52	*2.40*	71.69	*1.23*	71.61	*0.83*	69.27	*0.47*	69.25	*2.20*	68.13	*0.28*	69.67	*2.57*
Al_2O_3	15.76	*1.31*	15.12	*0.98*	14.94	*0.63*	15.32	*0.12*	15.35	*0.84*	15.83	*0.18*	15.65	*1.10*
TiO_2	0.95	*0.11*	0.42	*0.08*	0.45	*0.07*	0.57	*0.08*	0.57	*0.16*	0.58	*0.08*	0.59	*0.23*
FeO_{total}	6.62	*0.89*	1.38	*0.30*	1.56	*0.27*	2.07	*0.18*	2.06	*0.53*	2.27	*0.09*	1.80	*0.75*
MnO	0.31	*0.09*	0.14	*0.06*	0.19	*0.08*	0.21	*0.09*	0.11	*0.11*	0.13	*0.04*	0.10	*0.13*
MgO	4.00	*1.62*	0.26	*0.11*	0.29	*0.16*	0.50	*0.06*	0.53	*0.24*	0.65	*0.07*	0.57	*0.61*
CaO	6.19	*2.69*	1.44	*0.46*	1.36	*0.32*	1.74	*0.17*	1.74	*0.47*	2.10	*0.14*	1.59	*0.92*
Na_2O	4.20	*0.67*	4.45	*0.49*	4.39	*0.35*	4.72	*0.07*	4.61	*0.33*	4.78	*0.10*	4.42	*0.72*
K_2O	3.50	*0.65*	4.86	*0.55*	4.96	*0.42*	4.93	*0.08*	5.11	*0.28*	4.93	*0.19*	5.35	*0.64*
Cl	0.27	*0.15*	0.33	*0.13*	0.30	*0.11*	0.38	*0.06*	0.40	*0.04*	0.40	*0.06*	0.15	*0.11*
Anal diff [a]	0.67	*0.16*	-0.11	*0.12*	-0.04	*0.16*	0.29	*0.25*	0.27	*0.18*	0.18	*0.17*	0.12	*0.11*
Total (anal)	99.51		95.77		97.72		95.04		96.98		96.08		96.98	
n	*9*		*7*		*10*		*10*		*8*		*7*		*8*	

Tephra nb#	N-25		N-26		N-30		N-32		N-45		N-50		N-54	
(wt%)	avg.	±S.D.	avg.	±S.D.	avg.	±S.D.	avg.	±S.D.	avg.	±S.D.	avg.	±S.D.	avg.	±S.D.
SiO_2	69.57	*2.31*	71.62	*1.35*	68.82	*2.07*	67.97	*1.15*	67.18	*0.42*	64.60	*0.30*	66.62	*0.55*
Al_2O_3	15.58	*0.80*	15.45	*1.10*	15.41	*1.39*	15.55	*0.47*	16.24	*0.25*	16.51	*0.29*	16.54	*0.24*
TiO_2	0.52	*0.16*	0.45	*0.19*	0.64	*0.15*	0.67	*0.09*	0.64	*0.05*	0.76	*0.07*	0.62	*0.10*
FeO_{total}	1.87	*0.60*	0.99	*0.30*	2.47	*0.78*	2.53	*0.48*	2.65	*0.16*	3.71	*0.24*	2.69	*0.29*
MnO	0.15	*0.06*	0.09	*0.07*	0.12	*0.06*	0.24	*0.03*	0.16	*0.08*	0.21	*0.11*	0.19	*0.08*
MgO	0.47	*0.28*	0.22	*0.18*	0.49	*0.22*	0.84	*0.47*	0.71	*0.12*	1.27	*0.21*	0.76	*0.19*
CaO	1.77	*0.56*	1.37	*0.73*	1.82	*0.88*	2.28	*0.68*	1.97	*0.23*	2.77	*0.21*	2.51	*0.37*
Na_2O	4.63	*0.45*	4.58	*0.49*	4.35	*0.31*	4.69	*0.07*	4.82	*0.13*	4.87	*0.18*	4.92	*0.22*
K_2O	4.99	*0.49*	5.01	*0.81*	5.36	*0.70*	4.78	*0.21*	5.15	*0.38*	4.60	*0.23*	4.64	*0.32*
Cl	0.42	*0.17*	0.19	*0.06*	0.29	*0.10*	0.06	*0.07*	0.35	*0.07*	0.34	*0.06*	0.32	*0.04*
Anal diff [a]	0.04	*0.20*	0.05	*0.04*	0.23	*0.21*	0.11	*0.08*	0.16	*0.12*	0.36	*0.15*	0.18	*0.10*
Total (anal)	92.81		96.23		95.02		96.46		97.79		99.06		97.45	
n	*8*		*8*		*10*		*4*		*8*		*9*		*9*	

Appendix 3 *(continued)*

Tephra nb#	N-57		N-58		N-60		N-62		N-65		N-68		E-1	
(wt%)	avg.	±S.D.	avg.	±S.D.	avg.	±S.D.	avg.	±S.D.	avg.	±S.D.	avg.	±S.D.	avg.	±S.D.
SiO_2	64.40	*0.73*	61.64	*1.19*	62.02	*1.34*	65.98	*0.27*	65.78	*0.45*	67.64	*0.25*	64.65	*1.14*
Al_2O_3	16.68	*1.02*	16.95	*0.55*	16.79	*0.27*	16.33	*0.16*	16.44	*0.27*	15.89	*0.14*	16.69	*0.24*
TiO_2	0.82	*0.07*	0.95	*0.05*	0.98	*0.09*	0.81	*0.07*	0.69	*0.06*	0.62	*0.08*	0.77	*0.09*
FeO_{total}	3.48	*0.36*	4.80	*0.27*	4.91	*0.45*	3.31	*0.22*	3.06	*0.22*	2.90	*0.12*	3.77	*0.47*
MnO	0.15	*0.07*	0.22	*0.09*	0.16	*0.11*	0.18	*0.10*	0.12	*0.08*	0.12	*0.07*	0.13	*0.09*
MgO	1.22	*0.32*	1.65	*0.42*	1.89	*0.56*	0.78	*0.06*	0.82	*0.10*	0.84	*0.08*	1.23	*0.23*
CaO	3.31	*0.53*	4.16	*0.90*	3.70	*1.07*	1.78	*0.14*	2.14	*0.26*	2.17	*0.18*	3.04	*0.43*
Na_2O	4.73	*0.26*	4.71	*0.27*	4.89	*0.21*	4.89	*0.23*	5.20	*0.11*	4.77	*0.07*	4.58	*0.28*
K_2O	4.57	*0.42*	4.14	*0.39*	4.38	*0.51*	5.35	*0.15*	5.21	*0.19*	4.82	*0.09*	4.53	*0.17*
Cl	0.27	*0.03*	0.28	*0.06*	0.28	*0.06*	0.45	*0.13*	0.36	*0.09*	0.41	*0.03*	0.35	*0.05*
Anal diff [a]	0.38	*0.13*	0.50	*0.11*	-0.01	*0.20*	0.15	*0.16*	0.17	*0.15*	-0.18	*0.09*	0.24	*0.14*
Total (anal)	98.04		97.14		97.44		94.92		96.00		97.60		97.21	
n	*10*		*10*		*7*		*8*		*10*		*10*		*9*	

Tephra nb#	E-4		E-5		E-6		E-7		E-8		E-13		E-15	
(wt%)	avg.	±S.D.	avg.	±S.D.	avg.	±S.D.	avg.	±S.D.	avg.	±S.D.	avg.	±S.D.	avg.	±S.D.
SiO_2	68.26	*0.24*	56.26	*2.66*	57.41	*1.03*	55.63	*1.80*	71.17	*0.56*	70.09	*0.38*	66.93	*0.98*
Al_2O_3	16.06	*0.10*	16.11	*0.98*	16.61	*0.32*	16.76	*1.86*	14.77	*0.20*	15.04	*0.10*	16.09	*0.35*
TiO_2	0.44	*0.07*	1.05	*0.27*	0.99	*0.22*	1.09	*0.19*	0.46	*0.06*	0.55	*0.08*	0.69	*0.07*
FeO_{total}	2.29	*0.08*	7.94	*3.94*	6.43	*0.94*	7.51	*2.36*	1.69	*0.22*	1.89	*0.09*	2.77	*0.40*
MnO	0.15	*0.10*	0.31	*0.12*	0.38	*0.08*	0.33	*0.07*	0.18	*0.13*	0.18	*0.14*	0.19	*0.11*
MgO	0.62	*0.05*	3.23	*0.80*	2.73	*0.70*	3.46	*1.51*	0.35	*0.15*	0.46	*0.08*	0.84	*0.18*
CaO	2.13	*0.06*	6.64	*1.71*	5.85	*2.21*	7.10	*0.80*	1.63	*0.18*	1.58	*0.10*	2.46	*0.39*
Na_2O	4.66	*0.15*	4.25	*0.38*	4.64	*0.41*	4.19	*0.42*	4.51	*0.09*	4.64	*0.13*	4.80	*0.24*
K_2O	4.74	*0.09*	3.19	*0.47*	3.68	*0.67*	2.98	*0.27*	4.79	*0.17*	5.01	*0.17*	4.70	*0.28*
Cl	0.42	*0.12*	0.27	*0.06*	0.35	*0.03*	0.33	*0.12*	0.37	*0.04*	0.35	*0.02*	0.36	*0.05*
Anal diff [a]	0.22	*0.14*	0.75	*0.14*	0.91	*0.24*	0.61	*0.13*	0.09	*0.14*	0.21	*0.17*	0.18	*0.07*
Total (anal)	97.33		99.39		97.13		97.21		95.67		96.81		97.81	
n	*10*		*10*		*4*		*7*		*15*		*8*		*9*	

Tephra nb#	E-19		E-20		E-22		E-25		E-28		E-32		E-34	
(wt%)	avg.	±S.D.	avg.	±S.D.	avg.	±S.D.	avg.	±S.D.	avg.	±S.D.	avg.	±S.D.	avg.	±S.D.
SiO_2	68.69	*0.33*	66.74	*0.23*	64.76	*0.32*	64.15	*0.50*	67.34	*1.05*	63.07	*0.94*	62.57	*0.75*
Al_2O_3	15.79	*0.16*	16.25	*0.14*	16.59	*0.10*	16.92	*0.50*	16.26	*0.31*	16.70	*0.51*	16.67	*0.41*
TiO_2	0.57	*0.09*	0.70	*0.09*	0.76	*0.05*	0.73	*0.10*	0.63	*0.06*	0.94	*0.11*	0.94	*0.11*
FeO_{total}	2.47	*0.18*	3.06	*0.12*	3.67	*0.25*	3.54	*0.24*	2.53	*0.45*	4.39	*0.37*	4.79	*0.36*
MnO	0.13	*0.05*	0.15	*0.08*	0.17	*0.09*	0.15	*0.08*	0.09	*0.07*	0.12	*0.11*	0.22	*0.08*
MgO	0.72	*0.11*	0.98	*0.04*	1.18	*0.10*	1.13	*0.09*	0.60	*0.28*	1.25	*0.08*	1.78	*0.26*
CaO	1.95	*0.11*	2.21	*0.05*	2.71	*0.08*	3.09	*0.48*	2.18	*0.37*	3.04	*0.53*	3.21	*0.31*
Na_2O	4.69	*0.18*	4.94	*0.10*	5.29	*0.12*	5.14	*0.13*	5.06	*0.26*	4.90	*0.19*	4.89	*0.10*
K_2O	4.79	*0.21*	4.96	*0.07*	4.46	*0.08*	4.41	*0.29*	4.86	*0.35*	4.78	*0.36*	4.70	*0.17*
Cl	0.38	*0.07*	0.31	*0.07*	0.44	*0.06*	0.35	*0.06*	0.30	*0.10*	0.28	*0.09*	0.29	*0.03*
Anal diff [a]	-0.18	*0.12*	-0.29	*0.14*	-0.02	*0.15*	0.38	*0.15*	0.15	*0.20*	0.54	*0.20*	-0.06	*0.16*
Total (anal)	97.58		97.63		97.81		98.51		97.84		96.36		98.03	
n	*10*		*5*		*10*		*10*		*9*		*8*		*8*	

Tephra nb#	E-36		E-38		E-41		E-42		E-49		Kawakawa		E-52	
(wt%)	avg.	±S.D.	avg.	±S.D.	avg.	±S.D.	avg.	±S.D.	avg.	±S.D.	avg.	±S.D.	avg.	±S.D.
SiO_2	65.69	*0.85*	67.75	*0.37*	68.14	*0.86*	63.31	*1.32*	62.42	*1.70*	77.47	*0.33*	60.43	*0.86*
Al_2O_3	16.40	*0.30*	16.07	*0.36*	15.45	*0.28*	17.01	*0.54*	16.41	*0.97*	12.59	*0.08*	16.53	*0.73*
TiO_2	0.72	*0.06*	0.60	*0.03*	0.59	*0.05*	0.84	*0.14*	0.91	*0.17*	0.17	*0.06*	1.12	*0.25*
FeO_{total}	3.14	*0.27*	2.77	*0.11*	2.73	*0.21*	4.17	*0.63*	4.77	*1.37*	1.23	*0.09*	5.92	*1.00*
MnO	0.18	*0.11*	0.17	*0.09*	0.16	*0.13*	0.18	*0.13*	0.20	*0.08*	-0.02	*0.04*	0.20	*0.08*
MgO	0.76	*0.12*	0.78	*0.07*	0.61	*0.18*	1.37	*0.37*	1.69	*0.63*	0.13	*0.09*	1.58	*0.32*
CaO	2.05	*0.26*	2.09	*0.23*	1.91	*0.30*	3.37	*0.49*	3.49	*0.76*	1.21	*0.05*	3.74	*0.57*
Na_2O	5.13	*0.27*	4.89	*0.17*	4.79	*0.13*	5.10	*0.31*	5.06	*0.53*	3.84	*0.20*	4.94	*0.19*
K_2O	5.20	*0.28*	4.82	*0.22*	4.97	*0.19*	4.01	*0.28*	3.99	*0.51*	3.16	*0.16*	4.53	*0.27*
Cl	0.41	*0.10*	0.36	*0.05*	0.39	*0.06*	0.27	*0.03*	0.27	*0.11*	0.26	*0.05*	0.39	*0.04*
Anal diff [a]	0.32	*0.17*	-0.29	*0.11*	0.26	*0.12*	0.37	*0.14*	0.79	*0.94*	-0.05	*0.13*	0.61	*0.25*
Total (anal)	96.67		96.99		97.46		100.01		99.02		92.12		98.75	
n	*9*		*10*		*10*		*8*		*10*		*10*		*10*	

Appendix 3 *(continued)*

Tephra nb#	E-56		E-64		E-68		E-71		Okaia		E-76		E-79	
(wt%)	avg.	±S.D.	avg.	±S.D.	avg.	±S.D.	avg.	±S.D.	avg.	±S.D.	avg.	±S.D.	avg.	±S.D.
SiO_2	59.38	*1.73*	63.17	*1.09*	60.66	*0.77*	61.27	*1.09*	77.20	*0.15*	64.36	*0.31*	69.22	*0.69*
Al_2O_3	16.61	*0.93*	16.79	*0.46*	16.54	*0.77*	16.42	*0.65*	12.38	*0.10*	16.89	*0.17*	15.52	*0.26*
TiO_2	1.20	*0.20*	0.85	*0.07*	0.92	*0.14*	0.95	*0.08*	0.20	*0.08*	0.80	*0.06*	0.57	*0.07*
FeO_{total}	6.01	*0.90*	4.48	*0.90*	5.90	*0.57*	5.48	*0.77*	1.56	*0.09*	3.89	*0.14*	2.51	*0.29*
MnO	0.14	*0.09*	0.21	*0.12*	0.27	*0.10*	0.27	*0.10*	0.05	*0.07*	0.19	*0.11*	0.15	*0.03*
MgO	1.82	*0.83*	1.17	*0.45*	2.04	*0.46*	1.86	*0.80*	0.15	*0.07*	1.26	*0.10*	0.52	*0.14*
CaO	4.44	*1.01*	3.05	*0.28*	3.73	*0.70*	3.65	*0.39*	1.18	*0.10*	2.75	*0.09*	1.69	*0.19*
Na_2O	5.01	*0.28*	5.08	*0.16*	5.10	*0.12*	4.99	*0.23*	3.67	*0.19*	4.98	*0.20*	5.02	*0.22*
K_2O	4.42	*0.69*	4.42	*0.33*	3.94	*0.27*	4.05	*0.33*	3.27	*0.31*	4.33	*0.09*	4.33	*0.19*
Cl	0.32	*0.06*	0.39	*0.08*	0.40	*0.07*	0.32	*0.10*	0.27	*0.04*	0.24	*0.03*	0.35	*0.06*
Anal diff [a]	0.65	*0.27*	0.40	*0.16*	0.49	*0.17*	0.74	*0.25*	0.07	*0.05*	0.31	*0.18*	0.10	*0.07*
Total (anal)	99.18		98.64		104.62		104.59		98.69		98.37		101.76	
n	*9*		*9*		*9*		*10*		*11*		*9*		*8*	

Note: Glass analyses are normalised to 100% volatile free. Analytical (anal) totals and the [a]analytical difference (anal diff) from 100% are also shown. All Fe reported as FeO_{total}. Average (avg.) and 1 standard deviation (±S.D.) based on n (number of analyses per tephra). The complete compositional datasheet is available within the electronic appendices.

Appendix 4 *Depth, thickness, bulk grain-size, stratification, main characteristics, and modelled age of tephra layers from lake and peatland cores recovered during this study.*

Comp. tephra-nb[a]	Comp. short. depth (cm)[b]	Thick-ness (cm)[c]	Bulk grain size[d]	Stratifi-cation[e]	Main tephra characteristic[f]	Tm-group and gl chemistry[g]	Modelled tephra age (cal yr BP)[h]
Lake Richmond							
Ri-1	28.5	cryp	fa				424±11
Ri-2	36	0.5	fa		gr ash, bleached upper contact	11/12	517±10
Ri-3	38	cryp	fa				539±10
Ri-4	42	0.1	fa			12	581±12
Ri-5	51	0.05	fa				680±23
Ri-6	61	0.5	fa		gr ash	12	794±32
Ri-7	113.5	0.05	fa				1534±47
Ri-8	118	0.1	fa				1602±47
Ri-9	126	0.1	fa				1730±43
Ri-10	127	0.5	ca		lithic rich	6, TD	1739±43
Ri-11	129	0.1	fa				1771±41
Ri-12	129.5	0.1	fa				1778±41
Ri-13	130	0.1	fa				1785±41
Ri-14	134	0.1	fa				1853±38
Ri-15	135	0.1	fa				1870±37
Ri-16	136	0.1	fa				1886±37
Ri-17	139	0.1	fa				1938±35
Ri-18	141.5	0.1	fa				1983±35
Ri-19	142.5	0.1	fa				1999±35
Ri-20	150	1	ca	ig	gr ves pumice, sp lithics, bl frag	12, TD	2122±37
Ri-21	152	cryp	fa				2161±38
Ri-22	155	0.5	ca-fl			12, TD	2209±39
Ri-23	156.5	0.5	fa		gr ash	12	2228±40
Ri-24	158.5	0.5	ma		bl ash	11, TA	2258±41
Ri-25	164	0.5	ca			11	2355±42
Ri-26	167	2.5	ca	ig-ng	br-bl micves py pumice, lithic poor	11, TA	2365±42
Ri-27	171	cryp	fa			11	2445±41
Ri-28	171.5	0.5	ca		bl micves pumice		2445±41
Ri-29	173	0.05	fa			11	2476±41
Ri-30	176	2	ca		dgr-bl micves pumice, red scoria	11, bA-bTA-TA	2497±40
Ri-31	181	0.05	fa				2604±39
Ri-32	183.5	cryp	fa				2659±39
Ri-33	200	0.05	fa				2960±52
Ri-34	209.5	1	fa		gr ash, bleached upper contact	10, R	3201±61
Ri-35	220	cryp	fa				3398±52
Ri-36	220.5	0.1	fa				3405±51
Ri-37	221.5	0.1	fa				3422±50
Ri-38	222.5	0.1	fa				3438±49
Ri-39	225	0.1	fa				3483±46
Ri-40	227.5	1	fl-ml	m	wh f-ves pumice, lithic rich	10, R	3510±45
Ri-41	228.5	0.3	fa				3523±44
Ri-42	229.5	0.1	fa				3539±44
Ri-43	243	0.05	fa				3770±45
Ri-44	243.5	0.05	fa				3778±45
Ri-45	245.5	cryp	fa				3810±46
Ri-46	248	0.05	fa				3848±46
Ri-47	259	8	ca-fl	ig-ng	pgr ves pumice, banded, lithic rich	10, R	3893±46
Ri-48	259.5	0.03	fa				3900±46
Ri-49	273	cryp	fa				4070±37
Stent	287	1.5	fa		pwh ash	R	4279±47
Ri-50	294	0.3	fa			8	4315±50
Ri-51	302.5	8	ma-ca	m, ws	crys rich pgr pumiceous ash	9, TD	4328±51

Appendix 4 *(continued)*

Ri-52	304.5	cryp	fa				4371±53
Ri-53	307	cryp	fa				4424±56
Ri-54	309.5	cryp	fa				4476±57
Ri-55	313.5	1	fa				4538±57
Ri-56	323	0.1	fa				4732±52
Ri-57	324.5	0.3	fa				4757±51
Ri-58	329.5	3	ma	m, ws	crys rich pgr pumiceous ash	8, TD	4801±49
Ri-59	332.5	0.1	fa-ma				4866±46
Ri-60	337.5	4.5	ml	m	pgr ves pumice, banded, lithic poor	8, TD	4878±46
Ri-61	338.5	0.1	fa				4899±45
Ri-62	339.5	cryp	fa				4921±44
Ri-63	344.5	0.05	fa				5049±42
Ri-64	345	0.1	fa				5060±42
Ri-65	349	1	fa		gr ash, dispersed on top	tm spread	5145±42
Ri-66	353.5	0.05	fa-ma				5285±43
Ri-67	357.5	0.1	fa				5423±46
Ri-68	358.5	0.1	fa				5457±47
Ri-69	359.5	cryp	fa				5494±48
Ri-70	369.5	9	ml	m	pgr ves pumice, banded, lithic poor	9, TD-R	5534±48
Ri-71	370.5	0.1	fa				5568±47
Ri-72	371.5	0.1	fa				5601±48
Ri-73	372.5	cryp	fa				5641±48
Ri-74	373.5	0.5	fa-ma	ig	gr ash	8	5662±48
Ri-75	375	0.1	fa				5723±47
Ri-76	378.5	0.05	fa				5894±45
Ri-77	380	0.05	fa				5974±45
Ri-78	387	0.3	fa				6350±50
Ri-79	389	0.1	fa				6457±54
Ri-80	392	0.3	fa	ls			6605±60
Ri-81	393.5	0.3	fa	ls			6668±62
Ri-82	394.5	0.3	fa	ls			6704±64
Ri-83	398.5	0.3	fa	ls			6879±69
Ri-84	402.5	2	ma-ca	ng	gr ves pumice, lithic rich	3, TD	6960±70
Ri-85	403.5	0.3	fa	ls			6986±70
Ri-86	413	0.1	fa	ls			7277±64
Ri-87	416	0.1	fa	ls			7354±61
Ri-88	424.5	1	ml	ls	gr ves pumice, lithic rich	3	7535±53
Ri-89	426	0.5	fa	ls			7558±52
Ri-90	438.5	0.5	fa	ls			7813±39
Ri-91	441	0.5	fa	ls			7856±37
Ri-92	450	0.1	fa	ls			8054±32
Ri-93	451	0.1	fa	ls			8075±32
Ri-94	454.5	0.1	fa				8160±31
Ri-95	464	1	ca	m, ws	crys rich pgr pumiceous ash	8, TD	8401±33
Ri-96	464.5	0.1	fa-ma				8414±33
Ri-97	472	0.05	fa				8669±34
Ri-98	477.5	0.5	fa				8857±34
Ri-99	503	1	ca		gr-pgr ves-micves pumice, crys rich	2	9947±33
Ri-100	504.5	0.1	fa				10,017±33
Ri-101	505.5	0.1	fa				10,062±34
Ri-102	506.5	0.1	fa				10,107±35
Ri-103	507	0.1	fa				10,127±35
Ri-104	508	0.1	fa				10,173±36
Ri-105	509.5	0.5	ca		pgr ves pumice, crys & lithic rich	2	10,224±36
Ri-106	511	0.3	ca		lithic rich		10,285±38
Ri-107	512.5	0.5	ca				10,337±39
Ri-108	513.5	0.5	fa				10,362±39
Ri-109	516	1	ca	m, ws	gr ves pumice, crys rich	2, TD	10,440±41
Ri-110	518	0.5	ca				10,519±43
Ri-111	518.5	0.05	ca				10,543±43

Appendix 4 *(continued)*

Ri-112	520	0.5	fa				10,595±44
Ri-113	521.5	1.5	ml		pgr c-ves pumice, crys rich	5	10,595±44
Ri-114	525.5	3	ml				10,660±46
Ri-115	529.5	3	ml		pgr c-ves pumice, crys rich		10,741±45
Ri-116	530.5	0.5	fa-ca				10,782±45
Ri-117	538	5.5	ca-ml		pgr-gr c-ves pumice, crys&lithic rich	4	10,955±43
Ri-118	539.5	1	ca		pgr-gr c-ves pumice, lithic poor	7	11,000±44
Ri-119	542.5	1	fa				11,182±40
Ri-120	544.5	0.1	fa				11,359±36
Ri-121	556	4	ca		pgr ves pumice, crys rich	2, TD	12,042±24
Ri-122	559.5	0.5	ca				12,283±21
Ri-123	567.5	1	fa-ca	m	dgr ash, bl frag	2, TD	12,696±18
Ri-124	574.5	0.05	fa				12,944±24
Ri-125	584.5	4	ca		pgr-wh ves pumice		13,146±37
Ri-126	588.5	3	ca		pgr-wh ves pumice		13,178±40
Ri-127	608.5	0.05	fa	m, ws			13,766±91
Ri-128	641.5	1	ca		pgr-gr ves pumice, lithic poor		14,404±161
Ri-129	665.5	1	fa-ca		br ash		14,588±184
Ri-130	726.5	?	ml		dp in paleosol	8	unknown
Ri-131	727	0.1	fa				unknown
Ri-132	735	8	ca-ml	ig	pgr ves pumice, sp lithics	2, R	unknown
Tariki Swamp							
T-1	24	0.5	fl in fa	dp	wh ves pumice, sp pgr lithics		1736±42
T-2	33	1	ca		pgr ves pumice, sp lithics, bl frag	12, TD	1830±37
T-3	34.5	0.5	ca		gr lithics, bl frag, pumice poor	12	1841±36
T-4	51.5	7.5	ca-fl	ig-ng	pgr-gr micves pumice, red scoria	11, bTA-TA	1952±31
T-5	56.5	1	ca-fl		pgr ves pumice, sp lithics, bl frag	12	2005±29
T-6	61	1	ca	dpb, st	wh ves pumice, sp pgr lithics	12	2052±28
T-7	68	2	fl in ca	dp	pgr lithics	12	2118±28
T-8	74	2	ca	m	pgr ves pumice, sp lithics	12, TD	2170±29
T-9	82	2	ca	ig	br-bl micves py pumice, lithic poor	11, TA	2247±32
T-10	97	6.5	ca	ig	br-gr-bl micves py pumice	11, TA	2353±38
T-11	115	2	ma	dp	bl ash	11	2536±48
T-12	192.5	0.3	fa				3056±39
T-13	219	1	fl in fa	rew	lithics, wh pumice poor		3181±34
T-14	247.5	1	ml	rew	wh f-ves pumice, lithic rich	10, R	3433±41
T-15	268	?	ca-fl	dp/rew	pgr ves pumice, lithic poor, dp peat	10, R	3935±41
T-16	298	?	ca-ml	dp/rew	pgr ves pumice, lithic poor, dp paleosol	9, TD	5271±51
T-17	315	?	ca-cl	dp/rew	pgr ves pumice, lithic rich, dp paleosol	9, TD	6083±65
T-18	392	?	ca	dp/rew	lithic & crys rich, dp peat	2	10,522±194
T-19	436	5	ma	dp/rew	pgr ves pumice, lithic poor, dp peat	2	11,862±100
T-20	452	0.5	fa			2	12,022±100
T-21	464	7	ca		pgr-gr ves pumice, lithic rich, bl frag	2, TD	12,076±115
T-22	468	0.5	fa	m		2	12,121±128
T-23	479	10	ca-fl	mg	pgr-dgr ves pumice, banded, bl frag	1/2, TA-TD	12,135±132
T-24	487	4	ml	dpb, st	dgr ves pumice, sp lithics	1, TD spread	12,198±150
T-25	494	2.5	ma	dpb, st	crys rich ash	1	12,281±166
T-26	498	1	ca	dpb, st	lithic rich, dgr ves pumice poor	2, TD	12,343±176
T-27	510	1	ml	m	wh-pgr ves-micves pumice, lithic rich	3, TD-R	12,481±190
T-28	512	1	ml	m	wh-pgr ves-micves pumice, lithic rich	3, TD-R	12,506±191
T-29	519	0.5	fa		pgr pumiceous ash	3	12,679±199
T-30	550.5	0.3	fa			2	13,704±171

Appendix 4 *(continued)*

T-31	575.5	cryp	fa				14,508±110
T-32	582.5	cryp	fa	dp			14,725±115
T-33	588	cryp	fa	dp			14,887±119
T-34	596.5	cryp	fa	dp			15,119±124
T-35	603.5	0.5	fa			1	15,281±127
T-36	606	0.1	fa			1	15,336±127
T-37	608.5	0.5	fa			1	15,381±128
T-38	611	1	ca		br-dgr scoriaceous py pumice	1, TA	15,414±128
T-39	615	1	fa			1	15,476±127
T-40	617.5	0.3	fa			1	15,519±127
T-41	621.5	3	fa			1	15,538±126
T-42	626.5	4	fa			1	15,556±126
T-43	629.5	0.5	fa			1	15,600±125
T-44	631.5	0.5	ma		pbr-br ves pumice, lithic rich	1	15,626±124
T-45	634.5	2	ca	ng	lithic rich, br ves pumice poor	1, TA-TD	15,642±123
T-46	637.5	cryp	fa			1	15,689±120
T-47	648	0.3	ma			1	15,843±112
T-48	652.5	0.1	fa			1	15,907±109
T-49	654	0.3	fa				15,925±108
T-50	656	1	fa			1	15,939±107
T-51	658.5	1	ca		br scoriaceous pumice, bl frag	1, TA	15,960±106
T-52	659.5	0.5	ma		bl crys rich ash	1	15,968±106
T-53	676.5	1	ma-ca		br scoriaceous pumice, bl frag	1	16,185±98
T-54	703	1	ca			1, TA	16,493±102
T-55	749	1	ma-ca		dgr-br ves pumice, bl frag	1	16,800±99
T-56	754.5	2	ca-fl		pbr-br ves pumice, lithic rich	1	16,863±102
T-57	759	1.5	fa-ca		dbr scoriaceous pumice, ion-stained	1	16,890±104
T-58	772	3	ca		lithic & crys rich	1	16,976±111
T-59	777	2	ca		lithic & crys rich	1, TA-TD	17,027±116
T-60	783.5	0.5	fa			1, TA-TD	17,119±110
T-61	797.5	0.5	ma		br scoriaceous pumice	1	17,180±96
T-62	806.5	0.5	fa			1	17,218±89
T-63	814.5	1.5	ca		br-dbr scoriaceous pumice, bl frag	1	17,244±85
T-64	870.5	4	ca-ml	m	bl-dbr scoriaceous pumice, banded	1, TD	17,397±96
Ngaere Swamp							
N-1	8	0.5	ca				1847±111
N-2	15	1	ma	ws	wh-pgr ves pumice	12	1953±108
N-3	23.5	0.5	ca		wh ves pumice, bl frag		2094±103
N-4	30	0.5	ca				2201±100
N-5	40	1	ca				2360±95
N-6	54	8	ca	ig	pgr-gr micves pumice, red scoria	11, bA-bTA-TA	2448±92
N-7	69	3	ca-fl	ig	pgr-gr-bl micves py pumice, lithic rich	11	2603±83
N-8	113	2.5	ca-ml		wh f-ves pumice, lithic rich	10, R	3216±67
N-9	127	5	ca-ml		wh f-ves pumice, lithic poor	10, R	3365±65
N-10	157	cryp	fa	dp			4204±56
N-11	173	cryp	ca	dp			4680±55
N-12	177	cryp	ma	dp			4792±55
N-13	182	0.5	fa		pgr-gr lithics		4927±54
N-14	199	1	ca				5383±51
N-15	204	cryp	ca	dp			5492±49
N-16	207	cryp	ca	dp			5548±48
N-17	228	cryp	ca	dp			6107±45
N-18	271	4	ma	ws			6844±55
N-19	282.5	10	ca-fl	mg, sb	pgr ves pumice, lithic rich	9, TD-R	6862±53
N-20	307.5	1	ca				7049±34
N-21	321.5	2.5	ml	m	pgr ves pumice, lithic rich	3, TD	7124±38
N-22	327	2	ca-ml	m	pgr ves pumice, lithic rich	8, TD	7151±40

Appendix 4 *(continued)*

N-23	335	2.5	ca	sb-t, ws	pgr-gr ves-micves pumice, lithic rich	3, TD-R spread	7200±45
N-24	341	3.5	ca	dpb, st	pgr-gr ves-micves pumice, lithic rich	3	7226±47
N-25	347	1	ml	dp	pgr ves pumice	TD-R spread	7285±49
N-26	352	2	ca-ml	m		8, TD-R spread	7326±49
N-27	400	3	ca-fl	m	pgr-dgr lithics, banded, pumice poor		8090±46
N-28	417	0.5	ca				8336±46
N-29	428	1.5	ca-fl		gr-dgr lithics		8479±43
N-30	430	1	ml		pgr ves pumice	TD-R spread	8494±43
N-31	449.5	cryp	fa				8781±37
N-32	503	4	ca	ng, sb-t	pgr ves pumice with micves core	tm spread, TD	9519±36
N-33	514	0.5	ca in fa			2	9677±35
N-34	523	1	ca	dp			9796±34
N-35	532	1	ca			2	9914±35
N-36	542	4	ca	ig, sb	pgr ves pumice, crys rich	2	10,003±37
N-37	548	3	ca	ig		2	10,048±38
N-38	555	2	ca			2	10,124±41
N-39	559	3	ma	dp		2	10,139±42
N-40	562	0.5	ma			2	10,177±44
N-41	564	0.5	fa				10,200±45
N-42	566	2	ca-ml		gr c-ves pumice, crys rich, lithic poor	4	10,200±45
N-43	574	1.5	ma-ca				10,301±50
N-44	586	1.5	ca		pgr-gr ves pumice, crys rich, bl frag	2	10,471±56
N-45	594	1.5	ca		wh ves pumice	5, TD	10,580±59
N-46	597.5	1.5	ca		crys rich, wh pumice poor	5	10,614±59
N-47	611	1	ca		pgr c-ves pumice, crys rich	4	10,838±60
N-48	614	1.5	ma-ca		pgr c-ves pumice, crys rich	4	10,866±60
N-49	618.5	2	ca	ng	pgr c-ves pumice, crys rich	4	10,912±60
N-50	622	3	ca		pgr c-ves pumice, crys rich	4, TD	10,922±60
N-51	623	0.5	ca			4	10,931±60
N-52	634	4	ca-ml	m	wh ves pumice, lithic poor	7	11,065±63
N-53	636	1	ma-ca		wh ves pumice	7	11,084±64
N-54	642	4	ma	dpb, st	wh ves pumice	7, TD	11,123±65
N-55	683	0.5	ca			5	11,958±119
N-56	684	0.5	ca			5	11,969±119
N-57	699.5	3	ca	ig, sb-t	gr ves pumice, crys rich (augite)	2, TD	12,238±114
N-58	712.5	7	ca-ml	ig-ng	dgr-gr ves pumice, banded, bl frag	1, TA-TD	12,370±104
N-59	715	2	ca	dp	dgr-gr ves pumice, lithic rich, bl frag	1	12,382±102
N-60	721	1.5	ca		dgr-gr ves pumice, lithic rich, bl frag	1, TA-TD	12,486±90
N-61	724	2	ma-ca		dgr-gr ves pumice, lithic rich, bl frag	1	12,509±87
N-62	733	3	ma-ca		gr ves pumice, lithic poor, crys rich	1, TD	12,653±69
N-63	736	1	fa		lithic rich, pumice poor	1	12,701±65
N-64	741	1	ca-ml	m	pgr c-ves pumice, crys rich	2	12,799±60
N-65	749	2.5	ca-fl	m	pgr-gr ves pumice, lithic poor	2, TD	12,934±69
N-66	754	2	ca-fl		pgr-gr ves-micves pumice, lithic rich		13,005±77
N-67	768	cryp	ca		pgr ves pumice	3, TD	13,266±114
N-68	776	1	ma		crys rich pgr pumiceous ash	3, TD	13,400±136
Eltham Swamp							
E-1	47.5	4	ma	ws	wh-pgr ves pumice	2, TD	1532±76
E-2	58	0.5	ma-ca		wh ves pumice, lithic rich, bl frag		1829±64

Appendix 4 *(continued)*

E-3	68	2	ma-ca			12	2066±54
E-4	70.5	1	ma-ca			12, TD	2110±53
E-5	81	7	ca	ig	pgr-gr micves pumice, red scoria	11, bTA-TA	2214±49
E-6	97.5	7	ca	ig	gr-br-bl micves py pumice, lithic poor	11, TA	2501±39
E-7	117	1.5	ma-ca		pgr-gr micves pumice, red&bl scoria	11, bTA-TA	3042±33
E-8	140	3.5	ca-fl		wh f-ves pumice, lithic rich	10, R	3593±43
E-9	149	1	fl	dp			4120±35
E-10	154	1.5	ca		pgr ves pumice	8	4354±34
E-11	176	2	fl	dp			5567±42
E-12	191	2	ma	ws			6202±45
E-13	200	5	ca-ml	mg	pgr ves pumice, sp lithics	R	6366±44
E-14	217	4	ca-fl	dp			6721±40
E-15	230	6	ma-ca	sb, dpt	pgr-gr ves-micves pumice, lithic rich	3, TD	6936±39
E-16	234	1	ca		lithic rich, pumice poor		7022±40
E-17	237	0.5	ma		crys rich ash		7091±41
E-18	265	0.5	fa-ma	dp			7788±66
E-19	302	1	fa			3, TD	8244±71
E-20	344	2	ca		pgr ves pumice, crys & lithic rich	2, TD	9617±52
E-21	369	4.5	ca-fl		pgr c-ves pumice, crys rich, lithic poor	2	10,022±39
E-22	390	3	ma-ca		pgr c-ves pumice, crys rich (augite)	2, TD	10,307±38
E-23	393	1	ma-ml		lithic rich, pgr pumice poor	2/4	10,337±38
E-24	398	2	fa-ma			2	10,383±40
E-25	420	8	ca-fl	sb, dpt	pgr-gr ves pumice, crys rich, bl frag	2, TD	10,612±45
E-26	424	2	ma-ca			4	10,647±46
E-27	428	1	fl-ml		reworked E-28?		10,701±46
E-28	433.5	3	ca-ml	m	pgr c-ves pumice, crys rich	7, TD	10,746±46
E-29	436	1	fa				10,772±47
E-30	438	1	fa				10,790±47
E-31	493	3	fa				11,748±103
E-32	525	6	ca-ml	m	lithic rich, dgr pumice poor, bl frag	1, TD	12,230±119
E-33	529	2	ca-fl		gr-dgr ves pumice, lithic rich, bl frag	1	12,358±113
E-34	533	3	ma-ca		gr-dgr ves pumice, lithic rich, bl frag	1, TD	12,377±112
E-35	539.5	1	fa	dp			12,478±104
E-36	561	4	ma	dp	pgr-gr ves pumice, crys rich	2, TD	12,800±70
E-37	571	0.5	fa	dp			12,977±55
E-38	581	0.5	ca		wh-pgr ves pumice	3, TD	13,159±48
E-39	582.5	0.5	ma				13,178±48
E-40	593.5	1	fa-ma	dp		3	13,375±50
E-41	597.5	3.5	ma-ca	sb, dpt	pgr ves pumice, crys rich	3, TD	13,385±50
E-42	806.5	5	ma		crys rich pgr pumiceous ash	1, TD	23,472±141
E-43	811	1	ca				23,700±142
E-44	817	cryp	ca				24,071±143
E-45	819	0.1	ca				24,171±143
E-46	820	0.1	ma			2	24,211±143
E-47	830	0.3	ma			1	24,729±141
E-48	833.5	0.1	fa			1	24,890±139
E-49	842.5	2.5	ma	sb-t, m	crys rich pgr pumiceous ash	1, TA-TD	25,144±135
E-50	846	0.1	fa				25,271±132
Kawakawa	854	3	fa		pyell ash	R	25,447±125
E-51	856	1	fa		bl lithic rich ash	1	25,475±124
E-52	860	2.5	ma	sb-t, m	gr-dgr ves pumice, lithic rich, red frag	1, TA-TD	25,517±122
E-53	866	0.1	fa-ma		bl lithic rich ash		25,670±114

Appendix 4 *(continued)*

E-54	868	1.5	ca		gr-dgr ves pumice, lithic rich, red frag	1	25,682±114
E-55	869	cryp	fa				25,706±112
E-56	884	2	fa-ma	ig	dgr lithic rich ash	1, TA-TD	25,991±99
E-57	888.5	1	fa		bl ash		26,059±96
E-58	897	cryp	fa			1	26,212±91
E-59	899	cryp	fa-ma	dp			26,246±90
E-60	905	cryp	ma				26,344±88
E-61	919.5	2	fa		bl ash		26,537±89
E-62	923	cryp	ma-ca		gr-br c-vesicular pumice, lithic poor		26,589±90
E-63	924	0.1	ca		gr-br c-vesicular pumice, lithic poor		26,603±90
E-64	935	6	ca-fl	ig	iron-stained ves pumice, sp lithics	1, TD	26,679±92
E-65	941	1.5	ca		iron-stained (strongly altered)		26,748±94
E-66	974	0.1	ma		gr pumiceous ash		27,352±111
E-67	980.5	0.5	ca-fl	sb-t, m	gr-dgr ves pumice, lithic rich	1	27,495±114
E-68	982.5	2	ma	sb-t, ws	gr pumiceous ash	1, TA-TD	27,495±114
E-69	996	0.5	fa		iron-stained ash	1	27,855±115
E-70	1000	0.5	fa-ma		iron-stained ash with gr pumice frag		27,964±114
E-71	1011	2	ma-ca	sb-t, m	gr pumiceous ash	6, TA-TD	28,262±118
Okaia	1027	3	fa-ml		yell pumiceous ash	R	28,735±143
E-72	1032	2	ca-ml	m	iron-stained c-ves pumice		28,850±153
E-73	1043	2	ca-ml	m	iron-stained c-ves pumice, lithic rich		29,205±191
E-74	1054	3	ca-ml	m	dgr-gr ves pumice, banded, lithic poor	1	29,531±231
E-75	1062.5	7	ca-fl	m	pgr-gr ves pumice, banded, lithic poor	2, TD	29,593±240
E-76	1064	1	ma-ca		crys rich pgr pumiceous ash	2	29,614±242
E-77	1068	3	ma	ws	crys rich wh pumiceous ash	8	29,655±248
E-78	1073	2	ma		crys rich wh pumiceous ash	8	29,780±265
E-79	1083.5	8.5	ca-fl	mg	pgr-gr ves pumice, lithic poor	8, TD-R	29,855±274
E-80	1089	5	ca-fl		iron-stained ves pumice, lithic rich		29,872±276

*Note: Grey-highlighted rows represent the most prominent tephra layers within each composite core. The Taupo volcano-derived tephra layers (i.e., Stent, Kawakawa, Okaia) are marked in red. *The age of the Stent Tephra (4279±47 cal yr BP) is a mean age calculated from all three Lake Richmond cores (Fig. 3.1).*

[a] *Tephra numbers are based on each composite record (refer to Figs. 3.2 to 3.5).*

[b] *Depth is given as composite shortened depth (refer to 3.2.4.4)*

[c] *Abbr. as followed: cryp=crypto (tephra is not visible by naked eye, only identified in radiographic images), ?=unknown thickness, since tephra occurs dispersed in silty loam horizons*

[d] *Abbr. as followed: fa=fine ash (63-250µm), ma=medium ash (250-500µm), ca=coarse ash (500µm-2mm), fl=fine lapilli (2-4mm), ml=medium lapilli (4-16mm), cl=coarse lapilli (16-64mm)*

[e] *Abbr. as followed: ng=normal graded, ig=inverse graded, mg=multiple graded (shower bedded), m=massive, ws=well sorted, ls=lensing, dp=dispersed, s=sharp, b=bottom, t=top, (i.e., sb-t=sharp bottom and top)*

[f] *Abbr. as followed: gr=grey, wh=white, bl=black, br=brown, yell=yellow, p=pale, d=dark (i.e., dgr=dark grey), ves=vesicular, micves=microvesicular, f-ves=finely vesicular, c-ves= coarsely vesicular, sp=similar portion, dp=dispersed, rew=reworked, crys=crystal, py=porphyritic*

[g] *Titanomagnetite groups and glass shard chemistry (refer to Figs. 3.6, 3.7, and Table 3.2)*

[h] *Calibrated ages based on model shown in Fig. 3.1*

Appendix 5 *Electron microprobe-determined titanomagnetite compositions of tephra units from flank (proximal) and ring-plain (medial) localities.*

Sample#	Burrell		Te Popo		Kaupokonui		Manganui G		Curtis R.		Manganui F	
Location[a]	LM		LM & VS		CRS		CRS		CRS		LM & HH1	
(wt%)	avg.	±S.D.	avg.	±S.D.	avg.	±S.D.	avg.	±S.D.	avg.	±S.D.	avg.	±S.D.
TiO_2	6.11	*0.26*	7.59	*0.12*	9.27	*0.12*	6.23	*0.26*	6.39	*0.35*	6.32	*0.19*
Al_2O_3	3.11	*0.41*	2.13	*0.13*	3.19	*0.10*	6.22	*0.69*	2.58	*0.34*	6.60	*0.38*
FeO_t	82.78	*1.32*	83.76	*1.10*	79.55	*0.51*	80.28	*1.10*	83.52	*1.05*	79.82	*0.83*
MnO	1.00	*0.12*	1.39	*0.15*	0.92	*0.14*	0.74	*0.16*	1.15	*0.15*	0.59	*0.12*
MgO	2.88	*0.22*	2.08	*0.15*	3.23	*0.09*	3.56	*0.64*	2.02	*0.50*	3.89	*0.43*
Al_2O_3+MgO	6.00	*0.59*	4.20	*0.26*	6.42	*0.10*	9.78	*1.30*	4.60	*0.81*	10.49	*0.68*
Total	97.21	*0.86*	97.28	*1.18*	96.62	*0.44*	97.31	*0.39*	95.92	*0.57*	97.56	*0.38*
Fe_2O_3	56.56	*0.47*	54.63	*0.83*	49.87	*0.35*	53.20	*0.66*	55.47	*0.81*	52.80	*0.48*
FeO	31.89	*1.43*	34.60	*0.45*	34.67	*0.38*	32.41	*1.11*	33.61	*0.45*	32.31	*0.56*
Total recal	102.24	*0.78*	102.67	*1.22*	101.41	*0.53*	102.53	*0.41*	101.43	*0.50*	102.74	*0.37*
Ti	0.17	*0.01*	0.21	*0.00*	0.25	*0.00*	0.17	*0.01*	0.18	*0.01*	0.17	*0.00*
Al	0.13	*0.02*	0.09	*0.01*	0.14	*0.00*	0.26	*0.03*	0.11	*0.01*	0.27	*0.01*
Fe^{+3}	1.53	*0.01*	1.49	*0.01*	1.36	*0.01*	1.41	*0.02*	1.53	*0.03*	1.39	*0.02*
Fe^{+2}	0.96	*0.04*	1.05	*0.01*	1.05	*0.01*	0.95	*0.04*	1.03	*0.02*	0.95	*0.02*
Mn	0.03	*0.00*	0.04	*0.00*	0.03	*0.00*	0.02	*0.00*	0.04	*0.00*	0.02	*0.00*
Mg	0.15	*0.01*	0.11	*0.01*	0.17	*0.01*	0.19	*0.03*	0.11	*0.03*	0.20	*0.02*
Usp	0.17	*0.01*	0.21	*0.00*	0.25	*0.00*	0.16	*0.01*	0.18	*0.01*	0.17	*0.01*
n	*10*		*25*		*9*		*6*		*10*		*19*	

Sample#	Maketawa II		Maketawa I		Manganui E		Manganui D		Manganui D		Manganui D	
Location[a]	CRS		LM		LM		whole CRS		layer1-mid		layer2-bottom	
(wt%)	avg.	±S.D.	avg.	±S.D.	avg.	±S.D.	avg.	±S.D.	avg.	±S.D.	avg.	±S.D.
TiO_2	6.49	*0.15*	6.40	*0.08*	6.94	*0.28*	6.71	*0.56*	7.04	*0.51*	6.43	*0.41*
Al_2O_3	2.49	*0.10*	3.17	*0.12*	4.85	*0.19*	5.65	*0.88*	5.61	*0.43*	5.83	*0.94*
FeO_t	82.56	*0.43*	81.51	*0.63*	81.22	*0.47*	80.02	*1.18*	79.58	*0.56*	79.77	*1.20*
MnO	1.21	*0.17*	0.97	*0.16*	0.83	*0.10*	0.67	*0.16*	0.68	*0.08*	0.60	*0.09*
MgO	2.28	*0.09*	2.94	*0.09*	3.03	*0.19*	3.81	*0.51*	4.16	*0.18*	3.97	*0.53*
Al_2O_3+MgO	4.77	*0.10*	6.11	*0.14*	7.88	*0.35*	9.47	*1.30*	9.77	*0.48*	9.80	*1.39*
Total	95.39	*0.31*	95.37	*0.63*	97.24	*0.74*	97.18	*0.63*	97.49	*0.52*	96.83	*0.39*
Fe_2O_3	55.13	*0.56*	54.76	*0.46*	52.97	*0.61*	52.89	*0.95*	52.67	0.87	53.15	*0.94*
FeO	32.95	*0.18*	32.24	*0.40*	33.55	*0.52*	32.43	*0.85*	32.19	0.60	31.95	*0.78*
Total recal	100.79	*0.40*	100.74	*0.65*	102.40	*0.74*	102.35	*0.59*	102.56	0.57	102.07	*0.39*
Ti	0.18	*0.00*	0.18	*0.00*	0.19	*0.01*	0.18	*0.02*	0.19	0.01	0.17	*0.01*
Al	0.11	*0.00*	0.14	*0.00*	0.20	*0.01*	0.23	*0.04*	0.23	0.02	0.24	*0.04*
Fe^{+3}	1.53	*0.01*	1.51	*0.01*	1.42	*0.02*	1.40	*0.03*	1.39	0.02	1.41	*0.03*
Fe^{+2}	1.01	*0.01*	0.99	*0.01*	1.00	*0.02*	0.96	*0.03*	0.95	0.02	0.94	*0.03*
Mn	0.04	*0.01*	0.03	*0.00*	0.02	*0.00*	0.02	*0.00*	0.02	0.00	0.02	*0.00*
Mg	0.12	*0.00*	0.16	*0.01*	0.16	*0.01*	0.20	*0.03*	0.22	0.01	0.21	*0.03*
Usp	0.18	*0.00*	0.18	*0.00*	0.19	*0.01*	0.18	*0.02*	0.19	0.02	0.17	*0.01*
n	*10*		*10*		*6*		*46*		*10*		*10*	

Sample#	Manganui D		Manganui D		Manganui D		Manganui C		Manganui B		Manganui A	
Location[a]	layer2-top		layer3-mid		layer3-top		M		LM		M	
(wt%)	avg.	±S.D.	avg.	±S.D.	avg.	±S.D.	avg.	±S.D.	avg.	±S.D.	avg.	±S.D.
TiO_2	6.67	*0.39*	7.10	*0.62*	6.17	*0.14*	6.62	*0.22*	6.25	*0.27*	7.22	*0.21*
Al_2O_3	5.09	*0.27*	4.94	*0.44*	7.03	*0.23*	6.81	*0.24*	5.26	*0.42*	5.54	*0.26*
FeO_t	81.31	*0.99*	80.51	*0.88*	78.80	*0.51*	77.73	*0.85*	80.84	*0.49*	78.88	*0.54*
MnO	0.68	*0.15*	0.78	*0.24*	0.56	*0.15*	0.48	*0.12*	0.69	*0.15*	0.75	*0.09*
MgO	3.23	*0.25*	3.45	*0.26*	4.30	*0.23*	5.05	*0.32*	3.17	*0.09*	4.08	*0.18*
Al_2O_3+MgO	8.32	*0.47*	8.39	*0.58*	11.33	*0.27*	11.86	*0.33*	8.43	*0.47*	9.62	*0.37*
Total	97.38	*0.74*	96.98	*0.61*	97.20	*0.73*	96.99	*0.66*	96.58	*0.61*	96.84	*0.53*
Fe_2O_3	53.41	*0.95*	52.70	*1.12*	52.53	0.66	52.18	*0.56*	53.51	*0.43*	51.84	*0.44*
FeO	33.26	*0.32*	33.09	*0.58*	31.53	0.31	30.78	*0.58*	32.69	*0.26*	32.23	*0.47*
Total recal	102.54	*0.63*	102.23	*0.59*	102.35	0.69	102.11	*0.65*	101.75	*0.55*	101.83	*0.56*
Ti	0.18	*0.01*	0.19	*0.02*	0.16	0.00	0.17	*0.01*	0.17	*0.01*	0.19	*0.01*
Al	0.21	*0.01*	0.21	*0.02*	0.29	0.01	0.28	*0.01*	0.22	*0.02*	0.23	*0.01*
Fe^{+3}	1.43	*0.02*	1.41	*0.03*	1.38	0.01	1.37	*0.02*	1.44	*0.01*	1.38	*0.01*
Fe^{+2}	0.99	*0.01*	0.98	*0.02*	0.92	0.01	0.90	*0.01*	0.98	*0.01*	0.95	*0.02*
Mn	0.02	*0.00*	0.02	*0.01*	0.02	0.00	0.01	*0.00*	0.02	*0.00*	0.02	*0.00*
Mg	0.17	*0.01*	0.18	*0.01*	0.22	0.01	0.26	*0.02*	0.17	*0.00*	0.22	*0.01*
Usp	0.18	*0.01*	0.19	*0.02*	0.16	0.00	0.17	*0.01*	0.17	*0.01*	0.19	*0.01*
n	*10*		*10*		*9*		*6*		*10*		*10*	

Appendix 5 *(continued)*

Sample#	U. Inglewood		L. Inglewood		Korito		Kapuni-B		Kapuni-A		Kokowai	
Location[a]	M & EaS		LM		HH1		HS		HS		KK	
(wt%)	avg.	±S.D.	avg.	±S.D.	avg.	±S.D.	avg.	±S.D.	avg.	±S.D.	avg.	±S.D.
TiO_2	7.37	*0.17*	7.21	*0.19*	7.41	*0.25*	7.80	*0.15*	7.95	*0.08*	7.89	*0.16*
Al_2O_3	1.66	*0.16*	1.76	*0.09*	1.90	*0.13*	1.87	*0.08*	2.55	*0.15*	2.50	*0.11*
FeO_t	82.95	*0.50*	82.66	*0.44*	82.50	*0.45*	82.51	*0.43*	81.44	*0.52*	81.16	*0.48*
MnO	1.80	*0.15*	1.79	*0.16*	1.58	*0.14*	1.61	*0.17*	1.39	*0.18*	1.31	*0.14*
MgO	1.58	*0.15*	1.70	*0.08*	1.80	*0.14*	1.83	*0.10*	2.39	*0.19*	2.47	*0.12*
Al_2O_3+MgO	3.24	*0.23*	3.45	*0.14*	3.71	*0.17*	3.70	*0.13*	4.95	*0.20*	4.97	*0.16*
Total	95.78	*0.53*	95.57	*0.61*	95.50	*0.46*	95.98	*0.41*	96.11	*0.46*	95.73	*0.48*
Fe_2O_3	54.20	*0.42*	54.30	*0.39*	53.85	*0.47*	53.35	*0.62*	52.63	*0.32*	52.62	*0.38*
FeO	34.17	*0.35*	33.81	*0.29*	34.04	*0.30*	34.51	*0.39*	34.08	*0.57*	33.81	*0.40*
Total recal	101.07	*0.54*	100.81	*0.61*	100.77	*0.47*	101.20	*0.49*	101.21	*0.53*	100.85	*0.47*
Ti	0.21	*0.00*	0.20	*0.01*	0.21	*0.01*	0.22	*0.00*	0.22	*0.00*	0.22	*0.00*
Al	0.07	*0.01*	0.08	*0.00*	0.08	*0.01*	0.08	*0.00*	0.11	*0.01*	0.11	*0.00*
Fe^{+3}	1.51	*0.01*	1.52	*0.01*	1.50	*0.01*	1.48	*0.01*	1.45	*0.01*	1.45	*0.01*
Fe^{+2}	1.06	*0.01*	1.05	*0.01*	1.05	*0.01*	1.06	*0.01*	1.04	*0.02*	1.04	*0.01*
Mn	0.06	*0.00*	0.06	*0.00*	0.05	*0.00*	0.05	*0.01*	0.04	*0.01*	0.04	*0.00*
Mg	0.09	*0.01*	0.09	*0.00*	0.10	*0.01*	0.10	*0.01*	0.13	*0.01*	0.14	*0.01*
Usp	0.21	*0.00*	0.20	*0.00*	0.21	*0.01*	0.22	*0.01*	0.22	*0.00*	0.22	*0.00*
n	*20*		*10*		*19*		*10*		*9*		*40*	

Sample#	Tw-I		Manganui		E5-Mangatoki		E5-Mangatoki-b		E5-Mangatoki-c		E4-Tariki (upper)	
Location[a]	KK		MSt		MSt		MSt		MSt		MSt	
(wt%)	avg.	±S.D.	avg.	±S.D.	avg.	±S.D.	avg.	±S.D.	avg.	±S.D.	avg.	±S.D.
TiO_2	8.13	*0.32*	5.78	*0.13*	8.39	*0.13*	6.51	*0.13*	6.46	*0.04*	9.73	*0.13*
Al_2O_3	2.54	*0.12*	7.65	*0.22*	2.45	*0.17*	2.69	*0.11*	5.09	*0.11*	2.73	*0.06*
FeO_t	80.73	*0.62*	74.56	*0.79*	78.90	*0.43*	79.01	*0.44*	77.73	*0.70*	77.28	*0.40*
MnO	1.28	*0.13*	0.26	*0.03*	0.91	*0.07*	0.82	*0.03*	0.35	*0.06*	0.72	*0.07*
MgO	2.60	*0.11*	4.29	*0.08*	2.28	*0.14*	2.77	*0.47*	2.90	*0.06*	3.06	*0.06*
Al_2O_3+MgO	5.14	*0.15*	11.94	*0.22*	4.73	*0.26*	5.46	*0.57*	7.99	*0.17*	5.79	*0.08*
Total	95.73	*0.55*	92.86	*0.56*	92.93	*0.55*	91.79	*0.30*	92.53	*0.52*	93.51	*0.47*
Fe_2O_3	52.02	*0.83*	49.41	*0.53*	49.68	*0.37*	52.74	*0.08*	50.41	*0.40*	47.45	*0.26*
FeO	33.92	*0.42*	30.10	*0.37*	34.20	*0.36*	31.55	*0.51*	32.37	*0.34*	34.58	*0.25*
Total recal	100.76	*0.58*	97.48	*0.80*	97.91	*0.57*	97.07	*0.30*	97.58	*0.56*	98.28	*0.49*
Ti	0.22	*0.01*	0.16	*0.00*	0.24	*0.00*	0.19	*0.00*	0.18	*0.00*	0.27	*0.00*
Al	0.11	*0.00*	0.33	*0.01*	0.11	*0.01*	0.12	*0.00*	0.22	*0.01*	0.12	*0.00*
Fe^{+3}	1.44	*0.02*	1.35	*0.01*	1.41	*0.01*	1.51	*0.01*	1.41	*0.01*	1.33	*0.01*
Fe^{+2}	1.04	*0.01*	0.92	*0.01*	1.08	*0.01*	1.00	*0.02*	1.01	*0.01*	1.08	*0.00*
Mn	0.04	*0.00*	0.01	*0.00*	0.03	*0.00*	0.03	*0.00*	0.01	*0.00*	0.02	*0.00*
Mg	0.14	*0.01*	0.23	*0.00*	0.13	*0.01*	0.16	*0.03*	0.16	*0.00*	0.17	*0.00*
Usp	0.22	*0.01*	0.16	*0.00*	0.24	*0.00*	0.19	*0.00*	0.18	*0.00*	0.27	*0.00*
n	*10*		*6*		*13*		*2*		*2*		*13*	

Sample#	E4-Tariki (mid)		E4-Tariki (lower)		E3-Waipuku		E2-Kaponga		E1-Konini (*Kaponga)		Mahoe (*Konini)	
Location[a]	MSt		MSt		MSt		MSt		MSt		MSt	
(wt%)	avg.	±S.D.	avg.	±S.D.	avg.	±S.D.	avg.	±S.D.	avg.	±S.D.	avg.	±S.D.
TiO_2	9.16	*0.55*	8.20	*0.14*	7.61	*0.25*	8.77	*0.17*	8.84	*0.30*	10.45	*0.23*
Al_2O_3	2.61	*0.22*	2.77	*0.20*	2.98	*0.07*	3.55	*0.07*	3.59	*0.10*	3.76	*0.09*
FeO_t	75.94	*1.38*	78.45	*0.66*	78.97	*0.56*	75.71	*0.80*	76.95	*0.66*	75.59	*0.69*
MnO	0.74	*0.08*	0.82	*0.08*	0.77	*0.05*	0.60	*0.02*	0.58	*0.05*	0.57	*0.06*
MgO	2.96	*0.18*	2.55	*0.21*	2.65	*0.07*	3.36	*0.08*	3.49	*0.09*	3.64	*0.15*
Al_2O_3+MgO	5.57	*0.31*	5.32	*0.15*	5.63	*0.10*	6.91	*0.12*	7.07	*0.16*	7.41	*0.18*
Total	91.41	*1.43*	92.79	*0.66*	92.88	*0.73*	91.99	*0.99*	93.45	*0.80*	94.02	*0.71*
Fe_2O_3	47.15	*1.12*	49.73	*0.73*	50.89	*0.50*	47.45	*0.49*	48.40	*0.50*	45.35	*0.45*
FeO	33.51	*0.78*	33.70	*0.46*	33.18	*0.41*	33.02	*0.45*	33.40	*0.47*	34.79	*0.45*
Total recal	96.13	*1.51*	97.77	*0.71*	98.07	*0.72*	96.74	*1.03*	98.29	*0.82*	98.56	*0.74*
Ti	0.26	*0.02*	0.23	*0.00*	0.21	*0.01*	0.25	*0.00*	0.25	*0.01*	0.29	*0.01*
Al	0.12	*0.01*	0.12	*0.01*	0.13	*0.00*	0.16	*0.00*	0.16	*0.00*	0.16	*0.00*
Fe^{+3}	1.36	*0.02*	1.41	*0.01*	1.44	*0.01*	1.35	*0.01*	1.35	*0.01*	1.26	*0.01*
Fe^{+2}	1.07	*0.02*	1.06	*0.01*	1.04	*0.01*	1.04	*0.01*	1.04	*0.01*	1.07	*0.01*
Mn	0.02	*0.00*	0.03	*0.00*	0.02	*0.00*	0.02	*0.00*	0.02	*0.00*	0.02	*0.00*
Mg	0.17	*0.01*	0.14	*0.01*	0.15	*0.00*	0.19	*0.00*	0.19	*0.00*	0.20	*0.01*
Usp	0.26	*0.02*	0.23	*0.00*	0.21	*0.01*	0.25	*0.00*	0.25	*0.01*	0.29	*0.01*
n	*11*		*14*		*10*		*5*		*14*		*12*	

Appendix 5 *(continued)*

Sample#	Layer-256		Layer-256-b		aS		bS	
Location[a]	MSt		MSt		Oa		Oa	
(wt%)	avg.	*±S.D.*	avg.	*±S.D.*	avg.	*±S.D.*	avg.	*±S.D.*
TiO_2	9.77	*0.18*	6.93	*0.29*	7.27	*1.00*	7.96	*0.85*
Al_2O_3	4.12	*0.09*	6.08	*0.20*	3.08	*1.17*	2.62	*0.65*
FeO_t	75.21	*0.56*	75.83	*0.38*	83.58	*1.43*	83.06	*1.75*
MnO	0.55	*0.07*	0.33	*0.02*	1.21	*0.49*	1.34	*0.29*
MgO	3.68	*0.07*	3.47	*0.14*	2.44	*0.61*	2.43	*0.66*
Al_2O_3+MgO	7.80	*0.12*	9.55	*0.34*	5.51	*1.68*	5.05	*1.28*
Total	87.13	*24.11*	92.64	*0.30*	97.89	*0.46*	98.03	*0.99*
Fe_2O_3	45.82	*0.47*	48.59	*0.61*	54.70	*1.73*	53.86	*2.01*
FeO	33.98	*0.31*	32.11	*0.40*	34.36	*0.91*	34.60	*0.88*
Total recal	97.92	*0.63*	97.50	*0.35*	103.26	*0.51*	103.09	*0.73*
Ti	0.27	*0.00*	0.19	*0.01*	0.20	*0.03*	0.21	*0.02*
Al	0.18	*0.00*	0.26	*0.01*	0.13	*0.05*	0.11	*0.03*
Fe^{+3}	1.28	*0.01*	1.35	*0.01*	1.47	*0.05*	1.46	*0.06*
Fe^{+2}	1.05	*0.01*	0.99	*0.02*	1.03	*0.03*	1.04	*0.03*
Mn	0.02	*0.00*	0.01	*0.00*	0.04	*0.01*	0.04	*0.01*
Mg	0.20	*0.00*	0.19	*0.01*	0.13	*0.03*	0.13	*0.03*
Usp	0.27	*0.00*	0.19	*0.01*	0.20	*0.03*	0.22	*0.02*
n	*15*		*3*		*10*		*9*	

Note: Titanomagnetite compositions of individual tephra units are given as average (avg.) with 1 standard deviation (±S.D.), n = number of titanomagnetites analysed. The complete compositional datasheet is available within the electronic appendices. Multi- and/or bimodal compositions of some tephra units are noted with -b, -c (refer to Fig. 4.3).

[a] Sample localities (refer also to Fig. 4.2) as followed: Little Maketawa (LM), Vero Slip (VS), Curtis Ridge Section (CRS), Holly Hut (HH1), Maketawa hut (M), East Section (EaS), Hooker Shelter (HS), Kokowai (KK), Mangatoki Stream (MSt), Onaero Beach section (Oa)

[b] FeO, Fe_2O_3, cation proportions and Usp (mole fraction ulvöspinel) calculated as in Carmichael (1966).

**E1-Konini and Mahoe (Franks et al., 1991) = Kaponga and Konini (Alloway et al., 1995) (refer to Chapter 4)*

Appendix 6 *Electron microprobe-determined glass shard compositions of tephra units from flank (proximal) and ring-plain (medial) localities.*

Sample#	Burrell		Te Popo		Kaupokonui		Curtis Ridge		Manganui E		Manganui D	
Location[a]	LM		LM		CRS		CRS		LM		CRS	
(wt%)	avg.	±S.D.	avg.	±S.D.	avg.	±S.D.	avg.	±S.D.	avg.	±S.D.	avg.	±S.D.
SiO_2	65.70	*0.33*	69.42	*0.24*	62.24	*0.37*	68.20	*0.39*	59.23	*1.05*	55.90	*2.60*
Al_2O_3	16.91	*0.14*	15.79	*0.12*	16.46	*0.59*	15.73	*0.37*	17.33	*1.53*	15.84	*1.14*
TiO_2	0.55	*0.06*	0.49	*0.10*	0.85	*0.07*	0.49	*0.08*	0.92	*0.23*	1.30	*0.30*
FeO_{total}	3.17	*0.26*	2.10	*0.21*	5.04	*0.56*	2.84	*0.89*	5.86	*1.44*	8.16	*1.89*
MnO	0.21	*0.08*	0.13	*0.08*	0.23	*0.09*	0.17	*0.06*	0.23	*0.12*	0.27	*0.08*
MgO	0.97	*0.07*	0.37	*0.05*	2.14	*0.50*	0.71	*0.09*	2.35	*0.87*	4.00	*1.90*
CaO	2.69	*0.13*	1.55	*0.08*	4.06	*0.32*	2.23	*0.30*	5.56	*1.14*	6.71	*2.04*
Na_2O	4.64	*0.12*	4.77	*0.13*	4.54	*0.26*	4.63	*0.16*	4.80	*0.41*	4.18	*0.60*
K_2O	4.96	*0.08*	5.46	*0.10*	4.27	*0.20*	4.87	*0.09*	3.46	*0.42*	3.44	*0.83*
Cl	0.39	*0.07*	0.44	*0.03*	0.27	*0.08*	0.38	*0.03*	0.28	*0.06*	0.32	*0.07*
Anal diff[b]	-0.20	*0.10*	-0.53	*0.13*	-0.09	*0.11*	-0.26	*0.21*	-0.03	*0.25*	-0.12	*0.21*
Total (anal)	97.93		96.96		97.42		98.28		96.59		96.55	
n	*9*		*9*		*9*		*9*		*10*		*10*	

Sample#	Manganui C		Manganui B		Manganui A		U. Inglewood		L. Inglewood		Korito	
Location[a]	M		LM		M		M		LM		HH1	
(wt%)	avg.	±S.D.	avg.	±S.D.	avg.	±S.D.	avg.	±S.D.	avg.	±S.D.	avg.	±S.D.
SiO_2	55.68	*1.52*	58.02	*0.88*	58.27	*1.27*	71.68	*0.70*	70.92	*0.51*	69.72	*1.24*
Al_2O_3	15.79	*1.22*	16.78	*0.93*	16.67	*1.21*	14.58	*0.29*	14.93	*0.09*	15.25	*0.65*
TiO_2	1.51	*0.23*	0.98	*0.13*	1.21	*0.11*	0.45	*0.08*	0.41	*0.07*	0.52	*0.11*
FeO_{total}	8.65	*1.03*	6.76	*0.94*	6.88	*0.93*	1.99	*0.45*	2.03	*0.53*	2.48	*0.59*
MnO	0.30	*0.09*	0.34	*0.06*	0.26	*0.12*	0.09	*0.10*	0.21	*0.09*	0.11	*0.08*
MgO	3.46	*1.40*	2.97	*0.68*	2.49	*1.45*	0.36	*0.11*	0.48	*0.06*	0.52	*0.27*
CaO	6.29	*1.74*	6.52	*0.74*	5.41	*1.43*	1.45	*0.15*	1.58	*0.05*	1.74	*0.42*
Na_2O	4.14	*0.51*	4.29	*0.24*	4.64	*0.40*	4.40	*0.19*	4.51	*0.12*	4.67	*0.33*
K_2O	3.88	*0.71*	3.06	*0.34*	3.79	*0.43*	5.05	*0.23*	4.94	*0.14*	4.89	*0.47*
Cl	0.26	*0.05*	0.28	*0.09*	0.30	*0.03*	0.29	*0.12*	0.34	*0.05*	0.31	*0.10*
Anal diff[b]	0.05	*0.17*	-0.02	*0.22*	0.08	*0.12*	-0.33	*0.15*	-0.35	*0.16*	-0.19	*0.23*
Total (anal)	97.30		96.82		97.65		98.19		99.23		99.09	
n	*9*		*10*		*8*		*17*		*14*		*32*	

Sample#	Kapuni-B		Kapuni-A		Kokowai		Manganui		Inglewood		E5-Mangatoki	
Location[a]	HS		HS		KK		MSt		MSt		MSt	
(wt%)	avg.	±S.D.	avg.	±S.D.	avg.	±S.D.	avg.	±S.D.	avg.	±S.D.	avg.	±S.D.
SiO_2	69.87	*0.37*	67.26	*0.59*	67.09	*0.55*	53.32	*1.61*	70.74	*0.27*	70.77	*0.89*
Al_2O_3	15.03	*0.14*	15.89	*0.17*	16.21	*0.28*	18.48	*1.08*	15.28	*0.12*	15.20	*0.37*
TiO_2	0.51	*0.04*	0.56	*0.07*	0.61	*0.07*	0.99	*0.17*	0.41	*0.06*	0.43	*0.06*
FeO_{total}	2.57	*0.35*	3.10	*0.43*	2.92	*0.32*	8.32	*0.86*	1.92	*0.13*	2.06	*0.26*
MnO	0.13	*0.09*	0.15	*0.08*	0.18	*0.11*	0.13	*0.09*	0.11	*0.09*	0.12	*0.06*
MgO	0.48	*0.06*	0.74	*0.09*	0.79	*0.11*	3.75	*0.78*	0.39	*0.05*	0.43	*0.08*
CaO	1.65	*0.10*	2.30	*0.14*	2.29	*0.22*	8.63	*1.56*	1.82	*0.11*	1.57	*0.30*
Na_2O	4.67	*0.12*	5.09	*0.19*	5.01	*0.18*	3.97	*0.60*	4.66	*0.19*	4.44	*0.29*
K_2O	4.89	*0.08*	4.74	*0.11*	4.67	*0.21*	2.27	*0.50*	4.47	*0.12*	4.81	*0.15*
Cl	0.41	*0.04*	0.39	*0.04*	0.38	*0.07*	0.13	*0.05*	0.20	*0.03*	0.17	*0.04*
Anal diff[b]	-0.22	*0.14*	-0.21	*0.19*	-0.15	*0.20*	--	--	--	--	--	--
Total (anal)	97.81		98.14		98.64		97.71		98.96		97.19	
n	*11*		*10*		*28*		*15*		*14*		*19*	

Sample#	E4-Tariki (upper)		E4-Tariki (mid)		E4-Tariki (lower)		E3-Waipuku		E2-Kaponga		E1-Konini (*Kaponga)	
Location[a]	MSt		MSt		MSt		MSt		MSt		MSt	
(wt%)	avg.	±S.D.	avg.	±S.D.	avg.	±S.D.	avg.	±S.D.	avg.	±S.D.	avg.	±S.D.
SiO_2	68.97	*0.95*	68.44	*1.73*	68.26	*0.72*	68.63	*0.72*	65.71	*0.48*	65.45	*0.95*
Al_2O_3	15.67	*0.31*	15.81	*0.79*	16.44	*0.53*	16.16	*0.66*	16.80	*0.24*	16.72	*0.34*
TiO_2	0.58	*0.11*	0.50	*0.13*	0.51	*0.06*	0.45	*0.05*	0.62	*0.06*	0.63	*0.07*
FeO_{total}	2.60	*0.34*	2.98	*0.66*	2.52	*0.28*	2.64	*0.31*	3.28	*0.14*	3.34	*0.18*
MnO	0.07	*0.08*	0.09	*0.10*	0.07	*0.08*	0.08	*0.07*	0.15	*0.08*	0.09	*0.08*
MgO	0.64	*0.12*	0.72	*0.18*	0.61	*0.13*	0.65	*0.08*	1.00	*0.13*	1.06	*0.19*
CaO	1.95	*0.28*	2.31	*0.37*	2.05	*0.30*	2.17	*0.41*	2.58	*0.29*	2.83	*0.84*
Na_2O	4.60	*0.42*	4.62	*0.30*	4.69	*0.38*	4.64	*0.26*	5.07	*0.46*	5.18	*0.49*
K_2O	4.73	*0.27*	4.37	*0.27*	4.63	*0.20*	4.38	*0.28*	4.53	*0.17*	4.48	*0.25*
Cl	0.20	*0.07*	0.16	*0.07*	0.22	*0.06*	0.20	*0.03*	0.24	*0.02*	0.24	*0.06*
Anal diff[b]	--	--	--	--	--	--	--	--	--	--	--	--
Total (anal)	97.69		96.68		96.62		98.39		97.60		98.24	
n	*15*		*9*		*11*		*16*		*10*		*14*	

Appendix 6 *(continued)*

Sample#	Mahoe (*Konini)		Layer-256	
Location[a]	MSt		MSt	
(wt%)	±*S.D.*	±*S.D.*	avg.	±*S.D.*
SiO_2	63.96	*0.73*	62.89	*1.44*
Al_2O_3	17.03	*0.47*	17.48	*0.30*
TiO_2	0.76	*0.08*	0.69	*0.09*
FeO_{total}	4.07	*0.51*	4.65	*0.51*
MnO	0.11	*0.08*	0.16	*0.03*
MgO	1.27	*0.12*	1.44	*0.40*
CaO	3.01	*0.31*	3.66	*0.69*
Na_2O	5.07	*0.19*	5.02	*0.33*
K_2O	4.55	*0.26*	3.84	*0.33*
Cl	0.16	*0.03*	0.19	*0.02*
Anal diff[b]	--	--	--	--
Total (anal)	97.30		96.99	
n	*17*		*10*	

Note: Glass shard compositions of individual tephra deposits are given as average (avg.) with 1 standard deviation (±S.D.) based on n = number of glass shards analysed. Analytical (anal) totals and [b]the analytical difference (anal diff) from 100% are also shown. The complete compositional datasheet is available within the electronic appendices.
[a] Sample localities (refer also to Fig. 4.2) as followed: Little Maketawa (LM), Vero Slip (VS), Curtis Ridge Section (CRS), Holly Hut (HH1), Maketawa hut (M), East Section (EaS), Hooker Shelter (HS), Kokowai (KK), Mangatoki Stream (MSt).
**E1-Konini and Mahoe (Franks et al., 1991) = Kaponga and Konini (Alloway et al., 1995) (refer to Chapter 4)*

Appendix 7 *Whole-lapilli major and trace element compositions of lake and peatland tephra layers from Mt. Taranaki using X-ray fluorescence (XRF) spectrometry and laser ablation–inductively coupled plasma–mass spectrometry (LA-ICP-MS).*

	TS A								
sample	Ri-6	T-8	E-5	E-6	E-7	N-6	Ri-26	Ri-30	T-4A
XRF analyses of major elements (wt%)									
SiO_2	61.38	57.12	51.31	53.46	51.75	51.39	53.00	51.67	50.66
TiO_2	0.72	0.67	1.13	1.05	1.17	1.21	0.97	1.06	1.25
Al_2O_3	17.94	18.52	17.46	19.22	17.23	17.83	19.01	18.57	18.98
Fe_2O_3	5.62	5.22	7.86	5.69	7.21	6.76	9.32	10.12	8.26
MnO	0.13	0.16	0.14	0.15	0.13	0.13	0.17	0.18	0.17
MgO	1.97	3.94	6.00	4.31	6.09	6.11	3.56	4.14	4.90
CaO	5.38	9.32	12.83	11.63	13.23	13.07	9.23	9.94	11.80
Na_2O	4.15	3.87	2.93	3.56	3.00	2.97	3.74	3.47	3.02
K_2O	3.47	2.10	1.33	1.44	1.20	1.15	2.03	1.85	1.38
P_2O_5	0.30	0.29	0.22	0.22	0.21	0.21	0.30	0.29	0.27
LOI	0.02	0.01	0.01	0.00	0.01	0.01	0.00	0.00	0.01
Total	101.06	101.20	101.21	100.72	101.22	100.83	101.33	101.28	100.69
LA-ICP-MS analyses of trace elements (ppm)									
Cs	4.59	2.59	1.45	1.19	1.00	0.82	2.42	2.25	1.18
Ba	1210	790	550	677	538	565	753	691	582
Rb	83.21	46.51	23.61	23.60	20.71	18.27	43.01	36.70	24.16
Sr	610	735	633	761	658	654	699	678	716
Pb	17.69	13.42	7.82	9.42	8.38	9.79	10.70	8.93	8.59
Th	10.89	5.92	3.34	3.27	2.99	3.10	5.10	4.29	3.31
U	2.31	1.28	0.77	0.72	0.61	0.67	1.10	0.94	0.73
Zr	195	118	78	75	71	77	111	95	82
Nb	5.71	3.76	2.47	2.58	2.38	2.39	3.66	3.50	2.58
Hf	5.34	3.29	2.48	2.31	2.26	2.41	3.16	2.79	2.62
Ta	0.44	0.28	0.21	0.19	0.19	0.19	0.27	0.23	0.19
Y	19.87	20.46	17.56	19.19	16.75	17.91	19.69	19.49	21.13
La	24.95	17.39	11.17	11.42	10.26	10.25	16.19	14.22	12.23
Ce	41.71	31.56	21.63	22.42	20.30	19.74	29.86	26.54	23.25
Pr	5.10	4.17	3.01	3.00	2.78	2.86	3.86	3.53	3.36
Nd	22.81	18.96	14.66	15.14	14.14	14.57	18.20	17.05	17.47
Sm	4.73	4.56	3.80	4.09	3.81	3.91	4.33	4.36	4.67
Eu	1.31	1.39	1.29	1.44	1.22	1.36	1.36	1.32	1.52
Gd	4.25	4.36	3.83	4.16	3.85	4.07	4.31	4.07	4.64
Tb	0.61	0.65	0.60	0.64	0.57	0.63	0.66	0.61	0.74
Dy	3.60	4.01	3.60	3.87	3.46	3.62	3.88	3.82	4.23
Ho	0.71	0.76	0.69	0.75	0.67	0.73	0.77	0.77	0.85
Er	2.02	2.13	1.82	2.03	1.72	1.88	2.12	2.02	2.33
Tm	0.30	0.30	0.24	0.28	0.25	0.26	0.28	0.29	0.31
Yb	2.07	2.18	1.68	1.88	1.62	1.74	2.05	2.12	2.23
Lu	0.34	0.31	0.23	0.27	0.22	0.24	0.28	0.29	0.30
Sc	14.00	22.86	44.22	28.66	44.95	45.40	20.49	25.00	31.40
V	136	117	240	140	218	200	250	287	248
Cr	162	253	446	227	446	433	233	372	214
Co	11.33	14.10	23.31	14.80	22.14	20.34	22.34	24.69	22.31
Ni	28.87	16.23	27.63	10.45	25.59	29.74	13.87	28.60	9.14
Cu	68.69	43.20	70.66	37.14	57.14	48.19	89.59	64.25	68.16
Zn	59.62	53.19	48.26	43.03	42.72	39.01	75.71	78.02	64.94
Ga	19.20	18.07	19.70	20.18	18.93	20.54	20.60	19.94	21.00

Appendix 7 *(continued)*

			TS B					TS C	
sample	T-4B	T-10	E-8	N-8/9	Ri-34	Ri-40	Ri-47	E-13	E-16
XRF analyses of major elements (wt%)									
SiO_2	48.65	53.73	60.70	60.40	62.25	59.34	58.75	59.31	57.35
TiO_2	1.36	0.98	0.40	0.52	0.61	0.61	0.68	0.80	0.88
Al_2O_3	18.64	19.49	19.97	20.27	18.43	18.72	18.65	19.93	19.83
Fe_2O_3	9.24	6.76	2.81	2.99	5.09	5.99	6.74	3.11	3.49
MnO	0.17	0.15	0.14	0.14	0.16	0.17	0.19	0.14	0.14
MgO	5.60	4.18	2.24	2.24	1.37	1.81	2.08	2.80	3.17
CaO	12.45	10.77	7.92	8.18	5.68	6.97	7.30	9.24	9.87
Na_2O	2.72	3.63	4.41	4.44	4.59	4.22	4.24	4.23	3.98
K_2O	1.25	1.71	2.06	2.06	2.68	2.39	2.30	2.00	1.85
P_2O_5	0.26	0.28	0.06	0.30	0.24	0.29	0.28	0.34	0.40
LOI	0.01	0.00	0.01	0.02	0.01	0.01	0.02	0.02	0.02
Total	100.33	101.68	100.71	101.55	101.10	100.50	101.21	101.90	100.96
LA-ICP-MS analyses of trace elements (ppm)									
Cs	1.01	1.64	2.68	2.60	3.93	3.29	3.23	2.81	2.34
Ba	516	737	814	819	925	860	773	785	742
Rb	21.50	32.75	45.93	44.54	63.09	57.48	56.49	45.52	40.64
Sr	679	760	844	861	640	721	700	827	864
Pb	7.25	11.05	14.68	17.10	15.10	14.29	13.32	15.45	13.69
Th	2.72	4.25	7.19	7.37	7.87	7.33	6.62	6.06	5.87
U	0.60	0.89	1.42	1.60	1.78	1.65	1.46	1.27	1.24
Zr	76	97	124	134	159	137	138	128	119
Nb	2.31	3.24	3.66	3.86	5.03	4.12	4.38	4.39	4.12
Hf	2.45	2.85	3.35	3.68	4.27	3.79	3.84	3.68	3.49
Ta	0.16	0.24	0.28	0.29	0.37	0.29	0.31	0.32	0.29
Y	20.08	19.39	18.67	24.45	19.78	20.05	19.92	25.01	24.14
La	10.23	14.79	17.08	22.86	21.00	20.42	19.55	20.54	20.16
Ce	20.15	26.91	36.51	40.16	38.63	37.65	36.32	39.89	38.73
Pr	2.95	3.57	3.88	5.45	4.70	4.65	4.58	5.21	5.15
Nd	15.25	17.78	17.98	24.89	21.25	20.93	20.61	24.64	24.34
Sm	4.28	4.46	4.01	5.88	4.46	4.48	4.70	5.68	5.73
Eu	1.40	1.42	1.36	1.73	1.34	1.32	1.35	1.74	1.74
Gd	4.47	4.26	3.63	4.99	4.07	4.02	4.16	5.56	5.28
Tb	0.71	0.61	0.57	0.77	0.59	0.62	0.62	0.81	0.80
Dy	4.10	3.93	3.48	4.69	3.81	3.58	3.80	4.81	4.88
Ho	0.78	0.77	0.70	0.92	0.74	0.75	0.76	0.98	0.93
Er	2.22	1.97	1.94	2.47	2.14	2.12	2.10	2.69	2.49
Tm	0.29	0.27	0.28	0.37	0.30	0.31	0.30	0.38	0.36
Yb	1.94	1.99	2.08	2.54	2.20	2.15	2.07	2.55	2.40
Lu	0.27	0.28	0.30	0.37	0.34	0.32	0.31	0.37	0.35
Sc	35.67	27.60	12.41	12.46	8.18	9.61	11.57	16.27	18.23
V	294	192	40	42	86	104	129	54	71
Cr	206	247	147	144	149	172	581	180	123
Co	25.94	17.42	5.26	5.34	6.61	8.33	12.60	6.77	8.29
Ni	11.96	15.57	5.33	7.85	25.96	7.05	76.24	7.10	7.88
Cu	67.91	70.13	15.73	14.68	25.78	24.03	54.16	19.00	28.77
Zn	60.81	54.86	37.85	40.94	72.75	74.01	75.85	37.21	40.00
Ga	20.65	19.43	18.56	18.95	20.11	19.86	20.41	20.25	20.37

Appendix 7 *(continued)*

sample	N-19	N-21	N-22	Ri-51	Ri-60	Ri-70	Ri-88	TS D E-20	E-25
XRF analyses of major elements (wt%)									
SiO_2	59.22	58.16	58.11	57.52	56.42	57.46	57.03	57.84	55.91
TiO_2	0.70	0.54	0.72	0.78	0.83	0.80	0.81	0.72	1.01
Al_2O_3	19.98	19.67	19.99	18.72	18.71	18.27	18.74	19.46	19.79
Fe_2O_3	3.47	3.42	3.81	7.25	7.60	7.25	7.28	4.03	4.86
MnO	0.15	0.15	0.15	0.17	0.17	0.18	0.17	0.15	0.15
MgO	2.77	3.13	2.97	2.38	2.72	2.41	2.41	3.35	3.56
CaO	8.87	9.71	9.27	8.01	8.23	7.55	7.89	9.54	10.17
Na_2O	4.13	4.09	4.07	3.99	3.87	3.92	4.02	3.88	3.65
K_2O	2.10	1.85	1.99	2.21	2.30	2.49	2.25	1.92	1.76
P_2O_5	0.37	0.38	0.39	0.31	0.32	0.30	0.36	0.25	0.38
LOI	0.03	0.02	0.03	0.01	0.01	0.01	0.01	0.01	0.02
Total	101.77	101.10	101.46	101.34	101.17	100.63	100.97	101.14	101.23
LA-ICP-MS analyses of trace elements (ppm)									
Cs	2.66	2.53	2.58	3.20	3.32	3.84	3.06	2.33	2.12
Ba	793	750	768	700	774	776	807	721	648
Rb	48.08	41.15	44.19	54.53	57.29	62.96	54.55	39.83	38.91
Sr	786	869	826	689	693	625	716	814	835
Pb	14.93	15.21	15.27	13.19	13.49	14.69	13.31	14.68	12.70
Th	6.51	5.87	6.35	5.82	5.90	6.59	6.28	5.32	4.52
U	1.43	1.50	1.51	1.39	1.42	1.63	1.38	1.14	1.05
Zr	140	118	130	135	132	138	131	106	104
Nb	4.46	3.53	4.06	3.96	3.86	3.99	4.43	2.93	3.31
Hf	3.98	3.45	3.72	3.77	3.62	3.80	3.54	3.03	3.04
Ta	0.33	0.29	0.31	0.27	0.29	0.30	0.31	0.22	0.24
Y	26.18	24.50	25.19	19.64	19.80	19.13	21.81	19.88	20.67
La	22.45	21.19	21.48	17.35	17.41	17.43	19.32	17.77	16.56
Ce	42.04	38.73	40.01	33.32	33.38	34.03	37.00	34.84	32.58
Pr	5.61	5.24	5.38	4.29	4.27	4.27	4.75	4.47	4.22
Nd	26.94	25.02	25.54	19.69	19.64	19.46	22.34	21.37	20.66
Sm	6.22	5.87	5.86	4.32	4.57	4.28	5.08	4.94	4.79
Eu	1.74	1.71	1.73	1.32	1.31	1.26	1.46	1.50	1.48
Gd	5.73	5.53	5.50	4.10	4.09	3.93	4.69	4.69	4.64
Tb	0.81	0.80	0.83	0.61	0.62	0.60	0.72	0.72	0.68
Dy	5.10	4.95	4.93	3.79	3.74	3.57	4.17	3.97	4.01
Ho	1.01	0.95	0.97	0.74	0.75	0.71	0.80	0.78	0.80
Er	2.86	2.57	2.71	2.07	1.99	1.92	2.34	2.10	2.18
Tm	0.39	0.36	0.36	0.30	0.31	0.29	0.32	0.29	0.30
Yb	2.80	2.48	2.53	2.17	2.09	2.01	2.20	2.15	2.05
Lu	0.40	0.36	0.37	0.32	0.31	0.30	0.32	0.30	0.28
Sc	16.11	18.34	17.53	12.91	14.04	13.51	12.47	20.32	21.78
V	67	56	75	160	175	166	158	62	110
Cr	149	184	165	152	195	607	162	142	143
Co	7.93	7.69	9.15	12.82	14.82	14.97	12.35	9.22	11.69
Ni	6.31	7.40	7.06	7.04	9.92	75.21	6.13	6.22	6.95
Cu	24.06	32.35	34.06	33.88	46.84	63.55	38.12	42.18	51.70
Zn	46.62	39.97	47.16	76.85	77.91	74.62	81.36	43.69	51.02
Ga	20.92	19.30	20.04	20.12	20.64	20.02	21.17	17.93	21.09

Appendix 7 *(continued)*

sample	E-28	E-32	E2-36	E-41	N-32	N-36	N-46	N-49	N-52
XRF analyses of major elements (wt%)									
SiO_2	56.22	56.07	55.60	54.66	57.42	56.99	56.42	56.31	56.87
TiO_2	0.96	1.05	0.75	0.61	0.81	0.68	0.57	0.73	0.76
Al_2O_3	19.88	19.62	20.58	19.98	20.13	19.46	19.63	19.31	19.32
Fe_2O_3	4.48	4.64	3.79	4.28	4.52	4.64	4.28	5.90	5.72
MnO	0.14	0.14	0.16	0.18	0.15	0.16	0.15	0.16	0.15
MgO	3.33	3.61	3.83	4.29	2.98	3.49	3.76	3.54	3.03
CaO	9.73	10.05	11.53	12.13	8.97	9.93	10.45	9.44	8.93
Na_2O	3.88	3.87	3.64	3.31	3.84	3.85	3.83	3.81	3.96
K_2O	1.82	1.84	1.42	1.10	1.89	1.74	1.69	1.94	2.05
P_2O_5	0.42	0.26	0.19	0.30	0.33	0.36	0.13	0.34	0.37
LOI	0.02	0.01	0.01	0.01	0.03	0.02	0.01	0.01	0.02
Total	100.86	101.14	101.47	100.84	101.03	101.30	100.91	101.47	101.16
LA-ICP-MS analyses of trace elements (ppm)									
Cs	2.35	1.86	1.40	1.12	2.23	2.06	1.85	2.35	2.69
Ba	698	755	642	513	711	669	632	708	751
Rb	42.65	36.35	27.09	23.42	38.85	36.72	34.68	43.68	49.50
Sr	863	798	889	903	844	834	874	800	800
Pb	14.63	12.81	9.82	7.21	15.04	12.50	10.06	12.13	13.71
Th	5.30	4.95	3.52	2.87	4.97	4.68	4.10	5.19	6.15
U	1.28	1.01	0.70	0.59	1.28	1.12	0.98	1.22	1.48
Zr	117	103	83	73	103	103	99	113	129
Nb	3.89	3.45	2.68	2.64	3.11	3.09	2.82	3.35	3.82
Hf	3.25	3.06	2.45	2.07	3.02	3.11	2.94	3.16	3.65
Ta	0.29	0.26	0.19	0.20	0.27	0.22	0.20	0.26	0.28
Y	21.50	19.62	18.82	19.09	19.81	21.89	20.08	20.28	20.37
La	18.87	15.14	12.87	13.51	16.20	17.70	13.81	17.92	19.89
Ce	36.44	28.96	24.57	25.94	30.60	33.39	27.59	34.00	36.44
Pr	4.73	3.84	3.29	3.47	4.09	4.53	3.59	4.39	4.85
Nd	22.56	18.19	16.33	17.08	19.42	22.18	17.45	21.34	22.70
Sm	5.32	4.45	3.95	4.28	4.58	5.19	4.42	4.71	5.02
Eu	1.62	1.46	1.41	1.46	1.45	1.57	1.51	1.48	1.45
Gd	4.85	4.26	3.97	4.20	4.22	4.83	4.20	4.30	4.55
Tb	0.71	0.66	0.74	0.61	0.65	0.72	0.62	0.67	0.68
Dy	4.08	3.87	3.65	3.84	3.80	4.44	3.95	4.14	3.96
Ho	0.82	0.78	0.73	0.75	0.75	0.83	0.77	0.81	0.79
Er	2.28	2.07	1.94	2.02	2.06	2.41	2.03	2.10	2.11
Tm	0.32	0.28	0.28	0.29	0.28	0.31	0.29	0.31	0.29
Yb	2.17	2.02	1.92	1.94	2.03	2.20	2.02	2.06	2.05
Lu	0.31	0.28	0.27	0.28	0.29	0.32	0.29	0.31	0.30
Sc	19.91	29.62	24.99	25.44	18.29	20.38	23.31	19.99	17.59
V	104	106	63	67	85	82	86	131	128
Cr	132	138	150	119	116	141	190	187	139
Co	11.12	11.17	10.06	11.30	10.07	10.63	10.61	13.55	12.60
Ni	8.04	7.55	7.17	8.89	5.85	7.30	8.07	12.69	7.82
Cu	47.41	68.25	51.62	33.88	42.95	39.75	38.98	48.96	48.70
Zn	48.41	43.51	37.12	41.96	49.34	50.03	40.93	58.44	58.22
Ga	21.87	20.80	18.52	18.47	19.74	18.70	17.85	19.15	19.76

Appendix 7 *(continued)*

sample	N-57	N-58	N-65	Ri-113	Ri-117	T-21	T-23	T-24	TS E T-45
XRF analyses of major elements (wt%)									
SiO_2	53.31	53.21	53.56	55.17	55.75	54.78	54.82	54.88	54.57
TiO_2	1.01	1.06	0.92	0.94	0.86	1.06	1.04	1.07	1.19
Al_2O_3	18.98	18.59	20.00	18.52	18.85	19.65	19.59	19.40	18.53
Fe_2O_3	9.08	9.21	7.00	8.37	7.78	6.57	6.42	6.81	7.61
MnO	0.17	0.17	0.17	0.18	0.16	0.15	0.15	0.16	0.15
MgO	3.42	3.67	3.54	2.94	2.75	3.54	3.55	3.60	3.67
CaO	9.12	8.96	10.15	8.66	8.28	9.15	9.43	9.39	9.26
Na_2O	3.63	3.55	3.49	3.91	3.93	3.59	3.73	3.75	3.51
K_2O	1.82	1.95	1.57	2.08	2.19	1.88	1.89	1.96	2.26
P_2O_5	0.30	0.29	0.31	0.32	0.33	0.34	0.33	0.31	0.33
LOI	0.01	0.01	0.02	0.01	0.01	0.02	0.01	0.01	0.01
Total	100.84	100.66	100.70	101.09	100.87	100.70	100.95	101.33	101.08
LA-ICP-MS analyses of trace elements (ppm)									
Cs	1.93	2.09	1.72	2.60	2.94	2.03	2.16	2.06	2.29
Ba	695	717	685	687	746	701	735	749	866
Rb	37.27	40.20	31.42	48.18	54.02	39.81	41.36	41.88	51.03
Sr	765	702	809	724	730	748	740	728	649
Pb	11.21	11.57	10.77	12.39	13.13	11.36	12.06	11.21	10.83
Th	4.80	5.28	4.60	4.92	5.51	5.15	5.05	4.91	5.95
U	0.97	1.08	0.88	1.20	1.35	1.08	1.07	1.04	1.18
Zr	105	113	106	117	122	115	115	118	115
Nb	3.18	3.46	3.31	4.04	3.93	3.53	3.60	3.75	4.23
Hf	3.09	3.30	3.05	3.25	3.45	3.35	3.32	3.42	3.36
Ta	0.24	0.26	0.26	0.25	0.27	0.28	0.28	0.30	0.30
Y	19.31	20.83	20.72	19.63	18.55	21.33	20.98	21.90	23.12
La	15.50	16.70	15.70	17.31	17.52	16.91	16.95	17.28	18.94
Ce	29.39	31.55	30.14	33.73	33.68	31.90	32.39	32.18	35.52
Pr	3.90	4.21	4.00	4.30	4.28	4.24	4.25	4.22	4.57
Nd	19.21	20.44	19.87	20.60	19.51	20.31	20.58	20.80	21.64
Sm	4.58	4.77	4.80	4.76	4.55	4.86	4.99	4.92	5.22
Eu	1.40	1.46	1.53	1.40	1.30	1.48	1.52	1.53	1.55
Gd	4.35	4.52	4.52	4.27	4.04	4.69	4.53	4.85	5.09
Tb	0.65	0.71	0.70	0.63	0.63	0.70	0.74	0.76	0.75
Dy	3.63	4.23	4.16	3.82	3.46	4.22	4.13	4.58	4.73
Ho	0.75	0.85	0.81	0.74	0.67	0.82	0.80	0.86	0.90
Er	2.06	2.19	2.23	2.09	1.94	2.15	2.30	2.31	2.48
Tm	0.30	0.31	0.31	0.29	0.26	0.31	0.32	0.31	0.33
Yb	1.95	2.12	2.14	1.90	1.92	2.15	2.14	2.23	2.46
Lu	0.29	0.29	0.30	0.28	0.27	0.31	0.29	0.32	0.33
Sc	24.26	27.62	23.27	16.03	15.28	27.47	25.96	24.97	29.89
V	233	254	166	199	189	218	188	197	247
Cr	159	160	191	174	155	164	175	145	221
Co	20.22	21.77	15.91	16.89	16.13	15.99	15.27	16.33	18.16
Ni	9.07	9.75	9.46	8.30	6.78	7.12	6.71	5.49	13.26
Cu	75.56	96.56	69.40	94.08	64.16	68.88	78.72	75.48	95.51
Zn	74.91	78.70	65.50	82.12	76.72	62.84	60.48	64.60	65.20
Ga	20.70	20.01	19.57	20.66	20.77	20.54	20.58	21.03	20.46

Appendix 7 *(continued)*

sample	T-54	T-56	T-58	T-64	TS F E-49	E-52	E-56	E-61	E-64
XRF analyses of major elements (wt%)									
SiO_2	52.51	53.23	51.30	52.35	52.79	51.22	53.54	53.51	53.25
TiO_2	1.13	1.10	1.06	1.06	0.99	1.18	1.03	0.87	0.88
Al_2O_3	18.71	18.82	18.64	18.39	18.24	17.54	18.84	18.03	18.42
Fe_2O_3	9.50	9.09	9.85	9.76	6.07	8.55	6.21	7.03	9.13
MnO	0.17	0.19	0.18	0.19	0.17	0.17	0.14	0.15	0.17
MgO	4.03	3.79	4.04	3.94	5.06	5.09	4.10	4.82	3.45
CaO	9.05	9.20	10.00	9.41	12.31	11.97	10.77	10.95	9.16
Na_2O	3.49	3.51	3.41	3.62	3.05	2.97	3.42	3.27	3.51
K_2O	1.87	1.89	1.71	2.02	1.23	1.39	1.82	1.68	1.90
P_2O_5	0.28	0.26	0.28	0.31	0.19	0.20	0.24	0.20	0.28
LOI	0.00	0.01	0.01	0.00	0.01	0.00	0.00	0.00	0.01
Total	100.74	101.08	100.47	101.04	100.10	100.28	100.11	100.50	100.15
LA-ICP-MS analyses of trace elements (ppm)									
Cs	1.95	1.97	1.89	2.25	1.15	1.31	1.70	1.70	2.09
Ba	669	691	712	757	584	552	705	642	732
Rb	38.49	40.48	38.25	43.90	20.88	25.82	35.11	34.02	40.13
Sr	654	682	744	689	670	617	657	603	652
Pb	9.89	9.62	9.65	10.29	8.63	7.22	8.49	7.82	9.77
Th	4.59	4.65	4.83	5.16	3.06	3.40	4.48	3.90	5.09
U	0.99	0.96	0.95	1.12	0.70	0.72	0.91	0.87	1.04
Zr	98	97	94	100	82	78	103	94	110
Nb	3.73	3.85	3.49	3.90	2.37	2.63	4.20	3.52	3.86
Hf	2.77	2.86	2.72	2.90	2.39	2.49	2.90	2.69	3.23
Ta	0.25	0.27	0.25	0.27	0.16	0.19	0.28	0.25	0.28
Y	18.63	19.60	19.40	19.51	22.22	20.44	20.30	19.36	21.75
La	15.68	15.97	16.12	17.14	14.26	12.49	15.33	12.55	16.63
Ce	29.24	29.34	29.91	32.37	30.69	24.16	28.75	23.57	30.74
Pr	3.84	3.94	3.93	4.19	4.13	3.34	3.78	3.23	4.11
Nd	18.14	18.78	18.71	19.52	20.84	16.48	18.28	15.77	19.78
Sm	4.41	4.60	4.52	4.55	5.24	4.32	4.59	4.02	4.78
Eu	1.37	1.38	1.50	1.46	1.68	1.41	1.48	1.33	1.49
Gd	3.98	4.27	4.25	4.38	5.06	4.30	4.43	4.13	4.65
Tb	0.61	0.65	0.69	0.65	0.77	0.69	0.71	0.65	0.75
Dy	3.67	3.75	3.73	3.76	4.99	4.07	3.96	3.93	4.30
Ho	0.71	0.74	0.75	0.74	0.92	0.81	0.82	0.75	0.85
Er	1.92	2.00	2.09	2.05	2.44	2.25	2.15	2.09	2.34
Tm	0.28	0.29	0.27	0.28	0.34	0.29	0.30	0.29	0.31
Yb	1.98	2.05	1.92	1.96	2.21	2.05	2.03	1.93	2.25
Lu	0.29	0.29	0.26	0.27	0.31	0.29	0.30	0.30	0.33
Sc	26.48	27.58	23.97	22.10	36.51	39.07	30.72	34.50	21.08
V	285	268	274	269	174	263	171	188	208
Cr	212	220	226	273	193	301	229	265	176
Co	24.20	22.83	24.03	23.79	15.63	21.51	15.51	18.87	18.07
Ni	13.80	11.84	12.42	26.28	10.56	17.67	11.31	23.01	8.61
Cu	134.07	113.92	103.93	123.93	41.46	55.98	61.17	58.53	69.30
Zn	76.29	73.70	79.28	81.64	46.99	61.10	50.36	53.68	70.25
Ga	20.17	20.16	20.44	20.34	18.05	18.31	18.91	17.57	19.25

Appendix 7 *(continued)*

sample	E-68	E-71	E-74	E-79	Ri-130	Ri-132
XRF analyses of major elements (wt%)						
SiO_2	51.71	52.32	53.11	55.82	55.92	56.78
TiO_2	1.01	0.90	0.97	0.80	0.89	0.85
Al_2O_3	18.94	17.03	18.39	18.91	20.47	19.49
Fe_2O_3	9.03	8.83	8.68	7.31	6.33	6.33
MnO	0.18	0.21	0.18	0.18	0.17	0.16
MgO	4.02	5.27	3.67	2.84	3.32	3.39
CaO	10.68	11.69	9.36	8.55	8.70	9.10
Na_2O	3.30	3.03	3.63	3.72	3.34	3.60
K_2O	1.42	1.47	1.91	1.90	1.17	1.42
P_2O_5	0.23	0.24	0.30	0.31	0.30	0.24
LOI	0.00	0.00	0.00	0.01	0.03	0.02
Total	100.52	100.98	100.21	100.33	100.60	101.36
LA-ICP-MS analyses of trace elements (ppm)						
Cs	1.42	1.56	1.99	2.07	1.26	1.39
Ba	584	606	756	742	469	513
Rb	29.17	29.37	40.68	41.18	27.38	32.40
Sr	717	609	665	670	522	570
Pb	7.21	8.07	10.03	10.98	9.61	8.12
Th	3.37	3.86	5.05	4.91	3.86	3.90
U	0.72	0.84	1.10	1.09	0.94	0.84
Zr	87	85	111	118	91	106
Nb	3.58	2.71	4.07	4.04	3.53	3.69
Hf	2.58	2.64	3.19	3.27	2.74	3.08
Ta	0.25	0.21	0.29	0.30	0.27	0.28
Y	19.72	22.60	22.15	20.88	19.08	23.15
La	13.11	13.52	17.25	17.20	14.19	15.56
Ce	24.40	26.16	32.17	32.28	28.66	28.68
Pr	3.34	3.53	4.30	4.19	3.58	3.84
Nd	16.35	17.96	20.57	19.96	16.70	17.99
Sm	4.19	4.78	4.91	4.52	3.77	4.43
Eu	1.44	1.46	1.47	1.37	1.24	1.31
Gd	4.18	4.83	4.70	4.38	3.65	4.46
Tb	0.64	0.73	0.72	0.68	0.61	0.69
Dy	3.90	4.48	4.35	4.02	3.80	4.40
Ho	0.77	0.89	0.87	0.82	0.75	0.89
Er	2.06	2.59	2.35	2.22	2.00	2.51
Tm	0.29	0.35	0.33	0.33	0.29	0.35
Yb	2.03	2.29	2.30	2.24	2.10	2.47
Lu	0.29	0.34	0.31	0.34	0.30	0.37
Sc	24.24	32.04	21.79	15.70	18.55	22.64
V	253	230	225	161	152	170
Cr	190	203	192	124	143	175
Co	22.01	22.06	19.79	14.40	14.61	15.35
Ni	13.83	16.39	13.01	8.04	11.66	10.99
Cu	50.62	54.64	86.65	35.54	41.15	30.15
Zn	73.39	70.44	77.11	73.38	71.26	63.70
Ga	19.98	17.83	20.35	19.64	20.86	19.58

Note: TS = Tephra Sequence (see Chapter 3)

Appendix 8 *Titanomagnetite minor and trace element compositions of lake and peatland tephras from Mt. Taranaki using laser ablation–inductively coupled plasma–mass spectrometry (LA-ICP-MS).*

	TSA		Manganui								TSB			
Sample	E-1	Ri-20	T-4	T-4	T-10	N-6	E-6	E-7	Ri-30	Ri-26	E-8	Ri-40	Ri-40	Ri-47
(ppm)														
V	1753	104	70	26	46	25	43	23	73	21	8	11	37	12
S	557	531	790	582	967	695	870	613	626	618	273	320	683	322
Sc	31	13	13	11	11	11	13	10	23	13	6	11	15	5
Co	3540	2789	4086	3008	5201	3680	4519	3103	4358	3373	1425	1811	2539	1782
Ni	105	29	938	29	130	639	7	702	91	957	290	689	526	439
Ga	5239	4032	3310	2000	5691	2620	4688	2156	4168	2656	1034	2020	5802	1721
Ge	208	161	233	171	223	258	242	211	177	217	96	92	167	111
Cu	76	63	226	53	49	372	83	282	69	135	146	37	54	59
Zn	72	46	17	10	15	32	23	28	101	34	18	21	164	18
Sn	976	661	540	305	999	464	877	386	741	444	176	360	953	293
Cr	8	3	2	1	3	2	3	2	4	2	1	2	5	1
Mn	88	49	64	43	84	69	81	55	65	53	24	27	56	30
Sr	8	6	9	6	15	8	10	7	7	8	3	4	9	4
Y	15	1	1	0	1	0	1	0	9	1	0	0	0	0
Zr	18	0	0	0	0	0	0	0	1	0	0	0	0	0
Nb	120	27	7	3	12	6	11	5	33	5	3	13	36	4
Mo	10	2	0	0	1	0	1	0	3	0	0	1	5	0
P	1	0	0	0	0	0	0	0	0	0	0	0	1	0

			TSC											
Sample	Ri-47	N-9	Ri-51	Ri-60	Ri-60	Ri-70	Ri-84	Ri-84	Ri-95	N-19	N-21	N-21	N-22	N-24
(ppm)														
V	61	1634	19	124	41	876	218	476	47	27	31	141	15	29
S	650	400	370	660	520	519	656	649	537	635	512	616	446	819
Sc	15	7	7	9	15	7	18	20	11	7	16	10	19	9
Co	2792	1542	2210	3390	2378	2370	2894	3060	2540	2810	2683	3160	2834	4138
Ni	547	47	27	83	399	34	59	188	54	553	3646	151	42	3
Ga	6085	4196	1547	8165	4879	6637	6481	7065	6745	7993	6281	5875	3773	4741
Ge	177	101	125	189	157	137	192	202	165	155	184	197	145	196
Cu	61	24	34	54	32	26	63	68	39	37	61	71	40	58
Zn	149	25	8	21	46	29	46	46	30	29	31	34	45	17
Sn	1055	679	241	1194	786	996	1172	1257	1137	1403	1264	905	648	756
Cr	6	3	1	6	4	4	6	6	5	7	5	3	3	2
Mn	56	37	31	66	49	52	64	70	60	67	64	61	44	69
Sr	8	5	5	11	6	8	9	9	8	10	10	9	7	10
Y	15	11	0	1	2	5	15	33	0	0	2	0	0	0
Zr	0	5	0	0	0	3	1	3	0	0	0	0	0	0
Nb	45	18	2	42	28	24	82	101	25	27	36	18	23	8
Mo	6	2	0	3	3	2	5	7	3	3	5	1	2	1
P	1	0	0	1	0	1	1	1	1	1	1	0	0	0

			TSD											
Sample	N-26	E-15	N-32	N-36	N-37	N-45	N-45	N-46	N49	N-49	N-49	N-52	N-57	N-58
(ppm)														
V	13	76	34	20	39	31	31	22	36	26	36	26	34	42
S	335	579	481	626	682	642	642	502	645	652	645	331	780	792
Sc	7	9	11	11	20	13	13	10	13	14	13	21	11	15
Co	2038	2994	2848	3419	3215	2753	2753	2845	3248	3498	3248	1717	3626	3742
Ni	1258	366	19	182	920	106	106	82	211	29	211	145	517	332
Ga	1401	5514	4101	3980	7146	5675	5675	4689	6680	6870	6680	1392	7348	7582
Ge	138	178	163	203	188	176	176	169	183	196	183	112	211	205
Cu	202	62	35	93	44	37	37	67	49	33	49	99	65	87
Zn	19	31	41	28	59	42	42	36	38	34	38	23	47	48
Sn	259	1030	673	710	1208	932	932	947	1105	1137	1105	256	1185	1260
Cr	1	4	4	3	7	4	4	4	6	6	6	16	6	7
Mn	34	69	48	57	67	58	58	56	64	64	64	41	74	77
Sr	5	8	8	9	9	8	8	8	8	11	8	19	10	10
Y	0	3	0	0	0	0	0	0	0	0	0	15	0	1
Zr	0	0	0	0	0	0	0	0	0	0	0	15	0	0
Nb	3	26	21	14	35	29	29	21	32	32	32	18	26	37
Mo	0	3	1	1	4	3	3	2	3	3	3	15	3	4
P	0	1	0	0	1	0	0	0	1	1	1	15	1	1

Appendix 8 *(continued)*

Sample	N-62	N-64	N-65	N-68	E-25	E-36	E-36	E-41	TSE T-51	T-64
(ppm)										
V	40	15	26	132	31	36	63	21	18	43
S	632	383	748	508	601	514	459	596	555	1157
Sc	13	6	12	13	13	11	14	9	14	36
Co	3242	2347	3832	2852	3618	2905	3316	2662	3166	6413
Ni	148	335	39	40	355	535	160	2	221	84
Ga	6859	2389	5220	3467	2561	1839	3515	2436	1845	9106
Ge	194	146	227	164	212	198	168	157	196	159
Cu	94	72	89	42	192	322	51	94	251	49
Zn	46	21	34	38	24	30	23	12	21	7
Sn	1169	426	858	568	479	354	542	404	285	2243
Cr	6	2	3	2	2	1	5	2	1	15
Mn	70	41	69	49	52	47	45	44	42	104
Sr	9	6	9	7	8	6	6	7	6	13
Y	0	0	0	2	0	0	7	0	0	0
Zr	0	0	0	0	0	0	1	0	0	0
Nb	33	6	19	14	5	4	22	5	4	113
Mo	3	0	2	1	0	0	3	0	0	13
P	1	0	0	0	0	0	1	0	0	3

Note: TS = Tephra Sequence (see Chapter 3)